THE DEVELOPMENT AND APPLICATION OF TWO-TIME-SCALE TURBULENCE MODELS FOR NON-EQUILIBRIUM FLOWS

A thesis submitted to the University of Manchester
for the degree of Doctor of Philosophy
in the Faculty of Engineering and Physical Sciences

2012

By
Tania S. Klein
School of Mechanical, Aerospace and Civil Engineering

Contents

List of Tables

List of Figures

Nomenclature

Roman Symbols

A	Flatness parameter, $A = 1 - \frac{9}{8}(A_2 - A_3)$ in the HJ model; Amplitude in oscillatory flows
A_2	2-D stress invariant, $A_2 = a_{ij}a_{ij}$
A_3	3-D stress invariant, $A_3 = a_{ij}a_{jk}a_{ki}$
a_{ij}	Dimensionless Reynolds stress anisotropy tensor, $a_{ij} = \frac{\overline{u_i u_j}}{k} - \frac{2}{3}\delta_{ij}$
b_{ij}	Dimensionless Reynolds stress anisotropy tensor, $b_{ij} = \frac{\overline{u_i u_j}}{2k} - \frac{1}{3}\delta_{ij}$
C_f	Skin-friction coefficient, $C_f = \frac{\tau_w}{0.5\rho U_\infty^2}$
C_{P_1}	Coefficient of the source term in the ε_P equation
c_{p11}	Constant inside C_{P1}
c_{p12}	Constant inside C_{P1}
C'_{P_1}	Coefficient of the extra source term $k_P \frac{\partial U_l}{\partial x_m}\frac{\partial U_i}{\partial x_j}\epsilon_{lmk}\epsilon_{ijk}$ in the ε_P equation
C_{P_2}	Coefficient of the sink term in the ε_P equation
c_{p21}	Constant inside C_{P2}
c_{p22}	Constant inside C_{P2}
C_{T_1}	Coefficient of the source term in the ε_T equation
c_{t1}	Constant inside C_{T1}
C_{T_2}	Coefficient of the sink term in the ε_T equation
c_μ	Coefficient in the eddy viscosity expression
c_{ε_1}	Coefficient of the source term in the ε equation
c_{ε_2}	Coefficient of the sink term in the ε equation
D	Diameter
D_{ij}	Diffusion term in the Reynolds stress transport equation
E	Near-wall extra dissipation term in the LS and KS models; Flatness parameter $E = 1 - \frac{9}{8}(E_2 - E_3)$ in the HJ model
E_2	2-D dissipation rate tensor invariant $E_2 = e_{ij}e_{ij}$
E_3	3-D dissipation rate tensor invariant $E_3 = e_{ij}e_{jk}e_{ki}$
e_{ij}	Dimensionless dissipation rate anisotropy tensor, $e_{ij} = \frac{\varepsilon_{ij}}{\varepsilon} - \frac{2}{3}\delta_{ij}$
f	Frequency of oscillation
f_{BL}	extra term proposed in this work to be inserted into C_{P1}
f_1	Damping function of the source term in the ε equation; Extra term proposed in this work to be inserted into f_{BL}
f_2	Damping function of the sink term in the ε equation; Extra term proposed in this work to be inserted into f_{BL}
f_μ	Damping function of the eddy viscosity expression
H	Shape factor in boundary layers, $H = \frac{\delta^*}{\theta}$; Step height in BFS flows
J	Jacobian matrix

k	Total turbulent kinetic energy
k_P	Turbulent kinetic energy stored by the large scales of motion
k_T	Turbulent kinetic energy stored by the small scales of motion
K	Acceleration parameter in FPGBL cases, $K = \frac{\nu}{U_\infty^2}\frac{dU_\infty}{dx}$
$\hat{P}$	Instantaneous pressure
P	Mean pressure
p	Fluctuating pressure
P_k	Turbulent kinetic energy production rate, $P_k = -\overline{u_i u_j}\frac{\partial U_i}{\partial x_j}$
P_{ij}	Reynolds stresses production rate, $P_{ij} = -\left(\overline{u_i u_k}\frac{\partial U_j}{\partial x_k} + \overline{u_j u_k}\frac{\partial U_i}{\partial x_k}\right)$
q	twice the turbulent kinetic energy, $q = 2k$
Q	Jet velocity in unsteady backward facing step cases
r	Radial distance
R	Radius
Re	Reynolds number
Re_t	Turbulent Reynolds number, $Re_t = \frac{k^2}{\nu\varepsilon}$
Re_λ	Reynolds Taylor number, $Re_\lambda = \left(\frac{20}{3}Re_t\right)^{1/2}$
Re_{δ^*}	Reynolds number based on the displacement thickness, $Re_{\delta^*} = \frac{\delta^* U_\infty}{\nu}$
Re_θ	Reynolds number based on the momentum thickness, $Re_\theta = \frac{\theta U_\infty}{\nu}$
s_{ij}	Mean strain rate tensor, $s_{ij} = \frac{1}{2}\left(\frac{\partial U_i}{\partial x_j} + \frac{\partial U_j}{\partial x_i}\right)$
S_{ij}	Mean strain rate tensor, $S_{ij} = \frac{\partial U_i}{\partial x_j} + \frac{\partial U_j}{\partial x_i}$
St	Strouhal number, $St = \frac{f\ell}{U_b}$
SW	Term used in f_2 in the NT1 and NT2 models, $SW = \frac{S_{ij}S_{ij} - W_{ij}W_{ij}}{S_{ij}S_{ij} + W_{ij}W_{ij}}$
S_ϕ	General source term in Chapter 4
t	Time
T	Period, $T = \frac{1}{f}$
U, V, W	Mean velocity components
u, v, w	Fluctuating velocity components
u_i, u_j	Fluctuating velocity components
u', v', w'	rms of the fluctuating velocity, $u' = \sqrt{\overline{u^2}}$; in periodic flows: $u' = \sqrt{< u^2 >}$
U_b, U_m	Bulk velocity
U_c	Centreline velocity
$\hat{U}$	Instantaneous velocity
$\overline{u_i u_j}$	Reynolds stress tensor
$\overline{u_i u_j u_k}$	Triple velocity correlation
V	Volume
w_{ij}	Vorticity tensor, $w_{ij} = \frac{1}{2}\left(\frac{\partial U_i}{\partial x_j} - \frac{\partial U_j}{\partial x_i}\right)$
W_{ij}	Vorticity tensor, $W_{ij} = \frac{\partial U_i}{\partial x_j} - \frac{\partial U_j}{\partial x_i}$
x, y, w	Coordinate directions
x_i, x_j	Coordinate directions
X_R	Time-averaged reattachment point in BFS flows

Greek Symbols

δ Boundary layer thickness
δ_{ij} Kronecker delta
δ^* Displacement thickness, $\delta^* = \int_0^\infty \left(1 - \frac{U(y)}{U_\infty}\right) \mathrm{d}y$
ε Turbulent kinetic energy dissipation rate
$\tilde{\varepsilon}$ Isotropic eddy dissipation rate of the turbulent kinetic energy
ε_{ij} Viscous dissipation term in the Reynolds stress transport equation
ε_P Energy transfer rate between the large and small scales of motion
ε_T Energy transfer rate between the small scales of motion and the dissipation zone, thus treated as the turbulent kinetic energy dissipation rate, $\varepsilon_T = \varepsilon$
ϕ Generic turbulent quantity in Chapter 4; Phase shift in oscillatory flows.
ϕ_{ij} pressure-strain correlation term in Reynolds stress transport equation
Γ Diffusivity in Chapter 4
η Dimensionless shear, $\eta = \max\left[\frac{k}{\varepsilon}\sqrt{\frac{1}{2}S_{ij}S_{ij}}, \frac{k}{\varepsilon}\sqrt{\frac{1}{2}W_{ij}W_{ij}}\right]$; Kolmogorov length scale, $\eta = (\nu^3/\varepsilon)^{1/4}$; General curvilinear coordinate in Chapter 4
κ von Karmam constant, $\kappa = 0.41$; wavenumber in the turbulent kinetic energy spectrum
μ Molecular viscosity
μ_t Eddy viscosity
ϑ Velocity scale
ρ Density
ν Kinematic viscosity
ν_t Kinematic eddy viscosity
θ Momentum thickness, $\theta = \int_0^\infty \frac{U(y)}{U_\infty}\left(1 - \frac{U(y)}{U_\infty}\right) \mathrm{d}y$
σ Turbulent Prandtl number
τ Time scale
τ_w Wall shear stress
ω Specific eddy dissipation rate in the FM and WM models; angular frequency elsewhere, $\omega = 2\pi f$
ω^+ Dimensionless forcing frequency in oscillatory pipe flows, $\omega^+ = \frac{\omega\nu}{u_\tau{}^2}$
ω^* Turbulent Stokes number proposed by Tu and Ramaprian (1983b), $\omega^* = \frac{\omega D}{u_\tau}$
ξ General curvilinear coordinate in Chapter 4
ζ General curvilinear coordinate in Chapter 4

Other Symbols

ℓ Length scale
ℓ_m Mixing length
$\overline{}$ Time average
$<>$ Phase average

Superscripts

$+$ Non-dimensionalized with inner velocity $U_\tau = \sqrt{\frac{\tau_w}{\rho}}$
$*$ Corrected quantity in SIMPLE scheme
$'$ Correction value in SIMPLE scheme

Subscripts

B/b	Bottom node/face
BL	Asymptotic state in local equilibrium boundary layers
DF	Asymptotic state in decaying grid turbulence
E/e	East node/face
N/n	North node/face
P	Current node in numerical analyses
SF	Asymptotic state in homogeneous shear flows
S/s	South node/face
T/t	Top node/face in numerical analyses
W/w	West node/face
∞	Value at the free-stream
0	Initial condition

Acronyms

APGBL	Adverse Pressure Gradient Boundary Layer
ARS	Algebraic Reynolds Stress
BFS	Backward Facing Step
BFS-St0	Steady state backward facing step case (St=0)
BFS-St0127	Backward Facing Step case with St=0.275
BFS-st1	Backward Facing Step case with St=1
CFD	Computational Fluid Dynamics
CG	Chen and Guo's LEV MTS model
CV	Control Volume
DNS	Direct Numerical Simulation
EXP	Experimental data
EV	Eddy Viscosity
FM	Menter's SST model
FPGBL	Favourable Pressure Gradient Boundary Layer
GL	Gibson and Launder's RST model
G&M0	Normally strained case of Gence and Mathieu (1979) - pure straining
G&M05	Normally strained case of Gence and Mathieu (1979) - two consecutive opposite in sign plane strains
HJ	Hanjalic et al.'s LRN RST model
HM1	Homogeneous moderate shear case of Matsumoto et al. (1991)
HM2	Homogeneous highest shear case of Matsumoto et al. (1991)
HR	Launder and Spalding's standard $k-\varepsilon$ model
HRN	High Reynolds Number
HSF	Homogeneous Shear Flow
JSF	Oscillatory boundary layer case of Jensen et al. (1989)
K150	FPGBL case of Spalart (1986) with $K = 1.5 \times 10^{-6}$
K250	FPGBL case of Spalart (1986) with $K = 2.5 \times 10^{-6}$
K275	FPGBL case of Spalart (1986) with $K = 2.75 \times 10^{-6}$
KC	Kim and Chen's LEV MTS model
KS	Modified Craft et al.'s 1999 Cubic NLEV $k-\tilde{\varepsilon}$ model

LEV	Linear Eddy Viscosity (model)
LRN	Low Reynolds Number
LS	Launder and Sharma's LRN $k - \tilde{\varepsilon}$ model
M&P10	Low Reynolds number APGBL case of Marusic and Perry (1995)
M&P30	High Reynolds number APGBL case of Marusic and Perry (1995)
MTS	Multiple Time Scale
NG	Nagano et al.'s LRN LEV MTS model
NLEV	Non Linear Eddy Viscosity
NL1	Two-time-scale non-linear-eddy-viscosity-model developed using $\nu_t = c_\mu \frac{kk_P}{\varepsilon_P}$
NL2	Two-time-scale non-linear-eddy-viscosity-model developed using $\nu_t = c_\mu \frac{k^2}{\varepsilon_T}$
NSF	Normally Strained Flow
NT1	Two-time-scale linear-eddy-viscosity-model developed using $\nu_t = c_\mu \frac{kk_P}{\varepsilon_P}$
NT2	Two-time-scale linear-eddy-viscosity-model developed using $\nu_t = c_\mu \frac{k^2}{\varepsilon_T}$
RANS	Reynolds Averaged Navier Stokes
RST	Reynolds Stress Transport
SG	Speziale et al.'s SSG RST model
SHC	Homogeneous high shear case of Lee et al. (1990)
STREAM	Simulation of Turbulent Reynolds averaged Equations for All Mach numbers - CFD code used
S&J	APGBL case of Samuel and Joubert (1974)
STS	Single Time Scale
TC	Craft's TCL LRN RST model
TCL	Two Component Limit
TED	Turbulent Eddy Dissipation
TKE	Turbulent Kinetic Energy
T&R	Laterally distorting case of Tucker and Reynolds (1968) - normally strained case with pure straining
TS	Hanjalic et al.'s LEV MTS model
Tu&R05	Oscillatory pipe flow of Tu and Ramaprian (1983a) with f=0.5Hz (low frequency case)
Tu&R36	Oscillatory pipe flow of Tu and Ramaprian (1983a) with f=3.6Hz (high frequency case)
T3RE10A20	Oscillatory pipe flow of He and Jackson (2009) with T=3s, Re=10000 and A=20%
T3RE14A20	Oscillatory pipe flow of He and Jackson (2009) with T=3.14s, Re=14000 and A=20%
T10RE7A20	Oscillatory pipe flow of He and Jackson (2009) with T=10, Re=7000 and A=20%
U2	Homogeneous low shear case of Rogers and Moin (1987)
WM	Wilcox's LRN RST MTS model
W2	Homogeneous low shear case of Rogers and Moin (1987)
X2	Homogeneous lowest shear case of Rogers and Moin (1987)
ZPGBL	Zero Pressure Gradient Boundary Layer

Abstract

The reliable prediction of turbulent non-equilibrium flows is of high academic and industrial interest in several engineering fields. Most turbulent flows are often predicted using single-time-scale Reynolds-Averaged-Navier-Stokes (RANS) turbulence models which assume the flows can be modelled through a single time or length scale which is an admittedly incorrect assumption. Therefore they are not expected to capture the lag in the response of the turbulence in non-equilibrium flows. In attempts to improve prediction of these flows, by taking into consideration some features of the turbulent kinetic energy spectrum, the multiple-time-scale models arose. A number of two-scale models have been proposed, but so far their use has been rather limited.

This work thus focusses on the development of two-time-scale approaches. Two two-time-scale linear-eddy-viscosity models, referred to as NT1 and NT2 models, have been developed and the initial stages of the development of two-time-scale non-linear-eddy-viscosity models are also reported. The models' coefficients have been determined through asymptotic analysis of decaying grid turbulence, homogeneous shear flows and the flow in a boundary layer in local equilibrium. Three other important features of these models are that there is consistent partition of the large and the small scales for all above limiting cases, model sensitivity to the partition and production rate ratios and sensitivity of the eddy viscosity sensitive to the mean strain rates.

The models developed have been tested through computations of a wide range of flows such as homogeneous shear and normally strained flows, fully developed channel flows, zero-pressure-gradient, adverse-pressure-gradient, favourable-pressure-gradient and oscillatory boundary layer flows, fully developed oscillatory and ramp up pipe flows and steady and pulsated backward-facing-step flows.

The proposed NT1 and NT2 two-scale models have been shown to perform well in all test cases, being, among the benchmarked models tested, the models which best performed in the wide range of dimensionless shear values of homogeneous shear flows, the only linear-eddy-viscosity models which predicted well the turbulent kinetic energy in the normally strained cases and the only models which showed satisfactory sensitivity in predicting correctly the reattachment point in the unsteady backward facing step cases with different forcing frequencies. Although the development of the two-time-scale non-linear-eddy-viscosity models is still in progress, the interim versions proposed here have resulted in predictions of the Reynolds normal stresses similar to those of much more complex models in all test cases studied and in predictions of the turbulent kinetic energy in normally strained flows which are better than those of the other models tested in this study.

Declaration

No portion of the work referred to in this thesis has been submitted in support of an application for another degree or qualification of this or any other university or other institute of learning.

Copyright

Acknowledgements

Firstly, I would like to thank my supervisors, Dr. Tim Craft and Prof. Hector Iacovides, for being so supportive and attentive with me. I am grateful for all the rich discussions which greatly enhanced my understanding and development. Their guidance during these four years has been invaluable and I am glad to have had them as my supervisors from whom I learnt so much. Thank you!

I would also like to acknowledge the support of CNPq, National Council for Scientific and Technological Development - Brazil, for the PhD scholarship. This work was also supported by the School of MACE, through financial assistance via the Overseas Research Student (ORS) Scholarship, to whom I would also like to express my gratitude.

Regarding my work itself, I would like to thank Dr. He for providing unreported experimental data for the oscillatory pipe flow cases described in He and Jackson (2009).

Generally, I would like to thank all my friends in Manchester who surely improved my stay here, always supported my studies and made me have a great time during these last four years.

I would also like to thank my parents for being so supportive and for making my studies possible here at the University of Manchester.

Last, but absolutely not least, I would like to thank my husband, Alexandre Leoni Fonseca, for all his support and love which definitely motivated me throughout my PhD.

Chapter 1

Introduction

The major objective of this work is to develop modelling strategies suitable for a wide range of non-equilibrium flows using two-time-scale approaches.

Non-equilibrium flows consist of flows which are subjected to rapid changes such as an abrupt expansion or contraction, rapid variation in time and imposed pressure gradients, among many other conditions which can remove the flow from its equilibrium. These kinds of flows are commonly found in industry since they happen in valves, pumps, heat exchangers and other types of equipment as well as in the aerospace field where the curvature of the surfaces may cause such non-equilibrium states. Therefore, it is of engineering interest to have the ability to accurately predict non-equilibrium flows.

The motivation of using multiple-time-scale schemes thus lies in the fact that most of the available turbulence models, which are single-time-scale schemes, are not capable of reproducing the effects of turbulence in such flows, specially with regard to the lag in the response of the turbulence. It is believed that this inability is due to the fact that single-time-scale models assume spectral equilibrium and use a single time or length scale to characterize the behaviour of the whole flow which is, admittedly, a coarse approximation of the real physics of the flows and which is known to be unrealistic. On the other hand, two-time-scale models attempt to take into account some features of the turbulent kinetic energy spectrum by characterizing the flows with two time or length scales. One could therefore expect that such models will be more likely to be able to predict non-equilibrium flows where lags in the response of the turbulence to changes in the mean flow, caused by the energy transfer process across the spectrum, are more noticeable.

In this introduction chapter, the turbulence phenomenon itself and its main features will be described and discussed and aspects of the established turbulence modelling art will be briefly presented. An outline of this thesis will be then also presented where the main work developed in each chapter will be delineated.

1.1 Turbulence and Its Modelling

The concept of turbulence in the way it is used and studied at the present time was perhaps first introduced by Osborne Reynolds (Reynolds, 1883) after his famous experiment on the transition from laminar to turbulent flow. This experiment was performed at the University of Manchester in 1883 and consisted of investigating the behaviour of a dye when injected into a water pipe submitted to increasing flow rates. Reynolds' apparatus can be seen in Figure 1.1. For low flow rates, it was possible to completely follow the dye stream as a single line along the pipe. As the flow rate was increased, it became more and more difficult to distinguish the line of dye in the flow until the moment (and from this point on) when a single line of dye could no longer be visualized and the entire pipe was apparently coloured by the dye. As a result of this experiment, Reynolds identified a dimensionless factor, currently known as the Reynolds number, which could indicate whether a flow was laminar, turbulent or in transition from laminar to turbulent states: at low flow rates the flow is laminar and at high rates it becomes turbulent. For turbulent flows Reynolds proposed the decomposition of the instantaneous velocity to the average and fluctuating components and then produced the time-averaged Navier-Stokes equations which form the foundation of the RANS (Reynolds-Averaged Navier-Stokes) computations and turbulence modelling which will be discussed further in the thesis.

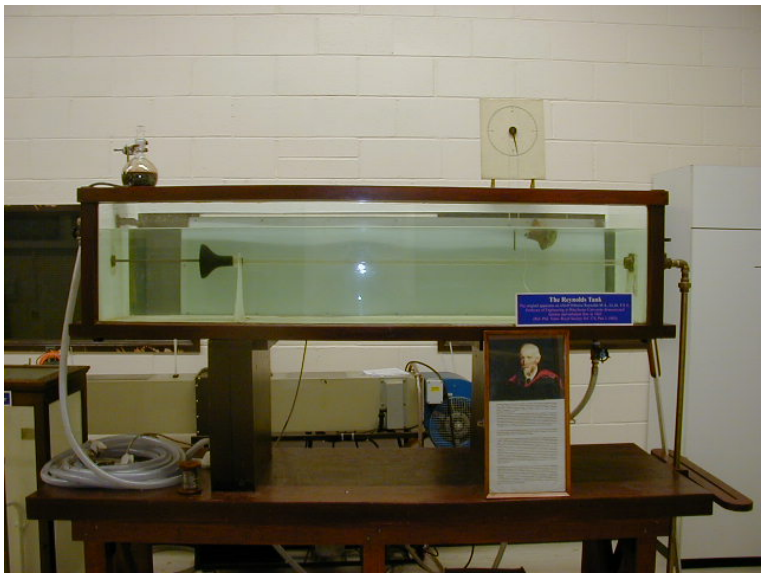

Figure 1.1: Reynolds' tank for the experiment about transition from laminar to turbulent flow

The turbulent flow is thus characterized by a random, unsteady, chaotic and three dimensional behaviour which is hard to describe and predict. Rotational flow structures, called eddies or vortices, are often visualized. Hence turbulence can be identified by its eddying motion with a wide spectrum of eddy sizes, implying a wide range of length scales. The largest eddy sizes have the same order of magnitude as the flow domain while the smallest are limited by the viscous forces and the kinetic energy of the fluctuating motion. When

the flow Reynolds number becomes higher and therefore the kinetic energy of the turbulent motion increases, the size of the smallest eddies needed to dissipate this energy is reduced. Therefore the higher the flow Reynolds number, the wider its eddy spectrum. The largest eddies are dominated by inertial forces and present a highly anisotropic arrangement. The smallest eddies exhibit high velocity gradients and as a result viscous effects are dominant, implying a tendency towards an isotropic structure. The process in which the energy contained in the main flow is transferred to the largest eddies is called vortex stretching, while the transfer of energy from these largest eddies to the smaller ones up to the point the viscous effects dissipate it is called the energy cascade. These concepts are widely used in the turbulence field as an attempt to comprehend and explain the turbulent motion. Hinze (1976); Rodi (1993); Versteeg and Malalasekera (1995) have written more extensively on this topic.

The turbulent kinetic energy spectrum thus illustrates the vortex stretching and cascade processes described above. Changes in the mean flow generate turbulent kinetic energy which is transferred to and stored by the large eddies of motion. These eddies break into smaller eddies which break into even smaller eddies and so on and thereby the turbulent kinetic energy is transferred across the different eddy sizes until they are so small that when broken, the turbulence kinetic energy is simply dissipated into heat by viscous forces.

With regard to industrial flows, one may either want to stimulate or avoid turbulence. In general, when the focus is on transfer processes, turbulence is desired. Indeed, momentum, heat and/or mass transfer can be optimized in a turbulent system due to its strong diffusive nature. This optimization is generally required in order to provide homogeneity (in mixtures, for example) and economy (when designing equipment, for example). On the other hand, when it is important to reduce frictional drag, as in the aerospace field, one may want to avoid or postpone the occurrence of turbulence. Whichever is the case, it is important to be able to understand and predict the turbulent effects.

The theoretical equations which describe any flow motion, including turbulent flows with all their complexities, are known as the Navier-Stokes equations when considering incompressible and Newtonian flows (which are the types of flows that will be considered in this work). To solve a single turbulent flow, a closed set of the time-dependent Navier-Stokes equations and the continuity equation must be solved for the three velocity components and the pressure. The main problem in predicting turbulence arises when one realizes that even the simplest flows do not have an analytical solution, and to solve numerically a turbulent flow, even the simplest ones require a huge computational effort. Such effort is due to the level of mesh refinement required to capture the eddies, from the largest to the smallest present in a turbulent flow. The method of solving numerically the full Navier-Stokes equations is called Direct Numerical Simulation (DNS). This technique has only become available in the last few decades when advances in computer technology provided enough storage capacity and speed to afford this kind of simulation. However, it is still not possible to carry out DNS for complex flows, and is restricted to simple geometries and low to moderate Reynolds numbers flows. Nevertheless DNS is considered an important tool for turbulence study development, as discussed by Moin and Mahesh (1998), and provides relevant databases which are

regularly used as reference data, especially for near wall effects as noted by Friedrich et al. (2001).

In general, engineers are interested in average behaviours, not in the full details of the turbulence structure. Fortunately, as Hinze (1976) points out, it is possible to identify average values of the main quantities (as velocity, pressure, temperature, etc) among the irregularities characteristic of the turbulent flows. As mentioned above, Osborne Reynolds was the first to propose the decomposition of the flow variables into their mean and fluctuating parts. It was this idea that gave rise to the so-called and widely used Reynolds-Averaged Navier-Stokes (RANS) turbulence models. The latter are usually applied in Computational Fluid Dynamics (CFD) in order to predict the mean quantities of the flows, but also the turbulent effects.

Computational Fluid Dynamics is the name given for a class of numerical tools which solve numerically the differential equations that govern fluid flows. As a general rule, the domain is discretized and boundary and/or inlet conditions are specified. The type of simulation which is intended to be solved defines the numerical methods as well as the mesh refinement that should be used. For example, when simulating with a Reynolds-Averaged modelling, one is not interested in capturing all the eddy size range and the mesh required is thus significantly coarser than the one needed to process a DNS. When one mentions a CFD simulation, one usually refers to Reynolds-Averaged processes and it was through this type of simulation that CFD became a popular tool in both the academic and industrial fields, allowing its users to predict more complex flows in a reasonable time. Nevertheless, CFD is still a strong research topic where researchers try to improve its numerical features. This is also true of the so called turbulence models.

Besides the RANS turbulence models already mentioned, there are other turbulence models available in the literature, such as large-eddy simulation, multiple point correlation turbulence models, PDF models, etc, which are, however, substantially more expensive in terms of computational resources and are consequently beyond the scope of this work and thus will not be described. Through a literature survey about RANS turbulence models, which will be presented in Chapter 2, it will be shown that numerous models of varying degree of complexity, but mostly single-scale, can be found in the scientific literature, which can reliably predict many flows. Nevertheless, for many kinds of flows, especially complex non equilibrium flows, there is still a requirement for turbulence model improvements. This work thus aims to develop two-time-scale models within the RANS framework suitable for non-equilibrium flows.

1.2 Outline of Thesis

The structure of this thesis will now be described and the main work developed in each chapter will be indicated as a guidance for its reading.

In this first chapter an overall background about turbulence and its modelling has been presented. This creates the scenario for the development of the present work which focused on turbulence modelling.

In Chapter 2 a literature survey about different kinds of turbulence models within the RANS framework has been carried out, presenting the main classes of turbulence models and showing their advantages and disadvantages as well as the physical processes they intend to model. Attention has been focussed on multiple-time-scale models since these are the object of study in this work.

In Chapter 3 the existing turbulence models which were used to simulate different test cases with non-equilibrium features are presented. The transport equations as well as the extra source terms and coefficients of each model are defined. In total, 13 turbulence models were used: 3 linear-eddy-viscosity models, 1 non-linear-eddy-viscosity model, 4 Reynolds-stress-transport models, 4 linear-eddy-viscosity two-time-scale models and 1 Reynolds-stress-transport two-time-scale model. Besides the intrinsic difference between each class of model, different features such as low-Reynolds-number approximations against the use of wall functions were also explored.

In Chapter 4 the Finite Volume method is discussed. The CFD code used in this work, the STREAM code, uses the Finite Volume method and is also described in this chapter. The fourth chapter thus aims to develop understanding of the numerical implementation of turbulence models into CFD codes and to make the STREAM code and its features familiar for future use.

In Chapter 5 the test cases simulated in this work are described, their inlet and boundary conditions as well as any other simulations set up are presented and the performance of the turbulence models, described in Chapter 3, in predicting them is discussed. A wide range of flows were assessed, including simple flows, such as fully developed channel flows and zero pressure gradient boundary layers, and non-equilibrium flows such as homogeneous shear flows, adverse-pressure gradient, favourable-pressure gradient and oscillatory boundary layers, normally strained flows, fully developed oscillatory and ramp up pipe flows and steady and unsteady backward facing step flows. This set of flows includes a wide range of different non-equilibrium features which are regularly used to assess the performance of new turbulence models and therefore are appropriate for the purposes of this work. This chapter is quite extensive due to the number of test cases used and the number of turbulence models tested.

In Chapter 6 the main outcome of this work is presented: the development of two two-time-scale linear-eddy-viscosity models, namely the NT1 and NT2 models. All stages which led to the final versions of these models are described in details and their performance in all test cases presented in Chapter 5 is assessed. It is shown that the new models developed perform well in all test cases and particularly improve predictions of homogeneous shear flows, normally strained flows and backward facing step cases.

In Chapter 7 the initial work carried out towards the development of two-time-scale non-linear-eddy-viscosity models is also described in detail. The performance of the two interim models developed, namely the NL1 and NL2 models, is also assessed in the test cases presented in Chapter 5.

Finally, in Chapter 8 the main conclusions about the complete work as a whole are presented and future work proposals will be also presented and discussed.

Chapter 2

Literature Survey

The purpose of this chapter is to present a literature survey on turbulence models and their applications and limitations up to the present time. The literature survey will focus on dynamic field models for incompressible single-phase Newtonian flows.

In order to discuss turbulence models, it is useful to start from the very beginning, where one can appreciate the reason why turbulence models are needed. As already mentioned, the momentum governing equations of incompressible single-phase Newtonian turbulent flows are the instantaneous Continuity (2.1) and Navier-Stokes (2.2) equations:

$$\frac{\partial \hat{U}_i}{\partial x_i} = 0 \tag{2.1}$$

$$\frac{\partial \hat{U}_i}{\partial t} + \hat{U}_j \frac{\partial \hat{U}_i}{\partial x_j} = -\frac{1}{\rho}\frac{\partial \hat{P}}{\partial x_i} + \nu \frac{\partial^2 \hat{U}_i}{\partial x_j \partial x_j} \tag{2.2}$$

In the above equations, summation applies in the repeated indexes and the circumflex accent indicates instantaneous quantities. Equations (2.1) and (2.2) constitute a closed set where the unknowns are $\hat{P}$, $\hat{U}_1 = \hat{U}$, $\hat{U}_2 = \hat{V}$ and $\hat{U}_3 = \hat{W}$. These variables can be expressed as in equation (2.3) by applying Reynolds' proposal of splitting each instantaneous variable into its mean and fluctuating parts:

$$\hat{U}_i = U_i + u_i \qquad \hat{P} = P + p \tag{2.3}$$

With regard to the averaging process, it is worth noting how the mean and fluctuating parts in equation 2.3 can be defined. For flows where the mean is steady (ie. where all the time-dependence is due only to turbulent fluctuations), a simple time-averaging may be used to define the mean quantities. In other cases the mean may be time-dependent (in flows with unsteady forcing, for example). In such cases a phase-averaging may be used if the flow is periodic, or ensemble-averaging if not. In the flows to be considered later all three forms of averaging will be implicitly employed, although for the modelling analysis below it does not

matter which is being considered.

The so called Reynolds Averaged Navier Stokes (RANS) equations are obtained by substituting equations (2.3) into equations (2.2) and (2.1) and averaging in order to obtain a set of equations for the mean quantities. The result of these algebraic manipulation is:

$$\frac{\partial U_i}{\partial x_i} = 0 \tag{2.4}$$

$$\frac{\partial U_i}{\partial t} + U_j \frac{\partial U_i}{\partial x_j} = -\frac{1}{\rho}\frac{\partial P}{\partial x_i} + \frac{\partial}{\partial x_j}\left(\nu \frac{\partial U_i}{\partial x_j} - \overline{u_i u_j}\right) \tag{2.5}$$

One should notice that equations (2.1) and (2.4) are the same, except for the fact that the divergence is being applied to the instantaneous velocity in the first equation and to the mean velocity in the second equation. This result is extremely convenient since it means that no additional term is required to calculate the mean quantities; that is, in principle, no information is lost due to this "change" of variables.

On the other hand, when comparing equations (2.2) and (2.5) one notices a new term, $-\overline{u_i u_j}$ appearing in the Reynolds-averaged form. This new term arises from the averaging process since the averaged product of two turbulent quantities is not necessarily zero. In fact, the autocorrelation of a velocity component with itself ($\overline{u^2}$, $\overline{v^2}$, $\overline{w^2}$) is never zero, unless that particular fluctuating velocity is always zero. When the product is not over the same two turbulent quantities it would only be zero if they were statistically independent, as noted by Versteeg and Malalasekera (1995). Indeed, the turbulent velocity fluctuations are usually not independent and account for important turbulent effects becoming much more significant than viscous terms in turbulent flow regions. When equation (2.5) is multiplied by the density ρ, the new term assumes the form $-\rho\overline{u_i u_j}$ which is known as the Reynolds stress.

One may notice that the new set of equations constituted by equations (2.4) and (2.5) now contains four equations (continuity equation and one for each velocity component from the RANS equation) and ten unknowns: P, U, V, W, $\overline{u^2}$, $\overline{v^2}$, $\overline{w^2}$, $\overline{uv}$, $\overline{uw}$ and $\overline{vw}$. Thus the six new introduced terms, the Reynolds stresses, characterize the so called closure problem. In order to close this equation system, it is necessary to introduce turbulence models, either in the form of algebraic expressions or additional transport equations to model the Reynolds stresses.

The first attempt to model the Reynolds stresses was proposed by Boussinesq in analogy to Newton's law of viscosity (where the shear stress is linearly proportional to the mean velocity gradient and the viscosity gives the slope), suggesting an analogy between the viscous and turbulent stresses, giving rise to the concept of a turbulent viscosity. Taking into account the turbulent kinetic energy definition, equation (2.7), Boussinesq's hypothesis is expressed as in equation (2.6):

$$\overline{u_i u_j} = -\nu_t\left(\frac{\partial U_i}{\partial x_j} + \frac{\partial U_j}{\partial x_i}\right) + \frac{2}{3}k\delta_{ij} \tag{2.6}$$

$$\text{where} \qquad 2k = \overline{u^2} + \overline{v^2} + \overline{w^2} \tag{2.7}$$

One may notice that this proposal suggests an algebraic way to calculate the Reynolds stresses and transfers the modelling challenge from the Reynolds stresses to the turbulent viscosity, ν_t. Turbulence models which apply the Boussinesq turbulent viscosity concept will thus attempt to model the turbulent viscosity. It is also important to call attention to the isotropic character of equation (2.6). In shear flows where $\frac{\partial U}{\partial x} = \frac{\partial V}{\partial y} = \frac{\partial W}{\partial z} = 0$, all the normal Reynolds stresses will assume the same value ($\overline{u^2} = \overline{v^2} = \overline{w^2} = \frac{2}{3}k$). This identity is known to be erroneous. However, in spite of this, equation (2.6) constitutes the base for many widely used and validated turbulence models.

In the literature, the turbulence models are most commonly classified into four groups: Zero Equation models, One Equation models, Two Equation models and Stress Transport models. Other classes of RANS turbulence models have also been investigated in the last few decades, such as the Algebraic Reynolds Stress models and the Multiple Time Scale models which may span across some of the above groups. Most of these types of turbulence models will be discussed in the following subsections, as part of a literature survey, and special attention will be given to the Multiple Time Scale models since it is believed they are more likely to be able to predict non equilibrium flows which will be the main focus of this study.

2.1 Zero Equation Models

The Zero Equation models are denoted as such because they do not solve any additional transport equations other than the Continuity and RANS equations. Therefore, they simply use an algebraic expression to model the turbulent viscosity. The pioneer on this work was Prandtl (1925) who initially observed that the turbulent viscosity could be modelled (following a dimensional analysis) as a product of a turbulent velocity scale (ϑ) and a length scale (ℓ), multiplied by a general dimensionless constant, as expressed in equation (2.8):

$$\mu_t = \rho C \vartheta \ell \tag{2.8}$$

Prandtl was investigating a simple 2D shear flow, where the only relevant mean velocity gradient is $\frac{\partial U}{\partial y}$ and the only important Reynolds stress is $\rho\overline{uv}$, and proposed a relation between the velocity scale and the mean shear rate as being $\vartheta \propto \ell_m |\frac{\partial U}{\partial y}|$, resulting in the following:

$$-\overline{uv} = \ell_m^2 \left|\frac{\partial U}{\partial y}\right| \frac{\partial U}{\partial y} \tag{2.9}$$

ℓ_m is known as the mixing length and the above equation is recognized as Prandtl's Mixing Length model. To fully close the system, the mixing length ℓ_m needs to be modelled. As

this new parameter represents a length scale, it is expected that it would vary as a function of the type of the flow. In practice, ℓ_m is usually expressed in the form of a ramp function whose linear part is proportional to the distance to the wall, as κy, κ being the von Karman constant evaluated as 0.41, and whose constant part assumes different values according to the kind of flow. Indeed, one may find tables (Rodi, 1993; Versteeg and Malalasekera, 1995) with different values (or expressions as functions of geometry and/or distance from the wall) for the constant part of ℓ_m for various flows, all of them having been determined by empirical observations. It is also valid to mention that the value of ℓ_m is usually reduced somewhat from the above value very near the wall, where viscous forces dominate. In this context, van Driest's (1956) damping near-wall function is the most widely used.

Equation (2.9) can be generalized to a form that could be applied in arbitrary strain fields. However, Zero Equation models do not generally give accurate prediction in other than rather simple flows due to the necessity of an expression for the mixing length which is hard to define for complex flows. They perform satisfactorily for simple 2D shear flows such as jets, mixing layers and zero pressure gradient boundary layers. However, for flows whose turbulence properties are not proportional to the mean flow length scale, they fail, not being, for example, capable of predicting separation and recirculation (Versteeg and Malalasekera, 1995) accurately as well as processes where convection and/or diffusion of turbulence are important (Rodi, 1993).

Prandtl's Mixing Length model is maybe the most popular and applied turbulence model among the Zero Equation models, however one can find in the literature a number of other algebraic turbulence models such as Smagorinsky (1963), Baldwin and Lomax and Cebeci and Smith (1974) mentioned by Speziale (1995).

2.2 One Equation Models

One Equation models overcome some of the limitations experienced by the Zero Equation models. They constitute a class of turbulence models which provide an additional transport equation to be solved. However they still also need an algebraic expression to close the system formed by the Continuity and the RANS equations.

The most famous One Equation model is known as the Kolmogorov-Prandtl model because the two workers arrived at the same proposal by independent ways (Rodi, 1993). Their proposals were based on defining the turbulent velocity scale as $k^{\frac{1}{2}}$. Since this turbulent quantity is associated with large eddies, this provides a velocity scale for the large scale turbulent eddies that is not purely dependent on the local mean flow, as is the case in the Zero Equation models. Following the general turbulent viscosity formulation - equation (2.8) - the turbulent viscosity can now be expressed as in equation 2.10 below where C'_μ is a dimensionless constant.

$$\nu_t = C'_\mu k^{\frac{1}{2}} \ell \tag{2.10}$$

The turbulent kinetic energy transport equation can be analytically derived from its definition stated in equation (2.7) which can also be written as $k = 0.5\overline{u_i^2}$. From this, one can derive $\frac{Dk}{Dt} = \frac{D}{Dt}\left(\frac{\overline{u_i^2}}{2}\right) = \overline{u_i \frac{Du_i}{Dt}}$. A transport equation for the fluctuating velocity u_i can be easily obtained by subtracting the RANS equation (2.5) from the instantaneous Navier Stokes equation (2.2), taking into account the decomposition of equation (2.3). Multiplying this equation by u_i and averaging, one can arrive at the exact turbulent kinetic energy transport equation:

$$\frac{\partial k}{\partial t} + U_j \frac{\partial k}{\partial x_j} = -\overline{u_i u_j}\frac{\partial U_i}{\partial x_j} - \nu \overline{\frac{\partial u_i}{\partial x_j}\frac{\partial u_i}{\partial x_j}} + \frac{\partial}{\partial x_j}\left(- \frac{\overline{u_i^2 u_j}}{2} - \frac{\overline{u_i p}}{\rho}\delta_{ij} + \nu \frac{\partial k}{\partial x_j}\right) \tag{2.11}$$

However, the above equation cannot, at this stage, be solved directly due to the last two terms on its right hand side. Evaluating the right hand side terms, one must call attention to the first term which is identified as turbulence production, $P_k = -\overline{u_i u_j}\frac{\partial U_i}{\partial x_j}$. This name arises from the fact that this same term is also present in the mean kinetic energy equation, but with the opposite sign, indicating that this is the process which transfers kinetic energy from the mean flow to the turbulent scales.

The second term on the right hand side of equation (2.11) also plays an important role in determining the turbulence behaviour. It is identified as the turbulent kinetic energy dissipation rate, $\varepsilon = \nu \overline{\frac{\partial u_i}{\partial x_j}\frac{\partial u_i}{\partial x_j}}$ (which is also called viscous eddy dissipation since it dissipates the turbulence effects by viscous action). This quantity is always positive since it consists of averaged squared turbulent velocity gradients. In One Equation models, ε is a modelled quantity, usually assuming the form $\varepsilon = C\frac{k^{3/2}}{\ell}$, where C is an empirical constant and ℓ a prescribed length scale.

The third term on the right hand side of equation (2.11) is identified as a diffusive process. All except the viscous diffusion need to be modelled. Its modelling is usually based on the presumption that the diffusive flux is proportional to the turbulent kinetic energy gradient. Therefore equation (2.11) is transformed into equation (2.12):

$$\frac{Dk}{Dt} = P_k - \varepsilon + \frac{\partial}{\partial x_j}\left[\left(\nu + \frac{\nu_t}{\sigma_k}\right)\frac{\partial k}{\partial x_j}\right] \tag{2.12}$$

This is the most common turbulent kinetic energy transport equation form, where Dk/Dt stands for the substantive derivative, defined as $\frac{Dk}{Dt} = \frac{\partial k}{\partial t} + U_j \frac{\partial k}{\partial x_j}$ and σ_k is the turbulent Prandtl number, usually assigned to unity, linking the diffusivity of k with the turbulent viscosity.

One may notice that the One Equation models still need an algebraic equation to model the turbulent length scale which is used in the turbulent viscosity and eddy dissipation expressions. The turbulent length scale is usually estimated by essentially the same empirical formulas used in the Zero Equation models.

An interesting observation pointed out by Rodi (1993) is that for local equilibrium, where convection and diffusivity can be neglected and then production is equal to dissipation, the One Equation model reduces to the Zero Equation model, making clear that Zero Equation models are more likely to be applicable only in local equilibrium flows.

There are other One Equation models available in the literature, not all of which propose an additional transport equation for the turbulent kinetic energy. Baldwin and Barth (1990) and Spalart and Allmaras (1992), for example, developed a transport equation for the turbulent viscosity (Speziale, 1995) while Bradshaw and co-workers (Bradshaw and Ferriss, 1967, 1973) proposed a transport equation for the shear stress (Rodi, 1993). However none of these escape from the necessity of empirical formulas such as length scale prescriptions which can then make the model difficult to apply in complex geometrical flows.

2.3 Two Equation Models

Following the logic for the last two turbulence models' nomenclature, it is quite intuitive that Two Equation models are those which provide two additional transport equations for the system composed by the Continuity and RANS equations. The reason they were developed is also sensible: to avoid the empirical and semi-empirical algebraic formulations for the turbulent velocity and length scales, since those experimental correlations restrict the turbulence model application to simple shear flows. The idea is to calculate two turbulence quantities through transport equations and use those turbulence quantities to infer turbulence velocity and length scales to be applied in the turbulent viscosity concept, constituting the minimum physically acceptable level of closure (Speziale, 1995).

The most famous turbulence model in this class is the $k-\varepsilon$ model which, as its name suggests, provides transport equations for the turbulent kinetic energy k and the turbulent eddy dissipation rate ε. The standard $k-\varepsilon$ model, referring to Jones and Launder's (1972b) work, proposes the k equation in the same form as presented in equation (2.12) and the ε equation as follows:

$$\frac{D\varepsilon}{Dt} = c_{\varepsilon 1}\frac{\varepsilon}{k}P_k - c_{\varepsilon 2}\frac{\varepsilon^2}{k} + \frac{\partial}{\partial x_j}\left[\left(\nu + \frac{\nu_t}{\sigma_\varepsilon}\right)\frac{\partial \varepsilon}{\partial x_j}\right] \tag{2.13}$$

There is an exact analytical transport equation for the quantity ε which can be obtained by manipulating the turbulent velocity transport equations in order to match the turbulent eddy dissipation definition. However, virtually all the terms appearing in this require modelling, and so the more empirically derived form of equation (2.13) is usually adopted.

Prandtl's general proposal for the turbulent viscosity, equation (2.8), is retained, but now no further correlations are necessary to express the turbulent velocity and length scales. The velocity scale is taken as $\vartheta = k^{\frac{1}{2}}$ as in the One Equation models and the turbulent length scale is now expressed as $\ell = \frac{k^{\frac{3}{2}}}{\varepsilon}$. Therefore, the turbulent viscosity assumes the form:

$$\nu_t = c_\mu \frac{k^2}{\varepsilon} \tag{2.14}$$

One may notice the presence of five constants to be determined. They are: σ_k (which normally assumes a value of unity) from the k equation, c_μ from the turbulent viscosity expression and $c_{\varepsilon 1}$, $c_{\varepsilon 2}$ and σ_ε from the ε equation. Briefly commenting on how these constants were determined, it is possible to say that the most common way of achieving values for these constants is to apply the turbulence model in a number of simplified and asymptotic flow states in order to guarantee some expected results. This way, c_μ can be determined by a local equilibrium analysis, $c_{\varepsilon 2}$ derived from decaying grid turbulence and $c_{\varepsilon 1}$ and σ_ε chosen from computer optimization and a relation between them (and $c_{\varepsilon 2}$) for the fully developed region of an equilibrium boundary layer.

The standard $k-\varepsilon$ model, usually used with the constants defined by Launder and Spalding (1974), thus consists of a linear eddy viscosity model with no low Reynolds number modifications, that is, no special treatment for near-wall regions. In spite of these drawbacks, the $k-\varepsilon$ model is widely used in the academic and industrial environments and is one of the turbulence models which has been most widely validated in terms of distinct simulated flows. It is believed to often give accurate prediction for relatively simple confined flows, but its performance is not reliable in general complex flows such as swirling flows and those with rapidly varying or high strain rates (Versteeg and Malalasekera, 1995).

There are many other Two Equation models available in the literature. Most of them consist of basically some improvements to the standard $k-\varepsilon$ model when applied to specific kinds of flows, aiming to expand the range of applicability of the model. Some of them propose different turbulent quantities to be solved by transport equations, usually replacing ε and keeping k. The following subsections will be dedicated to discuss briefly some alternative forms of Two Equation models.

2.3.1 Low-Reynolds-Number $k-\varepsilon$ Models

A number of researchers have worked on modifying the standard $k-\varepsilon$ model, aiming to be able to predict near-wall and viscous influenced behaviours. In a general way, their focus was directed to apply damping functions to the already used constants in order to allow them to still reproduce the log law profile and correctly predict the variables' values in the near-wall vicinity. In order to discuss these Low-Reynolds-Number models, from now on referred to as LRN models, the standard $k-\varepsilon$ model equations can be rewritten as in equations (2.15)-(2.18) below.

$$\nu_t = c_\mu f_\mu \vartheta \ell \qquad \text{or} \qquad \nu_t = c_\mu f_\mu \vartheta^2 \tau \tag{2.15}$$

$$\frac{Dk}{Dt} = P_k - \varepsilon + \frac{\partial}{\partial x_j}\left[\left(\nu + \frac{\nu_t}{\sigma_k}\right)\frac{\partial k}{\partial x_j}\right] \tag{2.16}$$

$$\frac{D\tilde{\varepsilon}}{Dt} = (c_{\varepsilon 1} f_1 P_k - c_{\varepsilon 2} f_2 \tilde{\varepsilon} + E)\tau^{-1} + \frac{\partial}{\partial x_j}\left[\left(\nu + \frac{\nu_t}{\sigma_\varepsilon}\right)\frac{\partial \tilde{\varepsilon}}{\partial x_j}\right] + \Pi_\varepsilon \tag{2.17}$$

$$\tilde{\varepsilon} = \varepsilon - D \tag{2.18}$$

Some models also introduce a new variable: $\tilde{\varepsilon}$. This variable is related to ε by equation (2.18) and is referred to as the isotropic eddy dissipation rate of the turbulent kinetic energy. One should notice that if the term D is zero, $\tilde{\varepsilon} = \varepsilon$. This concept was first introduced by Jones and Launder (1972b) who observed that it would be convenient to let $\tilde{\varepsilon}$ go to zero at a wall in equation (2.17). However, ε itself is not zero at a wall, so they introduced a form for D (Table 2.1(a)) that would ensure ε would take the correct wall value when $\tilde{\varepsilon}$ was set to zero at the wall. The term E was introduced in some models to provide additional near-wall dissipation. One should observe from their expressions in Tables 2.1(a) and 2.1(b) that in the bulk flow, where the local Reynolds number is high, the terms D and E are negligible. Jones and Launder (1972b) also proposed the constants c_μ and $c_{\varepsilon 2}$ to vary as functions of the local turbulent Reynolds number, which in the above models is taken as $Re_t = \frac{k^2}{\nu\tilde{\varepsilon}}$. They validated their model only for shear flows and that explains why in Tables 2.1(a) and 2.1(b) the derivatives of terms D and E are expressed only in terms of y, as presented in their paper, but of course a general form can be obtained. Jones and Launder (1972b) applied their turbulence model proposal to a few flows including zero and favourable pressure gradient boundary layers. In further work, (Jones and Launder, 1973) they expanded the model application, where, among the shear flows examined, one can mention: a fully developed flow in a pipe at high and low Reynolds numbers, a sink flow which is actually a boundary layer flow with a favourable pressure gradient, an asymptotic suction boundary layer, a plane channel flow at low Reynolds number and flows submitted to step changes in the levels of surface blowing and streamwise pressure gradients. In a general way, one can say that their model provided good predictions when compared to experimental data, except for transition regions.

Launder and Sharma (1974) developed an extension to Jones and Launder's (1972b; 1973) work, proposing new damping functions to c_μ and $c_{\varepsilon 2}$, still dependent on the turbulent Reynolds number. This was then validated for a spinning disk flow. According to Rodi and Mansour (1993) that was rated one of the best LRN models until 1984 in an review article.

Rodi and Mansour (1993) also proposed a LRN model, but focusing on modelling each term of the ε equation with the aid of available DNS data for a fully developed channel flow. The damping function for c_μ was determined as a function of the dimensionless distance to the wall y^+ and the damping function for $c_{\varepsilon 2}$ was made to vary with a new parameter $R_p = \frac{P_k/k}{0.3\sqrt{\varepsilon/\nu}}$, defined after an order of magnitude analysis of the ε-budget, which could be interpreted as a ratio between the dissipating motion and the production of turbulence timescales. The coefficients $c_{\varepsilon 1}$, $c_{\varepsilon 2}$, σ_k and σ_ε were kept as constants and their values were taken from Launder et al. (1975). Finally, the E term was modified, becoming an extended form of that of Jones and Launder (1972b). Its final form can be seen in Table 2.1(b). This model was all based on channel flow DNS databases which does not necessarily make it widely

applicable, unless also validated for other kinds of flow, as stated by the authors.

Cheng and Yang (2008) proposed a new LRN model by combining two damping functions from different authors (Park and Sung (1995) and Nomura et al. (2002)) into one. The idea was to account for viscous and near-wall effects by one of the damping functions and for non-equilibrium influences by the other. The resultant f_μ expression can be seen in Table 2.1(a). This model was validated in a 3D backward facing step flow, where the reattachment length was said to be in good agreement with experimental data.

The LRN models presented so far all considered the turbulent timescale in ν_t to be k/ε. Goldberg and Apsley (1997) proposed this timescale to be multiplied by $max(1, \xi^{-1})$, where $\xi = \frac{\sqrt{Re_t}}{C_\tau}$, Re_t is the already cited turbulence Reynolds number and C_τ was taken as $\sqrt{2}$ after an analysis for the viscous sublayer. This idea implies the timescale to be k/ε for high Reynolds numbers and to become the Kolmogorov scale for low Re_t. A damping function for the constant c_μ was determined by first analysing the turbulent viscosity in the near-wall region and subsequently extending it to the fully turbulent region, where f_μ should assume a value of unity, and applying some known relations involving the dimensionless distance to the wall. Lastly a new E term was also proposed based on canceling the corresponding non-zero destruction term near the wall. This term can be seen in Table 2.1(b) where S stands for the mean strain invariant $S = \sqrt{2 s_{ij} s_{ij}}$, $s_{ij} = \frac{1}{2}\left(\frac{\partial U_i}{\partial x_j} + \frac{\partial U_j}{\partial x_i}\right)$ and Q stands for the total kinetic energy. This model was validated for a flat plate near-wall flow, a fully developed pipe flow, a channel flow over a 2D hump, a flow over a slanted backward-facing step and a high lift aerofoil, all presenting good agreement with experimental data and performing as well as Lien and Leschziner's (1993) model which employed wall distance in its formulation.

Other authors have also proposed LRN models which do not depend upon the distance to the wall. Rahman and Siikonen (2005), for example, represented the time scale as shown in Table 2.1(a) which is never smaller than the Kolmogorov time scale, and this approach has also been applied by other authors. They proposed a damping function in the form of that stated in Table 2.1(a), where $f_\lambda = \tanh C_\lambda R_\lambda (1 + R_\lambda)$ and $R_\lambda = \sqrt{\frac{c_\mu Q}{\nu \max(S,W)}}$ and Q and S stand respectively for the total kinetic energy and the mean strain invariant, as already defined, and W is the mean vorticity invariant $W = \sqrt{2 w_{ij} w_{ij}}$, with $w_{ij} = \frac{1}{2}\left(\frac{\partial U_i}{\partial x_j} - \frac{\partial U_j}{\partial x_i}\right)$. The resulting damping function was stated as being valid for the whole flow field. The constant C_λ was evaluated as $C_\lambda = \beta c_\mu^{c_{\varepsilon 2}}$, with $\beta = \frac{0.5\tau \max(S,W)}{1+\tau\sqrt{S^2+W^2}}$. This parameter was also used to define the constant $c_{\varepsilon 1}$, and $c_{\varepsilon 2}$ was defined as a function of the latter as in Rahman and Siikonen (2003). The quantities σ_k and σ_ε were not kept as constants, being modelled with the aid of DNS data as can be seen in Table 2.1(b), where $f_\sigma = \frac{f_\mu}{\sqrt{\beta + f_\mu^3}}$. Besides this, an extra source term was suggested as a pressure diffusion term, to balance the ε equation in the limit of the near-wall region. This LRN model was evaluated for fully developed channel flows, a flat plate boundary layer with zero pressure gradients and a backward facing step flow where it performed well, giving good agreement with experimental data.

The constants, terms and damping functions generally represented in equations (2.15), (2.16), (2.17) and (2.18) for each one of the LRN models briefly commented on above can be

seen in Tables 2.1(a) and 2.1(b). For all turbulence models considered above, the constant c_μ assumed its classical value of 0.09 and the damping function f_1 was assigned as unity, hence these are not given separately in the tables. There are many other LRN $k-\varepsilon$ models available in the literature, but it is believed that the above sample of LRN models is enough to provide a broad and representative view of this class of turbulence model and its capabilities.

2.3.2 Non-Linear Eddy Viscosity Models

As already stated above, the standard eddy viscosity models based on Boussinesq's proposal for the turbulent viscosity imply an isotropic prediction of the normal Reynolds stresses in simple shear flows, where $\overline{u^2} = \overline{v^2} = \overline{w^2} = \frac{2}{3}k$. That may not be a problem for many shear-dominated flows where the only important Reynolds stresses are the shear ones, since they are the only ones that play an active role in the transport equations for these flows. However, for flows where the normal stresses play a role those turbulence models fail. In order to improve predictions without increasing drastically the computational effort, researchers developed the Non-Linear Eddy Viscosity models, from now on referred to as NLEV models, which can, in principle, give a better representation of the normal Reynolds stresses.

Speziale (1987) presented a NLEV model which incorporated a number of physical restrictions required for applicability. He stated these physical constraints as being three: dimensional and tensorial invariance, realizability (which accounts for k being always positive) and material frame indifference. Following these statements, a general non-linear proposal for the Reynolds stresses containing up to the cubic terms in mean strains can be written as by Craft et al. (1996b):

$$\begin{aligned}\overline{u_i u_j} =& \frac{2}{3}\delta_{ij}k - \nu_t S_{ij} \\ &+ c_1\frac{k}{\tilde{\varepsilon}}\nu_t\left(S_{ik}S_{jk} - \frac{1}{3}S_{kl}S_{kl}\delta_{ij}\right) + c_2\frac{k}{\tilde{\varepsilon}}\nu_t\left(W_{ik}S_{jk} + W_{jk}S_{ik}\right) + c_3\frac{k}{\tilde{\varepsilon}}\nu_t\left(W_{ik}W_{jk} - \frac{1}{3}W_{kl}W_{kl}\delta_{ij}\right) \\ &+ c_4\frac{k^2}{\tilde{\varepsilon}^2}\nu_t\left(S_{ki}W_{lj} + S_{kj}W_{li}\right)S_{kl} + c_5\frac{k^2}{\tilde{\varepsilon}^2}\nu_t\left(W_{il}W_{lm}S_{mj} + S_{il}W_{lm}W_{mj} - \frac{2}{3}S_{lm}W_{mn}W_{nl}\delta_{ij}\right) \\ &+ c_6\frac{k^2}{\tilde{\varepsilon}^2}\nu_t S_{ij}S_{kl}S_{kl} + c_7\frac{k^2}{\tilde{\varepsilon}^2}\nu_t S_{ij}W_{kl}W_{kl} \end{aligned} \tag{2.19}$$

where $S_{ij} = \left(\frac{\partial U_i}{\partial x_j} + \frac{\partial U_j}{\partial x_i}\right)$ and $W_{ij} = \left(\frac{\partial U_i}{\partial x_j} - \frac{\partial U_j}{\partial x_i}\right)$.

The main feature of a NLEV model is thus this non-linear way of expressing the Reynolds stresses by an algebraic formulation. One may notice that the first line of equation (2.19) is the standard linear eddy viscosity model, the second contains the quadratic terms and the last two lines the cubic ones. It is of value to add that a formulation for the turbulent viscosity ν_t is still required to close the system.

Table 2.1: Comparing LRN models

(a) Terms in ν_t expression and k equation

Model	f_μ	ϑ^2	ℓ	τ	D	σ_k
Jones and Launder (1972b)	$e^{\frac{-2.5}{1+Re_t/50}}$	k	$\frac{k^{3/2}}{\tilde{\varepsilon}}$	$\frac{k}{\tilde{\varepsilon}}$	$2\nu\left(\frac{\partial\sqrt{k}}{\partial y}\right)^2$	1.0
Launder and Sharma (1974)	$e^{\frac{-3.4}{(1+Re_t/50)^2}}$	k	$\frac{k^{3/2}}{\tilde{\varepsilon}}$	$\frac{k}{\tilde{\varepsilon}}$	$2\nu\left(\frac{\partial\sqrt{k}}{\partial y}\right)^2$	1.0
Rodi and Mansour (1993)	$1-\frac{e^{-0.0002y+}}{e^{0.00065y+^2}}$	k	$\frac{k^{3/2}}{\tilde{\varepsilon}}$	$\frac{k}{\tilde{\varepsilon}}$	0	1.0
Goldberg and Apsley (1997)	$\frac{1-e^{-0.01Re_t}}{1-e^{-\sqrt{Re_t}}}\max(1,\xi^{-1})$	k	$\frac{k^{3/2}}{\tilde{\varepsilon}}$	$\frac{k}{\tilde{\varepsilon}}\max(1,\xi^{-1})$	0	1.367
Rahman and Siikonen (2005)	$f_\lambda + C_\nu(1-f_\lambda)$	k	–	$\frac{k}{\tilde{\varepsilon}}\sqrt{1+\frac{C_T^2}{Re_t}}$	0	$\frac{\sigma_{\tilde{\varepsilon}}}{1-C_\nu f_\sigma}$
Cheng and Yang (2008)	$(1-e^{-y^+/87})(1-e^{-y^+/50.5})2.62\frac{1.2+0.646P_k/\tilde{\varepsilon}}{(1.2+P_k/\tilde{\varepsilon})^2}$	k	$\frac{k^{3/2}}{\tilde{\varepsilon}}$	$\frac{k}{\tilde{\varepsilon}}$	0	1.0

(b) Terms in ε equation

Model	$c_{\varepsilon 1}$	$c_{\varepsilon 2}$	f_2	E	σ_ε	Π_ε
Jones and Launder (1972b)	1.45	2.0	$1-0.3e^{-Re_t^2}$	$\frac{k}{\tilde{\varepsilon}}2\nu\nu_t\left(\frac{\partial^2 U}{\partial y^2}\right)^2$	1.3	0
Launder and Sharma (1974)	1.44	1.92	$1-0.3e^{-Re_t^2}$	$\frac{k}{\tilde{\varepsilon}}2\nu\nu_t\left(\frac{\partial^2 U}{\partial y^2}\right)^2$	1.3	0
Rodi and Mansour (1993)	1.44	1.90	$e^{2R_p^3}$	$0.5\frac{k}{\tilde{\varepsilon}}2\nu\nu_t\left(\frac{\partial^2 U}{\partial y^2}\right)^2 + 0.006\nu\frac{k^2}{\tilde{\varepsilon}^2}\frac{\partial k}{\partial y}\frac{\partial U}{\partial y}\frac{\partial^2 U}{\partial y^2}$	1.3	0
Goldberg and Apsley (1997)	1.42	1.83	1	$\frac{0.1c_{\varepsilon 2}}{0.01\sqrt{2}}\nu f_\mu S^2 e^{-0.231\sqrt{\frac{Q}{\nu S}}}$	1.367	0
Rahman and Siikonen (2005)	$1+\beta$	$1.33c_{\varepsilon 1}$	1	$2\frac{\nu_t}{\tau}\max\left(\frac{\partial(k/\tilde{\varepsilon})}{\partial x_j}\frac{\partial k}{\partial x_j},0\right)$	$\frac{C_T}{4C_\nu+f_\sigma}$	$-\frac{1}{2}\frac{\partial}{\partial x_j}\left(\nu\frac{\tilde{\varepsilon}}{k}\frac{\partial k}{\partial x_j}\right)$
Cheng and Yang (2008)	1.44	1.92	1	0	1.3	0

Equation (2.19) is written in terms of $\tilde{\varepsilon}$, the variable proposed by Jones and Launder (1972b). However, an equivalent non-linear expression for the Reynolds stresses may be written to suit any two-equation model, as Speziale (1987) did for a k-ℓ turbulence model.

Speziale's (1987) work concerned a quadratic NLEV model, therefore the above constants c_4, c_5, c_6 and c_7 were taken as zero. In his particular model, the constants c_2 and c_3 were also zero and he introduced a new term which he referred to as the frame-indifferent Oldroyd derivative of $\boldsymbol{S}$ (the strain invariant tensor). He proposed a NLEV model to be applied in $k-\ell$ and $k-\varepsilon$ turbulence models, writing equation (2.19) in terms of the length scale ℓ instead of ε and associating eddy dissipation to the length scale as $\varepsilon = \frac{k^{3/2}}{\ell}$. For the $k-\ell$ turbulence model, Speziale employed Mellor and Herring's (1973) transport equations and for the $k-\varepsilon$ form, Hanjalic and Launder's (1972) ε transport equation. For both, the turbulent viscosity was expressed as in equation (2.8), with the velocity scale $\vartheta = k^{1/2}$. His model was applied to a fully developed channel flow, a square duct and a backward-facing step flow. He verified the improvement achieved by the NLEV models in comparison to the standard linear $k-\varepsilon$ model, including a fair prediction of the normal stresses in the channel flow (except for the near-wall region), the correct physical form of the secondary flows in initial calculations of the square duct (which the linear model cannot capture) and much closer to experimental value for the reattachment length in the backward-facing step flow. Despite these good preliminary results, the model needed more testing for wider validation.

Craft et al. (1996b) noted a number of other quadratic NLEV models. Among them, one can mention Rubinstein and Barton's (1990) work, who applied the renormalization group theory developed by Yakhot and Orszag (1986) to arrive at values for the quadratic constants c_1, c_2 and c_3. However, based on the very different values for the constants c_1, c_2 and c_3 obtained by optimization for distinct flows by individual authors, Craft et al. (1996b) concluded that these quadratic NLEV models were only capable of slightly improving predictions compared to a linear eddy viscosity model. Hence, they proposed a cubic NLEV model, intended to return a more general applicability. In their work, the constants were determined by optimization over a wide range of flows, but special attention was given to simple shear flows to determine some parameters. The model was designed to be applied to low-Reynolds-number flow regimes, thus its turbulent viscosity formulation was in the form of equation (2.15) with c_μ varying with the strain invariants in the form $max(\tilde{S}, \tilde{W})$, where $\tilde{S}$ and $\tilde{W}$ are the dimensionless strain and vorticity invariants ($\tilde{S} = \frac{k}{\tilde{\varepsilon}}\sqrt{\frac{1}{2}S_{ij}S_{ij}}$ and $\tilde{W} = \frac{k}{\tilde{\varepsilon}}\sqrt{\frac{1}{2}W_{ij}W_{ij}}$) and f_μ varied with the turbulent Reynolds number. They adopted the D term suggested by Jones and Launder (1972b) in the k equation, but changed the E term expression in the $\tilde{\varepsilon}$ equation in order to reduce its dependence on the Reynolds number. An additional source term was also included in the ε equation: the so called Yap correction (Yap, 1987) which is a length scale correction, based on the normal distance to the wall. The model's performance was compared to that of Launder and Sharma's (1974) linear eddy viscosity model for a channel flow, a circular pipe flow, a pipe rotating about its own axis, a fully developed curved channel flow and a turbulent jet impinging normally onto a heated flat

plate. Craft et al.'s (1996b) model showed the better performance, especially in the latter flows, where non-linear effects were more important. However both models failed to predict the correct magnitude of the turbulent kinetic energy peak near the wall in the channel flow.

Two further developments in NLEV models arose from Craft et al.'s (1996b) turbulence model: one from the same authors, Craft et al. (1997), and the other by Craft et al. (1999). Craft et al. (1997) adopted the same general cubic stress strain model as indicated in equation (2.19), but proposed different expressions for the constants which now became functions of the turbulent Reynolds number, the mean strain invariants and the stress invariant A_2, defined as $A_2 = a_{ij}a_{ij}$, where $a_{ij} = \frac{\overline{u_i u_j}}{k} - \frac{2}{3}\delta_{ij}$ is the dimensionless Reynolds stress anisotropy tensor. The expressions for each constant were again obtained by optimization against DNS and experimental data of homogeneous shear flows over a range of the dimensionless strain rate, ensuring that the normal stresses should never be negative, irrespective of the dimensionless strain rate's magnitude, as well as swirling pipe and 2D straining curvature flows. In order to calculate the stress invariant A_2, a transport equation was solved for this quantity based on one derived from a full stress transport model. The k and ε equations were also not adopted in their standard formulation. The diffusive term in the k equation was modelled as in Daly and Harlow (1970), but with a new correlation for the constant within the model. The E term in the ε equation was adopted as in Rodi and Mansour (1993), but with different constants, and an extra source term was proposed in order to avoid the Yap (1987) correction, due to its dependence on the normal distance to the wall. The turbulence model was validated by being applied in a channel flow, in an axisymmetric flow through a pipe that rotates about its own axis, in a fully developed flow in a curved channel, for bypass transition in zero pressure boundary layers, in a turbulent impinging jet and in a flow around a turbine blade, where some adaptations and modifications were applied to the new model. In general, the new proposal provided better predictions, but did show some overprediction of the wall shear stress on the convex surface of the curved channel and did not capture the turbulence intensity far from the impinging point in the turbulent impinging jet flow particularly well. The authors concluded that the transport equation for the stress invariant was responsible for the better prediction of the normal stresses near the wall and that there was a deficiency for convex surface calculations.

In a refinement of the two equation NLEV model, Craft et al. (1999) evaluated Craft et al.'s (1996b) scheme for two particular non equilibrium cases: abrupt pipe expansion and an axisymmetric jet impinging onto a heated flat plate. They found that the dependence of the constant c_μ on the strain rate could lead to instabilities in the pipe expansion case, which was solved by suggesting a modified expression for c_μ. In order to avoid dependence on the normal distance to the wall, the Yap correction originally proposed was replaced by a length scale correction based on that proposed by Iacovides and Raisee (1997) whose constant was also modified into an expression depending on the turbulent Reynolds number and the mean stress invariants, in order to improve heat transfer prediction and not allow the time scale to be smaller than the Kolmogorov scale. When the modified turbulence model was applied to the axisymmetric jet impinging onto a heated flat plate case, it was found that

the Nusselt number was overpredicted, due to an overprediction of the wall-normal Reynolds stress $\overline{v^2}$. This observation led to a further reformulation of c_μ, which now also became a function of the dimensionless third invariant of the strain rate tensor $S_l = \frac{S_{ij}S_{jk}S_{ki}}{(S_{nl}S_{nl}/2)^{3/2}}$. This term was convenient because it solved the prediction problem and reduces to zero in simple shear flows, not altering the previous results already obtained for the abrupt expansion pipe case. This work was considered an extension in terms of applicability of the initial Craft et al. (1996b) turbulence model, improving prediction for sharp corner flows and increasing numerical stability.

Some NLEV models have been presented above, which serve to illustrate the general idea behind this class of turbulence models. In fact, any turbulence model which applies the turbulent viscosity concept and provides non-linear terms in the Reynolds stresses calculation could be classified as a NLEV model. That is the case, for example, of the Algebraic Reynolds Stress (ARS) models, which will be discussed further in a later section of this chapter.

2.3.3 Other Two Equation Models

Up to now, the turbulence models discussed were mainly of a $k-\varepsilon$ type. This section, though, will be dedicated to present some other popular turbulence models which are not of this kind. The first one which will be briefly described is the $k-\omega$ model, usually recognized as appropriate for near-wall flows. Subsequently, the Shear Stress Transport (SST) model will be presented as a combination of the $k-\varepsilon$ and $k-\omega$ models. Finally, the $k-\varepsilon-\overline{v}^2$ model will be discussed, in spite of not being strictly a Two Equation Model. It will be discussed here since it is often cited in different turbulence model formulations, in particular Two Equation Models.

The $k-\omega$ Turbulence Model

One of the more recent formulations of a $k-\omega$ model was developed by Wilcox (1988a). His intention was to propose a more appropriate scale-determining equation in order to improve prediction of two equation models. He thus proposed a transport equation for ω which is usually called the specific dissipation rate and is related to ε by $\omega = \frac{\varepsilon}{\beta^* k}$, where β^* is one of the model's dimensionless coefficients. According to Wilcox, one can also interpret ω as the rate of dissipation of turbulence per unit energy, with dimensions of $time^{-1}$. The k and ω equations were presented as:

$$\frac{Dk}{Dt} = P_k - \beta^*\omega k + \frac{\partial}{\partial x_j}\left[(\nu + \sigma^*\nu_t)\frac{\partial k}{\partial x_j}\right] \tag{2.20}$$

$$\frac{D\omega}{Dt} = \gamma\frac{\omega}{k}P_k - \beta\omega^2 + \frac{\partial}{\partial x_j}\left[(\nu + \sigma\nu_t)\frac{\partial \omega}{\partial x_j}\right] \tag{2.21}$$

This is still an eddy viscosity model, based on Boussinesq's turbulent viscosity concept, thus implying the isotropic Reynolds stress prediction in purely shear flows. The turbulent viscosity and the Reynolds stresses are then calculated as:

$$\nu_t = \gamma^* \frac{k}{\omega} \tag{2.22}$$

$$-\overline{u_i u_j} = 2\nu_t \left(s_{ij} - \frac{1}{3}\frac{\partial u_k}{\partial x_k}\delta_{ij} \right) - \frac{2}{3}k\delta_{ij} \tag{2.23}$$

Regarding the model's constants, the constant γ^* was taken as unity after a rescaling of ω through the governing and turbulent transport equations. A relation between $\frac{\beta^*}{\beta}$ was achieved by analysing the turbulence model's behaviour in decaying homogeneous isotropic turbulence flow. An incompressible zero pressure gradient boundary layer flow was then used to determine $\beta^* = \frac{9}{100}$, which implied $\beta = \frac{3}{40}$, and a relation between γ and β^*, β and σ. σ^* and σ were set as $\sigma^* = \sigma = 0.5$ after numerical computations of boundary layers with zero and adverse pressure gradients and defect-layer analysis, leading to $\gamma = \frac{5}{9}$.

Wilcox (1988a) also proposed wall boundary condition treatments for ω for no-slip and rough surfaces as well as surface mass injection. Simulations were performed for incompressible boundary layers with zero and adverse pressure gradients as well as with mass injection, compressible flat plate boundary layers and incompressible shear flows. The results were compared with experiments and predictions calculated with Jones and Launder's (1972b) model. Wilcox recommended that, in order to guarantee the desired ω behaviour near the smooth wall, the transport equations should only be solved for cells where the dimensionless distance to the wall y^+ was greater than 2.5, below which the expression for ω in the limit of the wall, which was defined as a function of y (the distance to the wall), was applied.

It was concluded that the $k-\omega$ model performed very well in all tested cases, presenting significant improvements over the other turbulence models. Although no near-wall damping functions and/or wall functions were presented, in further work (Wilcox, 1991) damping functions depending on the turbulent Reynolds number were introduced to correct the turbulent kinetic energy behaviour near the wall.

The SST Turbulence Model

The SST model arose as an attempt of Menter (1994) to combine the $k-\varepsilon$ and $k-\omega$ turbulence models in order to improve prediction of adverse pressure gradient boundary layers. Menter argued that the $k-\omega$ model would better fit the near-wall sublayer of the boundary layer, since it dispenses with damping functions, provides simple boundary conditions and remains numerically stable. On the other hand, the $k-\varepsilon$ model is more appropriate for the wake region of the boundary layer, since it more reliably predicts the eddy viscosity level, which is assumed to be important for strong adverse pressure gradient flow predictions, besides also being so for free shear flows.

The "simple" integration of the two turbulence models, keeping the eddy viscosity formulation of both models, gave rise to the baseline model (BSL model) which Menter identified as giving similar results to the $k-\omega$ model, except for the freestream instability of the latter. Menter (1994) then proposed a modification on the eddy viscosity formulation in order to

account for the transport of the principal turbulent shear stress, giving rise to the Shear Stress Transport (SST) model.

To implement the integration between the $k-\varepsilon$ and $k-\omega$ models, the former was rewritten in the same format of the latter (ie. solving transport equations for k and ω) by using the relation between the two turbulent variables $\varepsilon = \beta^* \omega k$. The resulting k equation became exactly the same as in the $k-\omega$ model, but the constant σ_k would have to assume a new value. The resulting "ε" equation resembled the ω equation, except for the constants and one additional source term which arises from the transformation of the original ε equation. Then, Menter (1994) proposed a blending function F_1 which should take a value of unity in the near-wall region and zero far from it. The term $(1 - F_1)$ was used to multiply the additional term arising from the original ε equation and each constant of the model was set as $\phi = F_1\phi_1 + (1 - F_1)\phi_2$, where ϕ_1 and ϕ_2 are the corresponding original $k-\omega$ and $k-\varepsilon$ model's constants, respectively. This way, it is possible to see that the model switches from one model to the other depending on distance to the wall since F_1 is defined in terms of this.

The SST model differs from the above BSL model by also including a modification of the turbulent viscosity formulation, as already noted above. By evaluating Johnson and King's (1985) turbulence model and the standard Boussinesq expression for the shear stress and taking into account experimental data of strong adverse pressure gradient flows, the eddy viscosity was proposed as $\nu_t = \frac{a_1 k}{max(a_1\omega, SF_2)}$, where S is the strain rate and F_2 a function designed to take a value of one for boundary layer flows and zero for free shear flows, where the eddy viscosity should become the same as in the $k-\omega$ model. The idea is to account for strong strain rates near the wall by decreasing the eddy viscosity, F_2 acting like a damping function in this region.

The model was considered versatile by making it easy to change the argument of the blending function F_1 in order to adjust the switching from the $k-\varepsilon$ to the $k-\omega$ model for any kind of flow. It was also pointed out that the general time of computation was not significantly affected, only the programming effort which must be done only once.

The BSL and SST models were applied in a range of different flow cases: zero and adverse pressure gradient boundary layer, free shear layer, backward facing step, airfoil and a transonic bump. Its performance was compared to the original $k-\omega$ model of Wilcox (1988a) and to Jones and Launder's (1972b) model. In a general way, the SST provided the best agreement with the experimental data used for comparison, the BSL and the original $k-\omega$ performed quite similarly, as already mentioned above, and the LRN $k-\varepsilon$ model presented the biggest discrepancies. None of the models were capable of correctly predicting the relaxation downstream of the reattachment point in the backward facing step flow. Nevertheless, the model was considered accurate as a whole, but was not validated for 3D flows.

The $k-\varepsilon-\overline{v}^2$ Model

The $k-\varepsilon-\overline{v}^2$ model was suggested by Durbin (1991). Its importance is more related to the many articles it inspired rather than its application as a turbulence model and that is the

reason why it is going to be commented upon here.

Durbin criticized the turbulence models which were applying damping functions to predict near-wall behaviour because of their empirical nature, although they may be useful for engineering purposes. Analysing the $k-\varepsilon$ eddy viscosity model formulation, its isotropy was identified as the main problem, since the near-wall region is quite anisotropic. To solve this problem, he suggested the turbulent viscosity to be expressed as $\nu_t = c_\mu \overline{v^2} \tau$, where τ is the time scale $\tau = max\left(\frac{k}{\varepsilon}, C_T\sqrt{\frac{\nu}{\varepsilon}}\right)$, where the constant C_T was defined by a near-wall limiting analysis. $\overline{v^2}$ was identified to be the proper velocity scale and the time scale formulation above avoids this reaching a smaller value than the Kolmogorov scale. A transport equation was suggested for $\overline{v^2}$ and its pressure-velocity term was calculated by an elliptic equation which incorporated part of the LRR model of Launder et al. (1975). The constants of the model were generally determined by evaluating the log law region together with DNS and experimental data of channel flows.

It is not the objective here to present all equations used to close the proposed system, therefore it is considered that the above brief description is enough to characterize the $k-\varepsilon-\overline{v}^2$ model developed by Durbin (1991). What is perhaps more important to add is that, this model would better suit a Three Equation model class, since it presents a third transport equation to be solved, but it was chosen to be included here due to its strong relation to the standard $k-\varepsilon$ model.

The Two Equation model subsection ends here. Generally reviewing what has been gone through, one should mention the standard $k-\varepsilon$ model, certainly the most representative turbulence model of this group, the LRN models, the NLEV model, the $k-\omega$ model and the SST model. Many of the main features of the Two Equation models have been presented and they provide a quite rich sample of turbulence model variations in order to illustrate how research has been developed. It should be noticed that the flows successfully predicted by this class of turbulence models were mainly 2D shear flows. That is related to weaknesses in predicting more complex flow systems. The next section will discuss the Reynolds Stress Transport models which emerge partly as a response to these deficiencies.

2.4 Reynolds Stress Transport Models

Although most of the turbulent flows mentioned so far have been shear dominated flows, complex and 3D turbulent flows are very often encountered in industry. While the former can often be acceptably predicted by Two Equation Models, as reported in the last section, engineers still need to be able to predict the latter accurately. It was in this context that the Reynolds Stress Transport models, from now on referred to as RST models, arose.

The RST models differ from the Two Equation Models by not calculating the Reynolds stresses by algebraic expressions, but by a transport equation for each one of the six components. Because of that, the RST models are also known as second order, or second moment closure, models. It will be shown further that the RST models still need a transport equation for the eddy dissipation ε. As a result, the RST models can have up to seven extra transport

equations to be solved together with the Navier-Stokes and Continuity equations. Needless to say, such a system will demand much more computational effort as well as required time of simulation than Two Equation models. However, one expects them to allow complex and 3D flow predictions to be obtained with an acceptable degree of confidence.

The exact transport equation for each Reynolds stress may be obtained by observing that $\frac{D\overline{u_i u_j}}{Dt} = \overline{u_j \frac{Du_i}{Dt}} + \overline{u_i \frac{Du_j}{Dt}}$. Hence, having derived the transport equation for the fluctuating velocity components u_i and u_j, by subtracting the average Navier-Stokes equation from its instantaneous form, then multiplying the first by u_j and the second by u_i and averaging; and finally making all necessary algebraic manipulations, one arrives at the exact form of the Reynolds stress transport equations which will be written here as in Launder and Sandham (2002):

$$\begin{aligned}
\frac{D\overline{u_i u_j}}{Dt} = & -\left(\overline{u_i u_k}\frac{\partial U_j}{\partial x_k} + \overline{u_j u_k}\frac{\partial U_i}{\partial x_k}\right) && \Big\} P_{ij} \\
& + \overline{\frac{p}{\rho}\left(\frac{\partial u_i}{\partial x_j} + \frac{\partial u_j}{\partial x_i}\right)} && \Big\} \phi_{ij} \\
& - \frac{\partial}{\partial x_k}\left(\overline{u_i u_j u_k} + \frac{\overline{pu_j}}{\rho}\delta_{ik} + \frac{\overline{pu_i}}{\rho}\delta_{jk} - \nu\frac{\partial \overline{u_i u_j}}{\partial x_k}\right) && \Big\} D_{ij} \\
& - 2\nu\overline{\frac{\partial u_i}{\partial x_k}\frac{\partial u_j}{\partial x_k}} && \Big\} \varepsilon_{ij}
\end{aligned} \tag{2.24}$$

Many important points must be discussed about the above equation. First, the physical meaning of each right hand side term will be defined: the first term, P_{ij}, is already known, being the production rate which acts to produce an increase in the Reynolds stress levels. The second term, ϕ_{ij}, stands for the pressure-strain correlation which acts as an energy redistributor, while the third term, D_{ij}, accounts for diffusion and acts as a spatial redistributor (Launder et al., 1984). The fourth term, ε_{ij}, represents dissipation by viscous influence, the first term of which is simply twice the eddy dissipation ε introduced earlier.

After describing each term in equation (2.24), they must be evaluated from a modelling point of view. The production term, as already commented, does not need any kind of modelling since it involves only the main variables to be calculated by the closed set of equations. On the other hand, the pressure-strain correlation, diffusion and dissipation terms will require modelling owing to the presence of terms which cannot be directly calculated. The pressure-strain correlation has an important characteristic that should be respected by any modelling attempt, which is that it has zero trace. This is often the most crucial term to be modelled as will be shown. With regard to the diffusion term, Launder et al. (1984) argued that the last three subterms which represent viscous diffusion could be neglected for high-Reynolds-number flows. Finally, and perhaps already starting some modelling, if the dissipation term is considered under high-Reynolds-number conditions, where isotropy of the small scales applies, Launder et al. (1984) demonstrated that the last two subterms of the

dissipation term are zero and the eddy dissipation should be expressed as $\varepsilon_{ij} = \frac{2}{3}\varepsilon\delta_{ij}$. Taking into account the above considerations, equation (2.24) can be rewritten as:

$$\frac{D\overline{u_i u_j}}{Dt} = -\left(\overline{u_i u_k}\frac{\partial U_j}{\partial x_k} + \overline{u_j u_k}\frac{\partial U_i}{\partial x_k}\right) + \overline{\frac{p}{\rho}\left(\frac{\partial u_i}{\partial x_j} + \frac{\partial u_j}{\partial x_i}\right)} - \frac{\partial}{\partial x_k}\left(\overline{u_i u_j u_k} + \frac{pu_j}{\rho}\delta_{ik} + \frac{pu_i}{\rho}\delta_{jk}\right) - \frac{2}{3}\varepsilon\delta_{ij} \quad (2.25)$$

From the above equation, it is possible to notice that a transport equation for the eddy dissipation, ε, will also be needed. Usually, its diffusion term is remodelled from that used in the $k-\varepsilon$ model and some additional terms may be included, but the main differences between existing RST models are still the different approaches for approximating each term in equation (2.25).

Some RST models will be discussed here, where the main differences and assumptions between them will be emphasized, as well as their performance over a range of flows to which they were applied. Starting with Hanjalic and Launder (1972), who adopted equation (2.25) as a starting point for modelling, one can identify two more terms which were dropped. The authors argued that based on some experimental results and lack of any other evidence, the pressure-velocity correlation within the diffusion term could be ignored, leaving only the triple velocity correlation to be modelled for the diffusion phenomenon. By evaluating transport equations for the triple velocity correlations, and based on some experimental results, the following expression was proposed for the triple correlation:

$$\overline{u_i u_j u_k} = c_s \frac{k}{\varepsilon}\left(\overline{u_i u_l}\frac{\partial \overline{u_j u_k}}{\partial x_l} + \overline{u_j u_l}\frac{\partial \overline{u_k u_i}}{\partial x_l} + \overline{u_k u_l}\frac{\partial \overline{u_i u_j}}{\partial x_l}\right) \quad (2.26)$$

In order to model the pressure strain correlation, one may find an exact expression for it by manipulating the instantaneous Navier-Stokes equation and solving the resulting Poisson equation for the instantaneous pressure. This exact expression cannot be used directly for solving the stress transport equation either, however it does make it possible to identify two interactions that contribute to the pressure strain correlation: the first between the fluctuating velocity components themselves and the second between these and the main flow, via the mean velocity gradients. As a result, the redistribution term was modelled as a sum of these two physical processes, $\phi_{ij} = \phi_{ij,1} + \phi_{ij,2}$. The first term, $\phi_{ij,1}$, was modelled by considering the decay of a non-isotropic homogeneous flow, where the mean strain rate was negligible, to its isotropic state where the shear stress should vanish. This suggested taking $\phi_{ij,1} = -c_{\phi 1}\frac{\varepsilon}{k}\left(\overline{u_i u_j} - \frac{2}{3}k\delta_{ij}\right)$, as previously proposed by Rotta (1951) and adopted by Hanjalic and Launder (1972). The second pressure-strain correlation term, $\phi_{ij,2}$, was proposed based on its exact expression for homogeneous flows where it is equal to the product of the mean strain rate and a fourth order tensor which then needs to be modelled. The fourth order tensor modelling was based on some symmetry and mass conservation constraints which led to a linear combination of the Reynolds stresses. The production and destruction terms in the ε equation were kept as in the Two Equation model, multiplied by their constants $c_{\varepsilon 1}$ and

$c_{\varepsilon 2}$ respectively, and the diffusion term was set to $c_{\varepsilon}\frac{\partial}{\partial x_k}\left(\frac{k}{\varepsilon}\overline{u_k u_l}\frac{\partial \varepsilon}{\partial x_l}\right)$ by analysing the exact transport equation for the diffusion of dissipation in the vicinity of a wall and in boundary layer flows.

Hanjalic and Launder (1972) simplified their model by applying it in a boundary layer flow, where only one transport equation was solved for the Reynolds shear stress, $\overline{u_1 u_2}$, and a second transport equation solved for half of the normal stresses summation which is the turbulent kinetic energy. The constants of the model were determined by considering homogeneous shear flows, grid decaying turbulence, the constant stress layer adjacent to a wall and computer optimization. The simplified version of the model was applied to several flows, including a fully developed asymmetrically ribbed flow in a plane channel, a symmetric annulus with internal diameter much smaller than the external tube diameter, a fully developed flow in an asymmetric annulus with a roughened core tube, a boundary layer developing in a uniform free stream, a plane wall jet, a plane jet in stagnant surroundings and a plane mixing layer, all of them at high Reynolds numbers, to fit the model's assumptions. As a whole, the model provided good velocity, kinetic energy and stresses predictions, but failed to capture the correct shear stress level and peak for the jet flows.

Launder et al. (1975) extended Hanjalic and Launder's (1972) work in order to improve the shear stress predictions. Initially, the authors kept the same expressions for the pressure-strain, diffusion and dissipation terms, but changed the original constants' values by reference to a homogeneous shear flow. A simplified model for $\phi_{ij,2}$, the second pressure-strain term, was also deduced from isotropic turbulence for comparison purposes. Near-wall flows were then considered and these indicated the necessity of an additional near-wall term to be accounted for in the pressure strain correlation. As a result, this term now became a combination of three parts: the two already considered, standing for turbulent-turbulent and turbulent-mean strain rate interactions, and a third for wall reflection: $\phi_{ij} = \phi_{ij,1} + \phi_{ij,2} + \phi_{ij,w}$. The constants of the latter part were determined by applying the turbulence model in a near-wall turbulent flow and comparing the results with experimental data. The eddy dissipation transport equation was also kept in the form proposed by Hanjalic and Launder (1972), but the constants were re-evaluated, by considering more experimental results. The remaining constants were determined by computer optimization. Both this simpler form of the model and the earlier form of Hanjalic and Launder (1972) were tested for a nearly homogeneous shear flow, a plane-strain distortion, an axisymmetric contraction, a plane mixing layer, a plane jet in stagnant surroundings, a plane jet in moving stream, a wake behind a thin flat plate, a symmetric plane channel flow, an asymmetric channel flow and a high-Reynolds-number flat plate boundary layer. In general, the complete version of the model performed well and better than the simplified one, although agreement with experimental data was not perfect. Despite this, the resulting turbulence model, which is usually referred to as the LRR model, has become one of the most widely used RST model.

Gibson and Launder (1978) started from Launder et al.'s (1975) simplified version and a previous work of both authors (Gibson and Launder, 1976) regarding buoyant effects in gravitational affected flows, in order to improve prediction of both atmospheric boundary

layers, which are ground affected, and free shear flows. The only term which was remodelled was the pressure-strain correlation, whose starting point was Launder et al.'s (1975) simplified version as already mentioned. In order to take into account wall proximity effects, the authors borrowed from Shir (1973) a proposed correction, $\phi'_{ij,1}$, to be added to $\phi_{ij,1}$, the first pressure-strain correlation term, and an analogous expression was derived, $\phi'_{ij,2}$, to be added as a correction to the second pressure-strain correlation term, $\phi_{ij,2}$. These two modelled correction terms, $\phi'_{ij,1}$ and $\phi'_{ij,2}$, depend on the unit vector and distance normal to the wall. Making an analogy to the LRR model, one could say that the new pressure-strain wall reflection part became: $\phi_{ij,w} = \phi'_{ij,1} + \phi'_{ij,2}$. The four constants associated with each one of the four pressure correction modelling terms ($\phi_{ij,1}$, $\phi_{ij,2}$, $\phi'_{ij,1}$ and $\phi'_{ij,2}$) were determined by applying the model to some simplified flows such as isotropic turbulence, free shear flows and near-wall turbulence. As one might expect, this turbulence model was also designed to take into account heat transfer and buoyancy. However, as this literature survey focuses only on momentum balance for incompressible Newtonian flows, those parts will not be discussed. The two target flows (atmospheric boundary layers and free shear flows) were used to validate the model which performed satisfactorily well for both flows.

Speziale et al. (1991) developed an RST model also for homogeneous high-Reynolds-number flows, considering local isotropy, and then only needing to model the pressure-strain correlation. The main difference between this model and the previous ones lies in a non-linear (more specifically quadratic) expression for the second term in the pressure-strain correlation, argued by the authors to not be much more complex than the previous RST models. Speziale et al. (1991) presented the pressure strain correlation no longer as the sum of two parts ($\phi_{ij,1}$ and $\phi_{ij,2}$), but as the most general expression this term could have in order to satisfy invariance when subjected to coordinate transformations. In order to satisfy this physical constraint, the Reynolds stress transport equation had Coriolis terms added. The Reynolds stress and eddy dissipation transport equations were derived for a plane homogeneous turbulence where the non trivial equilibrium solutions were found and used to reduce (from the general expression proposed) the pressure-strain correlation so that it fitted the same equilibrium state. The constants of the model were determined by computer optimization under return to isotropy, homogeneously strained turbulent flows starting from an isotropic state obeying the rapid distortion theory, homogeneous shear flows, rotating shear flows and decay of isotropic turbulence consistency problems.

Speziale et al. (1991) pointed out that their turbulence model does not satisfy certain extreme physical constraints. However, they argued that those constraints require higher orders (higher than quadratic) for the pressure-strain correlation, implying much higher computational efforts and leading sometimes to bad predictions. The model was named SSG and validated for four homogeneous turbulent flows (homogeneous turbulent flow, rotating shear flow, homogeneous plane strain turbulence and axisymmetric contraction and expansion in homogeneous turbulence) by comparing its results with experiments and the LRR model of Launder et al. (1975). In general, the SSG model performed better than the LRR, however deficiencies in capturing the correct time evolution of the turbulent kinetic energy in the

rotating and axisymmetric contraction and expansion flows remained. Analysing the range of solutions for the equilibrium state of rotating shear flows, the authors came to the conclusion that expressing the pressure-strain correlation from the Poisson equation solution for the fluctuating pressure p necessarily led to the above incorrect prediction. Despite this, the SSG model has also become a very popular RST model, often providing reasonable results, particularly for shear flows.

In contrast to the above RST models, Hanjalic et al. (1997) developed a Reynolds stress model for low-Reynolds-number flows, trying to avoid the use of wall functions which would be required with the previous described RST models which were designed only for high-Reynolds-number flows. As a result, their modelling of the redistribution, diffusion and dissipation terms in equation (2.24) assumed new features. To account for near-wall effects, the authors identified what they called the "flatness" parameters, A and E, representing the large and small scale behaviours, respectively, where $A = 1 - \frac{9}{8}(A_2 - A_3)$ and $E = 1 - \frac{9}{8}(E_2 - E_3)$. $A_2 = a_{ij}a_{ij}$ and $A_3 = a_{ij}a_{jk}a_{ki}$ are the turbulent stress tensor invariants, $E_2 = e_{ij}e_{ij}$ and $E_3 = e_{ij}e_{jk}e_{ki}$ are the dissipation rate tensor invariants, $a_{ij} = \frac{\overline{u_i u_j}}{k} - \frac{2}{3}\delta_{ij}$ is the dimensionless Reynolds stress anisotropy tensor, already mentioned, and $e_{ij} = \frac{\varepsilon_{ij}}{\varepsilon} - \frac{2}{3}\delta_{ij}$ is the dimensionless dissipation rate anisotropy tensor. Hanjalic et al. (1997) pointed out that A and E are appropriate parameters to be used to model proximity to the wall effects, since they behave differently through the flow domain. Besides that, these parameters could also represent the transition from 2 to 3 component turbulence, since for the former they are zero (and for the latter they are not) and they take the value of unity in isotropic turbulence.

With regard to the Reynolds stress transport equations, Hanjalic et al. (1997) proposed for the diffusion term a simple form of that proposed by Launder et al. (1975). The dissipation term was not treated as $\varepsilon_{ij} = \frac{2}{3}\varepsilon\delta_{ij}$ since that form is only accurate in high-Reynolds-number regions. The dissipation term was thus expressed depending upon a "blending" function that switches ε_{ij} from the above isotropic high-Reynolds-number form to another proposed by Hanjalic and Jakirlic (1993) in the near-wall region which depends on the unit vector normal to the wall, the turbulent Reynolds number and the Reynolds stresses themselves. Finally, the pressure-strain correlation was modelled by assuming $\phi_{ij} = \phi_{ij,1} + \phi_{ij,2} + \phi^w_{ij,1} + \phi^w_{ij,2}$, a general form adopted by Gibson and Launder (1978). Indeed, the form of the terms were actually the same as in the latter's work, but damping functions were introduced to the wall reflection terms and the constants of all terms were changed, being expressed in terms of the flatness parameters. The eddy dissipation transport equation was adopted as in Launder and Hanjalic (1976) (which is the same form of that proposed by Hanjalic and Launder (1972) with different constants and an extra term to account for the mean-field generation process in the exact eddy dissipation transport equation) with different constants and two new added terms. The first of these added terms, which for numerical convenience the authors did not activate in their own calculation, claiming it would be negligible in near-wall equilibrium flows, was intended to predict rotational flows effects; and the second stood for a length scale correction which does not depend on the distance to the wall as the Yap-correction does.

Hanjalic et al. (1997) applied their low-Reynolds-number RST model to several flows

(channel flows, oscillating and zero, adverse and favorable pressure gradient boundary layers, by-pass transition, 3D boundary layer under streamwise acceleration and transverse shear, developed and developing Couette flows at various pressure gradients in plane and wavy fixed wall, backward facing step flow, pipe expansion and flow over a surface mounted fence and rib) and concluded that, despite some imperfections in the prediction of transversal shear boundary layer and flow over a mounted fence, they could reach an overall good agreement with experimental and DNS data.

Concluding this section about RST models, one can note that the main features of this group of turbulence models were described and some representative models were discussed. As a whole, more high-Reynolds-number RST models than low-Reynolds-number approaches are found in the literature. With RST models, some complex turbulent flows which are poorly predicted by two equation models can be better represented, but they are significantly more computationally expensive than Two Equation models, which may be a barrier to their wider implementation.

2.5 Algebraic Reynolds Stress Models

The Algebraic Reynolds Stress models, which will be abbreviated as ARS models, emerged as an attempt to keep the RST models' features, but with less computational efforts involved. In order to do that, the differential transport equations for each of the Reynolds stresses were transformed into algebraic equations by either neglecting or approximating their transport and convective parts. Hence, for flows where these terms can actually be approximated like that, the ARS models should provide similar predictions to those from the full RST models, but economizing on time and computational cost. The following paragraphs will provide some examples of ARS models and their main ideas.

Pope (1975) was one of the pioneers to introduce an ARS model. Firstly, he proposed a general expression for the dimensionless Reynolds stress anisotropy tensor, $a_{ij} = \frac{\overline{u_i u_j}}{k} - \frac{2}{3}\delta_{ij}$ as a function of the dimensionless strain rate and vorticity tensors, $\tilde{s}_{ij} = \frac{1}{2}\frac{k}{\varepsilon}\left(\frac{\partial U_i}{\partial x_j} + \frac{\partial U_j}{\partial x_i}\right)$ and $\tilde{w}_{ij} = \frac{1}{2}\frac{k}{\varepsilon}\left(\frac{\partial U_i}{\partial x_j} - \frac{\partial U_j}{\partial x_i}\right)$, in the form of an infinite tensor polynomial which was transformed into a finite polynomial by the Cayley-Hamilton theorem and reduced by the fact that a_{ij} is symmetric and has zero trace. The general expression became:

$$\boldsymbol{a} = \sum_{\lambda} G^{\lambda} \boldsymbol{T}^{\lambda} \qquad \Rightarrow \qquad \overline{u_i u_j} = \frac{2}{3} k \delta_{ij} + k \sum_{\lambda} G^{\lambda} \boldsymbol{T}^{\lambda}_{ij} \tag{2.27}$$

where $\boldsymbol{T}^{\lambda}$ are the linearly, independent, symmetric zero trace tensors and G^{λ} are the function coefficients. For 2D flows, λ varies from 0 to 2, with the tensors expressed as:

$$\boldsymbol{T}^0 = \frac{1}{3}\boldsymbol{I}_3 - \frac{1}{2}\boldsymbol{I}_2 \qquad \boldsymbol{T}^1 = \boldsymbol{s} \qquad \boldsymbol{T}^2 = \boldsymbol{sw} - \boldsymbol{ws} \tag{2.28}$$

For 3D flows, λ varies from 1 to 10, with the base tensors being the following:

$$\begin{gathered}
\boldsymbol{T}^1 = \boldsymbol{s} \qquad \boldsymbol{T}^2 = \boldsymbol{sw} - \boldsymbol{ws} \qquad \boldsymbol{T}^3 = \boldsymbol{s}^2 - \frac{1}{3}\boldsymbol{I}\{\boldsymbol{s}^2\} \qquad \boldsymbol{T}^4 = \boldsymbol{w}^2 - \frac{1}{3}\boldsymbol{I}\{\boldsymbol{w}^2\} \\
\boldsymbol{T}^5 = \boldsymbol{ws}^2 - \boldsymbol{s}^2\boldsymbol{w} \qquad \boldsymbol{T}^6 = \boldsymbol{w}^2\boldsymbol{s} + \boldsymbol{sw}^2 - \frac{2}{3}\boldsymbol{I}\{\boldsymbol{sw}^2\} \qquad \boldsymbol{T}^7 = \boldsymbol{wsw}^2 - \boldsymbol{w}^2\boldsymbol{sw} \\
\boldsymbol{T}^8 = \boldsymbol{sws}^2 - \boldsymbol{s}^2\boldsymbol{ws} \qquad \boldsymbol{T}^9 = \boldsymbol{w}^2\boldsymbol{s}^2 + \boldsymbol{s}^2\boldsymbol{w}^2 - \frac{2}{3}\boldsymbol{I}\{\boldsymbol{s}^2\boldsymbol{w}^2\} \qquad \boldsymbol{T}^{10} = \boldsymbol{ws}^2\boldsymbol{w}^2 - \boldsymbol{w}^2\boldsymbol{s}^2\boldsymbol{w}
\end{gathered} \tag{2.29}$$

In both equations (2.28) and (2.29) a simplified notation is used, where $\boldsymbol{s}^2 = \tilde{s}_{ik}\tilde{s}_{kj}$, $\boldsymbol{sw} = \tilde{s}_{ik}\tilde{w}_{kj}$, $\boldsymbol{swws} = \tilde{s}_{ik}\tilde{w}_{kl}\tilde{s}_{lm}\tilde{s}_{mj}$, etc, $\{\cdot\}$ stands for the non zero independent invariants and $\boldsymbol{I_n}$ stands for the Kronecker delta of order n.

Commenting that the 3D system would be intractable, Pope (1975) determined the G coefficients only for 2D flows. To do so, he approximated the transport terms of the Reynolds stress transport equations of Launder et al. (1975), rewriting them in his same notation and by analogy arrived at an expression for the coefficients G^0, G^1 and G^2. As a result, the turbulent viscosity constant c_μ became a function of the strain rate and vorticity invariants which was noted as an important feature of the model. The model was only validated for a shear flow where $U = U(y)$ in order to highlight the difference between the proposed model and a linear eddy viscosity model in predicting the normal Reynolds stresses.

Gatski and Speziale (1993) were one of those who tried to extend Pope's (1975) work to 3D flows. They simplified the Navier-Stokes equations to a homogeneous turbulent flow in equilibrium, splitting the dissipation rate tensor into its isotropic and deviatoric parts. The latter was included in the pressure-strain correlation whose general form was represented as in Speziale et al. (1991). Algebraic manipulations were carried out to express the resultant governing equation in a dimensionless form whose solution was exactly the same as the form proposed by Pope (1975), equation (2.27), but with the dimensionless rate strain and vorticity tensors, $\boldsymbol{s}$ and $\boldsymbol{w}$, rescaled as functions of the coefficients of the pressure-strain general correlation. The linearly independent symmetric zero trace tensors, $\boldsymbol{T}^\lambda_{ij}$, had been already defined by Pope (1975), but the coefficients G^λ remained undetermined for λ higher than 3. With the aid of symbolic computational software, Gatski and Speziale (1993) obtained general expressions for all G^λ, hence extending the ARS model for a 3D flow. In order to check the result, the model was simplified to a 2D form, exactly matching Pope's (1975) work. The 3D version was evaluated for complex non equilibrium flows where a possibility was identified for a singular behaviour, explaining the instability and non convergence reported by others using these types of algebraic model. To solve this problem, Gatski and Speziale (1993) regularized the 2D simplified version of their model by a Padé approximation, since the 3D regularization would lead to intractable expressions. The constants of the regularized 2D model were determined based on the SSG model of Speziale et al. (1991) for homogeneous turbulent flows. The algebraic system was coupled to transport equations for the turbulent kinetic energy and eddy dissipation rate, in their standard high-Reynolds-number $k-\varepsilon$ model

forms, and the closed system including the Navier Stokes and Continuity equations was applied to some non trivial cases, including a homogeneous shear flow in a rotating frame and fully developed turbulent channel flow subjected to a spanwise rotation with constant angular velocity. The results were compared to experiments and/or DNS data, the SSG model and the standard $k-\varepsilon$ model. The outcome was that the ARS model performed similarly to the SSG RST model and both presented far better predictions than the $k-\varepsilon$ model. As a result, a new 2D ARS model was developed, but promising more stability for non equilibrium flows.

Taulbee (1992) proposed a rather different ARS model which was actually questioned by Gatski and Speziale (1993). Taulbee (1992) proposed an ARS model by writing a transport equation for the quantity $\frac{D}{Dt}\left(\frac{a_{ij}}{\tau\sigma}\right)$, where a_{ij} is the dimensionless stress anisotropy tensor, $\tau = \frac{k}{\varepsilon}$ is the turbulent time scale and $\sigma = \sqrt{S_{kl}S_{lk}}$, and setting $\frac{D}{Dt}\left(\frac{a_{ij}}{\tau\sigma}\right)$ to zero. Taulbee's objective was to account for convective effects and try to reproduce a general RST model's predictions for uniform shear flow. This proposed ARS model was written in a way to fit Pope's (1975) general 2D flow solution and after some simplifications, a system for 3D flows was determined. Besides the uniform shear flow, an uniform irrotational strain flow was also simulated and the results compared with those of an RST model. The improved ARS model fairly well reproduced the predictions of the latter. However, it might be commented that no applications for 3D flows were presented.

With regard to the ARS models presented, one can notice that a classical work (Pope, 1975) was described and two more recent works were discussed. As expected, both mentioned the former's work which became a reference for ARS models. Since the ARS models specify algebraic expressions for the Reynolds stresses to be solved together with the Navier-Stokes and Continuity equations, and usually one/two more transport equations, this group of turbulence models could be included as NLEV models. Indeed, the ARS models are NLEV models and the choice of presenting them separately from the latter's section was to focus on the different processes which lead them to be obtained, attempting to obey a logical order.

This section marks the end of the most common RANS turbulence model groups that one may find in the literature. The next section will be dedicated to the Multiple Time Scale models which, despite not being that modern, have been receiving more attention in the last few decades and may be the future for improving prediction of complex non equilibrium flows.

2.6 Multiple Time Scale Models

Despite the modelling improvements noted above, further refinements are still required to predict correctly a wide range of complex non equilibrium flows. In particular, flows submitted to rapid changes remain very difficult to simulate accurately with existing models. Such flows include those submitted to sudden expansions or contractions, flows where turbulence generation is suddenly interrupted (Hanjalic et al., 1980) or, the opposite, when turbulence is generated all of a sudden (Launder et al., 1984). Many of these flows feature a transition period or region in which it may not be appropriate to characterize the turbulence by a single

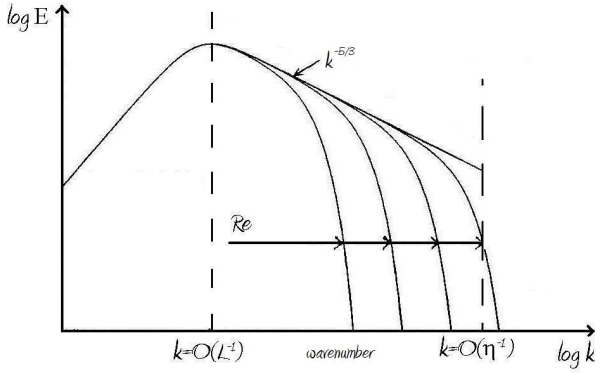

Figure 2.1: Turbulent Kinetic Energy Spectrum

length or time scale.

The total turbulent kinetic energy may be interpreted as the sum of the turbulent kinetic energy associated with each length scale characteristic of a flow, mathematically represented as the integral of the kinetic energy over the wavenumber range. The graphical representation of this process is called the energy spectrum which is illustrated in Figure 2.1. The wavenumber may be interpreted as the inverse of the length scale (Ferziger and Peric, 2002) and thus one may identify a wavenumber below which the mean strain plays a role and therefore provides turbulence production, and a wavenumber above which viscous effects dominate and the small eddies are immediately dissipated into heat. The former characterizes the energy containing range and the latter, the dissipation range. An intermediate range may or may not exist, depending upon the Reynolds number (Gatski et al., 1996; Mathieu and Scott, 2000). If it exists, it is called the inertial range and is characterized by a power law also indicated in Figure 2.1, and the higher the Reynolds number, the longer its domain. The wavenumber which limits the upper end of the energy containing range is of the order of magnitude of the inverse of the flow geometry (L in Figure 2.1) and the wavenumber associated with the onset of dissipation range is of the order of magnitude of the inverse of the Kolmogorov length scale (η in Figure 2.1). From this description, one may notice that distinct parts of the energy spectrum are responsible for different processes and a single time scale may not be representative enough to fully characterize the turbulence.

In order to account in a more realistic way for the physics behind the turbulent kinetic energy spectrum, and improve prediction of flows which would be strongly affected by it, the Multiple-Time-Scale turbulence models (MTS models) were developed. These, perhaps introduced by Hanjalic et al. (1980), usually divide the energy spectrum into three parts: production, transfer and dissipation regions. For each part, there would be a representative "slice" of the turbulent kinetic energy whose summation would then be the total kinetic energy. Considering that the turbulent kinetic energy is immediately dissipated when it enters the dissipation zone, there would be effectively only two turbulent kinetic energy partitions: the production, k_P, and transfer, k_T, ranges, where $k = k_P + k_T$. The transfer rate from production to transfer range is then ε_P and ε_T is the transfer rate from transfer to

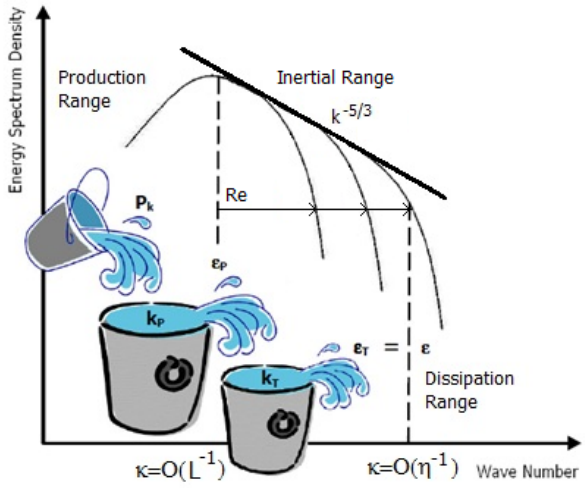

Figure 2.2: Turbulent Kinetic Energy Spectrum as proposed by Hanjalic et al. (1980)

dissipation range. Since the assumption has already been made that energy is immediately dissipated in the dissipation range, it follows that $\varepsilon_T = \varepsilon$, which thus represents spectral equilibrium between the transfer and dissipation zones. A generic such MTS model can then be expected to solve transport equations for k_P, k_T, ε_P and ε_T. The spectrum sketch for the framework just described is presented in Figure 2.2.

The main features, assumptions and results of the MTS models will be discussed in the following paragraphs through a literature review. The equations below are written in a way to match most MTS models which will be described, not comprising any particular turbulence model as a whole.

$$\frac{Dk_P}{Dt} = P_k - \varepsilon_P + D_{k_P} \tag{2.30}$$

$$\frac{Dk_T}{Dt} = \varepsilon_P - \varepsilon_T + D_{k_T} + \Pi_k \tag{2.31}$$

$$\frac{D\varepsilon_P}{Dt} = C_{P1} f_{P1} P_k \frac{\varepsilon_P}{k_P} - C_{P2} f_{P2} \frac{\varepsilon_P^2}{k_P} + C_{P3} \frac{P_k^2}{k_P} + C_{P4} W \varepsilon_P + D_{\varepsilon_P} + C'_{P1} P_{\varepsilon_P} \tag{2.32}$$

$$\frac{D\varepsilon_T}{Dt} = C_{T1} f_{T1} \frac{\varepsilon_P \varepsilon_T}{k_T} - C_{T2} f_{T2} \frac{\varepsilon_T^2}{k_T} + C_{T3} \frac{\varepsilon_P^2}{k_T} + C_{T4} W \varepsilon_T + D_{\varepsilon_T} + \Pi_\varepsilon \tag{2.33}$$

In Hanjalic et al.'s (1980) work, the transport equations for the turbulent kinetic energy contributions were defined as in equations (2.30) and (2.31) and the transfer and dissipation rates were modelled as in equations (2.32) and (2.33). No damping functions were considered in order to account for low-Reynolds-number flows or near-wall effects. Regarding diffusion, D_{k_P}, D_{k_T}, D_{ε_P} and D_{ε_T} were initially modelled as in the RST models with k and ε replaced

by k_P and ε_P, respectively, however further simplifications suggested the simpler gradient diffusion usually used in eddy-viscosity models. The pressure diffusion terms, Π_k and Π_ε, were neglected. Hanjalic et al. (1980) thus proposed a simple and basic type of MTS model where $C_{P3} = C_{P4} = C_{T3} = C_{T4} = 0$. However, they did make the generation of ε_P sensitive to different types of mean straining via the $P_{\varepsilon_P} = k_P \frac{\partial U_l}{\partial x_m} \frac{\partial U_i}{\partial x_j} \epsilon_{lmk} \epsilon_{ijk}$ term. The transport equations' coefficients were determined after analysing grid decaying turbulence in the limit of its equilibrium and optimizing their values for certain test flow cases, taking into account that both C_{P1} and C_{P2} and C_{T1} and C_{T2} of the ε_P and ε_T equations should not be constants at the same time otherwise it would not be possible to account for the interaction between large and small eddies.

The test flow cases used to validate Hanjalic et al.'s (1980) model were: decaying grid turbulence passed through a sudden contraction, axisymmetric and plane turbulent jets in stagnant surroundings and zero and adverse pressure gradient boundary layer flows. For these flows, the Reynolds stresses were calculated as $\overline{uv} = -0.10k \frac{k_P}{\varepsilon_P} \frac{\partial U}{\partial y}$ and $(\overline{u}^2 - \overline{v}^2) = \frac{k}{3}$, following the general Boussinesq's eddy viscosity concept. The results indicated better predictions of the MTS model when compared to the RS model of Launder et al. (1975) and the standard $k - \varepsilon$ model. The authors also proposed a transport equation for the Reynolds stresses consistent with the partitioned energy spectrum, basically replacing the ratio $\frac{\varepsilon}{k}$ by $\frac{\varepsilon_P}{k_P}$ in the RST model of Launder et al. (1975), however this model was not tested. The authors concluded that MTS models possess the potential to account for non equilibrium effects which the single scale models do not.

Kim and Chen (1989) also developed an MTS model based on Hanjalic et al.'s (1980) assumptions. The energy spectrum was interpreted in the same way, meaning that transport equations for k_P, k_T, ε_P and ε_T were required. The transport equations for k_P and k_T follow equations (2.30) and (2.31), but with Π_k set to zero, and the transport equations for ε_P and ε_T now include the terms multiplied by C_{P3} and C_{T3} respectively, which were defined as variable energy transfer functions. These terms act to increase the production rates of ε_P and ε_T and were designed to have a similar effect to the dependence of Hanjalic et al.'s coefficients on the ratios $\frac{k_P}{k_T}$ and $\frac{\varepsilon_P}{\varepsilon_T}$. Consequently, the model coefficients of Kim and Chen (1989) assumed constant values which were determined by reference to fully developed channel flow and a plane jet exhausting into a moving stream when equilibrium, asymptotic growth rate and asymptotic decay rate were reached. The model followed an eddy viscosity formulation, where c_μ was taken as $0.09 \frac{\varepsilon_T}{\varepsilon_P}$ in order to account for its dependence on the ratio between the turbulent kinetic energy production and dissipation rates. The model was tested for several cases and the ones presented in the paper were: wall jet issuing into moving stream, weakly coupled wake-boundary-layer interaction flow, turbulent backward facing step and confined coaxial swirling jet. All flows were solved by applying a wall function. The first two flow predictions were compared with experiments and an ARS model, indicating the MTS model's performance to be slightly better than the latter, although both reached good agreement with experimental data. The last two flows predictions were compared to experiments and the standard $k - \varepsilon$ model. As a whole, the MTS model followed the correct

trends indicated by the experimental data, yielding better performance than the $k-\varepsilon$ model, but still with no perfect match to measurements. Despite this, the authors concluded that the MTS model improved predictions of complex flows owing to its capability of modelling the cascade process of the turbulent kinetic energy spectrum.

Kim (1991) expanded Kim and Chen's (1989) MTS model, amongst other things incorporating a near-wall treatment. For this, the transport equations for k_P and k_T were solved over the whole domain whereas the transport equations for ε_P and ε_T were only solved for the regions far from the wall. In the near-wall region, ε_P and ε_T were calculated as $\varepsilon_P = \varepsilon_T = \frac{\varepsilon_1}{1-e^{-c_\mu^{3/2} Re_t/2\kappa^2}}$, where $\varepsilon_1 = \frac{c_\mu^{3/4} k^{3/2}}{\kappa y}$ and $Re_t = \frac{k^2}{\nu \varepsilon_1}$. In order to account for the near-wall region, the standard eddy viscosity expression was applied together with a damping function. This partial low-Reynolds-number MTS model (as named by the authors) was then applied to a divergent channel flow with a backward facing step. Predictions were performed for zero and six degrees of deflection of the channel top wall. Results were compared to experimental data as well as an ARS model and the standard $k-\varepsilon$ model. As a whole, the MTS model presented the better results, especially for the reattachment locations, however a perfect match with experiments was not reached. Again, the authors noted the improvement provided by the MTS model.

Kim and Benson (1992) also expanded the application of Kim and Chen's (1989) MTS model to a circular jet impinging in an uniform crossflow where a transport equation for the concentration was also included. The latter was modelled taking into account only convective and diffusive effects. The remaining equations were kept exactly as suggested by Kim and Chen (1989). The authors reached very good agreement with experimental data, reinforcing the capability of the MTS model in predicting strongly non equilibrium flows.

Chen and Guo (1991) proposed another MTS model for high-Reynolds-number flows. Based on those of Hanjalic et al. (1980) and Kim and Chen's (1989) work the authors developed an MTS model to account for rotational effects, by introducing the mean vorticity in the transport equations for ε_P and ε_T. The model's constants were determined by reducing the system of equations to consider the asymptotic decay rate of simple flows such as homogeneous grid turbulence. The transport equations assumed the general form expressed by equations (2.30)-(2.33) where $C_{P3} = C_{T3} = 0$ and C_{P4} and C_{T4} are different from zero. The Reynolds stresses were calculated in two different ways: first from the standard isotropic eddy viscosity formulation and secondly by an algebraic stress formulation in order to account for stress anisotropy. The latter was devised from an RST model, where the pressure-strain correlation was modelled similarly to Launder et al.'s (1975) simplified version and its constants were set as functions of a wall correction term which then depended upon the distance to the wall. The models were validated for grid generated rotating flows, 2D backward facing step flow and axisymmteric pipe expansion flow. The results were compared with experiments and an ARS $k-\varepsilon$ model as well as with the standard $k-\varepsilon$. The MTS model based on the ARS model presented an overall better result, as expected. The authors also argued that the computing time and storage costs were relatively low compared to the standard $k-\varepsilon$ model,

indicating one more positive feature of the MTS models.

Duncan et al. (1993) proposed an MTS model aiming to achieve good predictions in different flow situations without any extra term in ε_P and/or ε_T equations (which means C_{P3}, C_{P4}, C_{T3}, C_{T4}, C'_{P1}, Π_k and Π_ε in equations 2.30 to 2.33 to be all zero). In order to do that, Duncan et al. (1993) made C_{P1} and C_{T1} vary with two parameters: $\alpha = P_k/\varepsilon_P$ and $\beta = \varepsilon_P/\varepsilon_T$. The former was assumed to be 2.2 and the latter 1.05, both values based on homogeneous shear flow experiments which indicate that α/β should be near 2. C_{P2} was set as a constant and C_{T2} was made to vary with k_P/k_T and C_{P1}, both sink terms' coefficients being defined based on homogeneous decaying grid turbulence flows. This model was designed as a linear-eddy-viscosity model, the eddy viscosity being used as by Kim and Chen (1989), $\nu_t = c_\mu k^2/\varepsilon_P$. The model was assessed in planar mixing layers, planar jet and round jet flows and the results were compared to experiments and predictions of the standard $k-\varepsilon$ model and both models from Hanjalic et al. (1980) and Kim and Chen (1989). Reasonable results were achieved for all case, being worth mentioning that in the planar mixing layer and planar jet cases, the proposed model performed similarly to the standard $k-\varepsilon$ model, still better than the other two MTS models and in the round jet case, the proposed model performed similarly to Kim and Chen's model.

Nagano et al. (1997) later proposed a low-Reynolds-number MTS model for which all the damping functions f_{P1}, f_{P2}, f_{T1} and f_{T2} in equations (2.30)-(2.33) were applied. The turbulent kinetic energy spectrum partition adopted was the same Hanjalic et al. (1980) proposed. The authors did not take into consideration the variable transfer functions proposed by Kim and Chen (1989) nor the vorticity dependence suggested by Chen and Guo (1991), however pressure-diffusion terms were included in both k_T and ε_T transport equations. The diffusion terms for all transport equations (2.30)-(2.33) were defined as in the LRN single scale models, but using the appropriate partitioned variable, and a damping function was introduced to account for the increase of diffusion near the wall. The model constants were determined by considering the log law region of near-wall turbulent flow and homogeneous decaying flow. The main damping functions f_{P1}, f_{P2}, f_{T1} and f_{T2} which appear in equations (2.30)-(2.33) were determined in order to avoid divergence near the wall, and these were formulated as functions of the non-dimensional distance to the wall, y^*, defined not in terms of the friction velocity as usual, but in terms of the Kolmogorov velocity scale $u_\varepsilon = (\nu\varepsilon_T)^{0.25}$. The pressure-diffusion terms were determined by analysing k_P, k_T, ε_P and ε_T near the wall after expressing them as Taylor series expansions around $y = 0$. The model was validated for the following flows: homogeneous decaying flow, homogeneous shear flow, fully developed channel flow and turbulent boundary layers with zero, favorable and adverse pressure gradients. In general, the Reynolds stresses were calculated using the standard eddy viscosity formulation with a damping function to satisfy the near-wall behaviour, however for the adverse pressure gradient boundary layer flow they were calculated by an ARS model due to the activation of the irrotational straining effect by the P_{ε_P} term. The model performed in a fairly satisfactory way compared to experiments and other single scale turbulence models.

Rubinstein (2000) proposed a MTS approach based on spectrum integration which intended to make inertial range energy transfer different from energy dissipation, and at the same time to allow the MTS model to reduce to a STS model in self-similar flows such as decaying grid turbulence flows. In essence, that is already what the above mentioned MTS models do, since all solve a transport equation for ε_P, the inertial range energy transfer, and ε_T, the energy dissipation and all are intended to satisfy asymptotic states of self-similar flows. The model of Hanjalic et al. (1980) was indeed evaluated and confirmed to satisfy the above requirements. The main difference in Rubinstein's model lies in the equations for ε_P and ε_T which assume totally different forms than those of equations 2.32 and 2.33. All equations were derived for homogeneous flows where diffusion could be neglected. The ε_P and ε_T equations were derived using the method of moments, the order -1 being indicated as the more appropriate. In this method both sides of the spectrum equation was divided by κ^{order}, κ being the wavelength, and then integrated. Although this model was identified as more appropriate for the derivation of ε_P and ε_T equations, it presented deficiencies in establishing the sink terms of these equations. The proposed model was thus applied in a grid decaying turbulence flow using two different initial conditions. The results were not compared to experiments nor other turbulence models, but have shown the capability of predicting different energy decay rates. The author argued that this difference in the prediction of the energy decay rates for different initial conditions would not be possible to simulate with single-time-scale models.

Stawiarski and Hanjalic (2005) proposed a three equation MTS model. Instead of solving one transport equation for k_P and one for k_T, they proposed to solve only an equation for k, the total turbulent kinetic energy, which would depend only on the large-scale quantities, P_k, the conventional turbulent kinetic energy production being its source term and ε_P, the energy transfer flux, being its sink term. A transport equation for ε_T, the turbulent kinetic energy dissipation rate, was built, as a result of the spectrum integration method, by including both source terms from equations 2.32 and 2.33, but replacing k_P and k_T by k, and the sink term being the same sink term of equation 2.33, also with k_T replaced by k. A third equation was then derived for a generic variable $\phi = k^m \varepsilon_P^n \varepsilon_T^q$ which was supposed to model a large scale quantity, thus meaning that ε_T should not appear in its transport equation according to the authors. Asymptotic analysis were carried out for grid decaying turbulence, near-wall equilibrium and homogeneous shear flows and expressions were obtained for the model's coefficients as functions of the exponents of the generic variable ϕ. The authors thus presented the final results for two large scale variables: the spectral transfer flux $\phi = \varepsilon_P$ (m=0, n=1, q=0) and the so-called energy-length product kL (m=5/2, n=-1, q=0), $L = k^{3/2}/\varepsilon_P$ being an arbitrary length scale. In order to close the system of equations regarding the model's coefficients, some tests were carried out in order to find appropriate values for quantities such as k_P/k_T for grid decaying turbulence and near-wall equilibrium and $\alpha = P_k/\varepsilon_T$, $\beta = \varepsilon_P/\varepsilon_T$ and $\gamma = \frac{\varepsilon_T}{k}\frac{\partial k}{\partial \varepsilon_T}$ in homogeneous shear flows. Both versions of the proposed model (the one solving for ε_P and the one solving for kL) were then applied in normally strained flows and the version where kL was the large scale variable was identified as not providing the expected

behaviour for ε_P and ε_T. Besides, further analysis led to conclude that this version presented unclear source-sink relations and that a single source and sink term as originally proposed were not enough to characterize the correct energy transfer flux. The authors then concluded that ε_P was the most appropriate variable to represent the large scales. A final version of the model was presented where k_P/k_T was taken to be 1 in grid decaying turbulence and 4.3 in near-wall equilibrium. The homogeneous shear flow parameters were taken as $\alpha = 1.5$ (as suggested by Kim and Chen (1989)), $\beta = 1.05$ (as proposed by Kim and Chen (1989) and Duncan et al. (1993)) and $\gamma = 0.82$ (in spite of calculations having indicated that the correct value would be $\gamma = 1$, the authors argued that any value between 0.82 and 1 would be satisfactory). The final version of the model with ε_P was then applied in other normally strained cases (where production was provided, not calculated) and homogeneous shear flows and all were in reasonable agreement with experiments.

All the above mentioned MTS models were based on linear-eddy-viscosity schemes. The next paragraphs will mention a few attempts to include multiple-time-scale approaches into Reynolds-stress-transport models.

A slightly different approach in terms of the partition variables was proposed by Wilcox (1988b), based on his work on the $k-\omega$ model (Wilcox, 1988a), although its underlying physics are similar to those presented above (Kim and Chen, 1989; Kim, 1991). This model consists of splitting the Reynolds stress tensor into its lower (t_{ij}) and upper (T_{ij}) partition contributions. The lower partition is the one defined to be isotropic, to contain most of the vorticity and to dissipate quickly into heat, while the upper partition is characterized by being mostly inviscid. As a result, transport equations for the turbulent kinetic energy, for the specific dissipation rate and for the upper partition stress tensor are required. The first two were taken as in equations (2.20) and (2.21) for the $k-\omega$ model, but with a term added to the ω equation to account for vorticity, and the stress tensor equations were represented as:

$$\frac{\partial T_{ij}}{\partial t} + \frac{\partial}{\partial x_k}(u_k T_{ij}) = -P_{ij} + E_{ij} \tag{2.34}$$

where P_{ij} and E_{ij} stand for the production and the exchange of energy among the mean, upper and lower partition energies, respectively. Most of the novel physical modelling assumptions of the multiscale scheme proposed by Wilcox (1988b) were introduced to E_{ij}, and these will be briefly described here. In order to define a formulation for E_{ij}, homogeneous decaying turbulence where mean velocity gradients are negligible and a zero pressure gradient boundary layer were examined. The main assumption of the model is to consider that the large eddies decay at the same scale as the overall turbulence (broadly equivalent to assuming spectral equilibrium for the transfer and dissipation zones in the previous MTS models). This idea was argued by Wilcox to be supported by large-eddy simulation results. This model was applied to five homogeneous turbulence cases (decay of isotropic turbulence, system rotation, return to isotropy, plane strain and uniform shear), to viscous sublayer and three boundary layer classes (incompressible zero, adverse and favorable pressure gradient boundary layers,

compressible boundary layers and unsteady boundary layers for zero frequency, low and high amplitude cases). The model proved to provide good predictions compared to experimental data, although perfect agreement with the latter was not reached. Overall, its performance could be considered quite satisfactory.

Stawiarski and Hanjalic (2002) proposed a simplified Reynolds stress transport multiple-time-scale model, where the transport equations for the Reynolds stresses were kept just as in single-time-scale models, but with the dissipation rate ε replaced by ε_P, the spectral energy flux, in the diffusion and pressure redistribution terms. The authors used a wave-number-weighted spectrum integration method to derive the transport equations for two turbulence-scaling variables which were initially chosen as the dissipation rate ε_T and the energy-length product kL. The latter's transport equation was further converted into a ε_P transport equation due to previous bad experience of the authors with the kL variable just as in Stawiarski and Hanjalic (2005). The ε_T resultant of the weighted spectrum integration was subjected to a few modifications in order to account for a different time-scale (the high Reynolds number time scale being considered as k/ε_P) as the local Reynolds number of the flow decreased, just as proposed by Durbin (1991). Besides, an extra production term arose from the spectrum integration procedure in the ε_T equation. As a result, the latter included a source term based on the turbulent kinetic energy production, similar to those in single-time-scale models, and a similar source term to that of equation 2.33, but with k_T replaced by k. The model's coefficients were determined by evaluating the asymptotic states of grid decaying turbulence, homogeneous shear flows and near-wall equilibrium. The model was then applied in two normally strained cases, where the stresses were not calculated by the model, but interpolated from experimental data, in a channel flow and in an unsteady backward facing step case. Good agreement with experiments was achieved for the normally strained and channel flows, but for the backward facing step flows, the authors themselves agreed more tunning and refinement were necessary. Besides that, the two source terms in the ε_T equation were highlighted as responsible for solving the drawback of other two scale models which have only one source term in the ε_T equation and tend to overpredict the turbulent kinetic energy in backward facing step flows.

Cadiou et al. (2004) extended Stawiarski and Hanjalic's 2002 work, by applying the wave-number-weighted spectrum integration method to derive an equation for the Reynolds stresses too. The integration method is more detailed in this work and the choice of ε_P instead of kL as a large-scale variable was kept just as in Stawiarski and Hanjalic (2002) and Stawiarski and Hanjalic (2005). Similar analysis for the choice of a variable time-scale were made and the final ε_T equation was kept just as in Stawiarski and Hanjalic (2002). The model's coefficients were determined through asymptotic analysis of decaying grid turbulence, homogeneous shear flows and near-wall equilibrium, however this time the ratio k_P/k_T in near wall equilibrium was taken as 3, slightly different from in other works of the authors (Stawiarski and Hanjalic (2002), Stawiarski and Hanjalic (2005)). The applicability of the proposed scheme was tested in normally strained flows, where the stresses were again not calculated, but interpolated

from experiments, channel flow, unsteady backward facing step and flow around a square-sectioned cylinder. The authors stated that overall good agreement with the experiments were achieved for the last two flows, but no comparisons with experimental data were shown.

It might be of value to notice that the works of Stawiarski and Hanjalic (2002), Cadiou et al. (2004) and Stawiarski and Hanjalic (2005) presented a rather different approach to that proposed initially by Hanjalic et al. (1980) which was mostly followed by other authors. Although both classes of work are essentially the same, since they split the spectrum into the same regions, they present two essential differences: the equation for the turbulent kinetic energy k and for the dissipation rate ε_T. If we neglect diffusion for the sake of simplicity here, the transport equations for k_P and k_T, as presented in equations 2.30 and 2.31, can be added to provide the transport equation for k proposed by Hanjalic et al. (1980): $\frac{Dk}{Dt} = P_k - \varepsilon_T$ which is essentially the same proposed by single-time-scale models. On the other hand, Stawiarski and Hanjalic (2005) proposes $\frac{Dk}{Dt} = P_k - \varepsilon_P$ and Stawiarski and Hanjalic (2002), Cadiou et al. (2004) solve the Reynolds stresses based on the large eddies' time-scale which makes the total turbulent kinetic energy and the stresses dependent only on the large eddies. It is also worth mentioning that the large eddies' length scale in the latter work was taken as $k^{3/2}/\varepsilon_P$ where the total turbulent kinetic energy is used instead of k_P which is the actual turbulent kinetic energy of the production zone of the spectrum, according to the proposed spectrum split. It is also noticeable that while in equations 2.32 and 2.33 the terms are dimensionalized with k_P and k_T respectively in the denominator, in the works presented by Stawiarski and Hanjalic (2002), Cadiou et al. (2004) and Stawiarski and Hanjalic (2005), k is always used for this purpose and that is apparently an effect of the applied spectrum integration method. Now, regarding the ε_T equation, its form presented in 2.33 was built in a rather more intuitive way (Cadiou et al., 2004) while the form presented by Stawiarski and Hanjalic (2002), Cadiou et al. (2004) and Stawiarski and Hanjalic (2005) derives from a simplified spectral integration and the main result of that was an extra source term. However, the extra source term, when compared to equation 2.33 is the term which carries the turbulent kinetic energy production and which is found in the source term of the single-time-scale ε_T equation.

This completes the MTS models subsection as well as the general literature survey on turbulence models. Reviewing the MTS models presented, one can point out their improvements in predicting non equilibrium flows when compared to STS models. The MTS models better performance is usually related to splitting the turbulent kinetic energy spectrum and its modelling, making it possible to account for the different time and length scales associated with the smaller and larger eddies, thus implying a more reasonable representation of the physical processes involved. When accounting for different slices of the spectrum, parameters such as k_P/k_T and $\varepsilon_P/\varepsilon_T$ arise which enable more flexibility in the modelling process and allow lags in the turbulence to be better captured. Besides this, the simulation time and computational effort required are generally intermediate between Two Equation models and Reynold Stress models. As a result, the Multiple-Time-Scale turbulence models are believed to be one of the most appropriate (in terms of modelling and computational effort) ways to predict non-equilibrium flows where lags in the response of the turbulence are expected.

Chapter 3

Turbulence Models

This chapter aims to present the complete set of equations related to each turbulence model used during this work to simulate the test cases which will be discussed in chapter 5. The equations will be presented in the way they are applied in the in-house CFD code, STREAM, described in chapter 4. In some cases, there may be some differences between the model implemented in the latter and their respective original papers, which will thus be pointed out.

Before proceeding with the models' description, the production terms which will be used for the following turbulence models will be defined. The production rate of turbulent kinetic energy P_k, used by both eddy viscosity and RST models, is usually represented as:

$$P_k = -\overline{u_i u_j}\frac{\partial U_i}{\partial x_j} \tag{3.1}$$

The production rate of the stresses $\overline{u_i u_j}$, which appears in the stresses' transport equation of the RST models, is usually represented as:

$$P_{ij} = -\left(\overline{u_i u_k}\frac{\partial U_j}{\partial x_k} + \overline{u_j u_k}\frac{\partial U_i}{\partial x_k}\right) \tag{3.2}$$

As a general rule for all the turbulence models which will be described, δ_{ij} is the Kronecker delta which is 1 for $i = j$ and zero otherwise, μ is the molecular viscosity, μ_t is the turbulent viscosity, ν is the kinematic viscosity defined by $\nu = \frac{\mu}{\rho}$, ρ is the density, σ_ϕ is the turbulent Prandtl number for the quantity ϕ, Re_t is the turbulent Reynolds number and Φ_{ij} is the pressure strain correlation term in the RST models.

Three classes of turbulence models were considered in this work: eddy-viscosity models, Reynolds-stress-transport models and multiple-time-scale models. The following sections will present the turbulence models in order of simplicity within each class and their main differences will be highlighted.

A brief discussion about wall-functions for both the STS and MTS high-Reynolds-number turbulence models will also be presented.

3.1 Eddy-Viscosity Models

In this section, the eddy-viscosity models used in this work will be presented. As already commented in the Literature Survey, chapter 2, this is the most used class of turbulence model due to its simplicity and consequent less computational effort required.

The turbulence models which will be presented here are: Launder and Spalding's 1974 standard $k-\varepsilon$ model, Launder and Sharma's 1974 low-Reynolds-number $k-\varepsilon$ model, Menter's 1994 SST model and a modified version of the cubic non-linear eddy viscosity model of Craft et al. (1999).

3.1.1 Standard $k-\varepsilon$ Model

The standard $k-\varepsilon$ model of Launder and Spalding (1974) is a Two Equation model, as already mentioned before, and thus requires two transport equations, one for k and the other for ε, to describe the turbulence. These equations are implemented in the STREAM code through the following:

$$\frac{\partial(\rho k)}{\partial t}+\frac{\partial(\rho U_j k)}{\partial x_j}=\frac{\partial}{\partial x_j}\left[\left(\mu+\frac{\mu_t}{\sigma_k}\right)\frac{\partial k}{\partial x_j}\right]+\rho P_k-\rho\varepsilon \tag{3.3}$$

$$\frac{\partial(\rho \varepsilon)}{\partial t}+\frac{\partial(\rho U_j \varepsilon)}{\partial x_j}=\frac{\partial}{\partial x_j}\left[\left(\mu+\frac{\mu_t}{\sigma_\varepsilon}\right)\frac{\partial \varepsilon}{\partial x_j}\right]+\rho c_{\varepsilon 1}\frac{\varepsilon}{k}P_k-\rho c_{\varepsilon 2}\frac{\varepsilon^2}{k} \tag{3.4}$$

One may notice that in Launder and Spalding's paper the viscous part of the diffusion term is not present since it was written for high-Reynolds-number flows, where viscous effects would be negligible, except near the wall where a wall function should be applied. Despite this, the viscous part of equations (3.3) and (3.4) is included in the STREAM code, since it belongs to the exact k and ε equations, does not affect the calculations and may help stability.

The Reynolds stresses are then calculated by Boussinesq's eddy viscosity concept, where:

$$\overline{u_i u_j}=-\frac{\mu_t}{\rho}\left(\frac{\partial U_i}{\partial x_j}+\frac{\partial U_j}{\partial x_i}\right)+\frac{2}{3}k\delta_{ij} \tag{3.5}$$

and

$$\mu_t=\rho c_\mu \frac{k^2}{\varepsilon} \tag{3.6}$$

In the above equations, P_k is the production term given in equation (3.1) and c_μ, $c_{\varepsilon 1}$ and $c_{\varepsilon 2}$ are constants of the model whose values can be seen in Table 3.1 together with the values for σ_k and σ_ε. The values used in the STREAM code are the same as those proposed by Launder and Spalding (1974).

Table 3.1: Constants in the standard $k-\varepsilon$ model

c_μ	$c_{\varepsilon 1}$	$c_{\varepsilon 2}$	σ_k	σ_ε
0.09	1.44	1.92	1.0	1.3

3.1.2 Launder and Sharma's LRN $k-\varepsilon$ Model

The low-Reynolds-number $k-\varepsilon$ model of Launder and Sharma (1974) consists of two main differences from the standard $k-\varepsilon$ model. The first is the presence of damping functions in order to account for the near-wall region and the second is that the ε equation is solved for $\tilde{\varepsilon}$, where the latter represents the isotropic part of the turbulent eddy dissipation rate, ε. The k and $\tilde{\varepsilon}$ equations are thus:

$$\frac{\partial(\rho k)}{\partial t}+\frac{\partial(\rho U_j k)}{\partial x_j}=\frac{\partial}{\partial x_j}\left[\left(\mu+\frac{\mu_t}{\sigma_k}\right)\frac{\partial k}{\partial x_j}\right]+\rho P_k-\rho\tilde{\varepsilon}-2\mu\left(\frac{\partial\sqrt{k}}{\partial x_j}\right)^2 \tag{3.7}$$

$$\frac{\partial(\rho\tilde{\varepsilon})}{\partial t}+\frac{\partial(\rho U_j\tilde{\varepsilon})}{\partial x_j}=\frac{\partial}{\partial x_j}\left[\left(\mu+\frac{\mu_t}{\sigma_\varepsilon}\right)\frac{\partial\tilde{\varepsilon}}{\partial x_j}\right]+\rho c_{\varepsilon 1}\frac{\tilde{\varepsilon}}{k}P_k-\rho c_{\varepsilon 2}f_2\frac{\tilde{\varepsilon^2}}{k}+E+Y_c \tag{3.8}$$

Comparing equations (3.7) and (3.3), one may notice a new term in the former besides the presence of $\tilde{\varepsilon}$ instead of ε. Indeed, equations (3.7) and (3.3) are the same since $\varepsilon=\tilde{\varepsilon}+2\nu\left(\frac{\partial\sqrt{k}}{\partial x_j}\right)^2$. The latter term accounts for the value ε should assume at the wall (considering that $\tilde{\varepsilon}$ is zero there) and is negligible outside of the viscous sublayer.

Comparing equations (3.8) and (3.4), one may notice three new terms: a damping function in the sink term, and the two last terms in equation (3.8). The E term accounts for extra dissipation near the wall in order to improve k prediction in this region. Its expression suggested by Launder and Sharma and implemented in the STREAM code is:

$$E=2\mu\mu_t\left(\frac{\partial^2 U_i}{\partial x_k x_j}\right)^2 \tag{3.9}$$

The Y_c term stands for Yap's 1987 length scale correction. This term was not proposed initially by Launder and Sharma, but is implemented in the STREAM code for this turbulence model in order to improve its prediction in non-equilibrium flows. The Y_c term acts as a source term in equation (3.8) and is defined as:

$$Y_c=max\left[0.83\frac{\tilde{\varepsilon}^2}{k}\left(\frac{k^{1.5}}{2.5\tilde{\varepsilon}y}-1\right)\left(\frac{k^{1.5}}{2.5\tilde{\varepsilon}y}\right)^2,0\right] \tag{3.10}$$

As an eddy viscosity model proposal, the Launder and Sharma's model also applied Boussinesq's eddy viscosity formulation. However a damping function is introduced in the turbulent viscosity expression to account for near-wall effects. The Reynolds stresses and the turbulent viscosity are thus calculated as:

$$\overline{u_i u_j} = -\frac{\mu_t}{\rho}\left(\frac{\partial U_i}{\partial x_j} + \frac{\partial U_j}{\partial x_i}\right) + \frac{2}{3}k\delta_{ij} \tag{3.11}$$

$$\mu_t = \rho c_\mu f_\mu \frac{k^2}{\tilde{\varepsilon}} \tag{3.12}$$

In the above equations, P_k is again the production term given in equation (3.1), and the constants c_μ, $c_{\varepsilon 1}$ and $c_{\varepsilon 2}$ as well as σ_k and σ_ε assume the same values of these in the standard $k-\varepsilon$ model, presented in Table 3.1. The damping functions f_μ and f_2 can be seen in Table 3.2, where the turbulent Reynolds number is defined as $Re_t = \frac{k^2}{\nu\tilde{\varepsilon}}$.

Table 3.2: Damping Functions in Launder and Sharma's LRN $k-\varepsilon$ model

f_μ	f_2
$\exp\left(\frac{-3.4}{(1+Re_t/50)^2}\right)$	$1.0 - 0.3\exp\left(-Re_t^2\right)$

3.1.3 Menter's SST Model

As already mentioned in the literature review, the SST model combines the standard $k-\varepsilon$ model and the $k-\omega$ model of Wilcox (1988a) by rewriting both k and ε equations in terms of ω through the relation $\varepsilon = \beta^*\omega k$ and organizing them to appear in a similar format to the k and ω equations in Wilcox's model. The resulting k and "$\varepsilon - \omega$" equations are:

$$\frac{\partial(\rho k)}{\partial t} + \frac{\partial(\rho U_j k)}{\partial x_j} = P_k - \beta^*\rho\omega k + \frac{\partial}{\partial x_j}\left[(\mu + \mu_t\sigma_k)\frac{\partial k}{\partial x_j}\right] \tag{3.13}$$

$$\frac{\partial(\rho\omega)}{\partial t} + \frac{\partial(\rho U_j\omega)}{\partial x_j} = \frac{\gamma}{\nu_t}P_k - \beta\rho\omega^2 + \frac{\partial}{\partial x_j}\left[(\mu + \mu_t\sigma_\omega)\frac{\partial\omega}{\partial x_j}\right] + 2\rho(1-F_1)\sigma_{\omega 2}\frac{1}{\omega}\frac{\partial k}{\partial x_j}\frac{\partial\omega}{\partial x_j} \tag{3.14}$$

Equation (3.13) is exactly the same for both $k-\varepsilon$ and $k-\omega$ turbulence models, written in terms of ω. Equation (3.14) is equivalent to the ω equation of Wilcox (1988a) when $F_1 = 1$ and to the ε equation (written in terms of ω) of Jones and Launder (1972b) and Launder and Spalding (1974) when $F_1 = 0$. Hence, F_1 is the blending function which is used to switch between the $k-\omega$ and $k-\varepsilon$ models. Like the equation forms, the constants in the SST model also switch from the values used in the $k-\omega$ to the $k-\varepsilon$ values through the blending function F_1. The constants in equations (3.13) and (3.14), generally represented by ϕ, are defined as $\phi = \phi_1 F_1 + \phi_2(1-F_1)$ where the subscript "1" indicates the constants from the $k-\omega$ model and the subscript "2", the constants from the $k-\varepsilon$ model. Both set of constants can be seen in Table 3.3, where $\kappa = 0.41$ is the von Karman constant.

As both $k-\omega$ and $k-\varepsilon$ are eddy viscosity models, so is the SST model. Hence the

Reynolds stresses are calculated as:

$$\overline{u_i u_j} = -\frac{\mu_t}{\rho}\left(\frac{\partial U_i}{\partial x_j} + \frac{\partial U_j}{\partial x_i}\right) + \frac{2}{3}k\delta_{ij} \tag{3.15}$$

The SST model proposed a modification to the standard eddy viscosity formulation in order to differently account for boundary layer flows and free shear flows. The turbulent viscosity could assume its standard form for the former flow, but for the latter it was designed to assume the form proposed by Johnson and King (1985). In order to achieve this, another blending function F_2 was applied. When $F_2 = 1$, the turbulent viscosity is suitable for boundary layer flows and when $F_2 = 0$, for free shear flows. The general proposed form for the turbulent viscosity is:

$$\mu_t = \rho\frac{a_1 k}{max(a_1\omega, \Omega F_2)} \tag{3.16}$$

Both blending functions F_1 and F_2 can be seen in Table 3.4. The other parameters remaining to be defined can be seen in Table 3.5.

Table 3.3: Constants ϕ_1 and ϕ_2 in the SST model

σ_{k1}	$\sigma_{\omega 1}$	β_1	β^*	γ_1
0.85	0.5	0.0750	0.09	$\frac{\beta_1}{\beta^*} - \frac{\sigma_{\omega 1}\kappa^2}{\sqrt{\beta^*}}$
σ_{k2}	$\sigma_{\omega 2}$	β_2	β^*	γ_2
1.0	0.856	0.0828	0.09	$\frac{\beta_2}{\beta^*} - \frac{\sigma_{\omega 2}\kappa^2}{\sqrt{\beta^*}}$

Table 3.4: Blending functions in the SST model

F_1	arg_1	F_2	arg_2
$\tanh arg_1^4$	$min\left[max\left(\frac{\sqrt{k}}{0.09\omega y}, \frac{500\nu}{y^2\omega}\right), \frac{4\rho\sigma_{\omega 2}k}{CD_{kw}y^2}\right]$	$\tanh arg_2^2$	$max\left(2\frac{\sqrt{k}}{0.09\omega y}, \frac{500\nu}{y^2\omega}\right)$

Table 3.5: Auxiliary parameters in the SST model

Ω	a_1	CD_{kw}
$\frac{1}{2}\sqrt{\left(\frac{\partial U_i}{\partial x_j} - \frac{\partial U_j}{\partial x_i}\right)^2}$	0.31	$max\left(2\rho\sigma_{\omega 2}\frac{1}{\omega}\frac{\partial k}{\partial x_j}\frac{\partial \omega}{\partial x_j}, 10^{-20}\right)$

3.1.4 Modified Craft et al.'s Cubic NLEV $k-\varepsilon$ Model

Craft et al. (1999) proposed a cubic non-linear eddy viscosity $k-\varepsilon$ model where the equations for k and ε are:

$$\frac{\partial(\rho k)}{\partial t}+\frac{\partial(\rho U_j k)}{\partial x_j}=\frac{\partial}{\partial x_j}\left[\left(\mu+\frac{\mu_t}{\sigma_k}\right)\frac{\partial k}{\partial x_j}\right]+\rho P_k-\rho\tilde{\varepsilon}-2\mu\left(\frac{\partial\sqrt{k}}{\partial x_j}\right)^2 \tag{3.17}$$

$$\frac{\partial(\rho\tilde{\varepsilon})}{\partial t}+\frac{\partial(\rho U_j\tilde{\varepsilon})}{\partial x_j}=\frac{\partial}{\partial x_j}\left[\left(\mu+\frac{\mu_t}{\sigma_k}\right)\frac{\partial\tilde{\varepsilon}}{\partial x_j}\right]+\rho c_{\varepsilon 1}\frac{\tilde{\varepsilon}}{k}P_k-\rho c_{\varepsilon 2}f_2\frac{\tilde{\varepsilon^2}}{k}+E+Y_{dc} \tag{3.18}$$

One may notice some similarities in the above equations when compared to the k and ε equations of the LS model: the presence of an E term and a length scale correction, Y_{dc}, the damping function f_2 in the sink term of equation (3.18) and the same concept of splitting the turbulent eddy dissipation rate into its isotropic and near-wall region parts. The ε equation constants as well as the damping function f_2 were adopted as in the LS model, being thus expressed as in Tables 3.1 and 3.2, respectively. It is also valid to mention that the f_2 damping function is not proposed in Craft et al.'s 1999 work, but is implemented in the STREAM code as suggested by Momeni (2008).

The E term in equation (3.18) was remodelled by Craft et al. from that in the Launder and Sharma's 1974 scheme, assuming the form:

$$E=\begin{cases}0.0022\frac{\nu_t\tilde{S}k^2}{\tilde{\varepsilon}}\frac{\partial^2U_i}{\partial x_j\partial x_k} & \text{if } Re_t\leq 250\\ 0 & \text{if } Re_t>250\end{cases} \tag{3.19}$$

where the turbulent Reynolds number is $Re_t=\frac{k^2}{\nu\tilde{\varepsilon}}$.

The length scale correction Y_{dc} was also remodelled by Craft et al. (1999) who chose not to apply Yap's formulation due to its dependence on the normal distance to the wall. Instead, they adopted a correction based on local gradients of the turbulent length scale. In an attempt to improve prediction of separated and reattachment flows, Momeni (2008) proposed some modifications to Y_{dc} which is then the way the length scale correction is applied in the STREAM code:

$$Y_{dc}=max\left\{c_w min[(F+1)^2F^{0.4},20]max\left(\frac{\varepsilon^2}{k},0\right),0\right\} \tag{3.20}$$

All terms in the above equation can be found in Table 3.6, where the physical meaning of the term $\frac{d\ell_e}{dy}$ is the length scale gradient in near-wall equilibrium conditions.

The cubic expression proposed by Craft et al. for the Reynolds stresses is:

$$\begin{aligned}\overline{u_i u_j} =& \frac{2}{3}k\delta_{ij} - \nu_t S_{ij} \\ &+ c_1\frac{k}{\tilde{\varepsilon}}\nu_t\left(S_{ik}S_{jk} - \frac{1}{3}S_{kl}S_{kl}\delta_{ij}\right) + c_2\frac{k}{\tilde{\varepsilon}}\nu_t\left(W_{ik}S_{jk} + W_{jk}S_{ik}\right) + c_3\frac{k}{\tilde{\varepsilon}}\nu_t\left(W_{ik}W_{jk} - \frac{1}{3}W_{kl}W_{kl}\delta_{ij}\right) \\ &+ c_4\frac{k^2}{\tilde{\varepsilon}^2}\nu_t\left(S_{ki}W_{lj} + S_{kj}W_{li}\right)S_{kl} + c_5\frac{k^2}{\tilde{\varepsilon}^2}\nu_t\left(W_{il}W_{lm}S_{mj} + S_{il}W_{lm}W_{mj} - \frac{2}{3}S_{lm}W_{mn}W_{nl}\delta_{ij}\right) \\ &+ c_6\frac{k^2}{\tilde{\varepsilon}^2}\nu_t S_{ij}S_{kl}S_{kl} + c_7\frac{k^2}{\tilde{\varepsilon}^2}\nu_t S_{ij}W_{kl}W_{kl} \end{aligned} \tag{3.21}$$

where $S_{ij} = \frac{\partial U_i}{\partial x_j} + \frac{\partial U_j}{\partial x_i}$ and $W_{ij} = \frac{\partial U_i}{\partial x_j} - \frac{\partial U_j}{\partial x_i}$ and the eddy viscosity is given as:

$$\mu_t = \rho c_\mu f_{\mu p}\frac{k^2}{\tilde{\varepsilon}} \tag{3.22}$$

The coefficients in the above equations as well as the damping function $f_{\mu p}$ are presented in Tables 3.7 and 3.8. The form and values of these terms correspond to Momeni's 2008 work.

Table 3.6: Parameters related to Y_{dc}

c_w	F	η'
$\frac{[1.65min(Re_t/25,1)]^2(1-f_{FS})+0.3min(Re_t/40,1)f_{FS}}{0.8+0.7(\eta'/3.33)^4\exp(-Re_t/12.5)}$	$\left[\sqrt{\left(\frac{\partial \ell}{\partial x_j}\right)^2 - \frac{d\ell_e}{dy}}\right]\frac{1}{c_\ell}$	$max[max(\tilde{S},\tilde{W}),40]$

$\frac{d\ell_e}{dy}$	f_{FS}	c_ℓ	B_ε
$c_\ell[1-\exp(-B_\varepsilon Re_t)] + B_\varepsilon c_\ell Re_t\exp(-B_\varepsilon Re_t)$	$min\left[\frac{max(\frac{p_k}{\varepsilon},\exp(-\frac{Re_t}{50})^2,0)}{0.75},1\right]$	2.55	0.1069

Table 3.7: Coefficients in the Cubic NLEV model

c_μ	c_1	c_2	c_3	c_4	c_5	c_6	c_7
$min\left[0.09, \frac{1.2}{1+3.5\eta+f_{RS}}\right]$	-0.1	0.1	0.26	$-10c_\mu^2$	0	$-5c_\mu^2$	$5c_\mu^2$

Table 3.8: Damping functions and parameters in the Cubic NLEV model

$f_{\mu p}$	f_μ	f_{RS}
$f_\mu f_{FS} + (1-f_{FS})$	$1-\exp\left[-\sqrt{\frac{Re_t}{90}} - \left(\frac{Re_t}{400}\right)^2\right]$	$0.235[max(0,\eta-3.333)]^2\exp(-\frac{Re_t}{400})$

$\tilde{S}$	$\tilde{W}$	η
$\frac{k}{\tilde{\varepsilon}}\sqrt{\frac{1}{2}S_{ij}S_{ij}}$	$\frac{k}{\tilde{\varepsilon}}\sqrt{\frac{1}{2}W_{ij}W_{ij}}$	$max(\tilde{S},\tilde{W})$

3.2 Reynolds-Stress-Transport Models

In this section, four models will be presented. These are the most complex models which will be treated in this work. Since they solve transport equations for the Reynolds stresses, they are expected to provide better prediction of flows, but to demand a much higher computational effort.

The turbulence models which will be presented are: Gibson and Launder's 1978 model, the SSG model of Speziale et al. (1991), the low-Reynolds-number model of Hanjalic et al. (1997) and the low-Reynolds-number two-component-limit model of Craft (1998).

3.2.1 Gibson and Launder's RST Model

Gibson and Launder (1978) proposed a high-Reynolds-number RST model whose general equation for the Reynolds stresses $\overline{u_i u_j}$ is:

$$\frac{\partial(\rho\overline{u_i u_j})}{\partial t} + \frac{\partial(\rho U_j \overline{u_i u_j})}{\partial x_j} = \rho P_{ij} - \rho\frac{2}{3}\varepsilon\delta_{ij} + \rho\Phi_{ij} + \frac{\partial}{\partial x_k}\left[\left(\mu + \rho c_s \frac{k}{\varepsilon}\overline{u_k u_l}\right)\frac{\partial \overline{u_i u_j}}{\partial x_l}\right] \qquad (3.23)$$

It is of value to comment on the terms in the above equation. P_{ij} is the production rate of the Reynolds stresses expressed in equation (3.2). $\frac{2}{3}\varepsilon\delta_{ij}$ represents the dissipation terms for high-Reynolds-number flows where it is assumed that local isotropy holds (Launder et al., 1984). The diffusion term follows the Generalized Gradient Diffusion Hypothesis (GGDH) of Daly and Harlow (1970) whose diffusivity takes into consideration the Reynolds stresses in order to account for its anisotropy. Again, the viscous part of the diffusive term is included in the STREAM code and that is why it is represented in equation (3.23). Finally, the pressure-strain correlation term represents the effective contribution of Gibson and Launder's work. The pressure strain correlation is expressed as a sum of four terms: an interaction between the fluctuating velocity components themselves, $\phi_{ij,1}$, an interaction between these and the main flow, via a linear relation with the mean velocity gradients, $\phi_{ij,2}$, and two wall reflection terms. The latter are those which were actually proposed by Gibson and Launder as a new contribution since the former, $\phi_{ij,1}$ and $\phi_{ij,2}$, had been already proposed by Launder et al.

(1975). The equation for the modelled pressure-strain correlation is:

$$\Phi_{ij} = \phi_{ij,1} + \phi_{ij,2} + \phi_{ij,w1} + \phi_{ij,w2}$$

where:

$$\phi_{ij,1} = -C_1 \frac{\varepsilon}{k}\Big(\overline{u_i u_j} - \frac{2}{3}\delta_{ij}k\Big)$$

$$\phi_{ij,2} = -C_2\Big(P_{ij} - \frac{2}{3}\delta_{ij}P_k\Big)$$

$$\phi_{ij,w1} = C_1' \frac{\varepsilon}{k}(\overline{u_k u_m} n_k n_m \delta_{ij} - \frac{3}{2}\overline{u_k u_i} n_k n_j - \frac{3}{2}\overline{u_k u_j} n_k n_i)F$$

$$\phi_{ij,w2} = C_2'(\phi_{km,2} n_k n_m \delta_{ij} - \frac{3}{2}\phi_{ik,2} n_k n_i - \frac{3}{2}\phi_{jk,2} n_k n_i)F$$

$$\text{and} \qquad F = \frac{k^{3/2}}{2.5y\varepsilon} \tag{3.24}$$

In the above equation, P_k stands for the production rate of turbulence energy, given by equation (3.1), n_m is the component of the unit vector normal to the wall in the m direction and y, in the length scale function F, is the normal distance to the wall.

The RST model also requires an equation for the turbulent eddy dissipation rate ε. The equation adopted for Gibson and Launder's model in the STREAM code has a general form which can be expressed as:

$$\frac{\partial(\rho\varepsilon)}{\partial t} + \frac{\partial(\rho U_j \varepsilon)}{\partial x_j} = \frac{\partial}{\partial x_k}\left[\left(\mu + \rho c_\varepsilon \frac{k}{\varepsilon}\overline{u_k u_l}\right)\frac{\partial \varepsilon}{\partial x_k}\right] - \rho c_{\varepsilon 1}\frac{\varepsilon}{k}P_k - \rho c_{\varepsilon 2}\frac{\varepsilon^2}{k} \tag{3.25}$$

The diffusion term here is also of a GGDH type, again to give an anisotropic diffusivity. The constants of the model are presented in Table 3.9.

Table 3.9: Constants in Gibson and Launder's RST model

C_1	C_2	C_1'	C_2'	c_s	c_ε	$c_{\varepsilon 1}$	$c_{\varepsilon 2}$
1.8	0.6	0.5	0.3	0.22	0.18	1.44	1.92

3.2.2 The SSG RST Model

The SSG Reynolds stress transport model is also a high-Reynolds-number model, developed by Speziale et al. (1991). Its general equation form for the Reynolds stresses $\overline{u_i u_j}$ and the turbulent eddy dissipation rate ε are the same of those presented for the GL model, equation (3.23) and (3.25). The main difference between these two models lies in the pressure strain correlation expression.

Starting from the Poisson equation for the instantaneous pressure field, Speziale et al. (1991) developed a general solution, subjected to physical constraints, for the pressure strain

correlation which resulted in a non-linear formulation for the latter, where it varies quadratically with the anisotropy tensor defined by $b_{ij} = \frac{\overline{u_i u_j} - \frac{2}{3}k\delta_{ij}}{2k}$. The resulting expression for the pressure strain correlation Φ_{ij} is thus:

$$\begin{aligned}\Phi_{ij} = &-(C_1 + C_1^* \frac{\mathscr{P}}{\varepsilon})b_{ij} \\ &+ C_2\varepsilon(b_{ik}b_{kj} - \frac{1}{3}b_{mn}b_{mn}\delta_{ij}) \\ &+ (C_3 - C_3^*\sqrt{A})ks_{ij} \\ &+ C_4k(b_{ik}s_{jk} + b_{jk}s_{ik} - \frac{2}{3}b_{mn}s_{mn}\delta ij) + C_5k(b_{ik}w_{jk} + b_{jk}w_{ik})\end{aligned} \tag{3.26}$$

where $A = b_{ij}b_{ij}$ is the stress invariant and $s_{ij} = \frac{1}{2}\left(\frac{\partial U_i}{\partial x_j} + \frac{\partial U_j}{\partial x_i}\right)$ and $w_{ij} = \frac{1}{2}\left(\frac{\partial U_i}{\partial x_j} - \frac{\partial U_j}{\partial x_i}\right)$ are the mean strain and vorticity tensors.

One may notice that the first line in equation (3.26) is equivalent to the interaction between the fluctuating velocity components themselves, $\phi_{ij,1}$ used in the GL model. The second line contains the quadratically non-linear terms in the anisotropy tensor b_{ij}. The term in the third line is linearly dependent on the mean strain rate tensor, although its coefficient still depends on the anisotropy tensor and the other terms in the fourth line express the dependence of the pressure strain correlation on the interaction between the anisotropy tensor and the mean strain and vorticity tensors, respectively. It is also worth noting that there is no wall reflection term.

The constants of the SSG model can be found in Table 3.10.

Table 3.10: Constants in Speziale et al.'s RST model

C_1	C_1^*	C_2	C_3	C_3^*	C_4	C_5	c_s	c_ε	$c_{\varepsilon 1}$	$c_{\varepsilon 2}$
3.4	1.8	4.2	0.8	1.3	1.25	0.4	0.22	0.18	1.44	1.83

3.2.3 Hanjalic et al.'s LRN RST Model

Hanjalic et al. (1997) proposed a low-Reynolds-number Reynolds stress transport model. The general form of its transport equation for the Reynolds stresses is:

$$\frac{D(\rho\overline{u_i u_j})}{Dt} = \rho P_{ij} - \rho\varepsilon_{ij} + \rho\Phi_{ij} + \frac{\partial}{\partial x_k}\left[\left(\mu + \rho c_s \frac{k}{\varepsilon}\overline{u_k u_l}\right)\frac{\partial \overline{u_i u_j}}{\partial x_l}\right] \tag{3.27}$$

Hanjalic et al. proposed a similar expression for the pressure strain correlation to that proposed by Gibson and Launder (1978), where its coefficients were no longer constants, but expressed in terms of the denoted flatness parameters (A and E) which can be seen in Table

3.11. The pressure strain correlation is thus:

$$\begin{aligned}
&\Phi_{ij} = \phi_{ij,1} + \phi_{ij,2} + \phi_{ij,w1} + \phi_{ij,w2} \\
&\text{where} \\
&\phi_{ij,1} = -C_1 \varepsilon a_{ij} \\
&\phi_{ij,2} = -C_2 \Big(P_{ij} - \frac{2}{3}\delta_{ij} P_k \Big) \\
&\phi_{ij,w1} = C_1^w \frac{\varepsilon}{k} (\overline{u_k u_m} n_k n_m \delta_{ij} - \frac{3}{2}\overline{u_k u_i} n_k n_j - \frac{3}{2}\overline{u_k u_j} n_k n_i) f_w \\
&\phi_{ij,w2} = C_2^w (\phi_{km,2} n_k n_m \delta_{ij} - \frac{3}{2}\phi_{ik,2} n_k n_i - \frac{3}{2}\phi_{jk,2} n_k n_i) f_w
\end{aligned} \tag{3.28}$$

The other term in equation (3.27) which is different from the RST models presented above is the dissipation term. Since this is a low-Reynolds-number model, the common form adopted for it, $\varepsilon_{ij} = \frac{2}{3}\varepsilon\delta_{ij}$, could no longer be used since it would not be valid for the near-wall region. The proposed form for the dissipation was thus:

$$\varepsilon_{ij} = f_s \frac{\varepsilon}{k} \frac{(\overline{u_i u_j} + \overline{u_i u_k} n_j n_k + \overline{u_j u_k} n_i n_k + \overline{u_k u_l} n_k n_l n_i n_j) f_d}{1 + 1.5(\frac{\overline{u_p u_q}}{k}) n_p n_q f_d} + (1 - f_s)\frac{2}{3}\varepsilon\delta_{ij} \tag{3.29}$$

One may notice that the presence of the function f_s enables the expression for ε_{ij} to assume its high-Reynolds-number form when $f_s = 0$ which is supposed to happen far from the wall. The near-wall part was modelled as a function of the Reynolds stresses and the unit vector normal to the wall.

The ε equation in Hanjalic et al.'s model was not modelled as in the high-Reynolds-number models either. Instead, its equation was taken as:

$$\frac{\partial(\rho\varepsilon)}{\partial t} + \frac{\partial(\rho U_j \varepsilon)}{\partial x_j} = \frac{\partial}{\partial x_k}\left[\left(\mu + \rho c_\varepsilon \frac{k}{\varepsilon}\overline{u_k u_l}\right)\frac{\partial\varepsilon}{\partial x_k}\right] - \rho c_{\varepsilon 1}\frac{\varepsilon}{k}P_k - \rho c_{\varepsilon 2} f_2 \frac{\varepsilon\tilde{\varepsilon}}{k} + E - \Omega + S_\ell \tag{3.30}$$

The last three terms in the above equation are actually the ones which differentiate it from the standard ε equation in the previous high-Reynolds-number RST models. The E term is similar to the one used by Launder and Sharma (1974), but with GGDH influences:

$$E = \rho c_{\varepsilon 3}\frac{k}{\varepsilon}\overline{u_j u_k}\frac{\partial^2 U_i}{\partial x_j \partial x_l}\frac{\partial^2 U_i}{\partial x_k \partial x_l} \tag{3.31}$$

The Ω term in equation (3.30) was included in order to account for differences between rotational and irrotational straining. Its original formulation was $\Omega = -c_{\varepsilon_4} f_4 k W_k W_k$, where W_k is the vorticity tensor, but the authors themselves proposed in the same work a 2D simplified form for it which is the one applied in the STREAM code. The expression for Ω

is then:

$$\Omega = c^*_{\varepsilon_4}(\overline{v}^2 - \overline{u}^2)\frac{\partial U}{\partial x}\frac{\varepsilon}{k} \tag{3.32}$$

Although the above expression is not tensorially invariant, it is coded as $\overline{u^2}$ being interpreted as the normal stress in the streamwise direction and $\overline{v^2}$ in the cross-stream.

Finally, the last term in (3.30), S_ℓ, represents a length scale correction with no dependence on the distance to the wall which is designed to improve predictions in non equilibrium flows:

$$S_\ell = max\left\{\left[\left(\frac{1}{C_\ell}\frac{\partial \ell}{\partial x_n}\right)^2 - 1\right]\left(\frac{1}{C_\ell}\frac{\partial \ell}{\partial x_n}\right)^2, 0\right\}\frac{\varepsilon\tilde{\varepsilon}}{k}A \tag{3.33}$$

All the parameters, functions, coefficients and constants related to Hanjalic et al.'s model are presented in Tables 3.11, 3.12, 3.13 and 3.14.

Table 3.11: Parameters in Hanjalic et al.'s LRN RST model

A	E	C	F
$1-\frac{9}{8}(A_2-A_3)$	$1-\frac{9}{8}(E_2-E_3)$	$2.5AF^{0.25}f$	$min(0.6, A_2)$

Table 3.12: Damping and auxiliary functions in Hanjalic et al.'s LRN RST model

f_2	f_w	f	f_s	f_d
$1-\frac{c_{\varepsilon 2}-1.4}{c_{\varepsilon 2}}\exp\left[-\left(\frac{Re_t}{6}\right)^2\right]$	$min\left[\frac{k^{3/2}}{2.5y\varepsilon}, 1.4\right]$	$min\left[\left(\frac{Re_t}{150}\right)^{1.5}, 1\right]$	$1-\sqrt{A}E^2$	$(1+0.1Re_t)^{-1}$

Table 3.13: Invariants in Hanjalic et al.'s LRN RST model

a_{ij}	e_{ij}	A_2	E_2	A_3	E_3
$\frac{\overline{u_iu_j}}{k}-\frac{2}{3}\delta ij$	$\frac{\varepsilon_{ij}}{\varepsilon}-\frac{2}{3}\delta ij$	$a_{ij}a_{ji}$	$e_{ij}e_{ji}$	$a_{ij}a_{jk}a_{ki}$	$e_{ij}e_{jk}e_{ki}$

Table 3.14: Main coefficients in Hanjalic et al.'s LRN RST model

C_1	C_1^w	C_2	C_2^w	c_s	c_ε	$c_{\varepsilon 1}$	$c_{\varepsilon 2}$	$c_{\varepsilon 3}$	$c^*_{\varepsilon 4}$	C_ℓ
$C+\sqrt{A}E^2$	$max(1-0.7C, 0.3)$	$0.8\sqrt{A}$	$min(A, 0.3)$	0.22	0.18	1.44	1.92	0.25	1.16	2.5

3.2.4 Craft's 1998 Two-Component-Limit (TCL) LRN RST Model

The model which will be described here is based on the initial work of Craft et al. (1996a) which was extended by Craft and Launder (1996) and later modified by Craft (1998). The version effectively used here has also some further modifications already implemented in the

STREAM code, aimed at improving the stability of the simulations..

One important feature of the two-component-limit (TCL) scheme is that the model elements in the stress transport equations are designed to ensure a realizable stress field, for example, by ensuring the correct behaviour in two-component turbulence, when one of the fluctuating velocities is zero, for instance, close to a wall where the fluctuating velocity normal to it gets reduced much more than the other components. The model here presented also contains low-Reynolds number and near-wall corrections.

The idea of using this TCL model is to identify the advantages a much more complex model can bring in terms of prediction when compared to simple Reynolds Stress Transport turbulence models as the ones presented above.

Before presenting the transport equations, two terms, d_i and d_i^A, which are used in the TCL model's terms will be discussed. They were named as normalized length scale gradients and were first introduced by Craft et al. (1996a). Their expressions are:

$$d_i = \frac{N_i}{0.5 + \sqrt{N_k N_k}} \quad \text{where} \quad N_i = \frac{\partial(k^{3/2}/\varepsilon)}{\partial x_i} \tag{3.34}$$

$$d_i^A = \frac{N_i^A}{0.5 + \sqrt{N_k^A N_k^A}} \quad \text{where} \quad N_i^A = \frac{\partial(k^{3/2} A^{0.5}/\varepsilon)}{\partial x_i} \tag{3.35}$$

The authors argued that these terms are capable of sensitizing the model to the presence of a wall by making it sense the local inhomogeneity. The normalized length scale gradients would assume a value of 1 in very inhomogeneous areas which are usually in a near wall region and would be negligible in regions with small inhomogeneity. In the above equations, and subsequently in the model's equations and terms, A is the flatness parameter defined as $A = 1 - 9/8(A_2 - A_3)$, where $A_2 = a_{ij}a_{ij}$ and $A_3 = a_{ij}a_{jk}a_{ki}$ are the invariants of the stress anisotropy tensor $a_{ij} = \frac{\overline{u_i u_j}}{k} - \frac{2}{3}\delta_{ij}$.

The Reynolds stress equations follow a general form:

$$\frac{D\overline{u_i u_j}}{Dt} = P_{ij} + \Pi_{ij} - \varepsilon_{ij} + d_{ij} \tag{3.36}$$

where P_{ij} is the Reynolds stresses production term defined as $P_{ij} = -(\overline{u_i u_k}\partial U_j/\partial x_k + \overline{u_j u_k}\partial U_i/\partial x_k)$, Π_{ij} is the pressure correlation term, ε_{ij} is the dissipation and d_{ij} is the diffusion. As already noted, except for the production term, all terms require modelling. The modelling proposed by Craft (1998) will be presented below.

Starting from the pressure correlation term, Π_{ij}, this is treated as $\Pi_{ij} = \phi_{ij} - \frac{\overline{u_i u_j}}{k} d_k^p$, where the first term on the right hand side is the redistributive part and the second, the non-redistributive one. The only unknown term in the latter is d_k^p, the turbulent kinetic energy pressure-diffusion term, which is given by $d_k^p = -(1/\rho)\partial(\overline{pu_k})/\partial x_k$, where the correlation between fluctuating pressure and velocity is modelled by $\overline{pu_k} = -f_{pu1}\frac{k}{\varepsilon}u_i u_k \frac{\partial k}{\partial x_i} - f_{pu2}\frac{k^2}{\varepsilon}\frac{\partial k}{\partial x_k}$. The coefficients f_{pu1} and f_{pu2} are given in Table 3.15. It is of value to note that the expression

for the $\overline{pu_k}$ term is not the one proposed by Craft (1998), but a simpler expression already implemented in the STREAM code. The two formulations were tested in a plane channel flow, and no significant difference was seen in the results, therefore the above formulation already implemented in the STREAM code was kept.

The redistributive part of the pressure correlation term, ϕ_{ij}, is a much more complex term and has a general form of $\phi_{ij} = \phi_{ij1} + \phi_{ij2} + \phi_{ij1}^{inh} + \phi_{ij2}^{inh}$, where ϕ_{ij1} represents the slow pressure strain term, ϕ_{ij2} is the rapid pressure strain term and ϕ_{ij1}^{inh} and ϕ_{ij2}^{inh} are, respectively, the inhomogeneous parts of the slow and rapid pressure strain terms:

$$
\begin{aligned}
\phi_{ij1} =& -c_1\tilde{\varepsilon}\big[a_{ij} + c_1'\big(a_{ik}a_{kj} - \frac{1}{3}A_2\delta_{ij}\big)\big] - \tilde{\varepsilon}f_A' a_{ij} \\
\phi_{ij2} =& -0.6P_{ij} - \frac{1}{3}P_{kk}\delta_{ij} + 0.3a_{ijP_{kk}} \\
& - 0.2\left[\frac{\overline{u_k u_j u_l u_i}}{k}\left(\frac{\partial U_k}{\partial x_l} + \frac{\partial U_l}{\partial x_k}\right) - \frac{\overline{u_l u_k}}{k}\left(\overline{u_i u_k}\frac{\partial U_j}{\partial x_l} + \overline{u_j u_k}\frac{\partial U_i}{\partial x_l}\right)\right] \\
& - c_2[A_2(P_{ij} - D_{ij}) + 3a_{mi}a_{nj}(P_{mn} - D_{mn})] \\
& + c_2'\left(\frac{7}{15} - \frac{A_2}{4}\right)(P_{ij} - \frac{1}{3}P_{kk}\delta_{ij}) \\
& + 0.1c_2'[a_{ij} - \frac{1}{2}(a_{ik}a_{kj} - \frac{1}{3}\delta_{ij}A_2)]P_{kk} - 0.05c_2' a_{ij}a_{jk}P_{kl} \\
& + 0.1c_2'\left[\left(\frac{\overline{u_i u_m}}{k}P_{mj} + \frac{\overline{u_j u_m}}{k}P_{mi}\right) - \frac{2}{3}\delta_{ij}\frac{\overline{u_l u_m}}{k}P_{ml}\right] \\
& + 0.1c_2'\left[\frac{\overline{u_l u_i u_k u_j}}{k^2} - \frac{1}{3}\delta_{ij}\frac{\overline{u_l u_m u_k u_m}}{k^2}\right]\left[6D_{lk} + 13k\left(\frac{\partial U_l}{\partial x_k} + \partial\partial U_k\partial x_l\right)\right] \\
& + 0.2c_2'\frac{\overline{u_l u_i u_k u_j}}{k^2}(D_{lk} - P_{lk}) \\
\phi_{ij1}^{inh} =& f_{w1}\frac{\varepsilon}{k}\left(\overline{u_l u_k}d_l^A\delta_{ij} - \frac{3}{2}\overline{u_i u_k}d_j^A - \frac{3}{2}\overline{u_j u_k}d_i^A\right)d_k^A \\
& + f_{w2}\frac{\varepsilon}{k^2}\overline{u_l u_n}\left(\overline{u_n u_k}d_k^A\delta_{ij} - \frac{3}{2}\overline{u_i u_n}d_j^A - \frac{3}{2}\overline{u_j u_n}d_i^A\right)d_l^A \\
& + f_{w3}\nu\left(a_{il}\frac{\partial\sqrt{k}}{\partial x_l}\frac{\partial\sqrt{k}}{\partial x_j} + a_{jl}\frac{\partial\sqrt{k}}{\partial x_l}\frac{\partial\sqrt{k}}{\partial x_i} - \frac{2}{3}a_{nl}\frac{\partial\sqrt{k}}{\partial x_l}\frac{\partial\sqrt{k}}{\partial x_n}\delta_{ij} - \frac{4}{3}a_{ij}\frac{\partial\sqrt{k}}{\partial x_l}\frac{\partial\sqrt{k}}{\partial x_l}\right) \\
& + f_{w1}'\frac{k^2}{\varepsilon}\left(\overline{u_k u_l}\frac{\partial\sqrt{A}}{\partial x_k}\frac{\partial\sqrt{A}}{\partial x_l}\delta_{ij} - \frac{3}{2}\overline{u_i u_k}\frac{\partial\sqrt{A}}{\partial x_k}\frac{\partial\sqrt{A}}{\partial x_j} - \frac{3}{2}\overline{u_j u_k}\frac{\partial\sqrt{A}}{\partial x_k}\frac{\partial\sqrt{A}}{\partial x_i}\right) \\
\phi_{ij2}^{inh} =& f_1 k\frac{\partial U_l}{\partial x_n}d_l d_n\left(d_i d_j - \frac{1}{3}d_k d_k\delta ij\right)
\end{aligned}
\tag{3.37}
$$

It is also of value to comment that the ϕ_{ij2}^{inh} term is not implemented in the STREAM code, therefore the redistributive part of the pressure correlation term is better represented by $\phi_{ij} = \phi_{ij1} + \phi_{ij2} + \phi_{ij1}^{inh}$. However, one should expect no difference in predicting the current flow cases with the original Craft (1998) model and the one implemented in the STREAM code because Craft (1998) comments that the inhomogeneous part of the rapid pressure strain term, ϕ_{ij2}^{inh} which is not implemented in the STREAM code, is only effective in stagnating flows, like impinging jet flows, which is not the case in any of the five test cases here.

In equation (3.37), D_{ij} is given by $D_{ij} = -\overline{u_i u_k}\frac{\partial U_k}{\partial x_j} + \overline{u_j u_k}\frac{\partial U_k}{\partial x_i}$, $\tilde{\varepsilon}$ is defined as $\tilde{\varepsilon} =$

$\varepsilon - 2\nu\left(\frac{\partial\sqrt{k}}{\partial x_j}\right)^2$ and the coefficients (c_1, c_1', f_A', c_2, c_2', f_{w1}, f_{w2}, f_{w3} and f_{w1}') are presented in Table 3.16. Another feature of the TCL model presented here is that the velocity gradients in the rapid pressure strain term ϕ_{ij2} assume a "corrected" form in order to account for strong inhomogeneities in the mean velocity gradients (particularly close to a wall). Thus the so called effective velocity gradient is defined as:

$$\left.\frac{\partial U_i}{\partial x_j}\right|_{eff} = \frac{\partial U_i}{\partial x_j} + c_l l d_k^A \frac{\partial^2 U_i}{\partial x_k \partial x_j} \tag{3.38}$$

where the coefficient c_l, and the lengthscale l, are defined in Table 3.16.

The dissipation term in the stress equation (3.36) can be generally expressed as $\varepsilon_{ij} = (1-f_\varepsilon)(\varepsilon_{ij}' + \varepsilon_{ij}'' + \varepsilon_{ij}''')/D + \frac{2}{3} f_\varepsilon \varepsilon \delta_{ij}$, where $D = (\varepsilon_{kk}' + \varepsilon_{kk}'' + \varepsilon_{kk}''')/(2\varepsilon)$ and:

$$\begin{aligned}
\varepsilon_{ij}' =& \varepsilon \frac{\overline{u_i u_j}}{k} + 2\nu \frac{\overline{u_l u_n}}{k} \frac{\partial\sqrt{k}}{\partial x_l} \frac{\partial\sqrt{k}}{\partial x_n} \delta_{ij} + 2\nu \frac{\overline{u_l u_i}}{k} \frac{\partial\sqrt{k}}{\partial x_j} \frac{\partial\sqrt{k}}{\partial x_l} + 2\nu \frac{\overline{u_l u_j}}{k} \frac{\partial\sqrt{k}}{\partial x_i} \frac{\partial\sqrt{k}}{\partial x_l} \\
\varepsilon_{ij}'' =& \varepsilon \left(2 \frac{\overline{u_l u_k}}{k} d_l^A d_k^A \delta_{ij} - \frac{\overline{u_l u_i}}{k} d_l^A d_j^A - \frac{\overline{u_l u_j}}{k} d_l^A d_i^A \right) \\
\varepsilon_{ij}''' =& c_{\varepsilon s} \nu k \left(\frac{\partial\sqrt{k}}{\partial x_k} \frac{\partial\sqrt{k}}{\partial x_k} \delta_{ij} + 2 \frac{\partial\sqrt{A}}{\partial x_i} \frac{\partial\sqrt{A}}{\partial x_j} \right)
\end{aligned} \tag{3.39}$$

The coefficients $c_{\varepsilon s}$ and f_ε can be seen in Table 3.17. One may notice that the dissipation ε_{ij} reduces to its isotropic form $\varepsilon_{ij} = \frac{2}{3}\varepsilon\delta_{ij}$ far from the wall through the f_ε damping term. Therefore the terms in equation (3.39) were designed to model dissipation behavior near the wall.

Finally, the last term in the modelled stress transport equation, the diffusion d_{ij}, will be discussed. Craft (1998) adopted a form for d_{ij} based on the gradient of the triple moment $\overline{u_i u_j u_k}$, with an algebraic closure of the triple moment transport equations used to approximate $\overline{u_i u_j u_k}$. However, when testing this form in a range of channel flow cases some instabilities were encountered. As a result, in the present work the TCL model was run using the Generalized Gradient Diffusion Hypothesis (GGDH) form initially proposed by Daly and Harlow (1970), with the c_s coefficient presented in Table 3.17:

$$d_{ij} = \frac{\partial}{\partial x_k}\left[\left(\nu + c_s \frac{k}{\varepsilon} \overline{u_k u_l} \right) \frac{\partial \overline{u_i u_j}}{\partial x_l} \right] \tag{3.40}$$

The TCL model includes a transport equation for the homogeneous dissipation rate $\tilde{\varepsilon}$, already defined in the previous section as $\tilde{\varepsilon} = \varepsilon - 2\nu\left(\frac{\partial\sqrt{k}}{\partial x_j}\right)^2$. Its general form is then:

$$\frac{D\tilde{\varepsilon}}{Dt} = c_{\varepsilon 1} \frac{\tilde{\varepsilon} P_{kk}}{2k} - c_{\varepsilon 2} \frac{\tilde{\varepsilon}^2}{k} - c_{\varepsilon 2}' \frac{\tilde{\varepsilon}(\varepsilon - \tilde{\varepsilon})}{k} + \frac{\partial}{\partial x_l}\left[\left(\nu\delta_{lk} + c_\varepsilon \overline{u_l u_k} \frac{k}{\varepsilon} \right) \frac{\partial \tilde{\varepsilon}}{\partial x_k} \right] + c_{\varepsilon 3} \nu \overline{u_i u_j} \frac{k}{\varepsilon} \frac{\partial^2 U_k}{\partial x_i \partial x_l} \frac{\partial^2 U_k}{\partial x_j \partial x_l} + Y_E \tag{3.41}$$

The first, second and fourth terms on the right hand side of the above equation are the common terms usually found in the dissipation rate equations, being the production, destruction and diffusion terms of the dissipation rate, respectively. The third term was introduced to correct the profile of $\tilde{\varepsilon}$ near the wall, the fifth term was introduced to increase the dissipation in the near wall region in order to capture a better profile of the turbulent kinetic energy k, and finally, the sixth term was introduced as a length scale correction whose expression is:

$$Y_E = c_{\varepsilon l}\frac{\tilde{\varepsilon}^2}{k} max[F(F+1)^2, 0] \tag{3.42}$$

where $F = [\sqrt{\frac{\partial \ell}{\partial x_j}\frac{\partial \ell}{\partial x_j}} - c_\ell[1-\exp(-B_\varepsilon Re_t)] - B_\varepsilon c_\ell Re_t \exp(-B_\varepsilon Re_t)]/c_\ell$ and ℓ is the turbulent length scale $\ell = \frac{k^{3/2}}{\varepsilon}$. All coefficients in equations (3.41) and (3.42) can be seen in Table 3.18.

Table 3.15: Coefficients related to the non-redistributive part of the pressure correlation term

f_{pu1}	f_{pu2}	Re_t
$10\sqrt{A_2}/Re_t$	$-0.003 * min(1, Re_t/50)A^{1/4}$	$k^2/(\nu\varepsilon)$

Table 3.16: Coefficients related to the redistributive part of the pressure correlation term

c_1	c_1'	c_2	c_2'
$3.1 f_A f_{Re_t} A_2^{0.5}$	1.1	$min[0.55(1-\exp(-\frac{A^{1.5}Re_t}{100})), 3.2\frac{A}{1+S}]$	$min(0.6, A) + 3.5\frac{S-\Omega}{3+S+\Omega} - 2S_\ell$

f_A	f_{Re_t}	S	Ω
$\sqrt{A/14}$ $A < 0.05$ $\sqrt{A/0.7}$ $0.05 < A < 0.7$ $\sqrt{A}$ $A > 0.7$	$min(Re_t/160, 1)$	$\frac{k}{\varepsilon}\sqrt{\frac{1}{2}S_{ij}S_{ij}}$	$\frac{k}{\varepsilon}\sqrt{\frac{1}{2}\Omega_{ij}\Omega_{ij}}$

S_{ij}	Ω_{ij}	S_ℓ	f_{w1}
$\frac{\partial U_i}{\partial x_j} + \frac{\partial U_j}{\partial x_i}$	$\frac{\partial U_i}{\partial x_j} - \frac{\partial U_j}{\partial x_i}$	$S_{ij}S_{jk}S_{ki}/\sqrt{0.5S_{ln}S_{ln}}$	$0.4 + 1.6 f'_{Re_t}$

f_{w2}	f_{w3}	f'_{Re_t}	f''_{Re_t}
$0.1 + 0.8A_2 f''_{Re_t}$	$2.5\sqrt{A}$	$min[1, max(0.1 - \frac{Re_t-55}{20})]$	$min[1, max(0.1 - \frac{Re_t-50}{85})]$
f'_A	f'_{w1}	c_l	l
$\sqrt{A}f_{Re_t} + A(1-f_{Re_t})$	0.22	$0.7\sqrt{A(1-A)}$	$min[k^{3/2}/\varepsilon, 40(\nu^3/\varepsilon)^{1/4}]$

Table 3.17: Coefficients related to the dissipation and diffusion terms

$c_{\varepsilon s}$	f_ε	c_s
0.2	$A^{1.5}$	0.22

Table 3.18: Coefficients related to the dissipation rate equation

$c_{\varepsilon 1}$	$c_{\varepsilon 2}$	$c'_{\varepsilon 2}$	$c_{\varepsilon 3}$	$c_{\varepsilon l}$	c_{ε}	B_{ε}	c_{ℓ}
1.0	$\frac{1.92}{1+0.7max(A,0.25)A_2^{0.5}}$	1.0	0.875	0.5	0.15	0.1069	2.55

3.3 Multiple-Time-Scale Models

Since the major objective of this work is to develop a multiple-time-scale approach to improve prediction of non-equilibrium flows, it is sensible to assess the performance of some multiple-time-scale models available in the literature over a range of equilibrium and non-equilibrium flows in order to see how these models may be able to capture lags in the response of the turbulence.

Among the MTS models which will be tested, four are linear eddy viscosity models and one is a Reynolds stress transport model. All of them could be classified as two-time-scale models, since all are based on splitting the turbulent kinetic energy spectrum into three parts as already discussed in the Literature Survey. Figure 2.2 can be used for reference.

The first part of the spectrum is the production zone where turbulence is generated and the large scales store k_P of the total turbulent kinetic energy. According to the cascade process, the turbulent kinetic energy is transferred from the large to the small scales. Turbulent kinetic energy is thus transferred at a rate ε_P to the intermediate scales, which store k_T of the total turbulent kinetic energy. This range of length scales which store k_T is the second part of the spectrum, called the transfer range. The turbulent kinetic energy is then transferred to the even smaller scales at a rate ε_T. However, these even smaller scales are so small that the turbulent kinetic energy which is received is immediately dissipated into heat, thus characterizing the third part of the spectrum as the dissipation zone.

One may notice that according to the way the turbulent kinetic energy spectrum is modelled, the total turbulent kinetic energy k is given by $k = k_P + k_T$ and the turbulent eddy dissipation rate ε, used so far in the single-time-scale models, is simply $\varepsilon = \varepsilon_T$.

The multiple-time-scale models which will be described here use the above concept to model the turbulence. As one may have noticed, there are basically two scales being considered: the range of large length scales in the production zone and the range of length scales in the transfer zone. This is the reason why these models can be considered as two-time-scale models.

The turbulence models which will be presented are: the linear-eddy-viscosity models of Hanjalic et al. (1980), Kim and Chen (1989), Chen and Guo (1991), Nagano et al. (1997) and the Reynolds-stress-transport model of Wilcox (1988b).

3.3.1 TS model of Hanjalic et al. (1980)

The multiple-time-scale model proposed by Hanjalic et al. (1980) can be considered a reference for this class of turbulence models, since it was perhaps the first MTS model to approximate the turbulence kinetic energy spectrum as described above and therefore define the model

variables, k_P, k_T, ε_P and ε_T.

The model provides transport equations for each of the four variables k_P, k_T, ε_P and ε_T, presented in equation 3.43 to 3.46, in analogy to the STS LEV models, and uses the eddy-viscosity approach to calculate the Reynolds stresses as $\overline{u_i u_j} = \frac{2}{3}k\delta_{ij} - \nu_t\left(\frac{\partial U_i}{\partial x_j} + \frac{\partial U_j}{\partial x_i}\right)$, where ν_t, the eddy viscosity, is specified in a way to take into account the upper part of the spectrum: $\nu_t = c_\mu \frac{k k_P}{\varepsilon_P}$.

$$\frac{Dk_P}{Dt} = P_k - \varepsilon_P + c_\mu \frac{\partial}{\partial x_j}\left(\frac{k k_P}{\varepsilon_P}\frac{\partial k_P}{\partial x_j}\right) \tag{3.43}$$

$$\frac{Dk_T}{Dt} = \varepsilon_P - \varepsilon_T + c_\mu \frac{\partial}{\partial x_j}\left(\frac{k k_P}{\varepsilon_P}\frac{\partial k_T}{\partial x_j}\right) \tag{3.44}$$

$$\frac{D\varepsilon_P}{Dt} = C_{P1}P_k\frac{\varepsilon_P}{k_P} - C_{P2}\frac{\varepsilon_P^2}{k_P} + c_\mu \frac{\partial}{\partial x_j}\left(\frac{k k_P}{\varepsilon_P}\frac{\partial \varepsilon_P}{\partial x_j}\right) + C'_{P1}k_P\frac{\partial U_l}{\partial x_m}\frac{\partial U_i}{\partial x_j}\epsilon_{lmk}\epsilon_{ijk} \tag{3.45}$$

$$\frac{D\varepsilon_T}{Dt} = C_{T1}\frac{\varepsilon_P\varepsilon_T}{k_T} - C_{T2}\frac{\varepsilon_T^2}{k_T} + c_\mu \frac{\partial}{\partial x_j}\left(\frac{k k_P}{\varepsilon_P}\frac{\partial \varepsilon_T}{\partial x_j}\right) \tag{3.46}$$

The coefficients C_{P1}, C_{P2}, C_{T1} and C_{T2} are presented in Table 3.19. The term associated with the C'_{P1} coefficient in equation 3.45 was introduced in order to make the model more sensitive to normal straining. The value of this coefficient can be seen in Table 3.19 too.

One may have noted that the C_{P2} and C_{T1} coefficients were not specified as constants as is usually done in STS LEV models, but as functions of $\frac{k_P}{k_T}$ and $\frac{\varepsilon_P}{\varepsilon_T}$. Hanjalic et al. (1980) argued that since in this MTS model these ratios (which would respectively represent the shape and the equilibrium imbalance of the spectrum) were available, one should use them in order to relate the upper and the lower partitions and make them influence each other.

One may notice in equations 3.43 - 3.46 that the diffusion term is basically the same as usually used in eddy viscosity models, since c_μ can be inserted into the brackets and $c_\mu \frac{k k_P}{\varepsilon_P}$ can be replaced by ν_t. The diffusion terms thus become $\frac{\partial}{\partial x_j}\left(\nu_t \frac{\partial \phi}{\partial x_j}\right)$, where ϕ is each of the four main spectrum variables, which can be rewritten as $\frac{\partial}{\partial x_j}\left(\frac{\nu_t}{\sigma_\phi}\frac{\partial \phi}{\partial x_j}\right)$, σ_ϕ being the turbulent Prandtl number for ϕ and assuming the value of one. In the STREAM code, though, the diffusion term is actually implemented as $\frac{\partial}{\partial x_j}\left[\left(\nu + \frac{\nu_t}{\sigma_\phi}\right)\frac{\partial \phi}{\partial x_j}\right]$ in order to keep the viscous terms which would arise in the "exact" transport equations and might improve stability.

Table 3.19: Coefficients of the TS model of Hanjalic et al. (1980)

c_μ	C_{P1}	C_{P2}	C_{T1}	C_{T2}	C'_{P1}
0.09	2.2	$1.8 - 0.3\left(\frac{k_P}{k_T} - 1\right)/\left(\frac{k_P}{k_T} + 1\right)$	$1.08\frac{\varepsilon_P}{\varepsilon_T}$	1.15	-0.11

3.3.2 KC model of Kim and Chen (1989)

Kim and Chen (1989) proposed an MTS model based on Hanjalic et al.'s 1980 model, however they introduced an extra production term into the transfer rate equations. The transport equations for this model are presented below:

$$\frac{Dk_P}{Dt} = P_k - \varepsilon_P + \frac{\partial}{\partial x_j}\left[\left(\nu + \frac{\nu_t}{\sigma_k}\right)\frac{\partial k_P}{\partial x_j}\right] \tag{3.47}$$

$$\frac{Dk_T}{Dt} = \varepsilon_P - \varepsilon_T + \frac{\partial}{\partial x_j}\left[\left(\nu + \frac{\nu_t}{\sigma_k}\right)\frac{\partial k_T}{\partial x_j}\right] \tag{3.48}$$

$$\frac{D\varepsilon_P}{Dt} = C_{P1}P_k\frac{\varepsilon_P}{k_P} - C_{P2}\frac{\varepsilon_P^2}{k_P} + C_{P3}\frac{P_k^2}{k_P} + \frac{\partial}{\partial x_j}\left[\left(\nu + \frac{\nu_t}{\sigma_\varepsilon}\right)\frac{\partial \varepsilon_P}{\partial x_j}\right] \tag{3.49}$$

$$\frac{D\varepsilon_T}{Dt} = C_{T1}\frac{\varepsilon_P\varepsilon_T}{k_T} - C_{T2}\frac{\varepsilon_T^2}{k_T} + C_{T3}\frac{\varepsilon_P^2}{k_T} + \frac{\partial}{\partial x_j}\left[\left(\nu + \frac{\nu_t}{\sigma_\varepsilon}\right)\frac{\partial \varepsilon_T}{\partial x_j}\right] \tag{3.50}$$

Besides the coefficients values, which can be seen in Table 3.20, Kim and Chen (1989) also changed the expression for ν_t, taking the same expression usually used in STS LEV models: $\nu_t = c_\mu\frac{k^2}{\varepsilon_T}$. The authors argued that this expression would locate the partition $\frac{k_P}{k_T}$ in a higher or lower region of the spectrum, compared to its position in an equilibrium state.

Table 3.20: Coefficients of the KC model of Kim and Chen (1989)

c_μ	C_{P1}	C_{P2}	C_{P3}	C_{T1}	C_{T2}	C_{T3}	σ_k	σ_ε
0.09	1.24	1.84	0.21	1.28	1.66	0.29	0.75	1.15

3.3.3 CG model of Chen and Guo (1991)

Chen and Guo (1991) also proposed an MTS model based on the work of Hanjalic et al. (1980). The general features are the same, however they changed the constants and the expressions of the transport equations coefficients and also adopted a different expression for ν_t, being $\nu_t = c_\mu\frac{k^2}{\varepsilon_P}$.

The transport equations for this model are presented below, in equation 3.51 to 3.54, and the coefficients can be seen in Table 3.21.

$$\frac{Dk_P}{Dt} = P_k - \varepsilon_P + \frac{\partial}{\partial x_j}\left[\left(\nu + \frac{\nu_t}{\sigma_k}\right)\frac{\partial k_P}{\partial x_j}\right] \tag{3.51}$$

$$\frac{Dk_T}{Dt} = \varepsilon_P - \varepsilon_T + \frac{\partial}{\partial x_j}\left[\left(\nu + \frac{\nu_t}{\sigma_k}\right)\frac{\partial k_T}{\partial x_j}\right] \tag{3.52}$$

$$\frac{D\varepsilon_P}{Dt} = C_{P1}P_k\frac{\varepsilon_P}{k_P} - C_{P2}\frac{\varepsilon_P^2}{k_P} + C_{P3}W\varepsilon_P + \frac{\partial}{\partial x_j}\left[\left(\nu + \frac{\nu_t}{\sigma_\varepsilon}\right)\frac{\partial \varepsilon_P}{\partial x_j}\right] \tag{3.53}$$

$$\frac{D\varepsilon_T}{Dt} = C_{T1}\frac{\varepsilon_P\varepsilon_T}{k_T} - C_{T2}\frac{\varepsilon_T^2}{k_T} + C_{T3}W\varepsilon_T + \frac{\partial}{\partial x_j}\left[\left(\nu + \frac{\nu_t}{\sigma_\varepsilon}\right)\frac{\partial\varepsilon_T}{\partial x_j}\right] \tag{3.54}$$

The W term in equations 3.53 and 3.54 was described by the authors as the mean vorticity or angular velocity. The former was adopted to be implemented in the STREAM code.

Table 3.21: Coefficients of the CG model of Chen and Guo (1991)

c_μ	C_{P1}	C_{P2}	C_{P3}	C_{T1}	C_{T2}	C_{T3}	σ_k	σ_ε
0.09	1.42	$1.90\left(1 - 0.2\frac{k_T}{k_P} + 0.2\frac{k_T^2}{k_P^2}\right)$	-0.042	$0.96\left(1 + 0.01\frac{\varepsilon_T}{\varepsilon_P}\right)$	1.12	$-0.042\left(1 + 0.08\frac{\varepsilon_T}{\varepsilon_P}\right)$	0.75	1.0

3.3.4 NG model of Nagano et al. (1997)

Nagano et al. (1997) proposed a LEV MTS model, also based on the MTS model of Hanjalic et al. (1980), but with low Reynolds number (LRN) adaptations. To account for these effects the authors inserted damping functions into the modelled transport equations, presented below:

$$\frac{Dk_P}{Dt} = P_k - \varepsilon_P + \frac{\partial}{\partial x_j}\left[\left(\nu + f_t\frac{\nu_t}{\sigma_k}\right)\frac{\partial k_P}{\partial x_j}\right] \tag{3.55}$$

$$\frac{Dk_T}{Dt} = \varepsilon_P - \varepsilon_T + \frac{\partial}{\partial x_j}\left[\left(\nu + f_t\frac{\nu_t}{\sigma_k}\right)\frac{\partial k_T}{\partial x_j}\right] - \frac{1}{2}\nu\frac{\partial}{\partial x_j}\left(\frac{k}{\varepsilon_T}\frac{\partial\varepsilon_T}{\partial x_j}f_{w2}\right) \tag{3.56}$$

$$\frac{D\varepsilon_P}{Dt} = C_{P1}P_k\frac{\varepsilon_P}{k_P} - C_{P2}f_{P2}\frac{\varepsilon_P^2}{k_P} + \frac{\partial}{\partial x_j}\left[\left(\nu + f_t\frac{\nu_t}{\sigma_\varepsilon}\right)\frac{\partial\varepsilon_P}{\partial x_j}\right] + C'_{P1}\frac{\varepsilon_P}{k_P}(\overline{u}^2 - \overline{v}^2)\frac{\partial U}{\partial x} \tag{3.57}$$

$$\frac{D\varepsilon_T}{Dt} = C_{T1}f_{T1}\frac{\varepsilon_P\varepsilon_T}{k_T} - C_{T2}f_{T2}\frac{\varepsilon_T^2}{k_T} + \frac{\partial}{\partial x_j}\left[\left(\nu + f_t\frac{\nu_t}{\sigma_\varepsilon}\right)\frac{\partial\varepsilon_T}{\partial x_j}\right] + 0.5\nu\frac{\partial}{\partial x_j}\left[(1 - f_{w2})\frac{\varepsilon_T}{k}\frac{\partial k}{\partial x_j}f_{w2}\right] \tag{3.58}$$

The eddy viscosity ν_t was modelled as proposed by Hanjalic et al. (1980), $\nu_t = c_\mu\frac{kk_P}{\varepsilon_P}$. However, c_μ was not assigned to 0.09 as in the STS models and in the MTS models presented so far, but as a higher value which can be seen together with the other coefficients of this model in Table 3.22.

One may notice that the general formulation of the transport equations are basically the same as those presented so far for other MTS models. The main differences are the damping functions, which can be seen in Table 3.23, the pressure-diffusion terms inserted in equations 3.56 and 3.58 and the last term in equation 3.57 which was intended to act as an irrotational straining term, similar to the term introduced by Hanjalic et al. (1980) associated with the same constant. One may notice, though, that in a LEV model, $\overline{u^2} = \overline{v^2} = \overline{w^2}$ in simple shear

flows and therefore this term would vanish. Nagano et al. (1997) bypassed this problem by solving an algebraic stress model in flows where one would expect this term to improve prediction. As the focus of this project is not to test this model, but the MTS models' general features, this treatment was not employed in the STREAM code and this term was coded the way it is written here.

Table 3.22: Coefficients of the NG model of Nagano et al. (1997)

c_μ	C_{P1}	C_{P2}	C_{T1}	C_{T2}	σ_k	σ_ε
0.14	1.65	1.9	1.5	1.65	1.0	1.4

Table 3.23: Damping functions of the NG model of Nagano et al. (1997)

f_{P2}	f_{T1}	f_{T2}	f_t
$(1-f_{w2})(1-0.3f_{r2})$	$(1-f_{w2})$	$(1-f_{w2})(1-0.13f_{r2})$	$(1+3.5f_{r1})$
f_{r1}	f_{r2}	f_{w1}	f_{w2}
$e^{-\left(\frac{Re_t}{80}\right)^2}$	$e^{-\sqrt{\frac{Re_t}{12.5}}}$	$e^{-\left(\frac{y^*}{20}\right)^2}$	$e^{-\left(\frac{y^*}{3.3}\right)^2}$

3.3.5 WM model of Wilcox (1988b)

Wilcox (1988b) proposed a multiscale model based on his previous work on the $k-\omega$ LEV model. It is not exactly based on the model of Hanjalic et al. (1980), but the general treatment for the spectrum is similar.

This model was conceived as a Reynolds Stress Transport (RST) model so the division of the spectrum should take into account how to calculate the Reynolds stresses for the different partitions. The spectrum was split into two parts, the upper and the lower partitions. In the former, where the large scales dominate, the flow was taken to be inviscid. In the latter, the flow was taken to be isotropic and turbulent kinetic energy was assumed to be immediately dissipated into heat. The approach is thus based on the same split spectrum proposed by Hanjalic et al. (1980), but with additional considerations about the stresses rather than only the turbulent kinetic energy.

The transport equations then proposed follow below:

$$\frac{Dk}{Dt} = \overline{u_i u_j}\frac{\partial U_i}{\partial x_j} - \beta^*\omega k + \frac{\partial}{\partial x_j}\left[(\nu + \sigma^*\nu_t)\frac{\partial k}{\partial x_j}\right] \tag{3.59}$$

$$\frac{D\omega}{Dt} = \frac{\gamma\omega}{k}\overline{u_i u_j} - \beta\omega^2 - \xi\beta\omega\sqrt{2\Omega_{mn}\Omega_{mn}} + \frac{\partial}{\partial x_j}\left[(\nu + \sigma\nu_t)\frac{\partial \omega}{\partial x_j}\right] \tag{3.60}$$

$$\frac{D\overline{u_i u_j}}{Dt} = -P_{ij} + \frac{2}{3}\beta^*\omega k\delta_{ij} + \left(E_{ij} - E\delta_{ij}\right) + \frac{\partial}{\partial x_j}\left[(\nu + \nu_t)\frac{\partial \overline{u_i u_j}}{\partial x_j}\right] \tag{3.61}$$

$$\frac{Dk_u}{Dt} = (1-\hat{\alpha}-\hat{\beta})P - \beta^*\omega k\left(\frac{k_u}{k}\right)^{3/2} \tag{3.62}$$

where $\Omega_{ij} = \frac{1}{2}\left(\frac{\partial U_i}{\partial x_j} - \frac{\partial U_j}{\partial x_i}\right)$ is the vorticity, $P_{ij} = -\overline{u_i u_m}\frac{\partial U_j}{\partial x_m} - \overline{u_j u_m}\frac{\partial U_i}{\partial x_m}$ is the Reynolds stresses production, $P = \frac{1}{2}P_{mm}$ and E_{ij} is the energy exchange between the upper and the lower partition energies given by:

$$E_{ij} = -C_1\beta^*\omega\left(\overline{u_i u_j} + \frac{2}{3}k\delta_{ij}\right) + \hat{\alpha}P_{ij} + \hat{\beta}D_{ij} + \hat{\gamma}k\left(s_{ij} - \frac{1}{3}\frac{\partial U_k}{\partial x_k}\delta_{ij}\right) + \frac{2}{3}\omega k\left(\frac{k_u}{k}\right)^{3/2}\delta_{ij} \tag{3.63}$$

where $D_{ij} = \overline{u_i u_m}\frac{\partial U_m}{\partial x_j} + \overline{u_j u_m}\frac{\partial U_m}{\partial x_i}$, $s_{ij} = \frac{1}{2}\left(\frac{\partial U_i}{\partial x_j} + \frac{\partial U_j}{\partial x_i}\right)$ is the mean strain rate tensor and k_u, obtained from solving equation 3.62, is the upper partition turbulent kinetic energy.

The constants of the model can be found in Table 3.24 and $\nu_t = \frac{k}{\omega}$ is given as in the $k-\omega$ model.

Table 3.24: Coefficients of the WM model of Wilcox (1988b)

$\hat{\alpha}$	$\hat{\beta}$	β	β^*	$\hat{\gamma}$	γ	σ	σ^*	ξ	C_1
$\frac{42}{55}$	$\frac{6}{55}$	$\frac{3}{40}$	$\frac{9}{100}$	$\frac{1}{4}$	$\frac{4}{5}$	$\frac{1}{2}$	$\frac{42}{55}$	1.0	$1+4\left(\frac{k_u}{k}\right)^{3/2}$

3.4 Wall Function

High-Reynolds-number turbulence models neglect near-wall effects in their modelling and therefore should not be integrated to the wall as they will fail to give accurate predictions. In this case it is common to use wall functions to account for the near-wall viscosity-affected layers of the flow.

Wall functions are then empirical formulations that are designed to model the viscous sublayer and immediate outer layer adjacent to a wall in order to allow the high-Reynolds-number turbulence models to represent the flow from this point on. As a result, the first node, starting from the wall, should be located outside the viscous sublayer, implying the first node should be at a non-dimensional distance from the wall of $y^+ \approx 30$ or greater.

One advantage of using wall functions is associated with the time and effort of calculation that can be saved since the viscous sublayer is not being resolved, which would require a very fine grid and consequent computational resources. On the other hand, its disadvantage lies in the fact that the wall functions are empirical formulations, usually based on zero pressure gradient boundary layers, which may compromise their accuracy when applied to more complex flow cases.

The wall function which will be briefly described below is based on Chieng and Launder's 1980 work and will be presented in the way it is applied in the STREAM code.

The wall function applies the log law, but instead of using the friction velocity ($U_\tau = \sqrt{\frac{\tau_w}{\rho}}$,

where τ_w is the wall shear) as a velocity scale, it uses $c_\mu^{1/4}k^{1/2}$, which is equivalent to using the friction velocity in local equilibrium boundary layers, but avoids the problems associated with τ_w going to zero at separation/reattachment or impingement points. Then the log law is rewritten as:

$$\frac{c_\mu^{1/4}k^{1/2}U}{(\tau_w/\rho)} = \frac{1}{\kappa}\ln\left(y\frac{Ec_\mu^{1/4}\sqrt{k}}{\nu}\right) \tag{3.64}$$

where $\kappa = 0.41$ is the von Karmam constant and E is the log law constant usually taken as 9. The above equation is valid outside the viscous sublayer, within which the simpler linear law ($U^+ = y^+$) applies. Taking y_ν to be the viscous sublayer height, one can then provide a value for τ_w as follows:

$$\begin{aligned}\mu_w &= \begin{cases} \mu & \text{if } y \le y_\nu \\ \frac{y\rho\kappa c_\mu^{1/4}\sqrt{k}}{\ln(E(y/\nu)c_\mu^{1/4}\sqrt{k})} & \text{if } y > y_\nu \end{cases} \\ \tau_w &= \mu_w\frac{U}{y}\end{aligned} \tag{3.65}$$

where μ_w is the "eddy viscosity at the wall", y the distance from the first node to the wall, and U the velocity at the near-wall node. A value for ε is also provided for the first node as a function of the distance to wall as follows:

$$\varepsilon = \frac{k^{3/2}}{2.55y} \tag{3.66}$$

The equation for k is still solved for the first near-wall node, however the values of P_k and ε (for the eddy viscosity models) and the Reynolds stresses $\overline{u_iu_j}$ (for the RST models) are also estimated by the wall function.

The values of P_k and ε are not evaluated at the near-wall node, because they can be expected to vary rapidly across the near-wall cell, and a better approach is thus to consider cell-averaged values for them: $\overline{P_k}$ and $\overline{\varepsilon}$, respectively. Hence, the wall function approximates:

$$\overline{P_k} = \begin{cases} 0 & \text{if } 2y \le y_\nu \\ \left(\frac{\tau_w}{\rho}\right)^2\ln\left(\frac{2y}{y_\nu}\right)\frac{1}{2y\kappa c_\mu^{1/4}\sqrt{k}} & \text{if } 2y > y_\nu \end{cases} \tag{3.67}$$

$$\overline{\varepsilon} = \begin{cases} \frac{2\nu k}{y_\nu^2} & \text{if } 2y \le y_\nu \\ \frac{1}{2y}\left[\frac{2\nu k}{y_\nu} + ln\left(\frac{2y}{y_\nu}\right)\frac{c_\mu^{1/4}k^{3/2}}{\kappa}\right] & \text{if } 2y > y_\nu \end{cases} \tag{3.68}$$

For the RST models, the Reynolds stresses are approximated at the wall through an ARS model applied to boundary layer flows. For these kinds of flow, the general Reynolds stress

transport equation can be expressed as a function of $\frac{\overline{u_i u_j}}{k}$ and the mean strain rate S: $\frac{D}{Dt}\left(\frac{\overline{u_i u_j}}{k}\right) = f(\frac{\overline{u_i u_j}}{k}, S)$. For boundary layer flows, the value of S is known and $\frac{D}{Dt}\left(\frac{\overline{u_i u_j}}{k}\right)$ can be set to zero, thus implying a system where one can find the value of $\overline{u_i u_j}$ as a function of the turbulent kinetic energy k in wall-aligned coordinates:

$$\begin{aligned}
\overline{u}_t^2 &= 1.098k \\
\overline{u}_n^2 &= 0.247k \\
\overline{u}_b^2 &= 2k - \overline{u}_t^2 - \overline{u}_n^2 = 0.655k \\
\overline{u_t u_n} &= -0.255k \\
\overline{u_t u_b} &= \overline{u_n u_b} = 0
\end{aligned} \tag{3.69}$$

where $\overline{u}_t^2$, $\overline{u}_n^2$ and $\overline{u}_b^2$ are the normal Reynolds stresses aligned to the three wall coordinates in the streamwise, wall-normal and third directions and $\overline{u_t u_n}$, $\overline{u_t u_b}$ and $\overline{u_n u_b}$ are the Reynolds shear stresses also aligned to the three wall coordinates. These Reynolds stress components are then transformed into Cartesian coordinates and assigned as the values the Reynolds stresses should take at the first node near the wall.

This is then the wall function that was applied in this work together with the standard $k-\varepsilon$ model and the high-Reynolds-number RST models of Gibson and Launder (1978) and Speziale et al. (1991).

3.4.1 Wall Functions for the MTS models

Three of the MTS models described here are high-Reynolds-number models since they do not have any treatment for the region near the wall where the local turbulent Reynolds number becomes very low. That means they need to be used together with wall functions.

The wall function used for standard STS models have just been described above, however in order to be used together with MTS models, it needs some adaptations.

The velocity treatment remains the same, as do the modifications to evaluate P_k and ε used in the k (now k_P) equation. Instead of specifying just ε at the near wall node, from assuming equilibrium conditions (as done in the standard STS wall function), "equilibrium" values are set for k_T, ε_P and ε_T.

In a local equilibrium boundary layer, $\varepsilon_P = \varepsilon_T$. Therefore, the same treatment given to ε in STS models can also be applied to ε_P, for example, and then ε_T is set equal to ε_P.

It remains then to determine an appropriate value for k_T. Some initial calculations of simple channel flows performed in this study have shown that in the local equilibrium boundary layer $\frac{k_P}{k} \approx \frac{2}{3}$ and $\frac{k_T}{k} \approx \frac{1}{3}$ which implies that $\frac{k_P}{k_T} \approx 2$. That is a rough, but reasonable, approximation to apply for the wall function. The more correct way to do it would be to derive an exact expression for $\frac{k_P}{k_T}$ for each particular model through a local equilibrium boundary layer asymptotic analysis. However some tests were performed by applying this "real" value of $\frac{k_P}{k_T}$ for the KC model (because Kim and Chen (1989) provide

this relation), applying the ratio $\frac{k_P}{k_T} = 2$ as above, and also by solving the transport equation for k_T in the first node and no significant difference was found. Therefore, in the present work, the three high-Reynolds-number LEV MTS models (TS, KC and CG) were run by setting in the wall function that $\frac{k_P}{k_T} \approx 2$.

3.5 Concluding Remarks

The turbulence models which will be used in this work were all presented in detail in the way they are implemented in the STREAM code. One can notice that each model contains particular features which will be of use to evaluate the performance of the models in the test cases which will be discussed in chapter 5.

In the following chapters these models will be referred to using the acronyms presented in Table 3.25 which are the same acronyms used in the STREAM code to identify each one of the turbulence models.

Table 3.25: Turbulence models' acronym in STREAM code

Acronym	Model
HR	Launder and Spalding's standard $k-\varepsilon$ model
LS	Launder and Sharma's LRN $k-\varepsilon$ model
FM	Menter's SST model
KS	Modified Craft et al.'s Cubic NLEV $k-\varepsilon$ model
GL	Gibson and Launder's RST model
SG	Speziale et al.'s SSG RST model
HJ	Hanjalic et al.'s LRN RST model
TC	Craft's TCL LRN RST model
TS	Hanjalic et al.'s LEV MTS model
KC	Kim and Chen's LEV MTS model
CG	Chen and Guo's LEV MTS model
NG	Nagano et al.'s LRN LEV MTS model
WM	Wilcox's LRN RST MTS model

Chapter 4

Numerical Approaches

In order to predict turbulent flows one needs to solve numerically the closed set of equations comprised by the Navier-Stokes equations, continuity equation and those from the turbulence models discussed in the previous chapter. As this system consists of differential equations, it is necessary to discretize them and solve them numerically. Among the discretization techniques available in the literature, the three main ones are the Finite Difference, the Finite Volume and the Finite Element methods. The former is the simplest one, but presents some difficulties, for example in imposing conservation over the domain which is very important for flow simulations since their governing equations are conservation equations of momentum, heat and mass. The Finite Element method is the most complex, although it is similar to the Finite Volume one. Besides being relatively easy to apply, the Finite Volume method assures conservation, and because of that it became the most widely used discretization method in CFD codes. This is the method adopted here and will thus be described in this work.

The two main topics which will be covered in this Chapter are then the Finite Volume method and the main features of the STREAM code which was used in this work and also applies the Finite Volume method.

4.1 The Finite Volume Method

The Finite Volume method, from now on referred to as FV, consists of dividing the domain into small control volumes and integrating the set of equations over each one of them. In order to illustrate this technique, one can consider a general steady governing equation composed by a convection, a diffusion and a source term:

$$\frac{\partial(U_j\phi)}{\partial x_j} = \frac{\partial}{\partial x_j}\left(\Gamma_\phi \frac{\partial \phi}{\partial x_j}\right) + S_\phi \tag{4.1}$$

In the above equation, ϕ stands for any quantity such as velocity, temperature, concentration, Reynolds stress component, etc and Γ is its respective diffusivity. A general control volume over which equation (4.1) is integrated is illustrated in Figure 4.1, indicated by CV, where the capital letters indicate the node position and the lower case letters indicate face

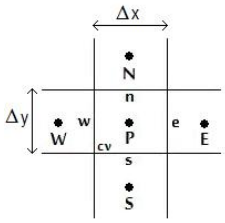

Figure 4.1: 2D Control Volume for the Finite Volume method

position. P is the node at the centre of the current cell over which the equations are to be integrated and W or w, E or e, N or n and S or s stand for its respective west, east, north and south node or face. The way the nodes are located in the control volume affects the numerical accuracy (Ferziger and Peric, 2002). In Figure 4.1 they are centered in the CV which is perhaps the most common way.

Integrating equation (4.1) over the control volume, one obtains:

$$\int_{CV} \frac{\partial(U_j\phi)}{\partial x_j}\,\mathrm{d}V = \int_{CV} \frac{\partial}{\partial x_j}\big(\Gamma_\phi \frac{\partial \phi}{\partial x_j}\big)\,\mathrm{d}V + \int_{CV} S_\phi\,\mathrm{d}V \tag{4.2}$$

In order to apply the divergence theorem, equation (4.2) can be rewritten as:

$$\int_{CV} \nabla\cdot(U\phi - \Gamma_\phi\nabla\phi)\,\mathrm{d}V = \int_{CV} S_\phi\,\mathrm{d}V \tag{4.3}$$

The volume integral on the left hand side of equation (4.3) can be transformed into a surface integral through the divergence theorem as:

$$\int_{\partial S} (U\phi - \Gamma_\phi\nabla\phi)\cdot n\,\mathrm{d}S = \int_{CV} S_\phi\,\mathrm{d}V \tag{4.4}$$

where ∂S and n stand for the control volume boundary and the unit vector normal to the surface, respectively. The surface integral argument, $(U\phi - \Gamma\nabla\phi)\cdot n$, represents the total net flux through the control volume surface, the first term, $(U\phi)\cdot n$, being the convective flux and the second term, $(\Gamma\nabla\phi)\cdot n$, the diffusive flux. Since the same integration is performed over each control volume in the domain and there is no overlapping between the control volumes boundaries, this method ensures conservation over the whole domain.

The volume integral of the source term over the control volume in equation (4.4) is usually approximated by the product of its average value in the control volume, $(S_\phi)_P$ (when P is located in the centre of the CV), and the CV volume, V_{CV}:

$$\int_{CV} S_\phi\,\mathrm{d}V \approx (S_\phi)_P V_{CV} \tag{4.5}$$

The surface integral in equation (4.4) is usually approximated by the summation of the total

flux through each one of the control volume faces ($f = w, e, n, s, t, b$):

$$\int_{\partial S} (U\phi - \Gamma_\phi \nabla\phi) \cdot n \, \mathrm{d}S \approx \sum_f (U\phi - \Gamma_\phi \nabla\phi)_f (n\Delta S)_f \tag{4.6}$$

Equations (4.5) and (4.6) are the discretized form of equation (4.1) and both approximations can be shown to be of second order accuracy. The governing equations are discretized by integrating over each control volume, giving rise to a system of algebraic equations where the number of unknowns is equal to the number of control volumes which is the number of equations in the system.

In order to illustrate this algebraic system and exemplify the discretization process, the method will be applied on a 2D rectangular grid for the general quantity ϕ governed by equation (4.1). Integrating thus equation (4.1) over the control volume illustrated in Figure 4.1, one obtains:

$$\iint_{CV} \left[\frac{\partial (U\phi)}{\partial x} + \frac{\partial (V\phi)}{\partial y} \right] \mathrm{d}x \, \mathrm{d}y = \iint_{CV} \left[\frac{\partial}{\partial x} \left(\Gamma_\phi \frac{\partial \phi}{\partial x} \right) + \frac{\partial}{\partial y} \left(\Gamma_\phi \frac{\partial \phi}{\partial y} \right) \right] \mathrm{d}x \, \mathrm{d}y + \iint_{CV} S_\phi \, \mathrm{d}x \, \mathrm{d}y \tag{4.7}$$

The above equation then becomes:

$$\left[\int U\phi \, \mathrm{d}y \right]_w^e + \left[\int V\phi \, \mathrm{d}x \right]_s^n = \left[\int \Gamma_\phi \frac{\partial \phi}{\partial x} \, \mathrm{d}y \right]_w^e + \left[\int \Gamma_\phi \frac{\partial \phi}{\partial y} \, \mathrm{d}x \right]_s^n + (S_\phi)_P \Delta x \Delta y \tag{4.8}$$

In the above equation, the left hand side comprises the convective term and the right hand side, the diffusive and source terms. The latter is already in its final form accordingly to equation (4.5). So it remains to treat the convective and diffusive parts. Starting with the latter, it can be approximated as:

$$\left[\int \Gamma_\phi \frac{\partial \phi}{\partial x} \, \mathrm{d}y \right]_w^e + \left[\int \Gamma_\phi \frac{\partial \phi}{\partial y} \, \mathrm{d}x \right]_s^n \approx \left[\Gamma_\phi \frac{\partial \phi}{\partial x} \Delta y \right]_w^e + \left[\Gamma_\phi \frac{\partial \phi}{\partial y} \Delta x \right]_s^n \tag{4.9}$$

The derivatives in equation (4.9) are usually approximated by a Central Difference Scheme (CDS) and the whole diffusion term assumes the form:

$$\left[\Gamma_\phi \frac{\partial \phi}{\partial x} \Delta y \right]_w^e + \left[\Gamma_\phi \frac{\partial \phi}{\partial y} \Delta x \right]_s^n = (\Gamma_\phi \Delta y)_e \frac{\phi_E - \phi_P}{\Delta x} - (\Gamma_\phi \Delta y)_w \frac{\phi_P - \phi_W}{\Delta x} + (\Gamma_\phi \Delta x)_n \frac{\phi_N - \phi_P}{\Delta y} - (\Gamma_\phi \Delta x)_s \frac{\phi_P - \phi_S}{\Delta y} \tag{4.10}$$

Now the diffusion term has been discretized. Recalling that the convective term in equation (4.8) is approximated similarly to the diffusive term, one has:

$$\left[\int U\phi\,\mathrm{d}y\right]_w^e + \left[\int V\phi\,\mathrm{d}x\right]_s^n \approx [U\phi\Delta y]_w^e + [V\phi\Delta x]_s^n \tag{4.11}$$

The right hand side in the above equation thus leads to:

$$[U\phi\Delta y]_w^e + [V\phi\Delta x]_s^n = \underbrace{[U\Delta y]_e}_{C_{xe}}\phi_e - \underbrace{[U\Delta y]_w}_{C_{xw}}\phi_w + \underbrace{[V\Delta x]_n}_{C_{yn}}\phi_n - \underbrace{[V\Delta x]_s}_{C_{ys}}\phi_s \tag{4.12}$$

In equation (4.12), the terms underbraced are the volume flow fluxes in the x and y directions through the east, west, north and south cell faces. One may notice that ϕ's value is required at the face, not at the node where its value is stored. In this case, another approximation will be necessary. Because of the non-linearity of the convective term, the approximation selected for the cell-face values of ϕ has a strong influence on both the accuracy and boundedness of the resulting numerical solution. In order to proceed with the discretization method, the interpolation method that will be adopted now is the upwind scheme which is perhaps the simplest one and usually assures stability, but compromises accuracy since it is only first order accurate. The upwind scheme consists of:

$$\phi_e = \begin{cases} \phi_P & \text{if } C_{xe} > 0 \\ \phi_E & \text{if } C_{xe} \leq 0 \end{cases} \tag{4.13}$$

Now equation (4.1) is totally discretized. Equations (4.10), (4.12) and (4.13) can be combined, substituted into equation (4.8) and reorganized in order to put the unknowns in an explicit way. The result of this algebraic manipulation is:

$$A_P\phi_P = A_E\phi_E + A_W\phi_W + A_N\phi_N + A_S\phi_S + (S_\phi)_P\Delta x\Delta y \tag{4.14}$$

where:

$$\begin{aligned} A_E &= (\Gamma_\phi\Delta y/\Delta x)_e + max(-C_{xe}, 0) \\ A_W &= (\Gamma_\phi\Delta y/\Delta x)_w + max(C_{xw}, 0) \\ A_N &= (\Gamma_\phi\Delta x/\Delta y)_n + max(-C_{yn}, 0) \\ A_S &= (\Gamma_\phi\Delta x/\Delta y)_s + max(C_{ys}, 0) \\ A_P &= A_E + A_W + A_N + A_S \end{aligned} \tag{4.15}$$

Equation (4.14) together with equation (4.15) represent the system of algebraic equations to be solved when the FV method is applied. In equation (4.15), except for A_P which is the sum of the other coefficients, the coefficients are formed by two terms: the first comes from the discretization of the diffusive term and the second, from the discretization of the convective one. One may also notice that if the interpolation method for the value of ϕ at the face in

the convective term is not the upwind scheme, equation (4.14) will remain the same and the second term in the coefficients' expression, equation (4.15), may change. There are many other interpolation methods available in the literature which usually increase accuracy, but may compromise stability. A regular practice thus is to firstly begin a simulation with the upwind scheme, and once the solution is partly converged to switch to a more accurate scheme. An example of a more accurate interpolation method will be presented in the STREAM code section.

4.1.1 Pressure Correction Schemes

The above discretization process applies to all governing equations, except for the continuity equation which represents the conservation of mass and, for incompressible flows where the density is taken as constant, it is linear in the velocities. Besides that, when one solves the system formed by the continuity equation and the Navier-Stokes equations for U, V, W and P, there is one transport equation to each velocity component and no governing equation for the pressure P, the continuity equation being the fourth equation to close the system. In this scenario, it is necessary to find a way to ensure the continuity equation is satisfied. The Semi Implicit Method for Pressure Linked Equations (SIMPLE) Scheme, developed by Patankar and Spalding (1972), is one of the most widely used schemes and is also the one employed in the STREAM code. Because of that, it will be used here to illustrate the coupling between the velocities and the pressure.

Recalling equation (4.1) for $\phi = U$, it becomes the Navier-Stokes equation for the U velocity component where the source term is thus the pressure gradient $-\frac{\partial P}{\partial x}$. Equation (4.14) can then be rewritten as follows:

$$A_P U_P = \sum_k A_k U_k + \left(-\frac{\partial P}{\partial x} \right)_P V_{CV} \tag{4.16}$$

where k stands for the nodes around the node P (which are E, W, N and S for a 2D grid). In this case, the source term also needs to be discretized. In a fully collocated grid, where all quantities are stored in the nodes, as Figure 4.1 suggests, the value of the pressure gradient at node P could be obtained by using a central difference between cell-face pressure values as:

$$\left(-\frac{\partial P}{\partial x} \right)_P V_{CV} \approx -\frac{P_e - P_w}{\Delta x} \Delta x \Delta y = (P_w - P_e) \Delta y \tag{4.17}$$

The above result can then be substituted in equation (4.16) and U_P isolated by dividing the whole equation by A_P:

$$U_P = \sum_k \frac{A_k U_k}{A_P} + \underbrace{\frac{\Delta y}{A_P}}_{D_U} (P_w - P_e) \tag{4.18}$$

In a 2D simulation, one would also solve the Navier-Stokes equation for the velocity component V. Similarly, its discretized form is obtained as:

$$V_P = \sum_k \frac{A_k V_k}{A_P} + \underbrace{\frac{\Delta x}{A_P}}_{D_V}(P_s - P_n) \tag{4.19}$$

When one solves equations (4.18) and (4.19) starting from initially guessed values for the pressure, the resulting U and V may not satisfy the continuity equation. A pressure correction scheme then suggests the insertion of corrections to the velocities U', V' and pressure P' as follows:

$$U^* = U + U' \qquad V^* = V + V' \qquad P^* = P + P' \tag{4.20}$$

where the $*$ indicates the corrected quantities and the $'$ indicates the correction. The idea is that the corrected quantities must satisfy both Navier-Stokes and continuity equations. In order to satisfy the former, equation (4.20) must be substituted into equations (4.18) and (4.19). The resulting equation is then subtracted from the original equations (4.18) and (4.19) for the "uncorrected" velocities and one finds an equation linking the velocity and pressure corrections:

$$U'_P = \sum_k \frac{A_k U'_k}{A_P} + D_U(P'_w - P'_e) \qquad V'_P = \sum_k \frac{A_k V'_k}{A_P} + D_V(P'_s - P'_n) \tag{4.21}$$

The SIMPLE scheme then suggests that the summations in the above equations (involving velocities at nodes other than P) are ignored. As a result, the corrections become linked by:

$$U'_P = D_U(P'_w - P'_e) \qquad V'_P = D_V(P'_s - P'_n) \tag{4.22}$$

Now it remains to satisfy the continuity equation. Following the discretization procedure already described in the previous subsection, the discretized form of the continuity equation for the corrected velocities is:

$$[(\rho U^*)_e - (\rho U^*)_w]\Delta y + [(\rho V^*)_n - (\rho V^*)_s]\Delta x = 0 \tag{4.23}$$

One may notice that the values of U^* and V^* are required at the control volume faces. Hence, one will need the corrections also at the faces. The same procedure as outlined above can be used to link cell face velocity corrections to pressure corrections, resulting in:

$$U'_e = D_U(P'_P - P'_E) \qquad U'_w = D_U(P'_W - P'_P) \qquad V'_n = D_V(P'_P - P'_N) \qquad V'_s = D_V(P'_S - P'_P) \tag{4.24}$$

Now the above expressions for the corrections can be combined with equation (4.20) to be substituted into the discretized continuity equation, equation (4.23). The result is a system of algebraic equations to be solved for the pressure correction P':

$$a_p P'_P = a_e P'_E + a_w P'_W + a_n P'_N + a_s P'_S - S_m \tag{4.25}$$

In the above equation, $S_m = [(\rho U)_e - (\rho U)_w]\Delta y - [(\rho V)_n - (\rho V)_s]\Delta x$ which is the mass imbalance since it is the discretized continuity equation for the "uncorrected" velocities U and V. One may also note that the pressure corrections are evaluated at the nodes and the coefficients are being calculated at the faces:

$$\begin{aligned} a_e &= \Delta y(\rho D_U)_e \\ a_w &= \Delta y(\rho D_U)_w \\ a_n &= \Delta x(\rho D_V)_n \\ a_s &= \Delta x(\rho D_V)_s \\ a_p &= a_e + a_w + a_n + a_s \end{aligned} \tag{4.26}$$

The above summarizes the SIMPLE scheme and shows how the continuity equation gives rise to a pressure correction equation which results in discretized equations for all variables in both Navier-Stokes and continuity equation. There are other pressure and pressure correction schemes available in the literature which try to reach convergence faster. However it is beyond the scope here to consider other alternatives.

4.1.2 Algebraic System Solution

Both systems above, namely equations (4.14) for the main variables and (4.25) for the pressure correction, must be numerically solved, since they may be non-linearly coupled. One should also notice that, if solving for only one direction - an 1D problem, these systems would be tridiagonal. One of the most commonly used numerical methods for these kinds of algebraic systems is called the Tridiagonal Matrix Algorithm (TDMA). The advantage of this method against many others is that the number of operations that must be done is proportional to the number of unknowns (m) instead of the number of positions in the full matrix (m^3) (Ferziger and Peric, 2002). Besides that, its implementation in a programming language is considered easy.

When solving for 2D or 3D problems, one may approximate the systems composed of

the discretized equations (4.14) and (4.25) as tridiagonal, in order to use the TDMA, by considering one-direction at a time. Thereby, the systems can be considered as a series of tridiagonal systems:

$$A_P\phi_P^n = A_E\phi_E^n + A_W\phi_W^n + [A_N\phi_N + A_S\phi_S + A_T\phi_T + A_B\phi_B + S_\phi]^{n-1} \tag{4.27}$$

$$A_P\phi_P^n = A_N\phi_N^n + A_S\phi_S^n + [A_E\phi_E + A_W\phi_W + A_T\phi_T + A_B\phi_B + S_\phi]^{n-1} \tag{4.28}$$

$$A_P\phi_P^n = A_T\phi_T^n + A_B\phi_B^n + [A_E\phi_E + A_W\phi_W + A_N\phi_N + A_S\phi_S + S_\phi]^{n-1} \tag{4.29}$$

where n stands for the current iteration, $n-1$ for the previous iteration and equation (4.27) is solved for the east-west direction, equation (4.28) for the north-south direction and equation (4.29) for the top-bottom direction.

The TDMA is the numerical method used in STREAM code where it is applied as discussed above. The TDMA is not going to be discussed here since it is not the focus of the chapter, however the TDMA as well as other numerical methods can be easily found in numerical methods and CFD related books such as Ferziger and Peric (2002).

4.1.3 Boundary Conditions

When solving differential equations, one must normally provide boundary conditions for the variables being solved for. Two types of boundary conditions will be discussed here because they are the most commonly used for flow simulations. The first is known as Dirichlet Condition and consists of specifying a value for the variable ϕ at the boundary. The second is the Neumann Condition where one specifies the value of the gradient of ϕ at the boundary.

To illustrate how the boundary conditions are applied in the FV method, one can consider a 2D problem where equation (4.14) will be applied with a boundary condition for the north face, as in Figure 4.2. So equation (4.14) can be rewritten as:

$$A_P \underbrace{\phi_{i,nj-1}}_{\phi_P} = A_E \underbrace{\phi_{i+1,nj-1}}_{\phi_E} + A_W \underbrace{\phi_{i-1,nj-1}}_{\phi_W} + A_N \underbrace{\phi_{i,nj}}_{\phi_N} + A_S \underbrace{\phi_{i,nj-2}}_{\phi_S} + \underbrace{S_{\phi_{i,nj-1}}}_{S_{\phi P}} \tag{4.30}$$

If the boundary condition is of Dirichlet type, one would simply set $\phi_{i,nj} = \gamma$ where γ is the value at the boundary, and equation (4.30) would become:

$$A_P\phi_{i,nj-1} = A_E\phi_{i+1,nj-1} + A_W\phi_{i-1,nj-1} + A_N\gamma + A_S\phi_{i,nj-2} + S_{\phi_{i,nj-1}} \tag{4.31}$$

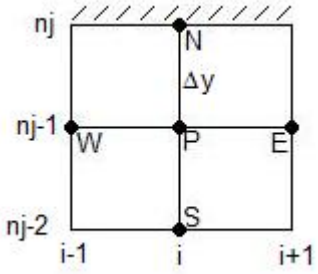

Figure 4.2: North boundary condition in a 2D problem

One may thus notice that there is no modification needed to the matrix coefficients for the Dirichlet boundary condition. Now, if the boundary condition is of Neumann type, one has:

$$\frac{\partial \phi_{i,nj}}{\partial y_{i,nj}} = \gamma \qquad \Rightarrow \qquad \frac{\phi_{i,nj} - \phi_{i,nj-1}}{\Delta y} = \gamma \qquad \Rightarrow \qquad \phi_{i,nj} = \phi_{i,nj-1} + \gamma \Delta y \tag{4.32}$$

where $\Delta y = y_{i,nj} - y_{i,nj-1}$ and γ is the value of the gradient of ϕ at the north face. Substituting the above equation into equation (4.30), one has for the Neumann boundary condition:

$$(A_P - A_N)\phi_{i,nj-1} = A_E\phi_{i+1,nj-1} + A_W\phi_{i-1,nj-1} + A_S\phi_{i,nj-2} + [S_{\phi_{i,nj-1}} + A_N\gamma\Delta y] \tag{4.33}$$

One may notice that the diagonal coefficient A_P and the source term are altered for the Neumann boundary condition:

$$\begin{aligned} A'_P &= (A_P - A_N) \\ S'_{\phi_{i,nj-1}} &= S_{\phi_{i,nj-1}} + A_N\gamma\Delta y \end{aligned} \tag{4.34}$$

where the prime indicates the new value of the A_P coefficient and the source term.

However, in the particular case where $\gamma = 0$ - symmetry conditions, for example, the Neumann boundary condition reduces to a Dirichlet boundary condition because equation (4.32) reduces to $\phi_{i,nj} = \phi_{i,nj-1}$. Hence, in this particular case there are no modifications needed for the matrix coefficients when Neumann boundary conditions are applied.

The procedure carried out above can be easily extended for any face of the domain and so the boundary conditions are applied together with the FV method.

4.1.4 General Procedure

This subsection simply aims to organize the steps one should follow to apply the discretization method described above. Thus, the general procedure to solve a set of discretized equations is:

1. Initially, to start calculation, one may provide the system with boundary conditions and initial guesses.
2. The discretized Navier-Stokes equations for all velocity components (U, V, and W) should be solved accordingly to equations (4.18) and (4.19).
3. Then, equation (4.25) must be solved for the pressure correction.
4. The velocity corrections should thus be calculated through equations (4.22) and (4.24), depending on where the velocity is being stored accordingly to the type of grid. For the fully collocated grid illustrated here, one should use equation (4.22) and obtain the value of the pressure at the faces through an interpolation technique.
5. The velocities must then be updated through equation (4.20).
6. Any other quantity should now be solved through equation (4.14).
7. Step 2 must be repeated until convergence.

Among the steps listed above, it still remains to discuss convergence criteria and relaxation. However these topics will be left for the next section where the STREAM code will be described.

4.2 STREAM Code

The STREAM code was developed following the general procedures of Lien and Leschziner (1994a). The acronym STREAM stands for Simulation of Turbulent Reynolds-averaged Equations for All Mach numbers (STREAM) which indicates the code is suitable for incompressible and compressible flows for a large range of Mach numbers.

The code is designed to apply the Finite Volume method on a 3D non-orthogonal fully collocated grid, which means it is written in general curvilinear (ξ, η, ζ) coordinates and stores all quantities only on the nodes which are defined to be centered in the control volumes. When using the curvilinear coordinates, one may choose between working with the Cartesian velocities U, V, and W or its components in the ξ, η, ζ directions. The former form presents the advantage of writing the governing equations for the Cartesian quantities. That was thus the form adopted in the STREAM code and its sketch can be seen in Figure (4.3).

The STREAM code can be interpreted as working with a dimensionless form of the governing equations which means all variables are supposed to be divided by a reference value. In this case, the resulting dimensionless form of the Navier-Stokes equations has the

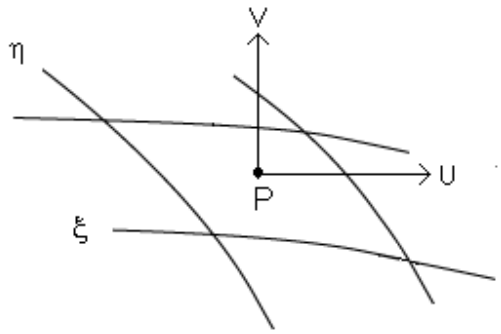

Figure 4.3: Cartesian velocities in a 2D curvilinear coordinate arrangement

same form as its dimensional one, but the viscosity plays the role of $1/Re$, with Re being the Reynolds number, formed by the reference quantities. One can find this implementation in Gant's (2002) work. The practical implication of that is that when simulating a case one may either set the viscosity as $1/Re$ and set the corresponding values such as velocity and geometric length scale to unity, or set the Reynolds number (which in this case will only serve to set the viscosity) as $\frac{1}{\mu}$, taking the viscosity, velocity and geometric lengths to match those of the case being studied.

One more important feature of the STREAM code which is actually a common practice among CFD codes is that the source terms in the discretized governing transport equations are split into two parts: an always negative, S_P, multiplied by ϕ, and S_U:

$$S_\phi = S_U + S_P \phi_P \tag{4.35}$$

S_U is not necessarily positive, unless ϕ is a definitely positive quantity such as the turbulent kinetic energy, the eddy dissipation rate and the normal stresses. The negative part is thus incorporated in the matrix coefficient A_P which becomes $A_P = A_E + A_W + A_N + A_S + A_T + A_B - S_P$ and the positive part remains on the right hand side of the system. This decomposition of the source term improves stability, by increasing the diagonal dominance of the coefficient matrix.

The following subsections will be dedicated to provide some important features regarding the convection and diffusion discretization in the curvilinear coordinates as well as convergence, relaxation and time dependence implementation.

4.2.1 Curvilinear Coordinates

Non-orthogonal grids are very useful for application in complex geometry cases, since they offer a more flexible approach than orthogonal grids. When non-orthogonal grids are implemented, general curvilinear coordinates can be used instead of Cartesian ones. If the physical variables as velocity, Reynolds stresses, etc remain in the Cartesian reference frame, these are now, however, treated as functions of the curvilinear coordinates. To transform the governing

equations it is thus necessary to relate derivatives with respect to the Cartesian coordinates to those with respect to the curvilinear coordinates.

In this subsection it will be shown how to relate the Cartesian derivatives of a general quantity φ to the curvilinear ones, which becomes necessary when applying the FV method over each control volume of the domain (also called cells), now in the curvilinear coordinates. The first step for doing so is to write the chain rule for the curvilinear coordinates derivatives:

$$\begin{bmatrix} \frac{\partial \varphi}{\partial \xi} \\ \frac{\partial \varphi}{\partial \eta} \\ \frac{\partial \varphi}{\partial \zeta} \end{bmatrix} = \underbrace{\begin{bmatrix} \frac{\partial x}{\partial \xi} & \frac{\partial y}{\partial \xi} & \frac{\partial z}{\partial \xi} \\ \frac{\partial x}{\partial \eta} & \frac{\partial y}{\partial \eta} & \frac{\partial z}{\partial \eta} \\ \frac{\partial x}{\partial \zeta} & \frac{\partial y}{\partial \zeta} & \frac{\partial z}{\partial \zeta} \end{bmatrix}}_{J^T} \begin{bmatrix} \frac{\partial \varphi}{\partial x} \\ \frac{\partial \varphi}{\partial y} \\ \frac{\partial \varphi}{\partial z} \end{bmatrix} \tag{4.36}$$

The above matrix equation should then be inverted, providing the desired Cartesian derivatives, in terms of the derivatives along the non-orthogonal grid directions:

$$\begin{bmatrix} \frac{\partial \varphi}{\partial x} \\ \frac{\partial \varphi}{\partial y} \\ \frac{\partial \varphi}{\partial z} \end{bmatrix} = \frac{1}{|J|} \begin{bmatrix} \frac{\partial y}{\partial \eta}\frac{\partial z}{\partial \zeta} - \frac{\partial y}{\partial \zeta}\frac{\partial z}{\partial \eta} & -\frac{\partial y}{\partial \xi}\frac{\partial z}{\partial \zeta} + \frac{\partial y}{\partial \zeta}\frac{\partial z}{\partial \xi} & \frac{\partial y}{\partial \xi}\frac{\partial z}{\partial \eta} - \frac{\partial y}{\partial \eta}\frac{\partial z}{\partial \xi} \\ -\frac{\partial x}{\partial \eta}\frac{\partial z}{\partial \zeta} + \frac{\partial x}{\partial \zeta}\frac{\partial z}{\partial \eta} & \frac{\partial x}{\partial \xi}\frac{\partial z}{\partial \zeta} - \frac{\partial x}{\partial \zeta}\frac{\partial z}{\partial \xi} & -\frac{\partial x}{\partial \xi}\frac{\partial z}{\partial \eta} + \frac{\partial x}{\partial \eta}\frac{\partial z}{\partial \xi} \\ \frac{\partial x}{\partial \eta}\frac{\partial y}{\partial \zeta} - \frac{\partial x}{\partial \zeta}\frac{\partial y}{\partial \eta} & -\frac{\partial x}{\partial \xi}\frac{\partial y}{\partial \zeta} + \frac{\partial x}{\partial \zeta}\frac{\partial y}{\partial \xi} & \frac{\partial x}{\partial \xi}\frac{\partial y}{\partial \eta} - \frac{\partial x}{\partial \eta}\frac{\partial y}{\partial \xi} \end{bmatrix} \begin{bmatrix} \frac{\partial \varphi}{\partial \xi} \\ \frac{\partial \varphi}{\partial \eta} \\ \frac{\partial \varphi}{\partial \zeta} \end{bmatrix} \tag{4.37}$$

In the above equations, J stands for the Jacobian matrix and $|J|$, its determinant. Now each derivative can be rearranged to provide:

$$\frac{\partial \varphi}{\partial x} = \frac{1}{|J|}\left\{ \frac{\partial}{\partial \xi}\left[\left(\frac{\partial y}{\partial \eta}\frac{\partial z}{\partial \zeta} - \frac{\partial y}{\partial \zeta}\frac{\partial z}{\partial \eta}\right)\varphi\right] + \frac{\partial}{\partial \eta}\left[\left(-\frac{\partial y}{\partial \xi}\frac{\partial z}{\partial \zeta} + \frac{\partial y}{\partial \zeta}\frac{\partial z}{\partial \xi}\right)\varphi\right] + \frac{\partial}{\partial \zeta}\left[\left(\frac{\partial y}{\partial \xi}\frac{\partial z}{\partial \eta} - \frac{\partial y}{\partial \eta}\frac{\partial z}{\partial \xi}\right)\varphi\right]\right\} \tag{4.38}$$

$$\frac{\partial \varphi}{\partial y} = \frac{1}{|J|}\left\{ \frac{\partial}{\partial \xi}\left[\left(-\frac{\partial x}{\partial \eta}\frac{\partial z}{\partial \zeta} + \frac{\partial x}{\partial \zeta}\frac{\partial z}{\partial \eta}\right)\varphi\right] + \frac{\partial}{\partial \eta}\left[\left(\frac{\partial x}{\partial \xi}\frac{\partial z}{\partial \zeta} - \frac{\partial x}{\partial \zeta}\frac{\partial z}{\partial \xi}\right)\varphi\right] + \frac{\partial}{\partial \zeta}\left[\left(-\frac{\partial x}{\partial \xi}\frac{\partial z}{\partial \eta} + \frac{\partial x}{\partial \eta}\frac{\partial z}{\partial \xi}\right)\varphi\right]\right\} \tag{4.39}$$

$$\frac{\partial \varphi}{\partial z} = \frac{1}{|J|}\left\{ \frac{\partial}{\partial \xi}\left[\left(\frac{\partial x}{\partial \eta}\frac{\partial y}{\partial \zeta} - \frac{\partial x}{\partial \zeta}\frac{\partial y}{\partial \eta}\right)\varphi\right] + \frac{\partial}{\partial \eta}\left[\left(-\frac{\partial x}{\partial \xi}\frac{\partial y}{\partial \zeta} + \frac{\partial x}{\partial \zeta}\frac{\partial y}{\partial \xi}\right)\varphi\right] + \frac{\partial}{\partial \zeta}\left[\left(\frac{\partial x}{\partial \xi}\frac{\partial y}{\partial \eta} - \frac{\partial x}{\partial \eta}\frac{\partial y}{\partial \xi}\right)\varphi\right]\right\} \tag{4.40}$$

The above results represent a tool that will be used in the following subsections to illustrate how some terms are discretized in the STREAM code.

4.2.2 The Continuity Equation

Starting with the continuity equation, one can write its integration over the control volume transformed into the curvilinear coordinates as follows:

$$\iiint \left[\frac{\partial(\rho U)}{\partial x}+\frac{\partial(\rho V)}{\partial y}+\frac{\partial(\rho W)}{\partial z}\right] \mathrm{d}x\,\mathrm{d}y\,\mathrm{d}z = \iiint \left[\frac{\partial(\rho U)}{\partial x}+\frac{\partial(\rho V)}{\partial y}+\frac{\partial(\rho W)}{\partial z}\right] |J|\,\mathrm{d}\xi\,\mathrm{d}\eta\,\mathrm{d}\zeta = 0 \quad (4.41)$$

Setting the general variable φ in equations (4.38), (4.39) and (4.40) as ρU, ρV and ρW, substituting into the above equation and grouping for each curvilinear derivative, one obtains:

$$\iiint \left\{ \frac{\partial}{\partial \xi}\left[\left(\frac{\partial y}{\partial \eta}\frac{\partial z}{\partial \zeta}-\frac{\partial y}{\partial \zeta}\frac{\partial z}{\partial \eta}\right)\rho U+\left(-\frac{\partial x}{\partial \eta}\frac{\partial z}{\partial \zeta}+\frac{\partial x}{\partial \zeta}\frac{\partial z}{\partial \eta}\right)\rho V+\left(\frac{\partial x}{\partial \eta}\frac{\partial y}{\partial \zeta}-\frac{\partial x}{\partial \zeta}\frac{\partial y}{\partial \eta}\right)\rho W\right]+\frac{\partial}{\partial \eta}\left[\cdots\right]+\frac{\partial}{\partial \zeta}\left[\cdots\right]\right\} \mathrm{d}\xi\,\mathrm{d}\eta\,\mathrm{d}\zeta \quad (4.42)$$

Considering that ξ, η and ζ are respectively associated with west-east, south-north and bottom-top directions and applying the FV method, one arrives at:

$$\begin{aligned} &\left\{ \iint \left[\left(\frac{\partial y}{\partial \eta}\frac{\partial z}{\partial \zeta}-\frac{\partial y}{\partial \zeta}\frac{\partial z}{\partial \eta}\right)\rho U+\left(-\frac{\partial x}{\partial \eta}\frac{\partial z}{\partial \zeta}+\frac{\partial x}{\partial \zeta}\frac{\partial z}{\partial \eta}\right)\rho V+\left(\frac{\partial x}{\partial \eta}\frac{\partial y}{\partial \zeta}-\frac{\partial x}{\partial \zeta}\frac{\partial y}{\partial \eta}\right)\rho W\right] \mathrm{d}\eta\,\mathrm{d}\zeta \right\}_w^e + \\ &\left\{ \iint \cdots \,\mathrm{d}\xi\,\mathrm{d}\zeta \right\}_s^n + \left\{ \iint \cdots \,\mathrm{d}\xi\,\mathrm{d}\eta \right\}_b^t \mathrm{d}\xi\,\mathrm{d}\eta = 0 \end{aligned} \quad (4.43)$$

Following the procedure already described in the FV section, the next step now is to approximate the derivatives and eliminate the integrals:

$$\begin{aligned} &\underbrace{\left[\frac{y_n-y_s}{\Delta\eta}\frac{z_t-z_b}{\Delta\zeta}-\frac{y_t-y_b}{\Delta\zeta}\frac{z_n-z_s}{\Delta\eta}\right]\Delta\eta\Delta\zeta}_{\Delta A_x^e}\rho_e U_e - \Delta A_x^w \rho_w U_w \\ &+ \Delta A_y^e \rho_e V_e - \Delta A_y^w \rho_w V_w + \Delta A_z^e \rho_e W_e - \Delta A_z^w \rho_w W_w \\ &+ \Delta A_x^n \rho_n U_n - \Delta A_x^s \rho_s U_s + \Delta A_y^n \rho_n V_n - \Delta A_y^s \rho_s V_s + \Delta A_z^n \rho_n W_n - \Delta A_z^s \rho_s W_s \\ &+ \Delta A_x^t \rho_t U_t - \Delta A_x^b \rho_b U_b + \Delta A_y^t \rho_t V_t - \Delta A_y^b \rho_b V_b + \Delta A_z^t \rho_t W_t - \Delta A_z^b \rho_b W_b = 0 \end{aligned} \quad (4.44)$$

In the above equation, ΔA_d^f ($f = e, w, n, s, t, b$ and $d = x, y, z$) is the projection of the f face area in the d direction, also called face area vectors which can be visualized in Figure 4.4.

Equation (4.44) can be rearranged to be expressed in terms of the mass fluxes through each face:

$$\begin{aligned} &\underbrace{\rho_e(\Delta A_x^e\ U_e + \Delta A_y^e\ V_e + \Delta A_z^e\ W_e)}_{C_e} - \underbrace{\rho_w(\Delta A_x^w\ U_w + \Delta A_y^w\ V_w + \Delta A_z^w\ W_w)}_{C_w} \\ &\underbrace{\rho_n(\Delta A_x^n\ U_n + \Delta A_y^n\ V_n + \Delta A_z^n\ W_n)}_{C_n} - \underbrace{\rho_s(\Delta A_x^s\ U_s + \Delta A_y^s\ V_s + \Delta A_z^s\ W_s)}_{C_s} \\ &\underbrace{\rho_t(\Delta A_x^t\ U_t + \Delta A_y^t\ V_t + \Delta A_z^t\ W_t)}_{C_t} - \underbrace{\rho_b(\Delta A_x^b\ U_b + \Delta A_y^b\ V_b + \Delta A_z^b\ W_b)}_{C_b} = 0 \end{aligned} \quad (4.45)$$

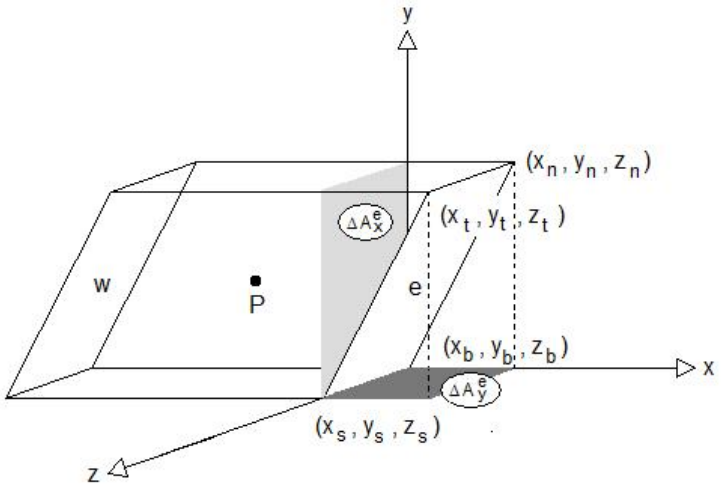

Figure 4.4: Area vectors for the east face in a general control volume

where C_f $(f = e, w, n, s, t, b)$ are the mass fluxes through each face. In the STREAM code, C_w of the next cell in the x (or ξ) direction is set equal to C_e of the current cell in order to ensure consistency of the fluxes and increase computational efficiency. The same logic is applied to the couples $C_s - C_n$ and $C_b - C_t$. One may notice that equation (4.45) is the mass imbalance (S_m).

Before proceeding with the SIMPLE Pressure Correction Scheme implementation, the convective and diffusive terms of a governing equation will first be discussed.

4.2.3 Convection Schemes

Integrating the expanded convective term in equation (4.1) for a general quantity ϕ over each control volume, and converting into the curvilinear coordinates, one obtains:

$$\iiint \left[\frac{\partial(\rho U\phi)}{\partial x} + \frac{\partial(\rho V\phi)}{\partial y} + \frac{\partial(\rho W\phi)}{\partial z}\right] \mathrm{d}x\,\mathrm{d}y\,\mathrm{d}z = \iiint \left[\frac{\partial(\rho U\phi)}{\partial x} + \frac{\partial(\rho V\phi)}{\partial y} + \frac{\partial(\rho W\phi)}{\partial z}\right] |J|\,\mathrm{d}\xi\,\mathrm{d}\eta\,\mathrm{d}\zeta \tag{4.46}$$

From its similarity to the continuity equation, where the argument on the gradient differs only by the presence of the quantity ϕ, one may readily obtain its discretized form:

$$C_e\phi_e - C_w\phi_w + C_n\phi_n - C_s\phi_s + C_t\phi_t - C_b\phi_b \tag{4.47}$$

That is exactly the expected result from the FV method description in the previous section. The important point to be emphasized here is the interpolation methods available in the STREAM code to calculate the values of ϕ at the faces and how they are inserted in the system's coefficients. When describing the FV method, the upwind scheme was used which

provided a convection contribution to the matrix coefficients as $max(\pm C_f, 0)$. It was commented that this method would provide stability, but not accuracy. Alternative methods available in the stream code are the QUICK, UMIST and Van Leer Schemes. These methods are supposed to improve accuracy, but sometimes can compromise stability as already mentioned. They are often implemented as deferred corrections, since they can be written as the upwind scheme plus additional terms. For example, the QUICK scheme for $Ce > 0$ provides:

$$\phi_e = \frac{3}{4}\phi_P + \frac{3}{8}\phi_E - \frac{1}{8}\phi_W \tag{4.48}$$

If the upwind scheme was being used, $\phi_e = \phi_P$. So, what is usually done is to write the deferred correction scheme in a way to incorporate the upwind scheme contribution into the matrix coefficient (thus taking it as $max(\pm C_f, 0)$), and including the remainder in the source term:

$$\phi_e = \underbrace{\phi_P}_{\text{to } A_E} + \underbrace{\left(-\frac{1}{4}\phi_P + \frac{3}{8}\phi_E - \frac{1}{8}\phi_W \right)}_{\text{to source term } S_U} \tag{4.49}$$

In most test cases in this work the UMIST interpolation technique was used. This method, developed by Lien and Leschziner (1994b), was intended to overcome some drawbacks in the QUICK scheme by limiting dispersive truncation errors. The UMIST scheme represents ϕ_e as:

$$\phi_e = \begin{cases} \underbrace{\phi_P}_{\text{to } A_E} + \underbrace{max\left[0, min\left(\phi_E - \phi_P, \phi_P - \phi_W, \frac{1}{4}\phi_P + \frac{1}{8}\phi_E - \frac{3}{8}\phi_W, \overbrace{-\frac{1}{4}\phi_P + \frac{3}{8}\phi_E - \frac{1}{8}\phi_W}^{QUICK}\right)\right]}_{\text{to source term } S_U} & \text{if } C_{xe} > 0 \\ \underbrace{\phi_E}_{\text{to } A_E} + \underbrace{max\left[0, min\left(\phi_P - \phi_E, \phi_E - \phi_{EE}, \frac{1}{8}\phi_P + \frac{1}{4}\phi_E - \frac{3}{8}\phi_{EE}, \overbrace{\frac{3}{8}\phi_P - \frac{1}{4}\phi_E - \frac{1}{8}\phi_{EE}}^{QUICK}\right)\right]}_{\text{to source term } S_U} & \text{if } C_{xe} \leq 0 \end{cases} \tag{4.50}$$

In the above equation the new subscript $_{EE}$ indicates the node to the east of the east node E. The term indicated as going to A_E is equivalent to the UPWIND scheme and all the other terms are incorporated in the positive source term S_U. One may notice that the UMIST scheme can be reduced to the QUICK scheme as indicated by the overbraces in equation 4.50.

4.2.4 Diffusion Schemes

In this subsection the discretization of diffusion terms in this non-orthogonal system will be developed. To exemplify its discretization process through the FV method, the U-momentum Navier Stokes equation will be used.

The Navier-Stokes equation, presented in equation 2.5, can be written as:

$$\frac{\partial U_i}{\partial t} + U_j \frac{\partial U_i}{\partial x_j} = -\frac{1}{\rho}\frac{\partial P}{\partial x_i} + \frac{\partial}{\partial x_j}\left[\nu\left(\frac{\partial U_i}{\partial x_j} + \frac{\partial U_j}{\partial x_i} - \frac{2}{3}\frac{\partial U_m}{\partial x_m}\right) - \overline{u_i u_j}\right] \tag{4.51}$$

One may notice that the above equation is the same as equation 2.5, since the only difference remains in the diffusive term and $\frac{\partial}{\partial x_j}\left(\frac{\partial U_j}{\partial x_i}\right) = \frac{\partial}{\partial x_i}\left(\frac{\partial U_j}{\partial x_j}\right) = 0$ and $\frac{\partial U_m}{\partial x_m} = 0$ according to the continuity equation. The reason why the Navier-Stokes equation is written as above in equation 4.51 is that its viscous term becomes similar to the term associated with the eddy-viscosity when using a linear eddy-viscosity model to represent the Reynolds stresses.

Thus the U-momentum Navier Stokes equation right hand side is:

$$\frac{\partial}{\partial x}\Bigg[\underbrace{-P + \mu\left(2\frac{\partial U}{\partial x} - \frac{2}{3}\frac{\partial U_m}{\partial x_m}\right) - \rho\overline{u}^2}_{-FLUXX}\Bigg] + \frac{\partial}{\partial y}\Bigg[\underbrace{\mu\left(\frac{\partial U}{\partial y} + \frac{\partial V}{\partial x}\right) - \rho\overline{uv}}_{-FLUXY}\Bigg] + \frac{\partial}{\partial z}\Bigg[\underbrace{\mu\left(\frac{\partial U}{\partial z} + \frac{\partial W}{\partial x}\right) - \rho\overline{uw}}_{-FLUXZ}\Bigg] \tag{4.52}$$

where the underbraced terms $-FLUXX$, $-FLUXY$ and $-FLUXZ$ are denoted as such for convenience purposes since that is the way these arguments are termed in the STREAM code. When comparing equation (4.52) with the general governing equation (4.1), one may notice that in this case, as $\phi = U$, the diffusive term to be discretized should be only:

$$\frac{\partial}{\partial x_j}\left(\Gamma\frac{\partial \phi}{\partial x_j}\right) = \frac{\partial}{\partial x}\left(\underbrace{\Gamma}_{D_1}\frac{\partial U}{\partial x}\right) + \frac{\partial}{\partial y}\left(\underbrace{\Gamma}_{D_2}\frac{\partial U}{\partial y}\right) + \frac{\partial}{\partial z}\left(\underbrace{\Gamma}_{D_3}\frac{\partial U}{\partial z}\right) \tag{4.53}$$

By comparing equations 4.52 and 4.53, one may notice that $D_1 = 2\mu$, $D_2 = \mu$ and $D_3 = \mu$. That is exactly how the STREAM code sees the diffusion part of the U momentum Navier Stokes equation. The diffusivities D_1, D_2 and D_3 are there termed as DIF11, DIF22 and DIF33 respectively.

When using linear eddy-viscosity turbulence models, one can take into account that $\rho\overline{u_i u_j} = -\mu_t\left(\frac{\partial U_i}{\partial x_j} + \frac{\partial U_j}{\partial x_i} - \frac{2}{3}\frac{\partial U_m}{\partial x_m}\right) + \rho\frac{2}{3}k\delta_{ij}$ and write equation 4.52 as:

$$\frac{\partial}{\partial x}\left[-P + (\mu+\mu_t)\left(2\frac{\partial U}{\partial x} - \frac{2}{3}\frac{\partial U_m}{\partial x_m}\right) - \frac{2}{3}k\right] + \frac{\partial}{\partial y}\left[(\mu+\mu_t)\left(\frac{\partial U}{\partial y} + \frac{\partial V}{\partial x}\right)\right] + \frac{\partial}{\partial z}\left[(\mu+\mu_t)\left(\frac{\partial U}{\partial z} + \frac{\partial W}{\partial x}\right)\right] \tag{4.54}$$

In this case it is easy to see, by comparing equations 4.53 and 4.54, that $D_1 = 2(\mu + \mu_t)$, $D_2 = \mu + \mu_t$ and $D_3 = \mu + \mu_t$. The reason to do that, instead of just using equation 4.53,

is to improve stability. For this same reason, when using Reynolds stress transport models, where in principle equation 4.53 should be used, one can use the effective viscosity concept.

The effective viscosity concept consists of expressing the Reynolds stresses as a part that is similar to that provided by an eddy-viscosity model, plus an additional contribution, so that the diffusion coefficient in equation 4.53, which is in principle only $\Gamma = \mu$, can be enhanced and stability can be improved. In order to obtain an appropriate split of the Reynolds stress for such a treatment, one can manipulate simplified algebraic versions of the transport equations. For example, in equations 3.23, one can neglect convective and diffusive terms, take the pressure-strain correlation as $\phi_{ij} = -C_1 \frac{\varepsilon}{k}\left(\overline{u_i u_j} - \frac{2}{3}\delta_{ij}k\right) - C_2\left(P_{ij} - \frac{2}{3}\delta_{ij}P_k\right)$ and group together terms involving the product $\overline{u^2}\frac{\partial U}{\partial x}$, to arrive at a form for $\overline{u^2}$ such as shown in equation 4.55. A similar treatment for the shear stress leads to $\overline{uv}$ as shown in equation 4.55 below:

$$\begin{aligned}
\overline{u^2} &= -\underbrace{\frac{k}{\varepsilon}\frac{(2-\frac{4}{3}C_2)}{C_1}\overline{u^2}}_{\nu_{t_{eff}}}\frac{\partial U}{\partial x} + \widehat{\overline{u^2}} \\
\overline{uv} &= -\underbrace{\frac{k}{\varepsilon}\frac{(1-C_2)}{C_1}\overline{v^2}}_{\nu_{t_{eff}}}\frac{\partial U}{\partial y} + \widehat{\overline{uv}}
\end{aligned} \tag{4.55}$$

where $\widehat{\overline{u_i u_j}}$ represents all terms in P_{ij} and P_k that were neglected and $\nu_{t_{eff}} = \mu_{t_{eff}}/\rho$ is taken as the effective viscosity since it plays the same role as the eddy viscosity. One may notice that the effective viscosity assumes different expressions depending on which Reynolds stress is being considered. For the normal stresses, the relation between the pressure strain correlation coefficients is $\frac{(2-\frac{4}{3}C_2)}{C_1}$ while for the shear stresses, it is $\frac{(1-C_2)}{C_1}$. The former is labeled C_{norm} and the latter C_{shear} in the STREAM code.

Thereby, equation 4.52 can be written as in equation 4.56 below, neglecting the $\widehat{\overline{u_i u_j}}$ terms in equation 4.55, and therefore the diffusivities in equation 4.53 become $D_1 = 2(\mu + \mu_{t_{eff}})$, $D_2 = \mu + \mu_{t_{eff}}$ and $D_3 = \mu + \mu_{t_{eff}}$.

$$\frac{\partial}{\partial x}\left[-P + (\mu+\mu_{t_{eff}})\left(2\frac{\partial U}{\partial x} - \frac{2}{3}\frac{\partial U_m}{\partial x_m}\right) - \frac{2}{3}k\right] + \frac{\partial}{\partial y}\left[(\mu+\mu_{t_{eff}})\left(\frac{\partial U}{\partial y} + \frac{\partial V}{\partial x}\right)\right] + \frac{\partial}{\partial z}\left[(\mu+\mu_{t_{eff}})\left(\frac{\partial U}{\partial z} + \frac{\partial W}{\partial x}\right)\right] \tag{4.56}$$

The other terms in equations 4.52, 4.54 or 4.56 which were not used in equation 4.53 are included in the $-FLUXX$, $-FLUXY$ and $-FLUXZ$ terms which, as will be discussed further in the text, will be accounted for within the positive source term S_U.

Similarly to the treatment given to the Navier-Stokes equation, it is easy to see that for the transport equations of the turbulent kinetic energy and the dissipation rate, $D_1 = D_2 = D_3 = \mu + \frac{\mu_t}{\sigma_\phi}$, where ϕ can be k, k_P, k_T, ε, ε_P, ε_T or ω. Equally, for the transport equations of $\overline{u_i u_j}$, the diffusivities will be $\mu + \rho C \frac{k}{\varepsilon}\overline{u_i u_j}$ if the GGDH form for diffusion is adopted which

is the case of all RST models used in this work.

Now one can thus integrate the diffusive part used as in equation 4.53 for the sake of simplicity:

$$\begin{aligned}&\iiint \left[\frac{\partial}{\partial x}\left(2\mu\frac{\partial U}{\partial x}\right)+\frac{\partial}{\partial y}\left(\mu\frac{\partial U}{\partial y}\right)+\frac{\partial}{\partial z}\left(\mu\frac{\partial U}{\partial z}\right)\right]\mathrm{d}x\,\mathrm{d}y\,\mathrm{d}z=\\&\iiint \left[\frac{\partial}{\partial x}\left(2\mu\frac{\partial U}{\partial x}\right)+\frac{\partial}{\partial y}\left(\mu\frac{\partial U}{\partial y}\right)+\frac{\partial}{\partial z}\left(\mu\frac{\partial U}{\partial z}\right)\right]|J|\,\mathrm{d}\xi\,\mathrm{d}\eta\,\mathrm{d}\zeta\end{aligned}\tag{4.57}$$

Hence, recalling equations (4.38), (4.39) and (4.40), one obtains:

$$\begin{aligned}\iiint\Bigg\{&\frac{\partial}{\partial\xi}\left[\left(\frac{\partial y}{\partial\eta}\frac{\partial z}{\partial\zeta}-\frac{\partial y}{\partial\zeta}\frac{\partial z}{\partial\eta}\right)2\mu\frac{\partial U}{\partial x}\right]+\frac{\partial}{\partial\eta}\left[\left(-\frac{\partial y}{\partial\xi}\frac{\partial z}{\partial\zeta}+\frac{\partial y}{\partial\zeta}\frac{\partial z}{\partial\xi}\right)2\mu\frac{\partial U}{\partial x}\right]+\frac{\partial}{\partial\zeta}\left[\left(\frac{\partial y}{\partial\xi}\frac{\partial z}{\partial\eta}-\frac{\partial y}{\partial\eta}\frac{\partial z}{\partial\xi}\right)2\mu\frac{\partial U}{\partial x}\right]+\\&\frac{\partial}{\partial\xi}\left[\left(-\frac{\partial x}{\partial\eta}\frac{\partial z}{\partial\zeta}+\frac{\partial x}{\partial\zeta}\frac{\partial z}{\partial\eta}\right)\mu\frac{\partial U}{\partial y}\right]+\frac{\partial}{\partial\eta}\left[\left(\frac{\partial x}{\partial\xi}\frac{\partial z}{\partial\zeta}-\frac{\partial x}{\partial\zeta}\frac{\partial z}{\partial\xi}\right)\mu\frac{\partial U}{\partial y}\right]+\frac{\partial}{\partial\zeta}\left[\left(-\frac{\partial x}{\partial\xi}\frac{\partial z}{\partial\eta}+\frac{\partial x}{\partial\eta}\frac{\partial z}{\partial\xi}\right)\mu\frac{\partial U}{\partial y}\right]+\\&\frac{\partial}{\partial\xi}\left[\left(\frac{\partial x}{\partial\eta}\frac{\partial y}{\partial\zeta}-\frac{\partial x}{\partial\zeta}\frac{\partial y}{\partial\eta}\right)\mu\frac{\partial U}{\partial z}\right]+\frac{\partial}{\partial\eta}\left[\left(-\frac{\partial x}{\partial\xi}\frac{\partial y}{\partial\zeta}+\frac{\partial x}{\partial\zeta}\frac{\partial y}{\partial\xi}\right)\mu\frac{\partial U}{\partial z}\right]+\frac{\partial}{\partial\zeta}\left[\left(\frac{\partial x}{\partial\xi}\frac{\partial y}{\partial\eta}-\frac{\partial x}{\partial\eta}\frac{\partial y}{\partial\xi}\right)\mu\frac{\partial U}{\partial z}\right]\Bigg\}\mathrm{d}\xi\,\mathrm{d}\eta\,\mathrm{d}\zeta\end{aligned}\tag{4.58}$$

which results in:

$$\begin{aligned}&\left\{\iint\left[\left(\frac{\partial y}{\partial\eta}\frac{\partial z}{\partial\zeta}-\frac{\partial y}{\partial\zeta}\frac{\partial z}{\partial\eta}\right)2\mu\frac{\partial U}{\partial x}\right]\mathrm{d}\eta\,\mathrm{d}\zeta\right\}_w^e+\left\{\iint\left[\left(\cdots\right)2\mu\frac{\partial U}{\partial x}\right]\mathrm{d}\xi\,\mathrm{d}\zeta\right\}_s^n+\left\{\iint\left[\left(\cdots\right)2\mu\frac{\partial U}{\partial x}\right]\mathrm{d}\xi\,\mathrm{d}\eta\right\}_b^t+\\&\left\{\iint\left[\left(-\frac{\partial x}{\partial\eta}\frac{\partial z}{\partial\zeta}+\frac{\partial x}{\partial\zeta}\frac{\partial z}{\partial\eta}\right)\mu\frac{\partial U}{\partial y}\right]\mathrm{d}\eta\,\mathrm{d}\zeta\right\}_w^e+\left\{\iint\left[\left(\cdots\right)\mu\frac{\partial U}{\partial y}\right]\mathrm{d}\xi\,\mathrm{d}\zeta\right\}_s^n+\left\{\iint\left[\left(\cdots\right)\mu\frac{\partial U}{\partial y}\right]\mathrm{d}\xi\,\mathrm{d}\eta\right\}_b^t+\\&\left\{\iint\left[\left(\frac{\partial x}{\partial\eta}\frac{\partial y}{\partial\zeta}-\frac{\partial x}{\partial\zeta}\frac{\partial y}{\partial\eta}\right)\mu\frac{\partial U}{\partial z}\right]\mathrm{d}\eta\,\mathrm{d}\zeta\right\}_w^e+\left\{\iint\left[\left(\cdots\right)\mu\frac{\partial U}{\partial z}\right]\mathrm{d}\xi\,\mathrm{d}\zeta\right\}_s^n+\left\{\iint\left[\left(\cdots\right)\mu\frac{\partial U}{\partial z}\right]\mathrm{d}\xi\,\mathrm{d}\eta\right\}_b^t\end{aligned}\tag{4.59}$$

One may notice that equations (4.38), (4.39) and (4.40) must be applied again in the first, second and third lines in the above equation, respectively. Owing to lack of space and simplicity, only the discretization of the ξ direction (west-east) for the X derivative will be shown. Hence, the first terms from the first, second and third lines of equation (4.59) become:

$$\begin{aligned}&\left\{\iint\left[\frac{1}{|J|}\left(\frac{\partial y}{\partial\eta}\frac{\partial z}{\partial\zeta}-\frac{\partial y}{\partial\zeta}\frac{\partial z}{\partial\eta}\right)^2 2\mu\frac{\partial U}{\partial\xi}+\frac{1}{|J|}\left(\cdots\right)2\mu\frac{\partial U}{\partial\eta}+\frac{1}{|J|}\left(\cdots\right)2\mu\frac{\partial U}{\partial\zeta}+\right.\\&\iint\frac{1}{|J|}\left(-\frac{\partial x}{\partial\eta}\frac{\partial z}{\partial\zeta}+\frac{\partial x}{\partial\zeta}\frac{\partial z}{\partial\eta}\right)^2\mu\frac{\partial U}{\partial\xi}+\frac{1}{|J|}\left(\cdots\right)\mu\frac{\partial U}{\partial\eta}+\frac{1}{|J|}\left(\cdots\right)\mu\frac{\partial U}{\partial\zeta}+\\&\left.\iint\frac{1}{|J|}\left(\frac{\partial x}{\partial\eta}\frac{\partial y}{\partial\zeta}-\frac{\partial x}{\partial\zeta}\frac{\partial y}{\partial\eta}\right)^2\mu\frac{\partial U}{\partial\xi}+\frac{1}{|J|}\left(\cdots\right)\mu\frac{\partial U}{\partial\eta}+\frac{1}{|J|}\left(\cdots\right)\mu\frac{\partial U}{\partial\zeta}\right]\mathrm{d}\eta\,\mathrm{d}\zeta\Bigg\}_w^e\end{aligned}\tag{4.60}$$

Terms that contain the non-orthogonal derivative $\frac{\partial U}{\partial\xi}$ at the east and west faces are treated

implicitly in the discretization process and are absorbed into the diffusive part of the coefficients of the discretized transport equation for U, through which the nodal value of U at location P is influenced by the nodal values at the surrounding locations, east, west, north, south, etc. The remaining terms in equation (4.60), which contain non-orthogonal derivatives $\frac{\partial U}{\partial \eta}$ and $\frac{\partial U}{\partial \zeta}$ at the east-west faces, are treated explicitly. They are transferred to the source term and are evaluated by using nodal values of U from the previous iterative level. For the north-south face terms, shown in equation (4.59) but not included in (4.60), it is the terms that contain the non-orthogonal derivative term $\frac{\partial U}{\partial \eta}$ that are treated implicitly and the rest explicitly and for the top-bottom faces, also not included in equation (4.60), the $\frac{\partial U}{\partial \zeta}$ terms are treated implicitly.

CDS is applied for the face derivatives, and the face area vectors are obtained in the same way as for the continuity equation:

$$\iint \left[\frac{1}{|J|}\left(\frac{\partial y}{\partial \eta}\frac{\partial z}{\partial \zeta}-\frac{\partial y}{\partial \zeta}\frac{\partial z}{\partial \eta}\right)^2 2\mu\frac{\partial U}{\partial \xi}\right] \mathrm{d}\eta\,\mathrm{d}\zeta = \frac{(2\mu)_e(\Delta A_x^e)^2}{|J|\Delta\xi\Delta\eta\Delta\zeta}(U_E-U_P)-\frac{(2\mu)_w(\Delta A_x^w)^2}{|J|\Delta\xi\Delta\eta\Delta\zeta}(U_P-U_W) \tag{4.61}$$

In the above equation, $|J|\Delta\xi\Delta\eta\Delta\zeta$ stands for the cell's volume V_{CV} (Lien and Leschziner, 1994a; Gant, 2002). The same procedure outlined here is done for all terms in equation (4.59), and one then arrives at expressions for the diffusive term contribution to the matrix coefficients of:

$$\begin{aligned}
De &= \frac{(2\mu)_e(\Delta A_x^e)^2}{V_{CV}} + \frac{(\mu)_e(\Delta A_y^e)^2}{V_{CV}} + \frac{(\mu)_e(\Delta A_z^e)^2}{V_{CV}} \\
Dw &= \frac{(2\mu)_w(\Delta A_x^w)^2}{V_{CV}} + \frac{(\mu)_w(\Delta A_y^w)^2}{V_{CV}} + \frac{(\mu)_w(\Delta A_z^w)^2}{V_{CV}} \\
Dn &= \frac{(\mu)_n(\Delta A_x^n)^2}{V_{CV}} + \frac{(2\mu)_n(\Delta A_y^n)^2}{V_{CV}} + \frac{(\mu)_n(\Delta A_z^n)^2}{V_{CV}} \\
Ds &= \frac{(\mu)_s(\Delta A_x^s)^2}{V_{CV}} + \frac{(2\mu)_s(\Delta A_y^s)^2}{V_{CV}} + \frac{(\mu)_s(\Delta A_z^s)^2}{V_{CV}} \\
Dt &= \frac{(\mu)_t(\Delta A_x^t)^2}{V_{CV}} + \frac{(\mu)_t(\Delta A_y^t)^2}{V_{CV}} + \frac{(2\mu)_t(\Delta A_z^t)^2}{V_{CV}} \\
Db &= \frac{(\mu)_b(\Delta A_x^b)^2}{V_{CV}} + \frac{(\mu)_b(\Delta A_y^b)^2}{V_{CV}} + \frac{(2\mu)_b(\Delta A_z^b)^2}{V_{CV}}
\end{aligned} \tag{4.62}$$

One may notice that all terms which are not included in the above implicit contributions, are, nevertheless, still evaluated in the $-FLUXX$, $-FLUXY$ and $-FLUXZ$ terms in equation (4.52). These terms should be integrated over the control volume, since they are the argument of derivatives in the original equation (4.52). As a result, and as already shown before, they will be multiplied by their respective area face vectors and their values will be needed at the cell faces which will then require interpolation:

$$\iiint \left[\frac{\partial(FLUXX)}{\partial x} + \frac{\partial(FLUXY)}{\partial y} + \frac{\partial(FLUXZ)}{\partial z}\right] \mathrm{d}x\,\mathrm{d}y\,\mathrm{d}z = \iiint \left[\frac{\partial(FLUXX)}{\partial x} + \frac{\partial(FLUXY)}{\partial y} + \frac{\partial(FLUXZ)}{\partial z}\right] |J|\,\mathrm{d}\xi\,\mathrm{d}\eta\,\mathrm{d}\zeta$$
$$\approx \underbrace{(\Delta A_x^e\ FLUXX_e + \Delta A_y^e\ FLUXY_e + \Delta A_z^e\ FLUXZ_e)}_{FLUX_e} - \underbrace{(\Delta A_x^w\ FLUXX_w + \Delta A_y^w\ FLUXY_w + \Delta A_z^w\ FLUXZ_w)}_{FLUX_w} + \cdots$$
$$= FLUX_e - FLUX_w + FLUX_n - FLUX_s + FLUX_t - FLUX_b \tag{4.63}$$

The fluxes $FLUX_f$ ($f = e, w, n, s, t, b$) are evaluated in a similar manner to the mass fluxes in the continuity equation. For example, $FLUX_w$ of the next cell in the x (or ξ) direction is set equal to $FLUX_e$ of the current cell in order to ensure consistency and save on computational effort.

The terms $-FLUXX$, $-FLUXY$ and $-FLUXZ$ also include the diffusive terms that were used to build the matrix coefficients in equation (4.62), and so the final contribution that appears in the discretized source term is in fact the flux differences of (4.63) minus the contributions included implicitly through the coefficient matrix parts.

Summarizing, the STREAM code applies the FV method for the governing equations written in form of equation (4.1) and all terms which are not convective are included in the $-FLUXX$, $-FLUXY$ and $-FLUXZ$ terms, from which are then subtracted the diffusive contributions included implicitly via the coefficient matrix. The integrated form of the terms $-FLUXX$, $-FLUXY$ and $-FLUXZ$, equation (4.63), are then included in the source term S_U.

The main discretized equation form in the STREAM code is thus given by:

$$\begin{aligned}
&A_P U_P = \sum_k A_k U_k + S_U \\
&\text{where } k = E, W, N, S, T, B \\
&A_E = De + max(-C_e, 0) \\
&A_W = Dw + max(C_w, 0) \\
&A_N = Dn + max(-C_n, 0) \\
&A_S = Ds + max(C_s, 0) \\
&A_T = Dt + max(-C_t, 0) \\
&A_B = Db + max(C_b, 0) \\
&A_P = A_E + A_W + A_N + A_S + A_T + A_B - S_P
\end{aligned} \tag{4.64}$$

Before proceeding with the pressure correction scheme analysis, it is worth mentioning some realizability constraints on the turbulence quantities that are imposed in the STREAM code. Amongst other things these ensure that the turbulent and apparent viscosities used in the above formulations cannot become negative.

The first constraint imposed is to ensure that k and ε, which are physically positive quantities, should always be calculated as such. This is done via a simple clipping limit on

the variables. The normal Reynolds stresses should also be positive (and less then $2k$), and the shear stresses should satisfy the Schwarz inequality, so the following limits are imposed on the Reynolds stresses:

$$\begin{aligned}
\overline{u}^2 &= min[2k, max(0, \overline{u}^2)] \\
\overline{v}^2 &= min[2k, max(0, \overline{v}^2)] \\
\overline{w}^2 &= min[2k, max(0, \overline{w}^2)] \\
\overline{uv} &= max[-\sqrt{\overline{u}^2\overline{v}^2}, min(\sqrt{\overline{u}^2\overline{v}^2}, \overline{uv})] \\
\overline{uw} &= max[-\sqrt{\overline{u}^2\overline{w}^2}, min(\sqrt{\overline{u}^2\overline{w}^2}, \overline{uw})] \\
\overline{vw} &= max[-\sqrt{\overline{v}^2\overline{w}^2}, min(\sqrt{\overline{v}^2\overline{w}^2}, \overline{uv})]
\end{aligned} \tag{4.65}$$

4.2.5 Pressure Correction Scheme

In order to discuss how the SIMPLE scheme is implemented in the STREAM code, it is useful to separate the pressure gradient contribution from the source term in equation (4.64):

$$A_P U_P = \sum_k A_k U_k + S_U + \iiint \left(-\frac{\partial P}{\partial x} \right) \mathrm{d}x\, \mathrm{d}y\, \mathrm{d}z \tag{4.66}$$

The development of the integral in equation 4.66 in the curvilinear system will thus lead to the following representation for the pressure contributions in the U-momentum equation:

$$\begin{aligned}
&\iiint \left(-\frac{\partial P}{\partial x} \right) \mathrm{d}x\, \mathrm{d}y\, \mathrm{d}z = \iiint \left(-\frac{\partial P}{\partial x} \right) |J|\, \mathrm{d}\xi\, \mathrm{d}\eta\, \mathrm{d}\zeta \approx \\
&(\Delta A_x^w\ P_w - \Delta A_x^e\ P_e) + (\Delta A_x^s\ P_s - \Delta A_x^n\ P_n) + (\Delta A_x^b\ P_b - \Delta A_x^t\ P_t)
\end{aligned} \tag{4.67}$$

Similarly, if the pressure gradient contribution in the V and W momentum Navier-Stokes equations is integrated over the control volume one obtains analogous forms, but for the face vector areas in the y and z directions. From the SIMPLE scheme described in the previous section, one can thus relate velocity and pressure corrections by:

$$\begin{aligned}
U'_P &= \underbrace{\frac{1}{A_P^U}}_{D_U} [(\Delta A_x^w\ P'_w - \Delta A_x^e\ P'_e) + (\Delta A_x^s\ P'_s - \Delta A_x^n\ P'_n) + (\Delta A_x^b\ P'_b - \Delta A_x^t\ P'_t)] \\
V'_P &= \underbrace{\frac{1}{A_P^V}}_{D_V} [(\Delta A_y^w\ P'_w - \Delta A_y^e\ P'_e) + (\Delta A_y^s\ P'_s - \Delta A_y^n\ P'_n) + (\Delta A_y^b\ P'_b - \Delta A_y^t\ P'_t)] \\
W'_P &= \underbrace{\frac{1}{A_P^W}}_{D_W} [(\Delta A_z^w\ P'_w - \Delta A_z^e\ P'_e) + (\Delta A_z^s\ P'_s - \Delta A_z^n\ P'_n) + (\Delta A_z^b\ P'_b - \Delta A_z^t\ P'_t)]
\end{aligned} \tag{4.68}$$

where A_P^U, A_P^V and A_P^W are the A_P coefficients for the U, V and W momentum Navier-Stokes equations respectively. However, since face velocities are needed in the discretized continuity equation, equivalent expressions to the above need to be written for the cell-face velocity corrections. To simplify these, one also neglects pressure correction differences arising from other than the perpendicular direction to the cell face, resulting in:

$$
\begin{array}{lll}
U'_e = \Delta A_x^e \; DU(P'_P - P'_E) & V'_e = \Delta A_y^e \; DV(P'_P - P'_E) & W'_e = \Delta A_z^e \; DW(P'_P - P'_E) \\
U'_w = \Delta A_x^w \; DU(P'_W - P'_P) & V'_w = \Delta A_y^w \; DV(P'_W - P'_P) & W'_w = \Delta A_z^w \; DW(P'_W - P'_P) \\
U'_n = \Delta A_x^n \; DU(P'_P - P'_N) & V'_n = \Delta A_y^n \; DV(P'_P - P'_N) & W'_n = \Delta A_z^n \; DW(P'_P - P'_N) \\
U'_s = \Delta A_x^s \; DU(P'_S - P'_P) & V'_s = \Delta A_y^s \; DV(P'_S - P'_P) & W'_s = \Delta A_z^s \; DW(P'_S - P'_P) \\
U'_t = \Delta A_x^t \; DU(P'_P - P'_T) & V'_t = \Delta A_y^t \; DV(P'_P - P'_T) & W'_t = \Delta A_z^t \; DW(P'_P - P'_T) \\
U'_b = \Delta A_x^b \; DU(P'_B - P'_P) & V'_b = \Delta A_y^b \; DV(P'_B - P'_P) & W'_b = \Delta A_z^b \; DW(P'_B - P'_P)
\end{array} \tag{4.69}
$$

Substituting then the corrected velocities $U^* = U + U'$, $V^* = V + V'$ and $W^* = W + W'$ into the continuity equation (4.45), one obtains:

$$
\begin{aligned}
& a_p P'_P = a_e P'_E + a_w P'_W + a_n P'_N + a_s P'_S - S_m \\
& \text{where} \\
& a_e = \rho_e[(\Delta A_x^e)^2 DU + (\Delta A_y^e)^2 DV + (\Delta A_z^e)^2 DW] \\
& a_w = \rho_w[(\Delta A_x^w)^2 DU + (\Delta A_y^w)^2 DV + (\Delta A_z^w)^2 DW] \\
& a_n = \rho_n[(\Delta A_x^n)^2 DU + (\Delta A_y^n)^2 DV + (\Delta A_z^n)^2 DW] \\
& a_s = \rho_s[(\Delta A_x^s)^2 DU + (\Delta A_y^s)^2 DV + (\Delta A_z^s)^2 DW] \\
& a_t = \rho_t[(\Delta A_x^t)^2 DU + (\Delta A_y^t)^2 DV + (\Delta A_z^t)^2 DW] \\
& a_b = \rho_b[(\Delta A_x^b)^2 DU + (\Delta A_y^b)^2 DV + (\Delta A_z^b)^2 DW] \\
& a_p = a_e + a_w + a_n + a_s + a_t + a_b - S_P
\end{aligned} \tag{4.70}
$$

where S_m stands for the mass imbalance, equation (4.45), and is stored in the "positive" source term S_U. S_P is the "negative" part of the source term and is the way to implement any case specific modification.

One important feature of the STREAM code is the interpolation method used to calculate U, V and W for the mass fluxes through each face (C_f) in equation (4.45): it uses the Rhie-Chow interpolation. This method makes it possible to use a fully collocated grid and at the same time account for the pressure at the nodes and at the faces in order to avoid the chequerboarding problem. The Rhie-Chow scheme can be interpreted as a linear interpolation of the velocities at the surrounding nodes added to a pressure smoothing term (Gant, 2002),

and can be written as:

$$U_e = \frac{1}{2}(U_P + U_E) + \frac{1}{2}[D_P^U(P_e - P_w) + D_E^U(P_{ee} - P_e) + (D_P^U + D_E^U)(P_P - P_E)] \quad (4.71)$$

That concludes the implementation of the SIMPLE scheme in the STREAM code, since the general procedure for solution is the same as outlined before.

4.2.6 Time Dependence Schemes

Everything presented so far has been for a steady system where time dependence is neglected. However, all governing equations have their unsteady parts which should also be discretized in order to be numerically solved. The time discretization schemes which will be discussed here will be focused on their implementation within the STREAM code, however the general guidelines about their theory will be also presented.

Starting with any generic time dependent equation, one has:

$$\frac{\partial \phi}{\partial t} = f(t, \phi(t)) \quad (4.72)$$

The simplest discretization method consists of integrating both sides from t^n to t^{n+1}, where $\Delta t = t^{n+1} - t^n$:

$$\int_{t^n}^{t^{n+1}} \frac{\partial \phi}{\partial t}\,\mathrm{d}t = \int_{t^n}^{t^{n+1}} f(t, \phi(t))\,\mathrm{d}t \qquad \Rightarrow \qquad \phi(t^{n+1}) - \phi(t^n) = \int_{t^n}^{t^{n+1}} f(t, \phi(t))\,\mathrm{d}t \quad (4.73)$$

From the above equation, one may notice that the discretization method now will depend on how the integral on the right hand side of equation (4.73) will be approximated. Two approximation techniques will be discussed here: the Fully Implicit method and the Trapezoidal Rule which is the basis for the Crank-Nicolson method. These methods will be presented because they are the ones applied in the STREAM code. However, other approximation methods can be found, for example, in Ferziger and Peric (2002).

The Fully Implicit approximation method consists of evaluating the integral using only the new time level, t^{n+1}:

$$\phi(t^{n+1}) - \phi(t^n) = f(t^{n+1}, \phi(t^{n+1}))\Delta t \quad (4.74)$$

On the other hand, the Trapezoidal Rule approximates the right hand side integral in equation (4.73) using a linear interpolation between t^n and t^{n+1}:

$$\phi(t^{n+1}) - \phi(t^n) = \frac{1}{2}[f(t^{n+1}, \phi(t^{n+1})) + f(t^n, \phi(t^n))]\Delta t \tag{4.75}$$

It can be shown through error analysis based on Taylor series expansions that this approximation method is more accurate than the first, however if the time step Δt is small enough both methods may present acceptable results.

Now it will be discussed how these methods are applied in the STREAM code. Starting from a complete generic governing equation in Cartesian coordinates, one has:

$$\frac{\partial(\rho\phi)}{\partial t} + \frac{\partial(\rho U_j \phi)}{\partial x_j} = \frac{\partial}{\partial x_j}\big(\Gamma \frac{\partial \phi}{\partial x_j}\big) + S_\phi \tag{4.76}$$

Following the general procedure outlined for the FV method, the next step is to integrate both sides, but now, also in relation to time:

$$\iiiint \frac{\partial(\rho\phi)}{\partial t}\,\mathrm{d}t\,\mathrm{d}x\,\mathrm{d}y\,\mathrm{d}z = \iiiint \Big[- \frac{\partial(\rho U_j \phi)}{\partial x_j} + \frac{\partial}{\partial x_j}\big(\Gamma \frac{\partial \phi}{\partial x_j}\big) + S_\phi \Big]\,\mathrm{d}t\,\mathrm{d}x\,\mathrm{d}y\,\mathrm{d}z \tag{4.77}$$

The above integral equation should now have its coordinates transformed from Cartesian to curvilinear:

$$\iiiint \frac{\partial(\rho\phi)}{\partial t}\,\mathrm{d}t|J|\,\mathrm{d}\xi\,\mathrm{d}\eta\,\mathrm{d}\zeta = \iiiint \Big[- \frac{\partial(\rho U_j \phi)}{\partial x_j} + \frac{\partial}{\partial x_j}\big(\Gamma \frac{\partial \phi}{\partial x_j}\big) + S_\phi \Big]|J|\,\mathrm{d}\xi\,\mathrm{d}\eta\,\mathrm{d}\zeta \tag{4.78}$$

The development of the right hand side of equation (4.78) is already known to be equation (4.64) for the generic variable ϕ. Hence, equation (4.78) can be rewritten and approximated as:

$$\Big[\int \frac{\partial(\rho\phi)}{\partial t}\,\mathrm{d}t \Big] \underbrace{|J|\Delta\xi\Delta\eta\Delta\zeta}_{V_{CV}} = \underbrace{-A_P\phi_P + \sum_k A_k\phi_k + S_U}_{f(t,\phi(t))} \tag{4.79}$$

Now the above equation is ready to use one of the time discretization methods discussed above. Starting with the Fully Implicit approximation, one can obtain:

$$[(\rho\phi_P)^{n+1} - (\rho\phi_P)^n]V_{CV} = f(t,\phi_P(t))^{n+1}\Delta t \Rightarrow \underbrace{\frac{V_{CV}}{\Delta t}\rho^{n+1}}_{\text{to } A_P}\phi_P^{n+1} = \underbrace{\frac{V_{CV}}{\Delta t}\rho^n\phi_P^n}_{\text{to } S_U} + f(t,\phi_P(t))^{n+1} \tag{4.80}$$

For the sake of simplicity, the superscripts n and $n+1$ are introduced to denote values at time levels t^n and t^{n+1} respectively. One may notice that the above system can be written in the same general form as equation (4.64), allowing the TDMA algorithm to still be applied in order to calculate the values at the new time level t^{n+1}. Hence, the final form for the Fully Implicit method in STREAM code is:

$$\begin{aligned}
(S_U^{n+1})^{new} &= S_U^{n+1} + \frac{V_{CV}}{\Delta t}\rho^n \phi_P^n \\
(A_P^{n+1})^{new} &= A_P^{n+1} + \frac{V_{CV}}{\Delta t}\rho^{n+1} \\
(A_P^{n+1})^{new}\phi_P^{n+1} &= \sum_k A_k^{n+1}\phi_k^{n+1} + (S_U^{n+1})^{new}
\end{aligned} \tag{4.81}$$

where A_P^{n+1} and S_U^{n+1} are the matrix coefficient A_P and the source term S_U calculated for the steady state through equation (4.64).

In case of applying the Trapezoidal Rule, also known as the Crank-Nicolson method, equation (4.79) becomes:

$$\begin{aligned}
&[(\rho\phi_P)^{n+1} - (\rho\phi_P)^n]V_{CV} = \frac{1}{2}[f(t,\phi_P(t))^{n+1} + f(t,\phi_P(t))^n]\Delta t \Rightarrow \\
&\underbrace{\frac{V_{CV}}{\Delta t}\rho^{n+1}}_{\text{to } A_P}\phi_P^{n+1} = \underbrace{\frac{V_{CV}}{\Delta t}\rho^n\phi_P^n}_{\text{to } S_U} + \frac{1}{2}f(t,\phi_P(t))^{n+1} + \underbrace{\frac{1}{2}f(t,\phi_P(t))^n}_{\text{to } S_U}
\end{aligned} \tag{4.82}$$

Again, the above system must be reorganized in order to assume the form of equation (4.64). The final form of the Crank-Nicolson method in STREAM code is thus:

$$\begin{aligned}
(S_U^{n+1})^{new} &= \frac{1}{2}S_U^{n+1} + \frac{1}{2}[-A_P\phi_P + \sum_k A_k\phi_k + S_U]^n + \frac{V_{CV}}{\Delta t}\rho^n\phi_P^n \\
(A_k^{n+1})^{new} &= \frac{1}{2}A_k^{n+1}, \text{ k=E,W,N,S,T,B} \\
(A_P^{n+1})^{new} &= \frac{1}{2}A_P^{n+1} + \frac{V_{CV}}{\Delta t}\rho^{n+1}
\end{aligned} \tag{4.83}$$

with A_P^{n+1} and S_U^{n+1} being the steady state matrix coefficient and source term in equation (4.64).

That concludes the temporal discretization methods applied in the STREAM code.

4.2.7 Cylindrical Coordinates

Cylindrical coordinates are a particular case of curvilinear coordinates which is very often used in both academia and industry since many times the flow geometry consists of a pipe, or similar, where it is convenient to take advantage of the axisymmetry inherent in the problem.

The Navier-Stokes equation as well as the transport equations for any turbulent quantity,

such as the turbulent kinetic energy, the eddy-dissipation rate, the Reynolds stresses and so on, can be converted from Cartesian coordinates to cylindrical coordinates. In order to illustrate how the STREAM code treats flows in cylindrical coordinates, the transport equation for a general variable ϕ, equation 4.1, will be converted from Cartesian coordinates to 2-D axisymmetric cylindrical coordinates.

One may notice that equation 4.1 does not include the unsteady term $\frac{\partial \phi}{\partial t}$ which will be here considered in order to make the analysis more complete. When the transformation to cylindrical polars is carried out, the resulting unsteady form of equation 4.1 can then be written in the form:

$$r\frac{\partial \phi}{\partial t} + \frac{\partial}{\partial x}(rU\phi) + \frac{\partial}{\partial r}(rV\phi) = \frac{\partial}{\partial x}\left(r\Gamma\frac{\partial \phi}{\partial x}\right) + \frac{\partial}{\partial r}\left(r\Gamma\frac{\partial \phi}{\partial r}\right) + rS_\phi \tag{4.84}$$

One may notice then that the both unsteady and source terms are multiplied by the radius r, that the convective part is formed just by the same regular convection terms (see terms inside bracket in the left hand side of equation 4.46), but with r inside the parenthesis, and that the diffusion term is formed just by the same diffusion terms, with the diffusivities Γ being multiplied by r (see left hand side of equation 4.53). That is, everything remains just the same, but multiplied by the radius r. When using cylindrical polars, the STREAM code thus uses the same discretization as described previously, with coefficients multiplied by the radius r as indicated by equation 4.84.

The procedure described above works for the U-momentum Navier-Stokes equation, the turbulent scalar quantities transport equations and the Reynolds normal stress $\overline{u^2}$ transport equation. However, when transforming the V and W-momentum Navier-Stokes equations and all other Reynolds stresses transport equations from Cartesian coordinates to cylindrical coordinates, some additional terms also appear, which are simply treated explicitly and thus included in the discretized source terms.

4.2.8 Under-Relaxation and Convergence

Under-relaxation and convergence are intrinsically related since the former helps one to reach the latter. The under-relaxation consists of a slow down procedure in the iteration process which then makes it more stable. Under-relaxation is necessary because the Navier-Stokes equations are non-linear. The way of moderating each variable update is thus:

$$\phi_P^{it} = {\phi_P}^{calc}\alpha_\phi + \phi_P^{it-1}(1-\alpha_\phi) \Rightarrow \phi_P^{calc} = \frac{\phi_P^{it}}{\alpha_\phi} - \phi_P^{it-1}\frac{(1-\alpha_\phi)}{\alpha_\phi} \tag{4.85}$$

where ϕ_P^{it} is the updated value of ϕ to be used in the next iteration, ${\phi_P}^{calc}$ is the value that would be obtained by simply solving the discretized equation forms as described above, ϕ_P^{it-1} is the previous iteration result and α_ϕ is the under relaxation factor for the variable ϕ. If the value of ${\phi_P}^{calc}$ is substituted into equation (4.64) for ϕ_P, one obtains:

$$\underbrace{\frac{{A_P}^{calc}}{\alpha_\phi}}_{A_P^{it}}\phi_P^{it} = \left[\sum_k A_k U_k\right]^{calc} + \underbrace{{S_U}^{calc} + \phi_P^{it-1}(1-\alpha_\phi)\frac{{A_P}^{calc}}{\alpha_\phi}}_{S_U^{it}} \tag{4.86}$$

Hence, the way the STREAM code applies the under relaxation is by modifying the diagonal coefficient A_P and then the source term S_U:

$$\begin{aligned} A_P^{it} &= \frac{{A_P}^{calc}}{\alpha_\phi} \\ S_U^{it} &= {S_U}^{calc} + \phi_P^{it-1}(1-\alpha_\phi)A_P^{it-1} \end{aligned} \tag{4.87}$$

The pressure is under-relaxed by simply adding a fraction of the calculated correction to it

$$P_P^{it} = {P_P}^{calc} + \alpha_P P'_P \tag{4.88}$$

Depending on the variable to be calculated one may define different values for the under relaxation factor. In the STREAM code, one may define an under relaxation factor to solve the U, V and W momentum Navier-Stokes equation (URFMOM) and another for the remained variables (URFTRB), except the pressure. Actually, one may also define an under relaxation factor for the pressure correction equation (URFP). The procedure of under relaxation is different with the latter because one solves an equation for its correction rather than for itself.

Unless where otherwise stated, for all simulations in this work, the typical values used were: URFMOM=URFTRB=0.35 and URFP=0.25.

The same logic should be applied for the corrected velocities. Since they just need to be multiplied by the relaxation factor (in this case URFMOM), that is implemented in the STREAM code by relaxing the coefficients D_U, D_V and D_W, respectively, for the U, V and W velocities, that is:

$$D_U^{it} = \alpha_U {D_U}^{calc} \qquad D_V^{it} = \alpha_V {D_V}^{calc} \qquad D_W^{it} = \alpha_W {D_W}^{calc} \tag{4.89}$$

With regard to the convergence criteria, the STREAM code calculates the residual as follows: for each node, a dimensionless flux imbalance of terms in the discretized transport equation, $RESOR_\phi$, is computed for each variable. This term is intrinsically dimensionless because all the equations in STREAM are written in a dimensionless form as already stated before.

$$RESOR_\phi = \frac{\sum_F A_F\phi_F + S_U - A_P\phi_P}{\sum_F A_F} \tag{4.90}$$

The root mean square residual is then calculated by averaging RESOR over the number of nodes:

$$RES = \sqrt{\frac{1}{N}\sum_{N} RESOR_{\phi}^{2}} \tag{4.91}$$

The advantage of using such a measure is that it gives values that are reasonably independent of the number of nodes. In the pressure correction equation, the mass imbalance is used to monitor convergence, and the residual is thus taken as:

$$RESOR_{P} = \frac{S_{U}}{\sum_{f} A_{f}} \tag{4.92}$$

4.3 Concluding Remarks

A brief overview of the FV method and the main features of the STREAM code have been presented. Some topics such as the time dependence treatment, under relaxation and convergence criteria have been described in a manner consistent with their implementation within the STREAM code. Indeed, the objective of this Chapter has been to show familiarity with the numerical tool used for the turbulent flow simulations.

Chapter 5

Simulated Flows

In this chapter the test cases used to assess the performance of the different turbulence models will be presented. A wide variety of flows was investigated, from simple and traditional flows such as fully developed channel flows and zero pressure gradient boundary layers to more complex flows such as oscillatory backward facing step flows. Apart from the first two simple flows just mentioned, all other test cases present some non-equilibrium features which is the main modelling focus of this work.

The purpose of this chapter is thus to present the flow cases simulated and discuss the performance of the turbulence models described in Chapter 3, which will form a basis for the model development work to be described in later chapters. The assessment of the performance of the turbulence models will generally follow a comparison between eddy-viscosity, Reynolds stress transport and multiple-time-scale models. The simulation results were compared with DNS and/or experimental data and these will be briefly discussed here as well.

When comparing DNS and experimental data with simulation, it is common to compare dimensionless variables. The main dimensionless variables employed here are defined as:

$$y^+ = \frac{y u_\tau}{\nu} \qquad U^+ = \frac{U}{u_\tau} \tag{5.1}$$

$$k^+ = \frac{k}{u_\tau^2} \qquad \overline{u_i u_j}^+ = \frac{\overline{u_i u_j}}{u_\tau^2} \qquad \varepsilon^+ = \frac{\varepsilon \nu}{u_\tau^4} \tag{5.2}$$

In the above, $\nu = \frac{\mu}{\rho}$ is the kinematic viscosity and u_τ is the friction velocity defined as $u_\tau = \sqrt{\frac{\tau_w}{\rho}}$, τ_w being the shear stress at the wall calculated through the expression $\tau_w = \mu \frac{\partial U}{\partial y}|_w$.

The cases which will be presented are: homogeneous shear and normally strained flows; fully developed channel flow; zero, adverse, favourable and oscillatory pressure gradient boundary layers; fully developed oscillatory and ramp-up pipe flows, and steady and unsteady backward facing step flows. The following sections provide a description of the above flows, defining the relevant parameters in each case. The inlet and boundary conditions used in the STREAM code will also be explained and finally, the results will be presented and discussed.

5.1 Homogeneous Constant Shear Flow

The first set of test cases consist of homogeneous shear flows in which the streamwise velocity U only depends on y, $U = U(y)$, and the shear $S = \frac{dU}{dy}$ is constant. There is then no need to solve the Navier-Stokes and continuity equations (nor, therefore, the pressure correction equation) and thus this problem is characterized by solving only for the turbulence. The flows are free from any wall influences, so the questions of handling wall effects in the modelling can be ignored here.

Although these flows are homogeneous in space, the turbulence develops in time, leading to non-equilibrium effects during the development. In fact, although some kind of equilibrium is reached (where the ratios $\frac{\overline{u_i u_j}}{k}$ become constant), the generation and dissipation rates of the turbulent kinetic energy are not balanced, with the DNS data suggesting $\frac{P_k}{\varepsilon}$ reaches an asymptotic value of around 1.8, implying a constant growth of k.

It is then reasonable to find out what asymptotic value the turbulence models predict for $\frac{P_k}{\varepsilon}$. The asymptotic method described below has been used in the past, first for STS models (Speziale, 1991) and more recently for MTS models (Stawiarski and Hanjalic, 2005). These approaches were extended here.

For STS models, one can arrive at the equilibrium value for $\frac{P_k}{\varepsilon}$ by noting that $\frac{D}{Dt}\left(\frac{P_k}{\varepsilon}\right) = 0$ and, as $P_k = -\overline{uv}\frac{dU}{dy}$, $\frac{D}{Dt}\left(\frac{\overline{uv}}{\varepsilon}\frac{dU}{dy}\right) = 0$, and since $\frac{dU}{dy}$ is constant, then $\frac{D}{Dt}\left(\frac{\overline{uv}}{\varepsilon}\right) = 0$. Writing this as $\frac{D}{Dt}\left(\frac{\overline{uv}}{k}\frac{k}{\varepsilon}\right) = 0$, and assuming that the ratio $\frac{\overline{uv}}{k}$ reaches some asymptotic value then one can look at $\frac{D}{Dt}\left(\frac{k}{\varepsilon}\right) = 0$. Recalling k and ε equations from any STS turbulence model described in Chapter 3 (note that for this flow they all reduce to the same form), one can find the value for $\frac{P_k}{\varepsilon}$ predicted by the models in the asymptotic state:

$$\frac{D}{Dt}\left(\frac{k}{\varepsilon}\right) = 0 = \frac{1}{\varepsilon}\frac{Dk}{Dt} - \frac{k}{\varepsilon^2}\frac{D\varepsilon}{Dt} = \frac{1}{\varepsilon}(P_k - \varepsilon) - \frac{k}{\varepsilon^2}\left(c_{\varepsilon 1}\frac{\varepsilon}{k}P_k - c_{\varepsilon 2}\frac{\varepsilon^2}{k}\right) = \frac{P_k}{\varepsilon} - 1 - c_{\varepsilon 1}\frac{P_k}{\varepsilon} + c_{\varepsilon 2}$$

$$\Rightarrow \qquad \frac{P_k}{\varepsilon} = \frac{1 - c_{\varepsilon 2}}{1 - c_{\varepsilon 1}} \tag{5.3}$$

Now, with the values of $c_{\varepsilon 1}$ and $c_{\varepsilon 2}$, one can determine, for each turbulence model, what is the expected value of $\frac{P_k}{\varepsilon}$ in the asymptotic state. Indeed, except for the SG model which uses a different value for $c_{\varepsilon 2}$, all turbulence models mentioned in the previous Chapter use the same values for $c_{\varepsilon 1}$ and $c_{\varepsilon 2}$. Hence, for the SG model, $\frac{P_k}{\varepsilon} = 1.89$ and for the others, $\frac{P_k}{\varepsilon} = 2.09$ in the asymptotic state.

For MTS models, one may use the relation $\frac{D}{Dt}\left(\frac{k_P}{\varepsilon_p}\right) = 0$ in order to find an asymptotic state for $\frac{P_k}{\varepsilon_P}$ and then $\frac{D}{Dt}\left(\frac{k_T}{\varepsilon_T}\right) = 0$ to find an asymptotic state for $\frac{\varepsilon_P}{\varepsilon_T}$. By combining both asymptotic states, one arrives at an expected asymptotic value for $\frac{P_k}{\varepsilon_P}\frac{\varepsilon_P}{\varepsilon_T} = \frac{P_k}{\varepsilon_T}$. For an MTS model such as those presented in Chapter 3, if no extra terms are considered and the coefficients are constants, which is the case for the NG model, one can find:

$$\frac{P_k}{\varepsilon_P} = \frac{1 - C_{P2}}{1 - C_{P1}} \qquad \frac{\varepsilon_P}{\varepsilon_T} = \frac{1 - C_{T2}}{1 - C_{T1}} \qquad \frac{P_k}{\varepsilon_T} = \frac{(1 - C_{P2})}{(1 - C_{P1})} \frac{(1 - C_{T2})}{(1 - C_{T1})} \tag{5.4}$$

For the other MTS models considered, CG, KC and TS, the analysis is not so straightforward due to the presence of extra terms in the ε_P and ε_T equations, however one can also arrive at asymptotic values for $\frac{P_k}{\varepsilon_T}$ for these models. This will be discussed in more detail in Chapter 6.

5.1.1 Simulated Cases

Three different DNS sources were chosen for these comparisons. The first is the DNS data from Matsumoto et al. (1991), which can be obtained online at *http://cfd.mace.manchester.ac.uk/ercoftac*, and provides two different cases (HM1 and HM2). The second consists of Rogers and Moin's 1987 DNS results for three different cases (C128U, C128W and C128X), which can also be found online at *ftp://torroja.dmt.upm.es/AGARD/chapter3/HOM23/*. The third source is Lee et al.'s 1990 case (SHC), available online at *ftp://torroja.dmt.upm.es/AGARD/chapter3/HOM25*.

Based on Jacobitz et al.'s 1997 work, who discussed the importance of initial conditions to the evolution of the turbulent kinetic energy in DNS of homogeneous shear flows, Al-Sharif (2007) pointed out that when performing RANS simulations of Rogers and Moin's DNS cases it was preferable to use their reported conditions at the non-dimensional time $St = 2$ as initial calculation conditions, rather than those at $St = 0$, since the DNS was started from arbitrary divergence-free spectrum initial conditions, therefore not providing fully turbulent initial conditions appropriate for RANS reproductions. A brief study was carried out confirming this hypothesis and therefore that is what will be applied here (denoted by cases $U2$, $W2$ and $X2$).

Relevant parameters and initial conditions for the cases considered here are summarized in Table 5.1, where the subscript 0 denotes the initial value of the variables and $\eta = \frac{k}{\varepsilon}\frac{dU}{dy}$ is the dimensionless shear. This parameter is very important and useful to characterize these homogeneous shear flows. St is the dimensionless time which can be interpreted as being a measure of the cumulative mean strain of the fluid (Mathieu and Scott, 2000). The names used to identify the cases reflect those used in the original DNS databases.

Table 5.1: Flow parameters and initial conditions for the homogeneous constant shear flow cases.

Case	DNS Source	$dU/dy = S$	η_0	k_0	ε_0	St_0	St_{max}	μ
X2	Rogers and Moin (1987)	$10\sqrt{2}$	1.1950	3.7159	43.9758	2	14	0.0050
U2	Rogers and Moin (1987)	$20\sqrt{2}$	1.6848	6.8336	114.7220	2	16	0.0100
W2	Rogers and Moin (1987)	$40\sqrt{2}$	2.0568	9.0519	248.9552	2	28	0.0200
HM1	Matsumoto et al. (1991)	30.0	4.7140	11.6387	74.0692	0	14	0.0120
SHC	Lee et al. (1990)	10.0	16.7624	0.0662	0.0395	0	16	0.0017
HM2	Matsumoto et al. (1991)	$20\sqrt{2}$	30.747	0.2007	0.1846	0	4	0.0120

5.1.2 Simulations Setup

As already mentioned, in a homogeneous constant shear flow one does not need to solve transport equations for the velocity field and the pressure correction.

Since the flow is homogeneous in space a simple square domain consisting of a 3x3 grid with zero gradient conditions on each boundary was employed, characterizing Dirichlet boundary conditions. The velocity was set as $U = Sy$, and the strain rate S and molecular viscosity for each case were set as given in Table 5.1.

The initial conditions were set as given in Table 5.2. When MTS models were used it was assumed that $\varepsilon_0 = \varepsilon_{P_0} = \varepsilon_{T_0}$ and $\frac{k_{P_0}}{k_{T_0}} = 2$.

Although spatial grid independence is irrelevant in these cases, since there is no spatial flow variations, checks should be performed to ensure time accuracy. In the results presented below, the timestep Δt was taken as $\Delta t = \frac{1}{10S}$. Tests showed that reducing this by a factor of 10 had no significant impact on the results, thus demonstrating numerical solution accuracy.

Table 5.2: Initial conditions (St=0) for each homogeneous constant shear flow case

Case	k_0	$\overline{u^2}_0$	$\overline{v^2}_0$	$\overline{w^2}_0$	$\overline{uv}_0$	ε_0
X2	3.7159	2.7310	2.3944	2.3064	-1.0260	43.9758
U2	6.8336	5.3404	3.9492	4.3775	-2.2044	114.7220
W2	9.0519	7.8435	4.5063	5.7540	-3.3173	248.9552
HM1	11.6387	7.7677	7.8242	7.6854	0.0141	74.0692
SHC	0.0662	0.0435	0.0447	0.0442	-0.0001	0.0395
HM2	0.20070300	0.13471836	0.13560217	0.13108600	-0.00238659	0.18462700

5.1.3 Results and Discussion

All cases listed in Table 5.1 were simulated with all the turbulence models presented in Chapter 3. One may notice in Table 5.1 that the cases are placed in order of increasing initial dimensionless shear, η_0, and can be divided into low shear cases ($X2$, $U2$ and $W2$), moderate shear ($HM1$) and high shear cases (SHC and $HM2$). In each case the predictions are grouped into generic model types (eddy-viscosity, stress transport and multi-scale models).

Starting by examining the lowest shear case, $X2$ (shown in Figures 5.1 to 5.9), one may notice from Figure 5.1 that the development of k was best predicted by the KC model, although apart from the CG, LS, TS and WM models, all other schemes also performed reasonably well. ε, in Figure 5.2, was best predicted by the HJ, NG and SG models, although the other models provided reasonable results too. The prediction of the Reynolds shear stress can be observed in both Figures 5.3 and 5.4. The profile of $\overline{uv}$ itself can be seen in the former where the HJ, KS, NG and SG models performed best. The profile of the shear component of the anisotropy tensor, a_{12} in Figure 5.4, was reasonably well predicted by all models. The normal components of the stress anisotropy tensor are presented in Figures 5.5, 5.6 and 5.7. As known, the LEV models will predict these as zero, since they predict isotropy for the Reynolds normal stresses in simple shear flows. The a_{11} and a_{22} components were best predicted by the KS and SG models, while the a_{33} component was best predicted by the

HJ, TC and WM models. $\frac{P_k}{\varepsilon}$, in Figure 5.8, was reasonably well predicted by all models except the CG model which, together with the TS model, did not reach an asymptotic value in the time simulated. All STS models do seem to tend to the asymptotic value predicted by equation 5.3. The performance of the models in predicting the dimensionless shear η, presented in Figure 5.9, is similar to that of $\frac{P_k}{\varepsilon}$.

The next case is $U2$ with a approximately 40% higher dimensionless shear. The results for this case are presented in Figures 5.10 to 5.12, showing the profiles of the turbulent kinetic energy, the eddy dissipation rate and the Reynolds shear stress only, since other comparisons are similar to those noted in the previous case. One may notice that the KS and SG models consistently provided the best predictions overall.

The last low shear case considered is the $W2$ case, with a dimensionless shear about 70% higher than that in the lowest shear case $X2$. Again, only profiles of k, ε and $\overline{uv}$ are being shown in Figures 5.13 to 5.15, since very similar analyses can be made for this case compared to those of the previous low shear cases, where the KS and SG models consistently provided the best predictions. In this case though the other models do not provide such reasonable results, tending either to underpredict or overpredict too much these turbulent quantities.

The only moderate shear case to be examined, $HM1$, has a dimensionless shear which is about four times bigger than that of the lowest shear case $X2$. The predictions of this case are presented in Figures 5.16 to 5.24. The turbulent kinetic energy (Figure 5.16), the eddy dissipation rate (Figure 5.17) and the Reynolds shear stress (Figures 5.18 and 5.19) were best predicted by the KS, HJ and WM models. One may notice that the other models tended to completely overpredict the profiles of k, ε and the magnitude of $\overline{uv}$. The normal components a_{11} and a_{22} of the stress anisotropy tensor were best predicted by the SG model, while the a_{33} component was best predicted by the TC and WM models. The profile of $\frac{Pk}{\varepsilon}$ was best predicted by the EV and RST models, while the MTS models tended to underpredict it, except for the CG and TS models which did not reach asymptotic values in the simulated time. The profile of η was best captured by the KS and HJ models.

Among the two high shear cases to be studied here, the lowest, SHC case, has a dimensionless shear which is about fourteen times that of the lowest shear case $X2$. The results for the SHC case are presented in Figures 5.25 to 5.33. By looking at Figure 5.25, one may notice that the KS model best predicts the turbulent kinetic energy profile, followed by the WM model which already overpredicts it a bit. All the other models clearly overpredict this quantity. The same happens in the prediction of the eddy dissipation rate in Figure 5.26 and the Reynolds shear stress $\overline{uv}$ in Figure 5.27. However, one may notice that the a_{12} profile was reasonably well predicted by all models, except the TS model. The normal components of the stress anisotropy tensor (Figures 5.29, 5.30 and 5.31) were also poorly predicted by all models, as was the dimensionless shear η in Figure 5.33. The profile of $\frac{Pk}{\varepsilon}$, presented in Figure 5.32, was reasonably well predicted by all models, except for the CG and TS schemes.

For the last case to be discussed, the highest shear case, $HM2$, only the profiles of the turbulent kinetic energy, the eddy dissipation rate and the Reynolds shear stress are presented in Figures 5.34 to 5.36, since there are few DNS data for comparison. In this case, the RST

models, including the MTS RST model WM, performed clearly best overall. It is worth noting that the change in the profile of $\overline{uv}$ presented by the KC model is due to unrealistically high values predicted by this model for the magnitude of the Reynolds shear stress until $St \approx 2$ which was thus clipped in the code.

Now that each case has been separately analysed, general comments may be made in order to compare the cases and the performance of the models.

The first and perhaps most important comment is how the models as a whole tend to perform better in the low shear cases. As the dimensionless shear increases, more of the models start to overpredict the turbulence quantities such as k and ε. An exception to this is the WM model, which clearly performed better in the moderate and high shear cases, and perhaps the SG model which performed reasonably well in most cases. The comparisons above suggest that most of the models are tuned to perform well over a certain limited range of dimensionless shear magnitudes, but do not do so well over a wide range of η values.

It is also worth noting that in all these homogeneous shear flow cases the HR and FM models performed precisely the same as each other. This result is obviously expected since the FM model should be entirely equivalent to the HR scheme far from walls.

Observing Figures 5.6(b), 5.7(b), 5.21(b), 5.22(b), 5.30(b) and 5.31(b), one may notice that the GL and HJ models tend to predict similar value for the Reynolds stress anisotropy components a_{22} and a_{33}. This is consistent in terms of the models since they use similar transport equations for free shear flows, where the damping functions of the HJ model should not be important. However, the fact that these profiles do not generally match the DNS data indicates an intrinsic deficiency which may be associated with the expression for the pressure-strain correlation of both models.

Another important comment is with regard to the KS model which also performed comparatively well as a whole over the range of η values tested here. The reason why this model stands out from the other eddy-viscosity model predictions is due to its c_μ dependence on the dimensionless shear η, whilst most of the other schemes which perform poorly in the moderate or high shear cases employ a constant c_μ. In all cases, except for the $HM1$ case, the KS model was run with the viscous damping term (f_μ in Table 3.8) set to unity, since initial simulations showed that inclusion of this significantly degraded the predictions due to it becoming active at the low Reynolds numbers of these flows. At least some of the deficiencies seen with the LS model may also be due to its f_μ damping function becoming active in these flows, although this hypothesis was not verified by setting it to unity in this case.

The predictions of $\frac{P_k}{\varepsilon}$ mainly confirm the expected asymptotic values of the various models, except for the CG and TS results which did not appear to reach constant asymptotic levels. The reason for this will be discussed in Chapter 6 when considering the desired asymptotic behaviour of models in these flows.

Overall, it is clear that the RST models, which do not rely on algebraic stress-strain relations, performed best, however they present much more complex formulations than the EV and LEV MTS models which, given their inherent limitations, did perform reasonably well in the low shear cases. It is also of value to call attention to the fact that the turbulence

models which presented generally the best performances were the SG and the KS models, both of which were designed taking into account at least some such simple shear flows, and have therefore been at least partly tuned for such cases.

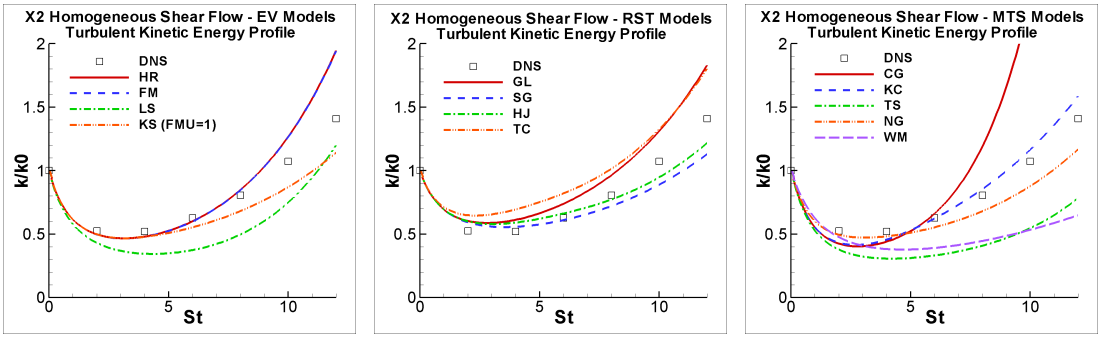

(a) (b) (c)

Figure 5.1: Prediction of the turbulent kinetic energy k for the homogeneous low shear case $X2$ by the: (a) eddy-viscosity models, (b) Reynolds stress transport models and (c) multiple-time-scale models. Models as in Table 3.25.

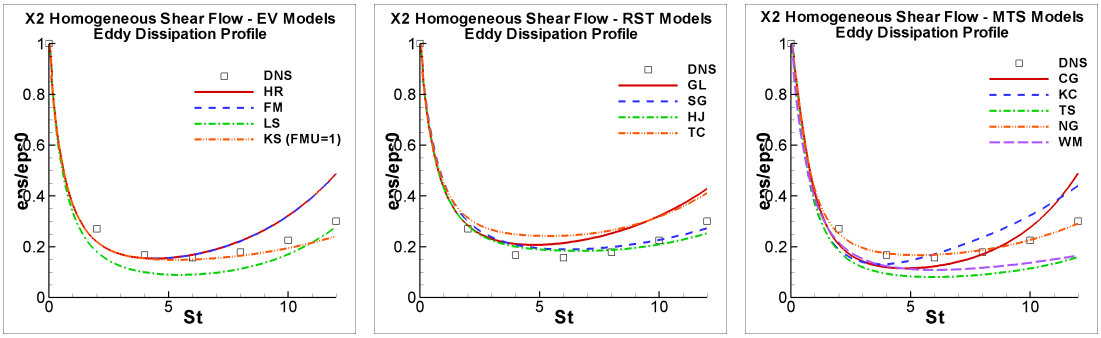

(a) (b) (c)

Figure 5.2: Prediction of the turbulent kinetic energy dissipation rate ε for the homogeneous low shear case $X2$ by the: (a) eddy-viscosity models, (b) Reynolds stress transport models and (c) multiple-time-scale models. Models as in Table 3.25.

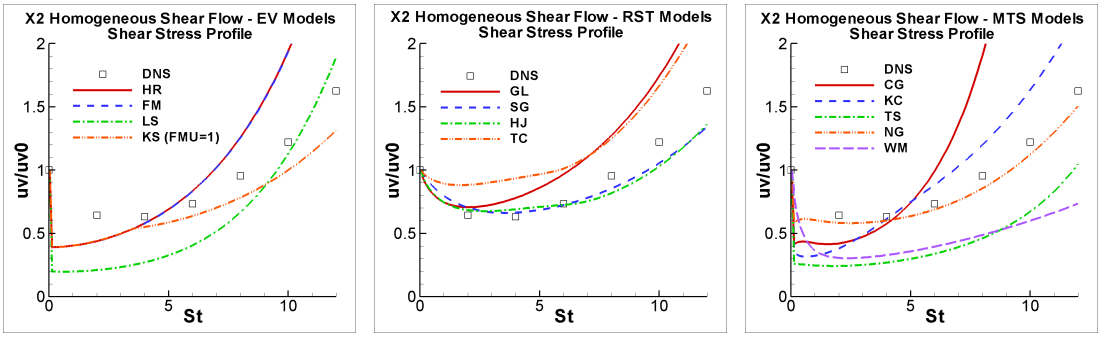

(a) (b) (c)

Figure 5.3: Prediction of the Reynolds shear stress $\overline{uv}$ for the homogeneous low shear case $X2$ by the: (a) eddy-viscosity models, (b) Reynolds stress transport models and (c) multiple-time-scale models. Models as in Table 3.25.

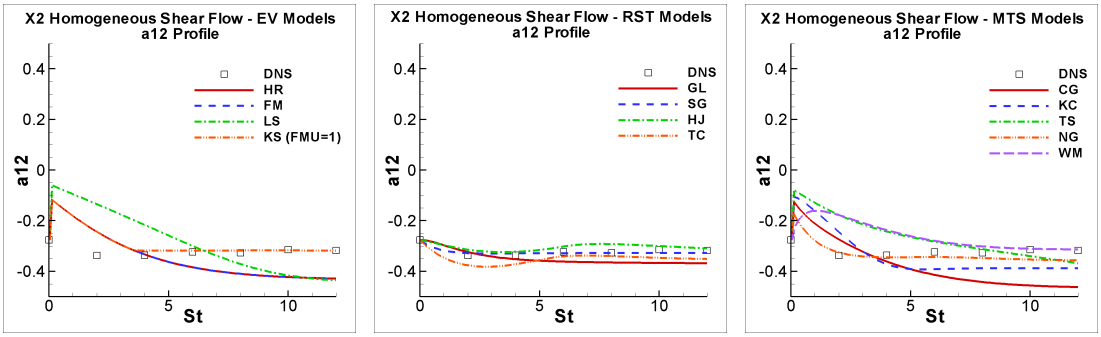

(a) (b) (c)

Figure 5.4: Prediction of the shear component a_{12} of the Reynolds stress anisotropy tensor for the homogeneous low shear case $X2$ by the: (a) eddy-viscosity models, (b) Reynolds stress transport models and (c) multiple-time-scale models. Models as in Table 3.25.

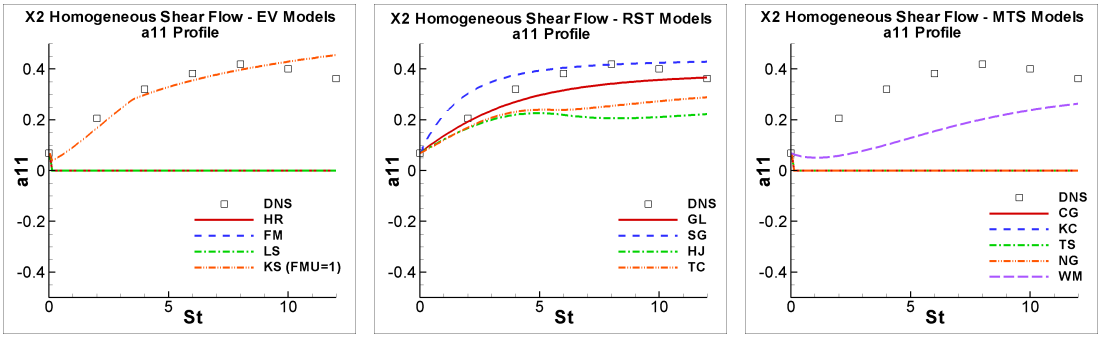

(a) (b) (c)

Figure 5.5: Prediction of the normal component a_{11} of the Reynolds stress anisotropy tensor for the homogeneous low shear case $X2$ by the: (a) eddy-viscosity models, (b) Reynolds stress transport models and (c) multiple-time-scale models. Models as in Table 3.25.

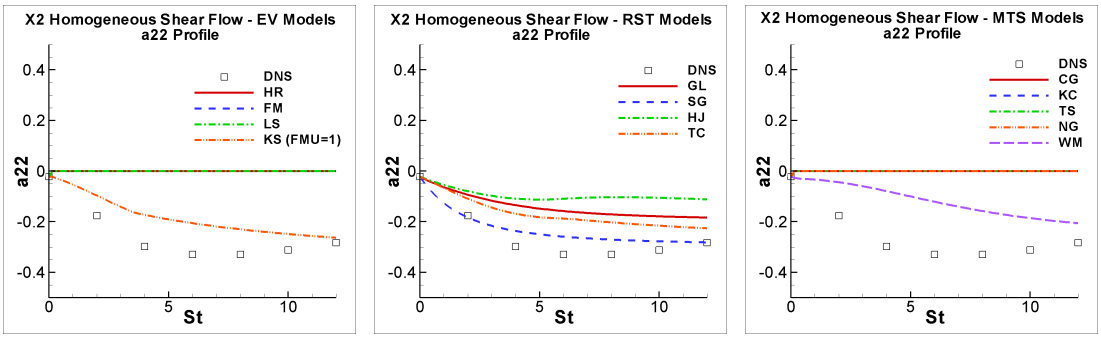

(a) (b) (c)

Figure 5.6: Prediction of the normal component a_{22} of the Reynolds stress anisotropy tensor for the homogeneous low shear case $X2$ by the: (a) eddy-viscosity models, (b) Reynolds stress transport models and (c) multiple-time-scale models. Models as in Table 3.25.

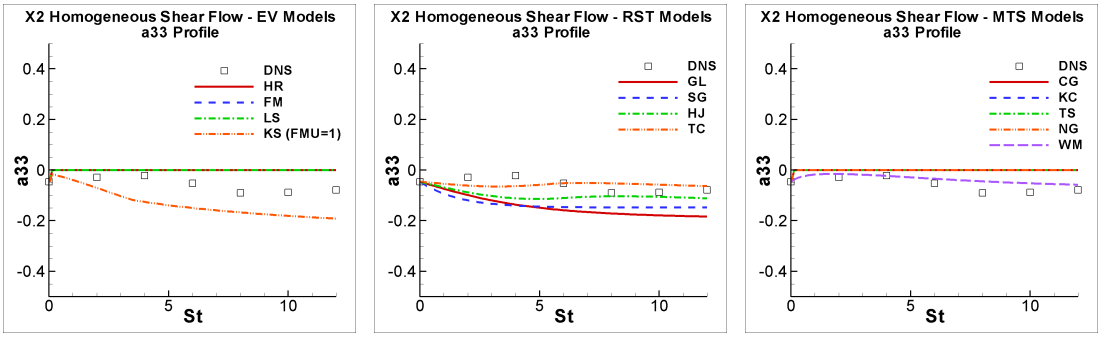

(a) (b) (c)

Figure 5.7: Prediction of the normal component a_{33} of the Reynolds stress anisotropy tensor for the homogeneous low shear case $X2$ by the: (a) eddy-viscosity models, (b) Reynolds stress transport models and (c) multiple-time-scale models. Models as in Table 3.25.

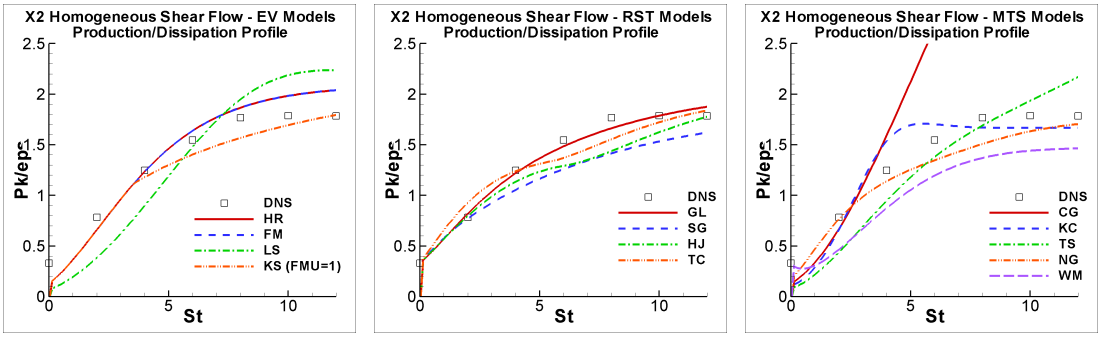

(a) (b) (c)

Figure 5.8: Prediction of the production to dissipation ratio, $\frac{P_k}{\varepsilon}$, for the homogeneous low shear case $X2$ by the: (a) eddy-viscosity models, (b) Reynolds stress transport models and (c) multiple-time-scale models. Models as in Table 3.25.

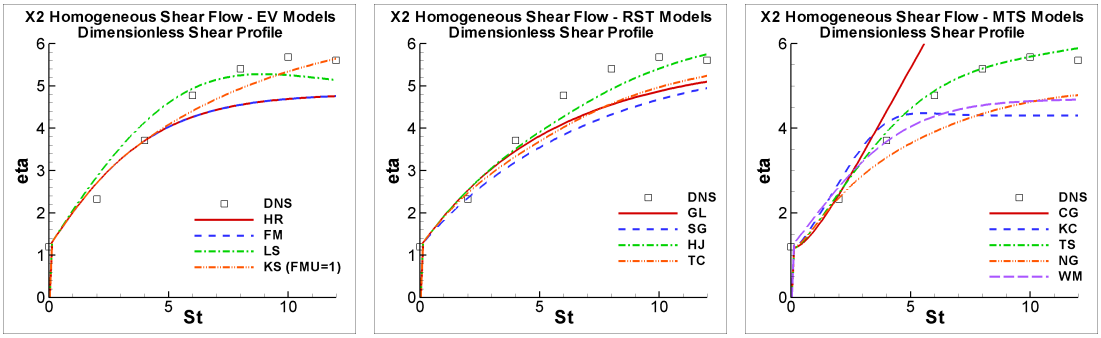

(a) (b) (c)

Figure 5.9: Prediction of the dimensionless shear $\eta = \frac{k}{\varepsilon}\frac{dU}{dy}$ for the homogeneous low shear case $X2$ by the: (a) eddy-viscosity models, (b) Reynolds stress transport models and (c) multiple-time-scale models. Models as in Table 3.25.

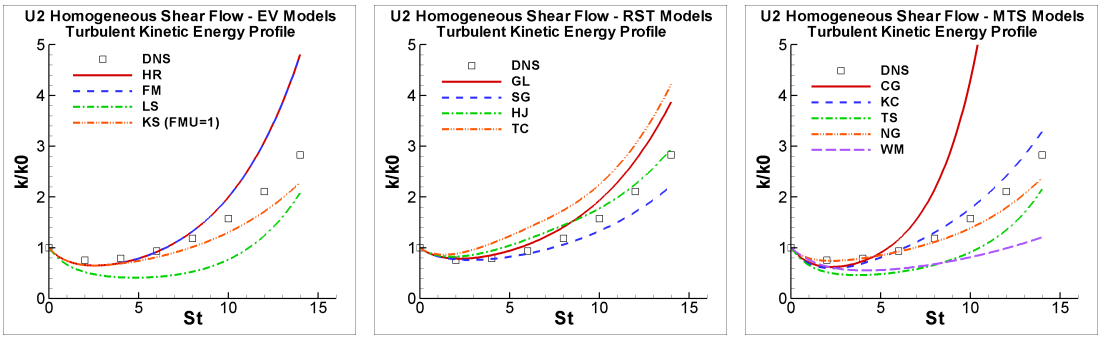

(a) (b) (c)

Figure 5.10: Prediction of the turbulent kinetic energy k for the homogeneous low shear case $U2$ by the: (a) eddy-viscosity models, (b) Reynolds stress transport models and (c) multiple-time-scale models. Models as in Table 3.25.

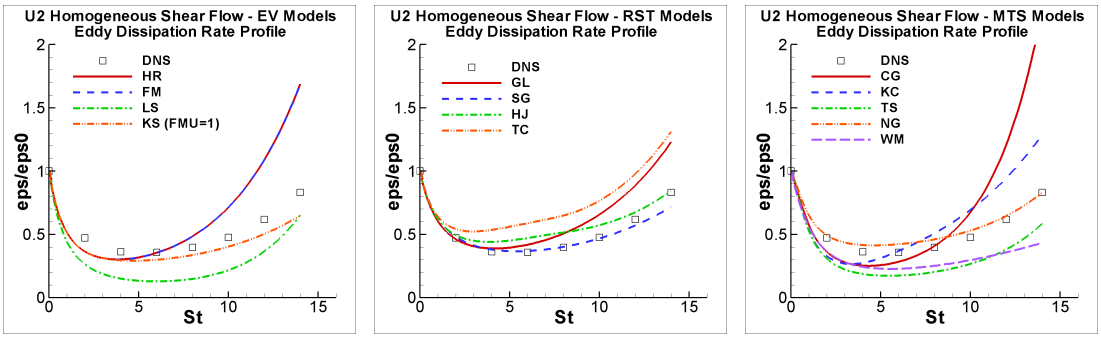

(a) (b) (c)

Figure 5.11: Prediction of the turbulent kinetic energy dissipation rate ε for the homogeneous low shear case $U2$ by the: (a) eddy-viscosity models, (b) Reynolds stress transport models and (c) multiple-time-scale models. Models as in Table 3.25.

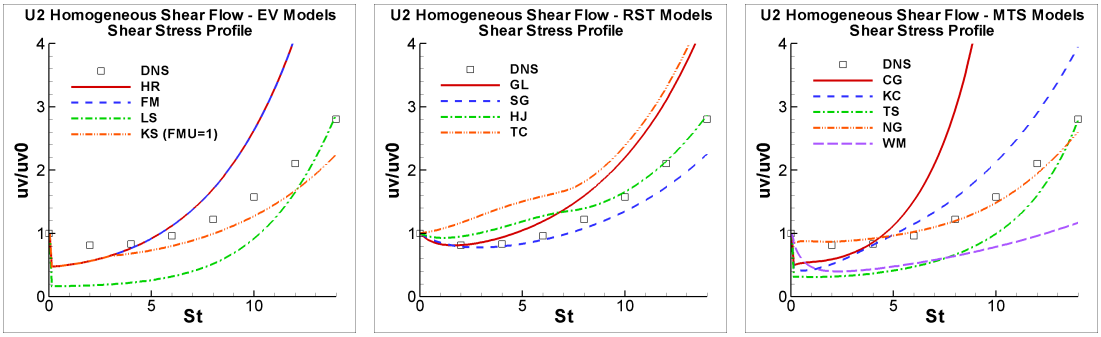

(a) (b) (c)

Figure 5.12: Prediction of the Reynolds shear stress $\overline{uv}$ for the homogeneous low shear case $U2$ by the: (a) eddy-viscosity models, (b) Reynolds stress transport models and (c) multiple-time-scale models. Models as in Table 3.25.

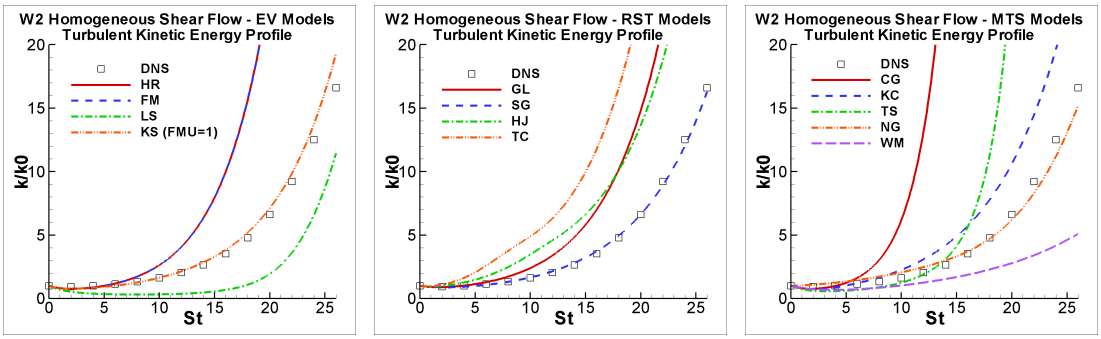

(a) (b) (c)

Figure 5.13: Prediction of the turbulent kinetic energy k for the homogeneous low shear case $W2$ by the: (a) eddy-viscosity models, (b) Reynolds stress transport models and (c) multiple-time-scale models. Models as in Table 3.25.

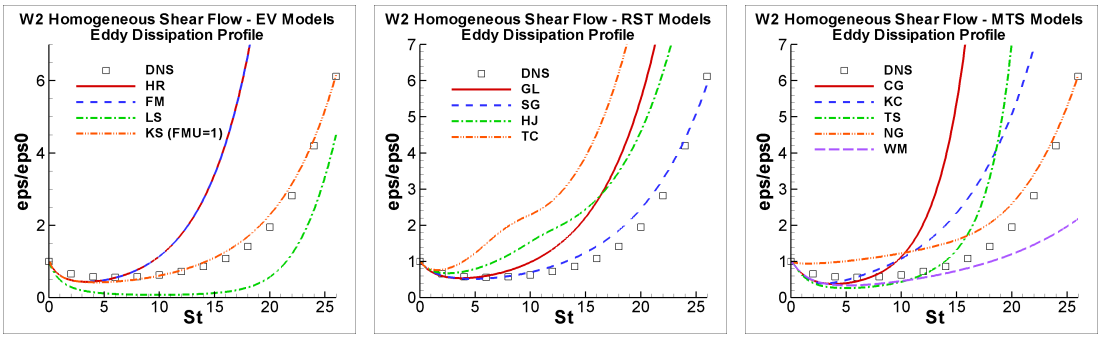

(a) (b) (c)

Figure 5.14: Prediction of the turbulent kinetic energy dissipation rate ε for the homogeneous low shear case $W2$ by the: (a) eddy-viscosity models, (b) Reynolds stress transport models and (c) multiple-time-scale models. Models as in Table 3.25.

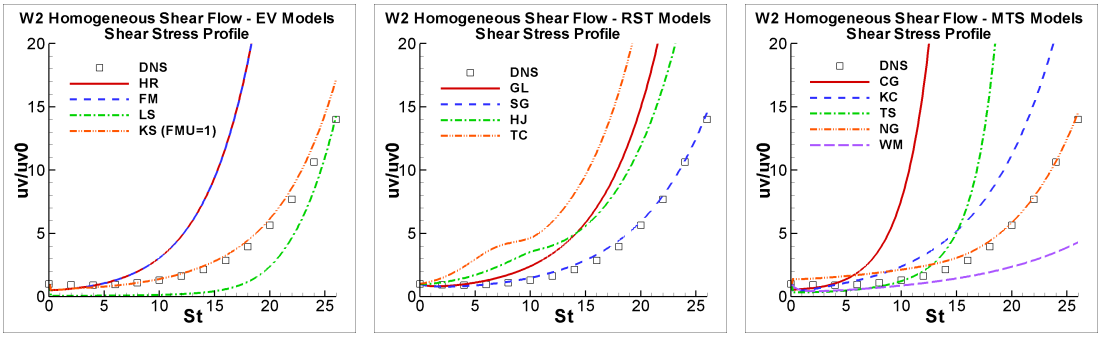

(a) (b) (c)

Figure 5.15: Prediction of the Reynolds shear stress $\overline{uv}$ for the homogeneous low shear case $W2$ by the: (a) eddy-viscosity models, (b) Reynolds stress transport models and (c) multiple-time-scale models. Models as in Table 3.25.

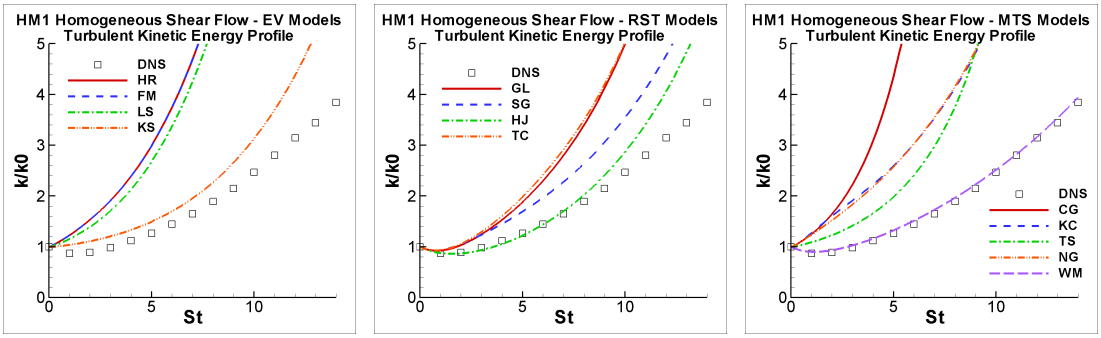

(a) (b) (c)

Figure 5.16: Prediction of the turbulent kinetic energy k for the homogeneous moderate shear case $HM1$ by the: (a) eddy-viscosity models, (b) Reynolds stress transport models and (c) multiple-time-scale models. Models as in Table 3.25.

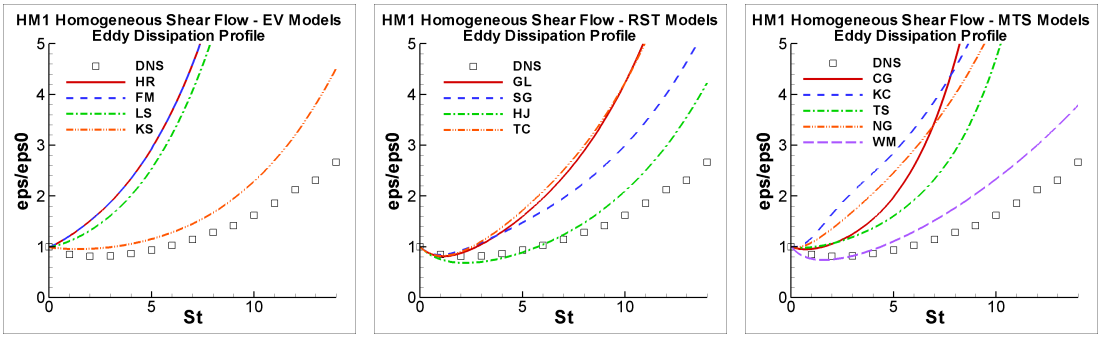

(a) (b) (c)

Figure 5.17: Prediction of the turbulent kinetic energy dissipation rate ε for the homogeneous moderate shear case $HM1$ by the: (a) eddy-viscosity models, (b) Reynolds stress transport models and (c) multiple-time-scale models. Models as in Table 3.25.

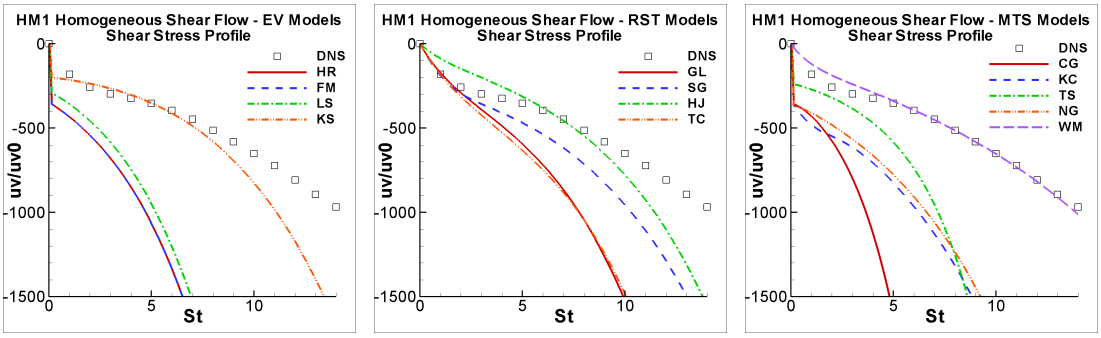

(a) (b) (c)

Figure 5.18: Prediction of the Reynolds shear stress $\overline{uv}$ for the homogeneous moderate shear case $HM1$ by the: (a) eddy-viscosity models, (b) Reynolds stress transport models and (c) multiple-time-scale models. Models as in Table 3.25.

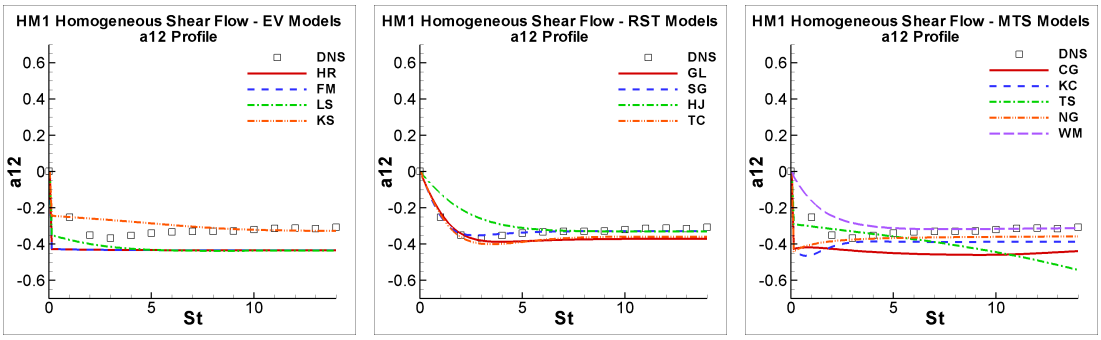

(a) (b) (c)

Figure 5.19: Prediction of the shear component a_{12} of the Reynolds stress anisotropy tensor for the homogeneous moderate shear case $HM1$ by the: (a) eddy-viscosity models, (b) Reynolds stress transport models and (c) multiple-time-scale models. Models as in Table 3.25.

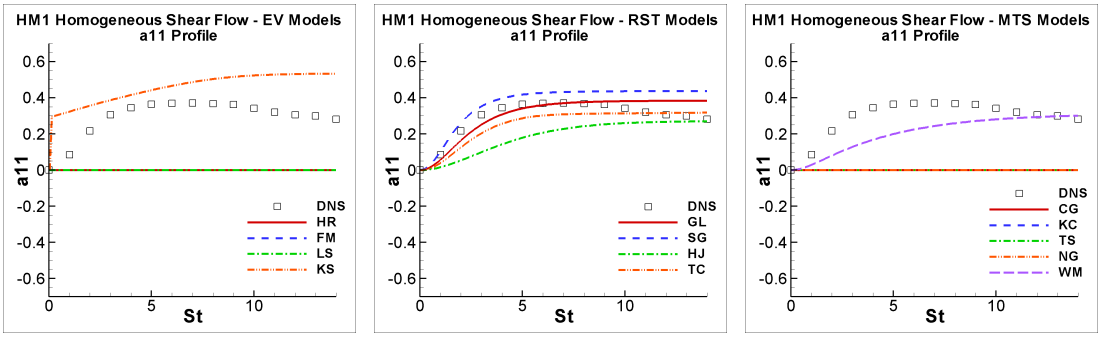

(a) (b) (c)

Figure 5.20: Prediction of the normal component a_{11} of the Reynolds stress anisotropy tensor for the homogeneous moderate shear case $HM1$ by the: (a) eddy-viscosity models, (b) Reynolds stress transport models and (c) multiple-time-scale models. Models as in Table 3.25.

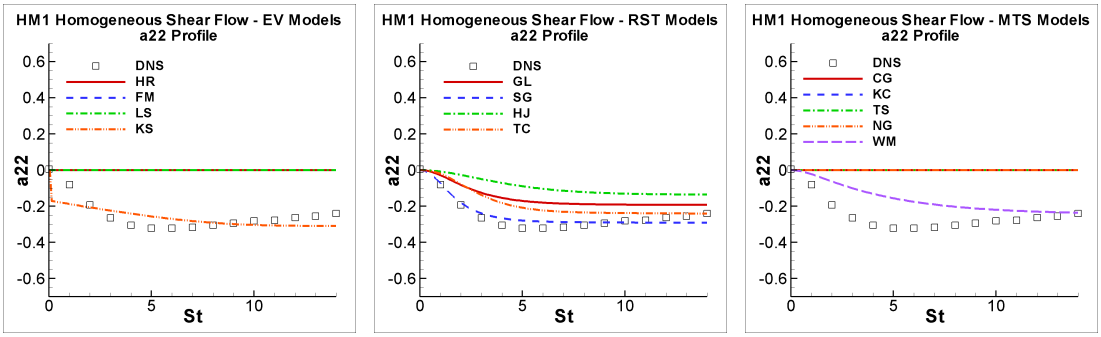

(a) (b) (c)

Figure 5.21: Prediction of the normal component a_{22} of the Reynolds stress anisotropy tensor for the homogeneous moderate shear case $HM1$ by the: (a) eddy-viscosity models, (b) Reynolds stress transport models and (c) multiple-time-scale models. Models as in Table 3.25.

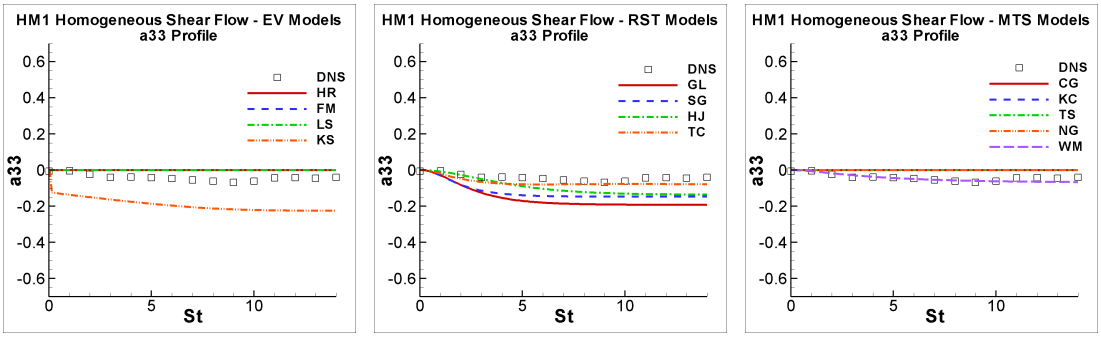

(a) (b) (c)

Figure 5.22: Prediction of the normal component a_{33} of the Reynolds stress anisotropy tensor for the homogeneous moderate shear case $HM1$ by the: (a) eddy-viscosity models, (b) Reynolds stress transport models and (c) multiple-time-scale models. Models as in Table 3.25.

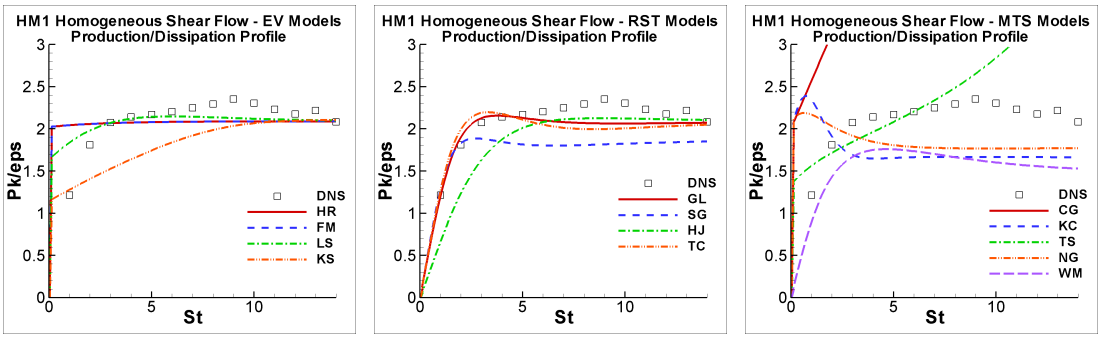

(a) (b) (c)

Figure 5.23: Prediction of the production to dissipation ratio, $\frac{P_k}{\varepsilon}$, for the homogeneous moderate shear case $HM1$ by the: (a) eddy-viscosity models, (b) Reynolds stress transport models and (c) multiple-time-scale models. Models as in Table 3.25.

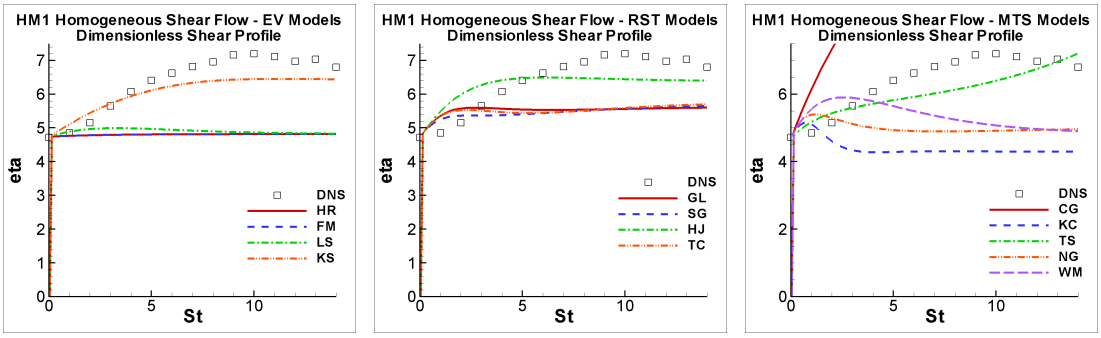

(a) (b) (c)

Figure 5.24: Prediction of the dimensionless shear $\eta = \frac{k}{\varepsilon}\frac{dU}{dy}$ for the homogeneous moderate shear case $HM1$ by the: (a) eddy-viscosity models, (b) Reynolds stress transport models and (c) multiple-time-scale models. Models as in Table 3.25.

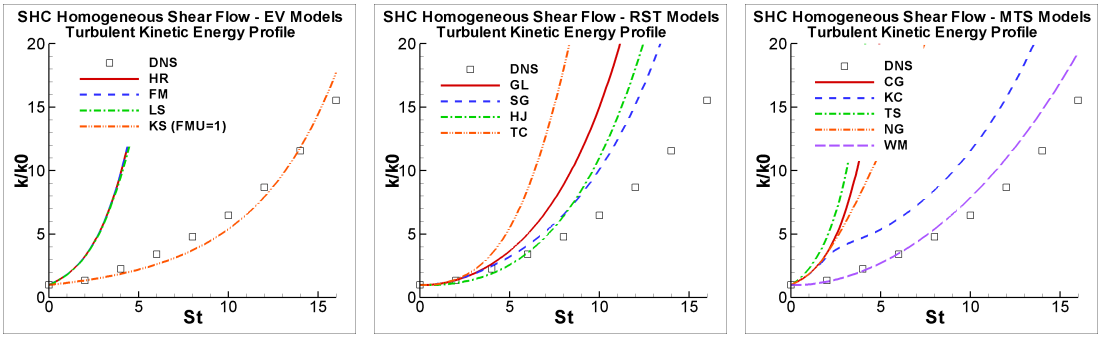

(a) (b) (c)

Figure 5.25: Prediction of the turbulent kinetic energy k for the homogeneous high shear case SHC by the: (a) eddy-viscosity models, (b) Reynolds stress transport models and (c) multiple-time-scale models. Models as in Table 3.25.

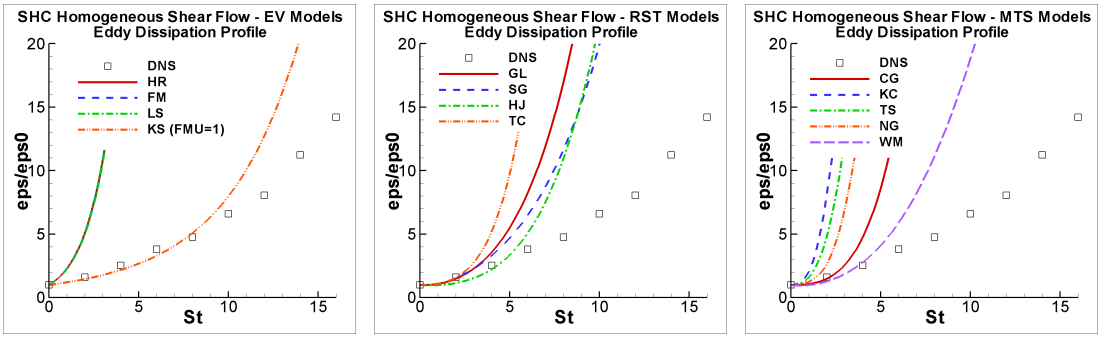

(a) (b) (c)

Figure 5.26: Prediction of the turbulent kinetic energy dissipation rate ε for the homogeneous high shear case SHC by the: (a) eddy-viscosity models, (b) Reynolds stress transport models and (c) multiple-time-scale models. Models as in Table 3.25.

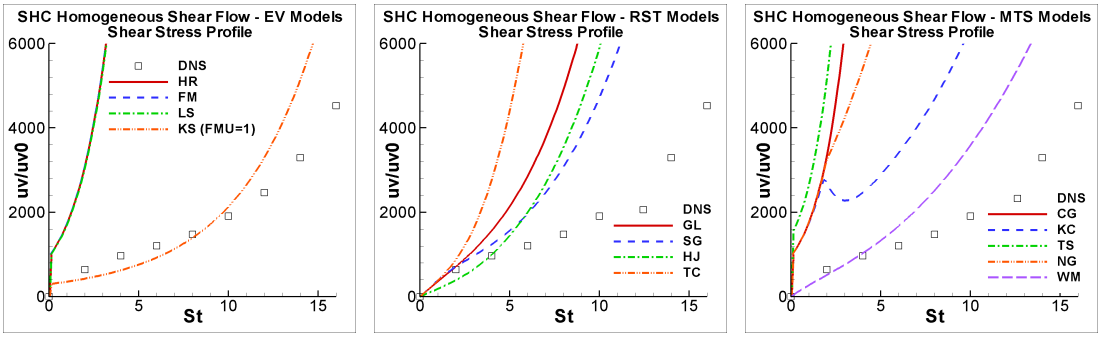

(a) (b) (c)

Figure 5.27: Prediction of the Reynolds shear stress $\overline{uv}$ for the homogeneous high shear case SHC by the: (a) eddy-viscosity models, (b) Reynolds stress transport models and (c) multiple-time-scale models. Models as in Table 3.25.

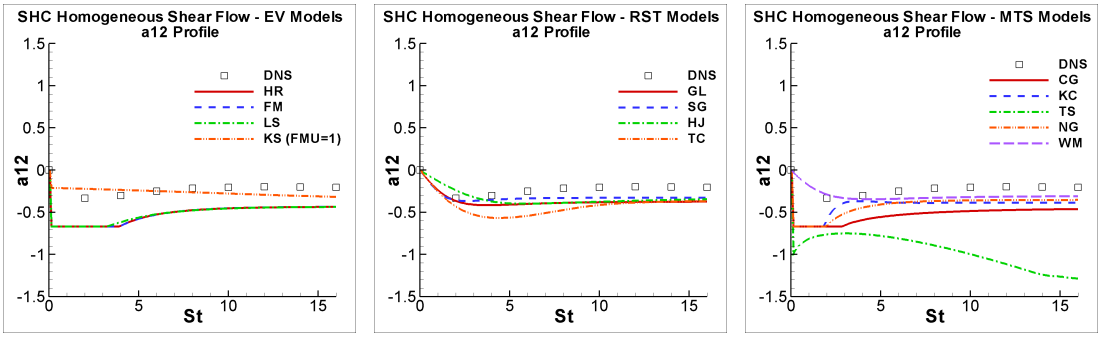

(a) (b) (c)

Figure 5.28: Prediction of the shear component a_{12} of the Reynolds stress anisotropy tensor for the homogeneous high shear case *SHC* by the: (a) eddy-viscosity models, (b) Reynolds stress transport models and (c) multiple-time-scale models. Models as in Table 3.25.

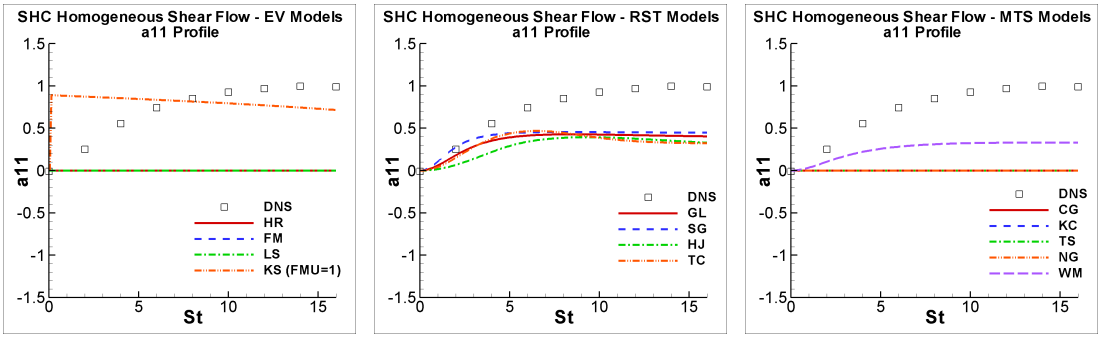

(a) (b) (c)

Figure 5.29: Prediction of the normal component a_{11} of the Reynolds stress anisotropy tensor for the homogeneous high shear case *SHC* by the: (a) eddy-viscosity models, (b) Reynolds stress transport models and (c) multiple-time-scale models. Models as in Table 3.25.

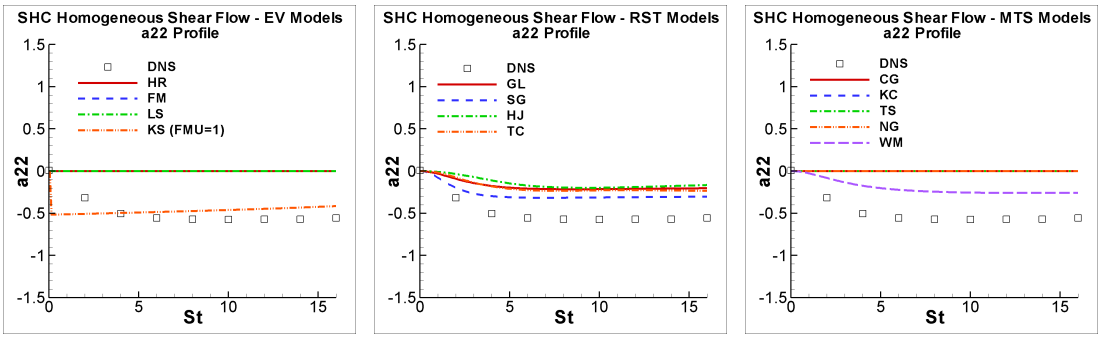

(a) (b) (c)

Figure 5.30: Prediction of the normal component a_{22} of the Reynolds stress anisotropy tensor for the homogeneous high shear case *SHC* by the: (a) eddy-viscosity models, (b) Reynolds stress transport models and (c) multiple-time-scale models. Models as in Table 3.25.

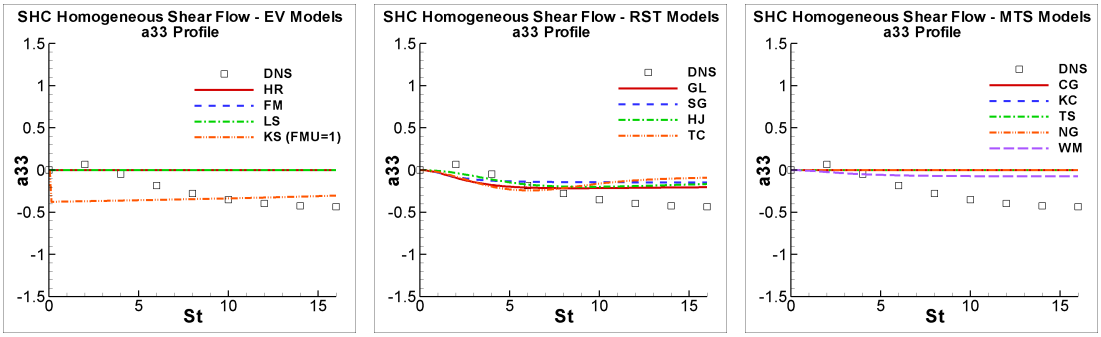

(a) (b) (c)

Figure 5.31: Prediction of the normal component a_{33} of the Reynolds stress anisotropy tensor for the homogeneous high shear case SHC by the: (a) eddy-viscosity models, (b) Reynolds stress transport models and (c) multiple-time-scale models. Models as in Table 3.25.

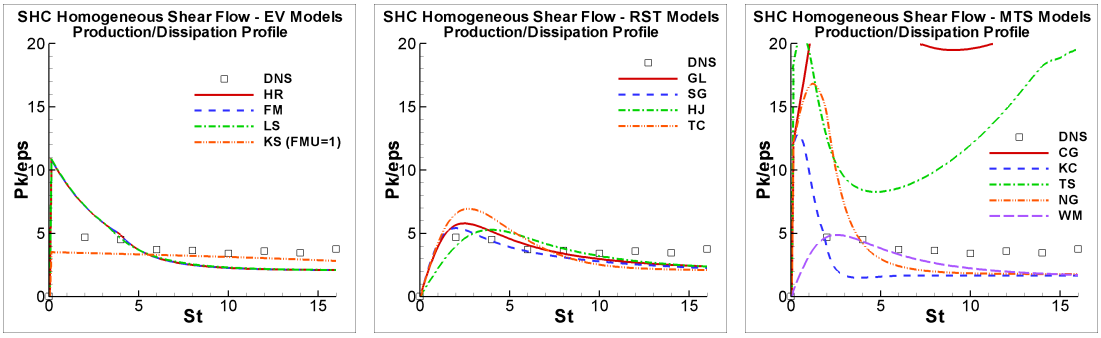

(a) (b) (c)

Figure 5.32: Prediction of the production to dissipation ratio, $\frac{P_k}{\varepsilon}$, for the homogeneous high shear case SHC by the: (a) eddy-viscosity models, (b) Reynolds stress transport models and (c) multiple-time-scale models. Models as in Table 3.25.

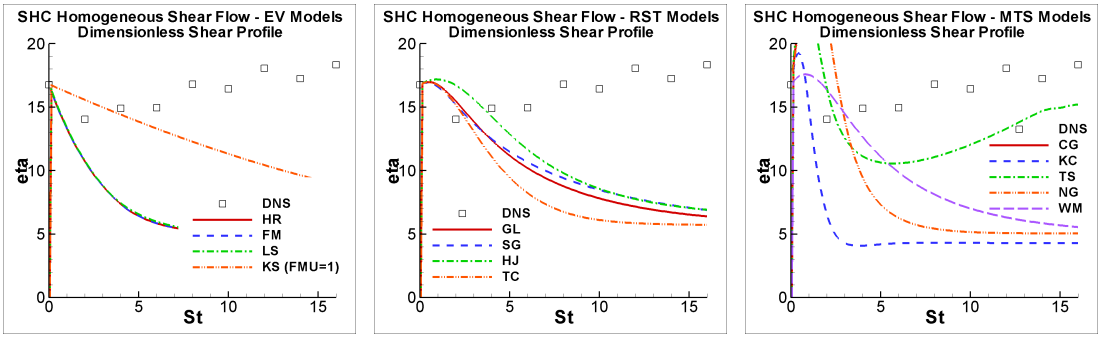

(a) (b) (c)

Figure 5.33: Prediction of the dimensionless shear $\eta = \frac{k}{\varepsilon}\frac{dU}{dy}$ for the homogeneous high shear case SHC by the: (a) eddy-viscosity models, (b) Reynolds stress transport models and (c) multiple-time-scale models. Models as in Table 3.25.

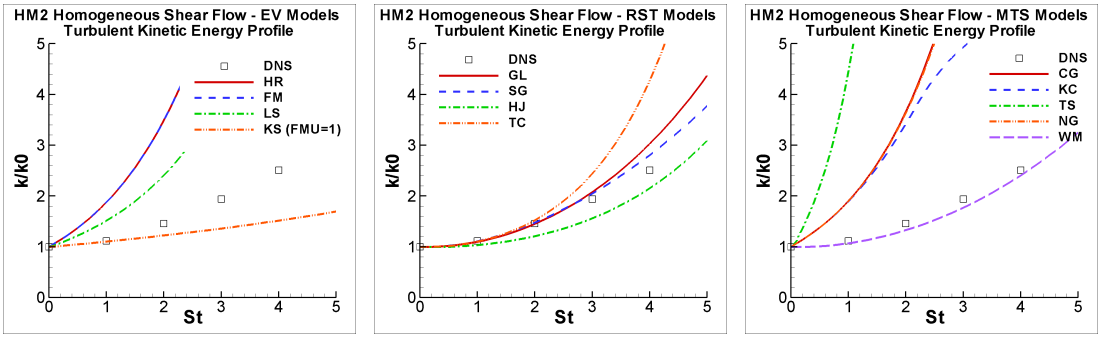

(a) (b) (c)

Figure 5.34: Prediction of the turbulent kinetic energy k for the homogeneous high shear case $HM2$ by the: (a) eddy-viscosity models, (b) Reynolds stress transport models and (c) multiple-time-scale models. Models as in Table 3.25.

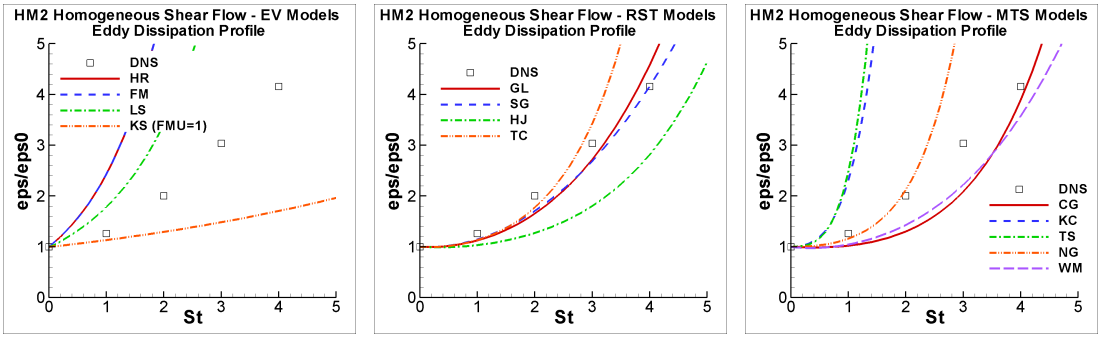

(a) (b) (c)

Figure 5.35: Prediction of the turbulent kinetic energy dissipation rate ε for the homogeneous high shear case $HM2$ by the: (a) eddy-viscosity models, (b) Reynolds stress transport models and (c) multiple-time-scale models. Models as in Table 3.25.

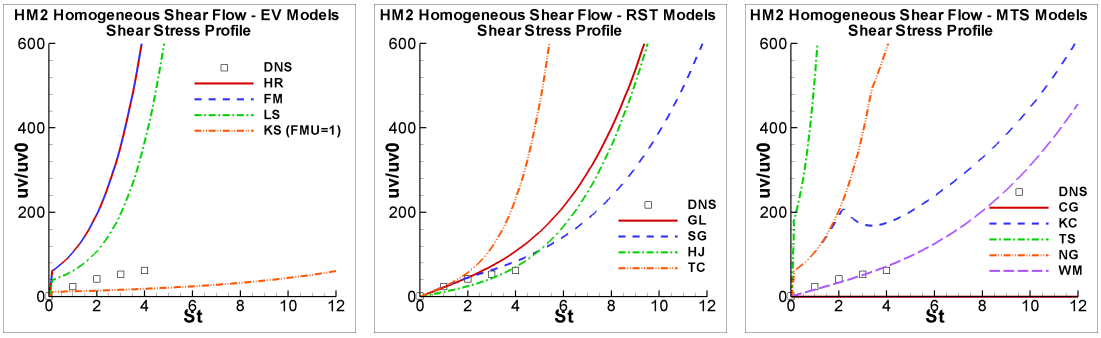

(a) (b) (c)

Figure 5.36: Prediction of the Reynolds shear stress $\overline{uv}$ for the homogeneous high shear case $HM2$ by the: (a) eddy-viscosity models, (b) Reynolds stress transport models and (c) multiple-time-scale models. Models as in Table 3.25.

5.2 Normally Strained Flow

This section is about homogeneous flows subjected to symmetric plane strain. The scenario consists of a constant velocity stream entering a channel in isotropic/quasi-isotropic turbulence conditions and facing a symmetric plane strain deformation of the channel. Here, one should understand by plane strain a deformation in the plane perpendicular to the main flow direction, caused only by normal strains. The symmetry comes from the fact that one imposes equal, but opposite in sign, strain rates in the two cross-stream directions, for example, as shown in Figure 5.37. The flow therefore presents an expansion in one direction and a contraction in the other, thus characterizing a non-equilibrium flow.

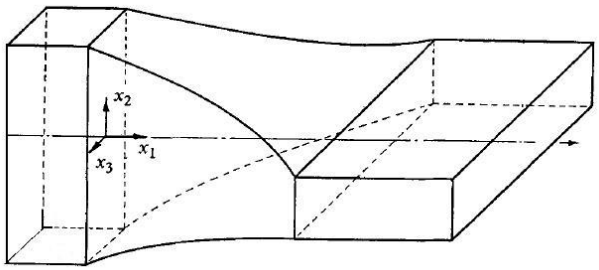

Figure 5.37: Representation of a pure plane strain, adapted from Tucker and Reynolds (1968)

One may notice that although this is a 3D flow, if one restricts attention to the central region of the duct, where immediate wall influences can be neglected, the turbulence may be considered as homogeneous, and developing only in the streamwise direction. Considering the centreline development, therefore, only a 1-dimensional simulation need be conducted.

The modelling challenge in this test case is thus the correct prediction of the non-isotropic normal stress field caused by the normal straining.

5.2.1 Simulated Cases

Three cases were simulated in this work. One from Tucker and Reynolds (1968) and two from Gence and Mathieu (1979).

The case reproduced here from Tucker and Reynolds (1968) - to be denoted by T&R - is the "laterally distorting tunnel". In this, a quasi-isotropic turbulence first developed for 2ft, and was then subjected to a constant symmetric plane strain for 8ft. Following this the flow was allowed to recover for a further 4ft. As Tucker and Reynolds (1968) performed an experimental work, they had to design a duct which would provide such plane strain. The tunnel used is illustrated in Figure 5.37, where the coordinates of the walls in the x_2 and x_3 directions, x_{2_w} and x_{3_w} respectively, are given by $x_{2_w} = x_{2_{w_0}} e^{\frac{D}{U_1} x_1}$ and $x_{3_w} = x_{3_{w_0}} e^{-\frac{D}{U_1} x_1}$ respectively (where $x_{2_{w_0}}$ and $x_{3_{w_0}}$ are the wall coordinates at the location where the straining is started, D is the magnitude of the normal strain rate ($D = -\frac{\partial U_2}{\partial x_2} = \frac{\partial U_3}{\partial x_3}$) and U_1, the streamwise velocity, is constant) in order to provide a constant cross-sectional area and a zero strain in the flow direction, as originally suggested by Townsend (1954).

Gence and Mathieu (1979) used an 0.8m long elliptical distorting duct, formed in two parts so they could alter the straining applied along the second half of the duct. They converted the x_2 and x_3 geometry curves initially proposed by Townsend (1954) and used by Tucker and Reynolds (1968) into elliptical coordinates to ensure a homogeneous normal straining. The authors performed five different cases which can be differentiated by the normal strain applied for the second half of the duct. A general representation of the normal strain in their experiment can be given by:

$$\begin{aligned} \frac{dV}{dy} &= \begin{cases} -D & \text{if } x \leq 0.4m \\ -D\cos(2\alpha) & \text{if } x > 0.4 \end{cases} \\ \frac{dW}{dz} &= \begin{cases} D & \text{if } x \leq 0.4m \\ D\cos(2\alpha) & \text{if } x > 0.4 \end{cases} \end{aligned} \tag{5.5}$$

Gence and Mathieu (1979) performed their experiment for five different values of α: 0, $\frac{\pi}{8}$, $\frac{\pi}{4}$, $\frac{3\pi}{8}$ and $\frac{\pi}{2}$. One may notice that for the first half of the duct (up to 0.4m), they applied a pure plane strain. Here only two cases were reproduced: $\alpha = 0$ (referred to here as G&M0) and $\alpha = \frac{\pi}{2}$ (referred to here as G&M05). The former represents a constant pure plane strain while the latter represents two consecutive opposite in sign plane strains. These two cases were chosen because they represent the more extreme cases and thus any lag effects are expected to be strongest in these two cases.

The main features of the three cases are presented in Table 5.3.

Table 5.3: General features of the normally strained cases

Case	Author	U_1	$D = \frac{dW}{dz}$ (s^{-1})
T&R	Tucker and Reynolds (1968)	20 ft/s	4.45
G&M0	Gence and Mathieu (1979)	18.6 m/s	32.23
G&M05	Gence and Mathieu (1979)	18.6 m/s	32.23 if $x < 0.4m$ -32.23 if $x > 0.4m$

5.2.2 Simulations Setup

As mentioned before, in order to reproduce the cases described above, only the centreline of the flow, where the only non-zero velocity is the streamwise one, U_1, and the only non-zero strains are $dU_2/dx_2 = dV/dy$ and $dU_3/dx_3 = dW/dz$, was simulated since it is a homogeneous flow.

The simulation was run as a 1D steady flow and allowed to develop in the x direction. The inlet conditions were set as described in the respective original papers and can be seen in Table 5.5. As the work of Tucker and Reynolds (1968) and Gence and Mathieu (1979) are experimental, the inlet value of the turbulent eddy dissipation rate, ε, was not provided and had to be estimated for the simulations. The inlet value of ε was thus taken as $\varepsilon_0 = \frac{k_0^{3/2}}{\ell_0}$, ℓ_0

being the length scale at the starting point of the simulation which was set in order to provide the same initial decay rate of the turbulent kinetic energy, k, as in the experiments. As will be discussed later, this parameter does influence the results of these simulations and one can notice from Table 5.5 that each model needed a different value of ℓ_0 in order to provide the correct decay of k reported in the experiments (see Figures 5.39, 5.44 and 5.46).

Table 5.4: Geometry and mesh of the normally strained cases

Case	Length	Grid 1 (X points)	Grid 2 (X points)
T&R	14 ft	130	200
G&M0	0.8 m	80	150
G&M05	0.8 m	80	150

As a 1D flow in the streamwise direction, only the length and number of points in the x direction needed to be defined. These details can be found in Table 5.4. Results on the two grids showed that those on the coarser one were grid independent, and so this was used for the results shown below.

One can notice from Tables 5.5 and 5.4 that the grids and inlet conditions of cases G&M0 and G&M05 are the same. In fact, the first half of the simulation (until x=0.4m) is the same for both cases. They differ from each other only in the second half, where the sign of the normal strains are changed in the G&M05 case.

Table 5.5: Inlet conditions for the normally strained cases

Case	k_0	$\overline{uu}_0$	$\overline{vv}_0$	$\overline{ww}_0$	ℓ_0	Model
T&R	0.908 ft^2/s^2	0.728 ft^2/s^2	0.552 ft^2/s^2	0.536 ft^2/s^2	0.050 ft	all STS and WM
					0.055 ft	KC,NG and TS
					0.060 ft	CG
G&M0	0.215 m^2/s^2	0.092 m^2/s^2	0.174 m^2/s^2	0.164 m^2/s^2	0.0115 m	NG
					0.0140 m	FM,HR
					0.0145 m	CG,KS
					0.0150 m	KC
					0.0165 m	SG
					0.0170 m	TS
					0.0175 m	LS
					0.0180 m	GL
					0.0200 m	HJ,TC,WM
G&M05	0.215 m^2/s^2	0.092 m^2/s^2	0.174 m^2/s^2	0.164 m^2/s^2	same as in G&M0 above	

5.2.3 Results and Discussion

Before evaluating the performance of the turbulence models, one may make an observation about the production of the turbulent kinetic energy P_k in eddy viscosity models. Such analysis has been used in the past, specially to evaluate the performance of LEV models in impinging jet flows (Craft et al., 1993).

In these 1-D contraction/expansion flows, where the only non-zero velocity component is U and the only non-zero strains are $\frac{\partial V}{\partial y}$ and $\frac{\partial W}{\partial z}$, P_k, given by $-\overline{u_i u_j}\frac{\partial U_i}{\partial x_j}$, becomes:

$$P_k = -\overline{v^2}\frac{\partial V}{\partial y} - \overline{w^2}\frac{\partial W}{\partial z} = \overline{v^2}\frac{\partial W}{\partial z} - \overline{w^2}\frac{\partial W}{\partial z} = (\overline{v^2} - \overline{w^2})\frac{\partial W}{\partial z} \tag{5.6}$$

One may notice from the above that depending on the values of $\overline{v^2}$ and $\overline{w^2}$, P_k can assume either positive or negative values. Besides, a sudden change in sign of the straining will change the sign of P_k for a while, since it will take the stresses some time to respond to the new straining.

In linear eddy viscosity turbulence models, where the Reynolds stresses are given by $\overline{u_i u_j} = -\nu_t\left(\frac{\partial U_i}{\partial x_j} + \frac{\partial U_j}{\partial x_i}\right) + \frac{2}{3}k\delta_{ij}$, the only non-zero Reynolds stresses used to calculate P_k are $\overline{v^2}$ and $\overline{w^2}$, given by $\overline{v^2} = -2\nu_t\frac{\partial V}{\partial y} + \frac{2}{3}k$ and $\overline{w^2} = -2\nu_t\frac{\partial W}{\partial z} + \frac{2}{3}k$. From the continuity equation, one knows that $\frac{\partial V}{\partial y} = -\frac{\partial W}{\partial z}$, thus the normal Reynolds stress $\overline{v^2}$ can be written as $\overline{v^2} = 2\nu_t\frac{\partial W}{\partial z} + \frac{2}{3}k$ and $P_k = -\overline{u_i u_j}\frac{\partial U_i}{\partial x_j}$ becomes:

$$P_k = (\overline{v^2} - \overline{w^2})\frac{\partial W}{\partial z} = (+2\nu_t\frac{\partial W}{\partial z} + \frac{2}{3}k + 2\nu_t\frac{\partial W}{\partial z} - \frac{2}{3}k)\frac{\partial W}{\partial z} = 4\nu_t\left(\frac{\partial W}{\partial z}\right)^2 \tag{5.7}$$

The above result indicates that the LEV models would always predict P_k as positive in these normally strained flows, which is not a general physical constraint, and, moreover, it shows the insensitivity of these models in predicting P_k when the normal strains have their sign suddenly changed which is an effect of these models not generally representing accurately the normal stresses. From equations 5.7 one can then infer that LEV models are not recommended for flows where there is change in sign of the normal strains, since they will provide wrong relevant results due to its formulation.

One can also evaluate P_k in NLEV models. Taking the general expression for the Reynolds stresses used in equation 3.21, in normally strained flows such as that considered above, one has $S_{22} = 2\frac{\partial V}{\partial y}$ and $S_{33} = 2\frac{\partial W}{\partial z} = -2\frac{\partial V}{\partial y} = -S_{22}$. So, the expressions for $\overline{v^2}$ and $\overline{w^2}$ become:

$$\begin{aligned}
\overline{v^2} &= \frac{2}{3}k - \nu_t S_{22} + \frac{c_1\nu_t}{3}\frac{k}{\varepsilon}(2S_{22}^2 - S_{33}^2) + c_6\nu_t\frac{k^2}{\varepsilon^2}S_{22}(S_{22}^2 + S_{33}^2) = \frac{2}{3}k + \nu_t S_{33} + \frac{c_1\nu_t}{3}\frac{k}{\varepsilon}S_{33}^2 - 2c_6\nu_t\frac{k^2}{\varepsilon^2}S_{33}^3 \\
\overline{w^2} &= \frac{2}{3}k - \nu_t S_{33} + \frac{c_1\nu_t}{3}\frac{k}{\varepsilon}(2S_{33}^2 - S_{22}^2) + c_6\nu_t\frac{k^2}{\varepsilon^2}S_{33}(S_{22}^2 + S_{33}^2) = \frac{2}{3}k - \nu_t S_{33} + \frac{c_1\nu_t}{3}\frac{k}{\varepsilon}S_{33}^2 + 2c_6\nu_t\frac{k^2}{\varepsilon^2}S_{33}^3
\end{aligned} \tag{5.8}$$

And now it becomes straightforward to calculate P_k:

$$P_k = (\overline{v^2} - \overline{w^2})\frac{\partial W}{\partial z} = \left(2\nu_t S_{33} - 4c_6\nu_t\frac{k^2}{\varepsilon^2}S_{33}^3\right)\frac{\partial W}{\partial z} = 4\nu_t\left(\frac{\partial W}{\partial z}\right)^2 - 32c_6\nu_t\frac{k^2}{\varepsilon^2}\left(\frac{\partial W}{\partial z}\right)^4 \tag{5.9}$$

Again, one can notice that P_k is insensitive to changes in the sign of the straining. It can be

then concluded that, in normally strained flows, models which calculate the Reynolds stresses through algebraic expressions based on the eddy-viscosity concept will always be insensitive to changes in sign of the straining and therefore not recommended for such flows.

It is also worth comparing the dimensionless straining history in the three cases, because, as it will be seen later, this appear to have an impact on the performance of the models. The parameter $\eta = \frac{k}{\varepsilon}\left|\frac{dV}{dy}\right|$ was then chosen to be plotted against a dimensionless streamwise distance defined as $x^* = \frac{x}{U}D$. Although there is no experimental data for η, the qualitative behaviour predicted by the different models is similar, and so Figure 5.38 shows the predicted development of η from the GL model which performed overall generally better than the other models. By observing Figure 5.38 one may say that the T&R case provides a steeper change in η than the other two cases of Gence and Mathieu (1979). Besides that, one may also note that the T&R case was strained over a longer dimensionless streamwise distance than the pure strained case G&M0. The kink in the profile of η in the G&M05 case is due to the change of sign of the normal straining.

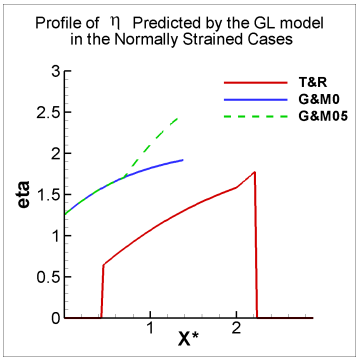

Figure 5.38: Profiles of η predicted by the GL model for the normally strained cases

The T&R case will be the first to be evaluated. The prediction of the turbulent kinetic energy can be seen in Figure 5.39. The KS, the GL and the SG models performed best in predicting this quantity, since they were the only models able to reach the peak of the turbulent kinetic energy immediately before the straining was interrupted at $x = 10ft$. For the same reason, the KS model performed best in predicting $\overline{u^2}$ in Figure 5.40. Most models tended to provide a too fast decay of the turbulent kinetic energy after the interruption of the straining. The Reynolds normal stress $\overline{v^2}$, in Figure 5.41, was best predicted by the GL and SG models and the latter best predicted the Reynolds normal stress $\overline{w^2}$ in Figure 5.42, although $\overline{w^2}$ tends to increase after the interruption of the straining whilst all turbulence models predicted that this Reynolds stress decreased when the straining is stopped.

It is worth noticing that the performance of the NLEV model KS was not so satisfactory in predicting the normal stresses $\overline{v^2}$ and $\overline{w^2}$ after the interruption of the straining and provided similar behaviour to that of the LEV models. The reason for that can be seen in equation 5.8, since when the straining is set to zero, the NLEV model reduces to a LEV model, predicting isotropy of the stresses just as the LEV models. As a consequence, the eddy viscosity models

show clearly where the straining started and stopped. The RST models produce a smoother development of the Reynolds stresses at both the start and end of the strained section, as a result of these models solving a transport equation for each Reynolds stress component.

Figure 5.43 shows the three non-zero components of the stress anisotropy tensor $b_{ij} = \frac{\overline{u_i u_j}}{q} - \frac{1}{3}\delta_{ij}$. Since the EV models are not expected to provide good results for the stress anisotropy, the figure shows results from the RST models only. One may notice that the STS RST models predicted the b_{33} component better than the other two although the b_{11} component is indeed less important in this case, since $\overline{u^2}$ is not used in the production term, and one can notice its lower order of magnitude. On the other hand, the WM model predicted the three normal components of the stress anisotropy tensor well until before the straining stopped. However, in the recovery region, once straining was removed, none of the turbulence models could follow the experimental data.

Now switching to evaluate the G&M0 case, it is of value to note that this case is essentially the same as the T&R: a pure normally strained flow. However, in the latter the straining is activated only in a section of the duct while in the G&M0 case the straining is activated all along the duct. Besides, the evolution and range of the dimensionless shear parameter η, shown in Figure 5.38, is steeper in the T&R case.

The prediction of the turbulent kinetic energy, presented in Figure 5.44, shows that the RST models performed best as a whole, the GL and TC models performing best. The same can be said about the prediction of the Reynolds normal stresses $\overline{u^2}$, $\overline{v^2}$ and $\overline{w^2}$, in Figure 5.45, where it can be noted that the non-linear-eddy-viscosity scheme is not able to correctly predict the initial magnitudes of the stresses which affects its whole subsequent performance. That is due to the stresses being calculated through algebraic expressions thus an inherent limitation of the EV models. The prediction of the linear-eddy-viscosity models are not shown, since they are not expected to predict correctly these quantities.

One may notice from the results presented in the T&R and G&M0 cases that the turbulence models were more capable of correctly reproducing the normally strained cases when the evolution of η was less steep, that is, in the G&M0 case.

Now moving on to the G&M05 case, it is worth recalling that, in this case, the eddy-viscosity models are expected to be insensitive to the change of sign in the normal strains. It is only worth then commenting on the performance of the RST models.

One may notice in Figure 5.46 the prediction of the turbulent kinetic energy. The RST models returned relatively similar predictions for the turbulent quantities, predicting a too fast return to the original configuration. The Reynolds normal stresses, presented in Figure 5.47 were perhaps best predicted by the HJ model, however all RST models provided reasonable results, except the SG model which tended to overpredict these quantities.

5.2.4 Concluding Remarks

These normally strained flows highlight one inherent limitation of the eddy-viscosity schemes, since they do not return correct normal stress values, and hence also predict P_k and k incorrectly. On the other hand, all RST models tested perfomed reasonably well, including the MTS WM model.

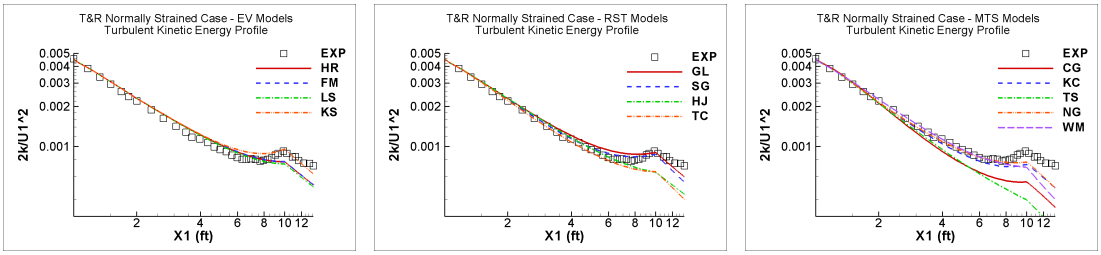

(a) (b) (c)

Figure 5.39: Profile of the turbulent kinetic energy in T&R normally strained case predicted by the: (a) eddy-viscosity models, (b) Reynolds stress transport models and (c) multiple-time-scale models and compared with the experiments of Tucker and Reynolds (1968). Models as in Table 3.25.

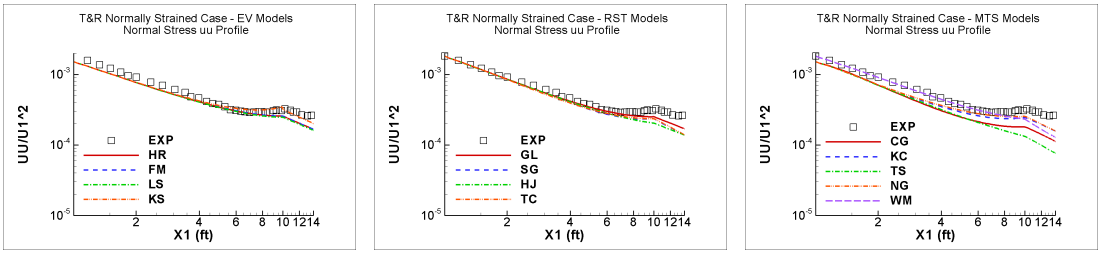

(a) (b) (c)

Figure 5.40: Profile of the Reynolds normal stress $\overline{u^2}$ in T&R normally strained case predicted by the: (a) eddy-viscosity models, (b) Reynolds stress transport models and (c) multiple-time-scale models and compared with the experiments of Tucker and Reynolds (1968). Models as in Table 3.25.

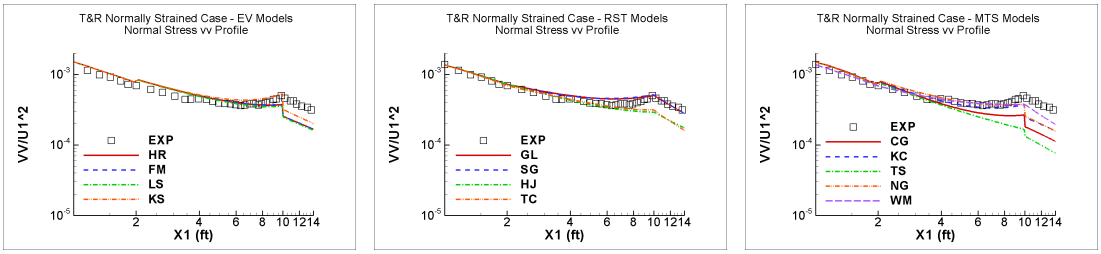

(a) (b) (c)

Figure 5.41: Profile of the Reynolds normal stress $\overline{v^2}$ in T&R normally strained case predicted by the: (a) eddy-viscosity models, (b) Reynolds stress transport models and (c) multiple-time-scale models and compared with the experiments of Tucker and Reynolds (1968). Models as in Table 3.25.

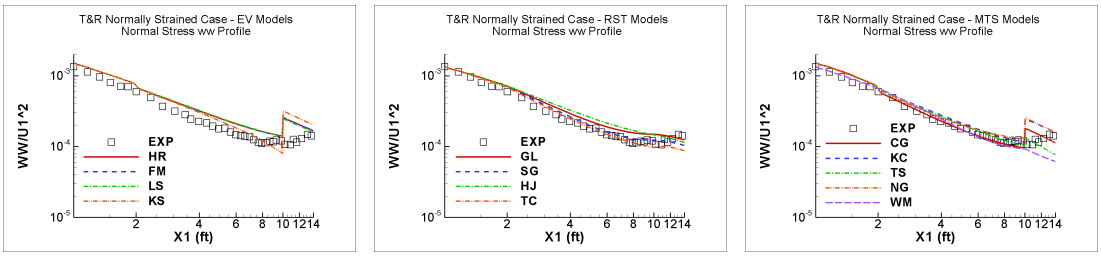

(a) (b) (c)

Figure 5.42: Profile of the Reynolds normal stress $\overline{w^2}$ in T&R normally strained case predicted by the: (a) eddy-viscosity models, (b) Reynolds stress transport models and (c) multiple-time-scale models and compared with the experiments of Tucker and Reynolds (1968). Models as in Table 3.25.

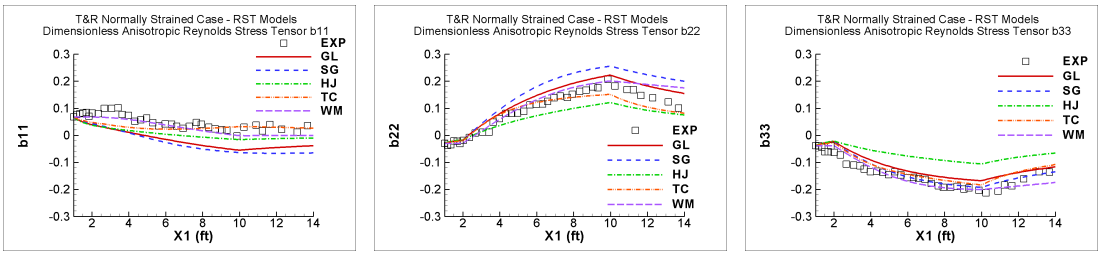

(a) (b) (c)

Figure 5.43: Profile of the normal components of the dimensionless Reynolds stress anisotropy tensor in T&R normally strained case predicted by the Reynolds stress transport models and compared with the experiments of Tucker and Reynolds (1968). Models as in Table 3.25.

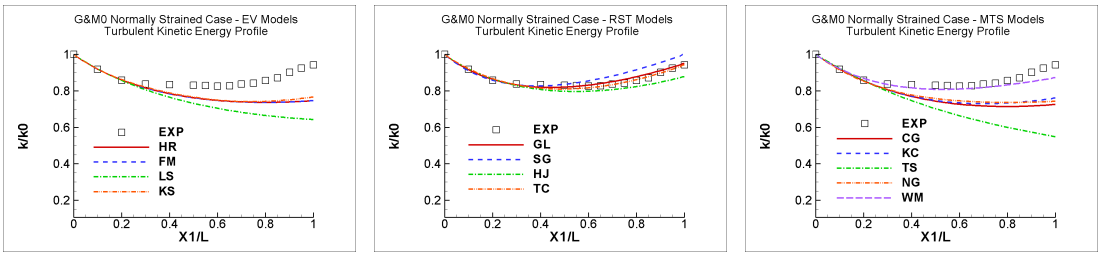

(a) (b) (c)

Figure 5.44: Profile of the turbulent kinetic energy in the G&M0 normally strained case predicted by the: (a) eddy-viscosity models, (b) Reynolds stress transport models and (c) multiple-time-scale models and compared with the experiments of Gence and Mathieu (1979). Models as in Table 3.25.

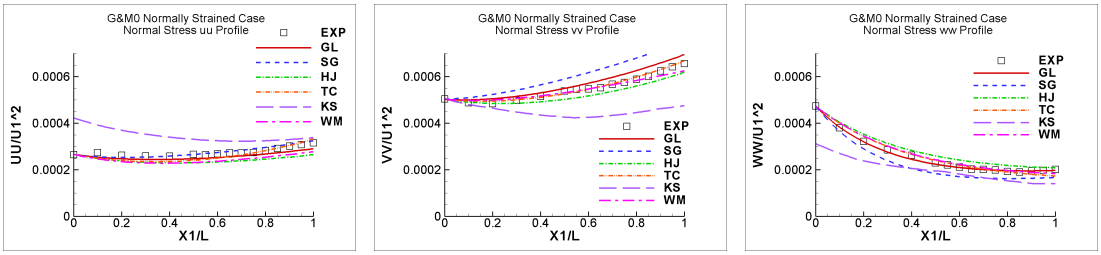

(a) $\overline{u^2}$ (b) $\overline{v^2}$ (c) $\overline{w^2}$

Figure 5.45: Profile of the Reynolds normal stresses in the G&M0 normally strained case predicted by the non-linear-eddy-viscosity and Reynolds stress transport models and compared with the experiments of Gence and Mathieu (1979). Models as in Table 3.25.

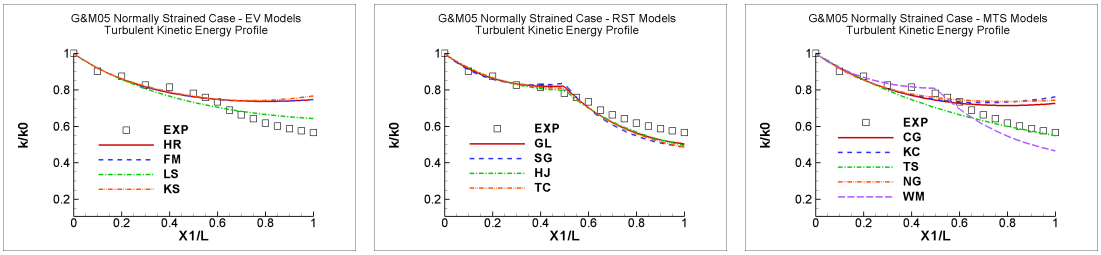

(a) (b) (c)

Figure 5.46: Profile of the turbulent kinetic energy in the G&M05 normally strained case predicted by the: (a) eddy-viscosity models, (b) Reynolds stress transport models and (c) multiple-time-scale models and compared with the experiments of Gence and Mathieu (1979). Models as in Table 3.25.

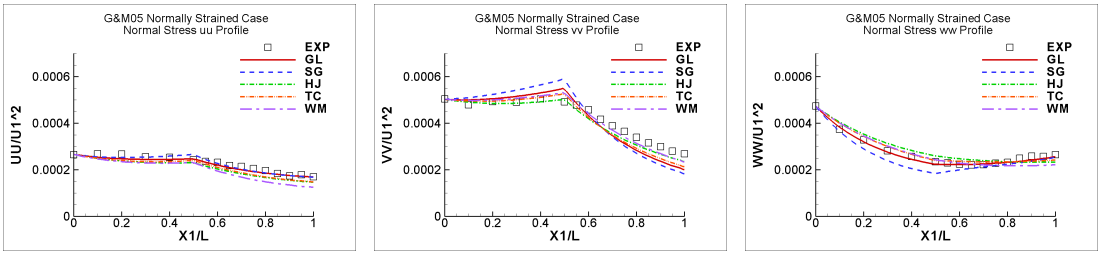

(a) $\overline{u^2}$ (b) $\overline{v^2}$ (c) $\overline{w^2}$

Figure 5.47: Profile of the Reynolds normal stresses in the G&M05 normally strained case predicted by the non-linear-eddy-viscosity and Reynolds stress transport models and compared with the experiments of Gence and Mathieu (1979). Models as in Table 3.25.

5.3 Fully Developed Channel Flow

Although the above flows have not involved any wall influences, a number of non-equilibrium flows to be considered below are wall-bounded, and thus the models' ability to account for the presence of a wall, as well as non-equilibrium effects, needs to be considered. As a prelude to these, two equilibrium wall-bounded flows are considered, namely fully developed plane channel flow and a zero pressure gradient boundary layer in order to first assess the models' performance in relatively simple wall-bounded flows without significant non-equilibrium effects.

A 2D fully developed channel flow is one of the simplest flows to be simulated. It consists of two parallel walls, one at the bottom and other at the top, both large enough to enable the system be considered 2D, between which a Newtonian incompressible fluid flows with a developed profile and constant pressure gradient which means it does not vary with time or the streamwise direction. This implies a steady flow where the streamwise velocity depends only upon the normal distance to the wall, $U = U(y)$. If the flow is laminar, the velocity profile is a parabola, the velocity being maximum at the half distance to the walls and zero at them. The more turbulent the flow, the flatter its velocity profile as shown in Figure 5.48.

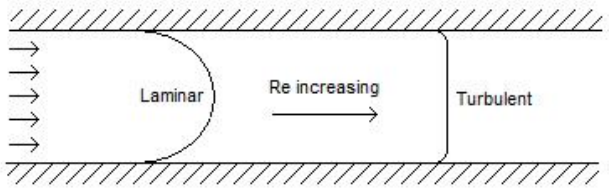

Figure 5.48: Velocity profile in fully developed channel flow

When simulating a fully developed channel flow, one wishes to reproduce the symmetry of the problem, besides, of course, to predict the correct velocity profile as well as the turbulent quantities.

5.3.1 Simulated Cases

The fully developed channel flow cases simulated in this work reproduce DNS results for four different Reynolds numbers based on the centreline velocity. Two test cases were taken from the ERCOFTAC database available at *http://cfd.mace.manchester.ac.uk/ercoftac/* namely the DNS of Kim et al. (1987) and the other two test cases carried out by Abe et al. (2004) were taken from the Kawamura Lab whose DNS database is available at *http://murasun.me.noda.tus.ac.jp/turbulence/index.html*. Table 5.6 provides each case specifications, where the Reynolds number based on the centreline velocity U_c and channel height h is $Re = \frac{hU_c\rho}{\mu}$ and that based on friction velocity is given by $Re_\tau = \frac{(h/2)u_\tau\rho}{\mu}$.

Table 5.6: Fully developed channel flow cases simulated

Author	Re	Re_τ
Kim et al. (1987)	6500	180
Kim et al. (1987)	15780	395
Abe et al. (2004)	24428	640
Abe et al. (2004)	41441	1020

5.3.2 Simulations Setup

As already mentioned in Chapter 4, the STREAM code can work with dimensionless variables where the Reynolds number is defined through the reference variables and then the viscosity assumes the value of $\frac{1}{Re}$. This way, the reference velocity, channel height and fluid density were set as 1, and the viscosity taken as $\mu = \frac{1}{Re}$ with the Reynolds number varying from case to case according to Table 5.6.

A simple rectangular domain was employed with no-slip walls at the top and bottom boundaries, which means the velocity as well as turbulent kinetic energy and Reynolds stresses are zero at them. In order to avoid a very long domain, necessary for the flow to become fully developed, a short domain length of one channel height was used, with periodic boundary conditions applied between the inlet (west) and outlet (east) faces and applying a bulk correction by scaling the velocity profile in the west face to give the desired mass flow rate. The value of the pressure at the inlet and outlet face nodes was set by linear extrapolation of the two following and two previous nodes, respectively.

The calculations were initialised with uniform values of most variables

$$
\begin{aligned}
&U_{initial} = 1.0 \\
&k_{initial} = \frac{3}{2}(IU_{initial})^2 \\
&\overline{u^2} = k_{initial} \qquad \overline{v^2} = 0.4k_{initial} \qquad \overline{w^2} = 0.6k_{initial} \qquad \overline{uv} = -\mu_t \frac{\partial U_{initial}}{\partial y} = 0.0
\end{aligned} \tag{5.10}
$$

where $I = \frac{\sqrt{2/3k}}{U}$ is the turbulence intensity which was set to 6%. One may notice that anisotropic values were provided for the Reynolds normal stresses. The value of ε was estimated through Norris and Reynolds's 1975 one equation model which thus does not give a uniform profile since it varies in terms of the distance to the wall.

When using MTS models, instead of initializing k and ε, one should provide initial values for k_P, k_T, ε_P and ε_T. The same initial conditions presented in equation 5.10 were kept by setting $\varepsilon_P = \varepsilon_T$ and by assuming a ratio $\frac{k_P}{k_T} = 2$.

Since low and high Reynolds number turbulence models are applied, two different meshes were designed. For low-Reynolds-number turbulence models, the mesh should be refined at the wall, providing $y^+ < 1$ at the first node, while for the high Reynolds number ones, it

should be coarse in this region, providing $y^+ \approx 30$ at the first node. Both grids were designed as 20x60, but with different distances from the first node to the wall, achieved by altering the grid expansion ratio. A test for grid independence was performed with a finer grid of 30x90 for each turbulence model, and no significant differences in the predictions were observed.

5.3.3 Results and Discussion

The results are presented in Figures 5.49 to 5.56 for the case with $Re = 6500$, 5.57 to 5.58 for the case with $Re = 15780$, 5.59 to 5.60 for the case with $Re = 24428$ and 5.61 to 5.62 for the case with $Re = 41441$.

Analysing the results for the channel flow with $Re = 6500$, one can notice that, overall, the turbulence models were able to predict to an acceptable level the log law ($U^+ = 2.44 \ln y^+ + 5$) in Figure 5.49. It is also of value to call attention to the fact that the DNS data lies slightly above the log-law at this low Reynolds number and so does the LS model. On the other hand, the HJ model underpredicted it a bit. At this low Reynolds number the effect of using a wall-function can be clearly seen in the high-Reynolds-number model results, since the near-wall node has to be placed at a rather large distance from the wall to ensure a reasonably large y^+ value here. The turbulence models which perhaps best predicted the DNS mean velocity profile were the FM, KS, TC, NG and WM models, all LRN forms as expected. The same analysis can be extended to the velocity profile plotted against $\frac{y}{H}$, Figure 5.50, where the symmetry of the flow can be seen.

With regard to the Reynolds shear stress $\overline{uv}$, Figure 5.51, one can notice that all models correctly predict it far from the wall, presenting a linear profile which confirms the fully developed state. The LRN models slightly overpredict the peak shear stress, whereas the HRN models cannot capture it, since the near-wall node in such low Reynolds number channel flows is typically beyond the $\overline{uv}$ peak, as noted above, so that y^+ can be reasonably large. The turbulence models which perhaps best predicted the Reynolds shear stress, including the near-wall region, were the LS, KS, NG and WM models.

The profile of ε, Figure 5.52, was well predicted in the region far from the wall by all models which were not applied with a wall function. The turbulence models which were used with wall functions only gave good agreement very far from the wall, near the centreline, which is not a great feature since the value of ε in this region is relatively low. None of the turbulence models were capable of correctly predicting the peak of the eddy dissipation rate at the wall, however the NG model provided the closest prediction. The LS and KS models, which solve a transport equation for $\tilde{\varepsilon}$, underpredicted the value of ε at the wall which means the turbulent kinetic energy gradient at the wall was underpredicted, since the exact expression used to account for the value of ε at the wall when $\tilde{\varepsilon} = 0$ is $2\mu\left(\frac{\partial\sqrt{k}}{\partial x_j}\right)^2$. The TC model was able to avoid this drawback.

The turbulence models as a whole captured the turbulent kinetic energy profile, Figure 5.53, to an acceptable level in the region far from the wall. The near-wall peak was best predicted by the RST model HJ and the MTS model NG, both LRN formulations. The

turbulent kinetic energy results are plotted using the same scales as the normal Reynolds stresses in Figures 5.54 to 5.56 so that one can easily compare their magnitude. Although the LEV models are not expected to provide the correct prediction of the latter, since they erroneously predict isotropy for the Reynolds normal stresses, their performance will also be presented for sake of comparison.

Regarding the Reynolds normal stress $\overline{u^2}$, Figure 5.54, this was underpredicted near the wall by all models, but correctly predicted in the bulk region by the RST models and the cubic NLEV (KS) model. $\overline{v^2}$, Figure 5.55, was overpredicted by all eddy viscosity models (since the DNS data show it to be less than $\frac{2}{3}k$), while the RST models were able to reproduce the bulk part of the flow in a more acceptable way. $\overline{w^2}$, Figure 5.56, was slightly overpredicted by all turbulence models. The SG model may be considered the one which best predicted the outer flow region and it is valid to mention that the HJ model was the one which best predicted the $\overline{u^2}$ peak near the wall.

The overall comments above on the case with the lowest Reynolds number can be generally extended to the other cases with higher Reynolds numbers, however some observations must be made. All the "problems" relative to the near-wall region tend to become less evident as the Reynolds number of the flow increases, as can be seen in Figures 5.57 to 5.62 where profiles of the velocity and turbulent kinetic energy are shown for the other three Reynolds number cases. This is due to the fact that the higher the Reynolds number, the thinner the viscous sublayer where most of the models fail to give good predictions. The log law profile (Figures 5.57, 5.59 and 5.61) as well as the turbulent kinetic energy (Figures 5.58, 5.60 and 5.62) tend to be better predicted as the Reynolds number increases.

Comparing the obtained predictions with the turbulence models' original papers, whenever possible, one may say that all models performed as expected, except for the HJ model which was expected to better predict the Reynolds normal stresses, especially near the wall, as well as match perfectly the log law. The result obtained here is consistent with the results obtained in this work for the boundary layer flow cases (which will be shown later in this Chapter) which perhaps indicates that there might have been some calibration of the damping functions which were not presented in Hanjalic et al.'s 1997 article and thus not implemented in the STREAM code.

As a whole, one can say that all models performed reasonably well, as expected, since this is a very simple and basic flow. It is difficult to discern the best model, however only the NLEV and RST models are able to correctly predict the Reynolds normal stresses. The use of a standard wall-function can somewhat degrade the predictions even in such a simple flow, especially at lower Reynolds numbers.

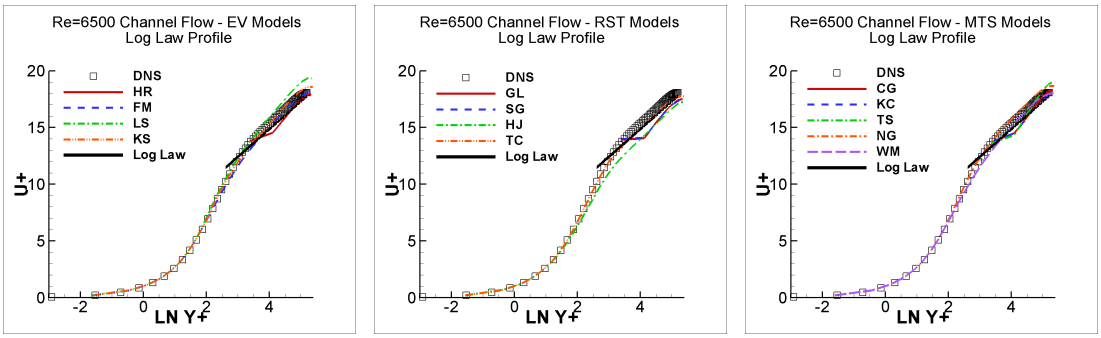

(a) (b) (c)

Figure 5.49: Prediction of the log law profile for the fully developed channel flow with Re=6500 by the: (a) eddy-viscosity models, (b) Reynolds stress transport models and (c) multiple-time-scale models. Models as in Table 3.25.

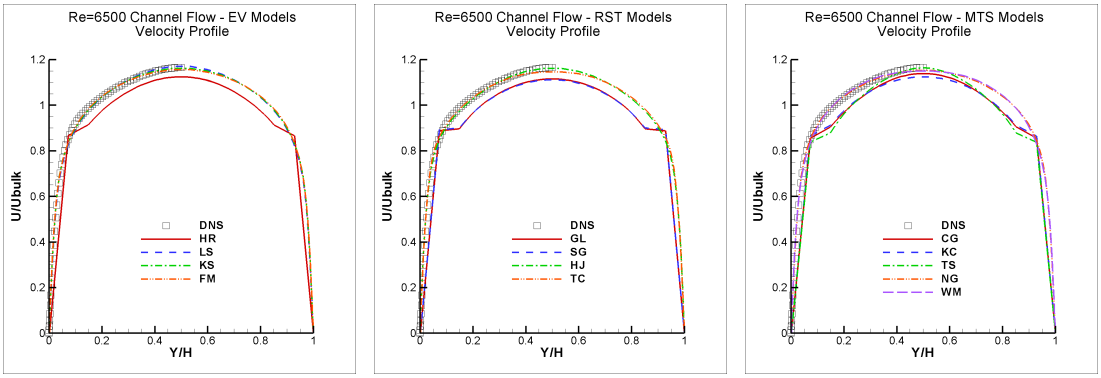

(a) (b) (c)

Figure 5.50: Prediction of the velocity profile for the fully developed channel flow with Re=6500 by the: (a) eddy-viscosity models, (b) Reynolds stress transport models and (c) multiple-time-scale models. Models as in Table 3.25.

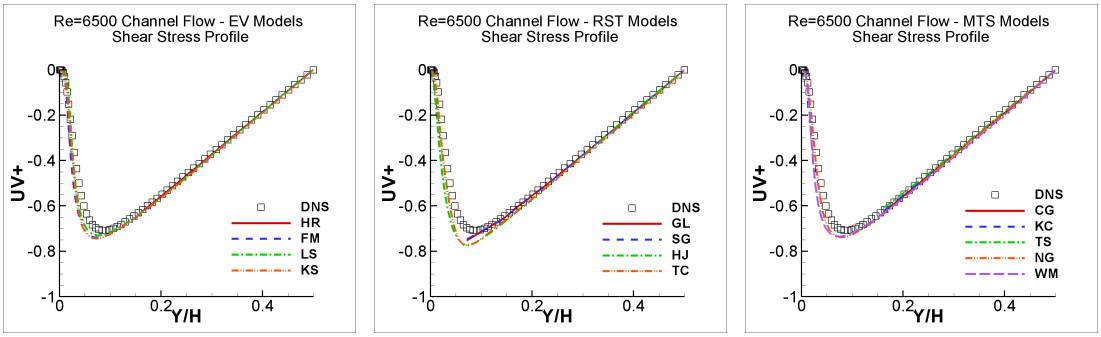

(a) (b) (c)

Figure 5.51: Prediction of the Reynolds shear stress $\overline{uv}$ for the fully developed channel flow with Re=6500 by the: (a) eddy-viscosity models, (b) Reynolds stress transport models and (c) multiple-time-scale models. Models as in Table 3.25.

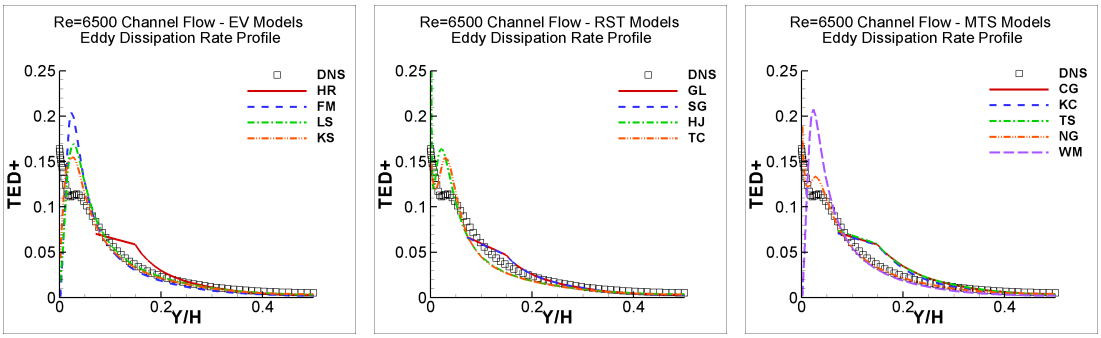

(a) (b) (c)

Figure 5.52: Prediction of the turbulent kinetic energy dissipation rate ε for the fully developed channel flow with Re=6500 by the: (a) eddy-viscosity models, (b) Reynolds stress transport models and (c) multiple-time-scale models. Models as in Table 3.25.

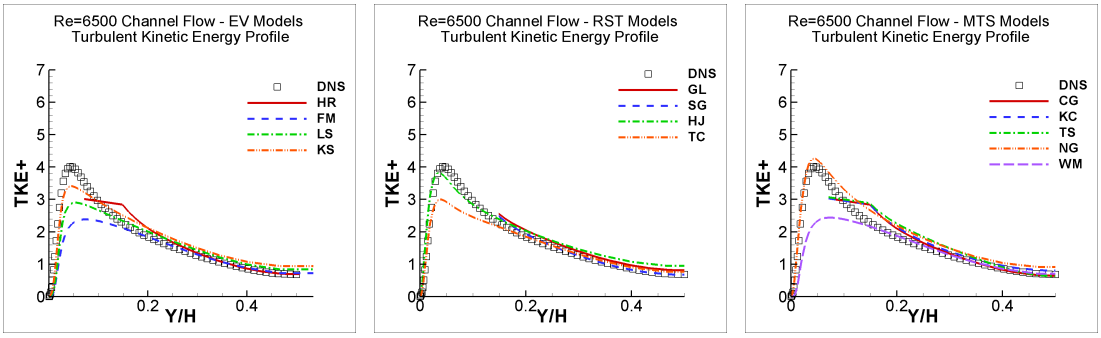

(a) (b) (c)

Figure 5.53: Prediction of the turbulent kinetic energy k for the fully developed channel flow with Re=6500 by the: (a) eddy-viscosity models, (b) Reynolds stress transport models and (c) multiple-time-scale models. Models as in Table 3.25.

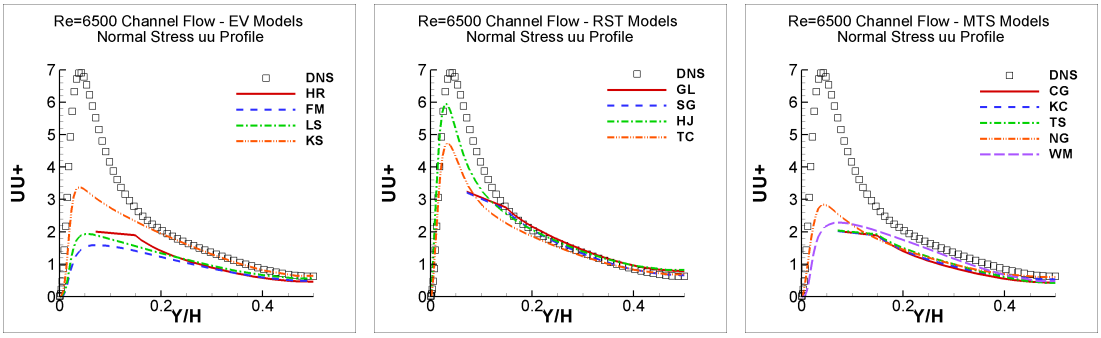

(a) (b) (c)

Figure 5.54: Prediction of the Reynolds normal stress $\overline{u^2}$ for the fully developed channel flow with Re=6500 by the: (a) eddy-viscosity models, (b) Reynolds stress transport models and (c) multiple-time-scale models. Models as in Table 3.25.

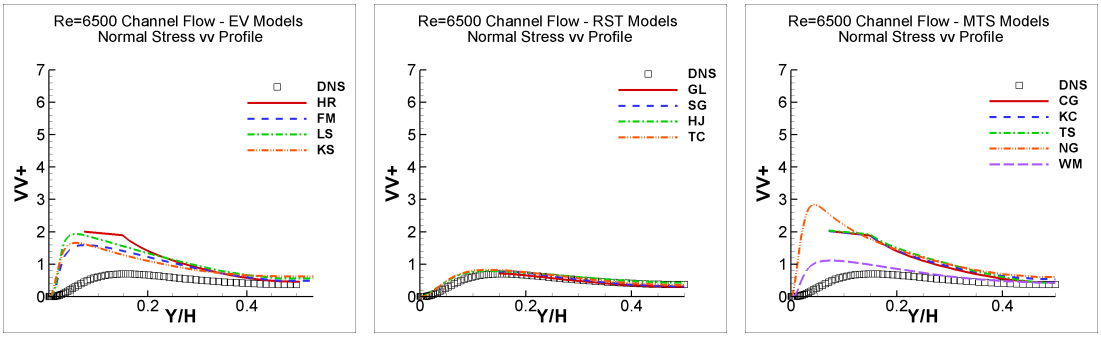

(a) (b) (c)

Figure 5.55: Prediction of the Reynolds normal stress $\overline{v}^2$ for the fully developed channel flow with Re=6500 by the: (a) eddy-viscosity models, (b) Reynolds stress transport models and (c) multiple-time-scale models. Models as in Table 3.25.

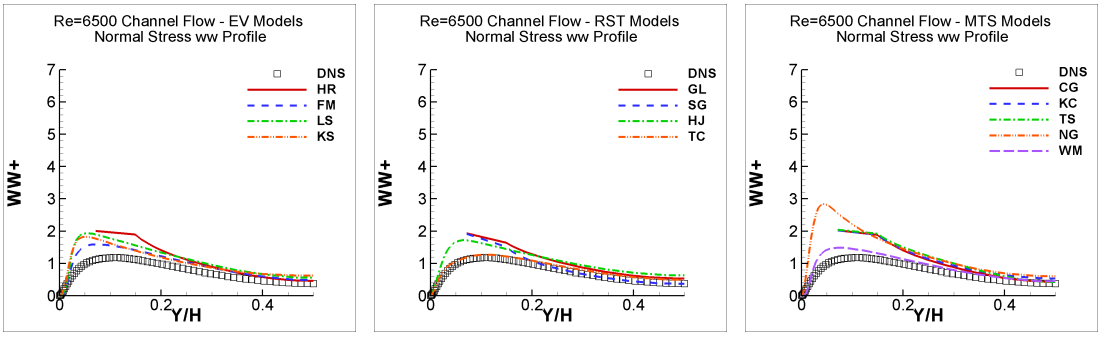

(a) (b) (c)

Figure 5.56: Prediction of the Reynolds normal stress $\overline{w^2}$ for the fully developed channel flow with Re=6500 by the: (a) eddy-viscosity models, (b) Reynolds stress transport models and (c) multiple-time-scale models. Models as in Table 3.25.

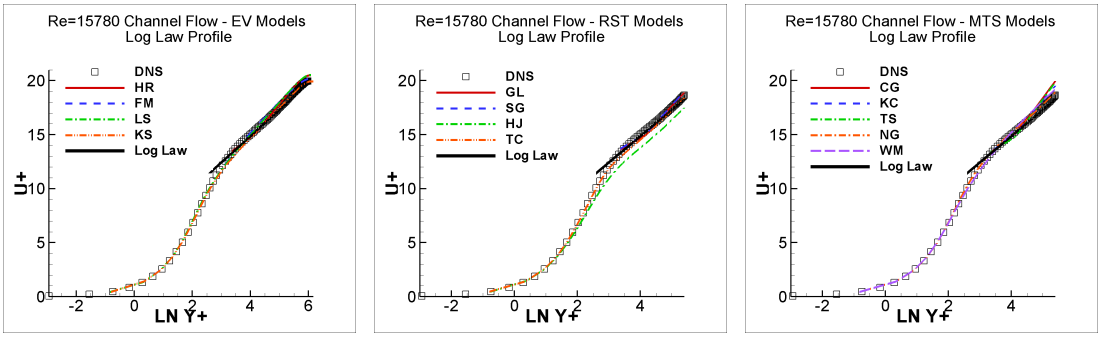

(a) (b) (c)

Figure 5.57: Prediction of the log law profile for the fully developed channel flow with Re=15780 by the: (a) eddy-viscosity models, (b) Reynolds stress transport models and (c) multiple-time-scale models. Models as in Table 3.25.

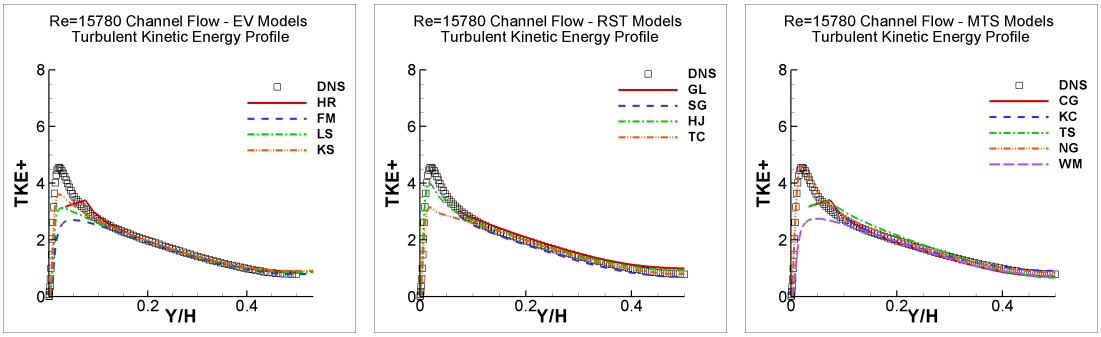

(a) (b) (c)

Figure 5.58: Prediction of the turbulent kinetic energy for the fully developed channel flow with Re=15780 by the: (a) eddy-viscosity models, (b) Reynolds stress transport models and (c) multiple-time-scale models. Models as in Table 3.25.

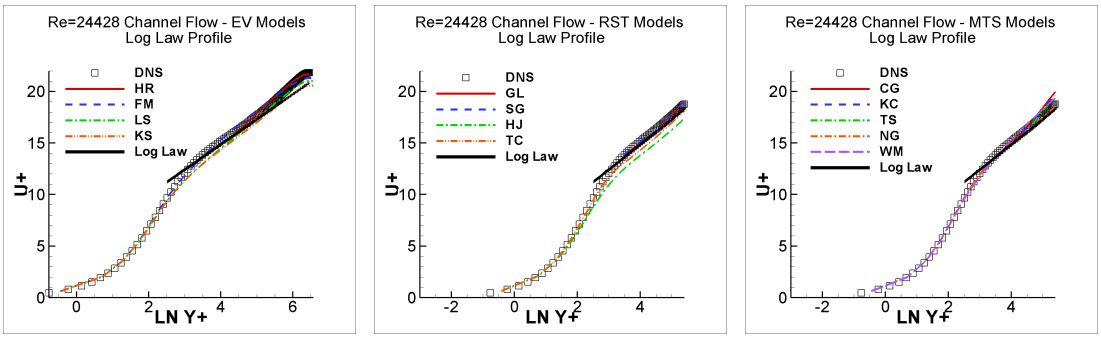

(a) (b) (c)

Figure 5.59: Prediction of the log law profile for the fully developed channel flow with Re=24428 by the: (a) eddy-viscosity models, (b) Reynolds stress transport models and (c) multiple-time-scale models. Models as in Table 3.25.

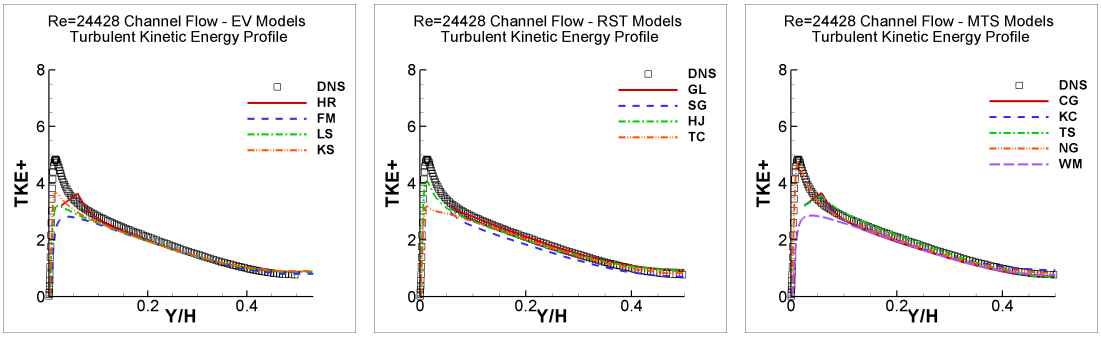

(a) (b) (c)

Figure 5.60: Prediction of the turbulent kinetic energy for the fully developed channel flow with Re=24428 by the: (a) eddy-viscosity models, (b) Reynolds stress transport models and (c) multiple-time-scale models. Models as in Table 3.25.

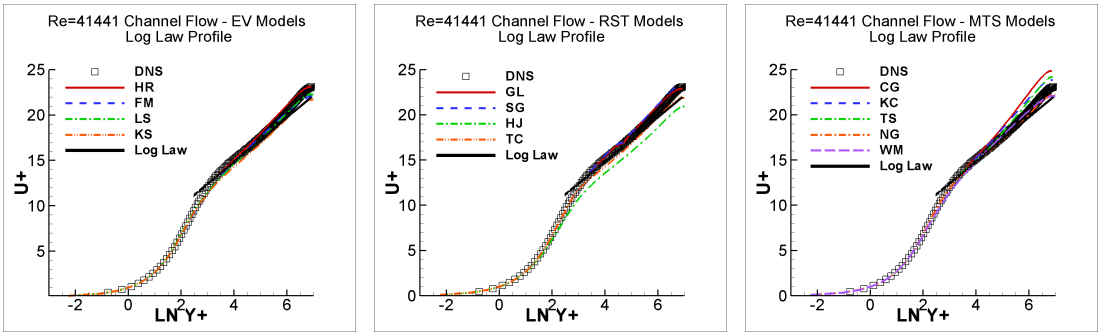

(a) (b) (c)

Figure 5.61: Prediction of the log law profile for the fully developed channel flow with Re=41441 by the: (a) eddy-viscosity models, (b) Reynolds stress transport models and (c) multiple-time-scale models. Models as in Table 3.25.

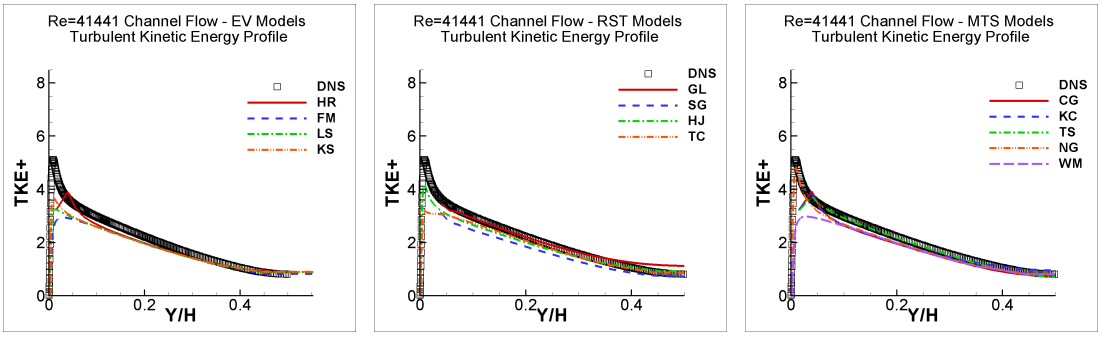

(a) (b) (c)

Figure 5.62: Prediction of the turbulent kinetic energy for the fully developed channel flow with Re=41441 by the: (a) eddy-viscosity models, (b) Reynolds stress transport models and (c) multiple-time-scale models. Models as in Table 3.25.

5.4 Zero Pressure Gradient Boundary Layer

The flow which will be considered in this section is a turbulent 2D zero pressure gradient boundary layer flow which is illustrated in Figure 5.63. The flow consists of a free stream approaching a flat plate with a uniform velocity profile of U_∞ without any imposed pressure gradient. At the moment the stream reaches the flat plate, a boundary layer starts to develop since the velocity at the plate is zero due to the no-slip condition. At the beginning of the plate the boundary layer is laminar. Further downstream it passes through the transition process and then becomes turbulent, leading to a profile illustrated in Figure 5.63. It is this turbulent region which will be considered in this work, in order to assess the performance of turbulence models in predicting it.

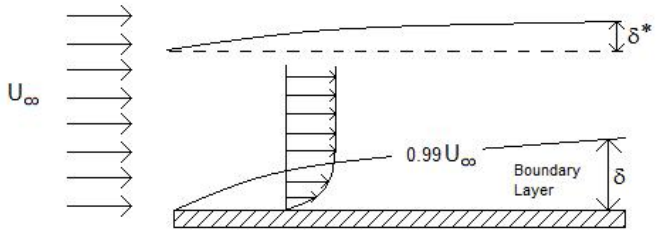

Figure 5.63: Zero pressure gradient boundary layer scheme

One may notice some similarity between the turbulent zero pressure gradient boundary layer flow and the fully developed channel flow, however there are two main differences. The first is physical, which is the fact that the boundary layer flow is an open flow, not bounded at the top as is the channel flow. The second difference lies in the fact that the channel flow is fully developed and so its velocity profile only depends on the normal distance to the wall. The turbulent boundary layer is a developing flow where the velocity profile varies as a function of the streamwise direction, hence $U = U(x, y)$. Needless to say, outside the boundary layer, where $U = U_\infty$, the streamwise velocity no longer varies in the streamwise direction.

When studying boundary layers it is common to define some parameters such as boundary layer thickness δ, the displacement thickness δ^*, the momentum thickness θ, the shape factor H and the skin-friction coefficient C_f.

The boundary layer thickness, as its name indicates, is the height of the boundary layer, which is a function of the streamwise distance x. It is defined as being the height where the velocity is 99% of the freestream velocity U_∞.

The displacement thickness represents the height an inviscid freestream would be shifted, which is equivalent to the loss of mass flow caused by the presence of the boundary layer. It is calculated through:

$$\delta^* = \int_0^\infty \left(1 - \frac{U(y)}{U_\infty}\right) \mathrm{d}y \tag{5.11}$$

The momentum thickness represents the height of the fluid layer with velocity U_∞ whose mass flux is equivalent to the momentum flux loss due to the presence of the boundary layer. It is calculated as:

$$\theta = \int_0^\infty \frac{U(y)}{U_\infty}\left(1 - \frac{U(y)}{U_\infty}\right) \mathrm{d}y \tag{5.12}$$

One may notice that the displacement and momentum thicknesses are integral parameters which means they need to be calculated through numerical integration in the y direction. When using a wall function these results need to be rather carefully interpreted, since the very near-wall velocity variation is not resolved.

The shape factor then arises as the ratio between the displacement thickness and the momentum thickness and is a dimensionless parameter which characterizes the flow. For turbulent zero pressure gradient boundary layers, one expects it to be about 1.4 (Mathieu and Scott, 2000). The shape factor H can thus be written as:

$$H = \frac{\delta^*}{\theta} \tag{5.13}$$

The skin-friction coefficient C_f is a measure of the drag imposed on the plate by the fluid. Therefore it is of high industrial importance. It is calculated through:

$$C_f = \frac{\tau_w}{0.5\rho U_\infty^2} \tag{5.14}$$

As the velocity profile in the turbulent boundary layer flow varies with both normal and streamwise directions, so do the other variables such as the turbulent kinetic energy, the eddy dissipation rate and the Reynolds stresses. Therefore, in order to compare profiles across the boundary layer, one should do so at a specific streamwise position. The streamwise position where the main variable profiles are evaluated is often defined through the dimensionless parameter Re_θ, which is the local Reynolds number expressed in terms of the momentum thickness θ and the freestream velocity U_∞:

$$Re_\theta = \frac{\theta U_\infty}{\nu} \tag{5.15}$$

Similarly, one may define a local Reynolds number as a function of the displacement thickness δ^*, which is then termed Re_δ^* and defined as:

$$Re_{\delta^*} = \frac{\delta^* U_\infty}{\nu} \tag{5.16}$$

This completes the set of parameters relevant for the study of a boundary layer flow. In this work, the parameter used to define at what streamwise position the simulation results will

be compared is Re_θ, since the cases which were being reproduced also used it.

5.4.1 Simulated Cases

In order to simulate the turbulent boundary layer flow, the DNS of Spalart (1988) and the experimental data of Smith (1994) were considered. Spalart (1988) provides the velocity and turbulent quantity profiles at three different Re_θ values: 300, 670 and 1410. The DNS database is available online at *http://cfd.mace.manchester. ac.uk/ercoftac/*. Smith (1994) provides the velocity and turbulent quantity profiles at two higher Re_θ values: 4981 and 13052. The experimental data is available online at *http://www.princeton.edu/ ∼gasdyn/*.

5.4.2 Simulations Setup

The domains used were simply rectangular, but of different sizes for the different cases to accommodate the greater streamwise development needed for the higher Reynolds number cases, with wall boundary conditions on the bottom, constant pressure at the top, and zero gradients at the outlet, except for the pressure which was set through linear extrapolation of the two preceding nodal values at the east face. It is of value to comment that there is no physical zero gradient at the outlet unless a fully developed state is reached, however, as the variable profiles will be evaluated at specific streamwise positions, it is usually sufficient to ensure, through the geometry, that the outlet will be far enough from the last downstream test position in order to not influence the results at this point. Zero gradient conditions were also applied at the north boundary for all variables except the pressure.

The inlet velocity and the fluid viscosity were set to match the values reported by each source of each case to be reproduced. The DNS of Spalart was performed using a scaling procedure to obtain profiles at a particular Re_θ, without simulating the full streamwise development. In the present calculations the data from the boundary layer transition test T3B (available online at *http://cfd.mace.manchester.ac.uk/ercoftac/*), providing hot-wire anemometry experimental data from the Rolls-Royce Applied Science Laboratory case, was used to provide inlet conditions. This case has 6% free-stream turbulence intensity, which was used initially, but resulted in far too high levels of turbulence in the free-stream. Therefore a lower value of 1.5% was actually used in the present work. The simulation run to reproduce Spalart's DNS is referred to in this work as Spalart case.

In essence, only one simulation needs to be performed for comparison with all the DNS and experimental data available, since the results can be compared in a dimensionless basis at fixed Re_θ. However, as the experimental data were provided in a dimensional basis, and all inlet conditions were clearly specified, it was decided to run a simulation for each experiment of Smith's work. Therefore two distinct simulations were run, the first for matching comparisons at $Re_\theta = 4981$, and being denoted in this work as case 4981, and the second extending further downstream to allow comparisons at $Re_\theta = 13052$, being denoted as case 13052.

The inlet conditions set for each simulated case are presented in Table 5.7, from where the remained variables had their inlet conditions set as:

$$k_{inlet} = \frac{3}{2}(IU_{inlet})^2 \qquad \varepsilon = \frac{k_{inlet}^{3/2}}{\ell}$$
$$\overline{u^2} = k_{inlet} \qquad \overline{v^2} = 0.4k_{inlet} \qquad \overline{w^2} = 0.6k_{inlet} \qquad \overline{uv} = -\mu_t \frac{\partial U_{inlet}}{\partial y} = 0.0 \tag{5.17}$$

The inlet turbulent lenghscale ℓ was estimated based on Chen's 1996 simulations of the T3B case for the Spalart case, and taken to be around 20% of the reported experimental boundary layer thickness for the 4981 and 13052 cases. Some simulations were performed varying ℓ in order to test the sensitivity of the simulations to it. These tests indicated that the values provided were reasonable, and the results were not particularly sensitive to them. For the simulations run with MTS models, the partitions $\varepsilon_P = \varepsilon_T$ and $\frac{k_P}{k_T} = 2$ were assumed at the inlet.

Table 5.7: Inlet conditions for the zero pressure gradient boundary layer flows

Case	Inlet Velocity	Density	Viscosity	Turbulence Intensity	Estimated ℓ (mm)
Spalart	9.4	1.2036	1.59×10^{-5}	0.015	5
4981	31.44	1.0	1.58×10^{-5}	0.005	10
13052	33.28	1.0	1.54×10^{-5}	0.005	10

Again, two different meshes were needed: one suitable for the high-Reynolds-number turbulence models (with the first node at a distance from the wall in order to provide $y^+ \approx 30$), which will be referred to as the Coarse mesh, and the other for the low-Reynolds-number turbulence models (with the first node at a distance from the wall in order to provide $y^+ < 1.0$), which will be referred to as Refined mesh. The geometry, as well as the mesh features for each simulation, are presented in Table 5.8, where NI stands for the number of grid lines in the x direction and NJ the number of grid lines in the y direction. The different domain lengths required with the wall-function or low-Reynolds-number approaches are associated with the performance of the low and high-Reynolds-number turbulence models in reaching the desired Re_θ number.

Again, a grid independence test was performed with the meshes referred to as Grid 1 and Grid 2 in Table 5.8 and no significant changes in the solutions were identified, thus justifying the results shown below being obtained on Grid 1.

5.4.3 Results and Discussion

Discussions for the Spalart case will only be carried out at $Re_\theta = 1410$, since it was found that the $Re_\theta = 300$ and $Re_\theta = 670$ stations were close enough to the flow domain inlet to be significantly affected by the precise inlet condition values applied. By $Re_\theta = 1410$ the flow had developed to be relatively independent of the inlet conditions.

One may notice that most turbulence models correctly predicted the loglaw at $Re_\theta = 1410$ and tended to overpredict the non-dimensional freestream velocity in Figure 5.64 (implying

Table 5.8: Geometry and mesh features for the zero pressure gradient boundary layer cases

Case	Mesh	Domain height (m)	Domain length (m)	Grid 1 NI	Grid 1 NJ	Grid 2 NI	Grid 2 NJ
Spalart	Refined	0.2	3.0	300	121	400	201
	Coarse			300	51	400	91
4981	Refined	0.2	5.0	500	201	700	301
	Coarse		3.0	300	51	400	91
13052	Refined	0.2	10.0	1000	201	1400	301
	Coarse		6.0	600	51	800	91

an underprediction of the wall shear stress). The TC model is the model which perhaps provided the best prediction of the velocity profile and the HJ model slightly underpredicts the log law. In the original paper of Hanjalic et al. (1997), they presented significantly better agreement with the log law for the zero pressure gradient boundary layer cases. However, this underprediction of the log law is consistent with the results obtained for the fully developed channel flow reported in section 5.1.

The turbulent kinetic energy, presented in Figure 5.65, was reasonably well predicted by all models, specially the FM, SG, KC and TS models. Its near-wall peak was best predicted by the HJ and NG models, both LRN schemes, which tended to slightly overpredict the turbulent kinetic energy profile across the boundary layer towards the outer stream. Similar analysis can be extended to the prediction of the Reynolds shear stress in Figure 5.66, however, all models correctly predicted its near-wall peak. The eddy dissipation rate was also generally correctly predicted by all models as shown in Figure 5.67.

The near-wall peak of the Reynolds normal stress $\overline{u^2}$ (Figure 5.68) was not captured by any turbulence model, but the HJ model clearly got closest. The freestream region, where $\overline{u^2}$ is nearly zero, was captured by all turbulence models, however the predicted reduction in turbulence levels across the boundary layer towards the outer stream did not follow the DNS trend for all models. The Reynolds normal stress $\overline{v^2}$ (Figure 5.69) was well predicted by all RST models which followed in essence the whole development of the variable. The Reynolds normal stress $\overline{w^2}$ (Figure 5.70) was well predicted by all models, including the LEV ones, indicating that in this case the magnitude of this quantity is approximately $\frac{2}{3}k$.

The results of Spalart (1988) regarding the boundary layer integral parameters have also been compared with the present calculations. Besides his own DNS results, Spalart (1988) provided data from Coles (1962) and other authors. One may notice that the skin-friction coefficient C_f (Figure 5.71) was better predicted by the LS, KS, HJ, TC and MTS models. The shape factor H (Figure 5.72) can be considered well predicted by all turbulence models since all of them reached the value of 1.4, characteristic of turbulent zero pressure gradients boundary layers, as already mentioned. The apparent discrepancies between the predicted curves and Spalart's data (particularly at lower Re_θ values) is believed to be due, as noted above, to the fact that the low Re_θ results are somewhat affected by the inlet conditions employed here. The boundary layer thickness is presented in order to demonstrate that the domain height of 0.2m was high enough, not interfering in the results, since the boundary

layer thickness at the end of the plate was only about 0.04m as can be seen in Figure 5.73. There were no DNS data available for comparison of δ.

Analysing case 4981, the log law (Figure 5.74) was reasonably well predicted by all models, although the KS, HJ, TC and NG models tended to slightly underpredict it. The SG and GL models, run with wall functions, exhibit a kink in in the velocity profile which could be avoided by using the effective viscosity numerical tool as described in Chapter 4. However, it was noticed that by using this, these models would clearly overpredict the velocity profile and it was preferred to have the kinks, but a correct velocity profile. The predictions of the Reynolds stresses in Figures 5.75, 5.76 and 5.77 are not very accurate, not following the correct trends. It is believed this is at least partly due to the profiles here still being affected by the inlet conditions, in the same way that the low Re_θ ones were in the Spalart case (although Re_θ is much higher here than in the Spalart case, as a different geometry was used, the physical development length at this location is still somewhat low). If the Spalart simulations had been continued further downstream, to Re=4981, the results might have matched the data much better. However, this test was, unfortunately, not performed.

Regarding the 13052 case, one may notice an improvement in the predictions by the turbulence models compared to the previous case. By observing Figure 5.78, one may notice that the log law region itself was well captured by all LRN models, but a little overpredicted by the HRN models, probably due to the influence of the wall-function used with these. The Reynolds normal stress $\overline{u^2}$ (Figure 5.79) was mostly well-predicted by the GL model, although the near-wall peak level was underestimated. The Reynolds normal stress $\overline{v^2}$ (Figure 5.80) was reasonably well captured by the RST models and the Reynolds shear stress $\overline{uv}$ (Figure 5.81) was well reasonably well predicted by all models, except the CG and NG models.

The profiles of the skin-friction coefficient, boundary layer thickness and shape factor are presented for both 4981 and 13052 cases together in Figures 5.82,5.83 and 5.84 respectively. All models predict reasonably well these boundary layer parameters, the KS and HJ models tending to overpredict the skin-coefficient and the KC and TS models tending to underpredict it. The CG and KC models overpredicted the boundary layer thickness at $Re_\theta = 13052$ and all models reached the expected value of 1.4 for the shape factor.

As a whole, one may observe that the k, $\overline{uv}$ and ε were reasonably well predicted by all turbulence models at high Re_θ values, which indicate they tend towards better predictions the more turbulent the boundary layer is. The weaknesses at lower Re_θ values perhaps indicate more a deficiency of the turbulence models in predicting the transition region, or in the prescription of exact inlet calculations for these cases, than the model performance in the turbulent boundary layer itself.

This test case and the channel flow cases were expected to be reasonably well predicted by all models. It was confirmed that all turbulence models tested here do represent these flows reasonably well, and the model development work to be described in chapter 6 will also use these basic flows for some initial model tuning and evaluation.

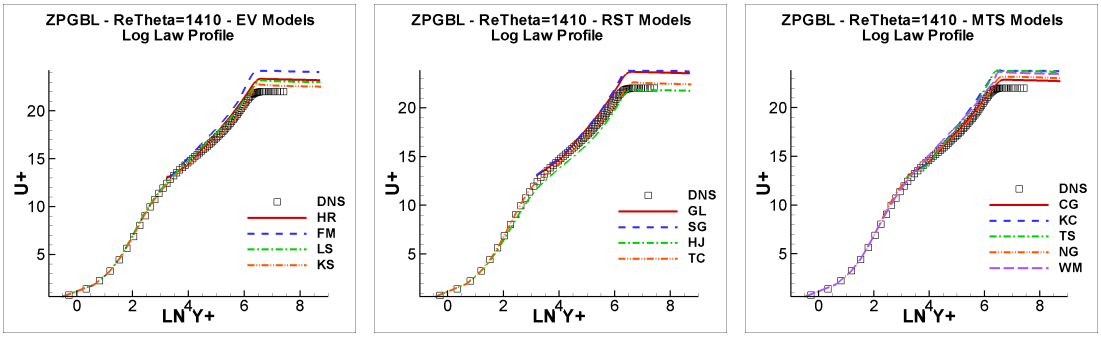

(a) (b) (c)

Figure 5.64: Profile of the mean velocity in a zero pressure gradient boundary layer at $Re_\theta = 1410$ compared to the DNS of Spalart (1988) predicted by: (a) eddy-viscosity models, (b) Reynolds stress transport models and (c) multiple-time-scale models. Models as in Table 3.25.

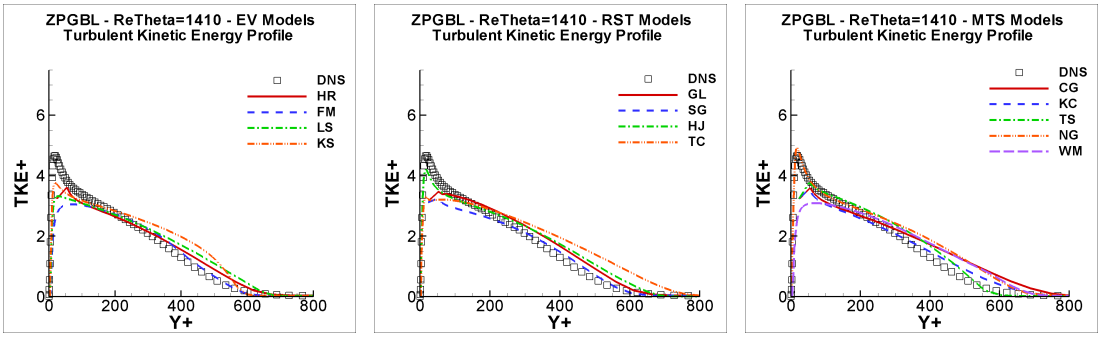

(a) (b) (c)

Figure 5.65: Profile of the turbulent kinetic energy k in a zero pressure gradient boundary layer at $Re_\theta = 1410$ compared to the DNS of Spalart (1988) predicted by: (a) eddy-viscosity models, (b) Reynolds stress transport models and (c) multiple-time-scale models. Models as in Table 3.25.

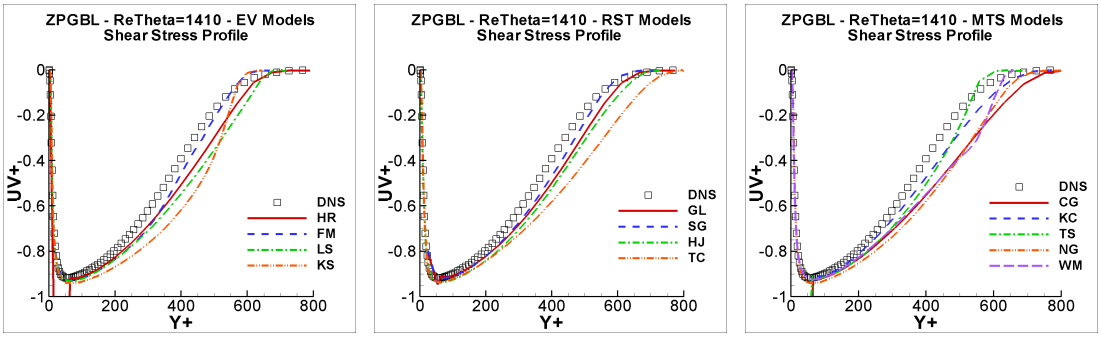

(a) (b) (c)

Figure 5.66: Profile of the Reynolds shear stress $\overline{uv}$ in a zero pressure gradient boundary layer at $Re_\theta = 1410$ compared to the DNS of Spalart (1988) predicted by: (a) eddy-viscosity models, (b) Reynolds stress transport models and (c) multiple-time-scale models. Models as in Table 3.25.

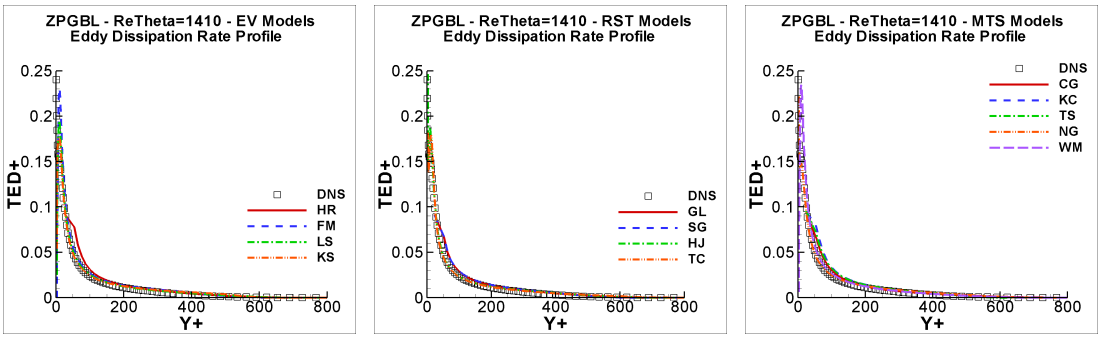

(a) (b) (c)

Figure 5.67: Profile of the turbulent kinetic energy dissipation rate e in a zero pressure gradient boundary layer at $Re_\theta = 1410$ compared to the DNS of Spalart (1988) predicted by: (a) eddy-viscosity models, (b) Reynolds stress transport models and (c) multiple-time-scale models. Models as in Table 3.25.

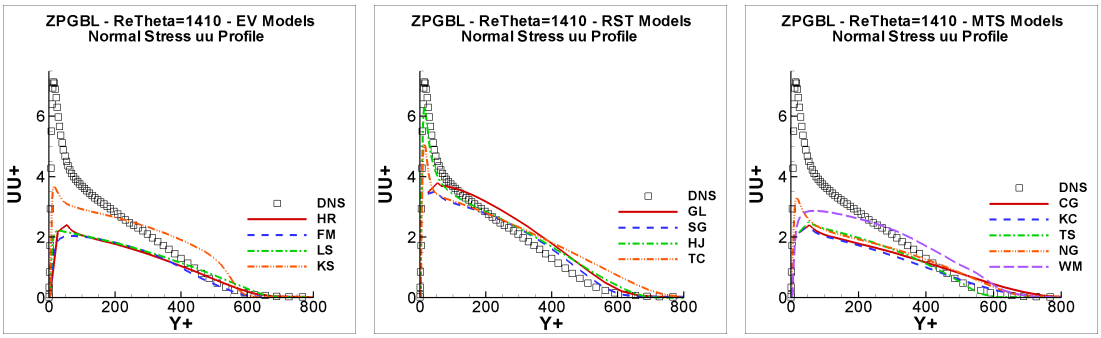

(a) (b) (c)

Figure 5.68: Profile of the Reynolds normal stress $\overline{u^2}$ in a zero pressure gradient boundary layer at $Re_\theta = 1410$ compared to the DNS of Spalart (1988) predicted by: (a) eddy-viscosity models, (b) Reynolds stress transport models and (c) multiple-time-scale models. Models as in Table 3.25.

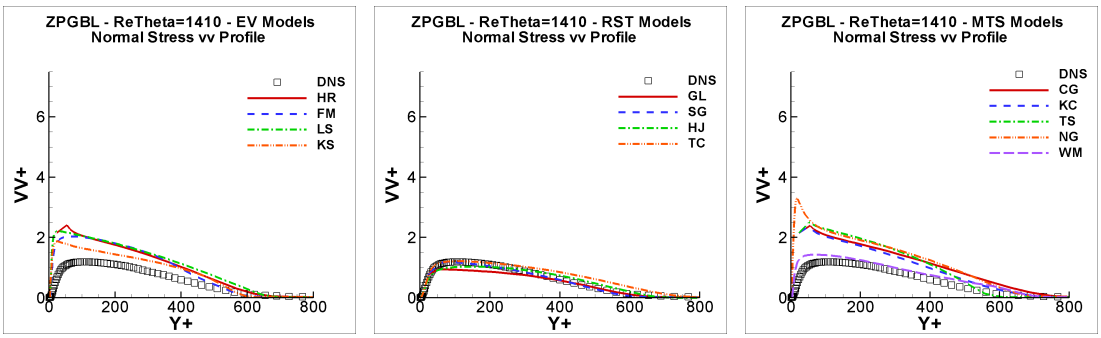

(a) (b) (c)

Figure 5.69: Profile of the Reynolds normal stress $\overline{v^2}$ in a zero pressure gradient boundary layer at $Re_\theta = 1410$ compared to the DNS of Spalart (1988) predicted by: (a) eddy-viscosity models, (b) Reynolds stress transport models and (c) multiple-time-scale models. Models as in Table 3.25.

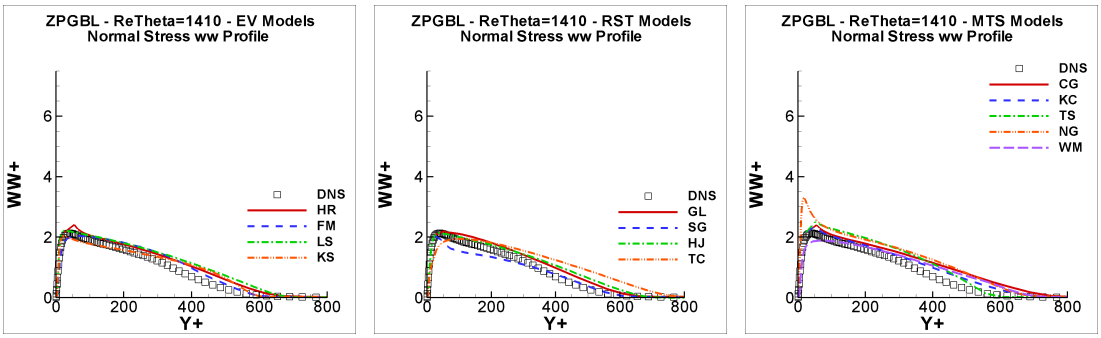

(a) (b) (c)

Figure 5.70: Profile of the Reynolds normal stress $\overline{w^2}$ in a zero pressure gradient boundary layer at $Re_\theta = 1410$ compared to the DNS of Spalart (1988) predicted by: (a) eddy-viscosity models, (b) Reynolds stress transport models and (c) multiple-time-scale models. Models as in Table 3.25.

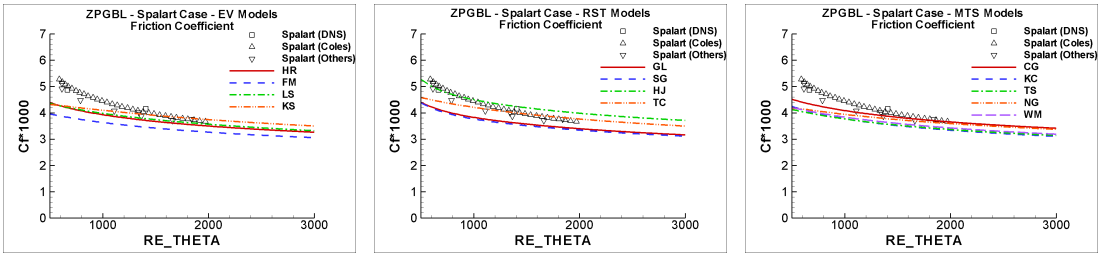

(a) (b) (c)

Figure 5.71: Profile of the skin-friction coefficient in a zero pressure gradient boundary layer compared to the DNS of Spalart (1988) predicted by: (a) eddy-viscosity models, (b) Reynolds stress transport models and (c) multiple-time-scale models. Models as in Table 3.25.

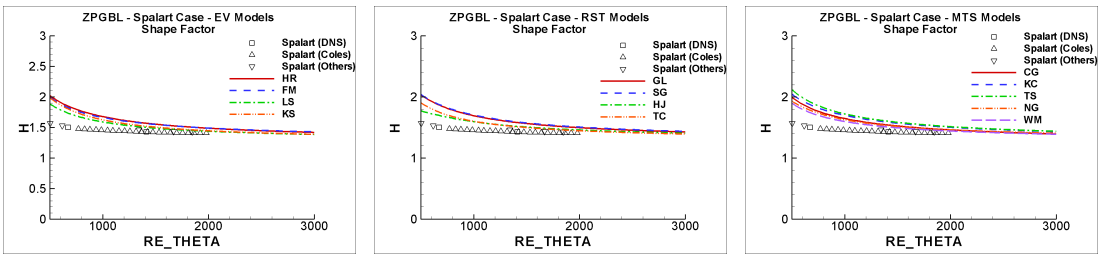

(a) (b) (c)

Figure 5.72: Profile of the shape factor in a zero pressure gradient boundary layer compared to the DNS of Spalart (1988) predicted by: (a) eddy-viscosity models, (b) Reynolds stress transport models and (c) multiple-time-scale models. Models as in Table 3.25.

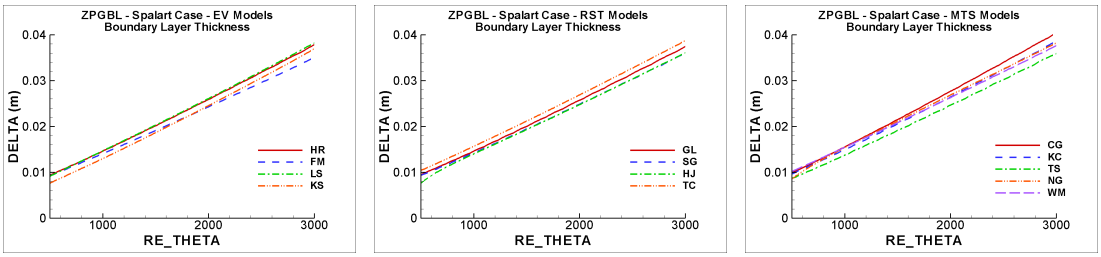

(a) (b) (c)

Figure 5.73: Profile of the boundary layer thickness in a zero pressure gradient boundary layer compared to the DNS of Spalart (1988) predicted by: (a) eddy-viscosity models, (b) Reynolds stress transport models and (c) multiple-time-scale models. Models as in Table 3.25.

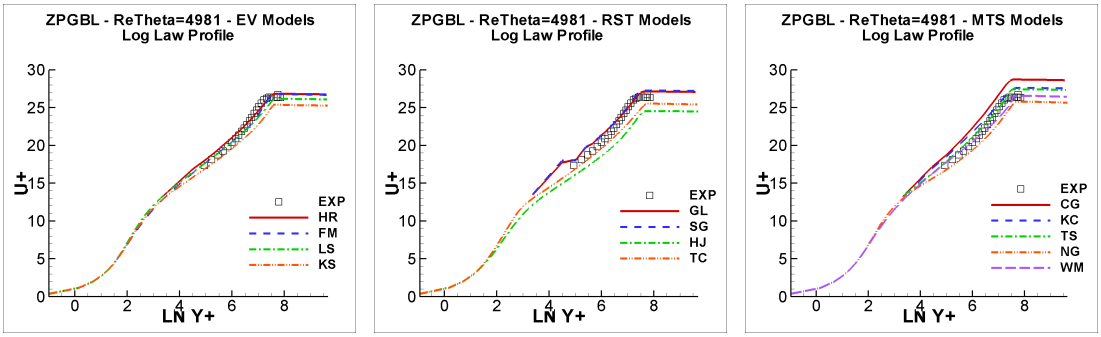

(a) (b) (c)

Figure 5.74: Profile of the mean velocity in a zero pressure gradient boundary layer at $Re_\theta = 4981$ compared to the experiments of Smith (1994) predicted by: (a) eddy-viscosity models, (b) Reynolds stress transport models and (c) multiple-time-scale models. Models as in Table 3.25.

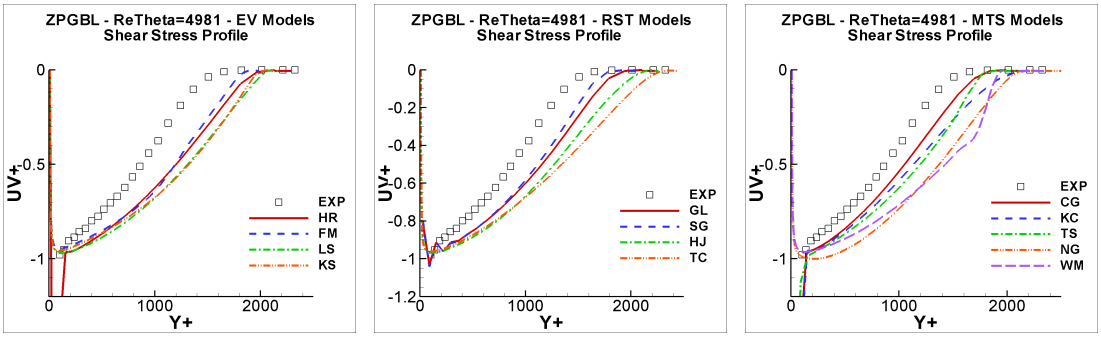

(a) (b) (c)

Figure 5.75: Profile of the Reynolds shear stress $\overline{uv}$ in a zero pressure gradient boundary layer at $Re_\theta = 4981$ compared to the experiments of Smith (1994) predicted by: (a) eddy-viscosity models, (b) Reynolds stress transport models and (c) multiple-time-scale models. Models as in Table 3.25.

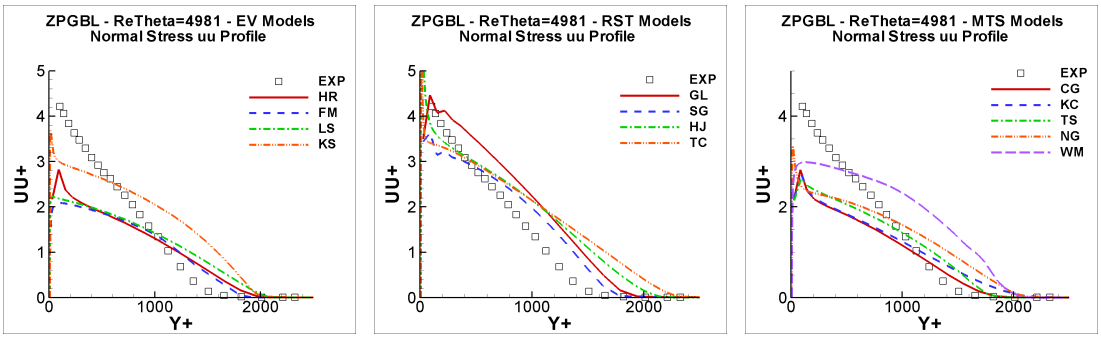

(a) (b) (c)

Figure 5.76: Profile of the Reynolds normal stress $\overline{u^2}$ in a zero pressure gradient boundary layer at $Re_\theta = 4981$ compared to the experiments of Smith (1994) predicted by: (a) eddy-viscosity models, (b) Reynolds stress transport models and (c) multiple-time-scale models. Models as in Table 3.25.

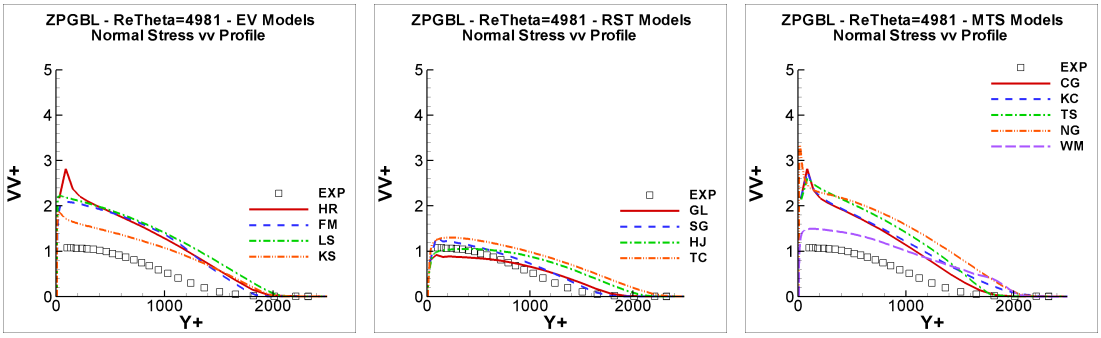

(a) (b) (c)

Figure 5.77: Profile of the Reynolds normal stress $\overline{v^2}$ in a zero pressure gradient boundary layer at $Re_\theta = 4981$ compared to the experiments of Smith (1994) predicted by: (a) eddy-viscosity models, (b) Reynolds stress transport models and (c) multiple-time-scale models. Models as in Table 3.25.

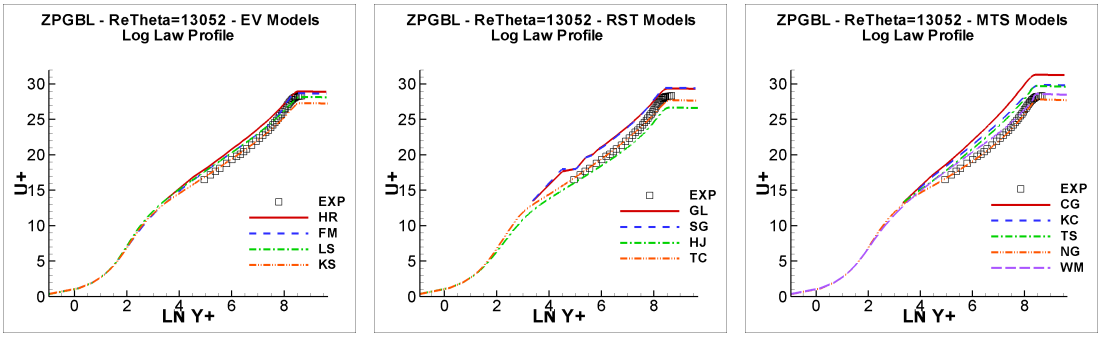

(a) (b) (c)

Figure 5.78: Profile of the mean velocity in a zero pressure gradient boundary layer at $Re_\theta = 13052$ compared to the experiments of Smith (1994) predicted by: (a) eddy-viscosity models, (b) Reynolds stress transport models and (c) multiple-time-scale models. Models as in Table 3.25.

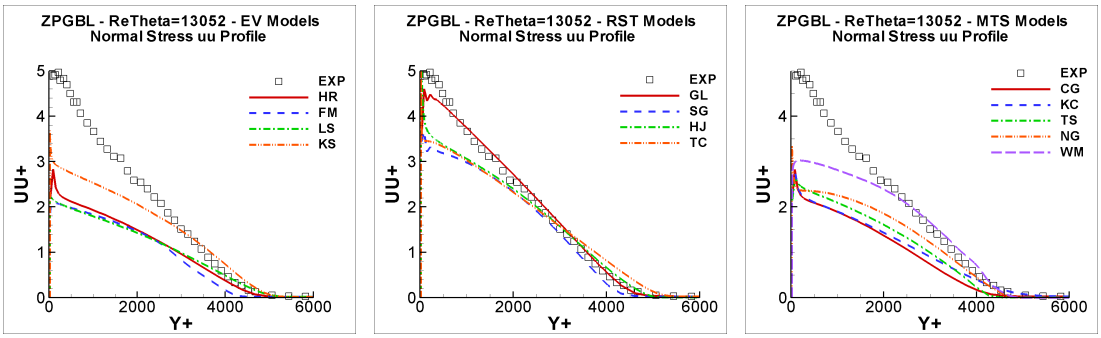

(a) (b) (c)

Figure 5.79: Profile of the Reynolds normal stress $\overline{u^2}$ in a zero pressure gradient boundary layer at $Re_\theta = 13052$ compared to the experiments of Smith (1994) predicted by: (a) eddy-viscosity models, (b) Reynolds stress transport models and (c) multiple-time-scale models. Models as in Table 3.25.

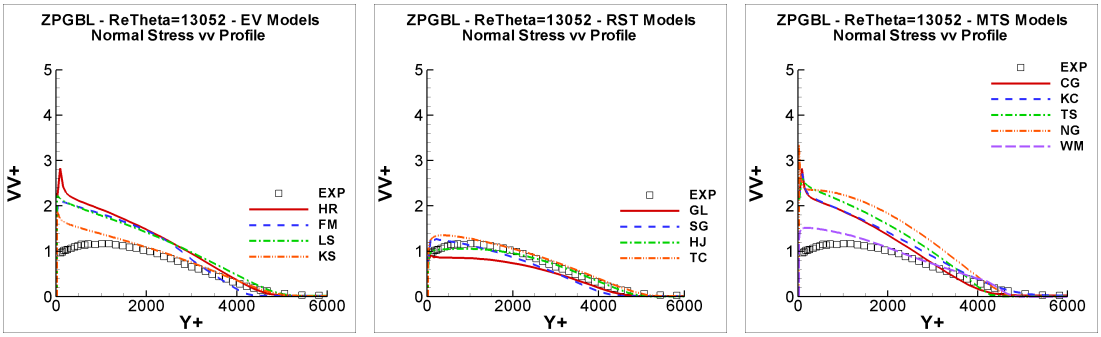

(a) (b) (c)

Figure 5.80: Profile of the Reynolds normal stress $\overline{v^2}$ in a zero pressure gradient boundary layer at $Re_\theta = 13052$ compared to the experiments of Smith (1994) predicted by: (a) eddy-viscosity models, (b) Reynolds stress transport models and (c) multiple-time-scale models. Models as in Table 3.25.

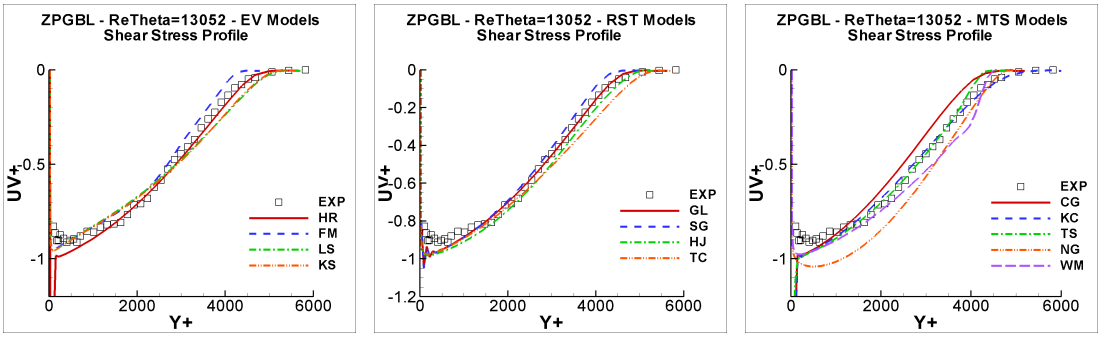

(a) (b) (c)

Figure 5.81: Profile of the Reynolds shear stress $\overline{uv}$ in a zero pressure gradient boundary layer at $Re_\theta = 13052$ compared to the experiments of Smith (1994) predicted by: (a) eddy-viscosity models, (b) Reynolds stress transport models and (c) multiple-time-scale models. Models as in Table 3.25.

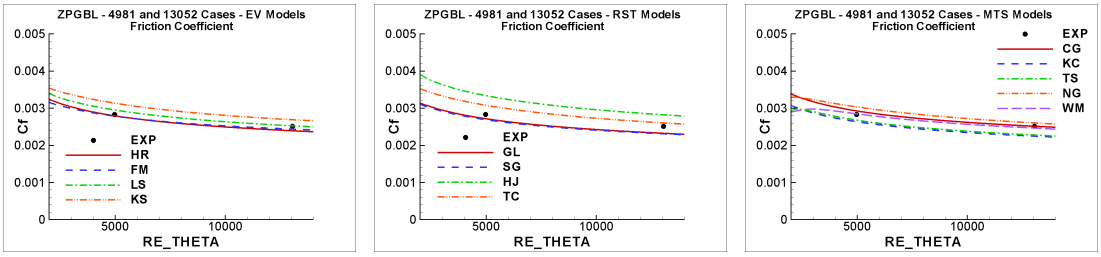

(a) (b) (c)

Figure 5.82: Profile of the skin-friction coefficient in a zero pressure gradient boundary layer compared to the experiments of Smith (1994) predicted by: (a) eddy-viscosity models, (b) Reynolds stress transport models and (c) multiple-time-scale models. Models as in Table 3.25.

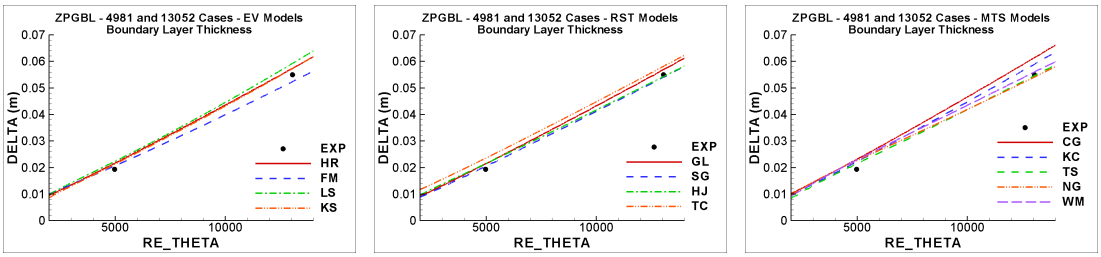

(a) (b) (c)

Figure 5.83: Profile of the boundary layer thickness in a zero pressure gradient boundary layer compared to the experiments of Smith (1994) predicted by: (a) eddy-viscosity models, (b) Reynolds stress transport models and (c) multiple-time-scale models. Models as in Table 3.25.

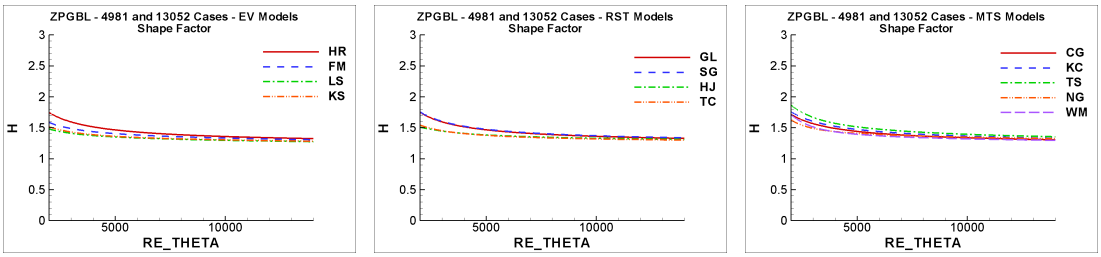

(a) (b) (c)

Figure 5.84: Profile of the shape factor in a zero pressure gradient boundary layer compared to the experiments of Smith (1994) predicted by: (a) eddy-viscosity models, (b) Reynolds stress transport models and (c) multiple-time-scale models. Models as in Table 3.25.

5.5 Adverse Pressure Gradient Boundary Layer

The adverse pressure gradient boundary layer consists of a boundary layer similar to that described in the previous section, but with a positive (adverse) pressure gradient in the streamwise direction. As the pressure increases along the x direction, the freestream velocity decreases which is why this kind of flow is also called decelerating flow. An adverse pressure gradient can be imposed by a variety of means, for example, it arises when the flow faces a convex surface or a deflected wall as shown in Figure 5.85. Therefore one may imagine how commonly it can be found in industry, and thus why it is an important kind of flow to accurately predict. As the pressure increases, the velocity profile tends towards an inflection point and if the pressure still rises, the flow may reverse, as shown by the development illustrated in Figure 5.85.

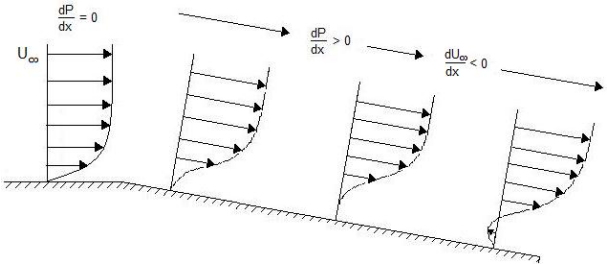

Figure 5.85: Adverse pressure gradient boundary layer

Needless to say, the streamwise velocity U will again vary in both x and y directions, but now there is no "fully developed" condition to be reached. The boundary layer parameters (δ, δ^*, θ, H, Re_θ, Re_δ and C_f) defined before in equations 5.11 to 5.16 are still used to characterize the adverse pressure gradient boundary layer flow.

5.5.1 Simulated Cases

Two different experimental works were reproduced here: one from Samuel and Joubert (1974) and the other from Marusic and Perry (1995). The latter is a more recent work while the former can be considered a classical work, having been modelled by many different authors: Menter (1994), Hanjalic et al. (1997), Nagano et al. (1997), etc.

Both Samuel and Joubert (1974) and Marusic and Perry (1995) defined the same dimensionless parameter C_p in order to express the pressure gradient they applied in their experiment:

$$C_p = \frac{P - P_\infty}{0.5\rho U_\infty^2} \tag{5.18}$$

where P_∞ and U_∞ are the freestream pressure and velocity at the inlet.

Samuel and Joubert (1974) reported measurements in a boundary layer with $Re_{bulk} = 1.7 \times 10^6$ per unit length, in which they applied an adverse pressure gradient beyond $x =$

$0.8m$. Profiles of the mean velocity and turbulence quantities were reported at six locations downstream of this, labelled T1 to T6, whose x coordinates are given in Table 5.9. The simulation set up to reproduce Samuel and Joubert's experiment will be referred to as case S&J in this work.

Marusic and Perry (1995) started to apply the adverse pressure gradient at $x \approx 1.5m$ and provided two cases where the only difference between them is the inlet freestream velocity U_∞. The case where the inlet velocity was $U_\infty = 10m/s$ will be referred to as M&P10 in this work and the case where $U_\infty = 30m/s$, M&P30. Marusic and Perry (1995) also provided measured profiles at 6 streamwise locations, whose coordinates are given in Table 5.9.

Table 5.9: x coordinates for profile output for each case

Case	T1 (m)	T2 (m)	T3 (m)	T4 (m)	T5 (m)	T6 (m)
S&J	1.04	1.44	1.79	2.38	2.89	3.39
M&P10	1.2	1.8	2.24	2.64	2.88	3.08
M&P30	1.2	1.8	2.24	2.64	2.88	3.08

The experimental data from Samuel and Joubert (1974) was digitized from their article, whilst that of Marusic and Perry (1995) was obtained from the following website: *http://www.mame.mu.oz.au/∼ivan/index.html*.

5.5.2 Simulations Setup

Since Samuel and Joubert (1974) provide all results in a dimensionless form, the inlet freestream velocity was here taken as unity, and the viscosity set to $\mu = 1/Re_{bulk}$, where Re_{bulk} is the Reynolds number reported above. The raw results from the simulations should then correspond to the non-dimensional quantities reported by $S\&J$. In the cases of Marusic and Perry (1995), their reported freestream velocities were used in the simulations.

The inlet conditions applied for each case are summarised in Table 5.10, which were used in conjunction with equation (5.17) to set the inlet turbulence parameters. The lengthscale, ℓ, was estimated, and sensitivity tests performed which showed its value did not greatly affect the results. The only exception to the use of these inlet conditions was the S&J case with the HJ model, for which use of this uniform inlet would have required a very long domain for the boundary layer to reach the desired thickness. In this case, an output profile from a zero pressure gradient boundary layer case simulated with the KS model was provided as inlet conditions for the simulation with the HJ model.

Table 5.10: Inlet conditions for the adverse pressure gradient cases

Case	U_∞	ρ	μ	I	ℓ (mm)
S&J	1.0	1.0	5.88×10^{-7}	0.015	10
M&P10	10.0	1.0	1.54×10^{-5}	0.03	10
M&P30	30.0	1.0	1.58×10^{-5}	0.03	10

The geometry was simply set as a rectangular domain and the boundary conditions were set similarly to the zero pressure gradient boundary layer cases, with no slip conditions at

the wall, linear extrapolation for the pressure at the west face, zero gradient for all variables at the east face (again, taking the domain length long enough so the result would not be influenced by the east boundary) and zero gradient for all variables except the pressure at the free surface (north face).

In order to impose the same pressure gradient as Samuel and Joubert (1974) and Marusic and Perry (1995) did, equation (5.18) was rewritten in the form $P(x) = 0.5\rho U_\infty^2 C_p(x) + P_\infty$ and the curve provided for C_p was fitted into a polynomial as a function of the streamwise coordinate x. This polynomial was then used to set the pressure along the upper boundary of the domain, ensuring the streamwise pressure gradient matched that in the experiment. By comparing Figures 5.86(a) and 5.86(b), one may notice that the pressure gradient increases more strongly in the Samuel and Joubert experiment. The locations where experimental data was made available, also described in Table 5.9, are also indicated in these Figures.

Regarding the imposed freestream pressure gradient, the streamwise location from where the non-zero values should start being applied in the simulation is another important issue. Initially, the simulations were set exactly as described in the experimental papers. However, in analysing the results it was noticed that the predicted boundary layer thickness where the adverse pressure gradient started was significantly lower than that reported in the measurements. The start of the adverse pressure gradient region was thus moved downstream, to a location where the boundary layer thickness coincided with that reported in the experimental cases (see Figures 5.92 and 5.101).

Since these simulations are wall-bounded, different grids are needed for the low and high-Reynolds number turbulence models in order to set the appropriate y^+ value at the first node. The geometry and grid features are presented in Table 5.11, where the Refined mesh refers to the one used with the LRN turbulence models and the Coarse one to the high-Reynolds-number models. Grid independence tests were performed with more refined grids (Grid 2 in Table 5.11) and the meshes presented for Grid 1 were shown to provide grid-independent results.

Table 5.11: Geometry and mesh features for the adverse pressure gradient boundary layer cases

Case	Domain height (m)	Domain length (m)	Mesh	Grid 1		Grid 2	
				NI	NJ	NI	NJ
S&J	0.2	4.8	Refined	360	75	400	121
			Coarse	360	41	400	71
M&P10	0.2	5.0	Refined	400	91	450	147
			Coarse	400	41	450	71
M&P30	0.2	5.0	Refined	400	91	450	147
			Coarse	400	41	450	71

5.5.3 Results and Discussion

The results for the simulation of the S&J case are presented from Figure 5.87 to 5.94; the results for the case M&P10, from Figure 5.95 to 5.103; and for the case M&P30, in Figures

5.104 to 5.108. The cases will be analysed and discussed in this order, however it may be of value to first observe the pressure development in the streamwise direction in order to understand better each case. This can be done by examining C_p in Figures 5.86(a) and 5.86(b) (The C_p curve for the M&P30 case is the same as for the M&P10 case), where one can also see the measurement stations' location. The results will be presented only for stations T5 and T6 for the S&J case and for stations T2, T4, T5 and T6 for the M&P cases for the sake of simplicity, since these stations do represent the evolution of the imposed pressure gradient.

Starting with the log law profile of the S&J case, one may observe in Figures 5.87 to 5.88 the evolution of the log law along the stations in the streamwise direction. Until station T5 ($x = 2.89m$) all turbulence models provided a similar and reasonable prediction of the log law, such as shown in Figure 5.87, the HJ model underpredicting it a bit, as already observed in the other flow cases. Between stations T5 and T6 there is a strong increase in the freestream pressure, and at station T6 ($x = 3.39$), none of the models were able to match the experimental velocity profile well, with the FM, HJ, NG and WM models arriving closest to it. Since the HJ model was underpredicting the log law at the other stations, it is not possible to know if its better performance at station T6 is due to its merit or due to a problem which has been making it underpredict the log law, although it did predict the log-law moving downward between T5 and T6. It is also worth noticing that those models which performed best are LRN models, indicating some limitations related to the use of wall functions.

The Reynolds stresses were output in the same dimensionless form Samuel and Joubert (1974) provided the results in their paper. With regard to the Reynolds shear stress, Figures 5.89 and 5.90, one may say that it was reasonably well predicted by the SG, GL and KC models at all stations (just like at station T5 in Figure 5.89), however at station T6 the near wall region was not so well predicted; this again is probably to do with the strong increase of the pressure from station T5 to T6. The only Reynolds normal stress whose results could be digitized from the experimental paper was $\overline{u^2}$ at station T3, whose prediction by all models can be found in Figure 5.91, where the HJ and the GL models are shown to perform best.

Evaluating the boundary layer parameters, in Figures 5.92 to 5.94, the boundary layer thickness, skin-friction and shape factor were reasonably well predicted by all models. Most models struggled to capture the value of these parameters at the last measurement station, however the FM, TC, NG and WM models performed well even at this location. One may notice that the shape factor is about 1.4 during much of the streamwise direction length, thus indicating the profile in this region was not so different from a turbulent zero pressure gradient boundary layer.

Now moving to the M&P10 case, one may observe that most models cannot follow the velocity profile (Figure 5.95) across all stations. The only two models which succeeded in this matter were the FM and the WM models, both LRN ω-based models, designed to perform well in adverse pressure gradient boundary layers. At the first stations all models performed reasonably well and one might notice that, at these stations, the imposed pressure gradient

is still quite weak and the flow still behaves, under some inertia, similarly to a zero pressure gradient boundary layer.

With regard to the Reynolds shear stress (Figure 5.96), one can notice that no model is actually able to follow the development of this stress along the stations. One might say though that the decay through to the free stream region was better predicted by the FM and the RST models, while the LEV MTS models perform better than the STS LEV models. The same analysis can be extended to the performance of the models in predicting the turbulent kinetic energy profiles in Figure 5.97.

The Reynolds normal stresses, presented in Figure 5.98, were not consistently well predicted by any RST or NLEV model. The SG model performs well in predicting $\overline{v^2}$, Figure 5.99, however it fails in predicting the other normal stresses. It is interesting to notice that the FM model is the only model which always predicts correctly the outer edge of the boundary layer, while all other turbulence models overpredict the thickness of the layer. It is always worth remembering that, apart from the WM model which performed reasonably well, the other MTS models which are being tested are LEV formulations which intrinsically limit their performance.

Analysing the boundary layer parameters in Figures 5.101 to 5.103 one may say that all turbulence models predicted these reasonably well, specially the boundary layer thickness. One may notice that only the FM and WM models are able to follow the skin-friction coefficient trend until the last station, which is consistent with the good mean velocity prediction of these models. Again, one may notice the value of 1.4 for the shape factor at the beginning of the measurements (where it was still essentially a turbulent zero pressure gradient boundary layer), which then increased.

The M&P30 case is essentially the same as the M&P10 and thus one would expect to obtain similar results from the turbulence models. Indeed, the velocity profile analysis described for the M&P10 case is still valid for the M&P30 and therefore the velocity profiles at different stations are not presented here. On the other hand, the Reynolds stresses presented some different results.

The Reynolds shear stress $\overline{uv}$ (Figure 5.104) was best predicted by the FM, SG and KC models which clearly follow the whole development of $\overline{uv}$. Most models still tend to overpredict the thickness of the outer layer. The turbulent kinetic energy (Figure 5.105) and the Reynolds normal stress $\overline{u^2}$ (Figure 5.106) are reasonably well captured along the stations by the GL model, while the other models provide similar behaviours to those of the previous case. The Reynolds normal stresses $\overline{v^2}$ (Figure 5.107) and $\overline{w^2}$ (Figure 5.108) were reasonably well captured by the WM model along the stations.

The boundary layer parameters were similarly predicted by the models compared to the M&P10 case (and therefore are not being presented here), that is, as a whole, all models performed reasonably well, with the FM and WM schemes standing out in capturing the skin-friction coefficient at the final stations.

Comparing the two cases of Marusic and Perry (1995), one may notice that as the inlet velocity increased, that is, as the flow Reynolds number increased, most models tended to

improve prediction. Such a behaviour might certainly be expected from the HRN models, since as the Reynolds number increases the thickness of the layer represented by the wall-function decreases.

To conclude this section, one may notice that most of the turbulence models tested here exhibit difficulties in correctly predicting the development of the mean velocity and turbulent quantities as the pressure gradient increases. Besides, and yet related to this, they tend to overpredict the thickness of the outer layer. The FM and WM models, which performed better in this respect, were calibrated to adverse pressure gradient boundary layer flows. Some of the RST models did not show clear improvements compared to simpler models such as EV models and it was noticeable that when comparing STS LEV models and MTS LEV models, the former was more adversely affected by some of the above weaknesses.

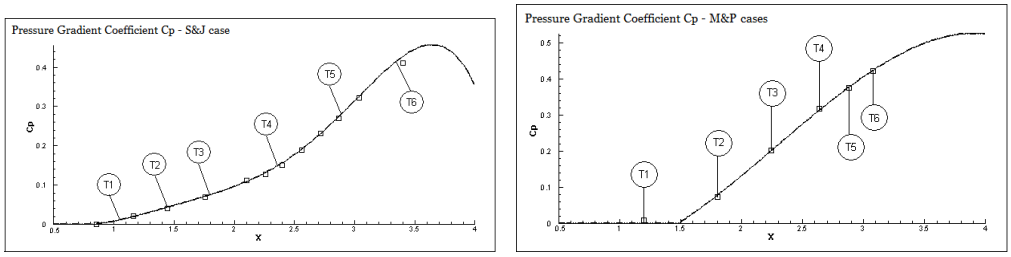

(a) S&J case (b) M&P cases

Figure 5.86: Pressure gradient coefficient profile for the adverse pressure gradient boundary layer cases.

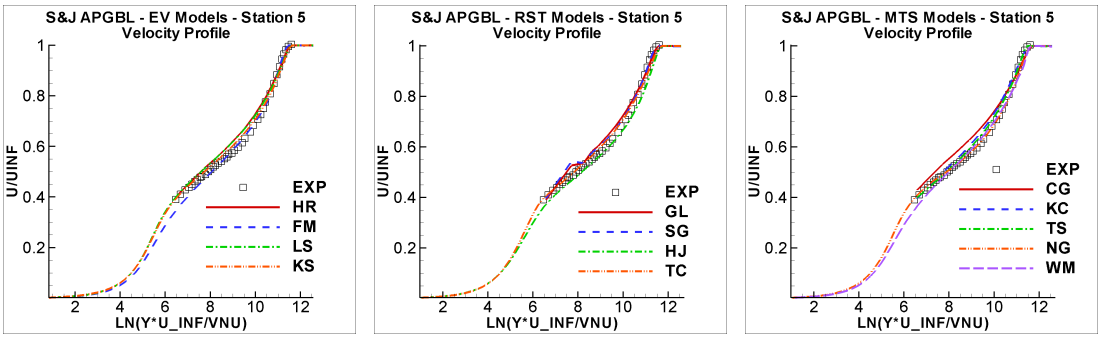

(a) (b) (c)

Figure 5.87: Log law profile at station T5 for the S&J case predicted by the: (a) eddy-viscosity models, (b) Reynolds stress transport models and (c) multiple-time-scale models. Models as in Table 3.25.

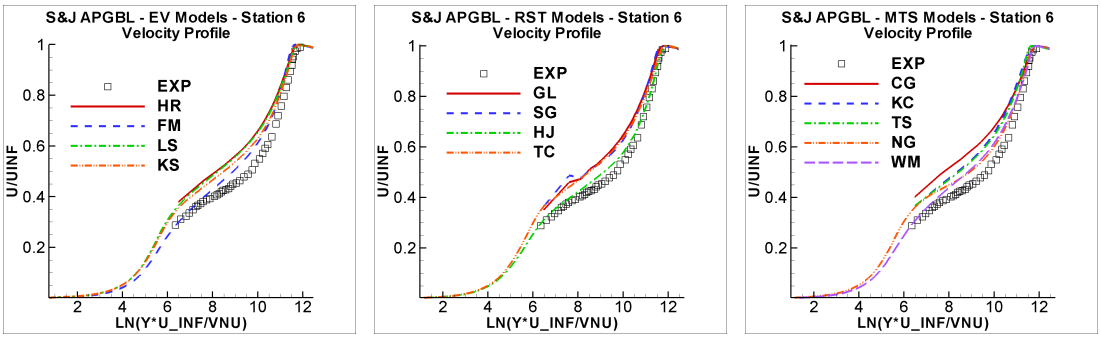

(a) (b) (c)

Figure 5.88: Log law profile at station T6 for the S&J case predicted by the: (a) eddy-viscosity models, (b) Reynolds stress transport models and (c) multiple-time-scale models. Models as in Table 3.25.

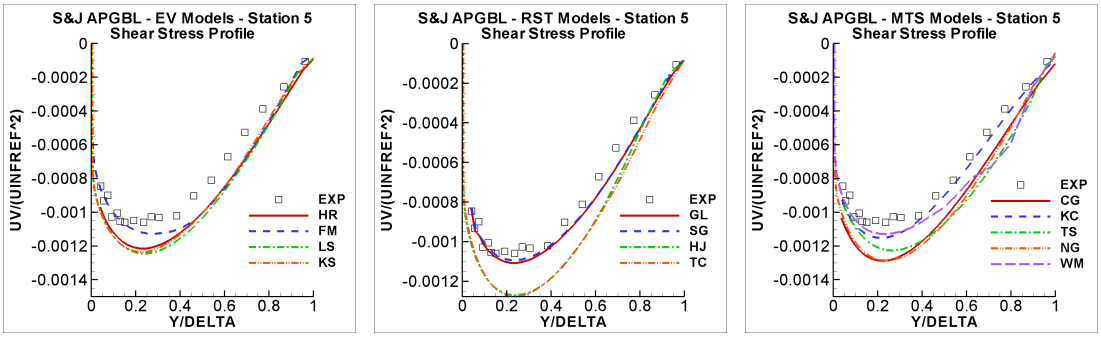

(a) (b) (c)

Figure 5.89: Reynolds shear stress profile at station T5 for the S&J case predicted by the: (a) eddy-viscosity models, (b) Reynolds stress transport models and (c) multiple-time-scale models. Models as in Table 3.25.

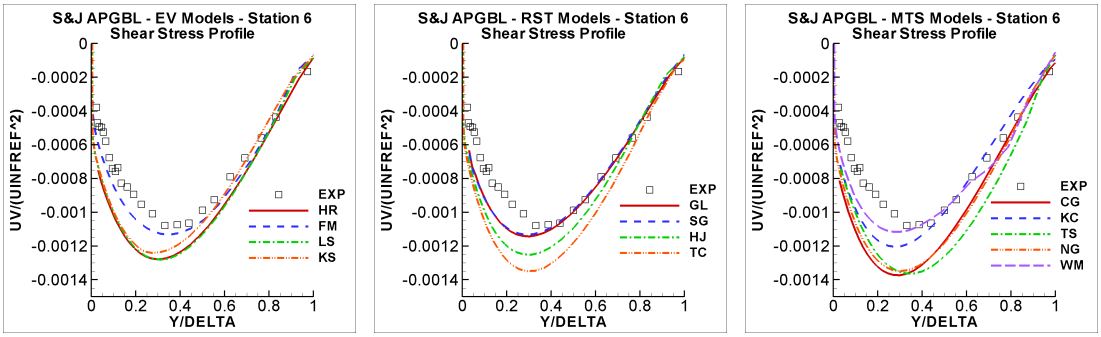

(a) (b) (c)

Figure 5.90: Reynolds shear stress profile at station T6 for the S&J case predicted by the: (a) eddy-viscosity models, (b) Reynolds stress transport models and (c) multiple-time-scale models. Models as in Table 3.25.

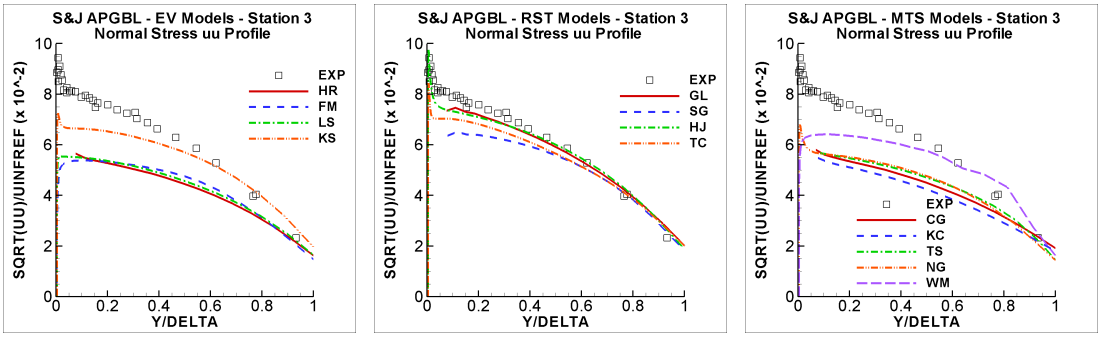

(a) (b) (c)

Figure 5.91: Reynolds normal stress $\overline{u^2}$ profile at station T3 for the S&J case predicted by the: (a) eddy-viscosity models, (b) Reynolds stress transport models and (c) multiple-time-scale models. Models as in Table 3.25.

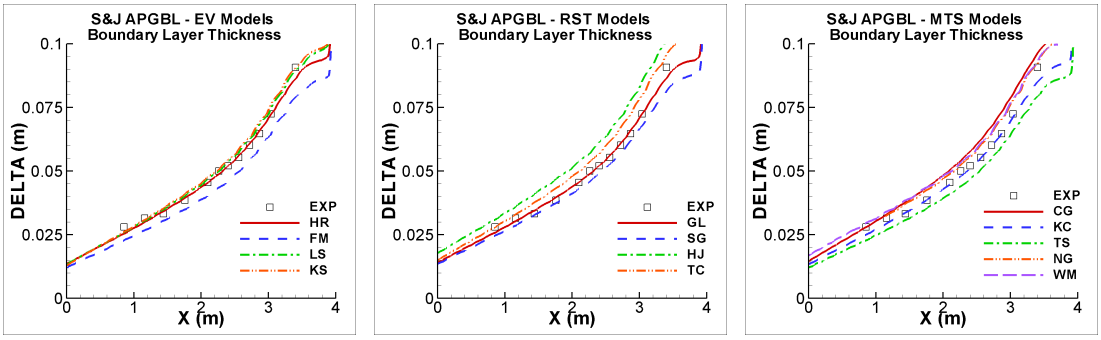

(a) (b) (c)

Figure 5.92: Boundary Layer thickness profile for the S&J case predicted by the: (a) eddy-viscosity models, (b) Reynolds stress transport models and (c) multiple-time-scale models. Models as in Table 3.25.

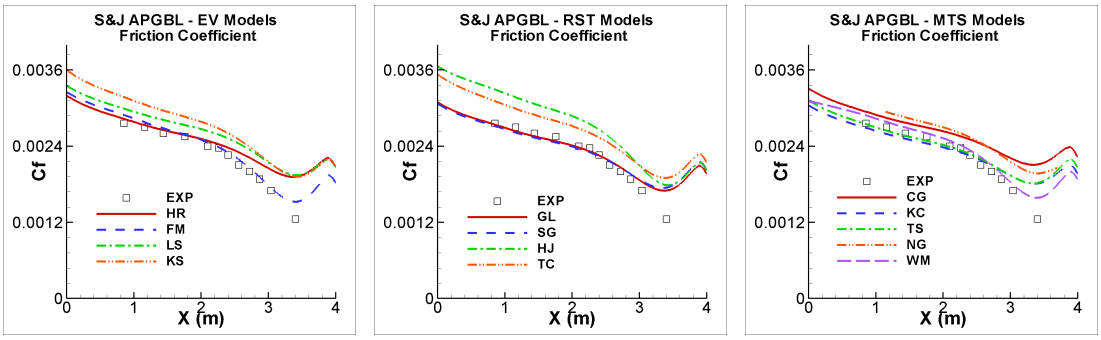

(a) (b) (c)

Figure 5.93: Skin-friction coefficient profile for the S&J case predicted by the: (a) eddy-viscosity models, (b) Reynolds stress transport models and (c) multiple-time-scale models. Models as in Table 3.25.

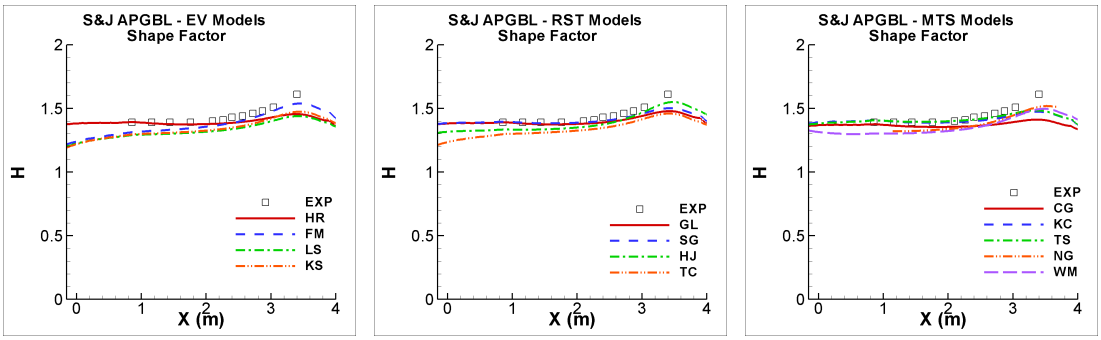

(a) (b) (c)

Figure 5.94: Shape Factor profile for the S&J case predicted by the: (a) eddy-viscosity models, (b) Reynolds stress transport models and (c) multiple-time-scale models. Models as in Table 3.25.

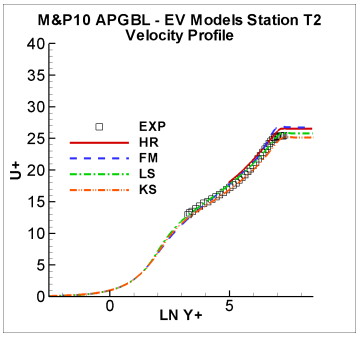

(a) EV models - station T2

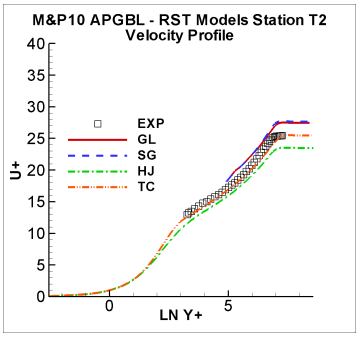

(b) RST models - station T2

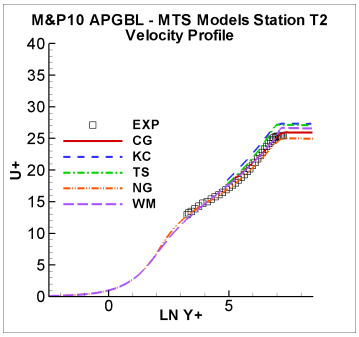

(c) MTS models - station T2

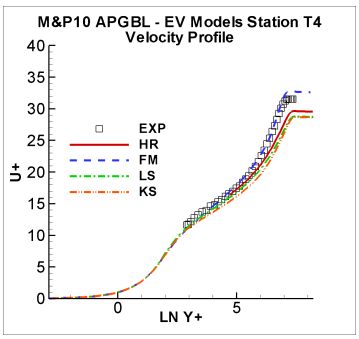

(d) EV models - station T4

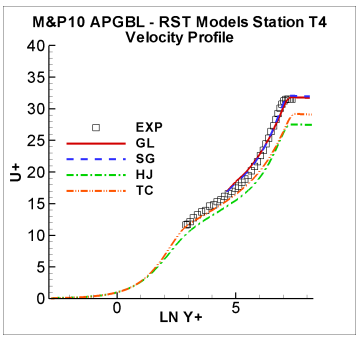

(e) RST models - station T4

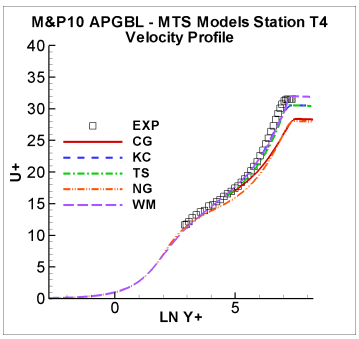

(f) MTS models - station T4

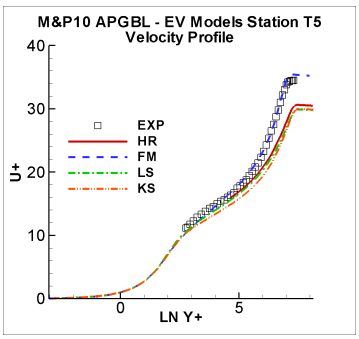

(g) EV models - station T5

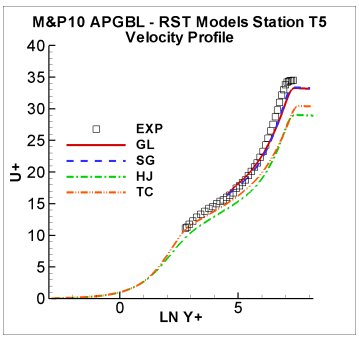

(h) RST models - station T5

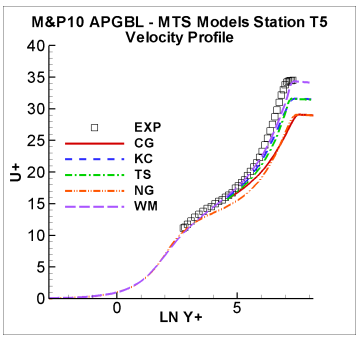

(i) MTS models - station T5

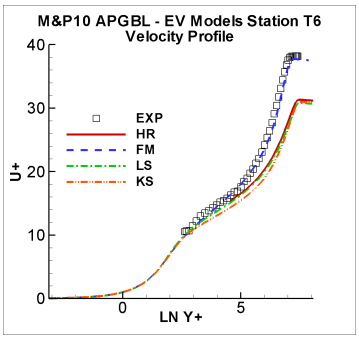

(j) EV models - station T6

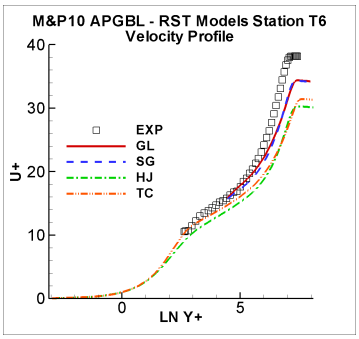

(k) RST models - station T6

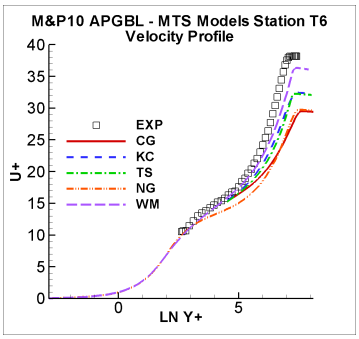

(l) MTS models - station T6

Figure 5.95: Log law profile at stations T2, T4, T5 and T6 for the M&P10 case predicted by the eddy-viscosity, Reynolds stress transport and multiple-time-scale models. Models as in Table 3.25.

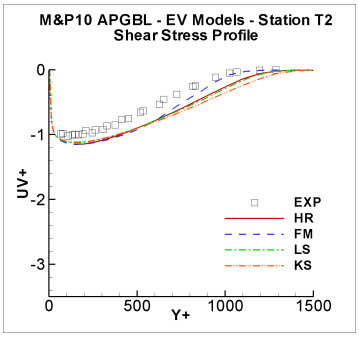

(a) EV models - station T2

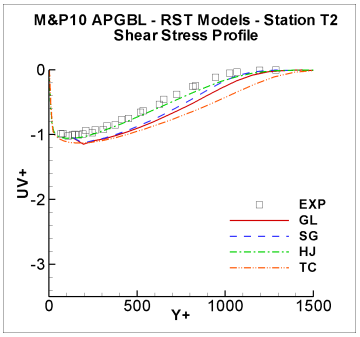

(b) RST models - station T2

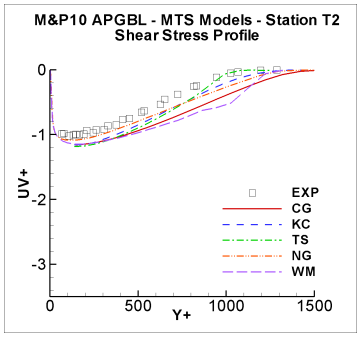

(c) MTS models - station T2

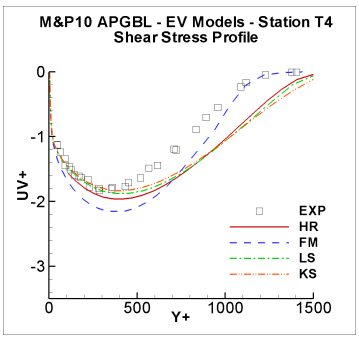

(d) EV models - station T4

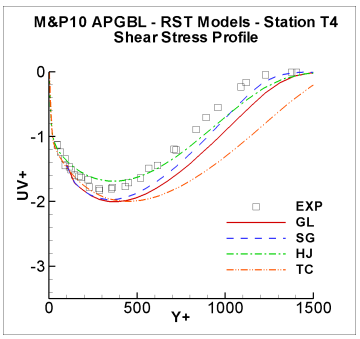

(e) RST models - station T4

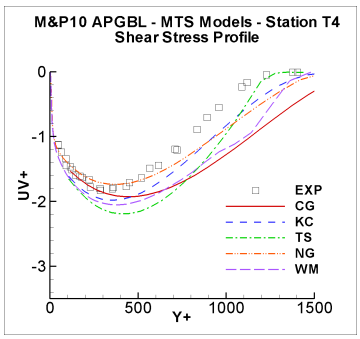

(f) MTS models - station T4

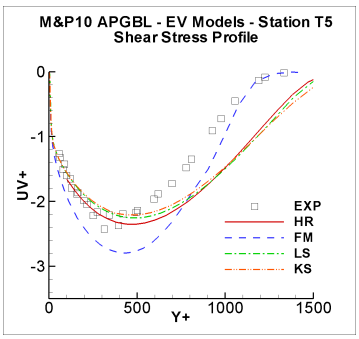

(g) EV models - station T5

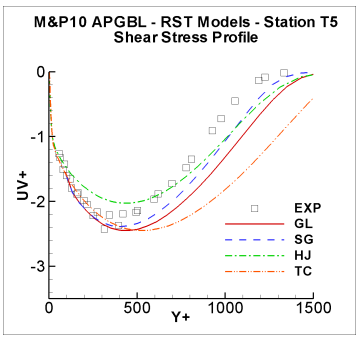

(h) RST models - station T5

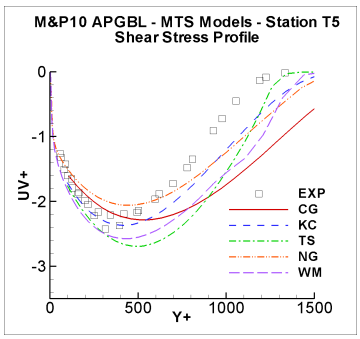

(i) MTS models - station T5

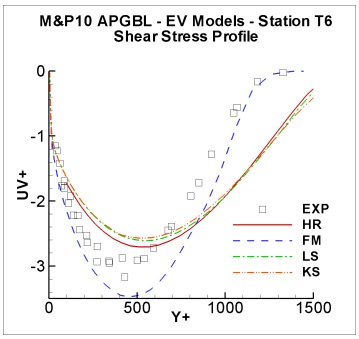

(j) EV models - station T6

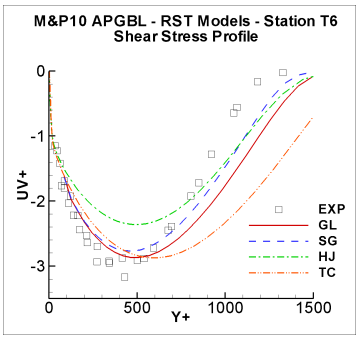

(k) RST models - station T6

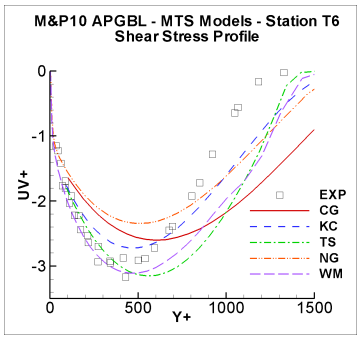

(l) MTS models - station T6

Figure 5.96: Reynolds shear stress at stations T2, T4, T5 and T6 for the M&P10 case predicted by the eddy-viscosity, Reynolds stress transport and multiple-time-scale models. Models as in Table 3.25.

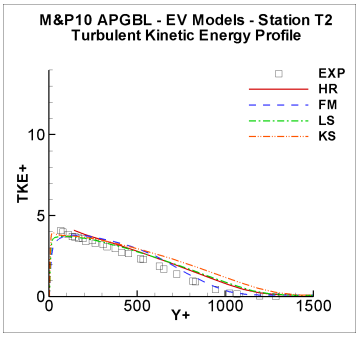

(a) EV models - station T2

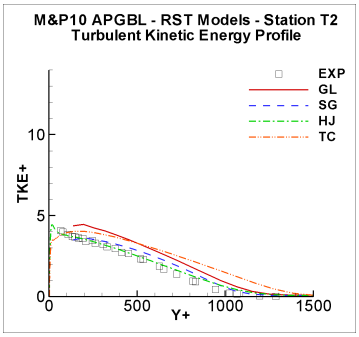

(b) RST models - station T2

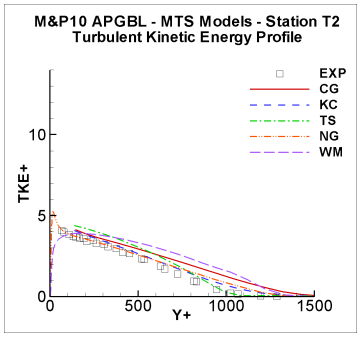

(c) MTS models - station T2

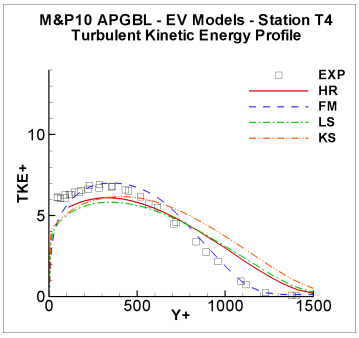

(d) EV models - station T4

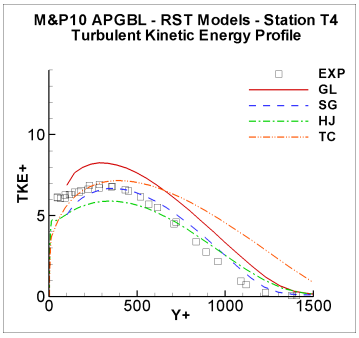

(e) RST models - station T4

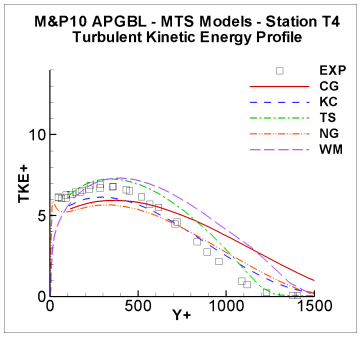

(f) MTS models - station T4

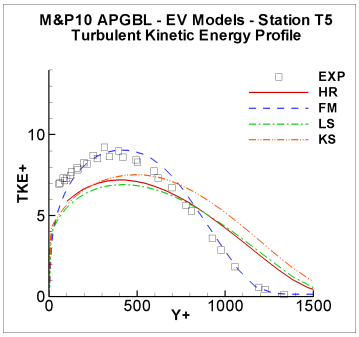

(g) EV models - station T5

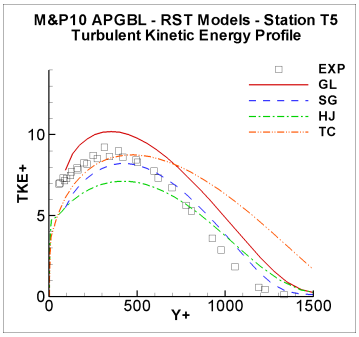

(h) RST models - station T5

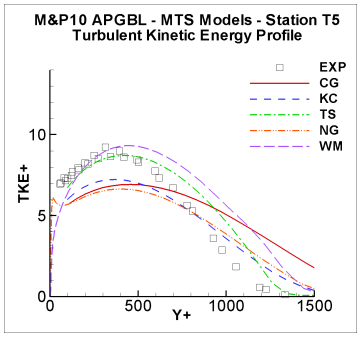

(i) MTS models - station T5

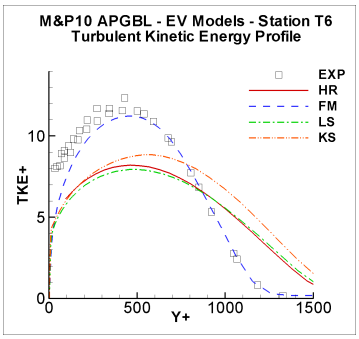

(j) EV models - station T6

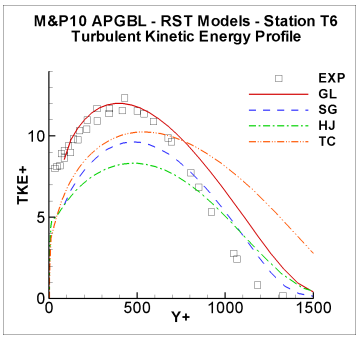

(k) RST models - station T6

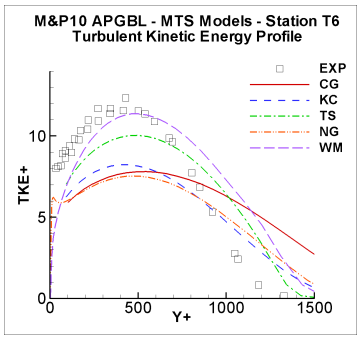

(l) MTS models - station T6

Figure 5.97: Turbulent kinetic energy at stations T2, T4, T5 and T6 for the M&P10 case predicted by the eddy-viscosity, Reynolds stress transport and multiple-time-scale. Models as in Table 3.25.

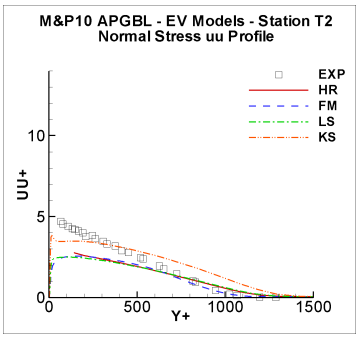

(a) EV models - station T2

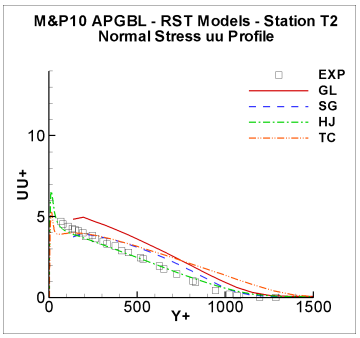

(b) RST models - station T2

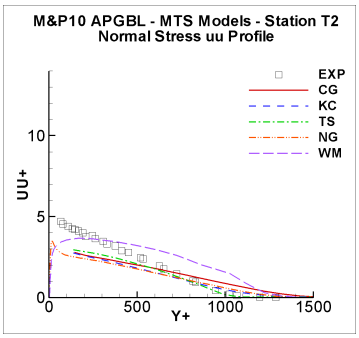

(c) MTS models - station T2

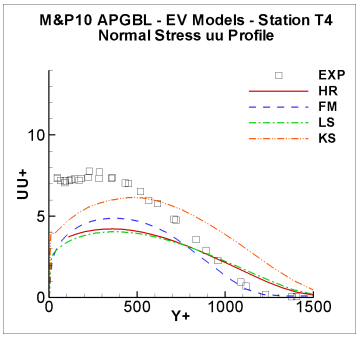

(d) EV models - station T4

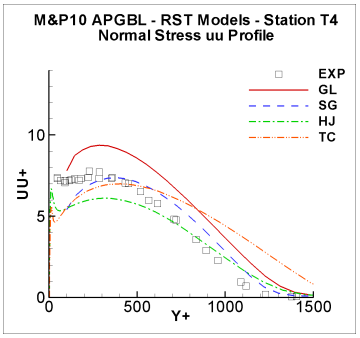

(e) RST models - station T4

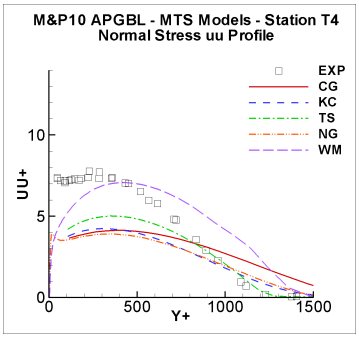

(f) MTS models - station T4

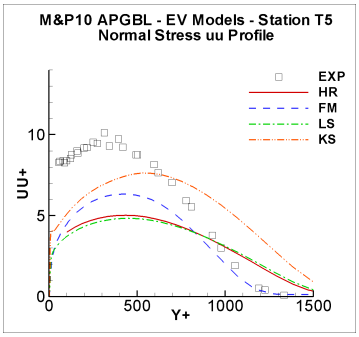

(g) EV models - station T5

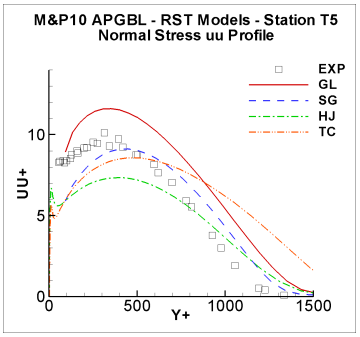

(h) RST models - station T5

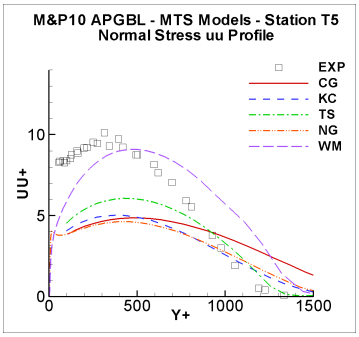

(i) MTS models - station T5

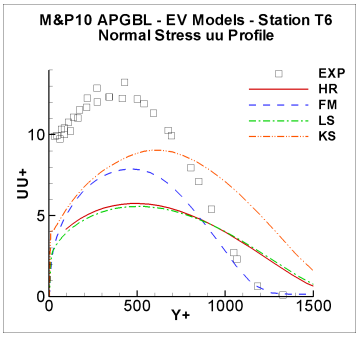

(j) EV models - station T6

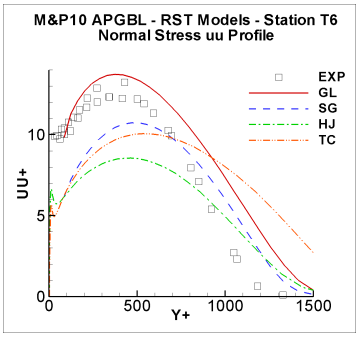

(k) RST models - station T6

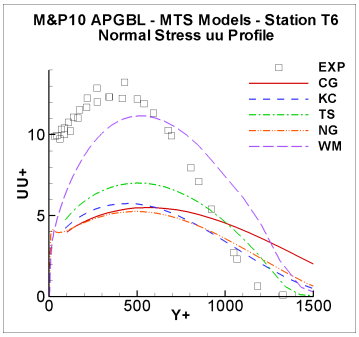

(l) MTS models - station T6

Figure 5.98: Reynolds normal stress $\overline{u^2}$ at stations T2, T4, T5 and T6 for the M&P10 case predicted by the eddy-viscosity, Reynolds stress transport and multiple-time-scale models. Models as in Table 3.25.

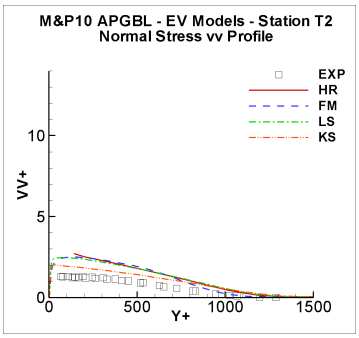

(a) EV models - station T2

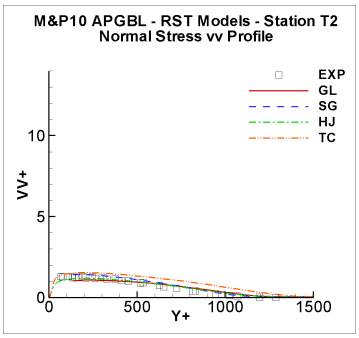

(b) RST models - station T2

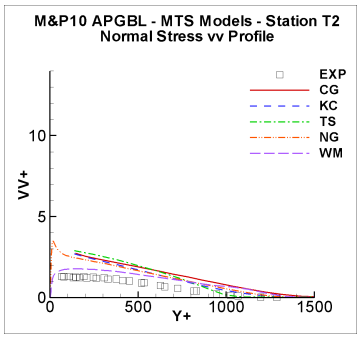

(c) MTS models - station T2

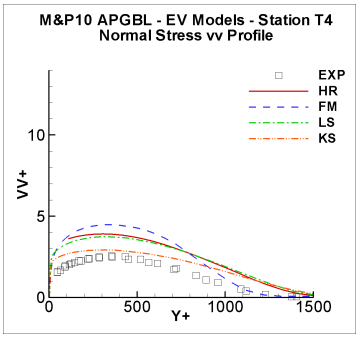

(d) EV models - station T4

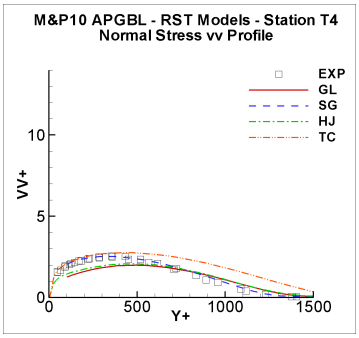

(e) RST models - station T4

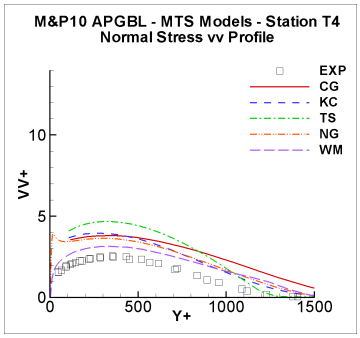

(f) MTS models - station T4

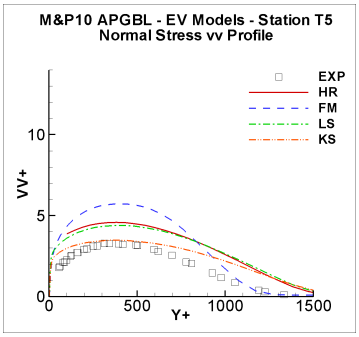

(g) EV models - station T5

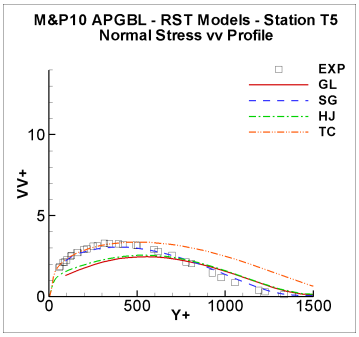

(h) RST models - station T5

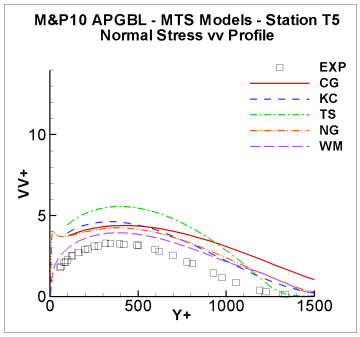

(i) MTS models - station T5

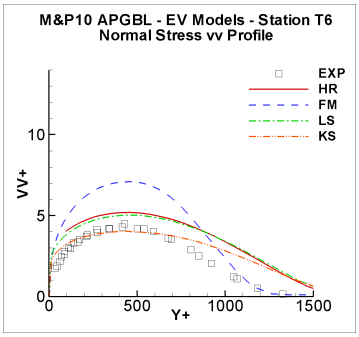

(j) EV models - station T6

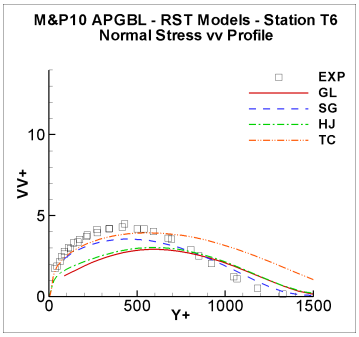

(k) RST models - station T6

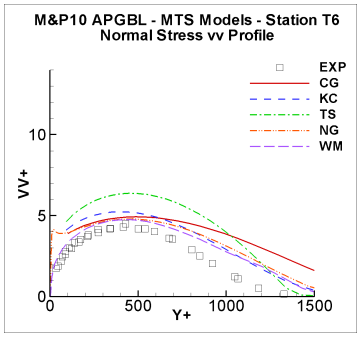

(l) MTS models - station T6

Figure 5.99: Reynolds normal stress $\overline{v^2}$ at stations T2, T4, T5 and T6 for the M&P10 case predicted by the eddy-viscosity, Reynolds stress transport and multiple-time-scale models. Models as in Table 3.25.

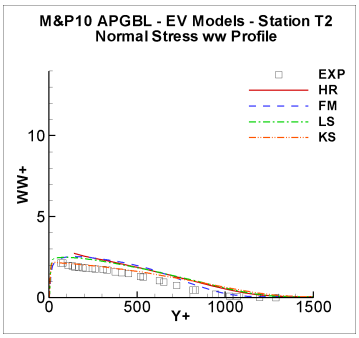

(a) EV models - station T2

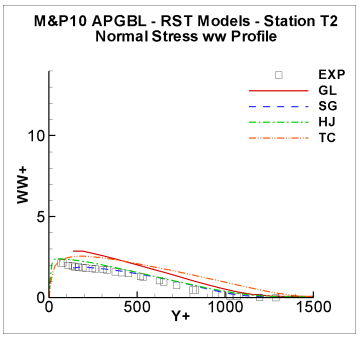

(b) RST models - station T2

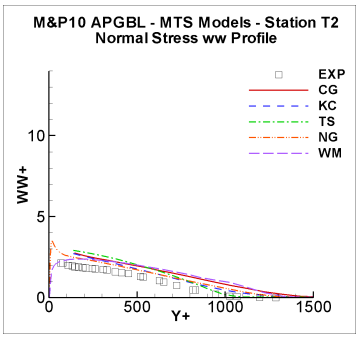

(c) MTS models - station T2

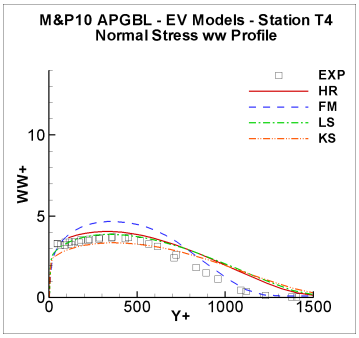

(d) EV models - station T4

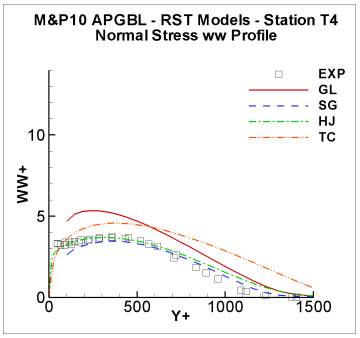

(e) RST models - station T4

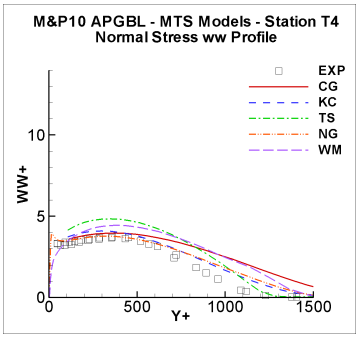

(f) MTS models - station T4

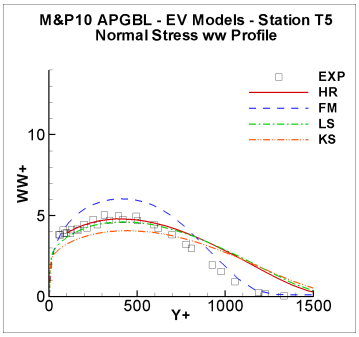

(g) EV models - station T5

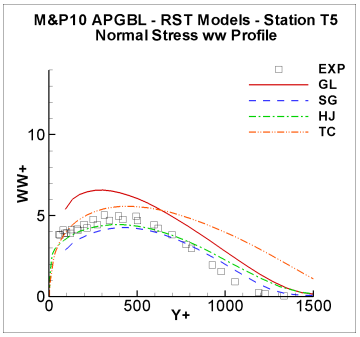

(h) RST models - station T5

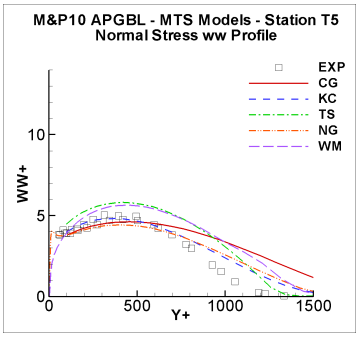

(i) MTS models - station T5

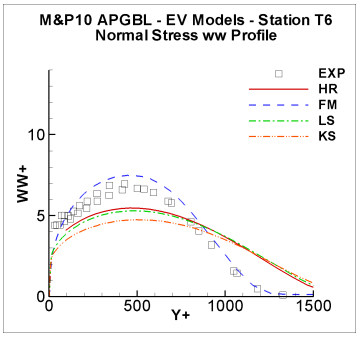

(j) EV models - station T6

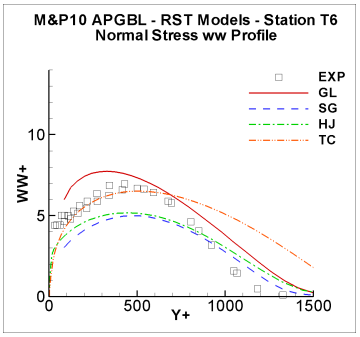

(k) RST models - station T6

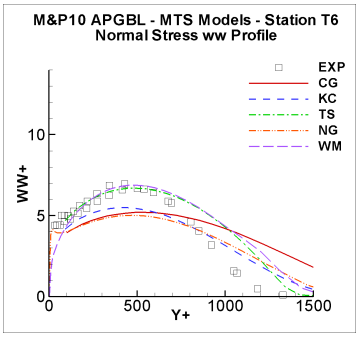

(l) MTS models - station T6

Figure 5.100: Reynolds normal stress $\overline{w^2}$ at stations T2, T4, T5 and T6 for the M&P10 case predicted by the eddy-viscosity, Reynolds stress transport and multiple-time-scale models. Models as in Table 3.25.

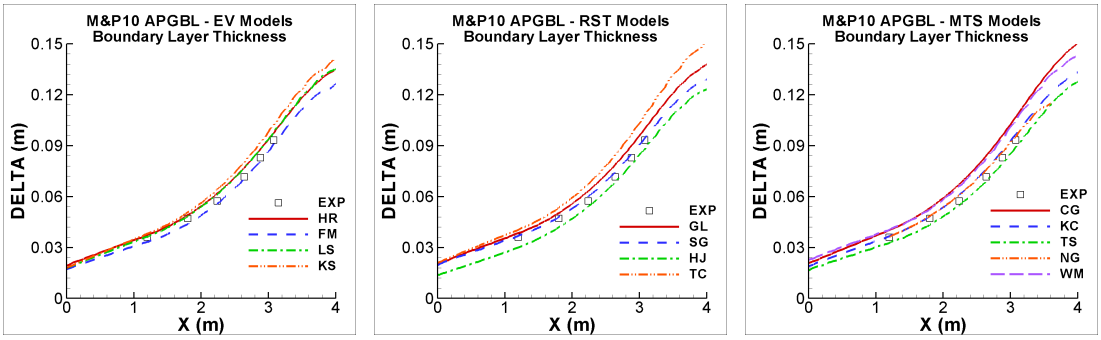

(a) (b) (c)

Figure 5.101: Boundary Layer thickness profile for the M&P10 case predicted by the: (a) eddy-viscosity models, (b) Reynolds stress transport models and (c) multiple-time-scale models. Models as in Table 3.25.

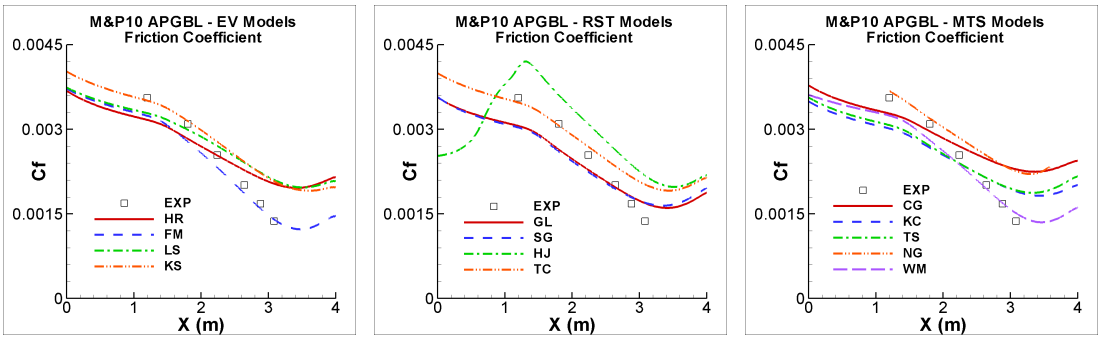

(a) (b) (c)

Figure 5.102: Skin-friction coefficient profile for the M&P10 case predicted by the: (a) eddy-viscosity models, (b) Reynolds stress transport models and (c) multiple-time-scale models. Models as in Table 3.25.

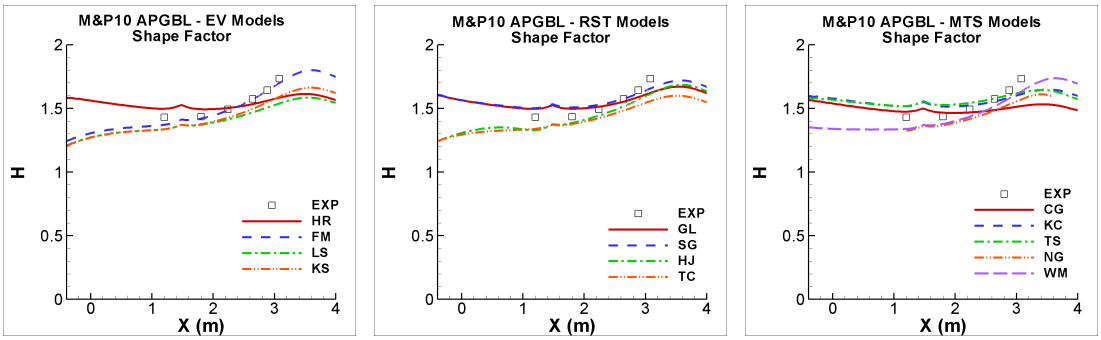

(a) (b) (c)

Figure 5.103: Shape Factor profile for the M&P10 case predicted by the: (a) eddy-viscosity models, (b) Reynolds stress transport models and (c) multiple-time-scale models. Models as in Table 3.25.

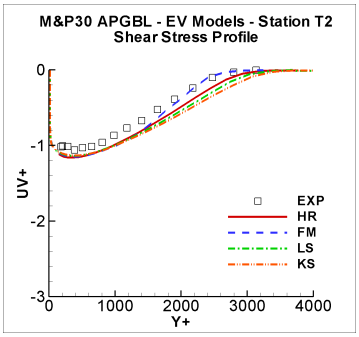

(a) EV models - station T2

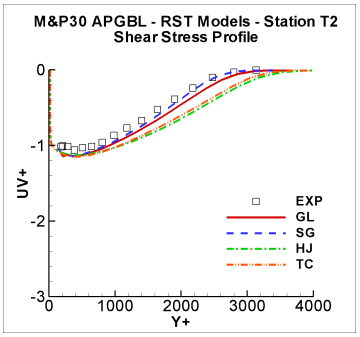

(b) RST models - station T2

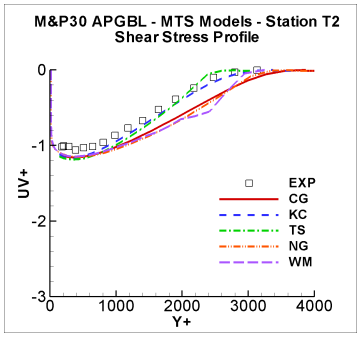

(c) MTS models - station T2

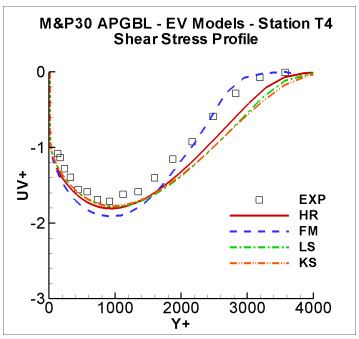

(d) EV models - station T4

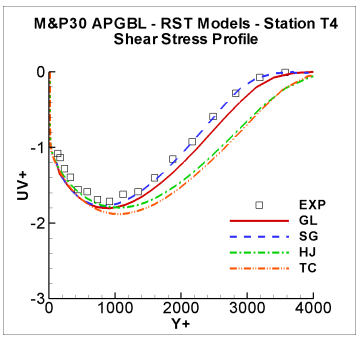

(e) RST models - station T4

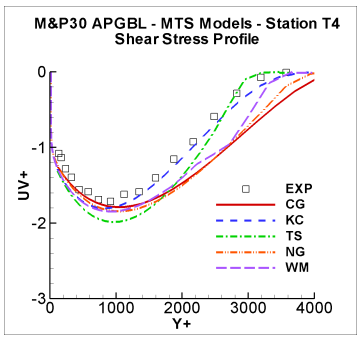

(f) MTS models - station T4

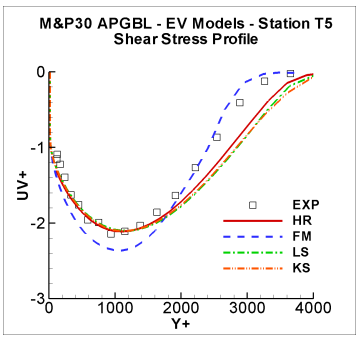

(g) EV models - station T5

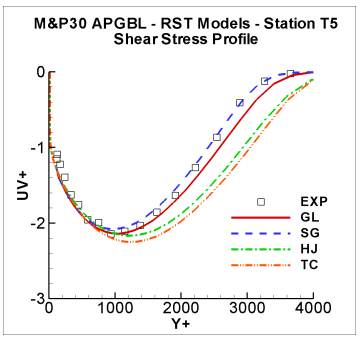

(h) RST models - station T5

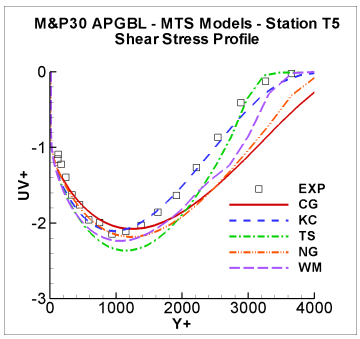

(i) MTS models - station T5

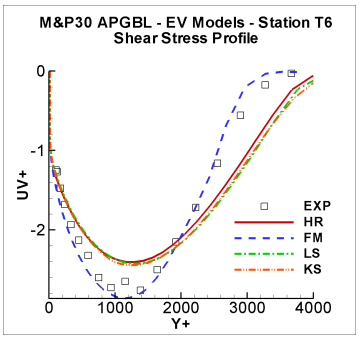

(j) EV models - station T6

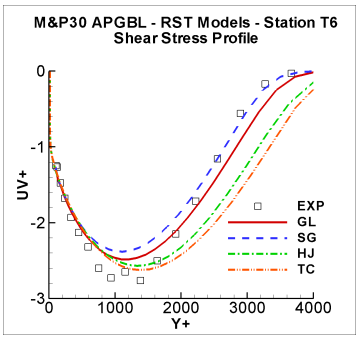

(k) RST models - station T6

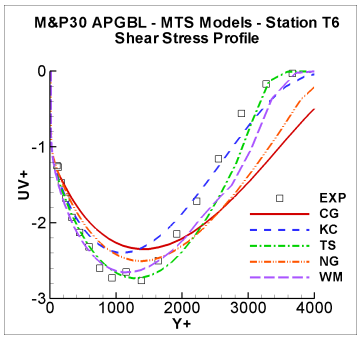

(l) MTS models - station T6

Figure 5.104: Reynolds shear stress at stations T2, T4, T5 and T6 for the M&P30 case predicted by the eddy-viscosity, Reynolds stress transport and multiple-time-scale models. Models as in Table 3.25.

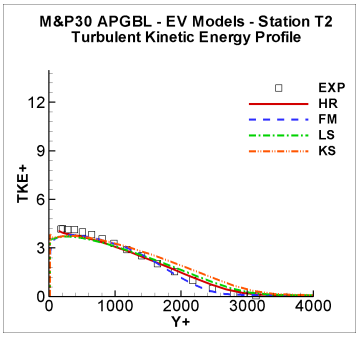

(a) EV models - station T2

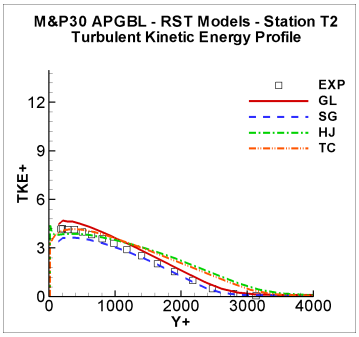

(b) RST models - station T2

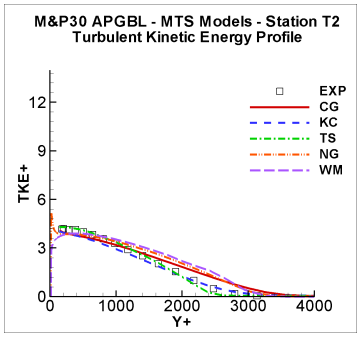

(c) MTS models - station T2

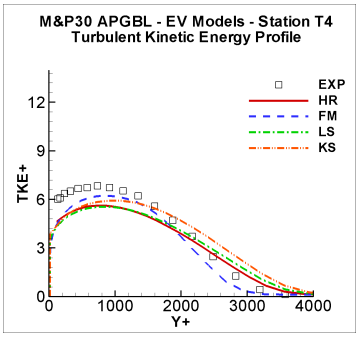

(d) EV models - station T4

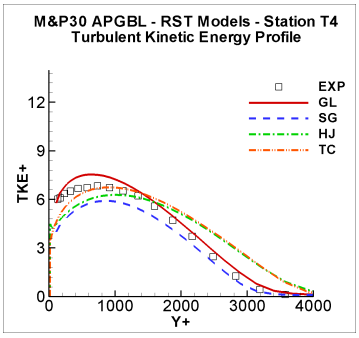

(e) RST models - station T4

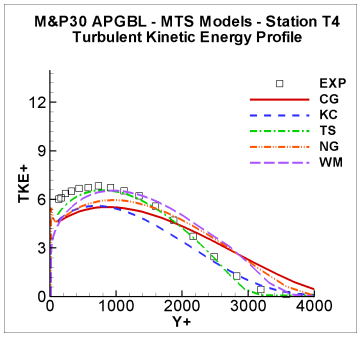

(f) MTS models - station T4

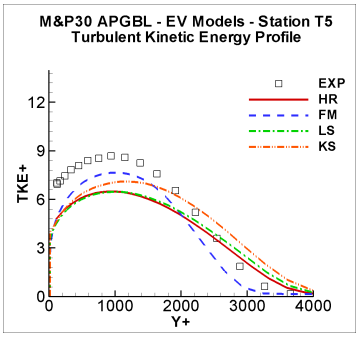

(g) EV models - station T5

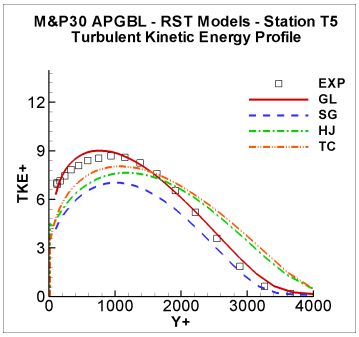

(h) RST models - station T5

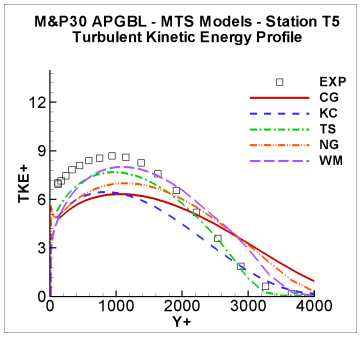

(i) MTS models - station T5

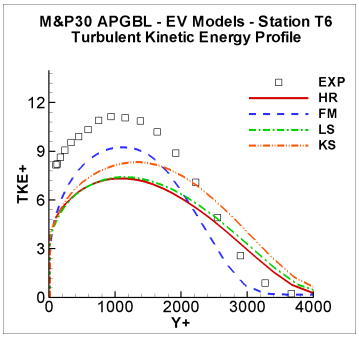

(j) EV models - station T6

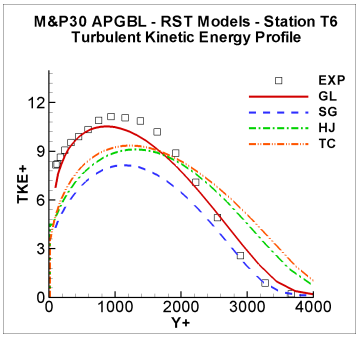

(k) RST models - station T6

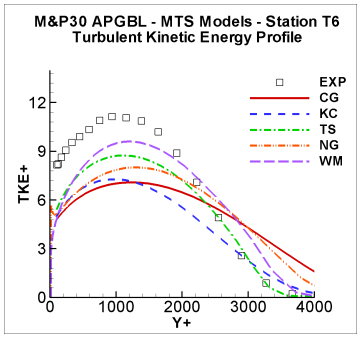

(l) MTS models - station T6

Figure 5.105: Turbulent kinetic energy at stations T2, T4, T5 and T6 for the M&P30 case predicted by the eddy-viscosity, Reynolds stress transport and multiple-time-scale models. Models as in Table 3.25.

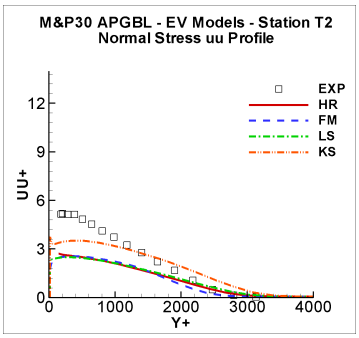

(a) EV models - station T2

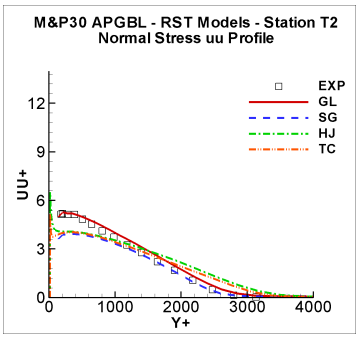

(b) RST models - station T2

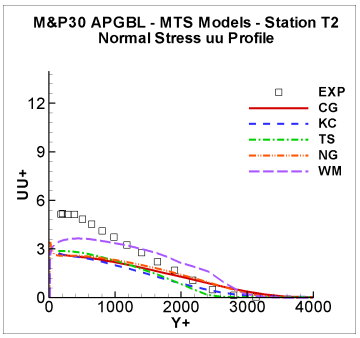

(c) MTS models - station T2

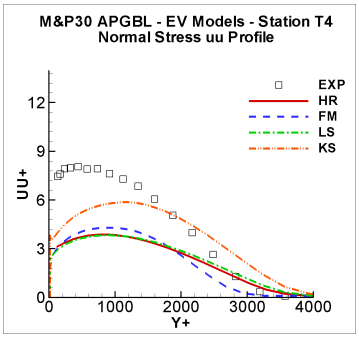

(d) EV models - station T4

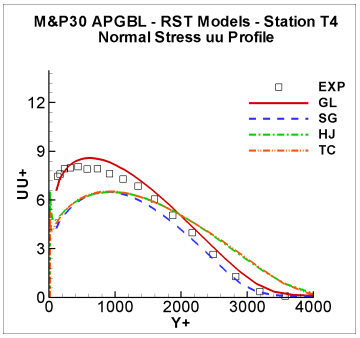

(e) RST models - station T4

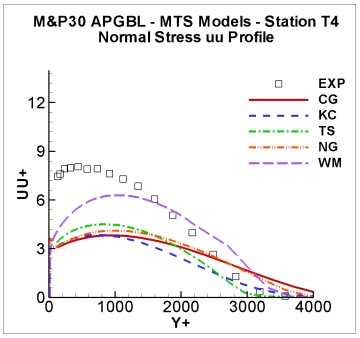

(f) MTS models - station T4

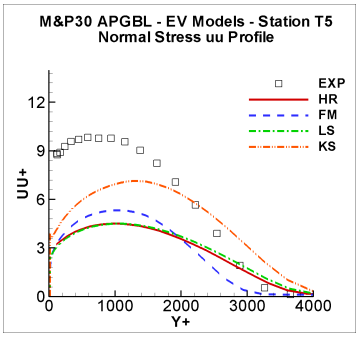

(g) EV models - station T5

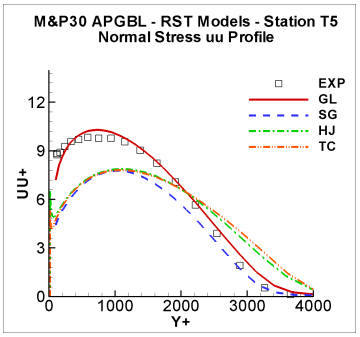

(h) RST models - station T5

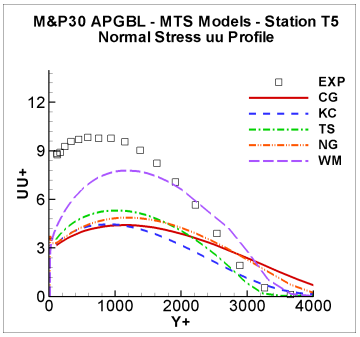

(i) MTS models - station T5

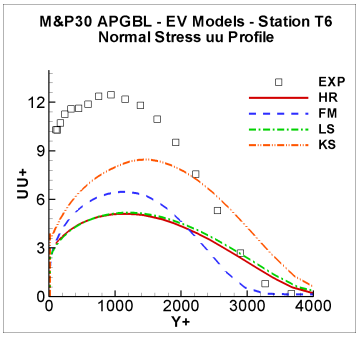

(j) EV models - station T6

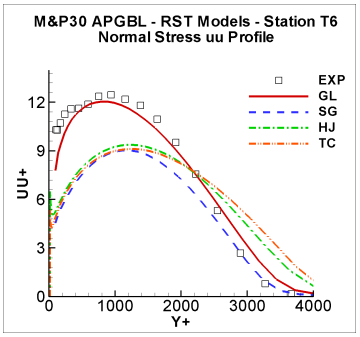

(k) RST models - station T6

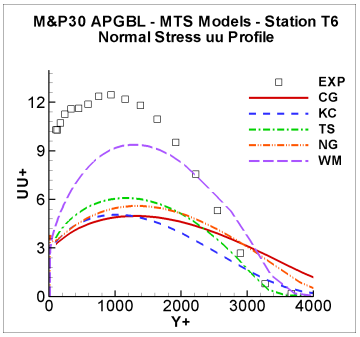

(l) MTS models - station T6

Figure 5.106: Reynolds normal stress $\overline{u^2}$ at stations T2, T4, T5 and T6 for the M&P30 case predicted by the eddy-viscosity, Reynolds stress transport and multiple-time-scale models. Models as in Table 3.25.

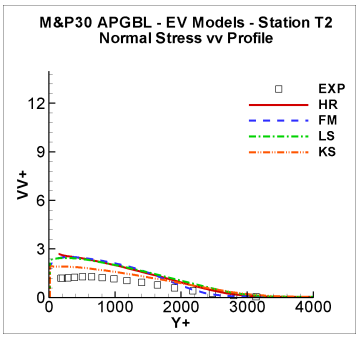

(a) EV models - station T2

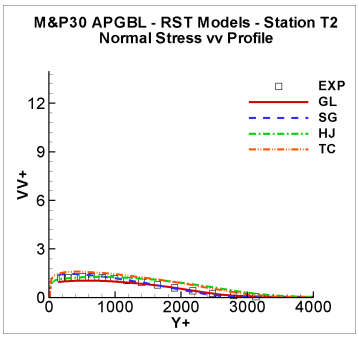

(b) RST models - station T2

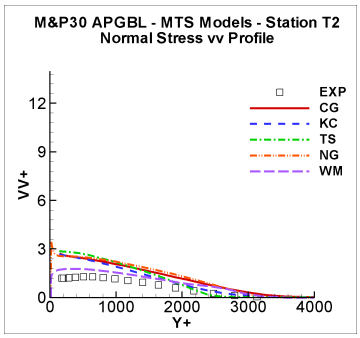

(c) MTS models - station T2

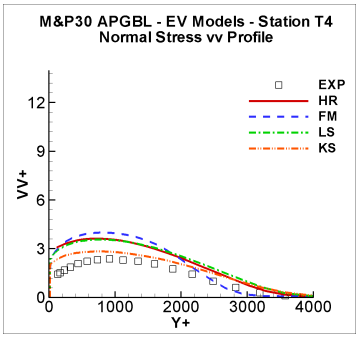

(d) EV models - station T4

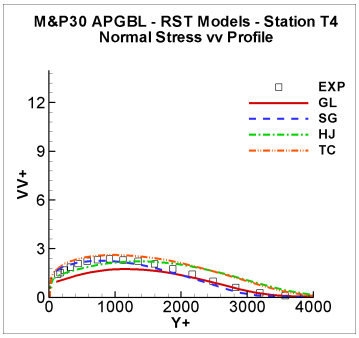

(e) RST models - station T4

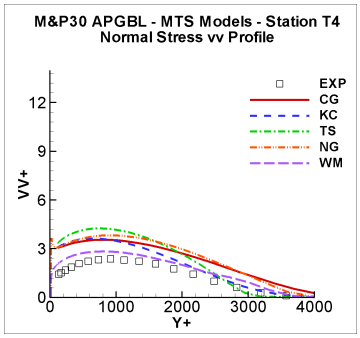

(f) MTS models - station T4

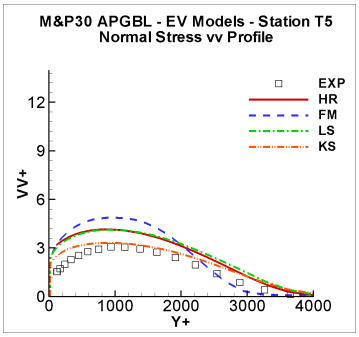

(g) EV models - station T5

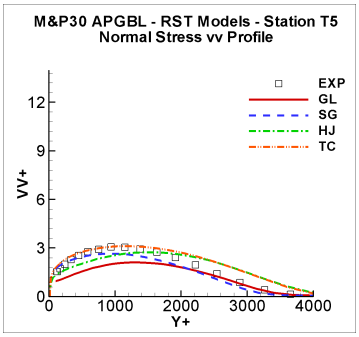

(h) RST models - station T5

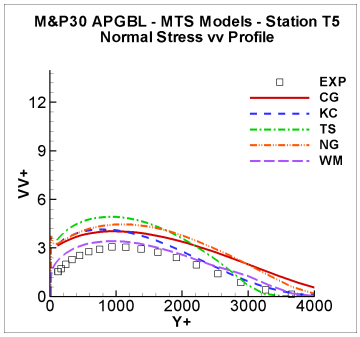

(i) MTS models - station T5

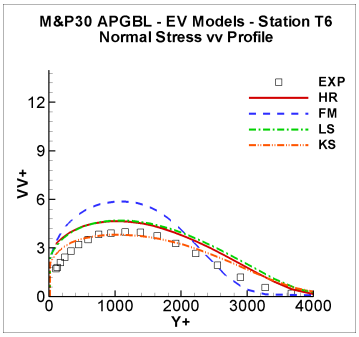

(j) EV models - station T6

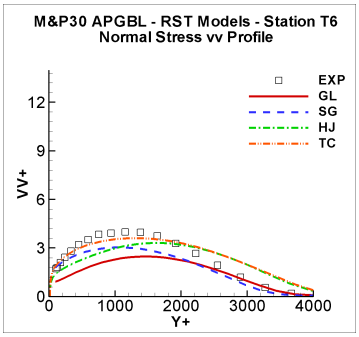

(k) RST models - station T6

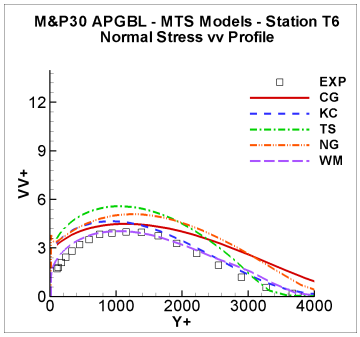

(l) MTS models - station T6

Figure 5.107: Reynolds normal stress $\overline{v^2}$ at stations T2, T4, T5 and T6 for the M&P30 case predicted by the eddy-viscosity, Reynolds stress transport and multiple-time-scale models. Models as in Table 3.25.

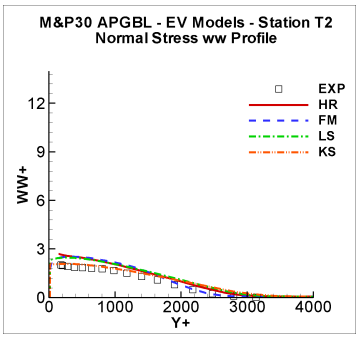

(a) EV models - station T2

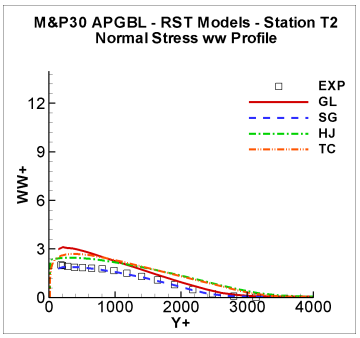

(b) RST models - station T2

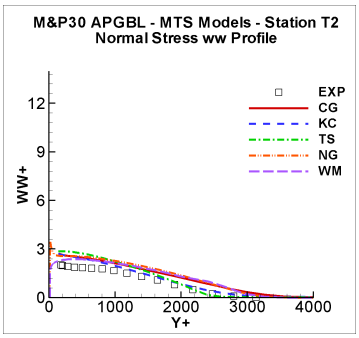

(c) MTS models - station T2

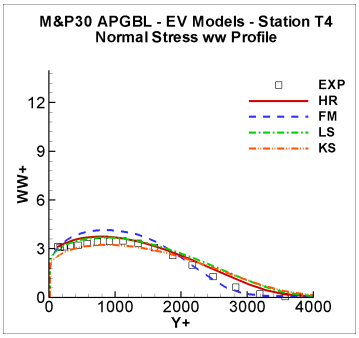

(d) EV models - station T4

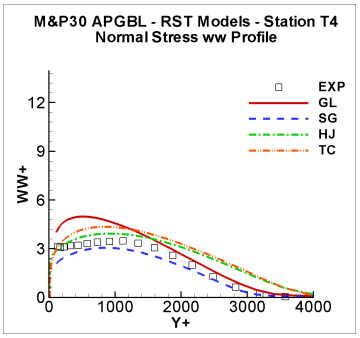

(e) RST models - station T4

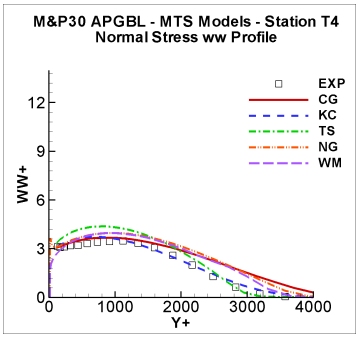

(f) MTS models - station T4

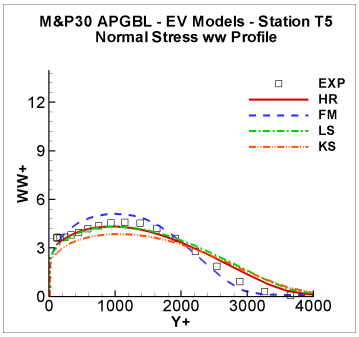

(g) EV models - station T5

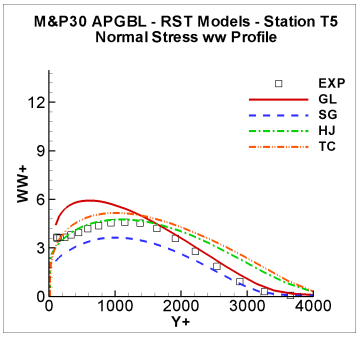

(h) RST models - station T5

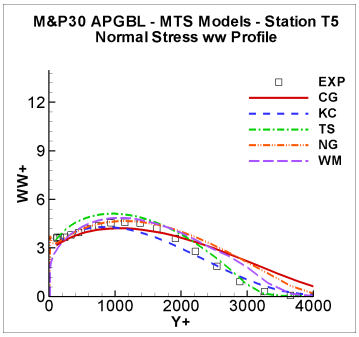

(i) MTS models - station T5

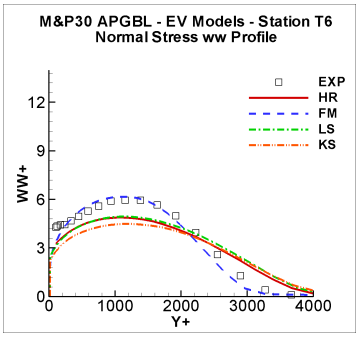

(j) EV models - station T6

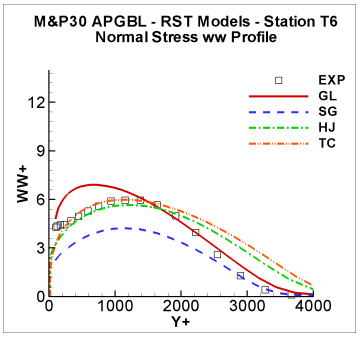

(k) RST models - station T6

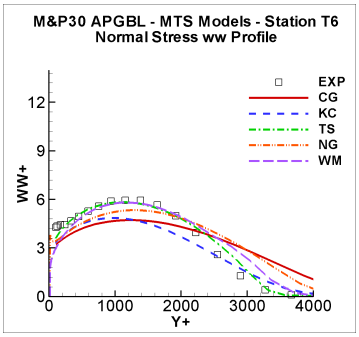

(l) MTS models - station T6

Figure 5.108: Reynolds normal stress $\overline{w^2}$ at stations T2, T4, T5 and T6 for the M&P30 case predicted by the eddy-viscosity, Reynolds stress transport and multiple-time-scale models. Models as in Table 3.25.

5.6 Favourable Pressure Gradient Boundary Layer

In the favourable pressure gradient boundary layer there is a negative pressure gradient driving the flow. As the pressure decreases along the streamwise direction, the freestream velocity increases which then justifies another name for this kind of flow which is accelerating flow.

One of the most particular and interesting characteristics of the favourable pressure gradient boundary layer is that it reaches a self-similar profile, since the velocity increases at the same rate the boundary layer thickness diminishes. When the self-similar state is then achieved, the dimensionless boundary layer parameters such as the skin-friction coefficient C_f, the shape factor H and the Reynolds number based on the displacement thickness, Re_δ, and momentum thickness, Re_θ, become constant.

A favourable pressure gradient can happen by being artificially imposed or in converging channels also called sink flows. When subjected to a favourable pressure gradient, the viscous sublayer becomes more dominant in the boundary layer (whose height decreases as the free stream velocity increases) and, among other effects, the flow may end up by laminarizing for sufficiently strong pressure gradients.

When dealing with favourable pressure gradients boundary layers, one usually defines the level of acceleration of a flow through the so-called acceleration parameter K which is defined as:

$$K = \frac{\nu}{U_\infty^2}\frac{dU_\infty}{dx} \tag{5.19}$$

The acceleration parameter definition can then be used to determine how the free-stream velocity increases with the streamwise direction. Equation (5.19) can be reorganized and integrated, providing:

$$U(x) = \frac{1}{\frac{1}{U_0} - \frac{K}{\nu}x} \tag{5.20}$$

where U_0 is the inlet free stream velocity. In the free stream region, where the flow can be considered steady and viscous effects can be neglected, Bernoulli's equation ($\frac{U^2}{2} + gh + \frac{P}{\rho} = constant$) can be employed in order to determine how the pressure varies as a function of the streamwise direction:

$$P_0 + \frac{1}{2}\rho U_0^2 = P_\infty + \frac{1}{2}\rho U_\infty^2 \qquad \Rightarrow \qquad P_\infty(x) = P_0 + \frac{\rho}{2}[U_0^2 - U_\infty^2(x)] \tag{5.21}$$

where P_0 is the inlet free stream pressure.

5.6.1 Simulated Cases

Jones and Launder (1972a) studied sink-flows in order to identify the maximum value the

acceleration parameter K could take before the flow laminarized. In their work, Jones and Launder could not report a single specific value for which the flow laminarized, however they determined a range of values ($K > 3 \times 10^{-6}$) over which laminarization could be expected to occur.

Spalart (1986) performed a further study about sink flows through DNS and compared his results with Jones and Launder's. In his work, Spalart defined $K = 2.75 \times 10^{-6}$ as the maximum value the acceleration parameter could have before laminarization would occur.

In this work, 2D turbulent favourable pressure gradient boundary layer flows have been simulated with three different acceleration parameters: $K = 1.5 \times 10^{-6}$, $K = 2.5 \times 10^{-6}$ and $K = 2.75 \times 10^{-6}$, since the objective is to simulate the turbulent boundary layer rather than the relaminarization process. The simulation results will be compared with Spalart's 1986 DNS which can be obtained online at *http://cfd.mace.manchester.ac.uk/ercoftac/*. The cases will be named here as K150, K250 and K275, corresponding to acceleration parameters of 1.5×10^{-6}, 2.5×10^{-6} and 2.75×10^{-6} respectively.

5.6.2 Simulations Setup

Since the comparisons made with the DNS data of Spalart will only be of dimensionless quantities, the exact flow properties used do not really matter. The inlet free-stream velocity and density were therefore set to unity, and the viscosity taken as $\mu = \frac{1}{Re_{bulk}}$.

The geometry of the case was again very simple consisting of a rectangle with boundary conditions set in the same way as in the previous flow cases: no-slip condition at the wall (south face), linear interpolation for the pressure at the inlet (west face), zero gradient for all variables at the outlet (east face) and zero gradient for all variables except the pressure for the free stream boundary (north face) where a pressure gradient was imposed by applying equation (5.21). The freestream velocity variation of equation (5.20) was not imposed, but it was checked that the computed profile did match this.

Calculations of a developing boundary layer were carried out, in order to ensure the domain length was long enough to achieve a self-similar state. It was then found that a domain length of 5.2m was sufficient for the boundary layer to achieve self-similarity. The domain height of 0.2m was also confirmed to ensure sufficient resolution of the boundary layer.

One may notice from equation (5.20) that one needs to ensure that $\frac{1}{U_0} - \frac{K}{\nu}x \geq 0$, since this expression is in the denominator and the velocity should not become infinite. As the domain length was already determined and the inlet free stream velocity was taken as unity, one can calculate the maximum bulk Reynolds number (recall that $\mu = \frac{1}{Re_{bulk}}$) for each case, that would ensure the above condition remained true, which is presented in Table 5.12 where the Reynolds number actually used in each simulation is also indicated.

The inlet conditions were initially set as in the previous boundary layer flows, following equation (5.17), where the turbulence intensity was set to 1.5% and the turbulent length scale was estimated as 10mm. The boundary layer was then allowed to develop for a streamwise

Table 5.12: Bulk Reynolds number for each favourable pressure gradient boundary layer case

Case	Maximum Re_{bulk}	Adopted Re_{bulk}
K150	128205	87489
K250	76923	63291
K275	69930	63291

distance of 0.8m before the favourable pressure gradient was applied. This worked for the high Reynolds number turbulence models, however it did not for the LS and KS models which resulted in a laminar solution for both K250 and K275 cases. This problem happened because the turbulent boundary layer (developing from a uniform inlet profile) was not totally developed before the non-zero pressure gradient was imposed, thus making it possible for E term in these models to induce a laminar profile. The problem was solved by first allowing the boundary layer to develop somewhat more under zero pressure gradient conditions. In order to avoid lengthening the domain, the previously computed zero pressure gradient boundary layer profiles were applied as inlet conditions for the LRN turbulence models. These then developed for a further 0.8m before the favourable pressure gradient was applied.

As a wall-bounded domain, different grids were necessary for the high and low Reynolds number turbulence models, being termed the Coarse and the Refined grids respectively. The geometry as well as the mesh specifications are presented in Table 5.13. Grid independence tests were performed with a refined grid of 500x201 and a coarse one of 500x151, and the results from the meshes presented in Table 5.13 can be considered grid independent.

Table 5.13: Geometry and mesh features for the adverse pressure gradient boundary layer cases

Case	Domain height (m)	Domain length (m)	Mesh	NI	NJ
K150	0.2	6.0	Refined	450	121
			Coarse	450	61
K250	0.2	6.0	Refined	450	151
			Coarse	450	71
K275	0.2	6.0	Refined	450	171
			Coarse	450	81

5.6.3 Results and Discussion

In order to illustrate the effect the acceleration parameter has on the mean velocity and turbulent quantities profiles, Figure 5.109 was built with the DNS data of Spalart (1986). One may observe that the velocity profile lies above the wake part of the log law and the turbulent quantities tend to have their peaks decreased near the wall as the acceleration parameter increases, in contrast to what happened in the adverse pressure gradient boundary layer flows and consistent with the tendency of laminarization of the favourable pressure gradient boundary layer flows.

Analysing the computed boundary layer parameters in Figures 5.110 to 5.112 for the

lowest acceleration parameter case, one may comment that the skin-friction coefficient as well as the shape factor attain reasonably constant values, characterizing the self-similar state this flow reaches. On the other hand, Re_θ values appear to continue changing downstream, although this was traced to imprecisions in the numerical integration procedure required to calculate the momentum thickness (any small departure from free-stream velocity in the outer domain can lead to large contributions in the integral for θ). These same checks for self-similarity were also performed for the other two higher acceleration parameters cases, and profiles of velocity and turbulence quantities across the boundary layer for comparison with the DNS data were taken at $x = 4m$ since the boundary layers had achieved self-similarity by this location.

Starting by analysing the case with the lowest acceleration parameter, $K = 1.5 \times 10^{-6}$, one may notice that the velocity profile (Figure 5.113) was reasonably well predicted by all models, apart from the LS and HJ models, since the former overpredicted it and the latter underpredicted the velocity profile. It is worth noticing that even the HRN models, run together with wall functions, presented good agreement with the velocity profile. The reason for that may be the high Reynolds number of the flow, which then attenuates the influence of the wall function, or even an effect of the wall function since the latter tends to make the models overpredict the velocity profile and because of that, the simulations' results end up matching the DNS because the latter does lie above the log law in favourable pressure gradient boundary layer flows. The LS and KS models probably overpredicted the velocity profile due to the E term (equations (3.8) and (3.9) for the LS model and (3.18) and (3.19) for the KS model) which tends to laminarize the solution in these acceleration flows. Although the TC model also has an E term in its modelled ε equation, it is of a more complex form, and does not appear to laminarize the flow so much at this low acceleration parameter. The difference seen between the HJ results here, and those published in their original paper are similar to those already discussed in the zero pressure gradient case.

The turbulent kinetic energy k (Figure 5.114) in the K150 case was overall best predicted by the KS, TC and NG models, since they best captured its near-wall peak and followed well the trend towards the outer layer. The near-wall peak of the eddy dissipation rate (Figure 5.115) was well captured by the NG model and its decay across the boundary layer was well predicted by most models, except the ones which were applied together with wall functions.

With regard to the Reynolds stresses in the K150 case, one may notice that the shear stress $\overline{uv}$ (Figure 5.116) was well predicted by the KS, FM and NG models. The near-wall peak of the Reynolds normal stress $\overline{u^2}$ (Figure 5.117) was captured by the HJ model, however the outer boundary layer was predicted better by most other models. Although the normal Reynolds stress $\overline{v^2}$ (Figure 5.118) was a bit overpredicted by the RST models, they still provided best predictions of this quantity, and the Reynolds normal stress $\overline{w^2}$ (Figure 5.119) had its near-wall peak overpredicted by all turbulence models while its profile in the outer part of the boundary layer was well captured by most models.

Now, analysing the K250 results, one may notice that the KS and NG models were the ones which best predicted the mean velocity profile in Figure 5.120. Most other models

tended to underpredict the velocity profile, specially the HRN models, used together with wall functions. Once the velocity departs from the log-law, it is not expected that these wall-functions would do well, since they put the near-wall velocity on the log-law. The Reynolds shear stress $\overline{uv}$ (Figure 5.121) was better predicted by the MTS models, in particular the NG model which captured the near-wall peak. The normal stresses were better predicted by the TC model as a whole, however the HJ model was the only RST model to reach the near wall peak of $\overline{u^2}$. The turbulent kinetic energy (Figure 5.125) and the eddy dissipation rate (Figure 5.126) was also better predicted by the NG model.

The analysis done for the K250 case is also totally valid for the K275 case. A sample of the results can be seen in Figures 5.127 to Figure 5.129. Indeed, the increase in the acceleration parameter from one case to the other is not that big and one may expect the results to be similar. It also shows a kind of insensitivity of the turbulence models to this small change in the flow configuration.

Tables 5.14, 5.15 and 5.16 present the boundary layer parameter results obtained in this work by the EV, RST and MTS models respectively, where the values for this work were evaluated at $x = 4m$, as discussed before. In Table 5.14 the results provided by the DNS of Spalart (1986) and those obtained by Deevy (2004) using the LS model are also presented. One may notice that Deevy's results are in broad agreement with the ones calculated in this work.

Comparing Tables 5.14, 5.15 and 5.16 in order to evaluate the performance of the turbulence models used here against the DNS data, one may notice that, overall, the NG model presented the closest prediction for all three boundary layer parameters. The TC model also performed very well in the K150 case. The skin-friction coefficient was acceptably well predicted by all models, except the HJ (too high) and the LS (too low) for the K150 case, while it was mostly overpredicted in the other higher acceleration cases. The values of Re_θ were not overall well predicted the models, except the TC and WM in the K150 case and the NG in the other two cases. However it must be recalled that the Re_θ profile did not reach a constant value (see Figures 5.112) and as this was associated with the numerical integration across the domain, it is not particularly useful to judge the turbulence models' performance by examining this. Finally, the shape factor was also mostly overpredicted by the turbulence models, but again the NG predicted quite well this factor.

Overall, one can say that the KS and specially the NG models were the schemes which performed best in this test case. Both are LRN models which makes sense with the previous comments about wall functions in favourable pressure gradient boundary layers. One may also comment that only the turbulence models with an E term in the ε equation are able to account for the laminarization process. The NG model has extra source terms in k_T and ε_T equations (equations 3.56 and 3.58) which are meant to improve near-wall prediction. On the other hand, the NG model is a LEV model and therefore employs a simpler stress-strain relation than the KS which is a NLEV model.

Table 5.14: Boundary layer parameters calculated by the EV models

Case	Parameter	DNS of Spalart (1986)	LS	FM	HR	KS	Deevy's LS
K150	C_f	0.0050	0.0045	0.0053	0.0051	0.0048	0.0044
	Re_θ	690	569	647	608	593	585
	H	1.42	1.49	1.45	1.58	1.47	1.48
K250	C_f	0.0052	0.0047	0.0059	0.0056	0.0050	0.0047
	Re_θ	415	379	470	446	387	366
	H	1.54	1.60	1.48	1.61	1.57	1.62
K275	C_f	0.0053	0.0048	0.0060	0.0057	0.0051	0.0048
	Re_θ	380	370	464	444	372	336
	H	1.54	1.59	1.47	1.63	1.58	1.64

Table 5.15: Boundary layer parameters calculated by each RST model

Case	Parameter	GL	HJ	SG	TC
K150	C_f	0.0052	0.0061	0.0052	0.0053
	Re_θ	623	757	621	693
	H	1.57	1.41	1.57	1.41
K250	C_f	0.0057	0.0065	0.0057	0.0058
	Re_θ	456	518	456	487
	H	1.60	1.45	1.60	1.44
K275	C_f	0.0058	0.0066	0.0058	0.0059
	Re_θ	452	499	452	475
	H	1.62	1.44	1.62	1.43

Table 5.16: Boundary layer parameters calculated by each MTS model

Case	Parameter	CG	KC	NG	TS	WM
K150	C_f	0.0052	0.0051	0.0049	0.0049	0.0054
	Re_θ	624	603	636	625	701
	H	1.56	1.59	1.44	1.60	1.41
K250	C_f	0.0057	0.0056	0.0052	0.0054	0.0061
	Re_θ	455	442	417	420	505
	H	1.60	1.62	1.54	1.67	1.44
K275	C_f	0.0058	0.0057	0.0052	0.0055	0.0062
	Re_θ	435	437	400	422	496
	H	1.64	1.64	1.55	1.69	1.43

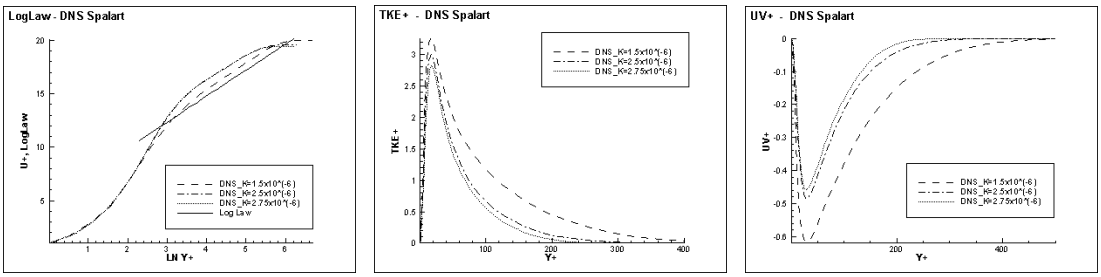

(a) Log law (b) Turbulent kinetic energy (c) Reynolds shear stress $\overline{uv}$

Figure 5.109: Profile of the mean velocity and turbulent quantities as a function of the acceleration parameter K accordingly to the DNS of Spalart (1986).

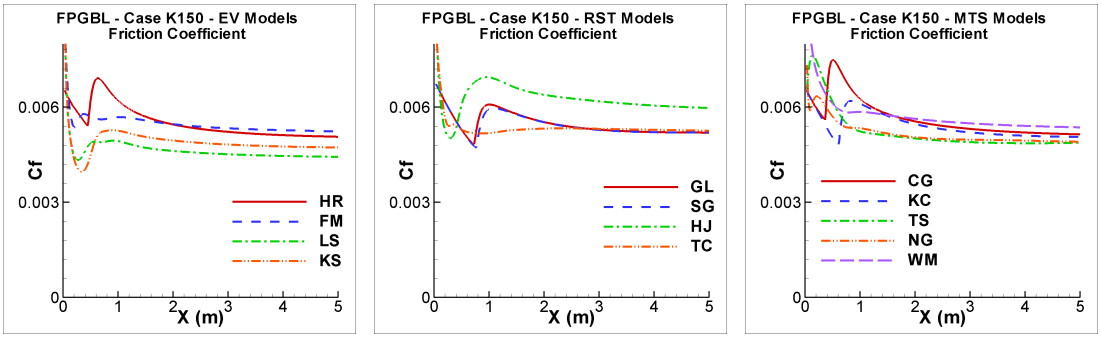

(a) (b) (c)

Figure 5.110: Skin-friction coefficient in the favourable pressure gradient boundary layer with $K = 1.5 \times 10^{-6}$ predicted by the: (a) eddy-viscosity models, (b) Reynolds stress transport models and (c) multiple-time-scale models. Models as in Table 3.25.

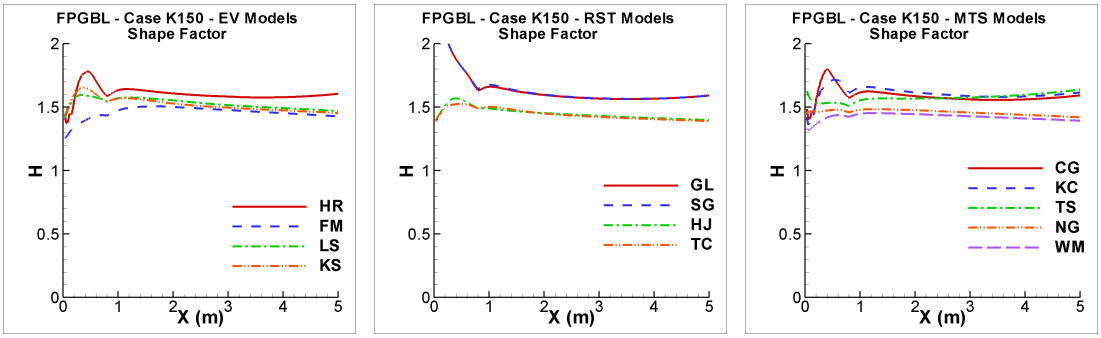

(a) (b) (c)

Figure 5.111: Shape factor in the favourable pressure gradient boundary layer with $K = 1.5 \times 10^{-6}$ predicted by the: (a) eddy-viscosity models, (b) Reynolds stress transport models and (c) multiple-time-scale models. Models as in Table 3.25.

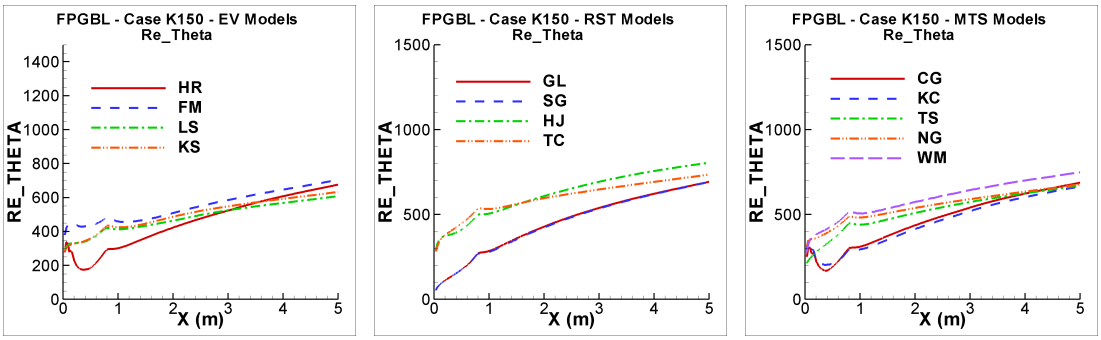

(a) (b) (c)

Figure 5.112: Re_θ in the favourable pressure gradient boundary layer with $K = 1.5 \times 10^{-6}$ predicted by the: (a) eddy-viscosity models, (b) Reynolds stress transport models and (c) multiple-time-scale models. Models as in Table 3.25.

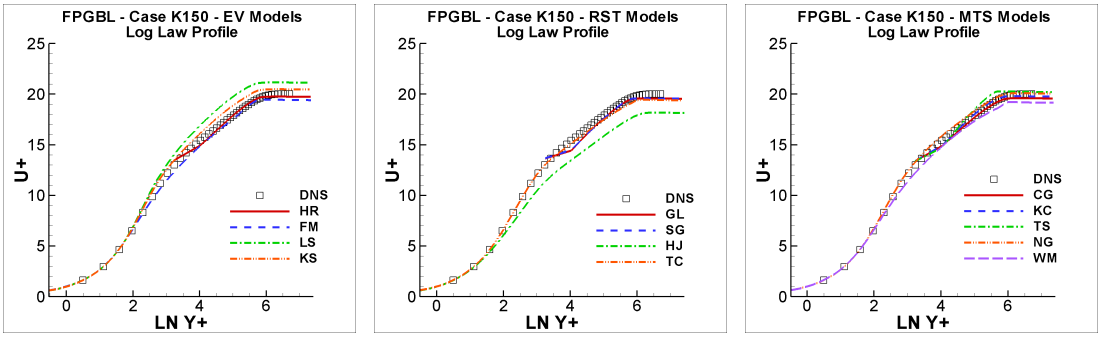

(a) (b) (c)

Figure 5.113: Profile of the mean velocity in the favourable pressure gradient boundary layer with $K = 1.5 \times 10^{-6}$ predicted by the: (a) eddy-viscosity models, (b) Reynolds stress transport models and (c) multiple-time-scale models and compared with the DNS of Spalart (1986). Models as in Table 3.25.

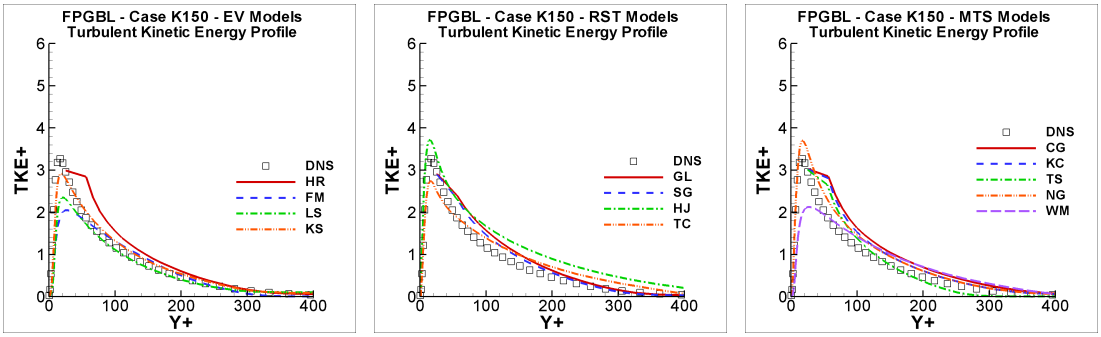

(a) (b) (c)

Figure 5.114: Profile of the turbulent kinetic energy in the favourable pressure gradient boundary layer with $K = 1.5 \times 10^{-6}$ predicted by the: (a) eddy-viscosity models, (b) Reynolds stress transport models and (c) multiple-time-scale models and compared with the DNS of Spalart (1986). Models as in Table 3.25.

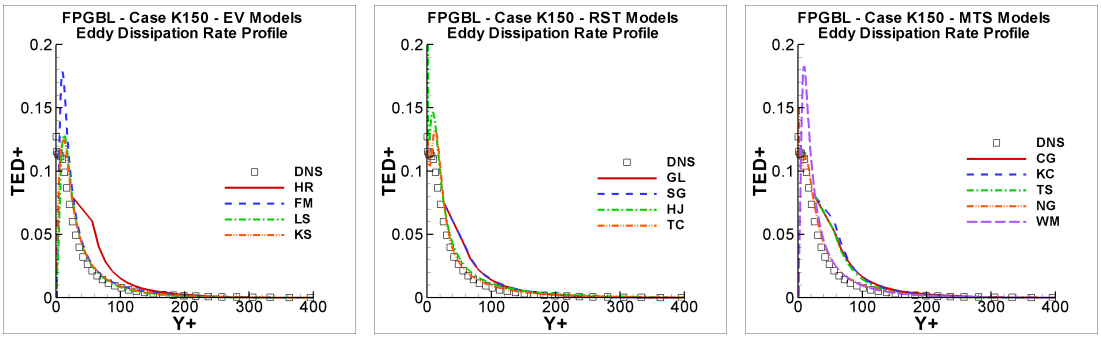

(a) (b) (c)

Figure 5.115: Profile of the turbulent kinetic energy dissipation rate in the favourable pressure gradient boundary layer with $K = 1.5 \times 10^{-6}$ predicted by the: (a) eddy-viscosity models, (b) Reynolds stress transport models and (c) multiple-time-scale models and compared with the DNS of Spalart (1986). Models as in Table 3.25.

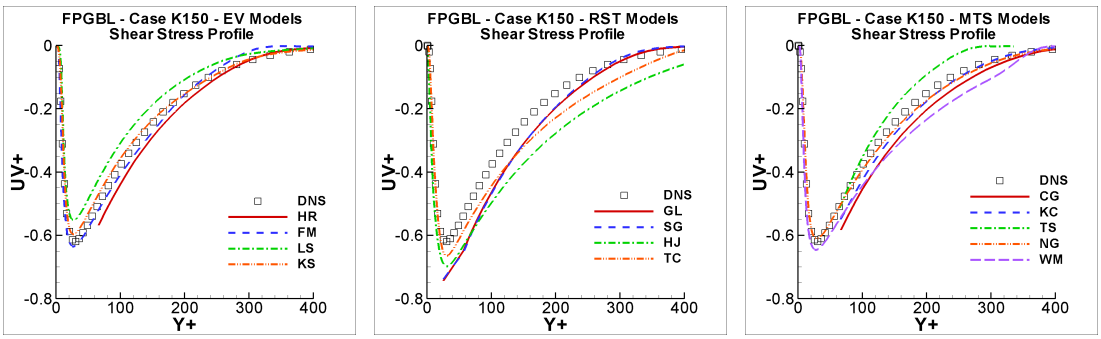

(a) (b) (c)

Figure 5.116: Profile of the Reynolds shear stress $\overline{uv}$ in the favourable pressure gradient boundary layer with $K = 1.5 \times 10^{-6}$ predicted by the: (a) eddy-viscosity models, (b) Reynolds stress transport models and (c) multiple-time-scale models and compared with the DNS of Spalart (1986). Models as in Table 3.25.

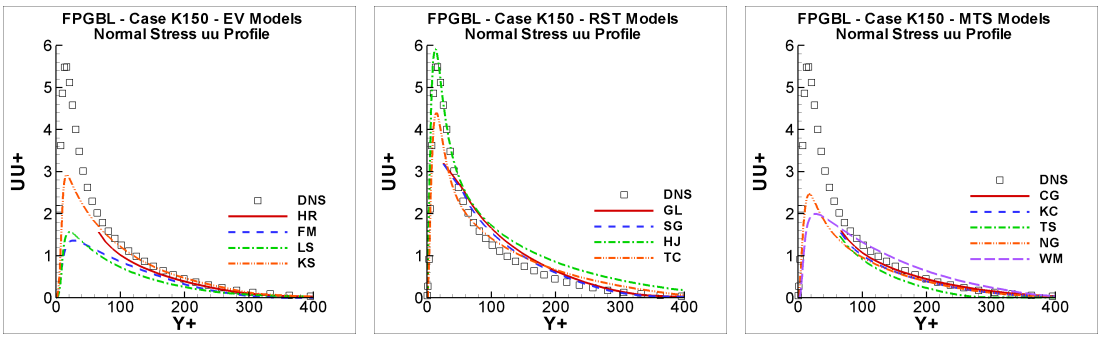

(a) (b) (c)

Figure 5.117: Profile of the Reynolds normal stress $\overline{u^2}$ in the favourable pressure gradient boundary layer with $K = 1.5 \times 10^{-6}$ predicted by the: (a) eddy-viscosity models, (b) Reynolds stress transport models and (c) multiple-time-scale models and compared with the DNS of Spalart (1986). Models as in Table 3.25.

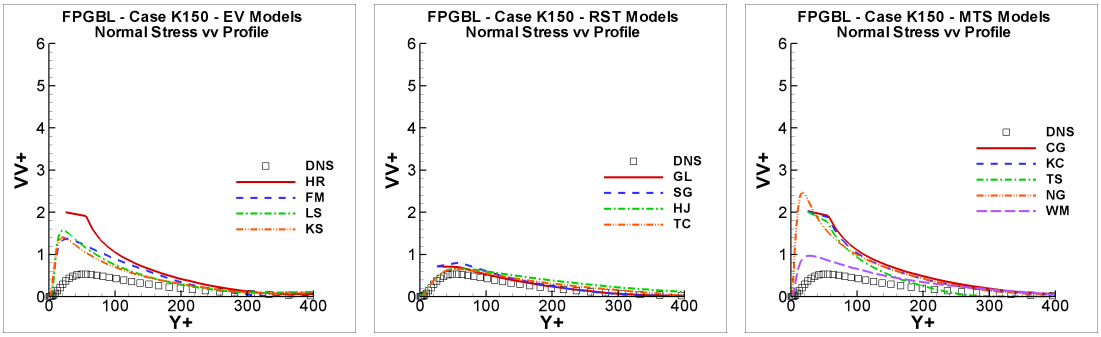

(a) (b) (c)

Figure 5.118: Profile of the Reynolds normal stress $\overline{v^2}$ in the favourable pressure gradient boundary layer with $K = 1.5\times10^{-6}$ predicted by the: (a) eddy-viscosity models, (b) Reynolds stress transport models and (c) multiple-time-scale models and compared with the DNS of Spalart (1986). Models as in Table 3.25.

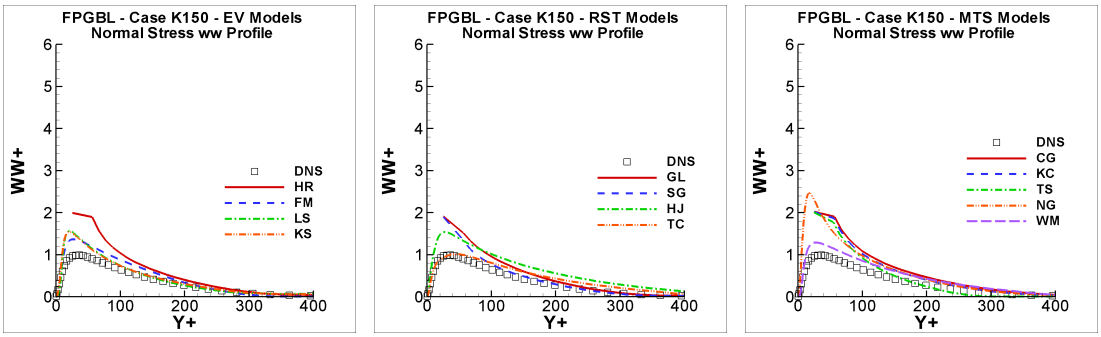

(a) (b) (c)

Figure 5.119: Profile of the Reynolds normal stress $\overline{w^2}$ in the favourable pressure gradient boundary layer with $K = 1.5\times10^{-6}$ predicted by the: (a) eddy-viscosity models, (b) Reynolds stress transport models and (c) multiple-time-scale models and compared with the DNS of Spalart (1986). Models as in Table 3.25.

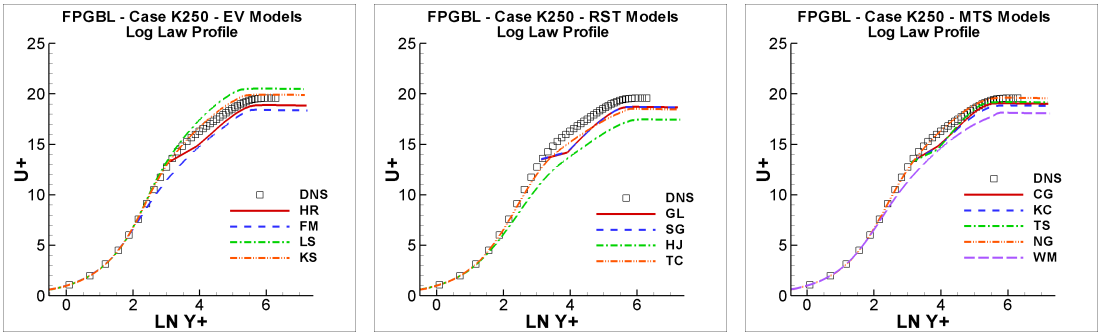

(a) (b) (c)

Figure 5.120: Profile of the mean velocity in the favourable pressure gradient boundary layer with $K = 2.5 \times 10^{-6}$ predicted by the: (a) eddy-viscosity models, (b) Reynolds stress transport models and (c) multiple-time-scale models and compared with the DNS of Spalart (1986). Models as in Table 3.25.

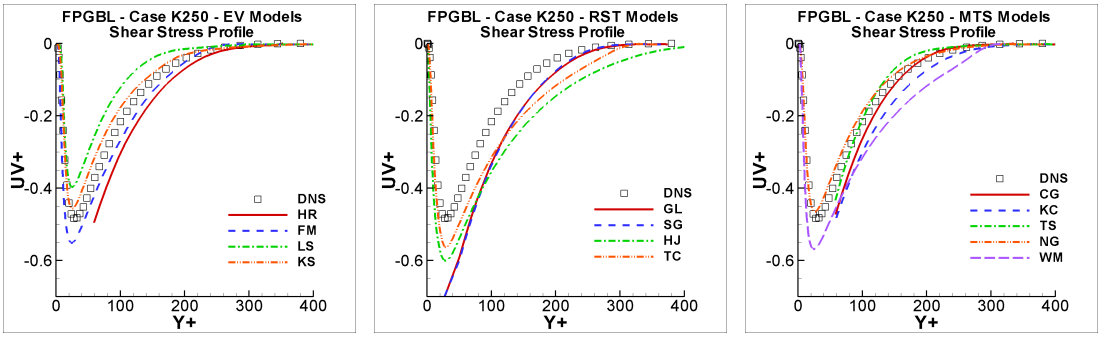

(a) (b) (c)

Figure 5.121: Profile of the Reynolds shear stress $\overline{uv}$ in the favourable pressure gradient boundary layer with $K = 2.5\times10^{-6}$ predicted by the: (a) eddy-viscosity models, (b) Reynolds stress transport models and (c) multiple-time-scale models and compared with the DNS of Spalart (1986). Models as in Table 3.25.

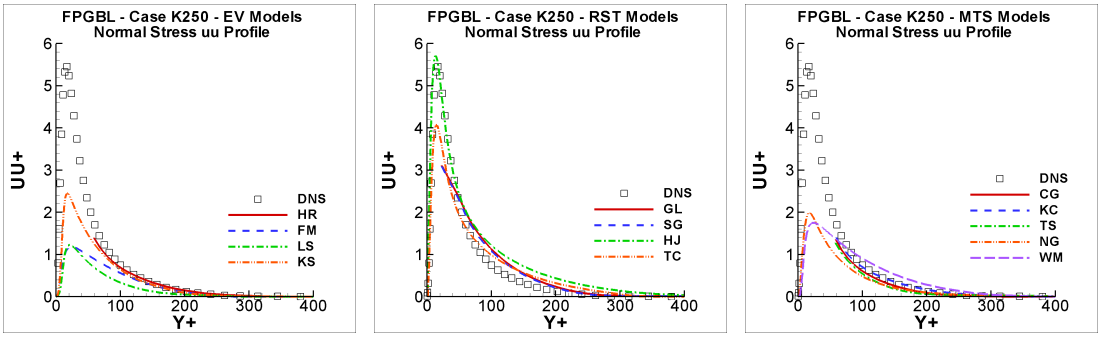

(a) (b) (c)

Figure 5.122: Profile of the Reynolds normal stress $\overline{u^2}$ in the favourable pressure gradient boundary layer with $K = 2.5\times10^{-6}$ predicted by the: (a) eddy-viscosity models, (b) Reynolds stress transport models and (c) multiple-time-scale models and compared with the DNS of Spalart (1986). Models as in Table 3.25.

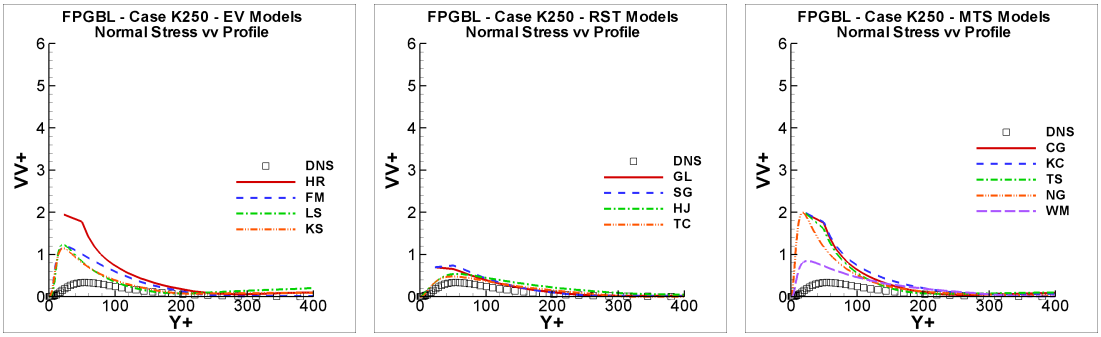

(a) (b) (c)

Figure 5.123: Profile of the Reynolds normal stress $\overline{v^2}$ in the favourable pressure gradient boundary layer with $K = 2.5\times10^{-6}$ predicted by the: (a) eddy-viscosity models, (b) Reynolds stress transport models and (c) multiple-time-scale models and compared with the DNS of Spalart (1986). Models as in Table 3.25.

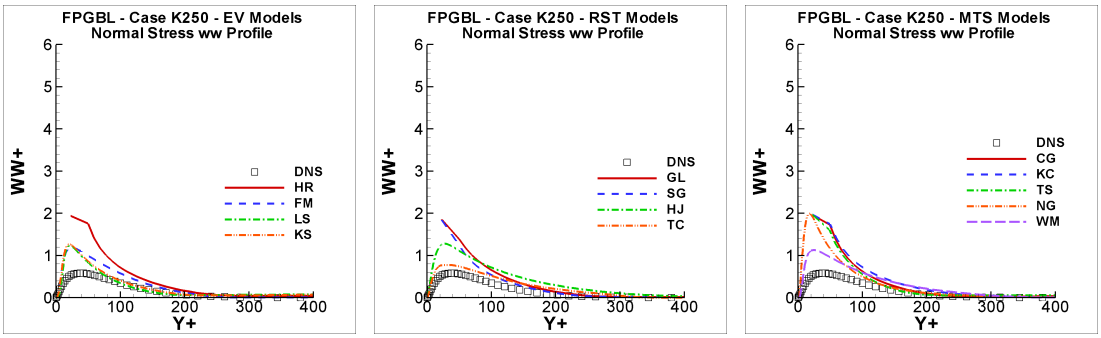

(a) (b) (c)

Figure 5.124: Profile of the Reynolds normal stress $\overline{w^2}$ in the favourable pressure gradient boundary layer with $K = 2.5\times10^{-6}$ predicted by the: (a) eddy-viscosity models, (b) Reynolds stress transport models and (c) multiple-time-scale models and compared with the DNS of Spalart (1986). Models as in Table 3.25.

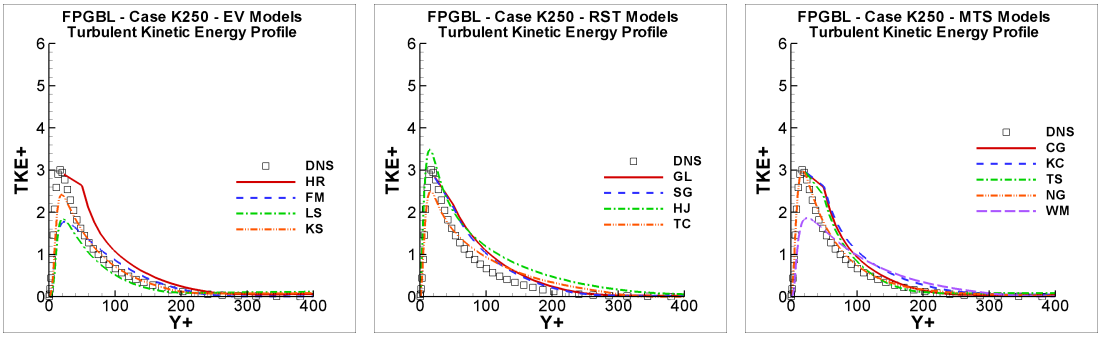

(a) (b) (c)

Figure 5.125: Profile of the turbulent kinetic energy in the favourable pressure gradient boundary layer with $K = 2.5\times10^{-6}$ predicted by the: (a) eddy-viscosity models, (b) Reynolds stress transport models and (c) multiple-time-scale models and compared with the DNS of Spalart (1986). Models as in Table 3.25.

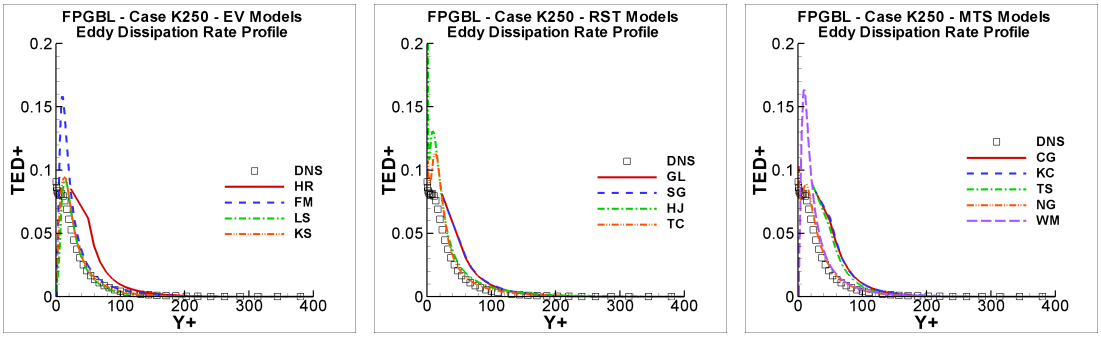

(a) (b) (c)

Figure 5.126: Profile of the turbulent kinetic energy dissipation rate in the favourable pressure gradient boundary layer with $K = 2.5 \times 10^{-6}$ predicted by the: (a) eddy-viscosity models, (b) Reynolds stress transport models and (c) multiple-time-scale models and compared with the DNS of Spalart (1986). Models as in Table 3.25.

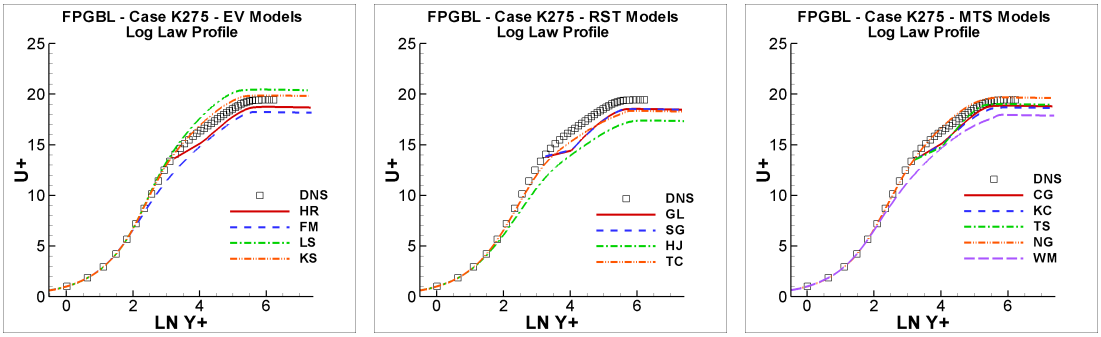

(a) (b) (c)

Figure 5.127: Profile of the mean velocity in the favourable pressure gradient boundary layer with $K = 2.75 \times 10^{-6}$ predicted by the: (a) eddy-viscosity models, (b) Reynolds stress transport models and (c) multiple-time-scale models and compared with the DNS of Spalart (1986). Models as in Table 3.25.

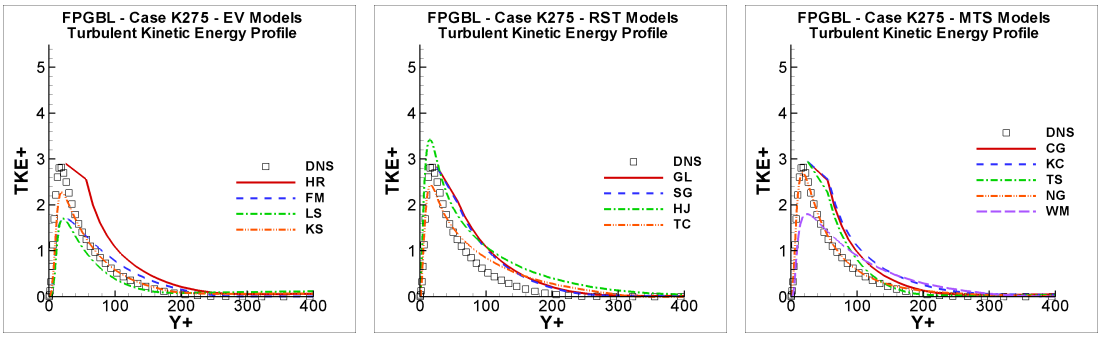

(a) (b) (c)

Figure 5.128: Profile of the turbulent kinetic energy in the favourable pressure gradient boundary layer with $K = 2.75 \times 10^{-6}$ predicted by the: (a) eddy-viscosity models, (b) Reynolds stress transport models and (c) multiple-time-scale models and compared with the DNS of Spalart (1986). Models as in Table 3.25.

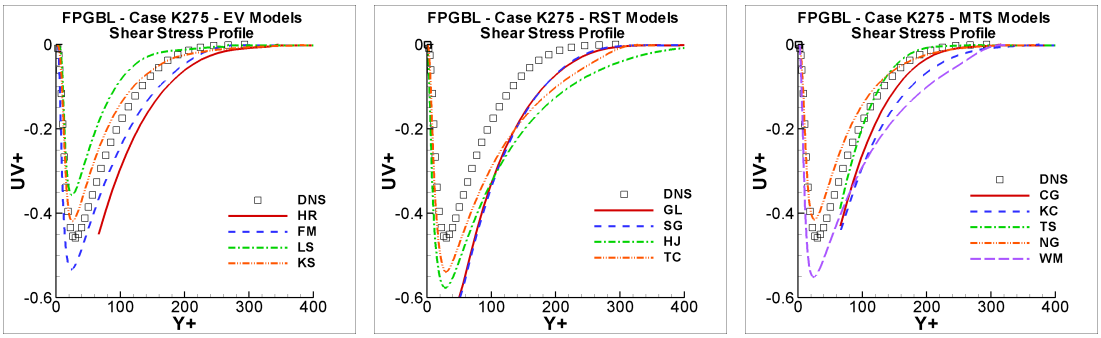

(a) (b) (c)

Figure 5.129: Profile of the Reynolds shear stress $\overline{uv}$ in the favourable pressure gradient boundary layer with $K = 2.75 \times 10^{-6}$ predicted by the: (a) eddy-viscosity models, (b) Reynolds stress transport models and (c) multiple-time-scale models and compared with the DNS of Spalart (1986). Models as in Table 3.25.

5.7 Oscillatory Flows

In this section oscillatory boundary layers and oscillatory pipe flows will be studied. In both cases a periodic sinusoidal oscillation is imposed about a reference velocity (free-stream velocity for the former and bulk velocity for the latter), however in the former case the time-mean reference velocity is zero and in the latter case it is not.

The main interest in these flows lies in how the oscillations imposed on the mean flow propagate to the turbulence and disturb the equilibrium state. When the free-stream or bulk velocity vary sinusoidally, all other quantities such as pressure gradient, wall-shear stress and turbulent quantities will also vary, however they might present phase shifts and time lags when compared to the velocity oscillation. How intense and how quickly the turbulence will be affected will then strongly depend upon the oscillation frequency. There are thus a range of frequencies which would promote non-equilibrium features which would then be interesting for this work.

These flows can also be viewed as providing favourable (velocity being accelerated) and adverse (velocity being decelerated) pressure gradients in sequence thus presenting the challenges of the flows examined earlier, as well as the transition from one to the other.

From a practical viewpoint, these periodic oscillatory flows, also referred to as pulsating flows, are also of great importance in engineering as mentioned by Tu and Ramaprian (1983a), Menendez and Ramaprian (1984), Shemer et al. (1985), Binder et al. (1995) and Scotti and Piomelli (2001), among others, who highlighted aerodynamics, turbomachinery and biofluids as the main fields where these flows take place.

As mentioned in the literature review, phase averaging is used in periodic time dependent flows. Flow quantities are thus decomposed into a time-mean, periodic, and fluctuating parts, represented by $q(x,t) = \overline{q}(x) + \widetilde{q}(x,t) + q'(x,t)$ where the phase average comprises the sum of the time-mean and periodic elements. The phase average will here be denoted by angle brackets, whilst time-averaged quantities will be denoted by an overbar, as in the preceding cases studied.

Below each of the oscillatory flows to be studied will be described and its results will be discussed in order to assess the performance of the turbulence models.

5.7.1 Oscillatory Boundary Layer Flow

In this case the freestream oscillation is imposed about a zero-mean velocity, so the flow totally reverses as illustrated in Figure 5.130.

Simulated Case

The case which will be simulated here is the test number 10 (and 11 which is the same, but the former was set to measure $< u^2 >^{1/2}$, $< v^2 >^{1/2}$ and $< uv >$ and the latter, $< w^2 >^{1/2}$) of the experimental work of Jensen et al. (1989) who performed experiments of oscillatory boundary layers for smooth and rough beds. The reason why this test case was chosen is

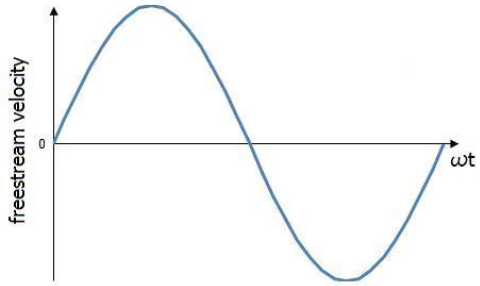

Figure 5.130: Velocity oscillating over its zero time-averaged value

that it represents a smooth bed test case where measurements of the Reynolds stresses were provided.

The free-stream velocity is imposed to vary as $U_\infty = U_{amp}\sin(\omega t)$, where $U_{amp} = 2m/s$ is the absolute amplitude and $\omega = 2\pi f$ is the angular frequency in radians. Jensen et al. (1989) did not vary the frequency range of oscillation, and their experiments were performed for a fixed period where $T = \frac{1}{f} = 9.72s$. This test case will be referred to in this work as the JSF case.

Simulations Setup

In order to simulate this test case, a 1D domain in the y direction was employed, and the x-directed pressure gradient specified to oscillate periodically (as determined from the reported free-stream velocity variation). By doing this, it was only necessary to solve the streamwise direction momentum equation together with the turbulence closure equations.

The simulation was set as unsteady and the pressure gradient was set to vary as $\frac{dP}{dx} = dP_{amp}\sin(\omega t)$, where dP_{amp} is the amplitude magnitude of the pressure gradient which would ensure the free-stream velocity varying with an amplitude magnitude of $U_{amp} = 2m/s$. It must be noticed that there is a phase shift between the pressure gradient and the velocity oscillation. This phase difference was calculated by Mao and Hanratty (1986) as being $-\frac{\pi}{2}$ and was here confirmed. In the presentation of the results below, the time has then been adjusted to give $\omega t = 0^o$ being the time at which the freestream velocity is zero.

Zero gradient boundary conditions were applied for all variables at the north free-stream boundary of the domain, whilst initial conditions were specified by providing the turbulent boundary layer profile of a previous zero pressure gradient boundary layer simulation.

A 1D grid was used, with 112 non-uniformly distributed points in the y direction for the LRN models, which ensured near-wall y^+ values smaller than one throughout the cycle. For the HRN schemes, a 56 node grid was used, which gave y^+ values of up to 60 during the cycle.

Since these are unsteady simulations, the time step must also be specified. As Jensen et al. (1989) provided experimental data every 15^o of the cycle, one would like to process simulation data at these same times. There would be then 24 points in the cycle to be output. The time step was therefore initially set by dividing the period T in 240 parts

($\Delta t = T/240 = 0.0405$), thus imposing 10 steps between each output point. In order to check the time step independence of the results, a refined time step of $\Delta t = 0.02025$ was also used. The results were basically the same, and the results reported below were obtained using the latter, since it resulted in better stability of the simulations. During the initial stages of some simulations it was found necessary to use an even smaller time step for some models, to ensure stability. In particular, the TC model had its first 100 time steps performed with $\Delta t = 0.00405$ and the NG and WM models had their first 200 time steps carried out with $\Delta t = 0.002025$.

The simulations were set to run over six cyclic periods, to ensure they had reached a developed state (in fact, periodicity generally was reached after only two). The simulation output was then taken from the first half of the last period. One may notice that since the time-averaged velocity is zero, the behaviour of the flow from $\omega t = 0^o$ to $\omega t = 180^o$ is totally symmetric to its behaviour from $\omega t = 180^o$ to $\omega t = 360^o$. Therefore, and accordingly with the experimental data provided by Jensen et al. (1989), only the first half, from $\omega t = 0^o$ to $\omega t = 180^o$ is presented.

Results and Discussion

The first check is whether the free-stream velocity and pressure gradient were set correctly. Both profiles can be found in Figure 5.131. Only predictions of the eddy-viscosity models are being shown since these profiles and their implementation are the same for all models. One can notice that the pressure gradient does present a $-\frac{\pi}{2}$ phase shift from the velocity profile and that the latter presents the correct amplitude, thus validating the implementation of the free-stream variation.

In Figure 5.132, one can see the predicted and measured variation of the absolute value of the wall shear stress τ_w. One may notice that interestingly, the LRN turbulence models significantly overpredicted the peak values of this quantity and that the GL, the SG and the KC models provide the best fit to the experimental data.

To give a more detailed picture of the flow behaviour, mean velocity and Reynolds stress profiles will be presented at four phase angles during the cycle ($\omega t = 30^o$, $\omega t = 60^o$, $\omega t = 105^o$ and $\omega t = 135^o$), chosen to give a good representation of the flow changes which occur during the cycle. As the streamwise velocity is varied through a sine function, the two first positions represent stages of the accelerating part and the last two positions represent stages of the decelerating part.

Looking firstly at the velocity profiles, normalized by the maximum friction velocity, in Figures 5.133 to 5.135, one can generally say that all models performed similarly and well. If one looks in more detail, one can notice that the models which are closer to the experimental data in the accelerating part are further away from them in the decelerating part and vice-versa. That would be consistent with the already observed phenomena of the turbulence models not being able to follow the subtle changes presented by the experimental data seen in the adverse pressure gradient boundary layer, for example.

The prediction of the Reynolds shear stress $< uv >$, normalized by the maximum friction velocity, expressed as $< uv+ >$, is presented in Figures 5.136 to 5.138. This quantity is reasonably well predicted by all turbulence models, however one may notice that the HRN models tend to overpredict the $< uv+ >$ values in the outer region as soon as the flow starts to be decelerated.

The prediction of the normal Reynolds stresses is presented in Figures 5.139 to 5.147. Although the linear-eddy-viscosity models are not expected to correctly predict these quantities, their results are being presented for sake of comparison, however the discussion will be based on the NLEV and RST models. The rms of the streamwise fluctuating velocity $< u^2 >^{1/2}$, normalized by the maximum friction velocity, expressed as $< u+ >$, can be seen in Figures 5.139 to 5.141. This represents essentially the prediction of the Reynolds normal stress $< u^2 >$. One may notice that all the turbulence models tend to underpredict this quantity, specially in the decelerating part of the cycle. The wall-normal fluctuating velocity $< v^2 >^{1/2}$, normalized by the maximum friction velocity, expressed as $< v+ >$, can be seen in Figures 5.142 to 5.144. One may notice that this quantity is much better predicted by all turbulence models as a whole and the same comment can be extended to the prediction of the fluctuating velocity $< w^2 >^{1/2}$, presented in Figures 5.145 to 5.147.

Overall, regarding the prediction of the Reynolds stresses, one could say that the HJ model performed best, however its prediction of the velocity profile was not among the best. Considering only the prediction of the velocity and Reynolds shear stress, one could say that the MTS models provided very reasonable results thus indicating the potential such models might have in predicting non-equilibrium flows.

In order to provide some more detail, the time-history of the velocity and the Reynolds stresses at specific locations across the boundary layer are shown. Figures 5.148 to 5.150 show profiles at $y = 4mm$ which corresponds to $y^+ \approx 350$. One may notice that the velocity peak is located at $\omega t \approx 80$ which is approximately where $< v^2 >^{1/2}$ and $< uv >$ peak, however $< u^2 >^{1/2}$ peaks at $\omega t \approx 110$ and none of the turbulence models are actually able to predict this phase shift between the velocity and the streamwise fluctuating velocity. However, as they predict the velocity profile correctly, they provide reasonable prediction for $< v^2 >^{1/2}$ and $< uv >$. The same qualitative analyses can be extended to the other two locations across the boundary layer, for instance, at $y = 9mm$ which is about $y^+ \approx 750$ (Figures 5.151 to 5.153) and $y = 26mm$ which is about $y^+ \approx 2200$ (Figures 5.154 to 5.156).

One may notice some significant differences in predictions though at the fourth point, at $y = 65mm$ which is about $y^+ \approx 5300$, presented in Figures 5.157 to 5.159. While all turbulence models predicted that the turbulence is already basically frozen, the experimental data still show some oscillations at this height (particularly in $< u^2 >^{1/2}$). No plots are presented even further from the wall, since there is no more experimental data available for comparison. These results show no significant difference between the general behaviours of the STS and MTS models.

As a general conclusion of this case, one could say that both velocity and Reynolds shear stress were well predicted by all turbulence models. The rms streamwise normal stress

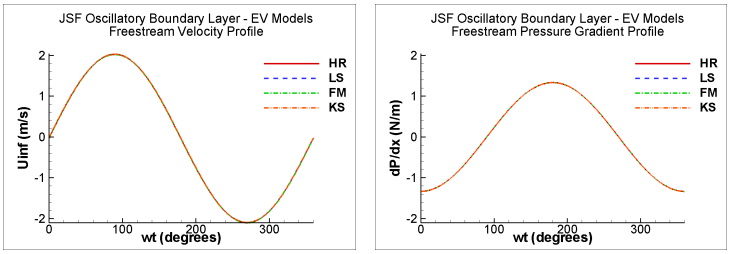

(a) velocity profile (b) pressure gradient profile

Figure 5.131: Checking the velocity and pressure gradient profiles for the JSF oscillatory boundary layer case with the eddy-viscosity models. Models as in Table 3.25.

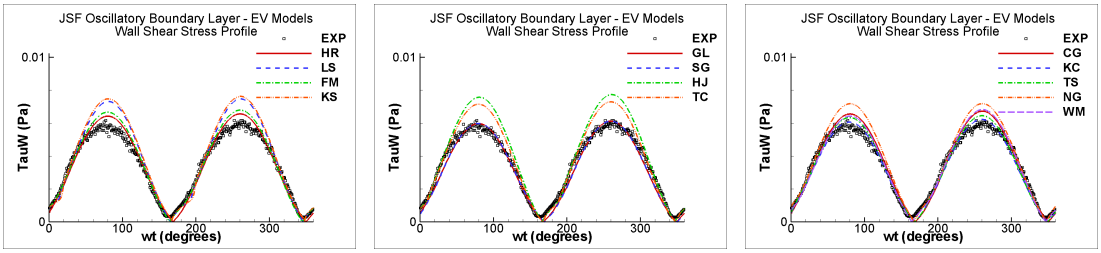

(a) (b) (c)

Figure 5.132: Prediction of the wall shear stress by the: (a) eddy-viscosity models, (b) Reynolds stress transport models and (c) multiple-time-scale models in the JSF oscillatory boundary layer case. Models as in Table 3.25.

component $< u^2 >^{1/2}$ was not captured by any RST model during the cycle and there was a clear phase shift in the measured data between u' and the mean velocity which was not captured by the RST models. The other two components of the fluctuating velocity were relatively well predicted throughout the cycle and did not show a significant phase shift in relation to the velocity. That would indicate a "deficiency" in the redistribution mechanism of the RST models which might then be improved if multiple time scales, such as the large and small time scales represented in the MTS models, were introduced into the redistribution process modelling.

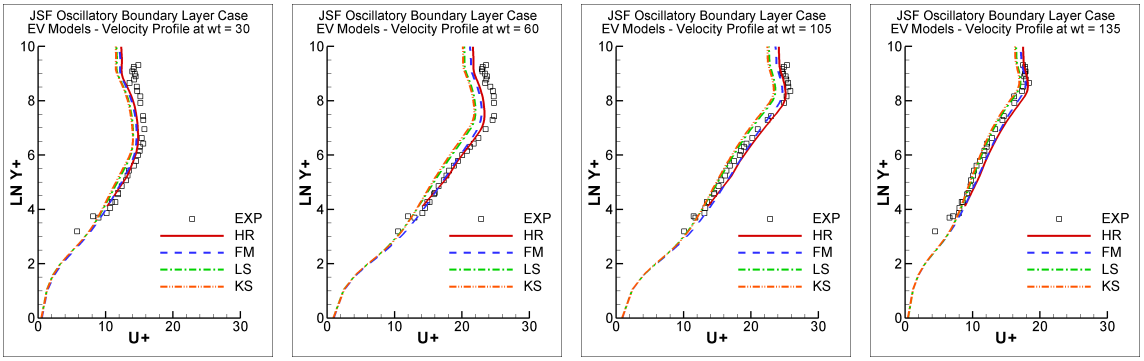

(a) (b) (c) (d)

Figure 5.133: Velocity profile at selected cycle positions in JSF oscillatory boundary layer case predicted by the eddy-viscosity models and compared with the experiments of Jensen et al. (1989). Models as in Table 3.25.

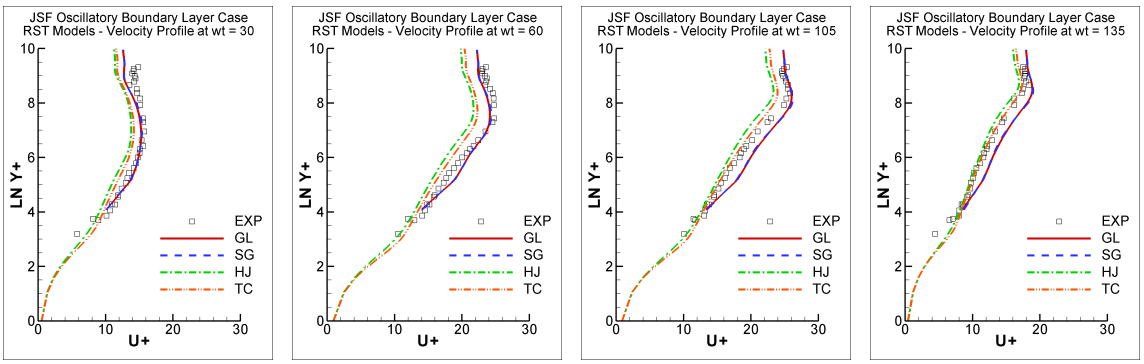

(a) (b) (c) (d)

Figure 5.134: Velocity profile at selected cycle positions in JSF oscillatory boundary layer case predicted by the Reynolds stress transport models and compared with the experiments of Jensen et al. (1989). Models as in Table 3.25.

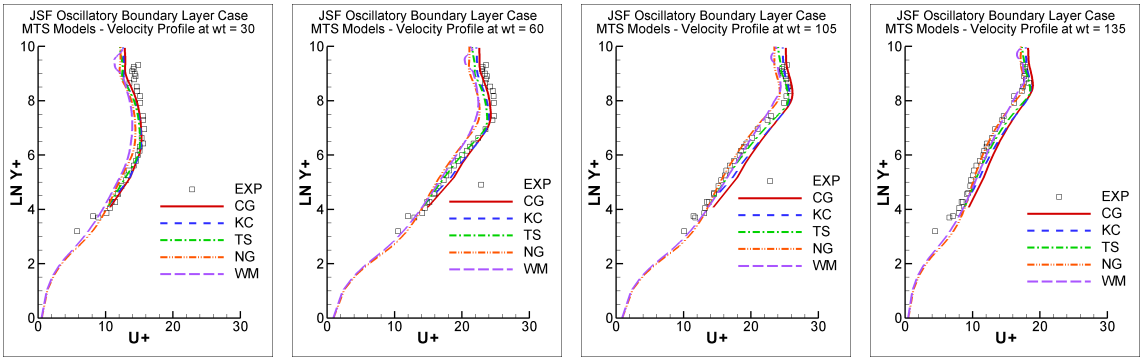

(a) (b) (c) (d)

Figure 5.135: Velocity profile at selected cycle positions in JSF oscillatory boundary layer case predicted by the multiple-time-scale models and compared with the experiments of Jensen et al. (1989). Models as in Table 3.25.

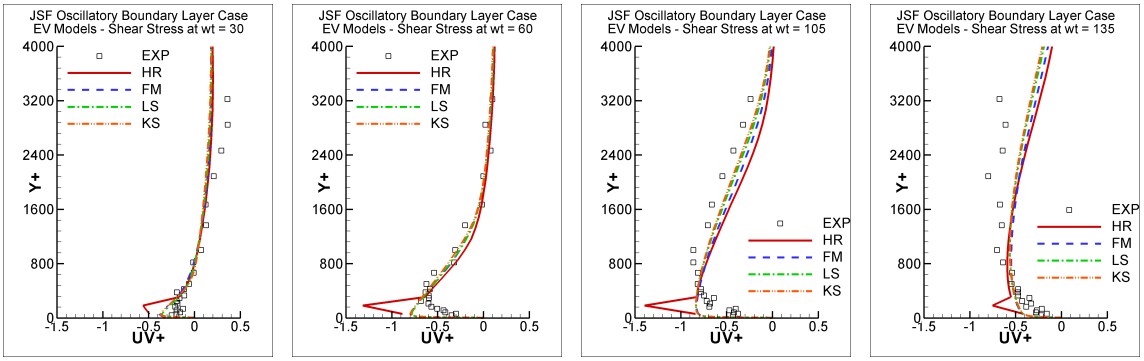

(a) (b) (c) (d)

Figure 5.136: Reynolds shear stress $< uv+ >$ profile at selected cycle positions in JSF oscillatory boundary layer case predicted by the eddy-viscosity models and compared with the experiments of Jensen et al. (1989). Models as in Table 3.25.

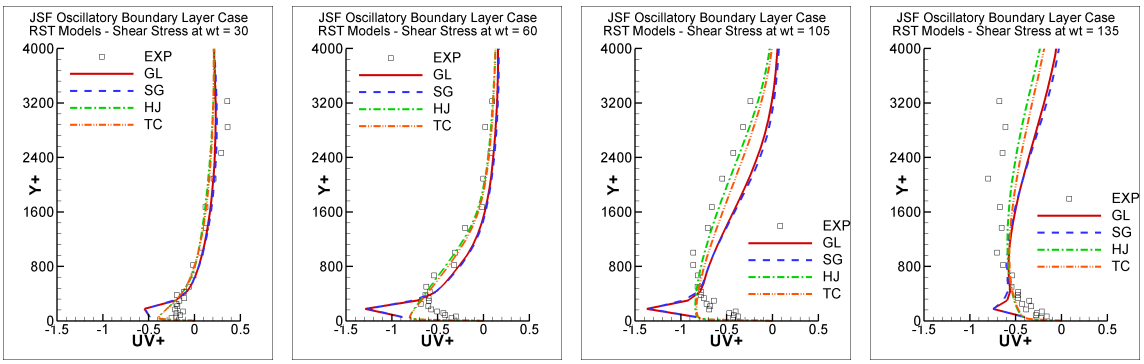

(a) (b) (c) (d)

Figure 5.137: Reynolds shear stress $< uv+ >$ profile at selected cycle positions in JSF oscillatory boundary layer case predicted by the Reynolds stress transport models and compared with the experiments of Jensen et al. (1989). Models as in Table 3.25.

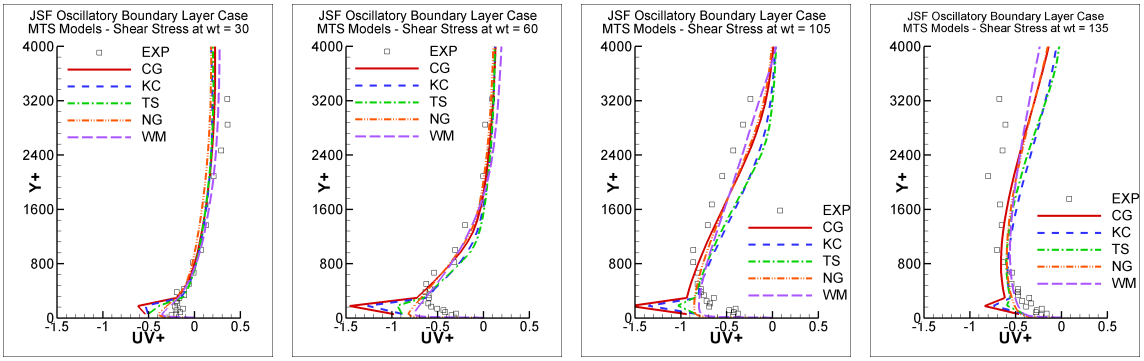

(a) (b) (c) (d)

Figure 5.138: Reynolds shear stress $< uv+ >$ profile at selected cycle positions in JSF oscillatory boundary layer case predicted by the multiple-time-scale models and compared with the experiments of Jensen et al. (1989). Models as in Table 3.25.

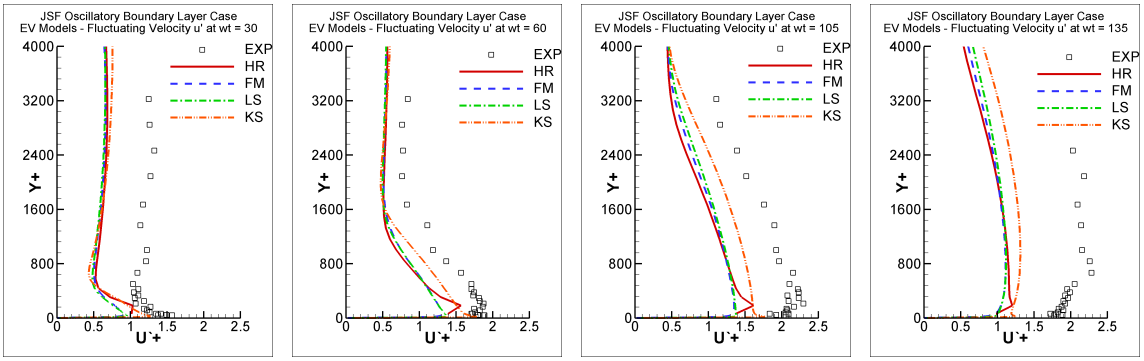

(a) (b) (c) (d)

Figure 5.139: Fluctuating velocity $< u+ >$ at selected cycle positions in JSF oscillatory boundary layer case predicted by the eddy-viscosity models and compared with the experiments of Jensen et al. (1989). Models as in Table 3.25.

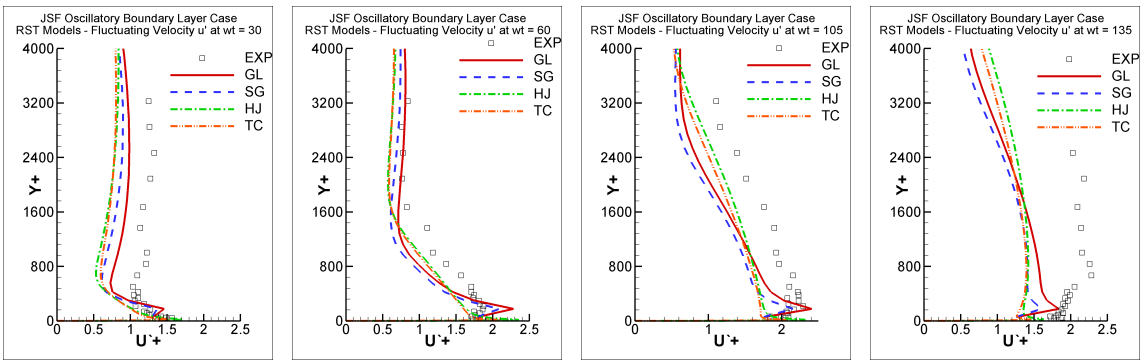

(a) (b) (c) (d)

Figure 5.140: Fluctuating velocity $< u+ >$ at selected cycle positions in JSF oscillatory boundary layer case predicted by the Reynolds stress transport models and compared with the experiments of Jensen et al. (1989). Models as in Table 3.25.

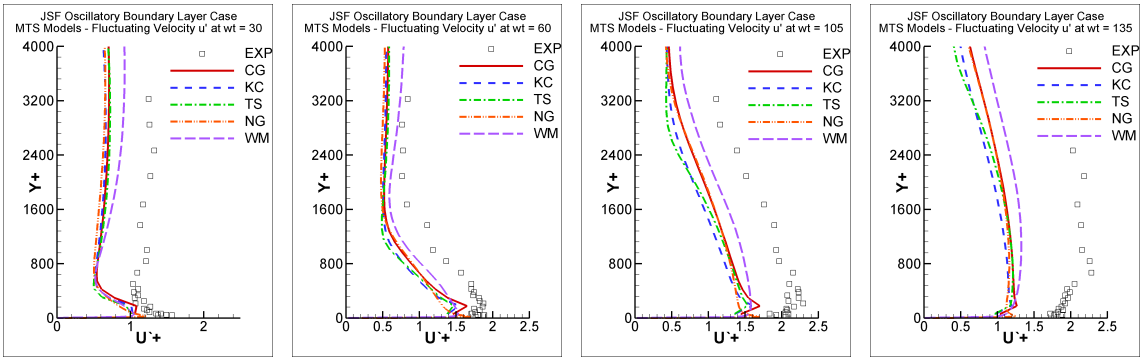

(a) (b) (c) (d)

Figure 5.141: Fluctuating velocity $< u+ >$ at selected cycle positions in JSF oscillatory boundary layer case predicted by the multiple-time-scale models and compared with the experiments of Jensen et al. (1989). Models as in Table 3.25.

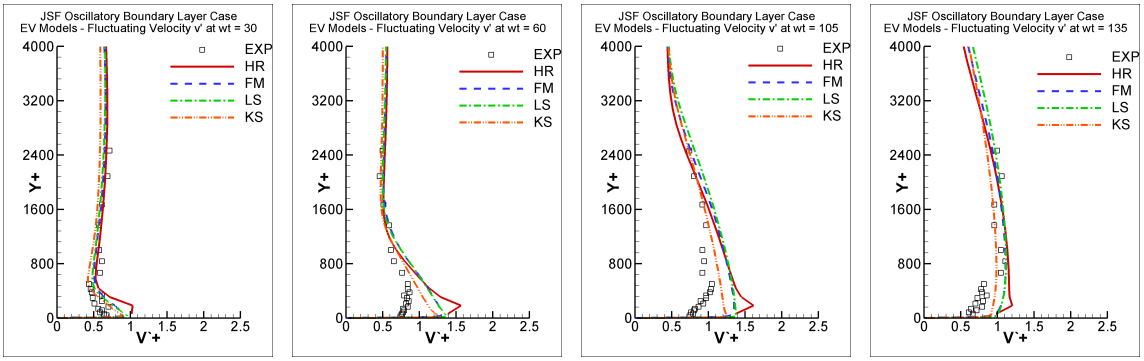

(a) (b) (c) (d)

Figure 5.142: Fluctuating velocity $< v+ >$ at selected cycle positions in JSF oscillatory boundary layer case predicted by the eddy-viscosity models and compared with the experiments of Jensen et al. (1989). Models as in Table 3.25.

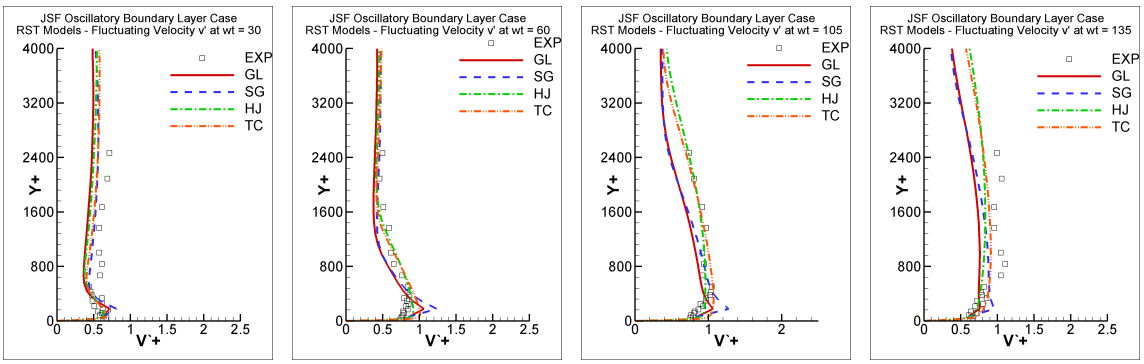

(a) (b) (c) (d)

Figure 5.143: Fluctuating velocity $< v+ >$ at selected cycle positions in JSF oscillatory boundary layer case predicted by the Reynolds stress transport models and compared with the experiments of Jensen et al. (1989). Models as in Table 3.25.

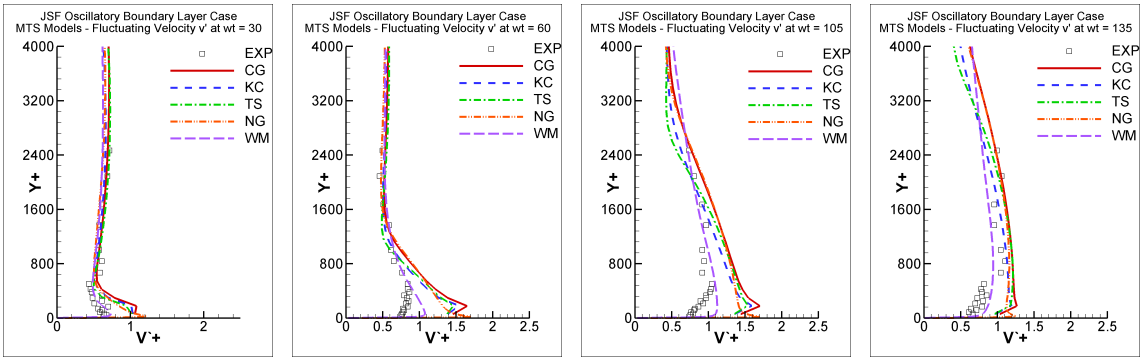

(a) (b) (c) (d)

Figure 5.144: Fluctuating velocity $< v+ >$ at selected cycle positions in JSF oscillatory boundary layer case predicted by the multiple-time-scale models and compared with the experiments of Jensen et al. (1989). Models as in Table 3.25.

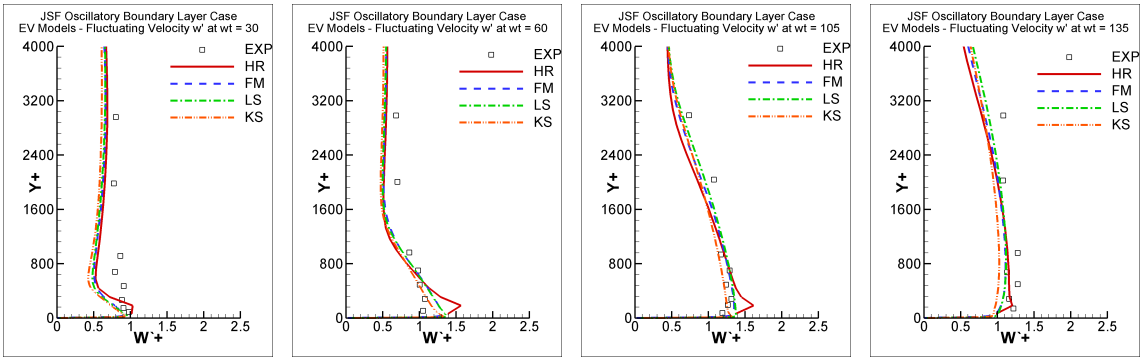

(a) (b) (c) (d)

Figure 5.145: Fluctuating velocity $< w+ >$ at selected cycle positions in JSF oscillatory boundary layer case predicted by the eddy-viscosity models and compared with the experiments of Jensen et al. (1989). Models as in Table 3.25.

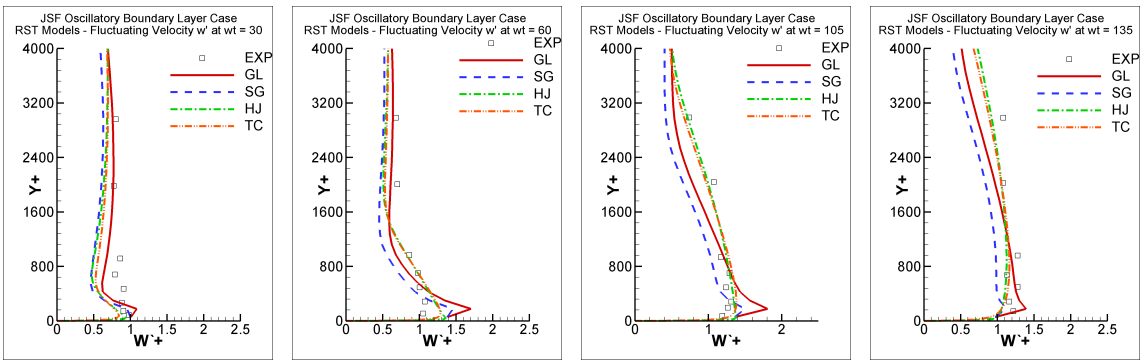

(a) (b) (c) (d)

Figure 5.146: Fluctuating velocity $< w+ >$ at selected cycle positions in JSF oscillatory boundary layer case predicted by the Reynolds stress transport models and compared with the experiments of Jensen et al. (1989). Models as in Table 3.25.

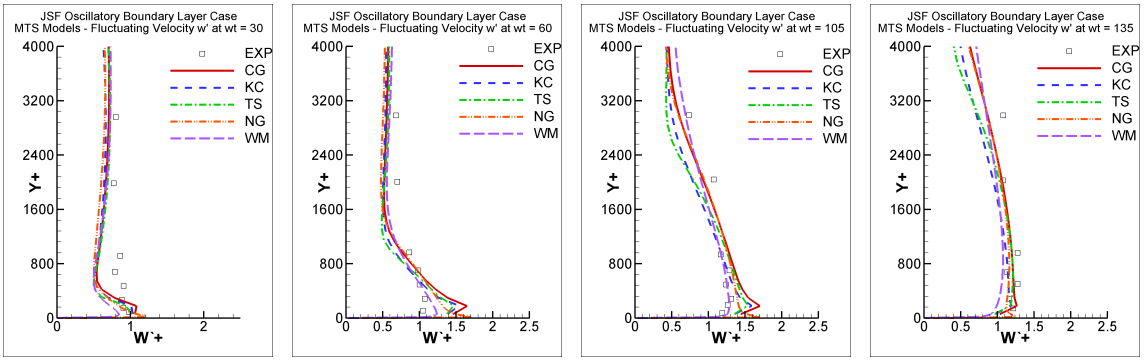

(a) (b) (c) (d)

Figure 5.147: Fluctuating velocity $< w+ >$ at selected cycle positions in JSF oscillatory boundary layer case predicted by the multiple-time-scale models and compared with the experiments of Jensen et al. (1989). Models as in Table 3.25.

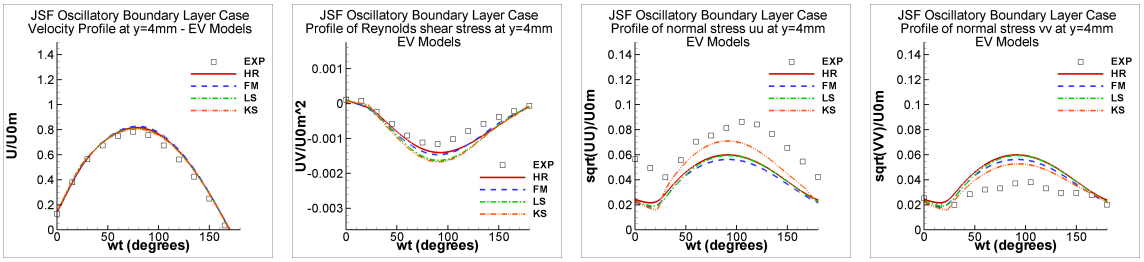

Figure 5.148: Prediction by the eddy-viscosity models of the velocity and Reynolds stresses at $y = 4mm$ in the JSF oscillatory boundary layer case. Models as in Table 3.25.

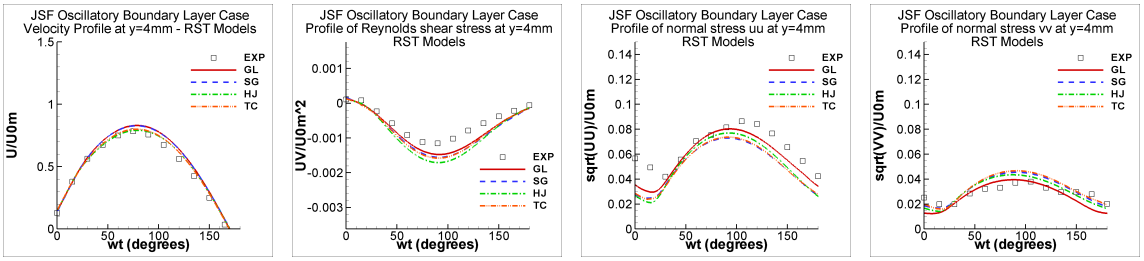

Figure 5.149: Prediction by the Reynolds stress transport models of the velocity and Reynolds stresses at $y = 4mm$ in the JSF oscillatory boundary layer case. Models as in Table 3.25.

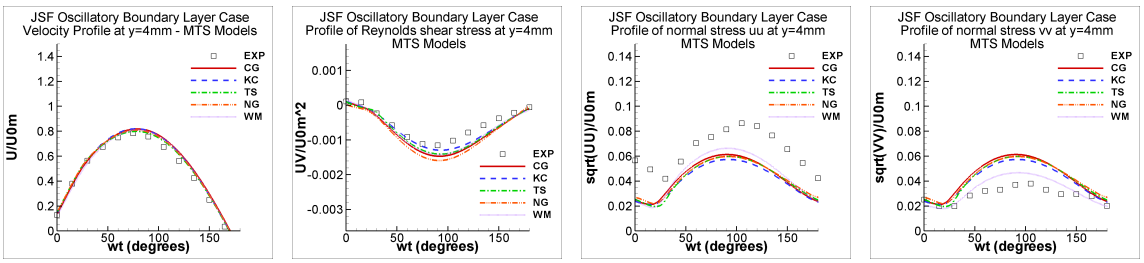

Figure 5.150: Prediction by the multiple-time-scale models of the velocity and Reynolds stresses at $y = 4mm$ in the JSF oscillatory boundary layer case. Models as in Table 3.25.

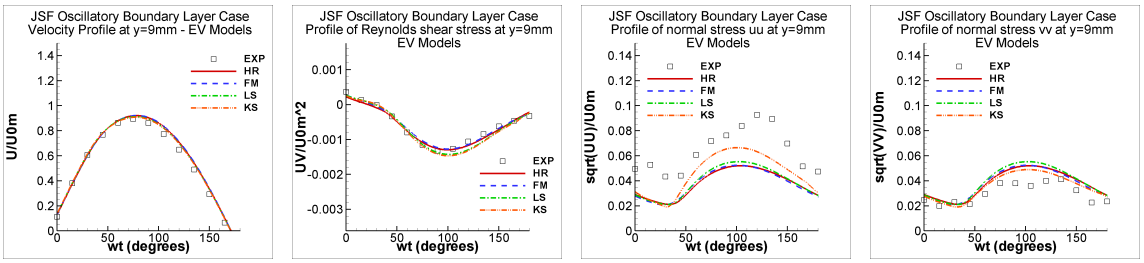

Figure 5.151: Prediction by the eddy-viscosity models of the velocity and Reynolds stresses at $y = 9mm$ in the JSF oscillatory boundary layer case. Models as in Table 3.25.

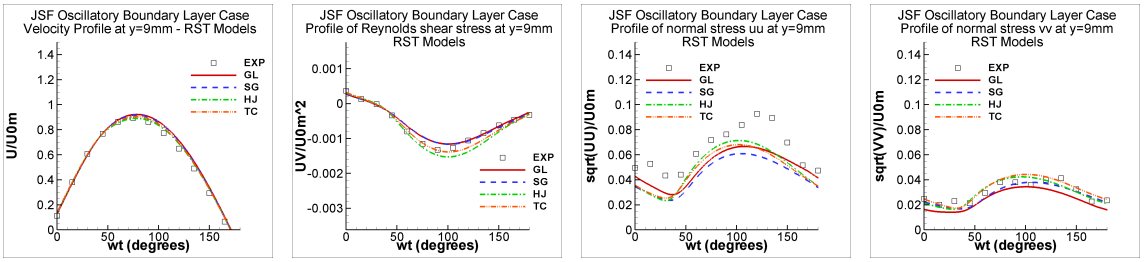

Figure 5.152: Prediction by the Reynolds stress transport models of the velocity and Reynolds stresses at $y = 9mm$ in the JSF oscillatory boundary layer case. Models as in Table 3.25.

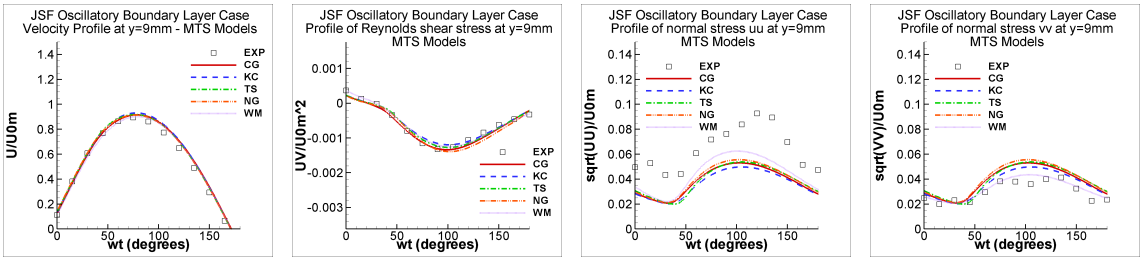

Figure 5.153: Prediction by the multiple-time-scale models of the velocity and Reynolds stresses at $y = 9mm$ in the JSF oscillatory boundary layer case. Models as in Table 3.25.

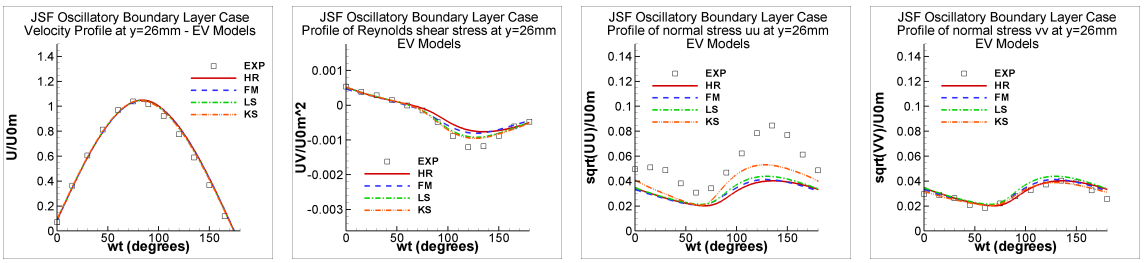

Figure 5.154: Prediction by the eddy-viscosity models of the velocity and Reynolds stresses at $y = 26mm$ in the JSF oscillatory boundary layer case. Models as in Table 3.25.

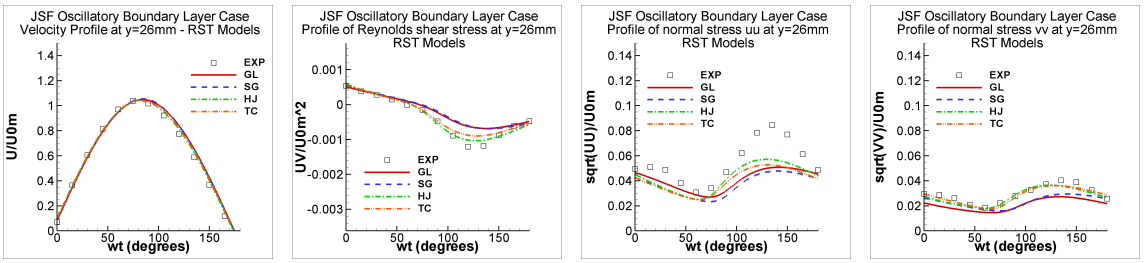

Figure 5.155: Prediction by the Reynolds stress transport models of the velocity and Reynolds stresses at $y = 26mm$ in the JSF oscillatory boundary layer case. Models as in Table 3.25.

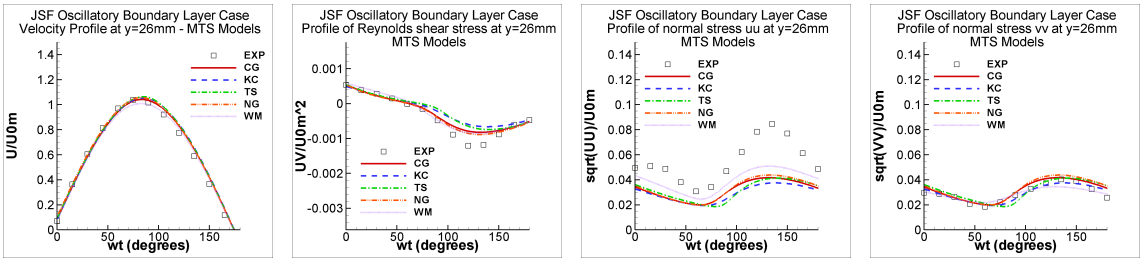

Figure 5.156: Prediction by the multiple-time-scale models of the velocity and Reynolds stresses at $y = 26mm$ in the JSF oscillatory boundary layer case. Models as in Table 3.25.

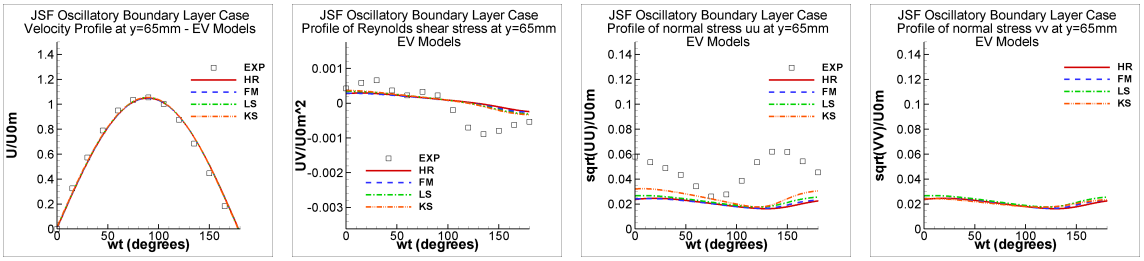

Figure 5.157: Prediction by the eddy-viscosity models of the velocity and Reynolds stresses at $y = 65mm$ in the JSF oscillatory boundary layer case. Models as in Table 3.25.

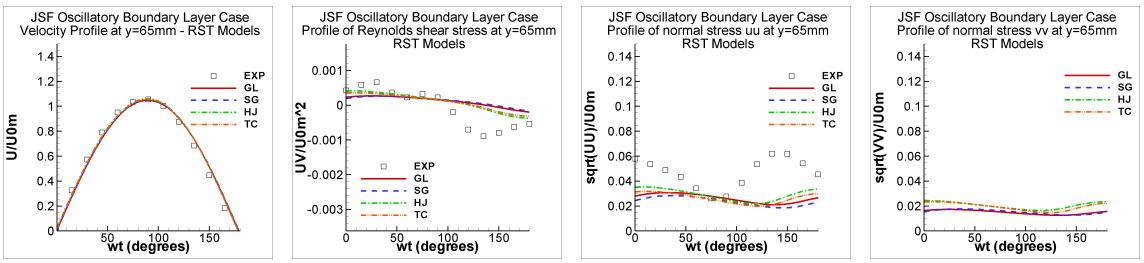

Figure 5.158: Prediction by the Reynolds stress transport models of the velocity and Reynolds stresses at $y = 65mm$ in the JSF oscillatory boundary layer case. Models as in Table 3.25.

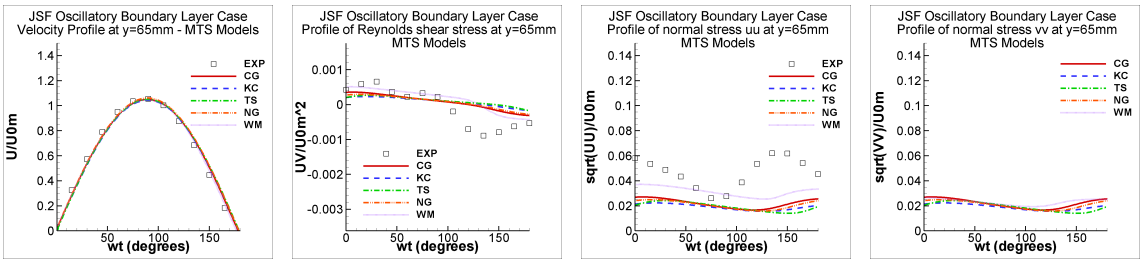

Figure 5.159: Prediction by the multiple-time-scale models of the velocity and Reynolds stresses at $y = 65mm$ in the JSF oscillatory boundary layer case. Models as in Table 3.25.

5.7.2 Oscillatory Pipe Flow

In these cases of oscillatory pipe flows, the time-averaged bulk velocity is non-zero, whilst the ensemble varies through a periodic function such as sine or cosine around this mean value. One may look at an example of a bulk velocity variation in Figure 5.160. Depending on the amplitude, the flow may reverse locally at some points through the cycle.

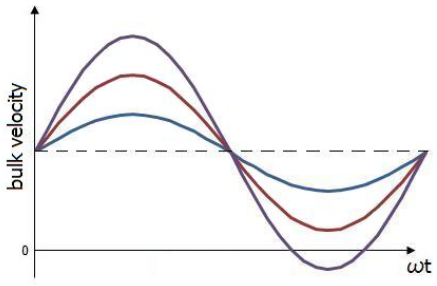

Figure 5.160: Velocity oscillating over its non-zero time-averaged value

For these oscillatory flows, it has been reported (Scotti and Piomelli, 2001; He and Jackson, 2009) that the amplitude does not affect the turbulence response, however the frequency is known to play an important role regarding the flows' equilibrium state and therefore its predictability by turbulence models.

One would expect that at very low or very high frequencies the flow would be closer to equilibrium. In the former case, the large time-scale, say the period of the flow, should be higher than the turbulent time-scale, say $\frac{k}{\varepsilon}$, giving the turbulence time to adjust itself to the mean flow, and thus behave almost as it would in a series of steady state flows as the cycle progresses. On the other hand, when the frequency is very high, the turbulent time-scale may be much higher than the large time-scale thus implying a frozen, static turbulence which would not respond to the oscillations in the main flow. Therefore the most interesting frequency range to be studied in order to capture non-equilibrium features would be an intermediate range, where both large and turbulent time-scales interact.

These oscillatory flows are commonly characterized by dimensionless parameters such as the Strouhal number St and the forcing frequency ω^+. The former is defined as $St = \frac{fL}{V}$ and the latter as $\omega^+ = \frac{\omega\nu}{{u_\tau}^2}$, where f is the oscillation frequency, L the characteristic length of the flow, V the time-mean velocity, $\omega = 2\pi f$ the angular frequency of oscillation, ν the kinematic viscosity and u_τ the time-mean friction velocity of the flow. According to Binder et al. (1995), there is a consensus that ω^+ is the most appropriate scaling parameter, since it is believed that the oscillating shear is confined in the inner layer of the flow.

According to Manna and Vacca (2008), an oscillatory pulsating flow needs three dimensionless parameters to be fully characterized, including the Reynolds number, based on the bulk velocity, of the flow. The authors also suggest parameters such as $Re_{l_s} = \frac{U_{amp} l_s}{\nu}$, $\Lambda = \frac{U_{amp}}{U_{ref}}$ and $\eta = \frac{R}{l_s}$, among other variations of the Strouhal number and the forcing frequency, where $l_s = \sqrt{\frac{2\nu}{\omega}}$ is the Stokes layer thickness, U_{ref} is a reference velocity such as the

bulk velocity or centreline velocity and R is the radius in a pipe flow.

There are several cases of oscillatory pipe flows with non-zero time-averaged bulk velocity values in the literature and they do present different ranges of frequencies, amplitudes and Reynolds numbers. The works also use different dimensionless parameters to classify the flows which sometimes makes them difficult to compare.

Tu and Ramaprian (1983b) argued that the Strouhal number St would not be appropriate for classifying such oscillating flows and proposed $\frac{\omega D}{u_\tau}$ as a more appropriate parameter which they called the turbulent Stokes number and which will be denoted here as ω^*. Indeed, the Strouhal number seems to be more widely used to rank flows involving separation (Sobey, 1982) and vortex shedding behind cylinders or spheres (Sakamoto and Haniu, 1990). Tu and Ramaprian (1983b) classified unsteady pipe flows into five frequency regimes, and noted that their two main experiments, presented in Tu and Ramaprian (1983a), fell into the intermediate-frequency and high-frequency regimes.

Tardu et al. (1994) indicated the dimensionless parameter $l_s^+ = \frac{l_s \overline{u_\tau}}{\nu}$ as the most appropriate which they referred to as Stokes-Reynolds number which is indeed directly correlated to the forcing frequency since $\omega^+ = \frac{2}{l_s^{+2}}$.

Scotti and Piomelli (2001) compared the work of four independent research groups (well represented by the works of Tu and Ramaprian (1983a), Mao and Hanratty (1986), Tardu et al. (1994) and Brereton et al. (1990) respectively for the Iowa, Illinois, Grenoble and Stanford groups), listing their forcing frequency ω^+, Reynolds number Re and relative amplitude of the flow Λ. They pointed to the low-frequency ($\omega^+ \approx 0.001$) and the medium frequency ($\omega^+ \approx 0.01$) ranges as the most interesting regarding non-equilibrium features. The referred experiments from the mentioned four groups encompassed these ranges, although, according to Scotti and Piomelli (2001), Tu and Ramaprian (1983a) provided experiments in the low ($\omega^+ \approx 0.0057$) and very low ($\omega^+ \approx 0.00079$) frequency regimes. However, using the data reported by Tu and Ramaprian (1983a), their experiments would appear to correspond to values of $\omega^+ \approx 0.001$ (low-frequency regime) and $\omega^+ \approx 0.008$ (medium-frequency regime), using the time-mean wall shear stress presented in Figure 9 of their paper to evaluate ω^+.

He and Jackson (2009) provided a set of experimental results and also tried to compare the works of the above mentioned authors. They proposed a dimensionless parameter $T^* = \frac{T u_\tau}{R}$ which, in essence, represents the same as the ω^* parameter proposed by Tu and Ramaprian (1983b). They concluded that these parameters would be more appropriate to characterize the outer and core flow while the Stokes-Reynolds number proposed by Tardu et al. (1994) (or alternatively, the forcing frequency) would be more appropriate for near-wall flows, specially at high frequencies.

He and Jackson (2009) presented a review of oscillatory flows about a non-zero mean velocity which, except for some specific issues, unified the previously-reported experiments and simulations as well as provided an explanation of the mechanisms by which turbulence is affected by imposed periodic unsteadiness. According to them, the imposed oscillation generates shear waves at the wall, due to the no-slip condition, which tend to propagate across the flow, thus affecting the turbulence. At very high frequencies ($\omega^+ > 2$), these shear

waves are confined in the near wall viscous sub-layer (as also stated by Tardu et al. (1994)) and therefore the inner and outer flows are decoupled, and the turbulence in the outer flow is not affected, and is therefore frozen. As the frequency is reduced and reaches a range where $0.04 \leq \omega^+ \leq 0.2$, the outer layer where the turbulence is frozen reduces and turbulence starts being affected by the pulsation in the mean flow, since the shear waves are no longer confined in the viscous sub-layer. However the coupling between the inner and outer layers remains weak. As one keeps reducing the frequency and it reaches a range where $0.01 \leq \omega^+ \leq 0.04$, the outer frozen layer is even smaller, which means the shear waves propagate well beyond the viscous sublayer, and the coupling between the inner and outer layers becomes stronger. This corresponds to the intermediate-frequency range in the scale described by He and Jackson (2009), where a significant response of the turbulence to the mean flow oscillation would be expected. The frequency can be reduced down to a point where no frozen outer layer exists any longer, when $\frac{\omega D}{u_\tau} \approx 10$. From this frequency down to $\frac{\omega D}{u_\tau} \approx 1$, the whole flow feels the effects of the imposed oscillation and phase lags between production and dissipation as well as asymmetry between acceleration and deceleration parts of the cycle occur. If the frequency is even further reduced, the turbulence is then forced to relax to a local time equilibrium, characterizing the quasi-steady state where the turbulence behaves as in a steady state flow. This regime would be achieved when $\frac{\omega D}{u_\tau} < 10^{-1}$, according to Tu and Ramaprian (1983b).

While Mao and Hanratty (1986), Tardu et al. (1994) and He and Jackson (2009) provided most of their results in terms of the fluctuating variables amplitude modulations and phase shifts to the reference velocity oscillation, Brereton et al. (1990) focused on mean quantities and Tu and Ramaprian (1983a) provided the classical results of velocity and the Reynolds stresses profiles through the cycle. Therefore, the latter was chosen to be initially reproduced here. As will be seen in the results and discussion section, the cases of Tu and Ramaprian (1983a) are apparently either in the too low or too high frequency ranges. Among the ten test cases performed by He and Jackson (2009), three were then selected to simulate the intermediate frequency range. In order to allow more detailed comparisons in these cases, S. He kindly provided more experimental results than those presented in their published work.

Simulated Cases

The cases that have been reproduced here are then the two experimental test cases performed by Tu and Ramaprian (1983a) and three test cases performed by He and Jackson (2009).

The two experimental test cases of Tu and Ramaprian (1983a) differ in the amplitude and frequency of the imposed oscillation. One case will be here referred to as TuR05 and the other as TuR36. Both are fully developed pipe flow cases where the ensemble bulk velocity was set to vary as $< U_m >= U_m(1 + A_{U_m} \cos(\omega t))$, where $U_m = 1m/s$ is the time-averaged bulk velocity, A_{U_m} the relative amplitude and $\omega = 2\pi f$, the frequency in radians. The values of A_{U_m} and f for each case are presented in Table 5.17. As the mean velocity, pipe diameter and the fluid, water, are the same, the Reynolds number based on the pipe diameter and time mean velocity of both cases is also the same, $Re = \frac{DU_m}{\nu} = 50000$.

The three selected test cases from He and Jackson (2009) differ in the Reynolds number and the frequency, all of them presenting the same amplitude which was 20% of the bulk velocity which was set to vary just as above: $< U_m >= U_m(1 + A_{U_m} \cos(\omega t))$. The case with $Re = 7000$ and period $T = 10s$ is here referred to as T10RE7A20, the case with $Re = 10000$ and $T = 3s$ is here referred to as T3RE10A20 and the case with $Re = 14000$ and $T = 3.26s$ is here referred to as T3RE14A20. These specifications are also presented in Table 5.17 which also gives the main dimensionless parameters discussed for all five test cases considered here.

One may notice that according to the forcing frequency ω^+, both cases from Tu and Ramaprian (1983a) could be considered as low-medium frequency cases (as they are generally referred to in the literature). However, by considering ω^*, and according to the frequency classification proposed by He and Jackson (2009), the TuR05 case would be in the low-frequency range while TuR36 would be in the high-frequency range, suggesting the former to be more interesting from the point of view of non-equilibrium features. However, He and Jackson (2009) reported the TuR05 case to be close to a quasi-steady flow. The three cases selected from the work of He and Jackson (2009) give both ω^+ and ω^* in an intermediate frequency range.

Table 5.17: Relative amplitude and frequency of the TuR05 and TuR36 cases

Case	Re	A_{U_m}	f (Hz)	$St = \frac{fD}{U_m}$	$\omega^+ = \frac{\omega\nu}{\overline{u_\tau}^2}$	$\omega^* = \frac{\omega D}{\overline{u_\tau}}$
TuR05	50000	0.64	0.5	0.025	0.001	3
TuR36	50000	0.15	3.6	0.180	0.008	20
T3RE10A20	10000	0.2	0.33	0.086	0.013	8
T3RE14A20	14000	0.2	0.31	0.057	0.007	6
T10RE7A20	7000	0.2	0.1	0.037	0.008	4

Simulations Setup

As the five cases are fully developed pipe flow cases, a number of simplifications can be made to reduce the computational requirements. The problem is thus solved as axisymmetric, in a cylindrical-polar coordinate system, the domain extending from $y = 0$ to $y = R$, where R is the pipe's radius. The flow is fully developed, meaning flow variables do not change in the streamwise direction, so a relatively short domain can be employed, with periodic boundary conditions connecting the east and west faces.

Therefore, the geometry was simply a short rectangle (the length in the streamwise direction does not matter since it is a fully developed flow), where the height is the same as the radius of the pipe in each experiment, being $R = 0.0250m$ for the cases from Tu and Ramaprian (1983a) and $R = 0.0254m$ for the cases from He and Jackson (2009).

The north face was set as the pipe wall, the bottom face is the axis where $V = 0$, $\overline{uv} = 0$ and zero gradients are applied to all other variables, and periodic boundary conditions were set between the east and west faces. In imposing the periodic conditions, a bulk mass flux correction was applied in order to ensure the correct mass flux through the pipe at each time

step.

The starting/initial conditions were used from a separate simulation of fully developed steady pipe flow at the Reynolds numbers indicated in Table 5.17 for each test case.

The grid was planned in order to provide the desired y^+ values at the near-wall node (according to the turbulence model type: for the LRN models, $y^+ < 1$ and for the HRN models $y^+ \approx 30$) of a fully developed pipe flow, with the same properties and geometrical conditions specified by each experiment. The number of control volumes in the y direction for the grids used in each simulation can be seen in Table 5.18. All grids were further refined and the results were confirmed to be grid independent.

Table 5.18: Grids used for each oscillatory pipe flow case

Case	number of control volumes in the y direction	
	HRN models	LRN models
TuR05	25	40
TuR36	25	40
T3RE10A20	22	90
T3RE14A20	25	100
T10RE7A20	18	70

In contrast to the JSF case, where the first half of the cycle is symmetric to the second half, since the mean velocity is zero, in the oscillatory pipe flow cases studied here, one must examine the whole cycle since the first half represents the decelerating part and the second, the accelerating one. Tu and Ramaprian (1983a) provided mean velocity and Reynolds stresses profiles every 45^o of the cycle, thus four in the decelerating part and four in the accelerating part. He and Jackson (2009) provided the amplitude and phase shift of the turbulent quantities and the velocity across the y direction, that is, along the radius of the pipe. This is done by fitting the variation of a turbulence quantity by its first harmonic: $< q(t,y) >=< q(y) > [1 + A_q \cos(\omega t - \phi_q)]$, where A_q and ϕ_q stand for the measured (in the experiments) and calculated (in the simulations) amplitude and phase shift of the turbulent quantity q.

The time step of the flow in each case was chosen to provide 40 steps every quarter of the cycle, thus 160 steps for the whole cycle. A refined time step of half this size was also tested in order to guarantee the former was small enough to provide accurate results. The total time of the simulation was set as five times the oscillation period for each case, thus ensuring the fully periodic state was reached.

Results and Discussion

All five test cases were simulated with all turbulence models presented in Chapter 3. The results will be discussed by case and a general analysis will be carried out at the end. Tu and Ramaprian (1983a) provided profiles of the oscillating bulk velocity which can be checked in Figure 5.161 for the eddy-viscosity models ensuring the simulations set up were in agreement with experiments.

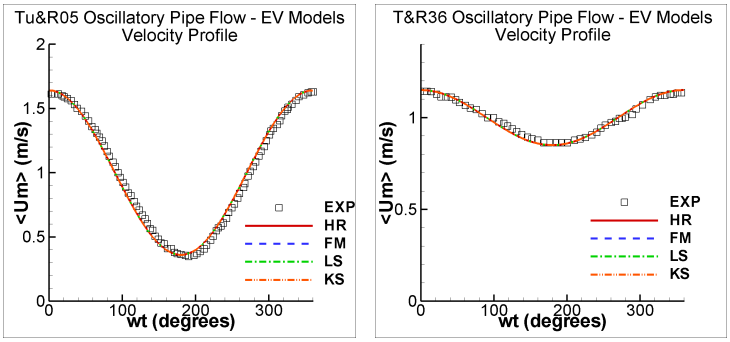

(a) Tu&R05 case (b) Tu&R36 case

Figure 5.161: Prediction of the velocity throughout the cycle by the eddy-viscosity models and compared with the experiments of Tu and Ramaprian (1983a). Models as in Table 3.25.

TuR05 Case The predictions of the wall shear stress are presented in Figure 5.162, in the form of $-\frac{<\tau_w>}{\rho U_m^2} \times 10^3$. One may notice that the models generally either fit the extremes of the cycle (early decelerating and late accelerating parts) or they fit the mid-part of the cycle. It is clear that the HRN schemes tend to fit the extremes better and underpredict $<\tau_w>$ in the middle of the cycle, while the LRN models predict $<\tau_w>$ well in the middle of the cycle, but overpredict the peak and underpredict the minimum values. The exception for this is the FM model which performs similarly to the HRN standard $k-\varepsilon$ model. It is also of value to notice that the wall shear stress is in phase with the bulk velocity and this is captured by all models.

Before looking at the predictions at specific times of the cycle, it is worth looking at some time-histories through the cycle at specific radial positions. Tu and Ramaprian (1983a) provided, for the TuR05 case, the histories of the rms streamwise normal Reynolds stress $<u^2>^{1/2}$, normalized by the time-mean velocity U_m, at three radial positions ($\frac{y}{R}=0.07$, $\frac{y}{R}=0.25$ and $\frac{y}{R}=0.95$, y being distance from the wall) and the histories of the Reynolds shear stress $<uv>$, normalized by the time-mean velocity squared, U_m^2, at two radial positions ($\frac{y}{R}=0.07$ and $\frac{y}{R}=0.63$).

In Figures 5.163 and 5.164, one can see the history of the Reynolds shear stress $\frac{<uv>}{U_m^2}\times 10^3$ at $\frac{y}{R}=0.07$ and $\frac{y}{R}=0.63$ respectively. Clearly, the models provide better prediction closer to the wall ($\frac{y}{R}=0.07$) than far from it ($\frac{y}{R}=0.63$). At $\frac{y}{R}=0.07$, all models predict the middle of the cycle reasonably well. One may notice though that all turbulence models presented are aligned in phase in predicting the minimum of $<uv>$. On the other hand, the profile of the Reynolds shear stress at $\frac{y}{R}=0.63$ was not captured by any turbulence model. The models provide profiles which do not match either the amplitude or the position of the peak. The phase shift between $\frac{<uv>}{U_m^2}\times 10^3$ and the bulk velocity also increases as one moves away from the wall: $\approx 45^o$ at $\frac{y}{R}=0.07$ and $\approx 130^o$ at $\frac{y}{R}=0.63$.

In Figures 5.165, 5.166 and 5.167, one can see the histories of the rms streamwise normal Reynolds stress $\frac{<u^2>^{1/2}}{U_m}$ at $\frac{y}{R}=0.07$, $\frac{y}{R}=0.25$ and $\frac{y}{R}=0.95$ respectively. One may notice that the oscillation near the wall is much stronger than far from it and that no turbulence

model was able to follow the whole behaviour of this quantity. At the furthest position from the wall, no model was able to follow the experiments' trend. One may also notice, by comparing the peaks in the decelerating part, that the experiments show a lag between the peak $\frac{<u^2>^{1/2}}{U_m}$ and bulk velocity values that becomes larger as one moves further away from the wall: $\approx 45^o$ at $\frac{y}{R} = 0.07$, $\approx 90^o$ at $\frac{y}{R} = 0.25$ and $\approx 150^o$ at $\frac{y}{R} = 0.95$. From these values, one could also say that $\frac{<u^2>^{1/2}}{U_m}$ and $\frac{<uv>}{U_m^2}$ seem to be in phase close to the wall. The models show the same qualitative trend, but the lag is underpredicted at each location.

Tu and Ramaprian (1983a) provided radial profiles of velocity, rms of the shear stress and rms of the streamwise fluctuating velocity varying along the y direction every 45^o of the cycle. Comparisons here show the profiles at $\omega t = 45^o$, $\omega t = 135^o$, $\omega t = 225^o$ and $\omega t = 135^o$; the first two positions representing the decelerating part of the cycle and the last two, the accelerating part, since the bulk velocity varied as a cosine function.

Velocity profiles at different times through the cycle, plotted in outer and wall coordinates, are presented in Figures 5.168 to 5.170. One can see that the velocity profiles are well captured by all turbulence models.

The prediction of the Reynolds shear stress $\frac{<uv>}{U_m^2} \times 10^3$ is presented in Figures 5.171 to 5.173. One may notice that none of the models were able to correctly predict the profile of this quantity at every cycle position, however, apart from the LS, KS, HJ and TC which are overpredicting too much in the beginning of the decelerating part, the other models can be considered as providing reasonable results.

The prediction of the rms streamwise normal Reynolds stress $\frac{<u^2>^{1/2}}{U_m}$ is presented in Figures 5.174 to 5.176. One may notice that among the models presented, most of them provide predictions close to experiments, however not fully following their trend. One can see that the turbulence intensity decreases while the flow is being decelerated and that the near wall peak vanishes in the first part of the acceleration phase, where the GL model performed best.

TuR36 Case With regard to the wall shear stress, presented in Figure 5.177, one may notice a kink in the measured data at around $\omega t = 120^o$ which could not be explained by Tu and Ramaprian (1983a) and that was not present in the TuR05 case. However they argued that the measurements were repeated, assuring accuracy, and the presence of the kink was confirmed. One may notice that none of the turbulence models was able to predict this kink; instead all predictions of the wall shear stress simply followed the bulk velocity cosine curve.

The time-histories of the Reynolds shear stress $\frac{<uv>}{U_m^2}$ at $\frac{y}{R} = 0.07$ and at $\frac{y}{R} = 0.79$ are presented in Figures 5.178 and 5.179 respectively. One may notice that none of the turbulence models are able to follow the experimental data, which shows a significantly stronger oscillation than the predictions. Further from the wall, at $\frac{y}{R} = 0.79$, the turbulence models predict almost no oscillation, while the experiments still show the influence of the periodicity. One may also notice that at the same position in the cycle where the kink in wall shear stress occurred, there is a kink in the measured Reynolds shear stress. This was also noticed by Tu and Ramaprian (1983a) who used this information to argue for the consistency

of their experiments. Again, none of the turbulence models were able to predict this. It could be that the kink is a result of the strong oscillations in the shear stress, not captured by the models. Despite the kink in $\frac{<uv>}{U_m^2}$ at $\frac{y}{R} = 0.07$, this quantity is clearly shifted from the bulk velocity by $\approx 45^o$ in this position, which puts it in phase with $\frac{<u^2>^{1/2}}{U_m}$ at this same position, and shows a $\approx 90^o$ shift at $\frac{y}{R} = 0.79$. It is not possible to determine if the measured $\frac{<u^2>^{1/2}}{U_m}$ and $\frac{<uv>}{U_m^2}$ remain in phase as one moves towards the centre of the pipe, since the time-histories for these quantities are given at different radial positions from the wall. Compared to the TuR05 case, the phase shift of $\frac{<uv>}{U_m^2}$ from the bulk velocity increased to $\approx 90^o$ at $\frac{y}{R} = 0.07$ and to $\approx 240^o$ at $\frac{y}{R} = 0.22$. At $\frac{y}{R} = 0.98$, $\frac{<uv>}{U_m^2}$ seems not to oscillate any more.

The time-histories of $\frac{<u^2>^{1/2}}{U_m}$ at $\frac{y}{R} = 0.07$, $\frac{y}{R} = 0.22$ and $\frac{y}{R} = 0.98$ are presented in Figures 5.180, 5.181 and 5.182 respectively. One may notice that the HJ model best predicts this quantity at $\frac{y}{R} = 0.07$ and $\frac{y}{R} = 0.22$. At $\frac{y}{R} = 0.98$, the SG model performed best together with the NG model which, as a LEV model, is indeed predicting $\frac{2}{3}k$. One may notice that the prediction of the rms streamwise normal Reynolds stress $\frac{<u^2>^{1/2}}{U_m}$ by these models seems to be in phase with the experiments.

The velocity profiles at different phase angles can be seen in Figures 5.183 to 5.185. Again, the profiles are shown at $\omega t = 45^o$, $\omega t = 135^o$, $\omega t = 225^o$ and $\omega t = 135^o$. One may notice that, overall, all turbulence models predicted the velocity profiles quite well.

The profiles of the Reynolds shear stress at different phase angles can be seen in Figures 5.186 to 5.188. One may notice that all turbulence models predicted basically the same profile for all phase angles, although this is only seen from $\omega t = 45^o$ to $\omega t = 135^o$ in the experiments. This results in a generally poor prediction of $\frac{<uv>}{U_m^2}$ by all models.

Profiles of the streamwise normal Reynolds stress at different phase angles can be seen in Figures 5.189 to 5.191. The experimental data, as well as the prediction of the turbulence models, barely change during the decelerating and accelerating parts, although from one part to the other the intensity does clearly change. In the decelerating part, the NLEV and RST models are able to predict $\frac{<u^2>^{1/2}}{U_m}$ reasonably well, while the LEV models underpredict it, as expected. In the accelerating part the measured intensity of the normal Reynolds stress decreases and the RST models are not able to follow it, remaining at the same levels as in the decelerating part. The same occurs for the LEV models which then fit the experimental data, although this is purely due to their earlier underprediction.

This frozen behaviour shown for the Reynolds stresses marks a clear and strong difference between the TuR05 and TuR36 cases. The latter case might, therefore, be classified as a high-frequency case. However, oscillation in the Reynolds shear stress could still be seen up to $\frac{y}{R} = 0.79$ as shown in Figure 5.179. Nevertheless, both STS and MTS models tend to show a frozen turbulence state through the cycle, except in the near-wall region.

The next cases which will be evaluated are those of He and Jackson (2009) whose experiments were carried out in intermediate frequency ranges.

T3RE10A20 Case According to the values of ω^+ and ω^* presented in Table 5.17, this is a case with an intermediate frequency, where one would expect more interaction between the

mean and turbulence scales than in the previous two cases. It would thus be a case where one would expect more effects on the turbulence caused by the imposed oscillation. Starting by evaluating the prediction of the amplitudes, presented in Figures 5.192 to 5.195, one can say that the amplitude of the velocity, in Figure 5.192, is reasonably well predicted by all models, except by the WM model close to the centre of the pipe. The GL and SG models seemed to be more affected by the use of a wall function, since their prediction in the near wall region was underpredicting the experimental data. On the other hand, the LS and KS models tended to overpredict the amplitude of the velocity in this region. As a whole, the LEV MTS models provided good predictions of the amplitude of velocity.

The amplitude of the Reynolds shear stress in Figure 5.193 was not so well predicted by all models. Most models tended to either capture the amplitude near the centre of the pipe or near the wall. The WM model did not provide a good prediction, but the other LEV MTS models did return acceptable predictions, the KC and TS models perhaps performing better than all other models.

The amplitude of the rms streamwise and wall-normal fluctuating velocities, respectively in Figures 5.194 and 5.195 are not expected to be captured by the LEV models and, as expected, these models underpredicted the former and were about the correct values for the latter. The model which best predicted these two quantities was the HJ model, however it overpredicted the amplitude of the Reynolds shear stress.

The prediction of the phase shift of the velocity is presented in Figure 5.196. One may notice that no model was able to capture the whole profile, since they would either correctly predict the centre of the pipe and overpredict the region closer to the wall ($r/R \approx 0.6$ - 0.8) or vice-versa. The KS, LS, HJ and WM models correctly predicted the shift at the centre while the other models correctly predicted the phase shift in the region closer to the wall.

The phase shift of the Reynolds shear stress, presented in Figure 5.197, was best predicted by the TS and WM models, although the latter deviated from the experimental data very close to the centre of the pipe. One can also notice the influence of the wall function in the HRN models' predictions, since in the near-wall region they all present the same rather abrupt decrease in phase shift. The HJ model also performed reasonably well while the other models failed to provide good predictions.

The phase shift of the rms streamwise and wall-normal fluctuating velocities, presented in Figures 5.198 and 5.199, was also best predicted by the HJ model. In spite of being a LEV model, the NG model also captured well the phase shift of u' which might indicate its good prediction in terms of phase shift of the turbulent kinetic energy, however no experimental data for this quantity was provided in the work of He and Jackson (2009).

T3RE14A20 Case This case has an absolute frequency very close to the previous case, as can be seen in Table 5.17, however, as the Reynolds number is higher, its dimensionless frequencies ω^+ and ω^* are lower, slightly above those in the Tu&R05 case.

The prediction of the velocity amplitude is presented in Figure 5.200 where clearly the LS, KS, HJ and TS models provided the best results. However, apart from the FM and WM

models, all other models provided reasonable results too. On the other hand, the amplitude of the shear stress, presented in Figure 5.201, was best predicted by the HR, FM, SG, GL and MTS LEV models.

The amplitude of the rms of the streamwise fluctuating velocity u', presented in Figure 5.202, was not fully captured by any model, the HJ and TC providing the closest results to the experiments. The same can be said of the amplitude of the rms wall-normal fluctuating velocity v' and it is worth noticing that no model predicted the decay of the v' amplitude in the near-wall region.

The velocity phase shift, presented in Figure 5.204, was well predicted by all models, except the CG model which tended to overpredict this quantity in the centre of the pipe.

The LS, KS, HJ, TS and WM models best predicted the phase shift of the shear stress, presented in Figure 5.205. Although the other models tended to underpredict this phase shift, they provided reasonable results.

All STS RST models provided equally reasonable results for the prediction of the phase shift of the rms of the normal fluctuating velocities u' and v', presented in Figures 5.206 and 5.207 respectively. Most LEV models, including the MTS models, also provided good predictions for the phase shift of the rms Reynolds normal stresses which might indicate their reasonable prediction of the phase shift of the turbulent kinetic energy.

T10RE7A20 Case This last case has the lowest Reynolds number and absolute frequency. Its resulting dimensionless frequencies ω^+ and ω^* are the lowest among the test cases selected from He and Jackson (2009), as can be seen in Table 5.17 being close to those of the Tu&R05 case.

The amplitude of the velocity, presented in Figure 5.208, was best predicted by the TS model, followed by the HR model. Most models tended to overpredict this quantity in the region close to the centre of the pipe.

The amplitude of the shear stress, presented in Figure 5.209 was best predicted by the FM and NG models. The influence of the wall function can be noticed in the near-wall peak prediction of these quantities by the HRN models. This is expected since the Reynolds number of this flow is rather low. Consistent with this observation, the two models which best performed here are LRN models.

The SG and GL models best predicted the amplitude of the normal rms Reynolds stress in Figures 5.210 and 5.211. Again, one could expect the LEV MTS models to predict reasonably the amplitude of the turbulent kinetic energy.

The phase shift of the velocity, presented in Figure 5.212, was best predicted by the TC and NG models, again LRN formulations. The same can be said of the prediction of the phase shift of the Reynolds shear stress, presented in Figure 5.213, however the WM model also performed well here. These three models also provided the best prediction of the rms streamwise and wall-normal fluctuating velocities, presented in Figures 5.214 and 5.215 respectively.

By comparing the three simulated cases of He and Jackson (2009), one may notice that the

case where the turbulence models perfomed best was the T3RE14A20, where the Reynolds number of the flow is the highest and the dimensionless frequencies are still in the intermediate frequency range, but probably towards the lower end of this range. The high Reynolds number of this flow means the influence of the wall function may be less than in the T10RE7A20 and T3RE10A20 cases where its effect on the near-wall behaviour was rather noticeable. In this sense, the HRN models might not be appropriate to run the T10RE7A20 case. The T3RE10A20 case, which represents a truly intermediate-frequency case, also has a rather low Reynolds number which does not allow one to judge definitively whether the HRN models do not perform well because of the wall function influence or due to intrinsic modelling limitations.

By comparing the cases from Tu and Ramaprian (1983a) and He and Jackson (2009), one could say that, despite the different form of presenting the results used by the authors making it rather difficult to compare the results, the models seemed to give better results in the latter cases. In the cases of Tu and Ramaprian (1983a), all models performed very similarly not allowing one to distinguish their features. That would again confirm the hypothesis of these cases being in the extremes of the frequency range which characterizes the interaction between the mean flow and the turbulence. On the other hand, the cases of He and Jackson (2009) presented a relatively low Reynolds number, possibly clouding any conclusions regarding the performance of the HRN turbulence models which were used together with wall functions.

By comparing the JSF oscillatory boundary layer case with the oscillatory pipe flow cases, one may notice that the turbulence models performed clearly better in the former, although there is still space for improvements. In the oscillatory boundary layer case, one could see the same phenomena observed in the adverse pressure gradient boundary layer cases in which the turbulence models, except the FM and WM, could not follow the subtle changes shown in the experiments. These two models did not follow the subtle changes shown in the experiments of Jensen et al. (1989) though.

Generally speaking, the RST models performed best in these oscillatory flows, however, given the limitation of linear-eddy-viscosity schemes, one could say that the MTS models did perform well too, usually providing better results than the single-time-scale LEV models. Thereby, these cases also indicate the potential of MTS models in predicting non-equilibrium flows.

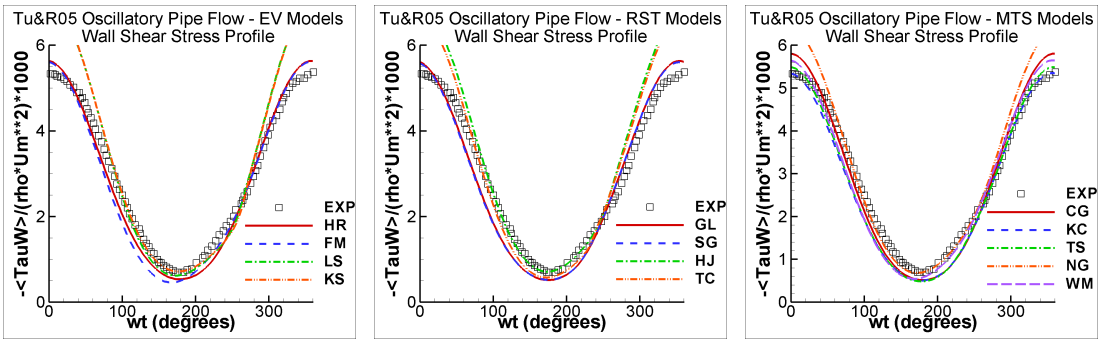

Figure 5.162: Prediction of the wall shear stress throughout the cycle by the (a) eddy-viscosity models, (b) Reynolds stress transport models and (c) multiple-time-scale models and compared with the experiments of Tu and Ramaprian (1983a) in the Tu&R05 oscillatory pipe flow case. Models as in Table 3.25.

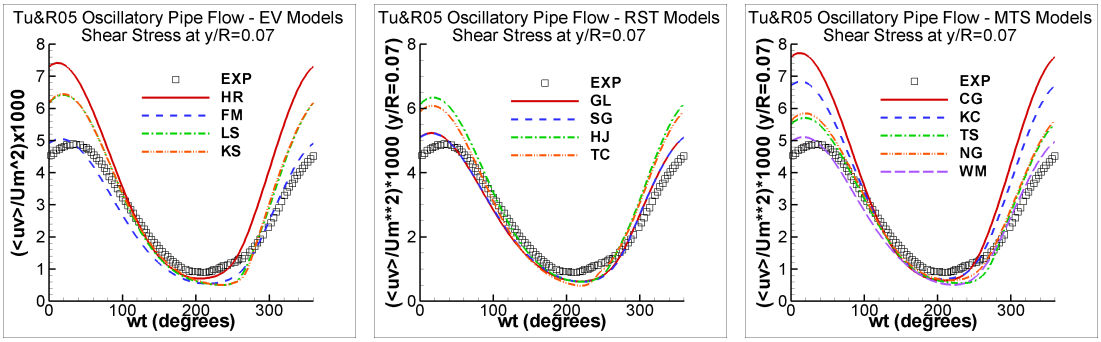

Figure 5.163: Prediction of the Reynolds shear stress at $y/R = 0.07$ throughout the cycle by the (a) eddy-viscosity models, (b) Reynolds stress transport models and (c) multiple-time-scale models and compared with the experiments of Tu and Ramaprian (1983a) in the Tu&R05 oscillatory pipe flow case. Models as in Table 3.25.

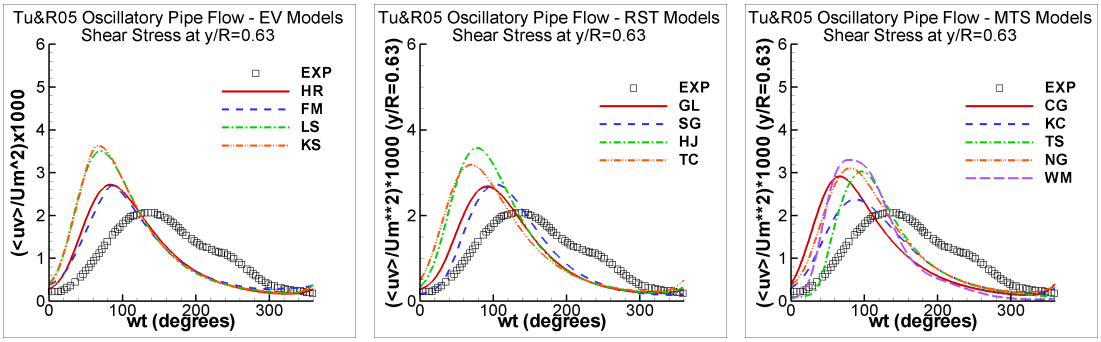

Figure 5.164: Prediction of the Reynolds shear stress at $y/R = 0.63$ throughout the cycle by the (a) eddy-viscosity models, (b) Reynolds stress transport models and (c) multiple-time-scale models and compared with the experiments of Tu and Ramaprian (1983a) in the Tu&R05 oscillatory pipe flow case. Models as in Table 3.25.

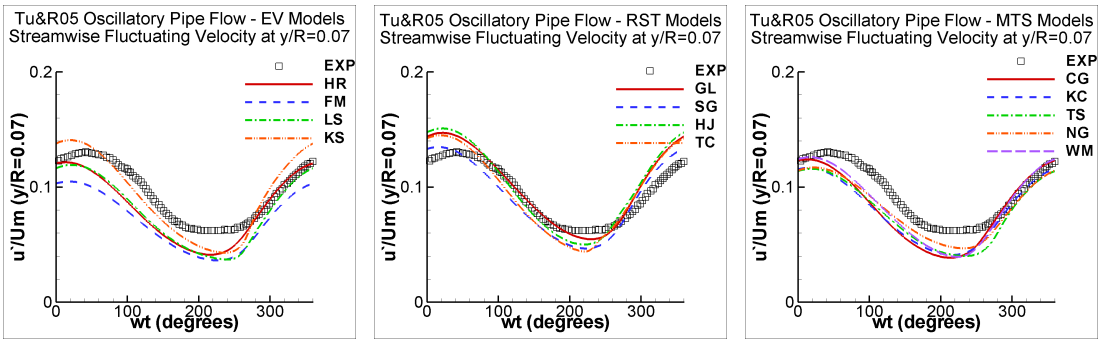

Figure 5.165: Prediction of the rms streamwise fluctuating velocity at $y/R = 0.07$ throughout the cycle by the (a) eddy-viscosity models, (b) Reynolds stress transport models and (c) multiple-time-scale models and compared with the experiments of Tu and Ramaprian (1983a) in the Tu&R05 oscillatory pipe flow case. Models as in Table 3.25.

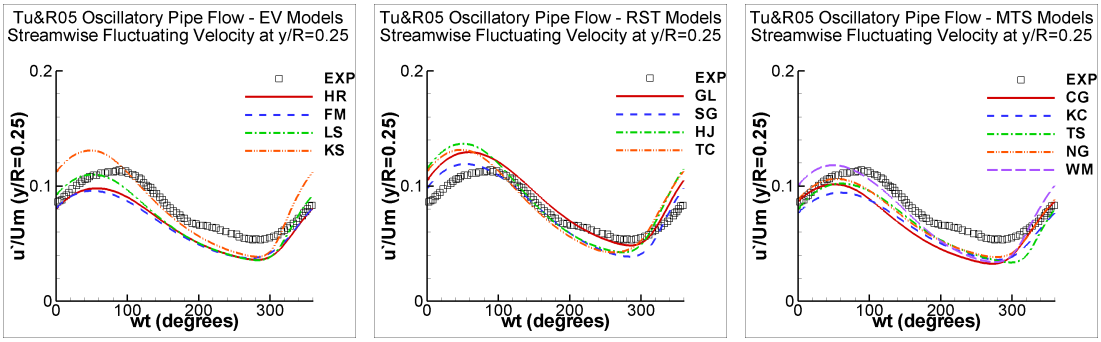

Figure 5.166: Prediction of the rms streamwise fluctuating velocity at $y/R = 0.25$ throughout the cycle by the (a) eddy-viscosity models, (b) Reynolds stress transport models and (c) multiple-time-scale models and compared with the experiments of Tu and Ramaprian (1983a) in the Tu&R05 oscillatory pipe flow case. Models as in Table 3.25.

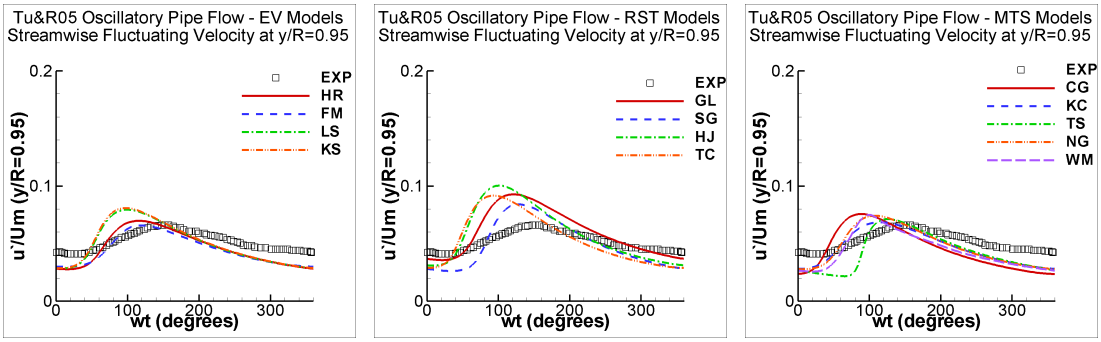

Figure 5.167: Prediction of the rms streamwise fluctuating velocity at $y/R = 0.95$ throughout the cycle by the (a) eddy-viscosity models, (b) Reynolds stress transport models and (c) multiple-time-scale models and compared with the experiments of Tu and Ramaprian (1983a) in the Tu&R05 oscillatory pipe flow case. Models as in Table 3.25.

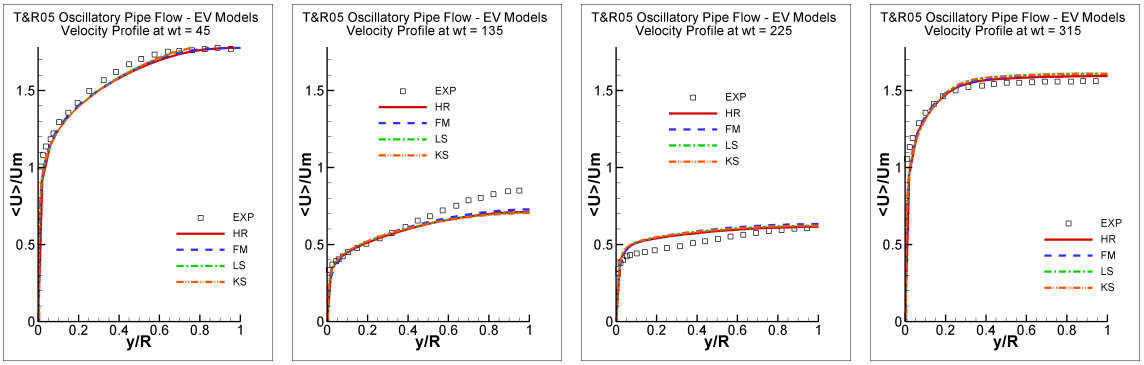

(a) (b) (c) (d)

Figure 5.168: Velocity profile at selected cycle positions in the Tu&R05 oscillatory pipe flow case predicted by the eddy-viscosity models and compared with the experiments of Tu and Ramaprian (1983a). Models as in Table 3.25.

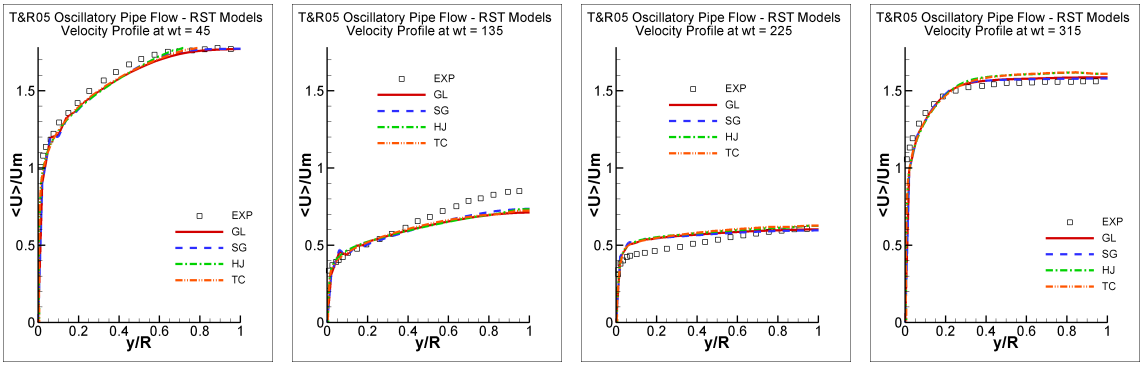

(a) (b) (c) (d)

Figure 5.169: Velocity profile at selected cycle positions in the Tu&R05 oscillatory pipe flow case predicted by the Reynolds stress transport models and compared with the experiments of Tu and Ramaprian (1983a). Models as in Table 3.25.

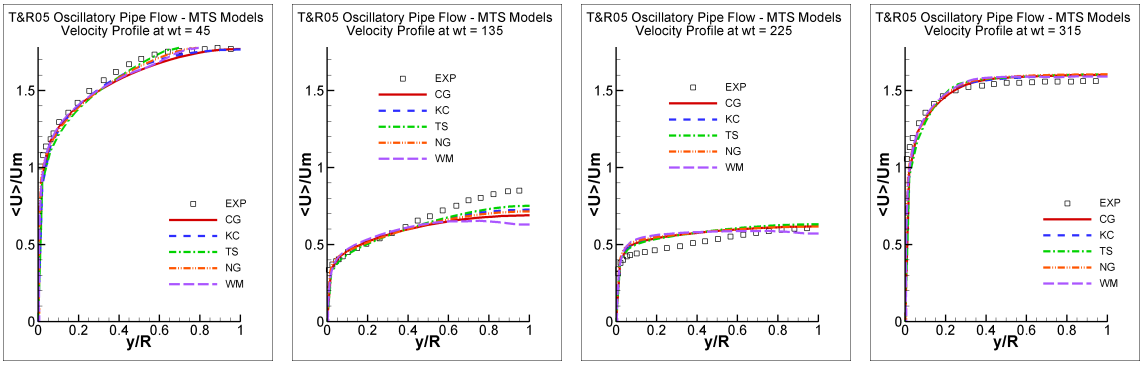

(a) (b) (c) (d)

Figure 5.170: Velocity profile at selected cycle positions in the Tu&R05 oscillatory pipe flow case predicted by the multiple-time-scale models and compared with the experiments of Tu and Ramaprian (1983a). Models as in Table 3.25.

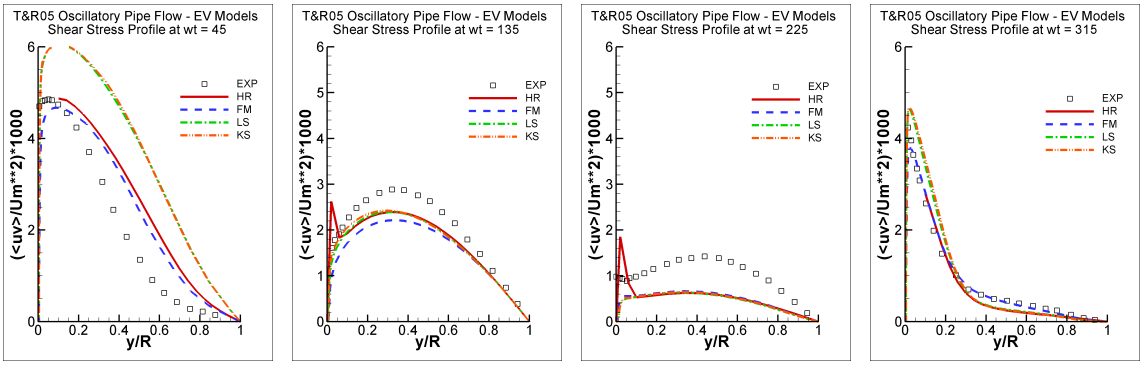

(a) (b) (c) (d)

Figure 5.171: Reynolds shear stress profile at selected cycle positions in the Tu&R05 oscillatory pipe flow case predicted by the eddy-viscosity models and compared with the experiments of Tu and Ramaprian (1983a). Models as in Table 3.25.

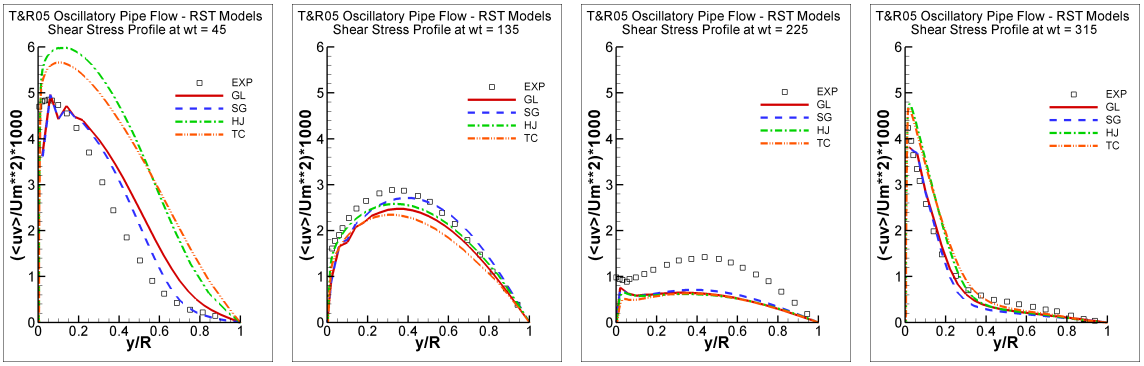

(a) (b) (c) (d)

Figure 5.172: Reynolds shear stress profile at selected cycle positions in the Tu&R05 oscillatory pipe flow case predicted by the Reynolds stress transport models and compared with the experiments of Tu and Ramaprian (1983a). Models as in Table 3.25.

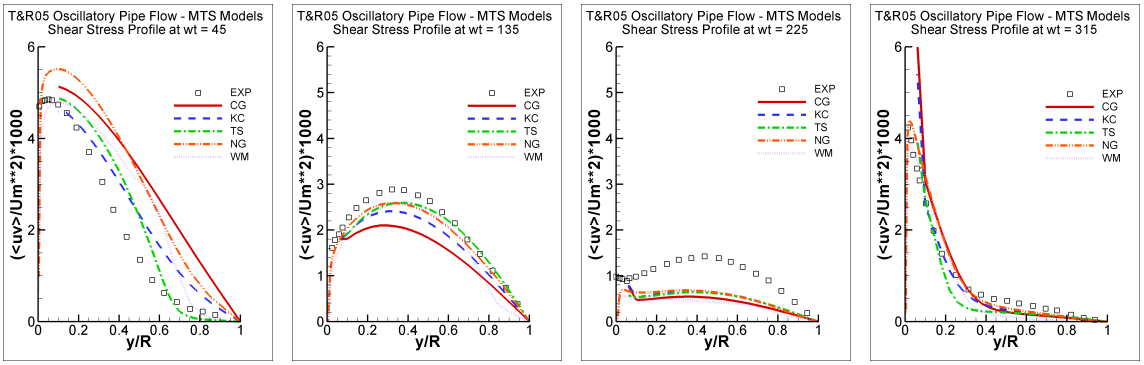

(a) (b) (c) (d)

Figure 5.173: Reynolds shear stress profile at selected cycle positions in the Tu&R05 oscillatory pipe flow case predicted by the multiple-time-scale models and compared with the experiments of Tu and Ramaprian (1983a). Models as in Table 3.25.

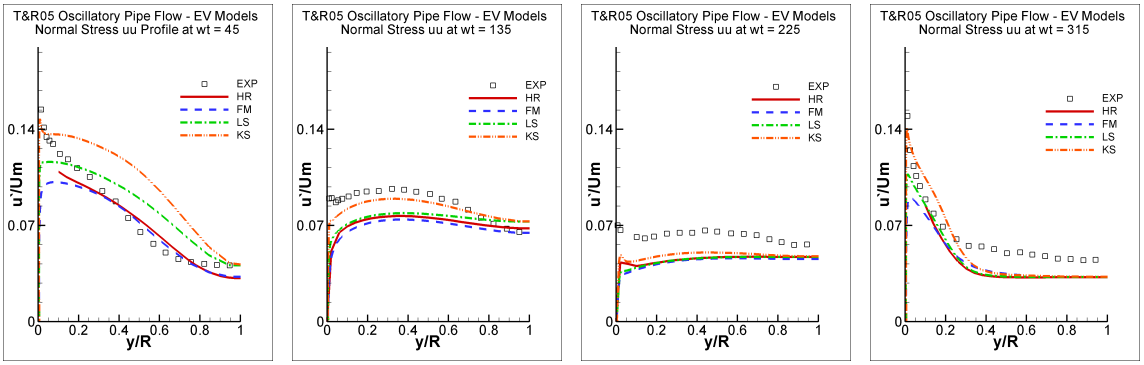

(a) (b) (c) (d)

Figure 5.174: Rms streamwise fluctuating velocity profile at selected cycle positions in the Tu&R05 oscillatory pipe flow case predicted by the eddy-viscosity models and compared with the experiments of Tu and Ramaprian (1983a). Models as in Table 3.25.

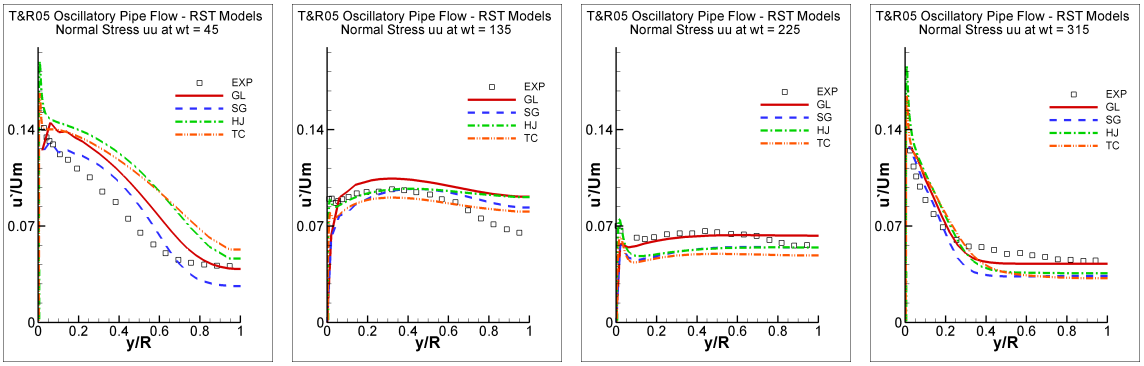

(a) (b) (c) (d)

Figure 5.175: Rms streamwise fluctuating velocity profile at selected cycle positions in the Tu&R05 oscillatory pipe flow case predicted by the Reynolds stress transport models and compared with the experiments of Tu and Ramaprian (1983a). Models as in Table 3.25.

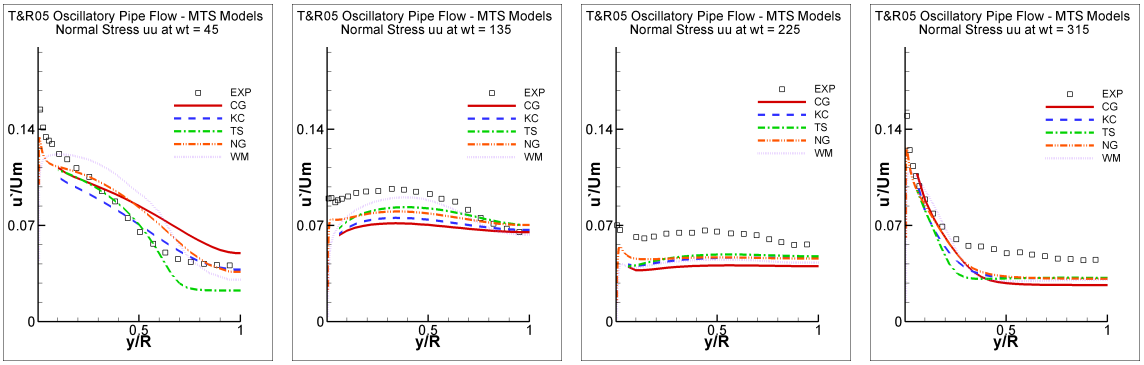

(a) (b) (c) (d)

Figure 5.176: Rms Streamwise fluctuating velocity profile at selected cycle positions in the Tu&R05 oscillatory pipe flow case predicted by the multiple-time-scale models and compared with the experiments of Tu and Ramaprian (1983a). Models as in Table 3.25.

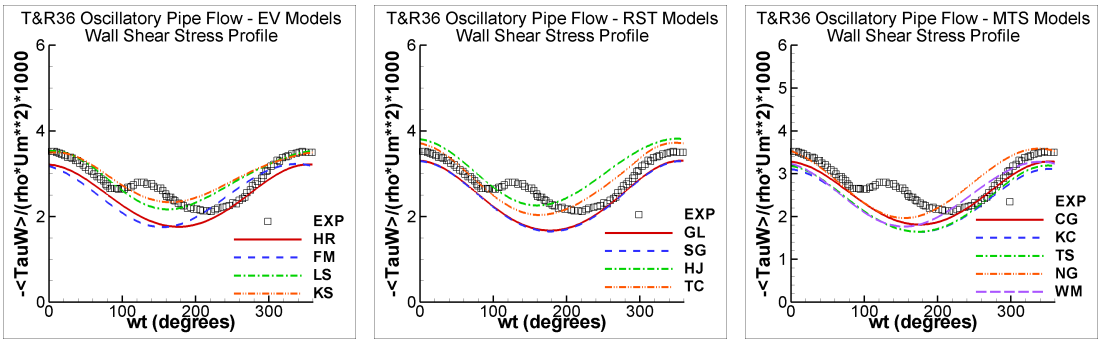

Figure 5.177: Prediction of the wall shear stress throughout the cycle by the (a) eddy-viscosity models, (b) Reynolds stress transport models and (c) multiple-time-scale models and compared with the experiments of Tu and Ramaprian (1983a) in the Tu&R36 oscillatory pipe flow case. Models as in Table 3.25.

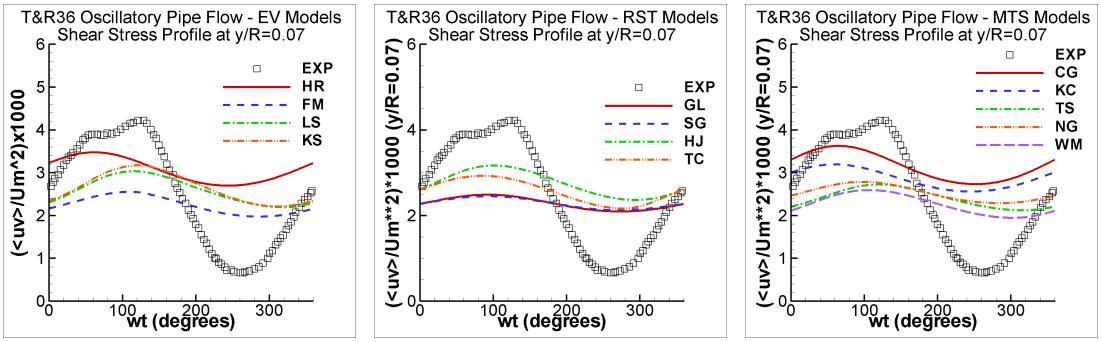

Figure 5.178: Prediction of the Reynolds shear stress at $y/R = 0.07$ throughout the cycle by the (a) eddy-viscosity models, (b) Reynolds stress transport models and (c) multiple-time-scale models and compared with the experiments of Tu and Ramaprian (1983a) in the Tu&R36 oscillatory pipe flow case. Models as in Table 3.25.

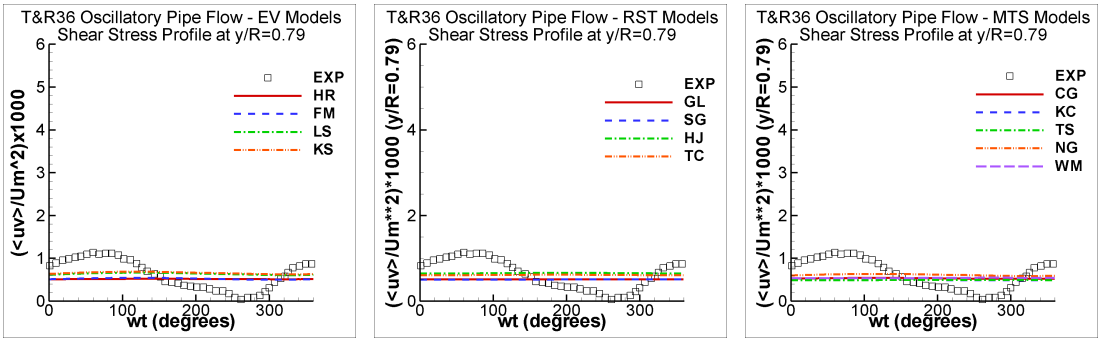

Figure 5.179: Prediction of the Reynolds shear stress at $y/R = 0.79$ throughout the cycle by the (a) eddy-viscosity models, (b) Reynolds stress transport models and (c) multiple-time-scale models and compared with the experiments of Tu and Ramaprian (1983a) in the Tu&R36 oscillatory pipe flow case. Models as in Table 3.25.

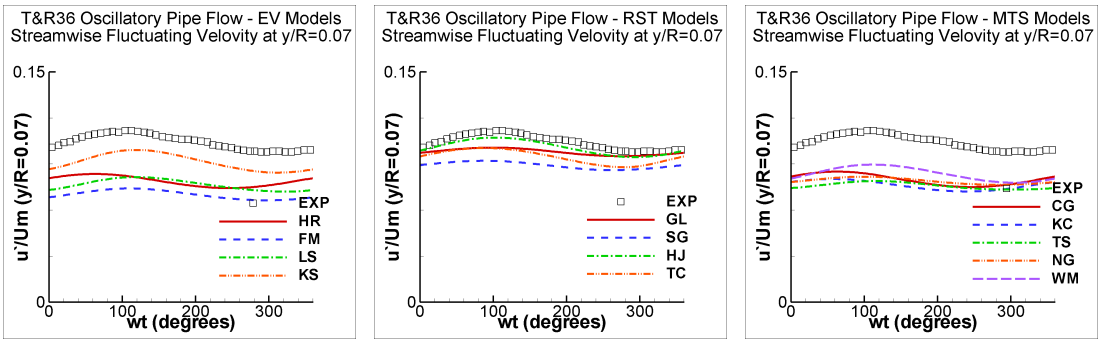

Figure 5.180: Prediction of the rms streamwise fluctuating velocity at $y/R = 0.07$ throughout the cycle by the (a) eddy-viscosity models, (b) Reynolds stress transport models and (c) multiple-time-scale models and compared with the experiments of Tu and Ramaprian (1983a) in the Tu&R36 oscillatory pipe flow case. Models as in Table 3.25.

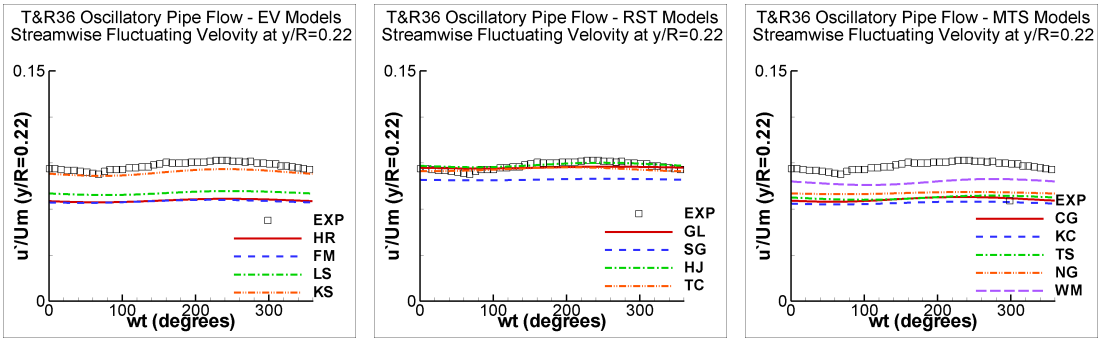

Figure 5.181: Prediction of the rms streamwise fluctuating velocity at $y/R = 0.22$ throughout the cycle by the (a) eddy-viscosity models, (b) Reynolds stress transport models and (c) multiple-time-scale models and compared with the experiments of Tu and Ramaprian (1983a) in the Tu&R36 oscillatory pipe flow case. Models as in Table 3.25.

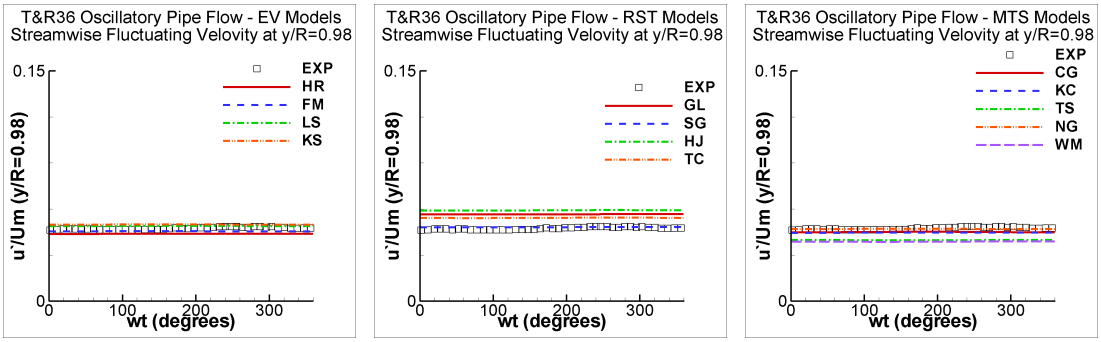

Figure 5.182: Prediction of the rms streamwise fluctuating velocity at $y/R = 0.98$ throughout the cycle by the (a) eddy-viscosity models, (b) Reynolds stress transport models and (c) multiple-time-scale models and compared with the experiments of Tu and Ramaprian (1983a) in the Tu&R36 oscillatory pipe flow case. Models as in Table 3.25.

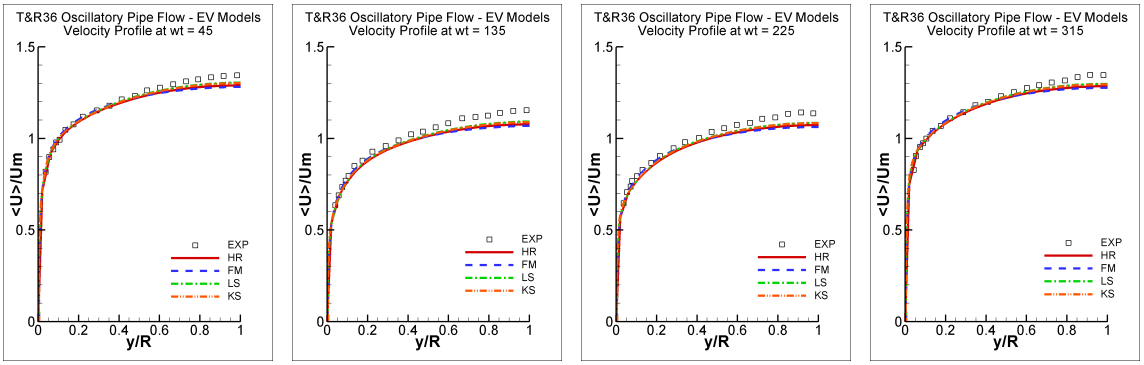

(a) (b) (c) (d)

Figure 5.183: Velocity profile at selected cycle positions in the Tu&R36 oscillatory pipe flow case predicted by the eddy-viscosity models and compared with the experiments of Tu and Ramaprian (1983a). Models as in Table 3.25.

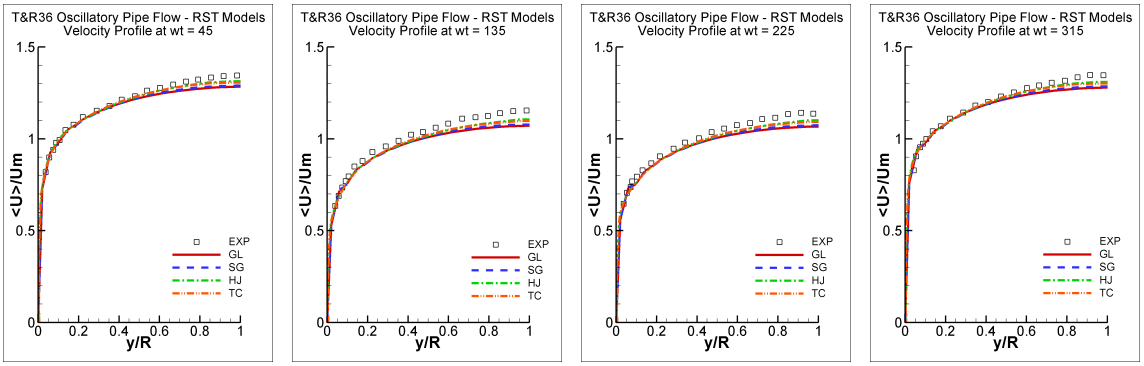

(a) (b) (c) (d)

Figure 5.184: Velocity profile at selected cycle positions in the Tu&R36 oscillatory pipe flow case predicted by the Reynolds stress transport models and compared with the experiments of Tu and Ramaprian (1983a). Models as in Table 3.25.

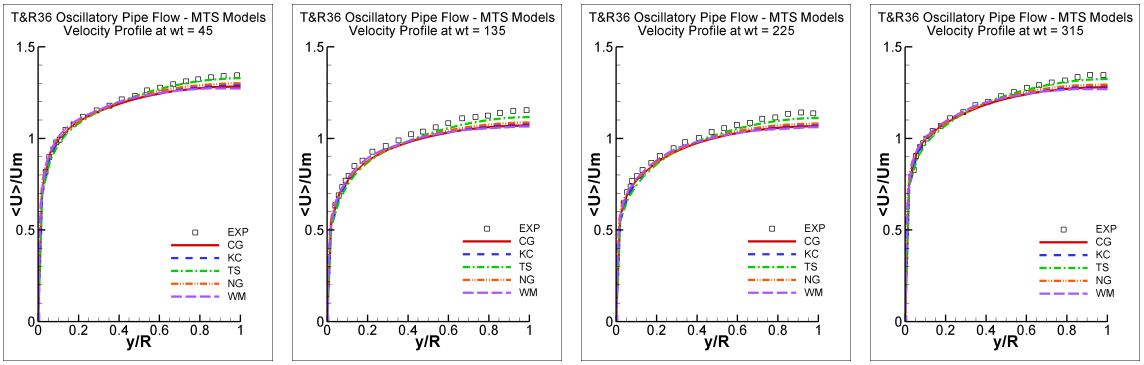

(a) (b) (c) (d)

Figure 5.185: Velocity profile at selected cycle positions in the Tu&R36 oscillatory pipe flow case predicted by the multiple-time-scale models and compared with the experiments of Tu and Ramaprian (1983a). Models as in Table 3.25.

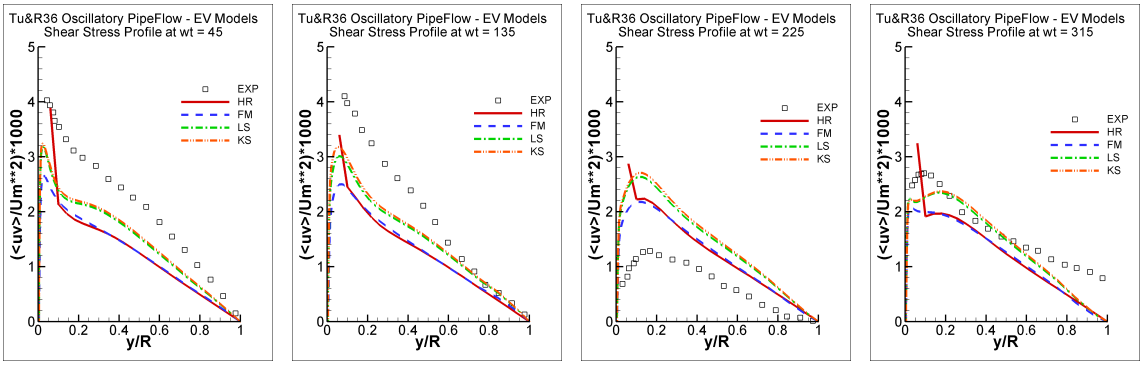

(a) (b) (c) (d)

Figure 5.186: Reynolds shear stress profile at selected cycle positions in the Tu&R36 oscillatory pipe flow case predicted by the eddy-viscosity models and compared with the experiments of Tu and Ramaprian (1983a). Models as in Table 3.25.

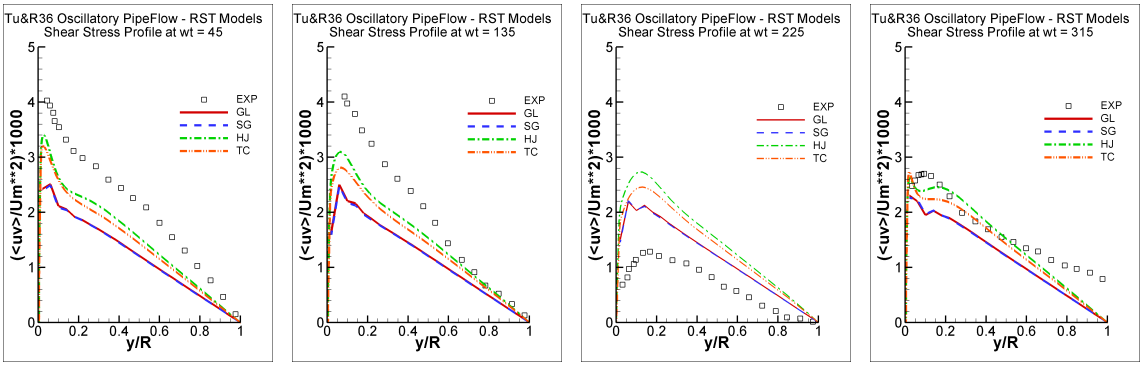

(a) (b) (c) (d)

Figure 5.187: Reynolds shear stress profile at selected cycle positions in the Tu&R36 oscillatory pipe flow case predicted by the Reynolds stress transport models and compared with the experiments of Tu and Ramaprian (1983a). Models as in Table 3.25.

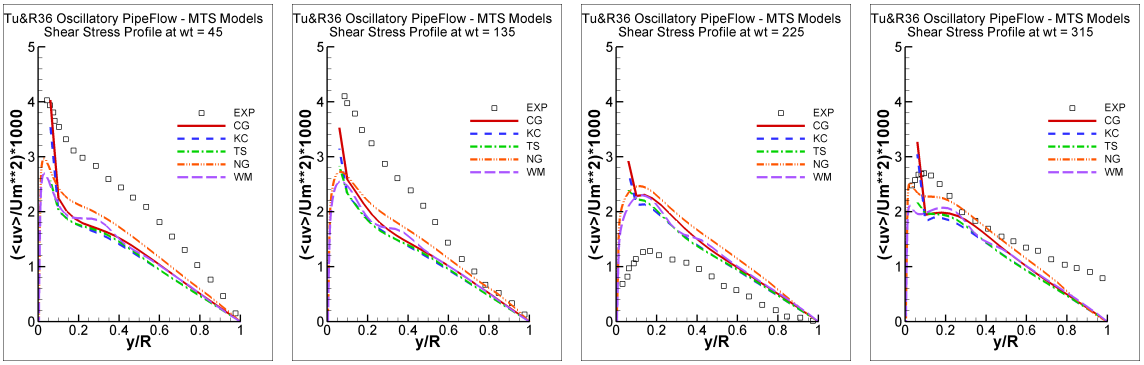

(a) (b) (c) (d)

Figure 5.188: Reynolds shear stress profile at selected cycle positions in the Tu&R36 oscillatory pipe flow case predicted by the multiple-time-scale models and compared with the experiments of Tu and Ramaprian (1983a). Models as in Table 3.25.

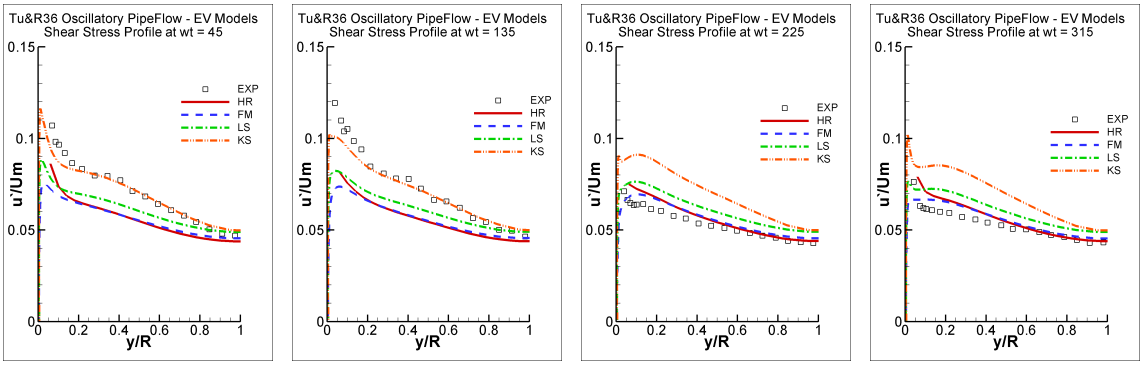

(a) (b) (c) (d)

Figure 5.189: Rms streamwise fluctuating velocity profile at selected cycle positions in the Tu&R36 oscillatory pipe flow case predicted by the eddy-viscosity models and compared with the experiments of Tu and Ramaprian (1983a). Models as in Table 3.25.

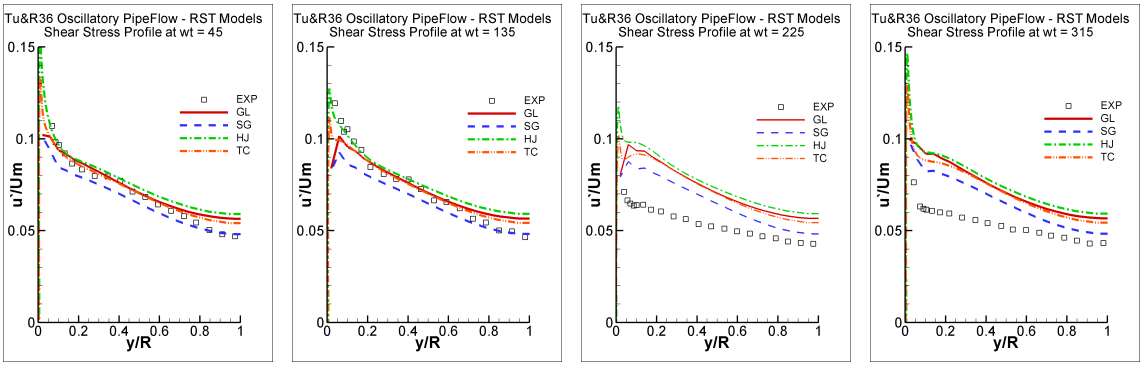

(a) (b) (c) (d)

Figure 5.190: Rms streamwise fluctuating velocity profile at selected cycle positions in the Tu&R36 oscillatory pipe flow case predicted by the Reynolds stress transport models and compared with the experiments of Tu and Ramaprian (1983a). Models as in Table 3.25.

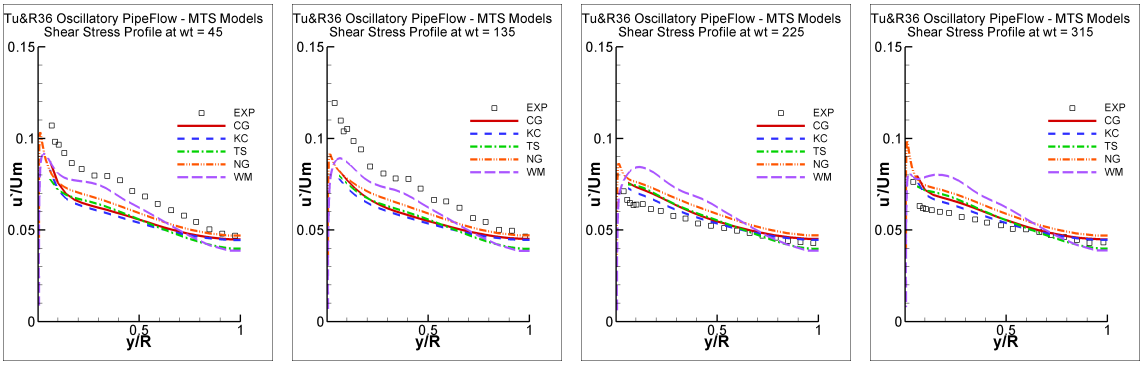

(a) (b) (c) (d)

Figure 5.191: Rms streamwise fluctuating velocity profile at selected cycle positions in the Tu&R36 oscillatory pipe flow case predicted by the multiple-time-scale models and compared with the experiments of Tu and Ramaprian (1983a). Models as in Table 3.25.

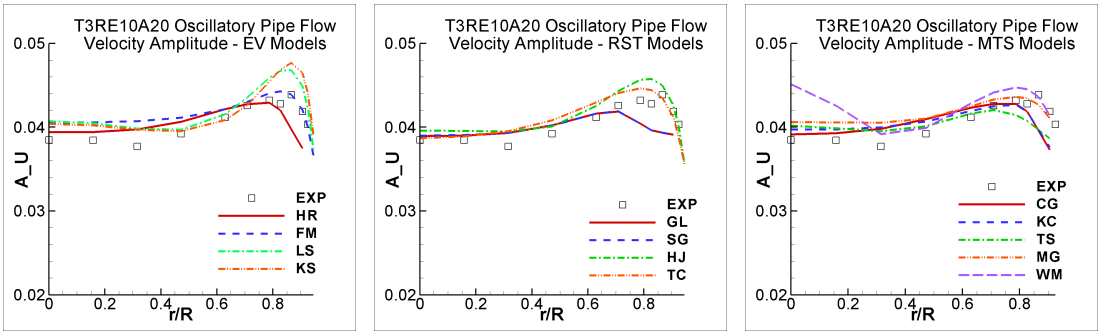

(a) (b) (c)

Figure 5.192: Prediction of the amplitude of velocity for the T3RE10A20 oscillatory pipe flow by the: (a) eddy-viscosity models, (b) Reynolds stress transport models and (c) multiple-time-scale models and compared with the experiments of He and Jackson (2009). Models as in Table 3.25.

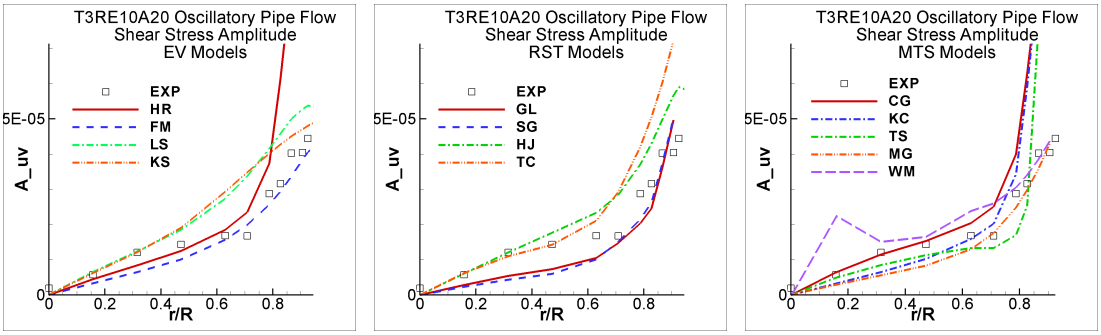

(a) (b) (c)

Figure 5.193: Prediction of the amplitude of Reynolds shear stress for the T3RE10A20 oscillatory pipe flow by the: (a) eddy-viscosity models, (b) Reynolds stress transport models and (c) multiple-time-scale models and compared with the experiments of He and Jackson (2009). Models as in Table 3.25.

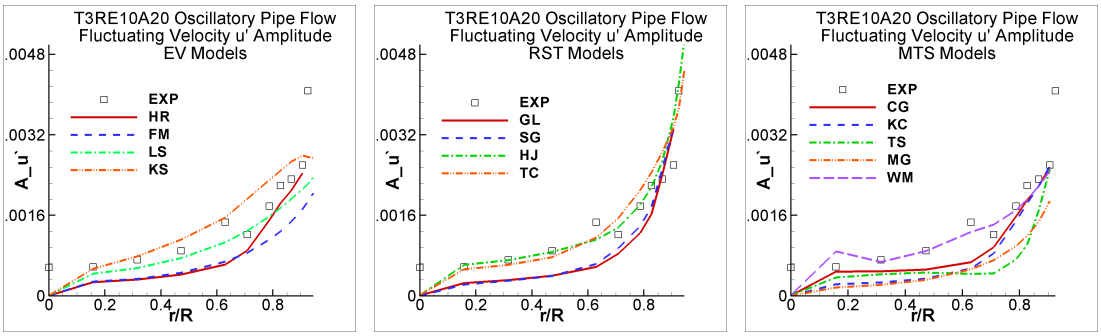

(a) (b) (c)

Figure 5.194: Prediction of the amplitude of rms streamwise fluctuating velocity for the T3RE10A20 oscillatory pipe flow by the: (a) eddy-viscosity models, (b) Reynolds stress transport models and (c) multiple-time-scale models and compared with the experiments of He and Jackson (2009). Models as in Table 3.25.

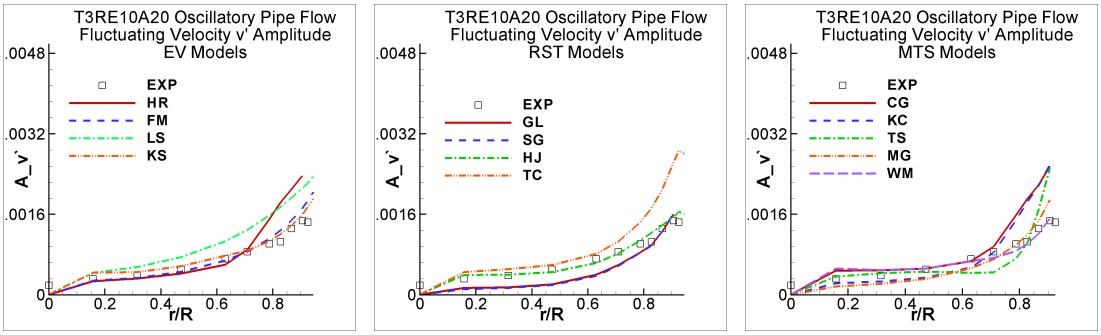

(a) (b) (c)

Figure 5.195: Prediction of the amplitude of rms wall-normal fluctuating velocity for the T3RE10A20 oscillatory pipe flow by the: (a) eddy-viscosity models, (b) Reynolds stress transport models and (c) multiple-time-scale models and compared with the experiments of He and Jackson (2009). Models as in Table 3.25.

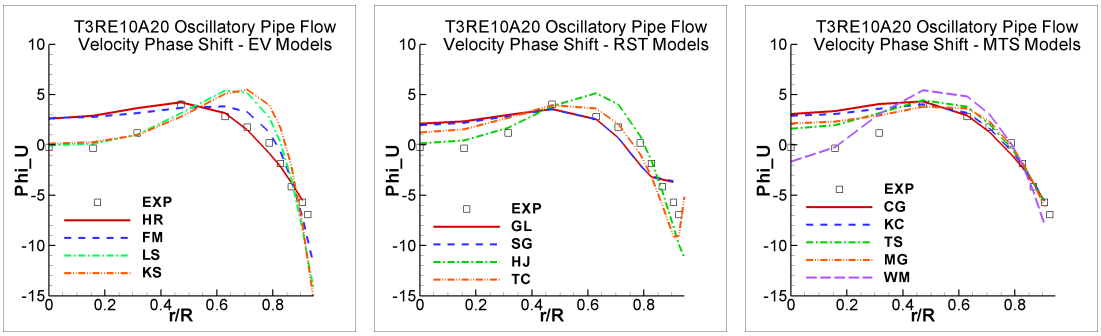

(a) (b) (c)

Figure 5.196: Prediction of the phase shift of velocity for the T3RE10A20 oscillatory pipe flow by the: (a) eddy-viscosity models, (b) Reynolds stress transport models and (c) multiple-time-scale models and compared with the experiments of He and Jackson (2009). Models as in Table 3.25.

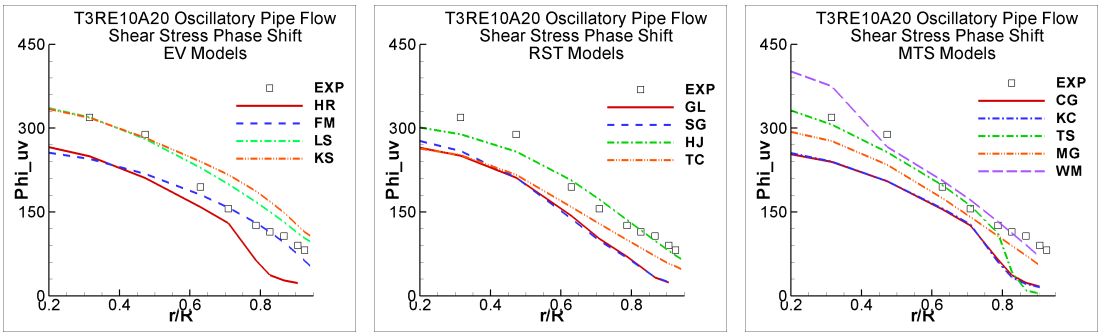

(a) (b) (c)

Figure 5.197: Prediction of the phase shift of Reynolds shear stress for the T3RE10A20 oscillatory pipe flow by the: (a) eddy-viscosity models, (b) Reynolds stress transport models and (c) multiple-time-scale models and compared with the experiments of He and Jackson (2009). Models as in Table 3.25.

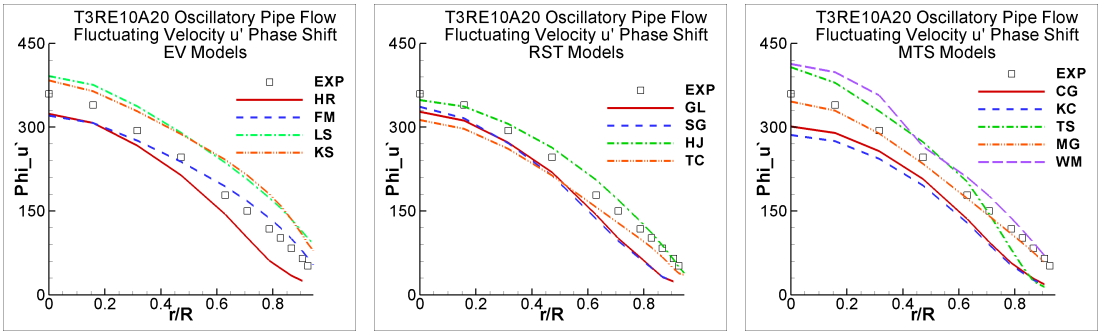

(a) (b) (c)

Figure 5.198: Prediction of the phase shift of rms streamwise fluctuating velocity for the T3RE10A20 oscillatory pipe flow by the: (a) eddy-viscosity models, (b) Reynolds stress transport models and (c) multiple-time-scale models and compared with the experiments of He and Jackson (2009). Models as in Table 3.25.

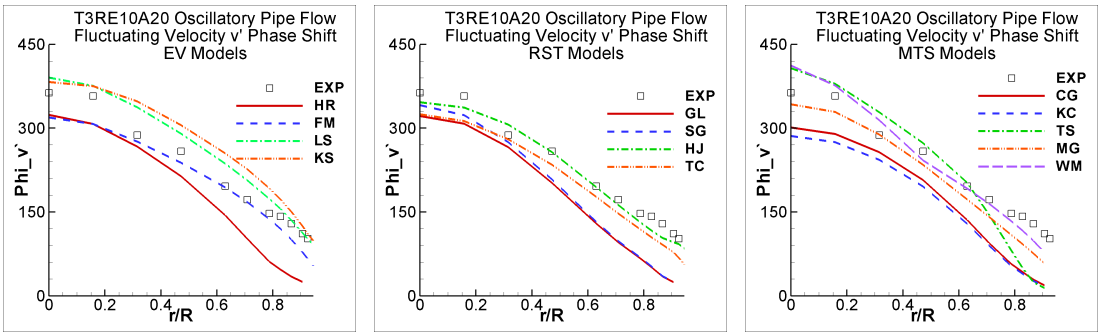

(a) (b) (c)

Figure 5.199: Prediction of the phase shift of rms wall-normal fluctuating velocity for the T3RE10A20 oscillatory pipe flow by the: (a) eddy-viscosity models, (b) Reynolds stress transport models and (c) multiple-time-scale models and compared with the experiments of He and Jackson (2009). Models as in Table 3.25.

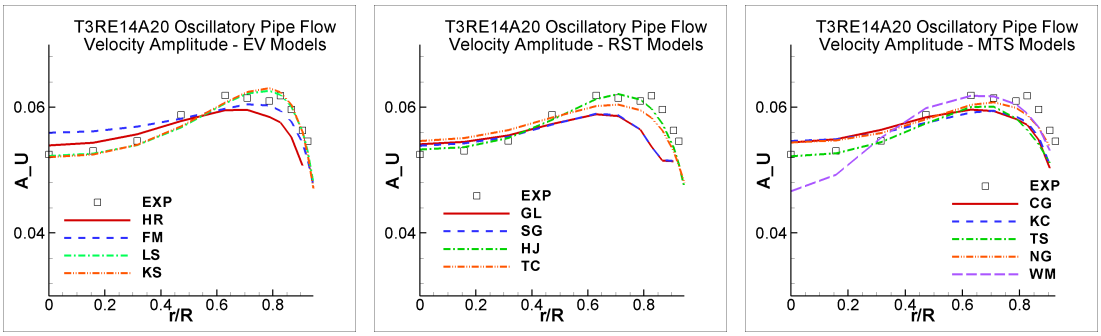

(a) (b) (c)

Figure 5.200: Prediction of the amplitude of velocity for the T3RE14A20 oscillatory pipe flow by the: (a) eddy-viscosity models, (b) Reynolds stress transport models and (c) multiple-time-scale models and compared with the experiments of He and Jackson (2009). Models as in Table 3.25.

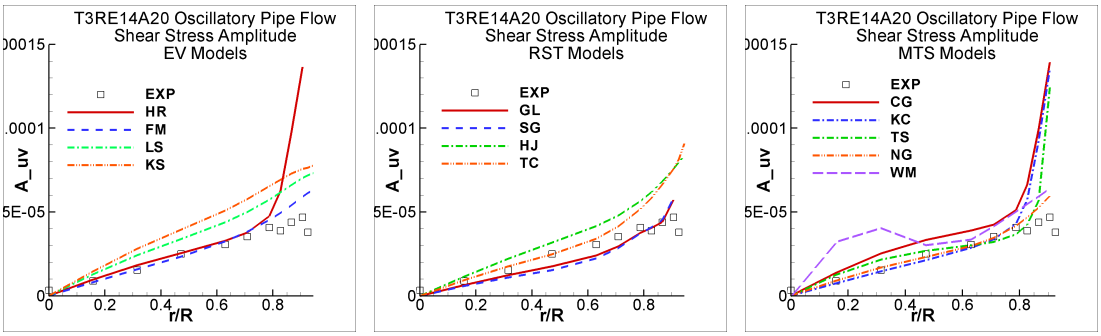

(a) (b) (c)

Figure 5.201: Prediction of the amplitude of Reynolds shear stress for the T3RE14A20 oscillatory pipe flow by the: (a) eddy-viscosity models, (b) Reynolds stress transport models and (c) multiple-time-scale models and compared with the experiments of He and Jackson (2009). Models as in Table 3.25.

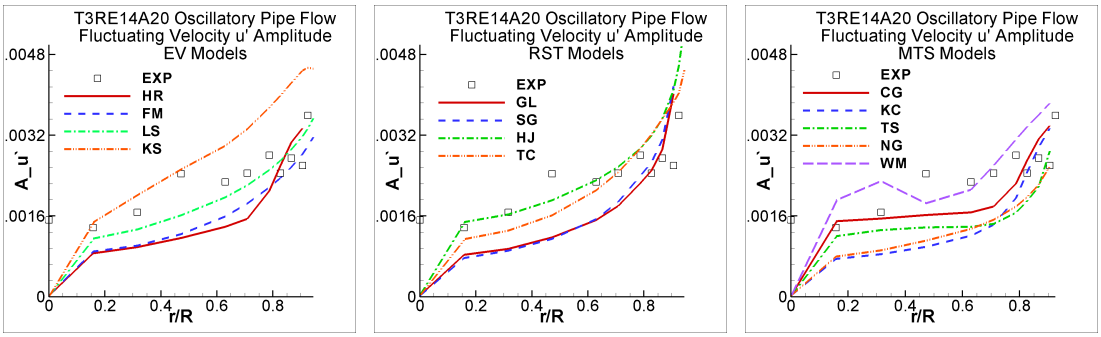

(a) (b) (c)

Figure 5.202: Prediction of the amplitude of rms streamwise fluctuating velocity for the T3RE14A20 oscillatory pipe flow by the: (a) eddy-viscosity models, (b) Reynolds stress transport models and (c) multiple-time-scale models and compared with the experiments of He and Jackson (2009). Models as in Table 3.25.

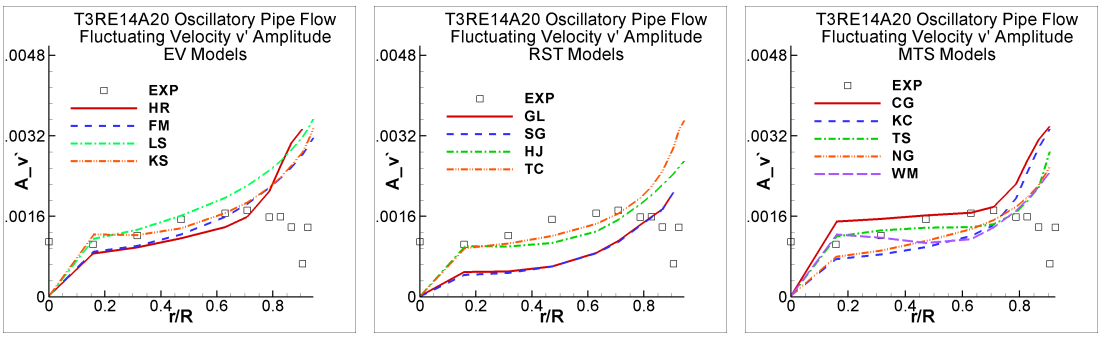

(a) (b) (c)

Figure 5.203: Prediction of the amplitude of rms wall-normal fluctuating velocity for the T3RE14A20 oscillatory pipe flow by the: (a) eddy-viscosity models, (b) Reynolds stress transport models and (c) multiple-time-scale models and compared with the experiments of He and Jackson (2009). Models as in Table 3.25.

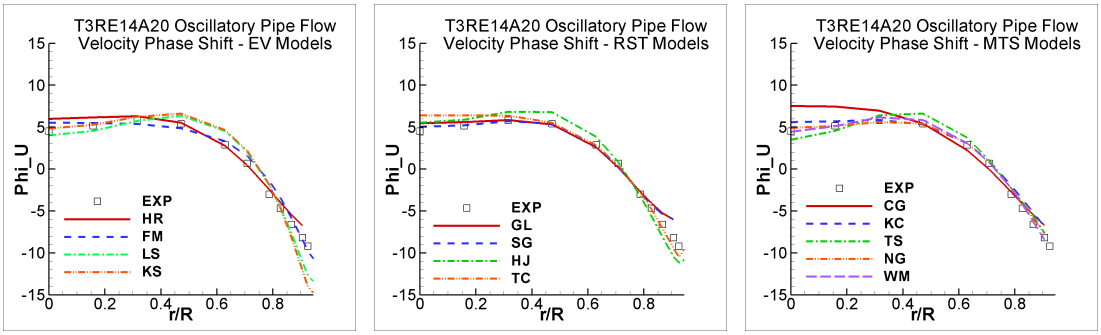

(a) (b) (c)

Figure 5.204: Prediction of the phase shift of velocity for the T3RE14A20 oscillatory pipe flow by the: (a) eddy-viscosity models, (b) Reynolds stress transport models and (c) multiple-time-scale models and compared with the experiments of He and Jackson (2009). Models as in Table 3.25.

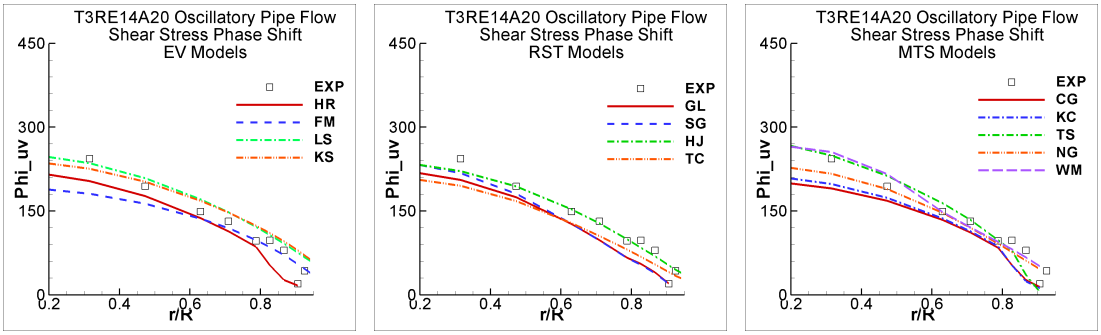

(a) (b) (c)

Figure 5.205: Prediction of the phase shift of Reynolds shear stress for the T3RE14A20 oscillatory pipe flow by the: (a) eddy-viscosity models, (b) Reynolds stress transport models and (c) multiple-time-scale models and compared with the experiments of He and Jackson (2009). Models as in Table 3.25.

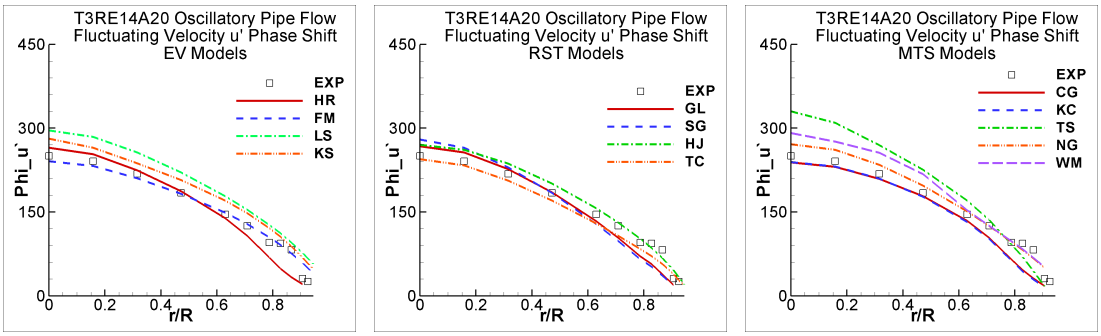

(a) (b) (c)

Figure 5.206: Prediction of the phase shift of rms streamwise fluctuating velocity for the T3RE14A20 oscillatory pipe flow by the: (a) eddy-viscosity models, (b) Reynolds stress transport models and (c) multiple-time-scale models and compared with the experiments of He and Jackson (2009). Models as in Table 3.25.

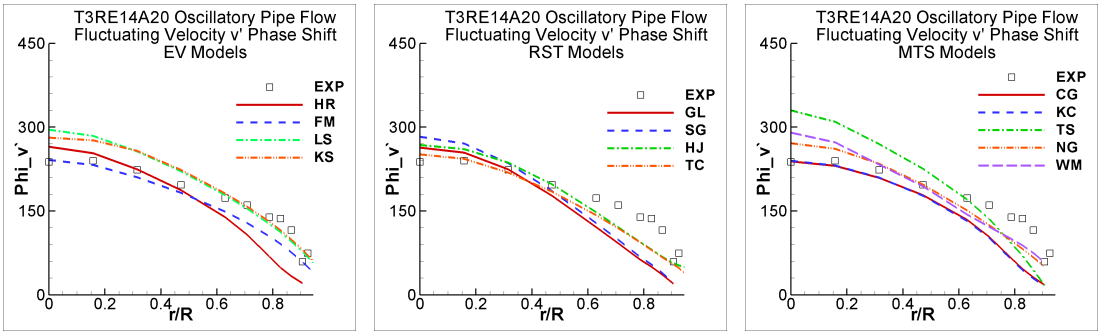

(a) (b) (c)

Figure 5.207: Prediction of the phase shift of rms wall-normal fluctuating velocity for the T3RE14A20 oscillatory pipe flow by the: (a) eddy-viscosity models, (b) Reynolds stress transport models and (c) multiple-time-scale models and compared with the experiments of He and Jackson (2009). Models as in Table 3.25.

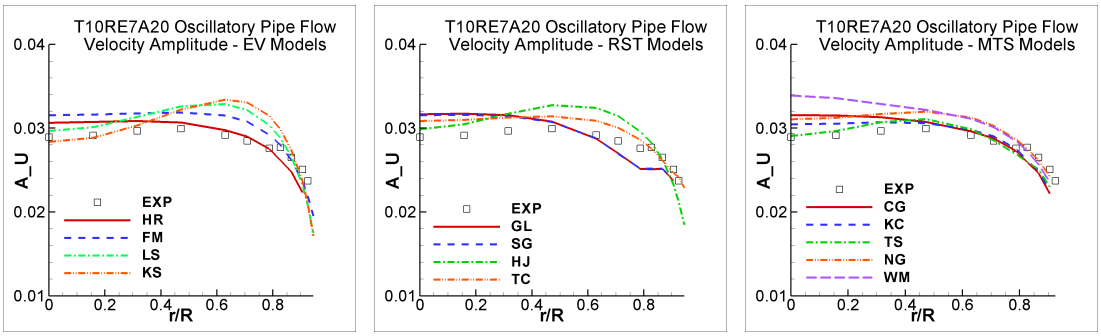

(a) (b) (c)

Figure 5.208: Prediction of the amplitude of velocity for the T10RE7A20 oscillatory pipe flow by the: (a) eddy-viscosity models, (b) Reynolds stress transport models and (c) multiple-time-scale models and compared with the experiments of He and Jackson (2009). Models as in Table 3.25.

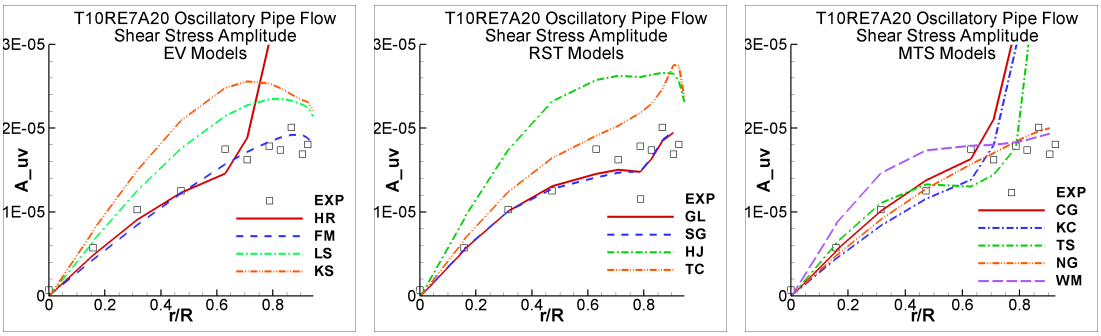

(a) (b) (c)

Figure 5.209: Prediction of the amplitude of Reynolds shear stress for the T10RE7A20 oscillatory pipe flow by the: (a) eddy-viscosity models, (b) Reynolds stress transport models and (c) multiple-time-scale models and compared with the experiments of He and Jackson (2009). Models as in Table 3.25.

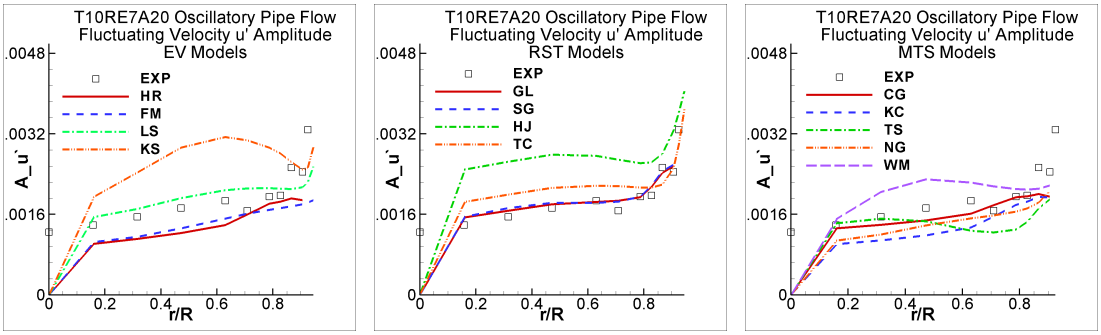

(a) (b) (c)

Figure 5.210: Prediction of the amplitude of rms streamwise fluctuating velocity for the T10RE7A20 oscillatory pipe flow by the: (a) eddy-viscosity models, (b) Reynolds stress transport models and (c) multiple-time-scale models and compared with the experiments of He and Jackson (2009). Models as in Table 3.25.

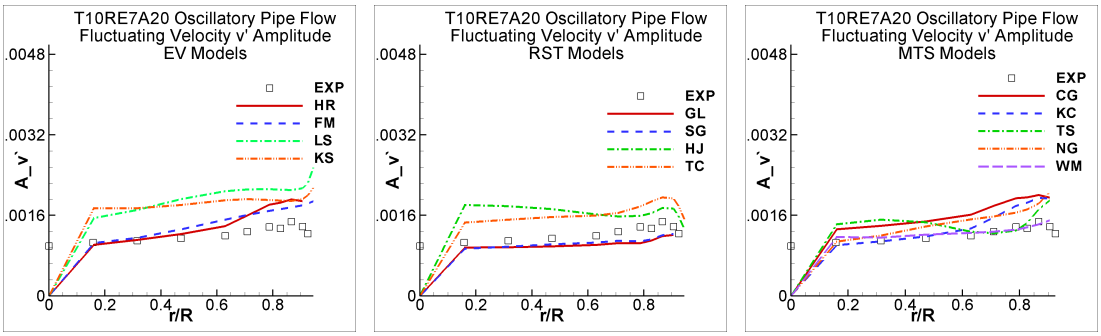

(a) (b) (c)

Figure 5.211: Prediction of the amplitude of rms wall-normal fluctuating velocity for the T10RE7A20 oscillatory pipe flow by the: (a) eddy-viscosity models, (b) Reynolds stress transport models and (c) multiple-time-scale models and compared with the experiments of He and Jackson (2009). Models as in Table 3.25.

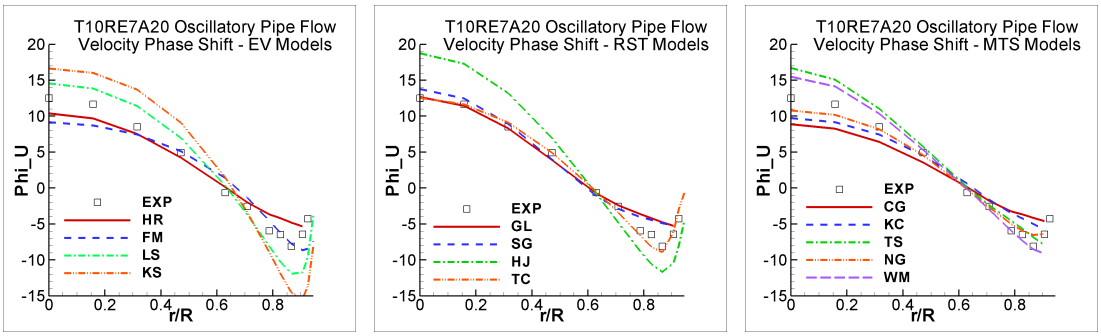

(a) (b) (c)

Figure 5.212: Prediction of the phase shift of velocity for the T10RE7A20 oscillatory pipe flow by the: (a) eddy-viscosity models, (b) Reynolds stress transport models and (c) multiple-time-scale models and compared with the experiments of He and Jackson (2009). Models as in Table 3.25.

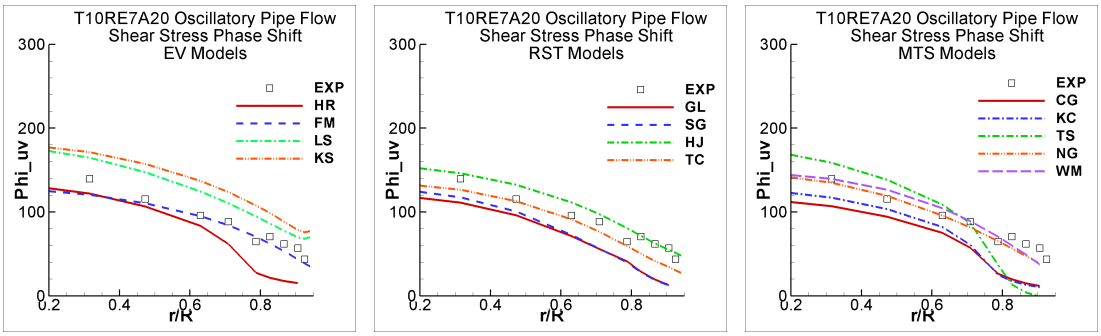

(a) (b) (c)

Figure 5.213: Prediction of the phase shift of Reynolds shear stress for the T10RE7A20 oscillatory pipe flow by the: (a) eddy-viscosity models, (b) Reynolds stress transport models and (c) multiple-time-scale models and compared with the experiments of He and Jackson (2009). Models as in Table 3.25.

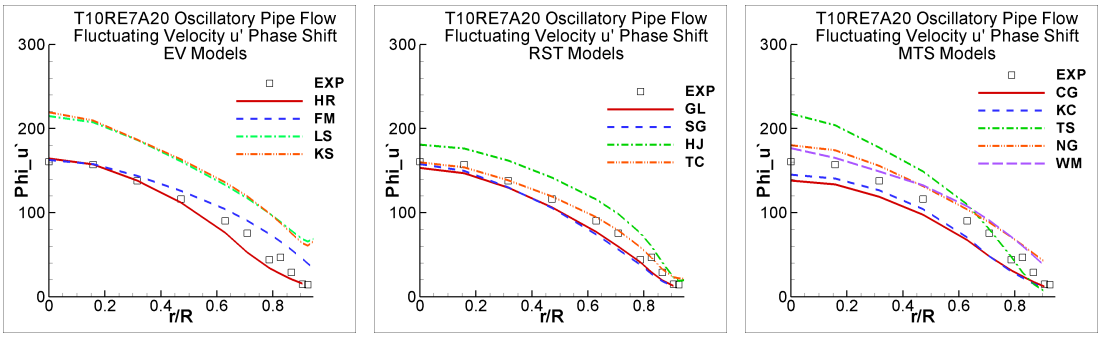

(a) (b) (c)

Figure 5.214: Prediction of the phase shift of rms streamwise fluctuating velocity for the T10RE7A20 oscillatory pipe flow by the: (a) eddy-viscosity models, (b) Reynolds stress transport models and (c) multiple-time-scale models and compared with the experiments of He and Jackson (2009). Models as in Table 3.25.

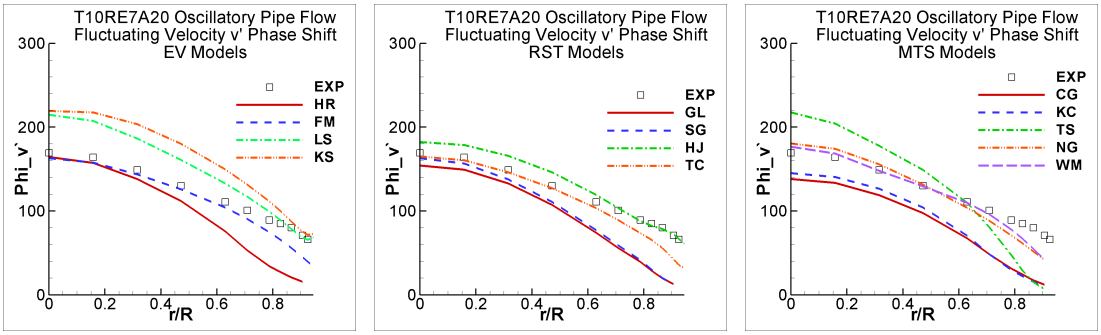

(a) (b) (c)

Figure 5.215: Prediction of the phase shift of rms wall-normal fluctuating velocity for the T10RE7A20 oscillatory pipe flow by the: (a) eddy-viscosity models, (b) Reynolds stress transport models and (c) multiple-time-scale models and compared with the experiments of He and Jackson (2009). Models as in Table 3.25.

5.8 Fully Developed Ramp Up Pipe Flow

This case again consists of an unsteady pipe flow, however the unsteadiness is not oscillatory, but monotonic. The bulk velocity of a fully developed pipe flow is set to increase or decrease linearly in time, characterized by a ramp profile. If the bulk velocity is increased in time, it is a ramp up flow; if the velocity decreases in time, it is a ramp down flow.

It was noted by He and Jackson (2000) that, in contrast to oscillatory pipe flows, non-periodic transient pipe flows, such as this one, have not been so widely explored experimentally. Nevertheless, this case is interesting as it features non-equilibrium effects which can be seen by the lag in time the turbulent quantities such as the turbulent kinetic energy and the Reynolds stresses need to respond to the imposed change in the bulk velocity, specially in regions further away from the wall. As noted by He and Jackson (2000), similarly to oscillatory pipe flows, the turbulent quantities start to respond to the imposed unsteadiness at the wall and then propagate its effects outwards into the flow up to its centre, as one will be able to see in the results, where the experimental data will be presented together with the predictions of the turbulent models.

While in oscillatory flows the frequency determines the lag in response and how much effect the turbulence will experience, in these ramp flows, the rate of acceleration and deceleration can play this role. However, it was noted that in accelerating flows, the influence of the acceleration rate becomes active only at very high rates. It was also observed by He and Jackson (2000) that for the same absolute slope in the ramp function, the turbulence needs more time to respond to the changing bulk velocity when the flow is accelerating compared to when it is decelerating. Another parameter which was identified by He and Jackson (2000) in influencing the lag in response of the turbulent quantities was the initial level of turbulence, say the initial Reynolds number of the flow. The lower the initial Reynolds number in an accelerating flow, the longer the turbulent quantities take to respond to the imposed change in the bulk velocity, thus implying a longer delay.

He and Jackson (2000) also studied the departure of the velocity and turbulent quantities profiles from the correspondent steady case at each Reynolds number of the flow. It was noticed that if the rate of acceleration was very slow, the variables profiles at each Reynolds number would be close to the steady state profile at the same Reynolds number. As the rate of acceleration increased, the profiles differed more from the corresponding steady state ones. The low acceleration rate cases could be then compared with the low frequency cases in oscillatory pipe flows. In order to identify how far from a series of steady states the ramp case would be, He and Jackson (2000) defined a parameter $\gamma = \frac{D}{U_{\tau_0}} \frac{1}{U_{b_0}} \frac{dU_b}{dt}$, where D is the pipe diameter, U_{τ_0} is the initial friction velocity, U_{b_0} is the initial bulk velocity of the flow and $\frac{dU_b}{dt}$ is the acceleration/deceleration rate. If γ is much less than 1, the flow is close to the steady state. The greater than unity this parameter is, the more different from the steady state the profiles of the turbulent quantities will be.

Based on the tests mentioned above, He and Jackson (2000) proposed a mechanism through which the unsteadiness imposed on the bulk velocity would propagate from the

near-wall region towards the centre of the pipe: due to the no-slip condition at the wall, the velocity gradients would increase in this region due to the change in the bulk velocity; that would than generate an increase in the turbulent kinetic energy production which would increase the axial component of the fluctuating velocity. Then, in a region further away from the wall, this axial component of the fluctuating velocity breaks up and turbulent kinetic energy is redistributed through pressure strain to the other components of the fluctuating velocity. That is when the shear stress starts to respond to the unsteadiness too. As the first region to be affected by the unsteadiness in the mean flow is the near wall region, where viscous effects dominates the transfer processes, a lag in the response of the turbulence might be expected, since the molecular diffusion is rather slow there.

These mechanisms of turbulence propagation are more likely to be reproduced by the RST models which model the energy redistribution process, however, when discussing the results, it will be assessed if the STS and MTS eddy-viscosity models are able to show part of the turbulence response behaviour through the prediction of the turbulent kinetic energy and shear stress.

5.8.1 Simulated Case

The experimental work of He and Jackson (2000), mentioned above, was used to set up a test case here. He and Jackson (2000) ran 10 ramp up and 9 ramp down fully developed pipe flows tests. Their cases explored different acceleration and deceleration rates as well as the initial Reynolds number of the flow. The main conclusions about these features were noted above. The case that was chosen to be reproduced here, in order to assess the performance of the turbulence models is their second ramp-up case where the Reynolds number of the flow, based on the bulk velocity and pipe diameter, was linearly increased from 7000 to 45200 over a period of 5 seconds with $\gamma = 6.1$. Considering the diameter of pipe and that the flow used for the experiments was water, that implied an increase in the bulk velocity from $0.138m/s$ to $0.891m/s$ in 5s. This is the only case for which time histories of all turbulence quantities, except the eddy-dissipation rate, were provided at four radial locations.

5.8.2 Simulations Setup

The set-up was the same as in the previous unsteady fully developed pipe flow simulations, the domain varying from $y = 0$ to $y = R$, where $R = 0.0254m$ is the pipe's radius.

The grid was planned in order to provide $y^+ < 1$ for the LRN models and $y^+ \approx 30$ for the HRN models in the near-wall node. The number of control volumes in the y direction for the grids used with the HRN models was 25 and with the LRN models, 40. Grid independence tests were carried out in order to ensure these grids would provide numerically accurate results.

A separate steady state fully developed flow with Reynolds number of 7000 was first simulated, and profiles from this taken as initial conditions for the unsteady simulation.

5.8.3 Results and Discussion

He and Jackson (2000) provided for the test case being reproduced here the profiles of velocity and turbulent quantities varying with the Reynolds number of the flow (or, equivalently, time) at four radial locations: at $r/R = 0$ (centre of the pipe), $r/R = 0.47$, $r/R = 0.83$ and $r/R = 0.93$, the latter being the positions closest to the wall. The simulations were thus set to provide equivalent time histories at these four locations. Profiles at $r/R = 0.93$ will not be shown for the HRN models, since in the grid used with these models, this position lies between the wall and the first near-wall node.

One can see in Figures 5.216, 5.217 and 5.218 that the velocity development at the four radial positions was well captured by all turbulence models. Only in the centre of the pipe, Figures 5.216(a), 5.217(a) and 5.218(a), is there a small disagreement between the experimental data and the predictions in the last 2 seconds of the acceleration, when the TS model performed best, providing the closest prediction.

The development of the turbulent kinetic energy can be seen in Figures 5.219, 5.220 and 5.221. From the experimental data one can see the lag in the response of the turbulence, where it first increases in the near-wall region, and later towards the pipe centre, the delay here being around 3.5 seconds. Starting by looking at the profiles of the turbulent kinetic energy at the centre of the pipe, Figures 5.219(a), 5.220(a) and 5.221(a), one may notice that most models predicted reasonably well the moment where the turbulent kinetic energy starts to increase, except for the HJ, TC and NG models which tended to underpredict the delay time and the TS model which overpredicted this delay, only predicting the turbulence kinetic energy to increase at about 4s. At $r/R = 0.47$, Figures 5.219(b), 5.220(b) and 5.221(b), almost the mid-distance from the centre to the wall, more models do not predict correctly the moment when the turbulent kinetic energy starts to build up, however the HR, FM, SG, GL, CG, KC and WM models still predict correctly this time delay. It is worth then noticing that, with regard to the prediction of the level of the turbulent kinetic energy after this delay time, the models tend to either predict it correctly at the centre of the pipe or at $r/R = 0.47$. The WM model is perhaps the model which provides the best prediction, considering both radial positions. At $r/R = 0.83$, where the lag in the response of the turbulence is quite small compared to that at the above radial positions, most models provided a overall profile which is in agreement with the experimental data, except for the HJ, SG and NG. At the radial position nearest to the wall, only the HJ and NG models provided results which differed too much from the experimental data. Most models predicted the turbulent kinetic energy profile at this position reasonably well, however none of them were able to predict the shift in the growing profile at about 2.5s. Most models predicted well the level of the turbulent kinetic energy from this moment on.

The development of the turbulent shear stress can be seen in Figures 5.222, 5.223 and 5.224. In the centre of the pipe, $\overline{uv} = 0$ due to the axisymmetric nature of the flow and therefore this profile is not shown. At $r/R = 0.47$, Figures 5.222(a), 5.223(a) and 5.224(a), all models predicted reasonably well the moment when the turbulent shear stress starts to build

up, approximately 3s, however its level after this time was not so well captured by all models, the LS, FM, GL, SG and WM performing best. At $r/R = 0.83$, Figures 5.222(b), 5.223(b) and 5.224(b), again, most models provide a overall good prediction of the development of $\overline{uv}$, except for the HJ and NG models which provide a too fast growth of this quantity. At $r/R = 0.93$, Figures 5.222(c), 5.223(c) and 5.224(c), only the HJ and NG models provided a too fast growth of $\overline{uv}$, as expected from their performance at the previous radial position, however, again, there is a shift in the growth profile of the Reynolds shear stress which was not captured by any model.

The development of the rms axial fluctuating velocity u' is presented in Figures 5.225, 5.226 and 5.227. The linear-eddy-viscosity models are expected to underpredict this quantity due to their inherent limitations. Among the NLEV and MTS models, one can say that the SG, GL and WM models performed best, considering all radial positions. It is worth noticing though, that while the turbulence models predict effectively no change in the profile of u' up to the moment it starts to build up, the experimental data predicts a smooth growth from the beginning of the imposed unsteadiness. Although the turbulence models predict correctly the starting level of the rms axial fluctuating velocity in the near-wall region, they fail to predict a step increase in the level of this quantity which the experiments show. As expected, the shift in the growth profile of u' at $r/R = 0.93$ was not predicted by any model. He and Jackson (2000) also provided profiles of the rms axial fluctuating velocity u', normalized by the local bulk velocity U_b. These results are presented in Figures 5.228, 5.229 and 5.230. The authors used these profiles, which are essentially the turbulence intensity profiles, to say that this quantity tends to be attenuated during the acceleration. Most models provided the correct trend from the centre of the pipe to $r/R = 0.83$, however, among the LRN models, the trend at $r/R = 0.93$ was only captured by the HJ model which, as seen before, tends to overpredict the u' profile after the shift in its growth profile.

The development of the rms radial fluctuating velocity v' is presented in Figures 5.231, 5.232 and 5.233 and its profile normalized by the local bulk velocity U_b is presented in Figures 5.234, 5.235 and 5.236. Similar analyses to those done with regard to the axial fluctuating velocity u' can be drawn here too, except that the profile of $\frac{v'}{U_b}$ at $r/R = 0.93$ was best predicted by the WM model, not the HJ.

The development of the circumferential fluctuating velocity w' is qualitative similar to that of the radial fluctuating velocity v' and therefore results are not being shown here.

To conclude this section, one can say that this case did present a clear lag in the response of the turbulence quantities which was not easily captured by the turbulence models. There is not a single model which could be pointed to as providing the best prediction for all quantities at all radial positions, however, it is clear the RST models are more appropriate to simulate these ramp up flows and the WM model perhaps performed best overall. Nevertheless, the LEV MTS did provide reasonable predictions, compared to STS models, again showing its potential of improving predictions in non-equilibrium flows.

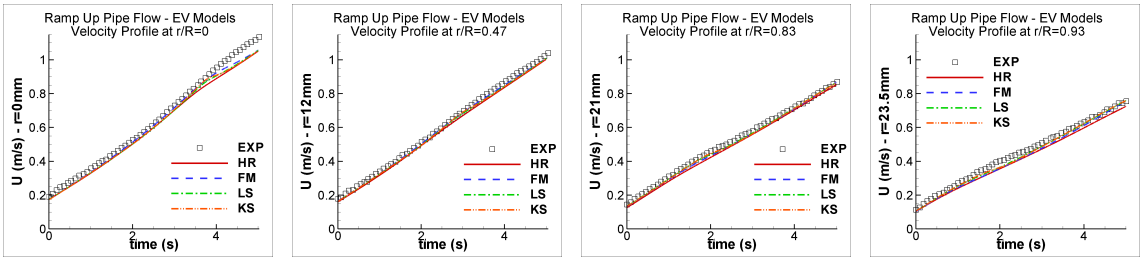

(a) (b) (c) (d)

Figure 5.216: Velocity profile at selected radial positions in the fully developed ramp up pipe flow case predicted by the linear-eddy-viscosity models and compared with the experiments of He and Jackson (2000). Models as in Table 3.25.

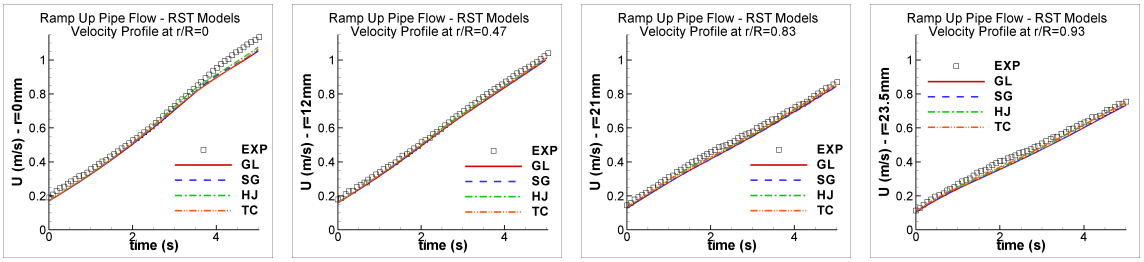

(a) (b) (c) (d)

Figure 5.217: Velocity profile at selected radial positions in the fully developed ramp up pipe flow case predicted by the Reynolds stress transport models and compared with the experiments of He and Jackson (2000). Models as in Table 3.25.

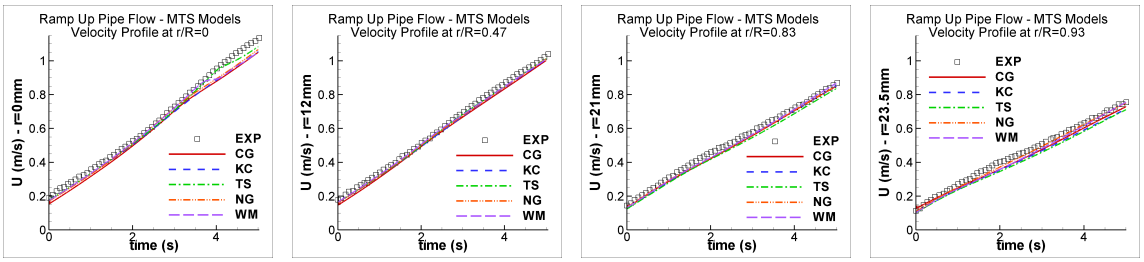

(a) (b) (c) (d)

Figure 5.218: Velocity profile at selected radial positions in the fully developed ramp up pipe flow case predicted by the multiple-time-scale models and compared with the experiments of He and Jackson (2000). Models as in Table 3.25.

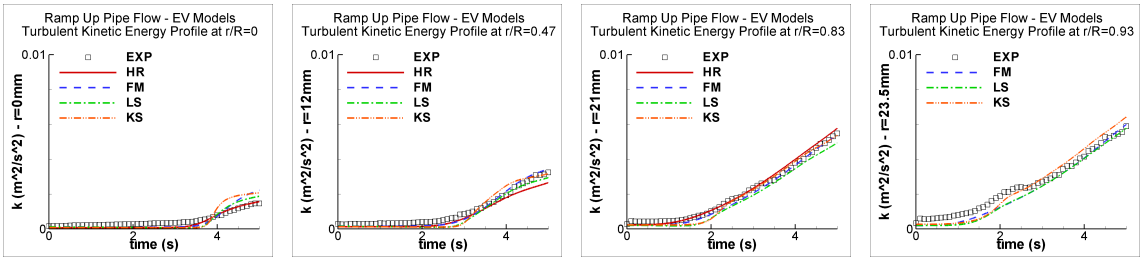

(a) (b) (c) (d)

Figure 5.219: Turbulent kinetic energy profile at selected radial positions in the fully developed ramp up pipe flow case predicted by the linear-eddy-viscosity models and compared with the experiments of He and Jackson (2000). Models as in Table 3.25.

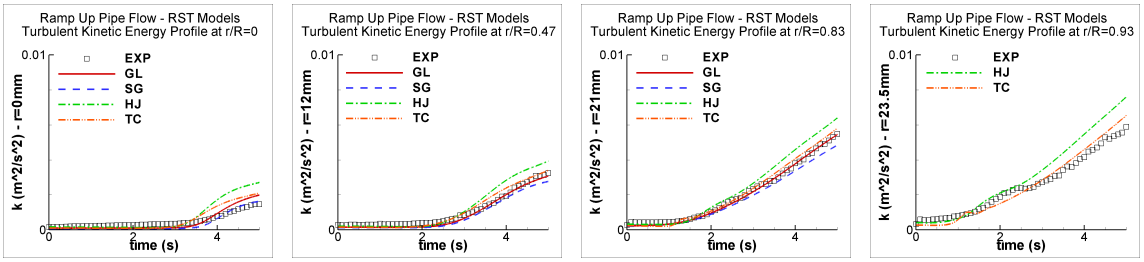

(a) (b) (c) (d)

Figure 5.220: Turbulent kinetic energy profile at selected radial positions in the fully developed ramp up pipe flow case predicted by the Reynolds stress transport models and compared with the experiments of He and Jackson (2000). Models as in Table 3.25.

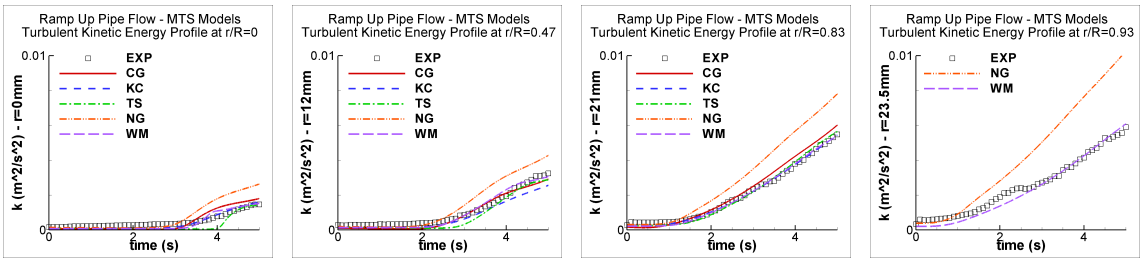

(a) (b) (c) (d)

Figure 5.221: Turbulent kinetic energy profile at selected radial positions in the fully developed ramp up pipe flow case predicted by the multiple-time-scale models and compared with the experiments of He and Jackson (2000). Models as in Table 3.25.

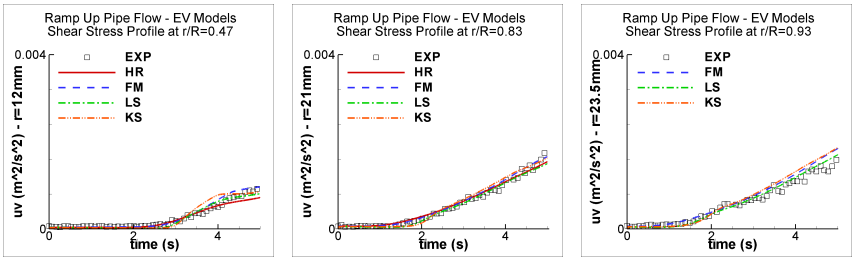

(a) (b) (c)

Figure 5.222: Reynolds shear stress profile at selected radial positions in the fully developed ramp up pipe flow case predicted by the linear-eddy-viscosity models and compared with the experiments of He and Jackson (2000). Models as in Table 3.25.

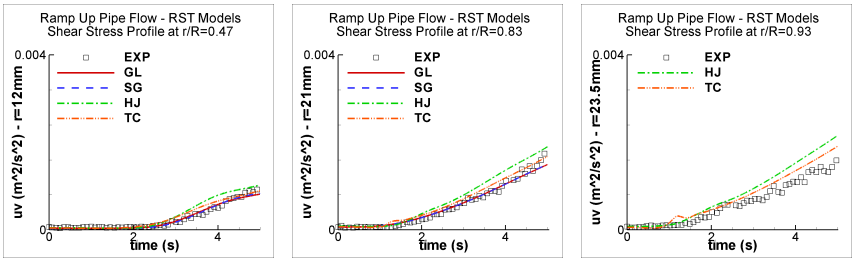

(a) (b) (c)

Figure 5.223: Reynolds shear stress at selected radial positions in the fully developed ramp up pipe flow case predicted by the Reynolds stress transport models and compared with the experiments of He and Jackson (2000). Models as in Table 3.25.

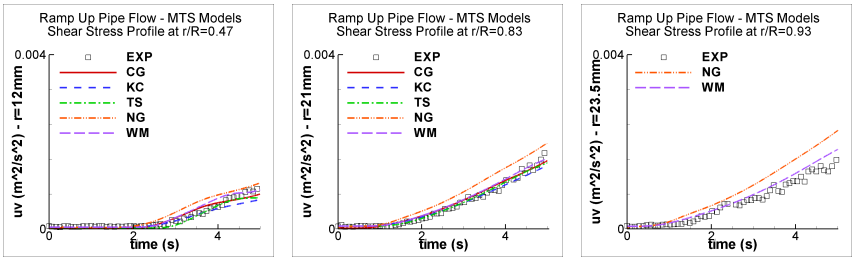

(a) (b) (c)

Figure 5.224: Reynolds shear stress at selected radial positions in the fully developed ramp up pipe flow case predicted by the multiple-time-scale models and compared with the experiments of He and Jackson (2000). Models as in Table 3.25.

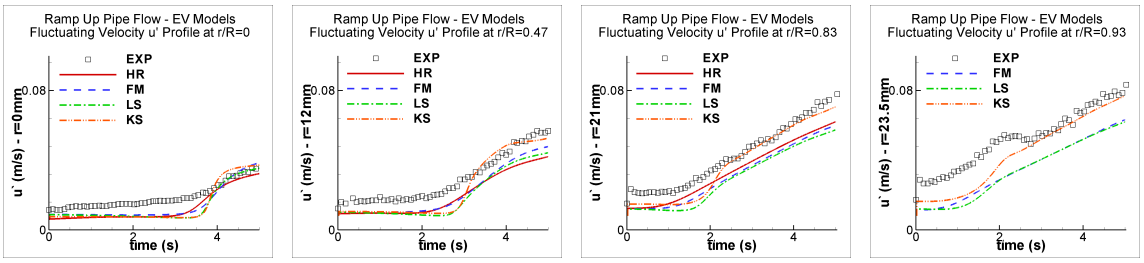

(a) (b) (c) (d)

Figure 5.225: Rms of fluctuating velocity u' profile at selected radial positions in the fully developed ramp up pipe flow case predicted by the linear-eddy-viscosity models and compared with the experiments of He and Jackson (2000). Models as in Table 3.25.

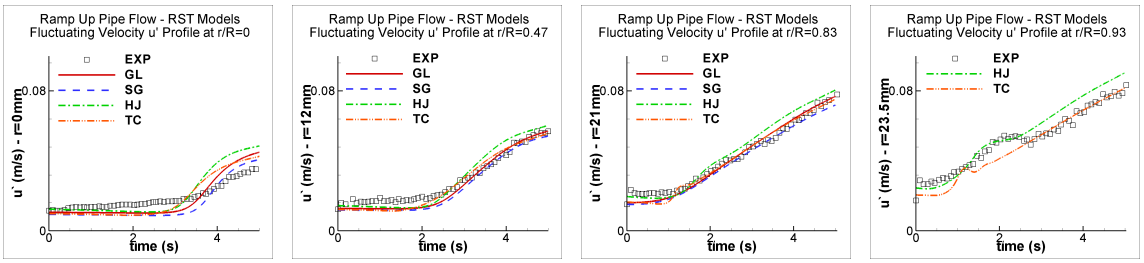

(a) (b) (c) (d)

Figure 5.226: Rms of fluctuating velocity u' profile at selected radial positions in the fully developed ramp up pipe flow case predicted by the Reynolds stress transport models and compared with the experiments of He and Jackson (2000). Models as in Table 3.25.

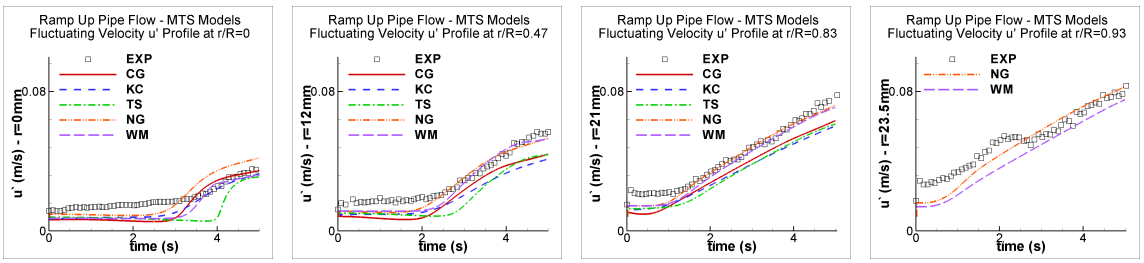

(a) (b) (c) (d)

Figure 5.227: Rms of fluctuating velocity u' profile at selected radial positions in the fully developed ramp up pipe flow case predicted by the multiple-time-scale models and compared with the experiments of He and Jackson (2000). Models as in Table 3.25.

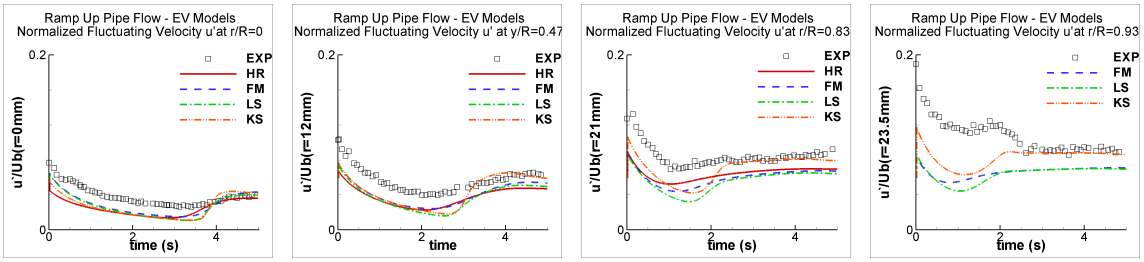

(a) (b) (c) (d)

Figure 5.228: Rms of fluctuating velocity u' normalized by the bulk velocity at selected radial positions in the fully developed ramp up pipe flow case predicted by the linear-eddy-viscosity models and compared with the experiments of He and Jackson (2000). Models as in Table 3.25.

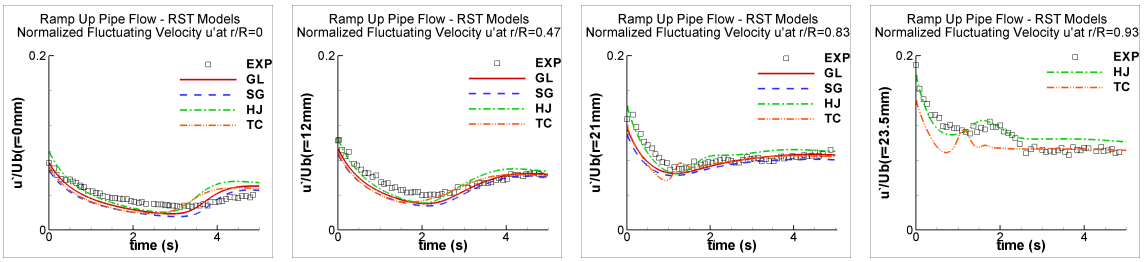

(a) (b) (c) (d)

Figure 5.229: Rms of fluctuating velocity u' normalized by the bulk velocity at selected radial positions in the fully developed ramp up pipe flow case predicted by the Reynolds stress transport models and compared with the experiments of He and Jackson (2000). Models as in Table 3.25.

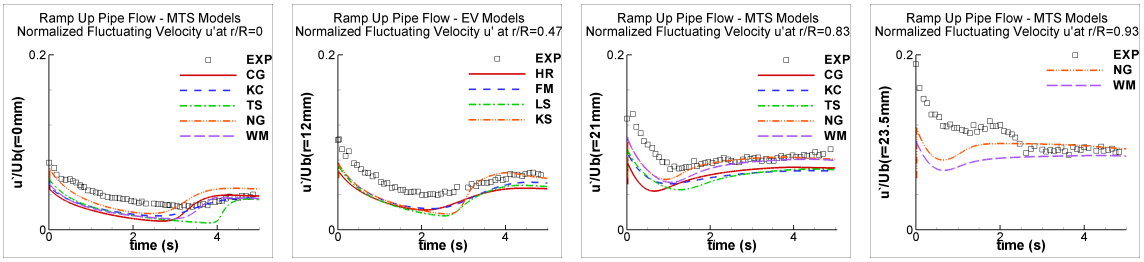

(a) (b) (c) (d)

Figure 5.230: Rms of fluctuating velocity u' normalized by the bulk velocity at selected radial positions in the fully developed ramp up pipe flow case predicted by the multiple-time-scale models and compared with the experiments of He and Jackson (2000). Models as in Table 3.25.

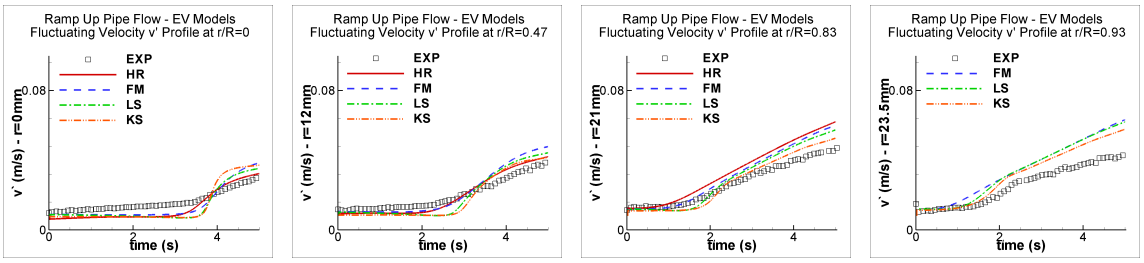

(a) (b) (c) (d)

Figure 5.231: Rms of fluctuating velocity v' profile at selected radial positions in the fully developed ramp up pipe flow case predicted by the linear-eddy-viscosity models and compared with the experiments of He and Jackson (2000). Models as in Table 3.25.

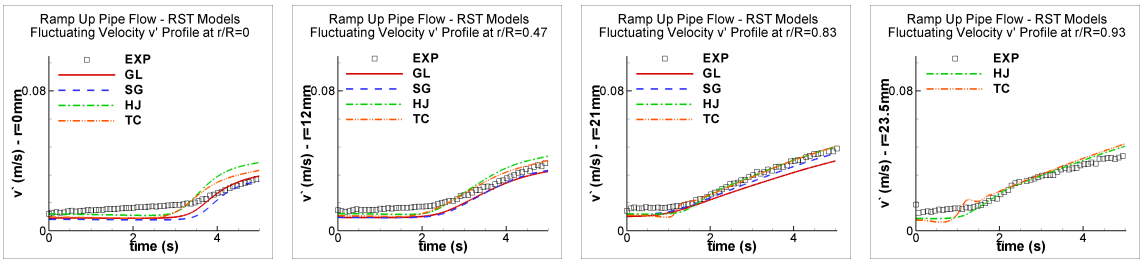

(a) (b) (c) (d)

Figure 5.232: Rms of fluctuating velocity v' profile at selected radial positions in the fully developed ramp up pipe flow case predicted by the Reynolds stress transport models and compared with the experiments of He and Jackson (2000). Models as in Table 3.25.

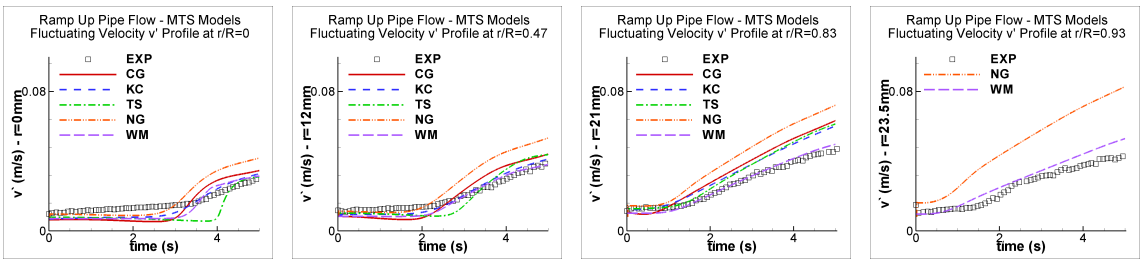

(a) (b) (c) (d)

Figure 5.233: Rms of fluctuating velocity v' profile at selected radial positions in the fully developed ramp up pipe flow case predicted by the multiple-time-scale models and compared with the experiments of He and Jackson (2000). Models as in Table 3.25.

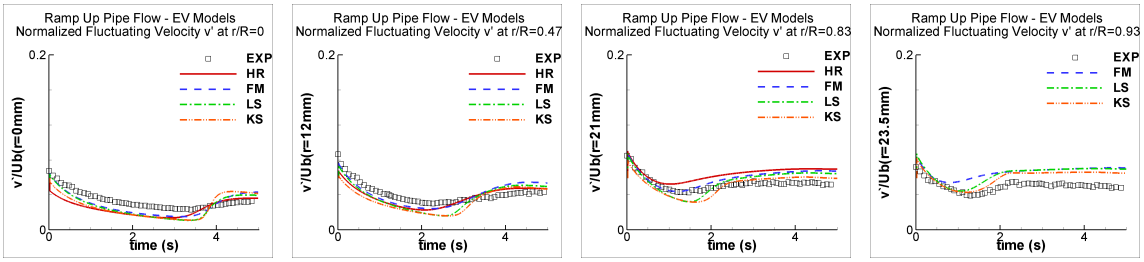

(a) (b) (c) (d)

Figure 5.234: Rms of fluctuating velocity v' normalized by the bulk velocity at selected radial positions in the fully developed ramp up pipe flow case predicted by the linear-eddy-viscosity models and compared with the experiments of He and Jackson (2000). Models as in Table 3.25.

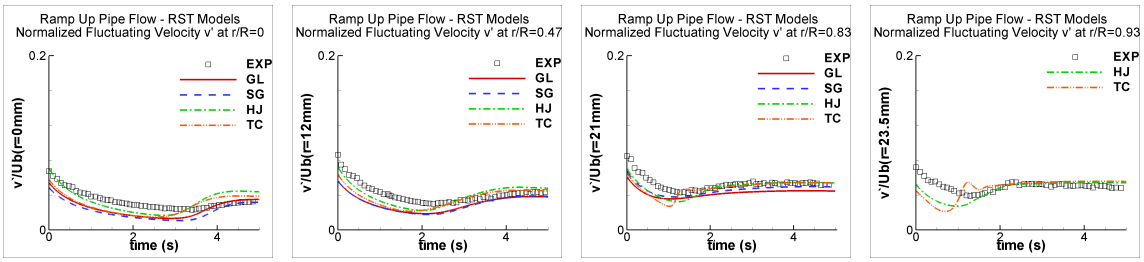

(a) (b) (c) (d)

Figure 5.235: Rms of fluctuating velocity v' normalized by the bulk velocity at selected radial positions in the fully developed ramp up pipe flow case predicted by the Reynolds stress transport models and compared with the experiments of He and Jackson (2000). Models as in Table 3.25.

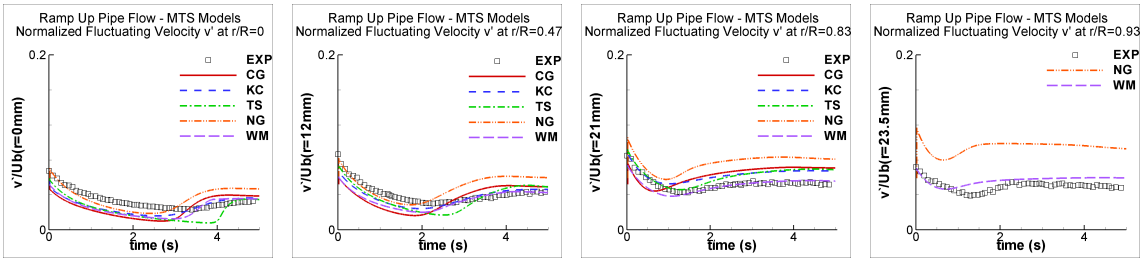

(a) (b) (c) (d)

Figure 5.236: Rms of fluctuating velocity v' normalized by the bulk velocity at selected radial positions in the fully developed ramp up pipe flow case predicted by the multiple-time-scale models and compared with the experiments of He and Jackson (2000). Models as in Table 3.25.

5.9 Backward Facing Step Flow

In a backward facing step flow, the flow originally in a channel faces a sudden expansion due to a step in the geometry, causing a sudden adverse pressure gradient which will lead to the reattachment of the flow in a position further downstream of the step. This process is illustrated in Figure 5.237. The presence of the step generates curved streamlines and recirculation zones which are confined between the step and the reattachment point, which thus becomes an important parameter to characterize the flow. From this description of the process, it becomes clear that non-equilibrium features are present, specially in the region between the step and the reattachment point. Downstream of the reattachment point, a new boundary layer develops.

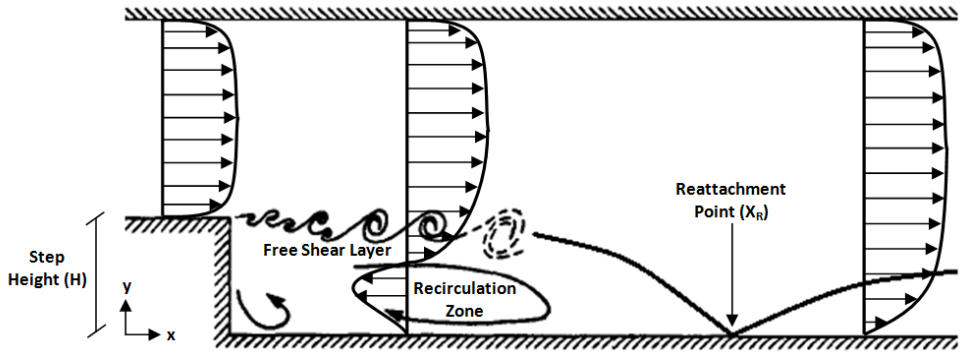

Figure 5.237: Backward facing step flow sketch. Adapted from Simpson (1996).

As commented by (Kasagi and Matsunaga, 1993), backward facing step flows are one of the simplest geometries to exhibit flow separation/reattachment, however they can still be considered as complex flows due to the physical phenomena involved in the process, as mentioned above. Besides that, as they are commonly found in industry and are of interest to several engineering fields, they are considered important flows to evaluate the performance of turbulence models. Ra et al. (1990) also highlighted the importance of flows where reattachment is present due to the rapid rise of pressure and heat transfer at the reattachment zone.

Lien and Leschziner (1994c) highlighted the importance of turbulence stress anisotropy in the curved and highly turbulent free shear layer formed due to separation. According to them, although the anisotropy in such a shear layer is smaller than in the boundary layer preceding separation, it influences the mean flow in the former much more than in the latter due to the strong interaction between curvature strain and normal stresses and the influence of the anisotropy of the normal stresses on the turbulent shear stress. As far as prediction of backward facing step flows by RANS turbulence models is concerned, Lien and Leschziner (1994c) argued that, although many research groups around the world had been using Reynolds stress transport models to predict such separating flows due to their capability of predicting anisotropy of the normal stresses, most of the standard forms of these models tend to provide excessive levels of anisotropy and low recovery of the flow profile after

the reattachment, which was being solved by excessively elaborated improvements. As a result of that, Lien and Leschziner (1994c) turned their attention to the use of non-linear eddy-viscosity models.

Momeni (2008) also carried out an extensive review of both experimental and computational works available in the literature regarding backward facing step flows. Although he did study steady backward facing step flows, his main interest was in exploring the modelling of flow control via a periodic injection/suction at the step corner, using the measured data of Chun and Sung (1996) for comparison. In the context of the present study, the resulting unsteady flow could be expected to exhibit significant non-equilibrium features, particularly at certain forcing frequencies.

Chun and Sung (1996) and Yoshioka et al. (2001) both studied experimentally the influence of periodic perturbation in backward facing step flows, by introducing a sinusoidally oscillatory jet at the step edge. The range of Reynolds number they studied was different, the former being much higher than the latter, although Yoshioka et al. (2001) concluded that the effect of the flow forcing was not particularly sensitive to the Reynolds number. Simpson (1996), who also did an extensive review about separated flows, arrived at similar conclusions for steady state backward facing steps and states that the reattachment length normalized by the step height depends mostly on the expansion ratio of the backward facing step case, for flows characterized by a Reynolds number based on the step height above 10^4, which is the case of Chun and Sung's experiments, but not of Yoshioka et al.'s. Both Chun and Sung (1996) and Yoshioka et al. (2001) concluded that there is a frequency range of the forcing, corresponding to a Strouhal number around 0.2, where the reattachment length would be minimized. Chun and Sung (1996) also studied the influence of the amplitude of perturbation on the reattachment point and minimal frequency range, and concluded that it did not affect the St range where the minimum reattachment length occurred, although it did affect the size of the minimum reattachment length which was observed to decrease linearly with the amplitude when the latter was plotted on a logarithmic scale.

As noted above, backward facing step flows can be considered as challenging flows for both experiments and turbulence models, with significant non-equilibrium effects expected to be present, particularly when introducing unsteady flow control via the jet forcing described above. These cases have thus been selected as the final set of flows to be studied in the present work.

5.9.1 Simulated Cases

Three cases from Chun and Sung (1996) were selected to be reproduced here. All of them are at a Reynolds number Re_H, based on the step height H and U_0, the bulk velocity just before the step ($x/H = -0.02$), equal to 33000. Although that is not a very high Reynolds number, it is among the highest Reynolds number cases found in the literature where relevant experimental data was provided for both steady and forced cases, as described above. In

addition, Momeni (2008) also simulated these three test cases and used two of the single-time-scale models in use in this work, the LS and KS models. So these three cases from Chun and Sung (1996) seem appropriate to evaluate the performance of existing and new models.

The steady case will be referred to as the BFS-St0 case. The two unsteady cases differ in the value of the forcing frequency. In both cases the velocity of the oscillatory jet can be expressed as $Q = A_0 U_0 \sin(\omega t)$, where $Q = \sqrt{U^2 + V^2}$ is the total velocity, A_0 is the amplitude of oscillation at $(x, y) = (-0.02H, 0.01H)$ and $\omega = 2\pi f$ is the angular frequency. The two cases studied here correspond to $f = 77Hz$ (giving a Strouhal number $St = \frac{fH}{U_0}$ of 0.275) and $f = 280Hz$, giving $St = 1$. These will be referred to as cases BFS-St0275 and BFS-St1 below.

All three cases were tested by Chun and Sung (1996) and verified to be 2-D and the expansion ratio of the flow was 1.5: it started in a channel with a $2H$ height and after the step, the new channel had a $3H$ height. The step height was $H = 0.05m$. The inlet bulk velocity was $14m/s$ and the fluid used in the experiments was air, thus the density was set as $\rho = 1.2kg/m^3$ and the viscosity as $\mu = 2.545 \times 10^{-5} kg/sm$ in order to ensure $Re_H = 33000$. It was reported that at the inlet there was a boundary layer of thickness $\delta/H = 0.41$ with momentum thickness Reynolds number $Re_\theta = \frac{\theta U_0}{\nu}$ of 1340.

It is of value to mention that Chun and Sung (1996) referred to the reference velocity U_0 as the freestream velocity, but here, in line with Momeni (2008), it was taken to be the bulk velocity, since the inlet corresponds to only a partially developed channel flow.

5.9.2 Simulations Setup

The domain was set just as in Figure 5.237, the length upstream of the step being set as $5H$ and the length downstream of the step, $30H$. The point $(x, y) = (0, 0)$ was set at the edge of the step, that is, the channel extended from $-5H$ to 0 in the x direction and from 0 to $2H$ in the y direction, and after the step the expanded channel extended from 0 to $30H$ in the x direction and from $-H$ to $2H$ in the y direction.

As for boundary conditions, all walls were set as no-slip and for all variables, except the pressure, zero gradient was applied at the outlet of the channel. A bulk pressure correction to ensure mass conservation was applied to set the pressure at the outlet in order to improve stability and facilitate convergence. The idea is to set the pressure at the outlet face equal to the cell-centre pressure plus a pressure drop ΔP. So the pressure at the east face is set as $P_e = P_P + \Delta P$. An iterative scheme is then used, in which corrections $\Delta P'$ are calculated and added to ΔP, to obtain the desired outlet mass flow. The procedure to find the desired $\Delta P'$ is described in Mostafa (2007) and is similar to that used for the SIMPLE pressure correction scheme. It will be briefly described here as well.

To apply the bulk pressure correction at the east face, the discretized form of the 2-D U-momentum equation, equation 4.18, can be recalled. In this equation, P_e is the pressure at the east boundary face, and P_w is the pressure at the west face, which is simply obtained from interpolation between nodal values. The correction $\Delta P'$ is associated with a velocity

correction $\Delta U'_P$. So equation 4.18 can be rewritten as:

$$U_P + \Delta U'_P = \sum_k \frac{A_k(U_k + \Delta U'_k)}{A_P} + \frac{\Delta y}{A_P}(P_w + \Delta P' - P_e) \tag{5.22}$$

Subtracting equation 4.18 from the above equation, provides:

$$\Delta U'_P = \sum_k \frac{A_k \Delta U'_k}{A_P} + \frac{\Delta y}{A_P}\Delta P' \tag{5.23}$$

As in the SIMPLE scheme, the first term in the right hand side of the above equation can be neglected which yields:

$$\Delta U'_P = \frac{\Delta y}{A_P}\Delta P' \tag{5.24}$$

As one wants to ensure overall mass conservation, the mass flow rate at the inlet, M_{in}, must be the same as the mass flow rate at the outlet which is $\sum \rho(U_P + \Delta U'_P)\Delta y$. By substituting $\Delta U'_P$ from equation 5.24, one can write:

$$M_{in} = \sum \rho(U_P + \frac{\Delta y}{A_P}\Delta P')\Delta y = \sum \rho U_P \Delta y + \Delta P' \sum \rho \frac{\Delta y^2}{A_P} \tag{5.25}$$

Considering that $\sum \rho U_P \Delta y$ is the current (at each iteration) mass flow rate at the outlet, M_{out}, the above equation can be rearranged to provide an explicit expression to calculate $\Delta P'$:

$$\Delta P' = \frac{M_{in} - M_{out}}{\sum \rho \frac{\Delta y^2}{A_P}} \tag{5.26}$$

This bulk pressure correction was used in both steady and unsteady cases.

Since the reported inflow conditions consist of a partially developed channel flow, a separate developing channel flow simulation was carried out, with a bulk velocity of $U_0 = 14m/s$, and suitable profiles were extracted from this to provide inlet conditions for the steady state backward-facing step flow. Inlet profiles using this procedure were generated using the HR, GL, KC, FM and LS models, and employed for the rest of the calculations. Chun and Sung (1996) reported the free-stream turbulence intensity level just before the step being less than 0.6%. In the present calculations though a higher level was prescribed at the domain inlet resulting in something close to 5% at the step edge for the sake of stability of the LRN models. Indeed, the KS model only converged for this higher inlet turbulence intensity level. In the work of Momeni (2008), it was not mentioned which initial turbulence intensity level was used, however from the presented profiles it was probably close to 5% too.

With the above settings, the computed velocity profile at $x = -0.02H$, just before the

step, was output in order to check that it matched the reported experimental conditions. This profile can be seen in Figure 5.238. Although the velocity profile was matching, the inlet Re_θ and δ/H parameters were slightly different, Re_θ varying from approximately 1295 to 1500 and δ/H from 0.38 to 0.5, depending on the model.

The jet injection in the unsteady cases was applied in the eight control volumes just before the step, reproducing the $1mm$ width of the experimental orifice used for the injection. In these eight cells, the velocity in the x and y directions, U and V, as $U = Q\cos(45^o)$ and $V = Q\sin(45^o)$, equivalently to the jet being injected at a 45^o angle which was the case in the experiment. Turbulent quantities and the pressure also had to be specified in these eight cells. The latter was set equal to the next node in the y direction. The turbulent kinetic energy was set based on a 1% turbulence intensity related to the jet total velocity, $k_0 = 1.5(0.01 * Q)^2$, the normal stresses were set as $\overline{u^2}_0 = k_0$, $\overline{v^2}_0 = 0.4 * k_0$ and $\overline{w^2}_0 = 0.6 * k_0$, the shear stress was set to zero and the eddy dissipation rate was set by considering the ratio $\nu_t/\nu = 5$, providing $\varepsilon_0 = 0.09 * k_0/(5\nu)$. When MTS models were used, the ratios $k_P/k_T = 2$ and $\varepsilon_P/\varepsilon_T = 1$ were used.

Chun and Sung (1996) specified the amplitude of the pulsed jet, A_0, as the difference between the time-averaged forced velocity, Q_{forced}, and unforced velocity, $Q_{unforced}$, normalized by the inlet bulk velocity U_0, that is, $A_0 = (Q_{forced} - Q_{unforced})/U_0$, measured at $(x/H, y/H) = (-0.02, 0.01)$. However, when setting up the simulation, the amplitude of oscillation must be defined at the jet inlet, since that is the boundary condition for this part of the domain. Momeni (2008) established that, in order to set $A_0 = 0.07$, the ratio ν_{rms}/U_0 should be 1.4, where $\nu_{rms} = \sqrt{\frac{1}{T}\int_0^T [Q(t)]^2 dt}$. As the jet velocity varies as $Q(t) = BU_0\sin(\omega t)$, B being the amplitude imposed at the jet inlet, and since $\omega T = 2\pi$, ν_{rms}^2 can be developed:

$$\frac{1}{T}\int_{t=0}^{t=T} [BU_0\sin(\omega t)]^2 dt = \frac{B^2U_0^2}{\omega T}\int_{x=0}^{x=\omega T}\sin^2 x dx = \frac{B^2U_0^2}{\omega T}\frac{1}{2}\left[x - \frac{\sin(2x)}{2}\right]_0^{\omega T} = \frac{B^2U_0^2}{2} \tag{5.27}$$

As $\nu_{rms}/U_0 = 1.4$ in order to have A_0=0.07, according to Momeni (2008), the above result can be used to calculate B:

$$\sqrt{\frac{B^2U_0^2}{2}} = 1.4U_0 \Rightarrow B = 1.4\sqrt{2} \tag{5.28}$$

This value for B was then used as an initial guess to find A_0 in the present simulations. A_0 depends on the value of B, but also on the imposed frequency and unforced velocity $Q_{unforced}$ which varies slightly from model to model, specially in the HRN models where a coarse interpolation must be done in order to find $Q_{unforced}$ at $y/H = 0.01$, since the first node provides $y/H = 0.0167$. In order to calculate the unforced velocity predicted by the HRN models, a linear interpolation was done using the first and second nodes and that was extrapolated to find the velocity at $y/H = 0.01$. The values of $Q_{unforced}$ for each model as

well as the value of B used in each model for each unsteady case are presented in Table 5.19.

Table 5.19: Unforced velocity at $(x/H, y/H) = (-0.02, 0.01)$ and applied forcing jet amplitude.

Model	$Q_{unforced}$	Jet amplitude B at $(x/H, y/H) = (0, 0)$	
		$St = 0.275$	$St = 1$
HR	7.9	$1.29\sqrt{2}$	$1.65\sqrt{2}$
GL	7.0	$1.065\sqrt{2}$	$1.45\sqrt{2}$
SG	7.5	$1.1\sqrt{2}$	$1.55\sqrt{2}$
CG	7.5	$0.92\sqrt{2}$	$1.58\sqrt{2}$
KC	7.7	$1.257\sqrt{2}$	$1.565\sqrt{2}$
LS	7.3	$1.3\sqrt{2}$	$2.6\sqrt{2}$
FM	7.4	$1.3\sqrt{2}$	$2.57\sqrt{2}$
KS	7.5	$1.4\sqrt{2}$	$2.7\sqrt{2}$

In the steady state simulations, the models other than the HR, GL, SG and LS were started from the converged results of one of these models. The unsteady cases were started with the results from the steady state simulation run with each respective model.

Separate grids were built for the HRN and LRN models, formed from 3 blocks as shown in Figures 5.253 to 5.262, the first being the channel upstream of the step, the second being the continuation of the upstream step, but after the step, and the third being only the lower part of the channel after the step.

For the HRN grid a total of 180 cells were used in the x-direction. From the inlet to $x = -0.02H$ a grid contraction ratio of 1.1 was applied, with eight uniform cells between this and the step corner (these formed the jet injection slot for the forced cases). Beyond the step an expansion ratio of 1.115 was applied until $x = 15H$, beyond which the grid spacing was uniform. In the y-direction, a grid expansion ratio of 1.015 was applied from $y = 0$ until $y = H$ and the same, symmetric, distribution was applied until $y = 2H$. The same procedure was used beyond the step, from $y = -H$ until $y = 0$, however the expansion ratio was slightly smaller, 1.01. In total, 70 control volumes in the y direction were used. So this HRN model grid can be generically described as a 180x70 grid and can be seen in Figure 5.239.

The LRN grid was built following a similar structure to the HRN one, but with a larger number of cells, and smaller near-wall cells. The total number of cells in the x direction was 240, with slightly smaller grid expansion ratios than in the HRN grid. The total number of cells in the y direction was 180, with slightly higher grid expansion ratios than in the HRN grid. This grid for the LRN models can be described as a 240x180 grid and can be seen in Figure 5.240.

In Figure 5.241 a zoom is given in the step corner region in order to show the 8 uniform control volumes just before the step and to compare the distribution of the cells in the y direction for both HRN and LRN models. One can then clearly see the difference in the height of the first cell near the wall for each grid in order to allow the desired y^+ values in the first node.

Grid independence tests were carried out and the HRN models were tested with the above grid and a more refined grid with specifications 240x90 while the LRN models were tested with the above grid and a coarser one of 180x160. For illustration, the prediction of the wall shear stress, wall pressure coefficient and maximum streamwise Reynolds stress with both grids is shown in Figures 5.242 and 5.243 for predictions with the HR, GL and KC models in the former and with the LS and NG models in the latter, where one can see that no significant changes are seen with the much more refined grid and therefore grid independence can then be confirmed. Although the above tests suggest the grids adopted are sufficient for accuracy, it should be noted that the TS model failed to converge on the finer HRN grid, as did the KS and TC models on the coarser LRN grid, suggesting these schemes may be less stable than the others in this case.

The prediction of y^+ in the first near-wall node can be seen in Figures 5.244 and 5.245 for the HR model representing the HRN models and the LS representing the LRN models. One can see that, before the step, the HRN calculations give y^+ a bit lower than 30 and the LRN models, a bit higher than 1, as commented on above. After the step, the y^+ values decrease slightly along the top wall, consistent with the decrease in the mean velocity due to the expansion of the channel. Along the bottom wall, as the reattachment point is approached, y^+ decreases to zero, since the velocity and wall shear stress will also decay to this value. After the reattachment point, similar values to those on the top wall are reached. Along the vertical wall of the step the values of y^+ are quite low for the HRN models and quite high for the LRN models, however, that is inevitable since it was deemed more important to have a smooth expansion, and not too fine streamwise grid, in the main channel region immediately before and after the step.

The last setup to be described is the time step used in the unsteady cases. Each cycle was divided into 400 time steps, so in the BFS-St0275 case, which has a period $T = \frac{1}{77}s$, the time step used was $\Delta t = 3.247 \times 10^{-5}s$ and in the BFS-St1 case, which has a period $T = \frac{1}{280}s$, the time step used was $\Delta t = 8.929 \times 10^{-6}$. A time step independence test was carried out using a more refined time step in which each forcing cycle was divided into 1200 steps. The results of this test are presented in Figure 5.246 and Figure 5.247 for the BFS-St0275 and BFS-St1 cases respectively where predictions of the HR, KC, GL and LS models show that no significant differences can be found in the profiles of the time-averaged wall shear stress, wall pressure coefficient and maximum streamwise Reynolds stress by refining the time-step.

The number of cycles needed to reach a fully periodic state for each model starting from their steady state result in each of the unsteady cases are presented in Table 5.20. Most models achieved a simple periodic solution with the same period as the forcing, one exception being the GL model which achieved periodicity every 2 cycles, the other being the SG and KS models which did not show any kind of periodic behaviour. As the results Chun and Sung (1996) provided are all time-averaged, it was then decided to average the last 10 cycles of all models. Having achieved a periodic state, a further 40 cycles were run for each model, and the variation of local reattachment point and wall shear stress at four positions downstream of the step can be seen in Figures 5.248 to 5.250 for the last 10 cycles of the $BFS - St0275$

and $BFS - St1$ cases.

Table 5.20: Number of cycles necessary to reach a fully periodic state in the unsteady backward facing step cases.

Model	St=0.275	St=1
HR	15	40
GL	30	60
SG	65*	75
CG	10	30
KC	20	50
LS	10	30
FM	12	50
KS	60*	-

In the low frequency case, the SG and KS models presented some particular features regarding the fully periodic state, despite having reached convergence. As can be seen in Figure 5.249, they could not reach a fully periodic state. The star in Table 5.20 for these models indicate then the number of cycles to reach an apparent irregular periodic state. For the SG model, more than 150 cycles were tried, but profiles similar to those of Figure 5.249(c) were encountered. The KS model, which takes much more time than the SG model to run, had more than 70 cycles run and the same occurred: profiles similar to those of Figure 5.249(a) were found. The last 10 cycles of the last simulation tried with these models were averaged. Their profiles are in Figures 5.249(b) and 5.249(d). The results for the SG model, seemed reasonable compared to the results provided by the other models, however the results provided by the KS model were not. As the main scope here is not the results provided by any particular model, the predictions of the KS model will not be presented in the discussions for the $BFS - St0275$ case. In Figure 5.250(f) one can see that the KS model did not reach a periodic state at all in the high frequency case and again its results will not be used for the results discussion.

5.9.3 Results and Discussion

As in all other test cases, these backward facing step cases were run with all models presented in Chapter 3. However, as mentioned before, it was not possible to achieve convergence with all models, and these will be identified as the results are discussed case-by-case below.

First, the steady backward facing step case will be discussed. In the steady state case, only the HJ and WM models did not converge so the predictions of these models will not be presented, and they will be considered less stable than the other models. With regard to stability, the KS model can also be considered less stable, since it only converged for a specific grid and initial turbulence intensity level, as commented on above. The FM model can also be considered less stable than the LS, since among all tests carried out in terms of different grids and initial turbulence intensity levels, the latter and the HRN models, except the TS model, proved to be the most stable ones.

Before discussing the velocity and turbulence quantity profiles, the prediction of the reattachment point by each turbulence models will be assessed, since this is a key parameter of these flows. The reattachment point in the $BFS - St0$ case predicted by each model can be seen in Table 5.21. One may notice that the NG and KS models best predicted the reattachment point in the steady state backward facing step case. The LS and FM schemes provided a moderate underprediction, while the KC model provided a moderate overprediction of the reattachment length. The HR, SG and GL models gave a greater than 10% underprediction of the reattachment length and the CG, TS and TC models provided an extreme underprediction of this parameter, more than 40% less than the experimental value. Tests showed that the extremely short reattachment length given by the TS and CG models was due to the extra irrotational production term in the ε_P equation (equations 3.45 and 3.53). The underprediction given by the TC model might be associated with its complex redistribution term, presented in equation 3.37. One noticeable feature from the above is that the best predictions came from LRN models, whilst those used with wall-functions generally returned worse results.

Table 5.21: Reattachment point in the steady backward facing step case of Chun and Sung (1996).

Model/Experiment	Reattachment point (x/H)	% Error
Experiment	7.8	-
HR	6.42	−17.73
LS	7.21	−7.51
FM	7.35	−5.75
KS	8.03	2.95
GL	6.59	−15.45
SG	6.95	−10.85
TC	4.66	−40.22
CG	4.20	−46.14
KC	8.44	8.17
TS	4.14	−46.89
NG	7.74	−0.76

The prediction of the reattachment point is directly related to the prediction of the wall-shear stress and wall-pressure coefficient which are presented in Figures 5.251 and 5.252 respectively. One may notice that the wall-pressure coefficient C_P, defined by Chun and Sung (1996) as $C_P = (P - P_0)/(0.5\rho U_0^2)$, P_0 and U_0 being the static pressure and streamwise mean velocity measured at $x/H = -2.0$ in the steady state respectively, were best predicted by the KS, SG, NG and KC models, consistent with their good predictions of the reattachment point. When looking at the profiles of the wall-shear stress, one may notice that some models show a small secondary recirculation in the step corner and, indeed, Chun and Sung (1996) reported separation at $x/H \approx 1$. Unfortunately, they did not provide measurements of the wall-shear stress, but one can infer the predicted presence of this small secondary recirculation by the models from the change in sign of τ_{wall}.

The presence of a separation zone as well as the reattachment zone can also be seen by evaluating the stream function Φ, defined as $\Phi = \int U dy - \int V dx$. The contour plot of this parameter provided by each turbulence model can be seen in Figures 5.253 to 5.263. It can be noted that among the HRN models, only the RST models were able to predict a small secondary recirculation in the step corner. Among the LRN models, only the NG model failed to do so. It can then be inferred that both the presence of LRN approaches and Reynolds normal stress predictions tend to promote the formation of the secondary corner vortex. For instance, by comparing the HR and LS models, which are essentially the same model, but the former used with wall-function and the latter being a LRN scheme, one can see the influence in the prediction of separation. The FM, KS and GL models provided the separation closer to $x/H \approx 1$, thus being closer to the experiments. It is not possible to compare the size and shape of the separation and reattachment bubbles, since these were not provided by Chun and Sung (1996).

With all this now in mind, one can look at Figures 5.264, 5.265 and 5.266 to evaluate the velocity profile at five positions downstream of the step, at $x/H = 1, 3, 5, 7, 9$. All other turbulent quantities will also be presented at these same positions. One can notice that, apparently, the turbulence models which best predicted the velocity profiles were the HR, FM and LS models, which, among others, underpredicted the reattachment point. One of the explanations for this in the downstream recovery region is that most RANS turbulence models often tend to predict a rather slow recovery of the post-reattachment channel profile, so the models which predict the reattachment point correctly tend to not provide the correct velocity profile after the reattachment point, which is then what is observed. Both the KS and NG models, which best predicted the reattachment point, overpredict the velocity profile in the shear layer after reattachment, that is at $x/H = 9$. One can see that, apart from the CG, TS and TC models, which far underpredicted the reattachment point, all models provide velocity profiles which are in agreement with the experiments up to $x/H = 7$, which is the last measured point before the reattachment point.

Chun and Sung (1996) also provided measured profiles of the streamwise Reynolds normal stress $\overline{u^2}$, which are compared with the predicted profiles in Figures 5.267, 5.268 and 5.269. One may notice that, apart from the CG and TS models at $x/H = 1$ and $x/H = 3$, the linear-eddy-viscosity models tended to provide levels of $\overline{u^2}$ closer to the experiments than the NLEV and RST models tested. That is in agreement with the comments of Lien and Leschziner (1994c), mentioned above, about the tendency of RST models to provide high levels of anisotropy.

The predictions of the other two Reynolds normal stresses are presented in Figures 5.270 to 5.275. One may notice that, as expected, the profiles provided by the linear-eddy-viscosity models are not different from those presented for the streamwise Reynolds normal stress $\overline{u^2}$, which is expected. The low levels of these other normal stresses agree again with the comments of Lien and Leschziner (1994c). The behaviour noted for the Reynolds normal stresses is also generally seen in the turbulent kinetic energy which is presented in Figures 5.276 to 5.278.

The profiles of the Reynolds shear stress and eddy-dissipation rate predicted by the turbulence models are also presented in Figures 5.279 to 5.281 for the former and in Figures 5.282 to 5.284 for the latter. One may notice that the correct prediction of the reattachment point is related to not so high levels of shear stress in the shear layer. The profile of eddy-dissipation is higher in the shear layer, as expected due to the higher rates of turbulent kinetic energy production, however it can be noted that the models which provided a too early reattachment of the flow, presented higher levels of ε near the bottom wall.

The results for the low frequency case, $BFS - St0275$, are presented in Figures 5.285 to 5.290. The TS, HJ, NG, TC, WM models did not converge for this case and the KS model, despite converging, did not reach a periodic state. Hence, the results for these models will not be presented. A few tests, where terms were deactivated and coefficients were adjusted, also indicated that the instability of the TS model is again related to its extra source term in equation 3.45. From the 13 models used in the previous test cases, only 7 are being considered for this case and therefore, instead of presenting the results divided into the three main turbulence models classes, as has been done so far, these 7 models were divided into two classes: the single-time-scale linear-eddy-viscosity models (HR, LS and FM) and the others: the single-time-scale Reynolds-stress-transport models (GL and SG) and the two-time-scale linear-eddy-viscosity models (CG and KC).

Before looking at the time-averaged variables profiles, the time-averaged reattachment point predicted by each model for this case is presented in Table 5.22. As can be seen, the measured reattachment length at this forcing frequency is much lower than in the steady case. This frequency, $St = 0.275$, is actually the frequency which provides the lowest reattachment point at $Re_H = 33000$ and $A_0 = 0.07$, according to the experiments of Chun and Sung (1996). One may notice that very few models are actually able to follow this trend.

If one looks only at Table 5.22, one might say that the standard $k - \varepsilon$ model, the HR model, provided the best result. Not only the best result, but exactly the value measured in the experiments. However, recalling its prediction of the reattachment point in the steady state, Table 5.21, one may notice that it underpredicted significantly this parameter in that case. A closer comparison of the two tables indicates that the models which underpredicted the reattachment point in the steady state case tended to provide the best results in this low frequency case. The models which provided closer prediction of the reattachment point in the steady state, tended to overpredict this parameter in the $BFS - St0275$ case. From this it can be seen that the models do, generally, give a reduction in the recirculation length in the forced case, compared to the steady case, but this reduction is significantly underestimated.

One can now look in Figures 5.285 and 5.286 at the time-averaged profiles of the wall shear stress, wall-pressure coefficient and the forward-flow time fraction. The latter is an experimentally measured parameter, defined as the fraction of time for which the near-wall flow was directed in downstream direction, Ra et al. (1990). They reported the reattachment point to be where this fraction takes the value of 0.5. Consistently with Table 5.22, one may see that the time-averaged wall shear stress changes sign at the reattachment location x/H indicated, and γ_P also takes a value of 0.5. Apart from the CG model, which completely

Table 5.22: Time-averaged reattachment point in the unsteady backward facing step case of Chun and Sung (1996) with $St = 0.275$.

Model/Experiment	Reattachment point (x/H)	% Error
Experiment	5.0	-
HR	5.01	0.20
LS	5.29	5.77
FM	6.16	23.14
GL	6.14	22.86
SG	5.51	10.21
CG	3.83	−23.38
KC	7.21	44.2

underpredicts the reattachment point, all models provide good agreement with the time-averaged wall pressure coefficient. There are no experimental data to compare the prediction of the time-averaged wall shear stress with, but one may notice that, in contrast to the steady state case, where some models clearly indicated a small secondary recirculation zone, no model shows such a feature in the time-averaged flow. Chun and Sung (1996) indeed reports that no secondary corner recirculation was identified in the unsteady cases. For this reason, together with the fact that there are no experimental data regarding the size and shape of the reattachment bubble, the stream function contour plots for each model will not be presented since no additional information can be taken from them.

The profiles of the time-averaged velocity can be seen in Figures 5.287 and 5.288. One may notice that the CG model provided the best results, matching the experimental data at all positions downstream of the step. However, as noted above in the steady state case results, the reason for that is its underprediction of the reattachment point which gives more time for the model to recover towards the post-reattachment channel flow. After the CG model, the single-time-scale linear-eddy-viscosity models presented the best agreement with the experiments, and these also returned best agreement with the reattachment location. Nevertheless, none of these models were able to match the velocity profile after the reattachment point, this again being related to a slow predicted recovery after reattachment. The KC model, which most overpredicted the reattachment point, provides similar velocity profiles to the GL and SG models which overpredicted less this parameter, confirming the comment of Lien and Leschziner (1994c) on the slow predicted recovery of RST models.

The profiles of the time-averaged streamwise Reynolds normal stress are presented in Figures 5.289 and 5.290. One may notice that the GL model provided good agreement with the experiments up to $x/H = 5$, however after this point it has high inertia and is not capable of reducing the turbulence intensity level. That is probably related to its slow post-reattachment recovery. Most LEV models provide levels of $\overline{u^2}$ which are in reasonable agreement with the experimental data, specially after the reattachment point. Again, one may notice a relation between the level of $\overline{u^2}$ before the reattachment point and the prediction of the latter.

The same qualitative analyses carried out for the other turbulent quantities (the Reynolds

normal stresses $\overline{v^2}$ and $\overline{w^2}$, the Reynolds shear stress, the turbulent kinetic energy and the eddy-dissipation rate) in the steady state case can be extended for both unsteady cases, where mainly one can notice a relation between the turbulence level in the shear region and the prediction of the reattachment point, which is totally expected from the physical description of the backward facing step case. As Chun and Sung (1996) did not provide experimental data for these quantities, their profiles will not be shown here for the unsteady cases.

The results for the high frequency case are presented in Figure 5.291 to 5.296. The TS, HJ, NG, TC, WM and KS models did not converge or reach the fully periodic state for this case either. Hence, as before, the results provided by the 7 models which provided a converged and fully periodic solution will be divided into the STS LEV models and the other models which include two STS RST models and two MTS LEV models.

Starting by looking at the time-averaged reattachment point predicted by each turbulence model, presented in Table 5.23, one may notice that, at this high frequency, the reattachment point reported in the experiments is slightly higher than that in the steady state and all turbulence models are consistent in this sense, meaning that, qualitatively, the results are similar to those discussed for the steady state. The model which returned the closest result was the FM model, followed by the SG and LS models. The CG model consistently underpredicts excessively the reattachment length, followed by the standard $k-\varepsilon$ model, HR model. The GL and KC models provide acceptable results, the former slightly underpredicting and the latter slightly overpredicting this parameter.

Table 5.23: Time-averaged reattachment point in the unsteady backward facing step case of Chun and Sung (1996) with $St = 1$.

Model/Experiment	Reattachment point (x/H)	% Error
Experiment	8.1	-
HR	6.67	−17.62
LS	7.56	−6.69
FM	8.30	2.42
GL	7.22	−10.82
SG	7.66	−5.45
CG	4.44	−45.13
KC	9.15	12.92

The time-averaged profiles of the wall shear stress, wall-pressure coefficient and the forward-flow time fraction are presented in Figures 5.291 and 5.292. The profiles of the time-averaged wall shear stress are in agreement with the reattachment points presented in Table 5.23 and so is the distribution of γ_P. All models, apart from the GL model, do not predict a secondary recirculation zone and that is in agreement with the findings of Chun and Sung (1996). For the same reasons discussed in the previous low frequency case, contour plots for the stream function will not be presented here since they will not contribute to the analysis. The profile of the wall pressure coefficient was well captured by the HR, KC, GL and SG models. The LS and FM models provided a too low minimum value which is in agreement with their wall shear stress prediction. The CG model, as expected from its gross

underprediction of the reattachment point provides a wrong profile, increasing C_P too fast.

The time-averaged velocity profiles are presented in Figures 5.293 and 5.294. One may notice that all models, except for the CG model, provide good agreement with the experiments even after the reattachment point, however, all of them fail to follow the shear region at $x/H = 7$. The post-reattachment recovery seems not to be so slow in this case and that might be an effect of the high frequency unsteadiness. Another explanation could be that the slightly later reattachment point, $X_R = 8.1$ in this case, is fairly close to the final measurement location, $x/H = 9$, and so the profiles only show the very initial stages of the post-reattachment recovery.

The profiles of the time-averaged streamwise Reynolds stress are presented in Figures 5.295 and 5.296. Again, one can say that the LEV models provide reasonable agreement with the experiments, but this time the GL model provides better agreement with the experimental data up to $x/H = 7$ and again seems to keep this level at $x/H = 9$ by inertia.

5.9.4 Concluding Remarks

To conclude the analysis of the backward facing step cases, one may look at Table 5.24 where the reattachment points predicted by each model in each case are summarized. One may notice that no model is actually able to follow completely the experiments. They all follow the general trend, $X_{R_{St=0.275}} < X_{R_{St=0}} < X_{R_{St=1}}$, however they fail to capture the magnitude of the differences. The models which underpredict considerably the reattachment point in the steady and high frequency cases, predict reasonably well the low frequency case and vice versa.

Overall, the models which performed best were the FM, LS and SG models. Although the latter did not actually reach a fully periodic state, since its time-averaged profiles did not appear to show any significant anomalies they were included in the comparisons above. The fact that the FM and LS models performed best might make one wonder whether it is the use of a LRN approach which is the important feature in predicting these flows. Unfortunately, these two models were the only LRN models which converged for all three cases and RST and MTS approaches could not be evaluated together with LRN schemes.

RST models did not seem to provide a clear advantage over the LEV models. Although the latter are not expected to correctly predict the Reynolds normal stresses, they provided overall the best agreement with the experimental data for the streamwise component $\overline{u^2}$. The same can be said of the MTS models. The CG clearly failed, always underpredicting the reattachment point and the KC model tended to always overpredict this parameter, specially in the low frequency case.

Among all the test cases evaluated, these backward facing step cases are clearly the most complex ones with the strongest non-equilibrium features. In contrast to a number of the other cases where most models performed reasonably well, in these test cases no model performed very satisfactorily. It was not possible to notice the strong influence of the anisotropy, as pointed out by Lien and Leschziner (1994c), since the LEV models performed

overall better than the RST models. It was not possible to identify clear advantages brought from the MTS schemes either. This case thus become an important test case in the scope of this work where it is intended to developed MTS models which perform well in non-equilibrium flows.

Table 5.24: Comparison of the prediction of the reattachment point in the three backward facing step cases.

Model/Experiment	St=0	St=0.275	St=1
Experiment	7.8	5.0	8.1
HR	6.42	5.01	6.67
LS	7.21	5.29	7.56
FM	7.35	6.16	8.30
GL	6.59	6.14	7.22
SG	6.95	5.51	7.66
CG	4.20	3.83	4.44
KC	8.44	7.21	9.15

To avoid repetition, conclusions of the performance of the models over the entire range of flows considered in this chapter are presented in Chapter 8.

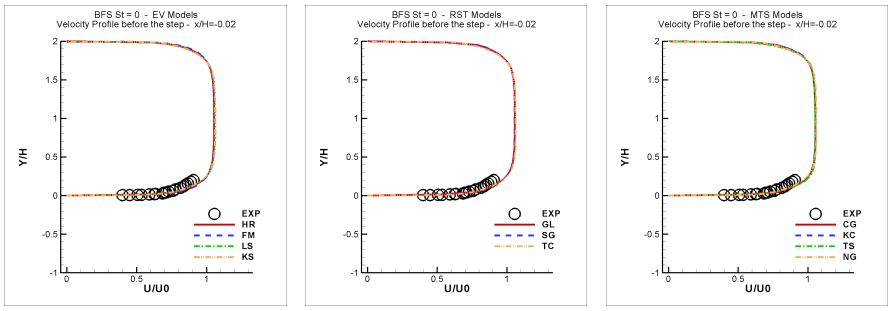

(a) (b) (c)

Figure 5.238: Prediction of the velocity profile before the step, at $x/H = -0.02$, by the (a) eddy-viscosity models, (b) Reynolds-stress-transport models and (c) multiple-time-scale models in the steady state backward facing step case of Chun and Sung (1996). Models as in Table 3.25.

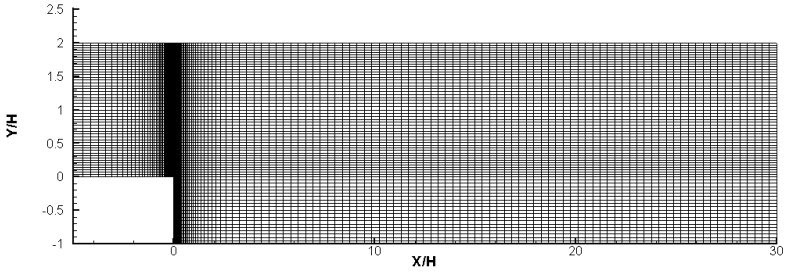

Figure 5.239: 180x70 grid used for the HRN models.

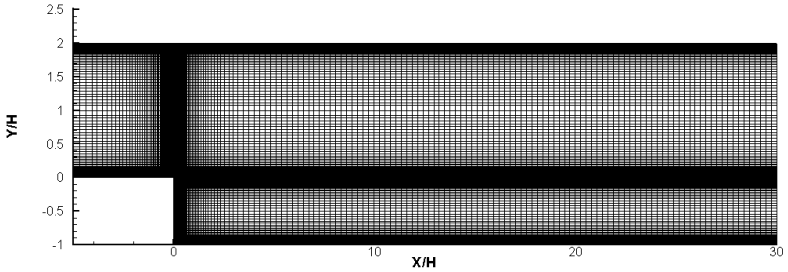

Figure 5.240: 240x180 grid used for the LRN models.

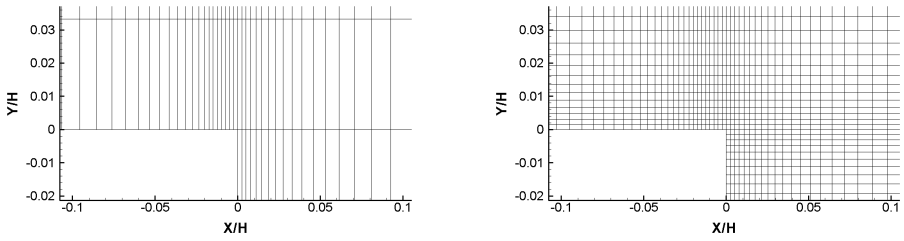

(a) (b)

Figure 5.241: Zoom in the step corner region in the (a) HRN models grid and in the (b) LRN models grid.

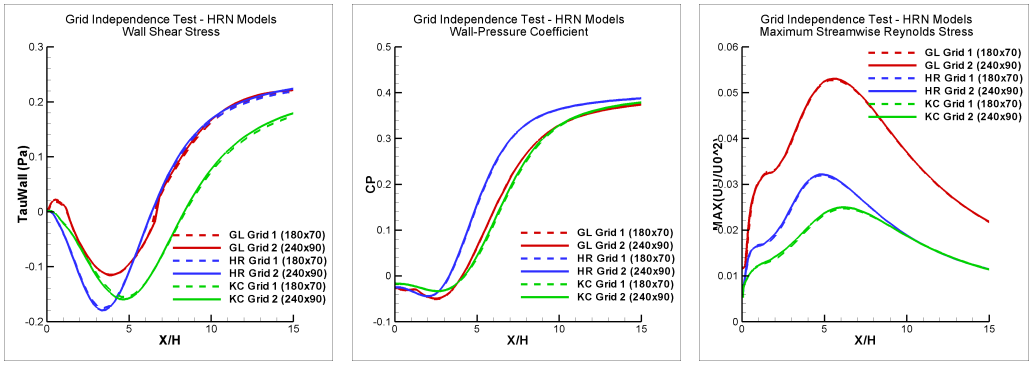

(a) (b) (c)

Figure 5.242: Prediction of (a) wall-shear-stress, (b) wall-pressure coefficient and (c) maximum $\overline{u^2}$ by the HR, GL and KC models, representing the HRN models, using the two tested grids, verifying the grid independence test.

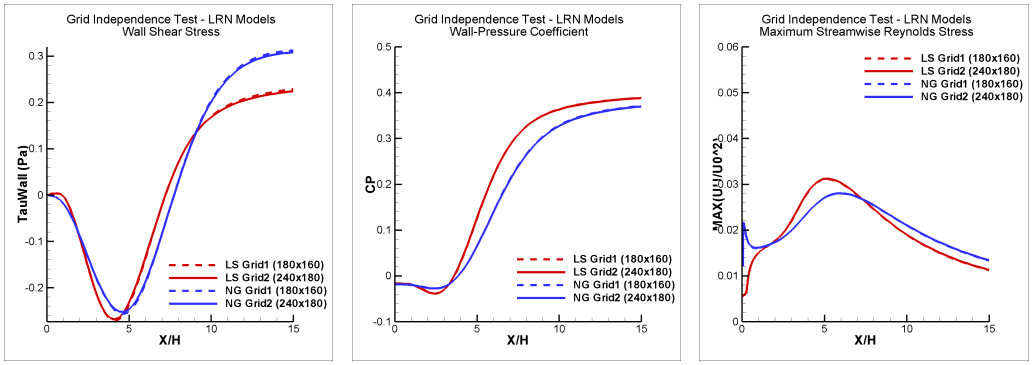

(a) (b) (c)

Figure 5.243: Prediction of (a) wall-shear-stress, (b) wall-pressure coefficient and (c) maximum $\overline{u^2}$ by the LS and NG models, representing the LRN models, using the two tested grids, verifying the grid independence test.

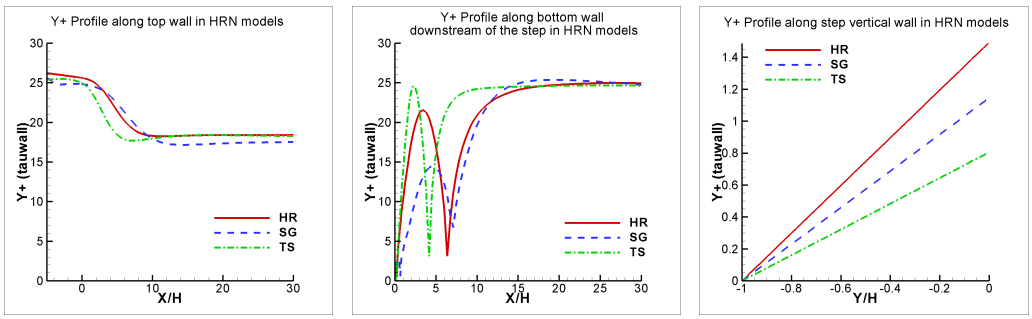

(a) (b) (c)

Figure 5.244: Prediction of y^+ in the first near-wall node of the (a) top wall, (b) bottom wall after step and (c) step vertical wall by the HR, GL and KC models, representing the HRN models.

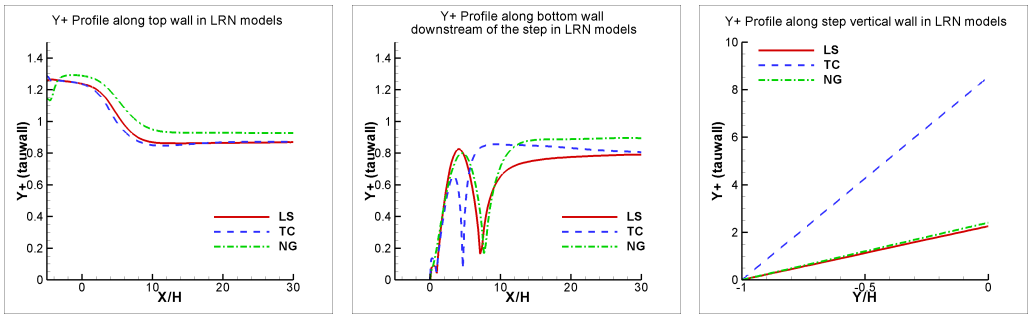

(a) (b) (c)

Figure 5.245: Prediction of y^+ in the first near-wall node of the (a) top wall, (b) bottom wall after step and (c) step vertical wall by the LS, NG and TC models, representing the LRN models.

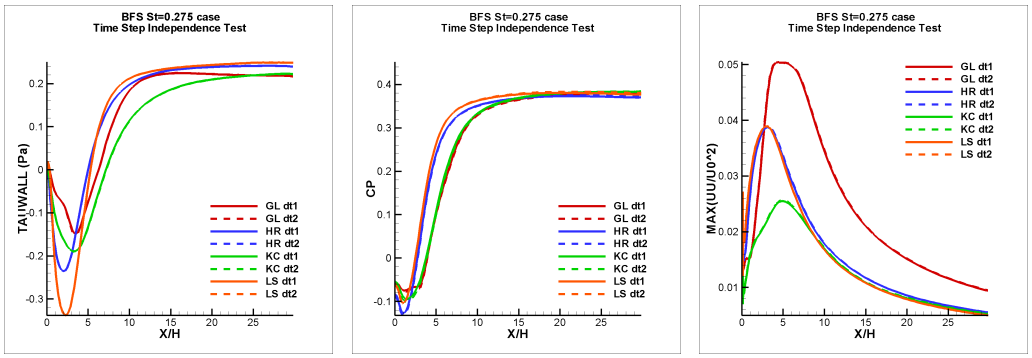

(a) (b) (c)

Figure 5.246: Prediction of (a) wall-shear-stress, (b) wall-pressure coefficient and (c) maximum $\overline{u^2}$ by the HR, GL and KC models, representing the HRN models, and the LS model, representing the LRN models, using the two tested time steps in the St=0.275 unsteady case of Chun and Sung (1996), verifying the time step independence test.

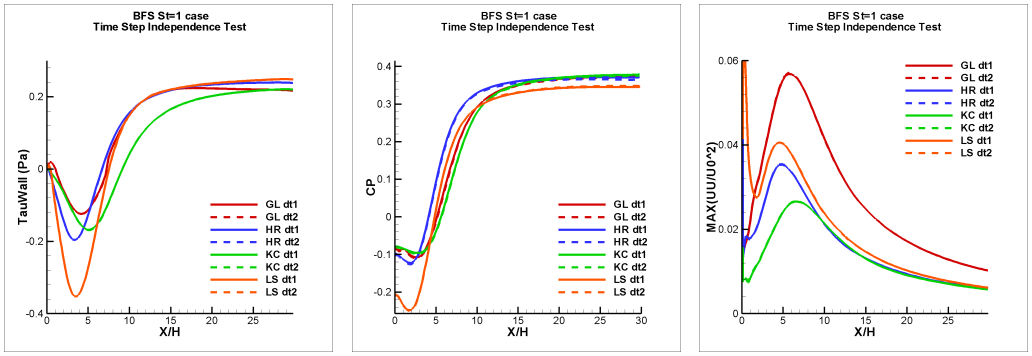

(a) (b) (c)

Figure 5.247: Prediction of (a) wall-shear-stress, (b) wall-pressure coefficient and (c) maximum $\overline{u^2}$ by the HR, GL and KC models, representing the HRN models, and the LS model, representing the LRN models, using the two tested time steps in the St=1 unsteady case of Chun and Sung (1996), verifying the time step independence test.

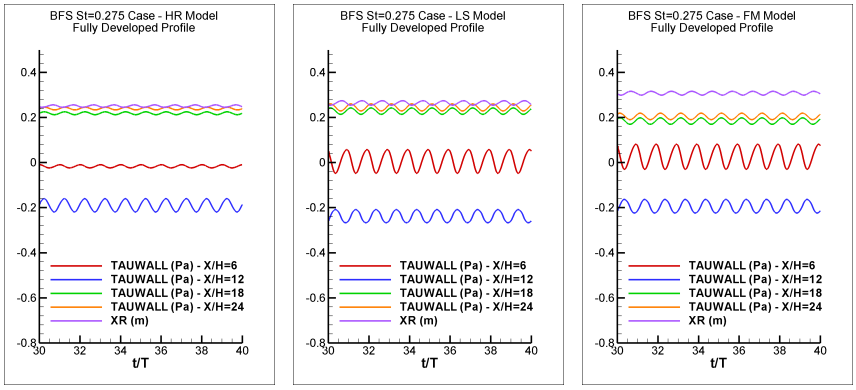

(a) HR model (b) LS model (c) FM model

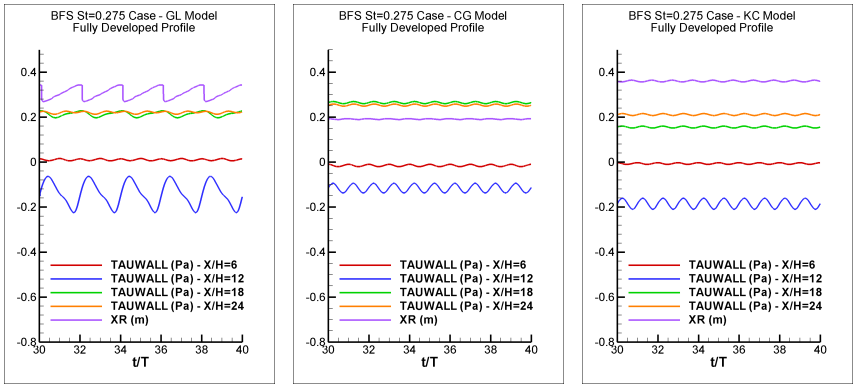

(d) GL model (e) CG model (f) KC model

Figure 5.248: Prediction of the reattachment point and τ_w at four positions downstream of the step at the last 10 cycles where the averaging process was carried out for the six turbulence models which reached the fully developed state in the $BFS - St0275$ case. Models as in Table 3.25.

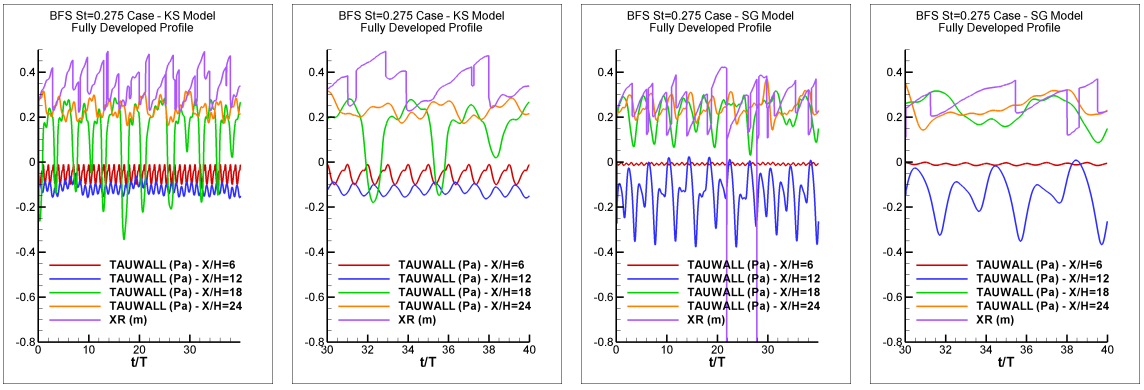

(a) KS model - 40 cycles (b) KS - last 10 cycles (c) SG model - 40 cycles (d) SG - last 10 cycles

Figure 5.249: Prediction of the reattachment point and τ_w at four positions downstream of the step at the last 40 cycles and at the last 10 cycles where the averaging process was carried out for the two turbulence models which could not reach a fully developed state in the $BFS - St0275$ case. Models as in Table 3.25.

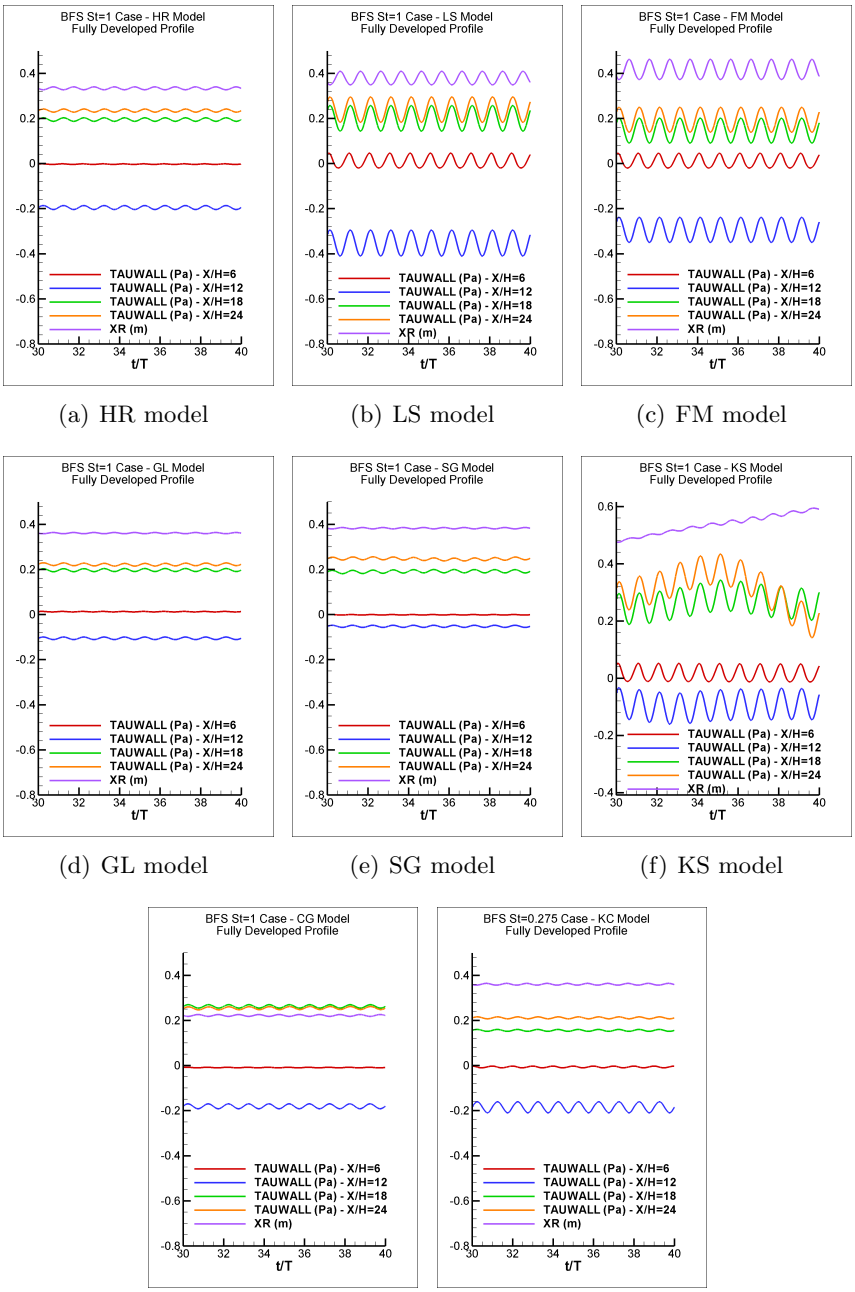

(a) HR model (b) LS model (c) FM model

(d) GL model (e) SG model (f) KS model

(g) CG model (h) KC model

Figure 5.250: Prediction of the reattachment point and τ_w at four positions downstream of the step at the last 10 cycles where the averaging process was carried out in the $BFS - St1$ case. Models as in Table 3.25.

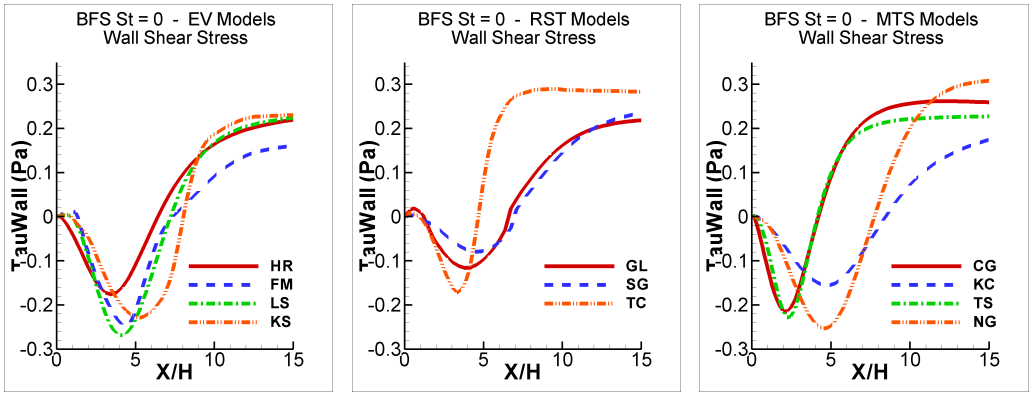

(a) (b) (c)

Figure 5.251: Prediction of the wall-shear-stress by the (a) eddy-viscosity models, (b) Reynolds-stress-transport models and (c) multiple-time-scale models in the steady state backward facing step case of Chun and Sung (1996). Models as in Table 3.25.

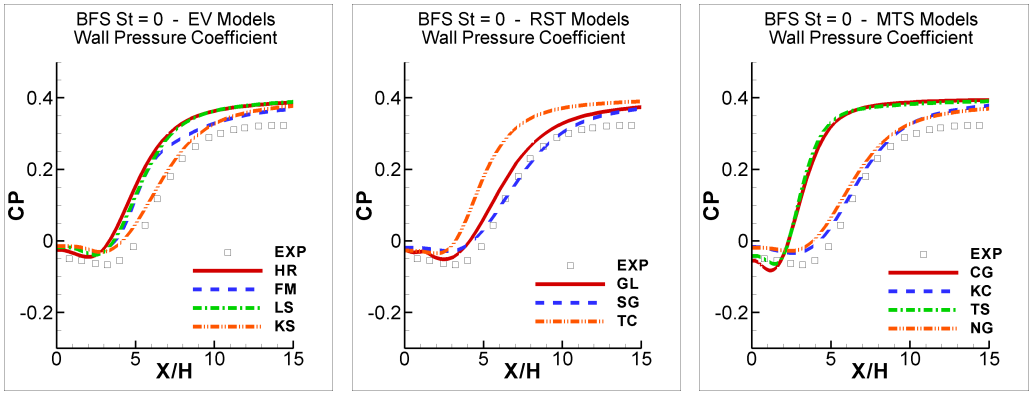

(a) (b) (c)

Figure 5.252: Prediction of the wall-pressure coefficient by the (a) eddy-viscosity models, (b) Reynolds-stress-transport models and (c) multiple-time-scale models in the steady state backward facing step case of Chun and Sung (1996). Models as in Table 3.25.

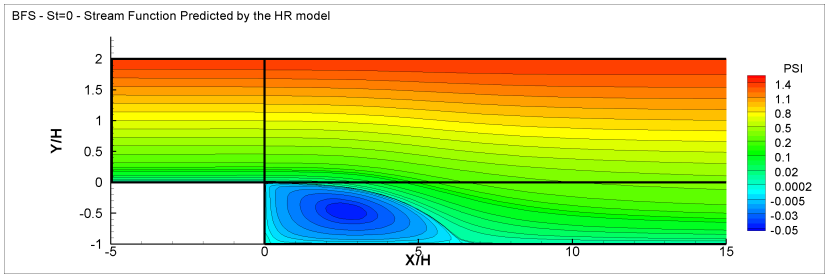

Figure 5.253: Prediction of the stream function by the HR model in the steady state backward facing step case of Chun and Sung (1996). Models as in Table 3.25.

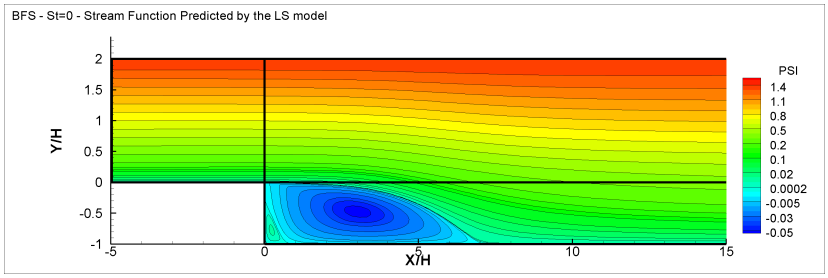

Figure 5.254: Prediction of the stream function by the LS model in the steady state backward facing step case of Chun and Sung (1996).

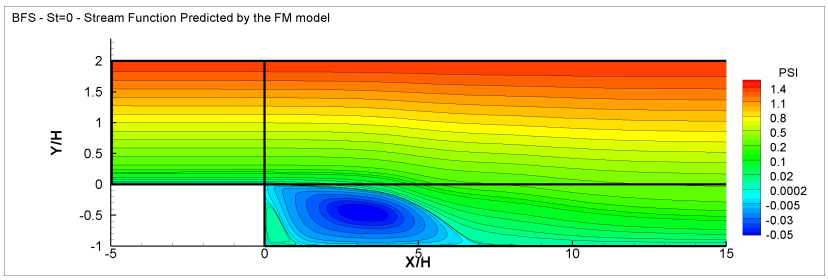

Figure 5.255: Prediction of the stream function by the FM model in the steady state backward facing step case of Chun and Sung (1996).

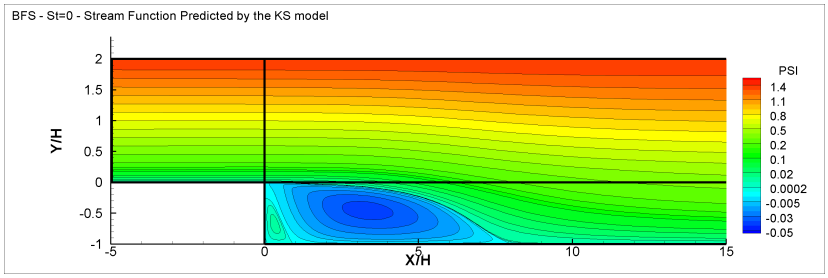

Figure 5.256: Prediction of the stream function by the KS model in the steady state backward facing step case of Chun and Sung (1996).

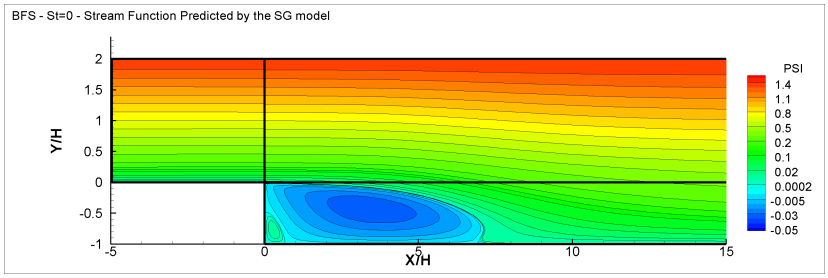

Figure 5.257: Prediction of the stream function by the SG model in the steady state backward facing step case of Chun and Sung (1996).

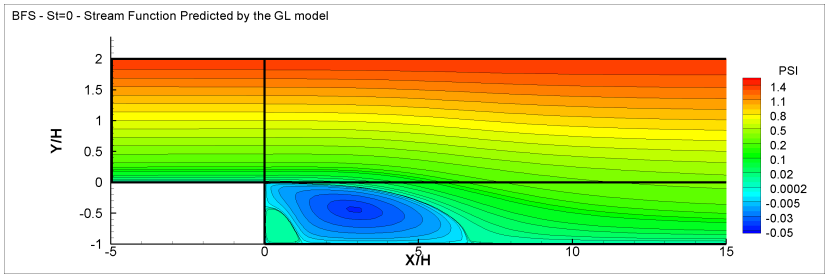

Figure 5.258: Prediction of the stream function by the GL model in the steady state backward facing step case of Chun and Sung (1996).

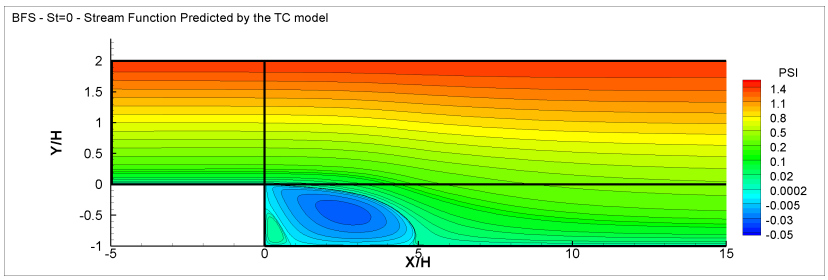

Figure 5.259: Prediction of the stream function by the TC model in the steady state backward facing step case of Chun and Sung (1996).

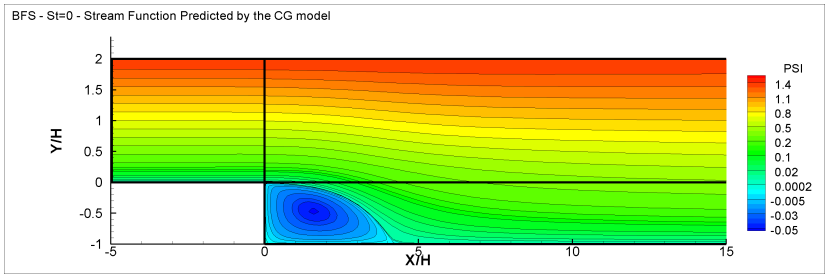

Figure 5.260: Prediction of the stream function by the CG model in the steady state backward facing step case of Chun and Sung (1996).

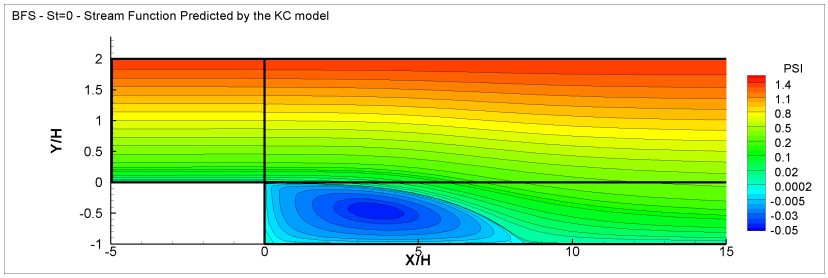

Figure 5.261: Prediction of the stream function by the KC model in the steady state backward facing step case of Chun and Sung (1996).

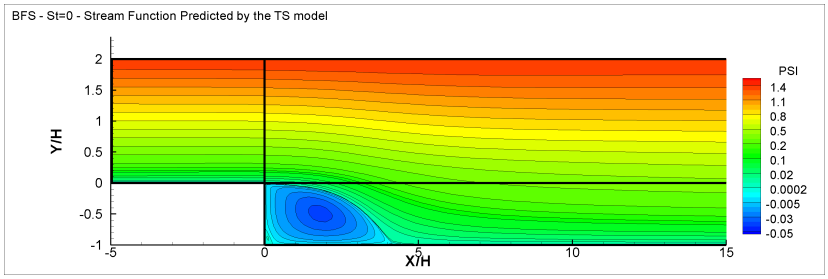

Figure 5.262: Prediction of the stream function by the TS model in the steady state backward facing step case of Chun and Sung (1996).

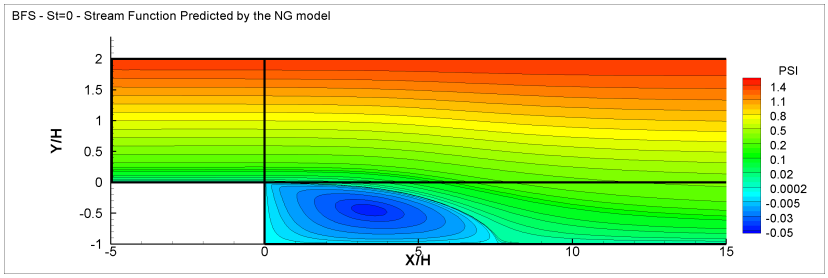

Figure 5.263: Prediction of the stream function by the NG model in the steady state backward facing step case of Chun and Sung (1996).

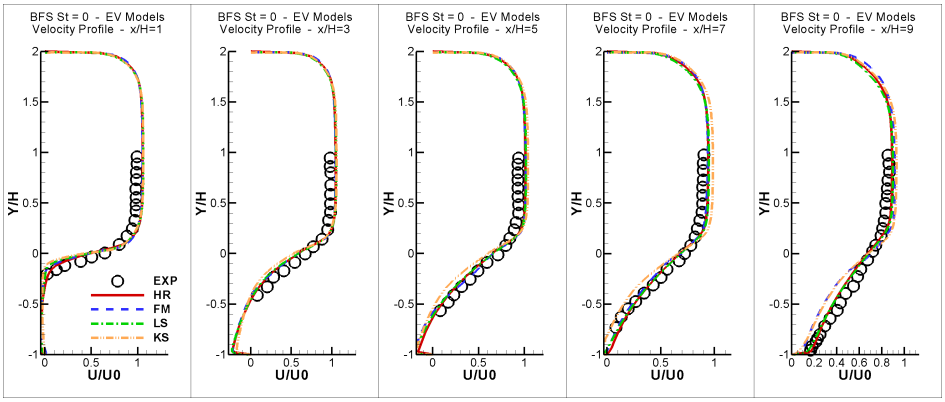

Figure 5.264: Prediction of the velocity profile at five positions downstream of the step $x/H = 1, 3, 5, 7, 9$ by the eddy-viscosity models in the steady state backward facing step case of Chun and Sung (1996). Models as in Table 3.25.

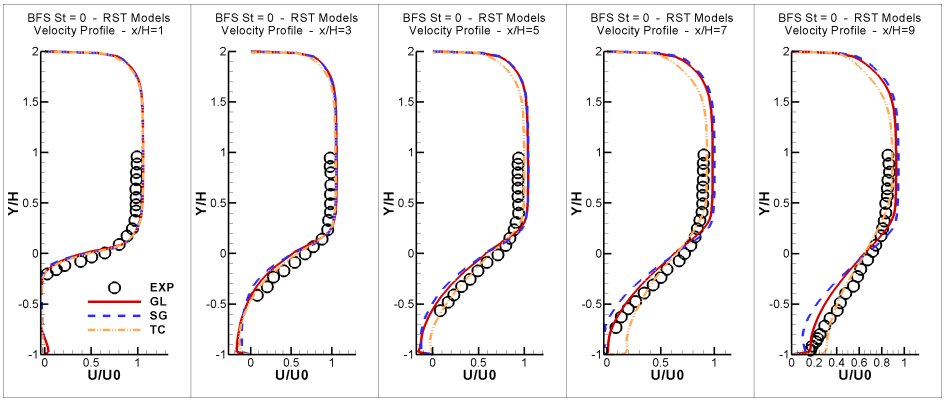

Figure 5.265: Prediction of the velocity profile at five positions downstream of the step $x/H = 1, 3, 5, 7, 9$ by the Reynolds-stress-transport models in the steady state backward facing step case of Chun and Sung (1996). Models as in Table 3.25.

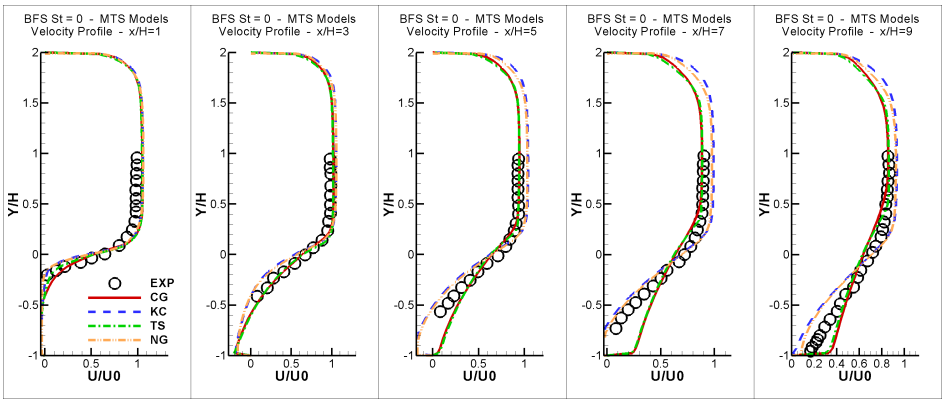

Figure 5.266: Prediction of the velocity profile at five positions downstream of the step $x/H = 1, 3, 5, 7, 9$ by the multiple-time-scale models in the steady state backward facing step case of Chun and Sung (1996). Models as in Table 3.25.

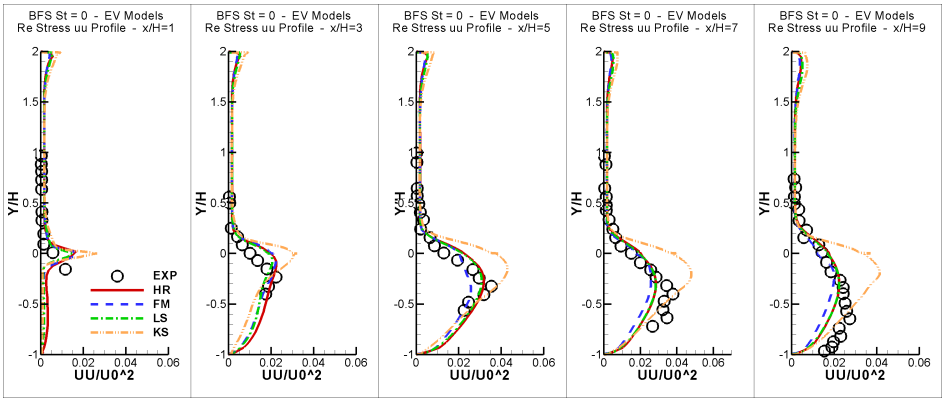

Figure 5.267: Prediction of the streamwise Reynolds normal stress profile at five positions downstream of the step $x/H = 1, 3, 5, 7, 9$ by the eddy-viscosity models in the steady state backward facing step case of Chun and Sung (1996). Models as in Table 3.25.

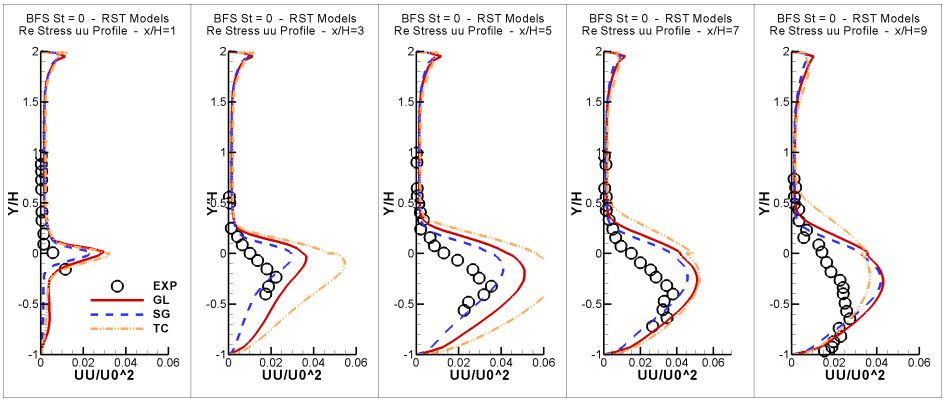

Figure 5.268: Prediction of the streamwise Reynolds normal stress profile at five positions downstream of the step $x/H = 1, 3, 5, 7, 9$ by the Reynolds-stress-transport models in the steady state backward facing step case of Chun and Sung (1996). Models as in Table 3.25.

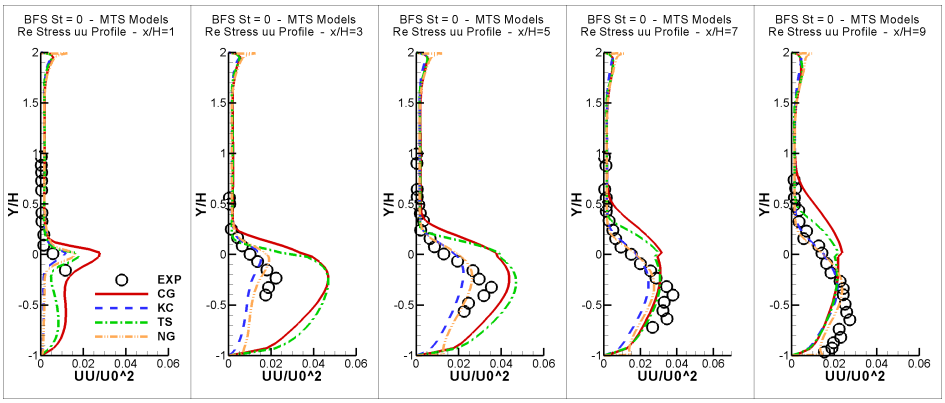

Figure 5.269: Prediction of the streamwise Reynolds normal stress profile at five positions downstream of the step $x/H = 1, 3, 5, 7, 9$ by the multiple-time-scale models in the steady state backward facing step case of Chun and Sung (1996). Models as in Table 3.25.

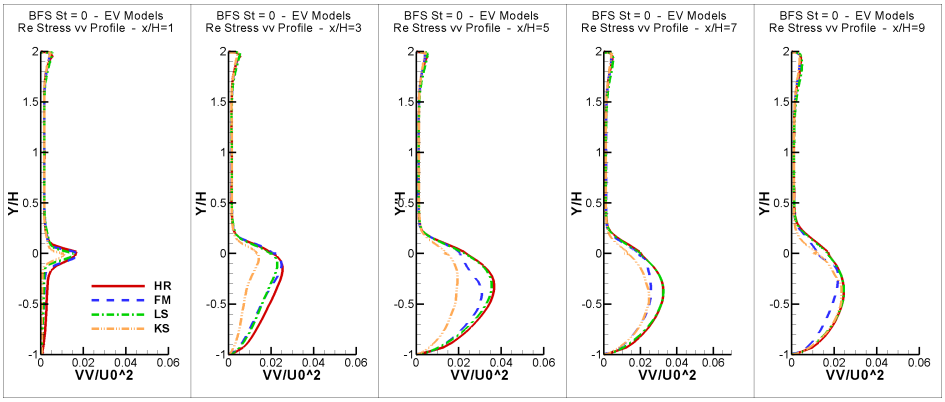

Figure 5.270: Prediction of the wall-normal Reynolds normal stress profile at five positions downstream of the step $x/H = 1, 3, 5, 7, 9$ by the eddy-viscosity models in the steady state backward facing step case of Chun and Sung (1996). Models as in Table 3.25.

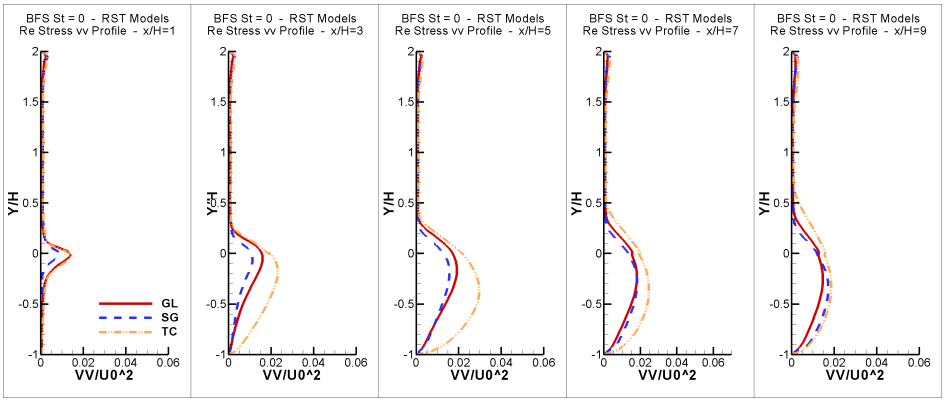

Figure 5.271: Prediction of the wall-normal Reynolds normal stress profile at five positions downstream of the step $x/H = 1, 3, 5, 7, 9$ by the Reynolds-stress-transport models in the steady state backward facing step case of Chun and Sung (1996). Models as in Table 3.25.

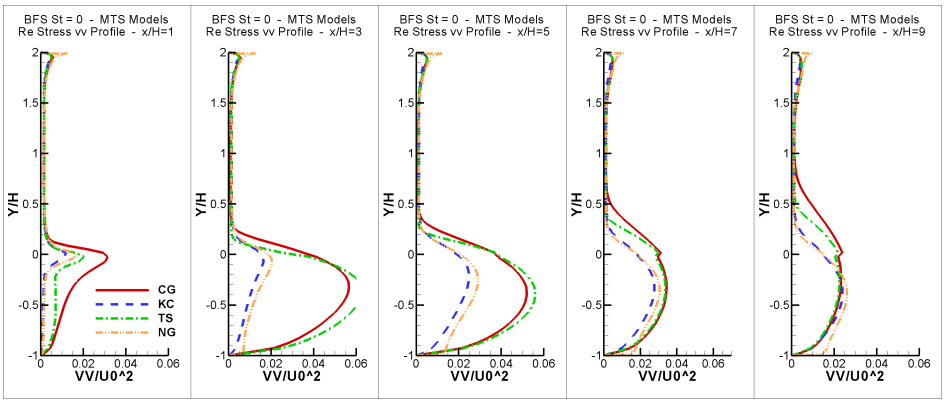

Figure 5.272: Prediction of the wall-normal Reynolds normal stress profile at five positions downstream of the step $x/H = 1, 3, 5, 7, 9$ by the multiple-time-scale models in the steady state backward facing step case of Chun and Sung (1996). Models as in Table 3.25.

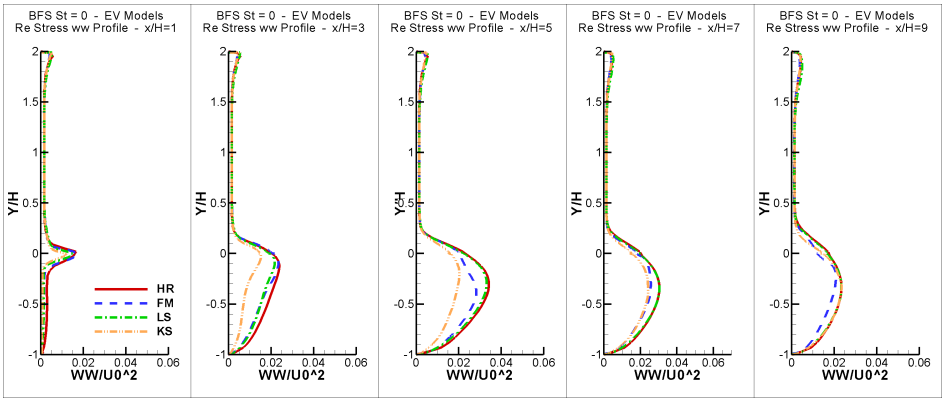

Figure 5.273: Prediction of the $\overline{w^2}$ Reynolds normal stress profile at five positions downstream of the step $x/H = 1, 3, 5, 7, 9$ by the eddy-viscosity models in the steady state backward facing step case of Chun and Sung (1996). Models as in Table 3.25.

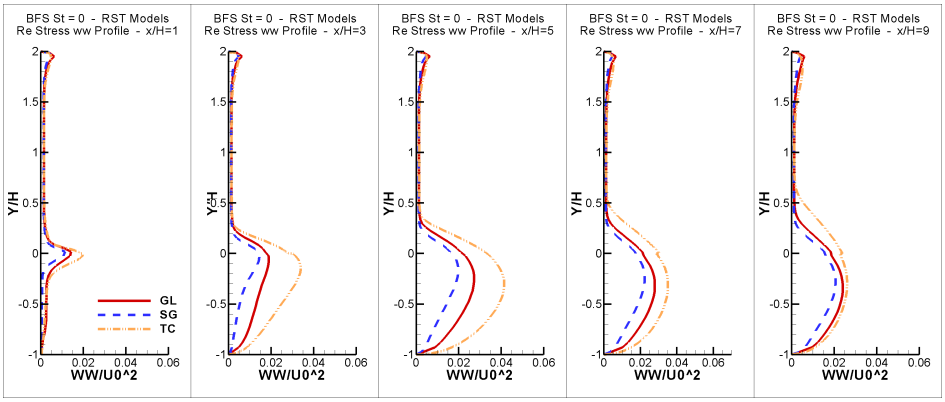

Figure 5.274: Prediction of the $\overline{w^2}$ Reynolds normal stress profile at five positions downstream of the step $x/H = 1, 3, 5, 7, 9$ by the Reynolds-stress-transport models in the steady state backward facing step case of Chun and Sung (1996). Models as in Table 3.25.

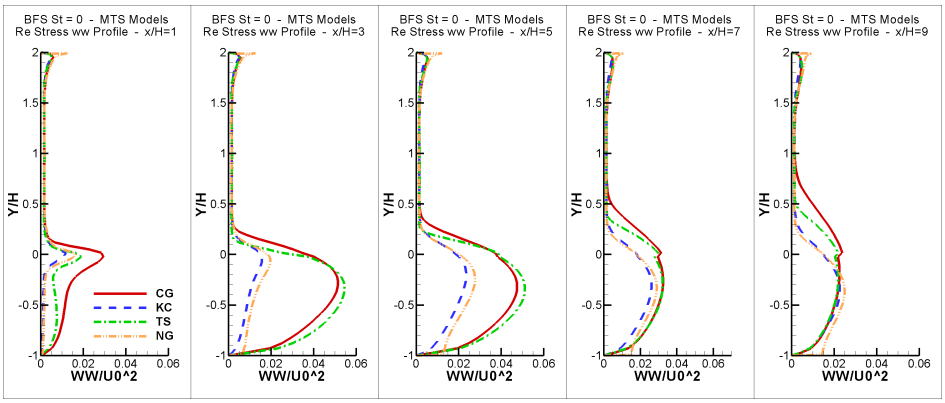

Figure 5.275: Prediction of the $\overline{w^2}$ Reynolds normal stress profile at five positions downstream of the step $x/H = 1, 3, 5, 7, 9$ by the multiple-time-scale models in the steady state backward facing step case of Chun and Sung (1996). Models as in Table 3.25.

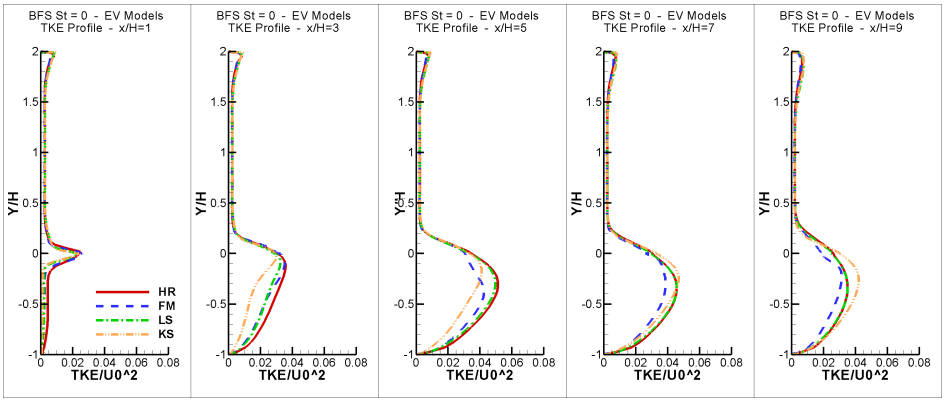

Figure 5.276: Prediction of the turbulent kinetic energy profile at five positions downstream of the step $x/H = 1, 3, 5, 7, 9$ by the eddy-viscosity models in the steady state backward facing step case of Chun and Sung (1996). Models as in Table 3.25.

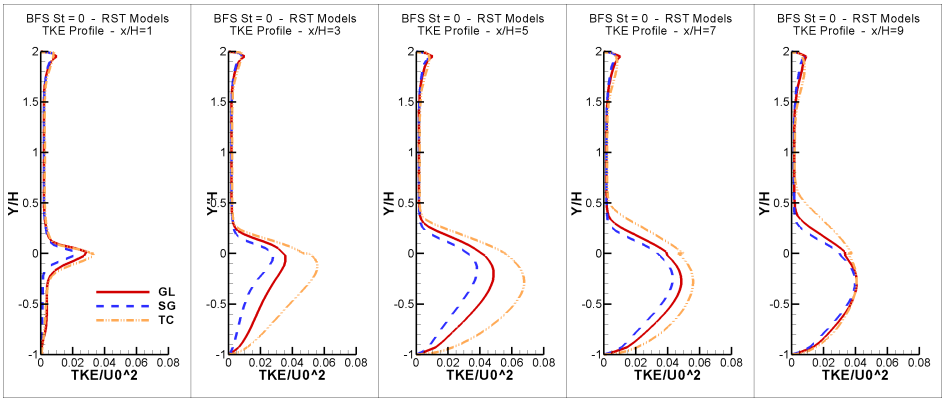

Figure 5.277: Prediction of the turbulent kinetic energy profile at five positions downstream of the step $x/H = 1, 3, 5, 7, 9$ by the Reynolds-stress-transport models in the steady state backward facing step case of Chun and Sung (1996). Models as in Table 3.25.

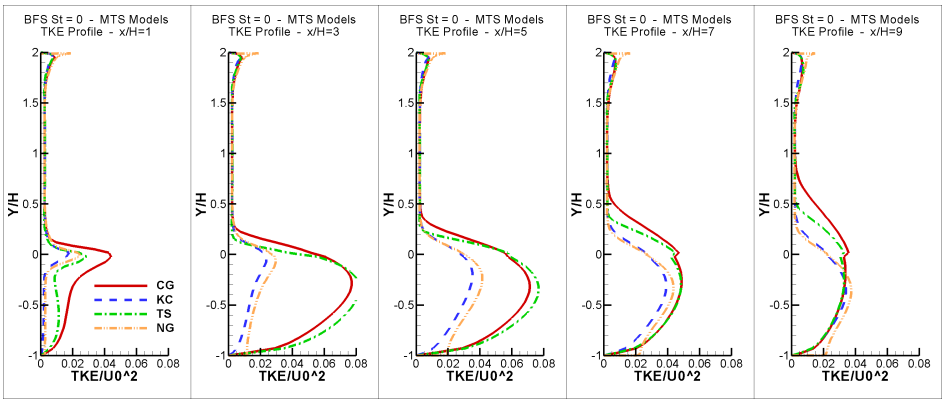

Figure 5.278: Prediction of the turbulent kinetic energy profile at five positions downstream of the step $x/H = 1, 3, 5, 7, 9$ by the multiple-time-scale models in the steady state backward facing step case of Chun and Sung (1996). Models as in Table 3.25.

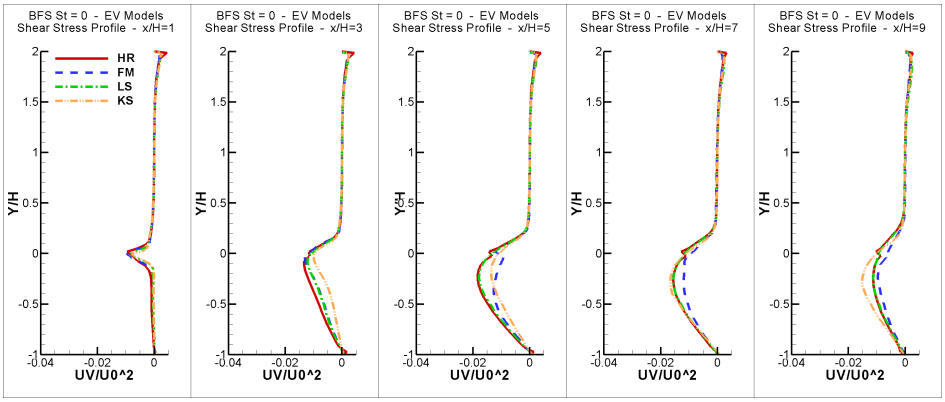

Figure 5.279: Prediction of the Reynolds shear stress profile at five positions downstream of the step $x/H = 1, 3, 5, 7, 9$ by the eddy-viscosity models in the steady state backward facing step case of Chun and Sung (1996). Models as in Table 3.25.

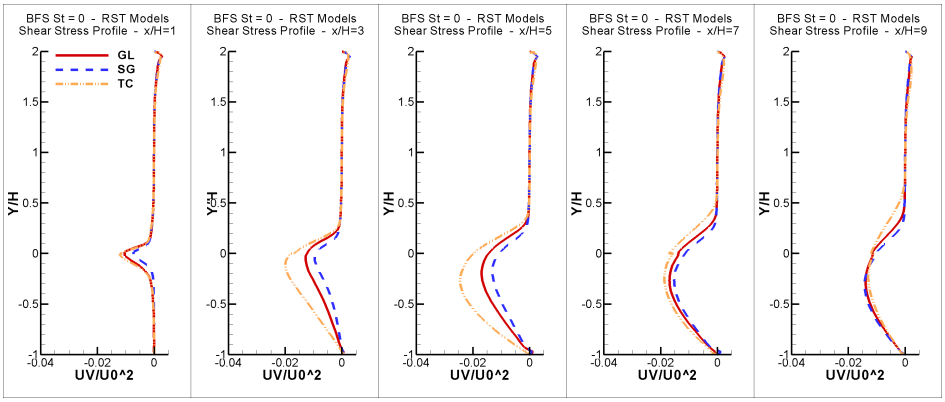

Figure 5.280: Prediction of the Reynolds shear stress profile at five positions downstream of the step $x/H = 1, 3, 5, 7, 9$ by the Reynolds-stress-transport models in the steady state backward facing step case of Chun and Sung (1996). Models as in Table 3.25.

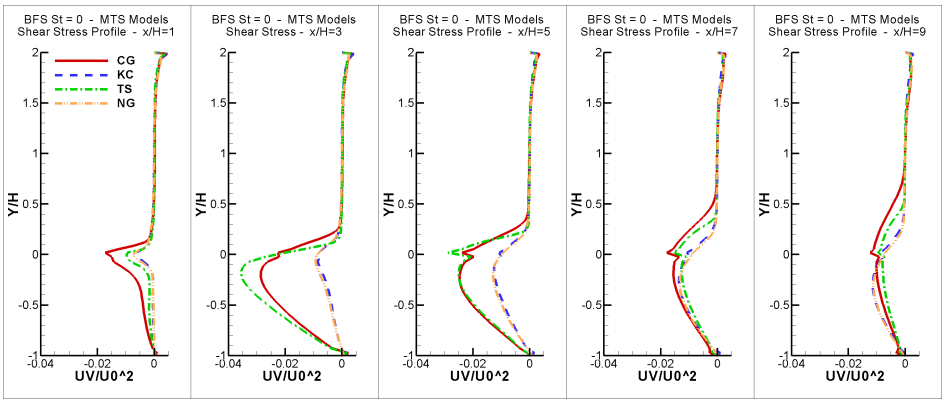

Figure 5.281: Prediction of the Reynolds shear stress profile at five positions downstream of the step $x/H = 1, 3, 5, 7, 9$ by the multiple-time-scale models in the steady state backward facing step case of Chun and Sung (1996). Models as in Table 3.25.

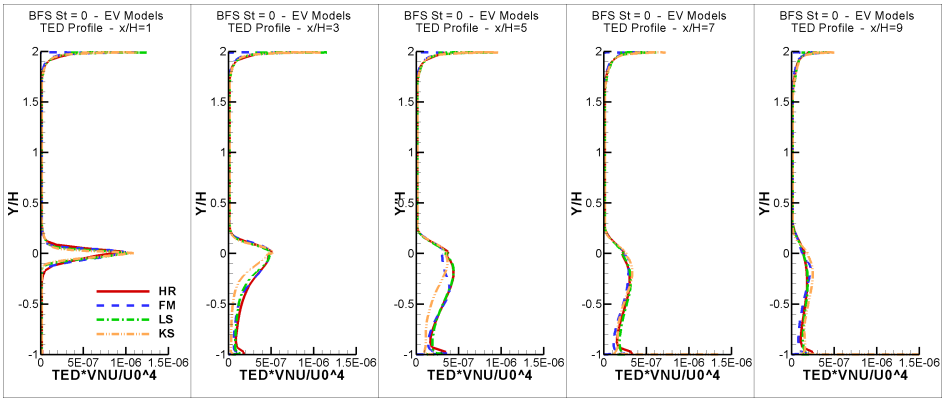

Figure 5.282: Prediction of the eddy-dissipation rate profile at five positions downstream of the step $x/H = 1, 3, 5, 7, 9$ by the eddy-viscosity models in the steady state backward facing step case of Chun and Sung (1996). Models as in Table 3.25.

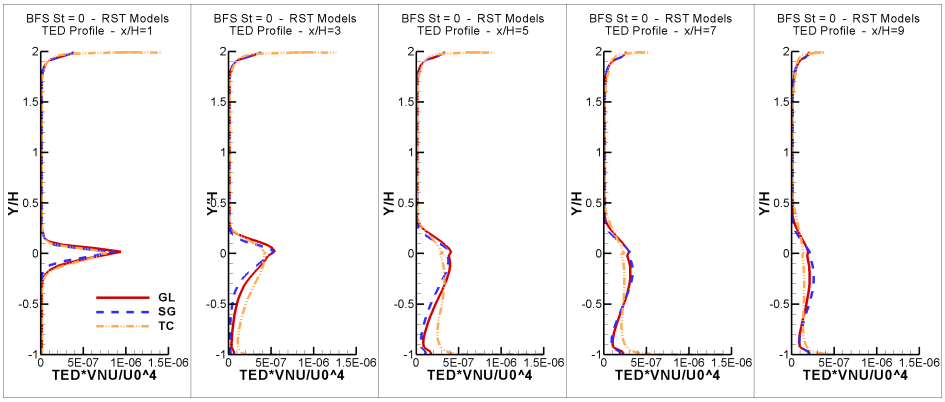

Figure 5.283: Prediction of the eddy-dissipation rate profile at five positions downstream of the step $x/H = 1, 3, 5, 7, 9$ by the Reynolds-stress-transport models in the steady state backward facing step case of Chun and Sung (1996). Models as in Table 3.25.

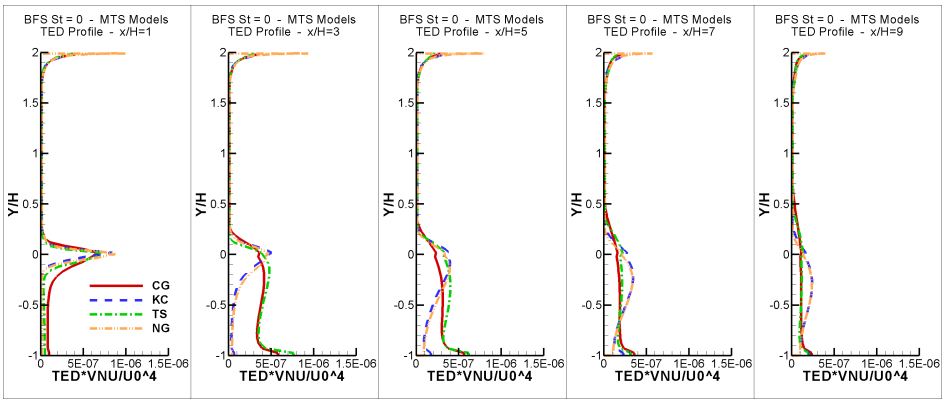

Figure 5.284: Prediction of the eddy-dissipation rate profile at five positions downstream of the step $x/H = 1, 3, 5, 7, 9$ by the multiple-time-scale models in the steady state backward facing step case of Chun and Sung (1996). Models as in Table 3.25.

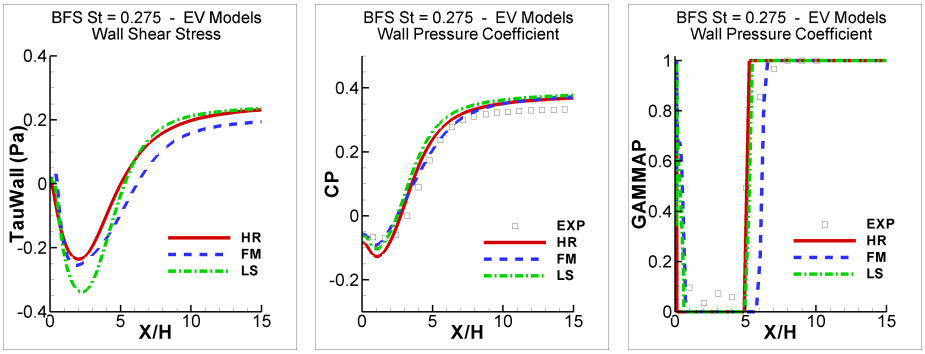

(a) (b) (c)

Figure 5.285: Prediction by the singe-time-scale eddy-viscosity models of (a) time-averaged wall-shear-stress, (b) time-averaged wall-pressure coefficient, (c) forward-flow time fraction in the unsteady backward facing step $BFS - St0275$ case. Models as in Table 3.25.

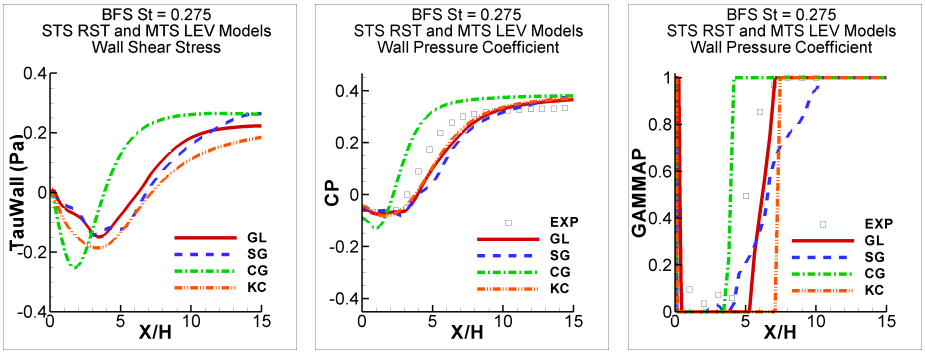

(a) (b) (c)

Figure 5.286: Prediction by the singe-time-scale Reynolds-stress-transport and two-time-scale linear-eddy-viscosity models of (a) time-averaged wall-shear-stress, (b) time-averaged wall-pressure coefficient, (c) forward-flow time fraction in the unsteady backward facing step $BFS - St0275$ case. Models as in Table 3.25.

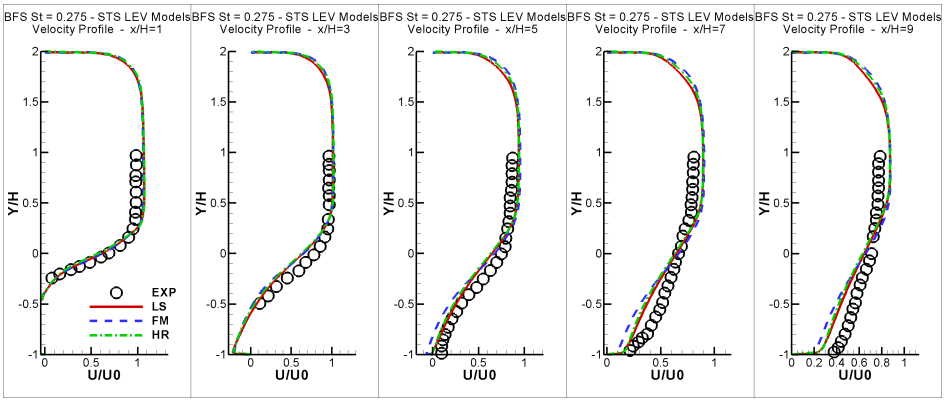

Figure 5.287: Prediction of the time-averaged velocity profile at five positions downstream of the step $x/H = 1, 3, 5, 7, 9$ by the singe-time-scale eddy-viscosity models in the unsteady backward facing step $BFS - St0275$ case. Models as in Table 3.25.

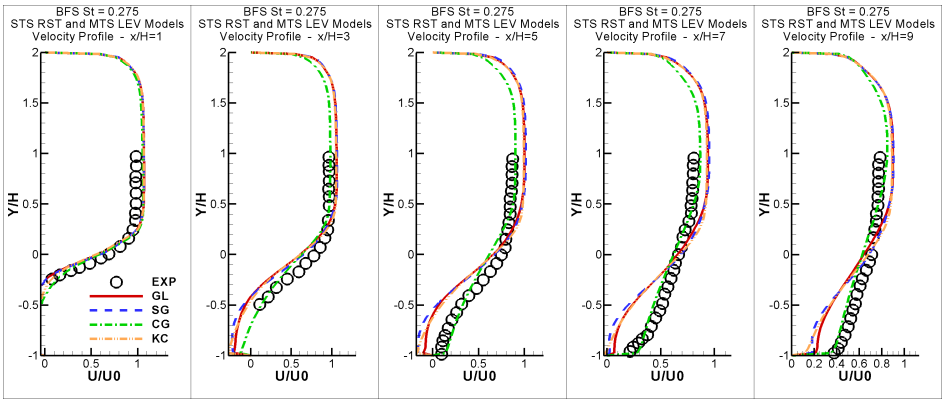

Figure 5.288: Prediction of the time-averaged velocity profile at five positions downstream of the step $x/H = 1, 3, 5, 7, 9$ by the singe-time-scale Reynolds-stress-transport and two-time-scale linear-eddy-viscosity models in the unsteady backward facing step $BFS - St0275$ case. Models as in Table 3.25.

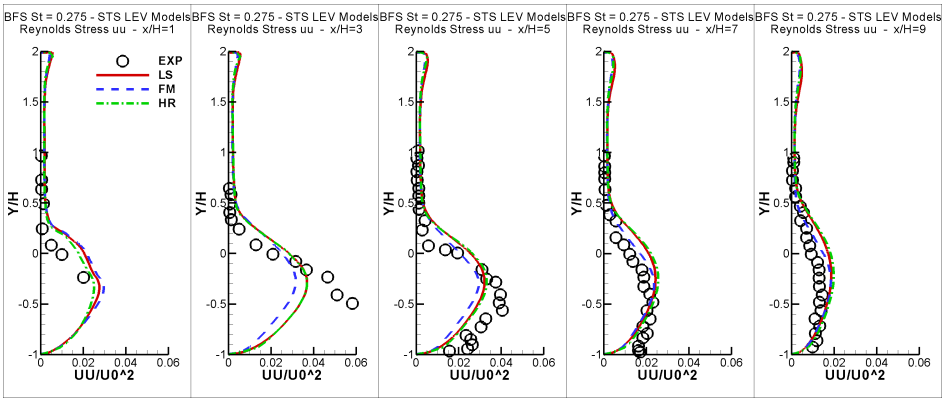

Figure 5.289: Prediction of the time-averaged streamwise Reynolds normal stress profile at five positions downstream of the step $x/H = 1, 3, 5, 7, 9$ by the singe-time-scale eddy-viscosity models in the unsteady backward facing step $BFS - St0275$ case. Models as in Table 3.25.

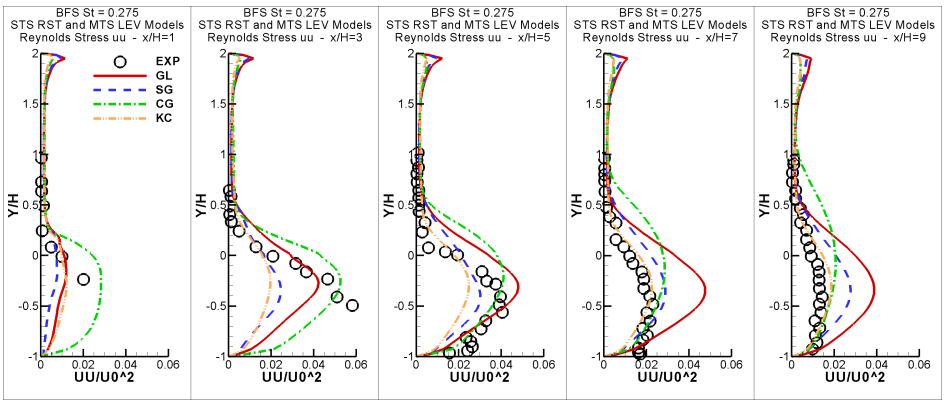

Figure 5.290: Prediction of the time-averaged streamwise Reynolds normal stress profile at five positions downstream of the step $x/H = 1, 3, 5, 7, 9$ by the singe-time-scale Reynolds-stress-transport and two-time-scale linear-eddy-viscosity models in the unsteady backward facing step $BFS - St0275$ case. Models as in Table 3.25.

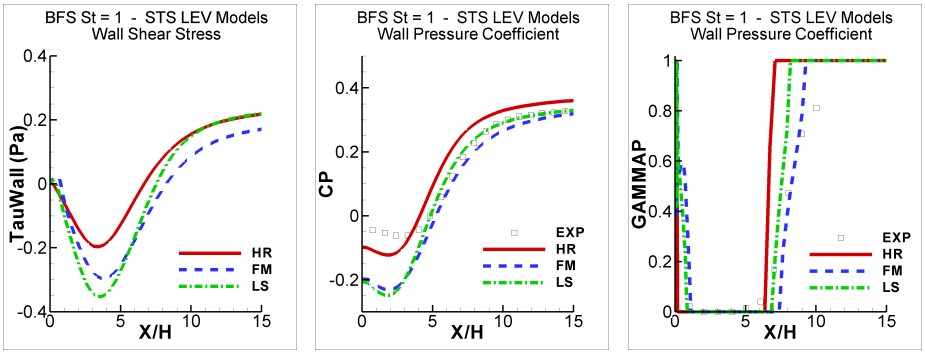

(a) (b) (c)

Figure 5.291: Prediction by the singe-time-scale eddy-viscosity models of (a) time-averaged wall-shear-stress, (b) time-averaged wall-pressure coefficient, (c) forward-flow time fraction in the unsteady backward facing step $BFS - St1$ case. Models as in Table 3.25.

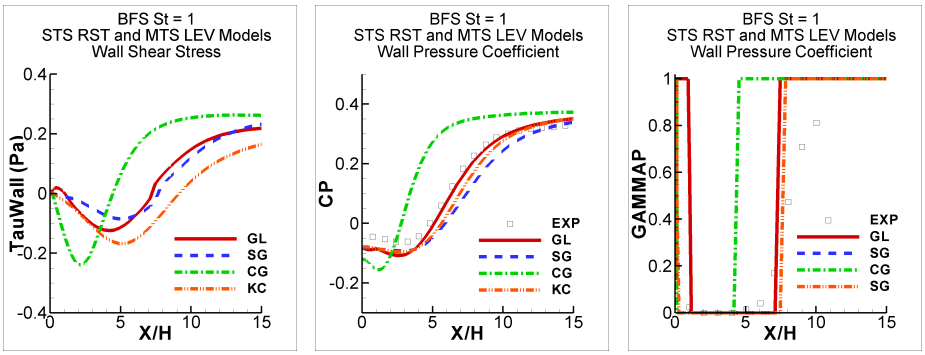

(a) (b) (c)

Figure 5.292: Prediction by the singe-time-scale Reynolds-stress-transport and two-time-scale linear-eddy-viscosity models of (a) time-averaged wall-shear-stress, (b) time-averaged wall-pressure coefficient, (c) forward-flow time fraction in the unsteady backward facing step $BFS - St1$ case. Models as in Table 3.25.

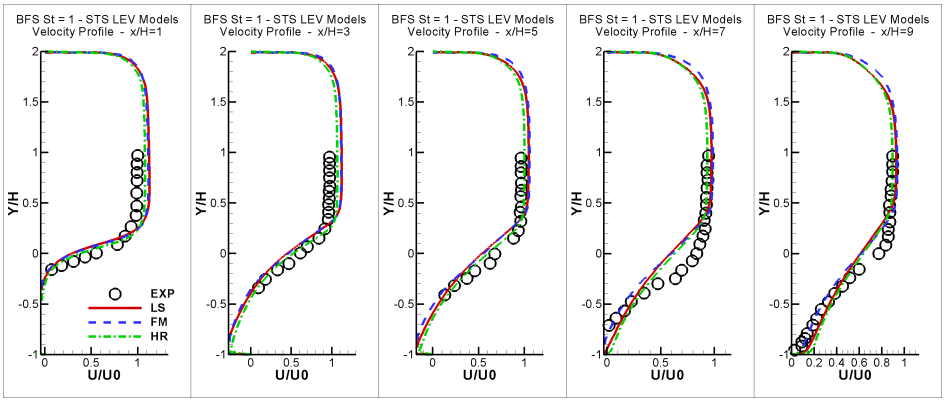

Figure 5.293: Prediction of the time-averaged velocity profile at five positions downstream of the step $x/H = 1, 3, 5, 7, 9$ by the singe-time-scale eddy-viscosity models in the unsteady backward facing step $BFS - St1$ case. Models as in Table 3.25.

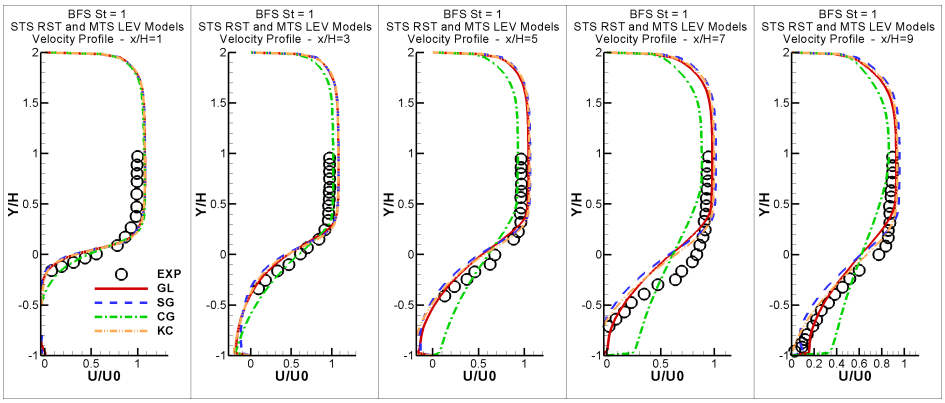

Figure 5.294: Prediction of the time-averaged velocity profile at five positions downstream of the step $x/H = 1, 3, 5, 7, 9$ by the singe-time-scale Reynolds-stress-transport and two-time-scale linear-eddy-viscosity models in the unsteady backward facing step $BFS - St1$ case. Models as in Table 3.25.

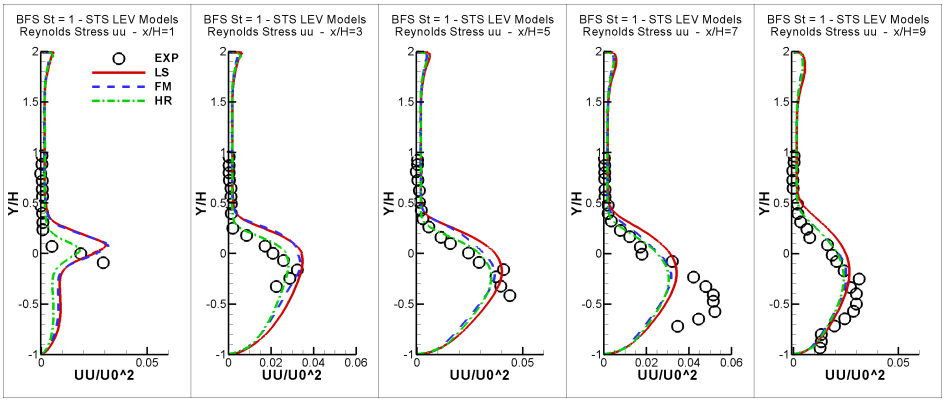

Figure 5.295: Prediction of the time-averaged streamwise Reynolds normal stress profile at five positions downstream of the step $x/H = 1, 3, 5, 7, 9$ by the singe-time-scale eddy-viscosity models in the unsteady backward facing step $BFS - St1$ case. Models as in Table 3.25.

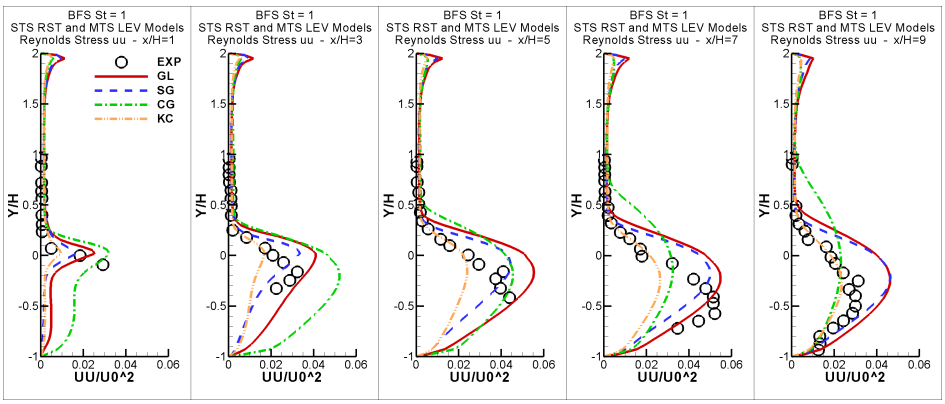

Figure 5.296: Prediction of the time-averaged streamwise Reynolds normal stress profile at five positions downstream of the step $x/H = 1, 3, 5, 7, 9$ by the singe-time-scale Reynolds-stress-transport and two-time-scale linear-eddy-viscosity models in the unsteady backward facing step $BFS - St1$ case. Models as in Table 3.25.

Chapter 6

Development of Two-Time-Scale Linear-Eddy-Viscosity Models

This chapter aims to present all the stages which led to the final version of the two two-time-scale linear-eddy-viscosity models developed in this work, which will be referred to as NT1 and NT2 models. As will be shown later, the main difference between the two models is in the expression for ν_t, the eddy viscosity, which results in different terms in the ε_P and ε_T equations and different values and expressions for the coefficients.

The development process for each model can be broken down into a number of discrete stages, with each subsequent stage resulting in further improved versions. A version was defined always when the general set of terms, expressions and coefficients were considered satisfactory in all test cases. This chapter will thus present each stage of development separately.

The final version of the models will be then used to simulate all test cases presented and discussed in the previous chapter and its effectiveness will be assessed through comparisons with the predictions of a selection of turbulence models used so far and also with DNS and/or experimental data.

6.1 First Versions of the NT1 and NT2 Models

The first step to identify how to start to develop or improve an MTS model was to evaluate the performance of existing MTS models, which was presented in the previous chapter. Based on this, the TS model was chosen as a base model to start off. This model was chosen mainly because it also served as a base for the developments of the other MTS models investigated in this work. Besides that, this model could also be chosen by elimination of the others. An LEV model would be preferable owing to its simplicity, so the WM could be discarded (although it could also be discarded by being an RST model and not bringing consistent advantages in predicting the Reynolds stresses in all tested cases). Among the LEV MTS schemes, the NG presented some stability problems which were associated with its high tuning of the near-wall region, which did provide good results, but does not represent what one wishes to start from.

A high-Reynolds-number form of turbulence model version emerges then as more appropriate since it does not require a specific near-wall treatment, which would need special attention when the partition variables (k_P, k_T, ε_P and ε_T) are considered. Besides, most cases tested are at a reasonably high Reynolds number, where one would then expect wall-functions not to be a problem. The CG model performed generally worse than the KC and TS models. These models presented reasonably good results in some flows, but performed poorly in some other flows. Consequently, as the TS model forms the basis of many of the MTS models, it was then chosen as a starting point.

The criteria used to chose a base model have just been described and now the procedures and analyses carried out to developed the first versions of the NT1 and NT2 models will be presented.

6.1.1 Study of the $\frac{k_P}{k_T}$ and $\frac{\varepsilon_P}{\varepsilon_T}$ ratios

As the MTS models presented and discussed so far are based on a division of the turbulent kinetic energy spectrum, from this the four main turbulent quantities emerge, k_P, k_T, ε_P and ε_T. The ratios $\frac{k_P}{k_T}$ and $\frac{\varepsilon_P}{\varepsilon_T}$, which respectively represent the shape and the equilibrium imbalance of the spectrum, thus emerge as important parameters to be studied.

The evolution of the $\frac{k_P}{k_T}$ and $\frac{\varepsilon_P}{\varepsilon_T}$ ratios was then assessed in order to enrich the understanding of the performance of the MTS models. This analysis could also clarify how the spectrum is divided by each turbulence model. By the time the first versions of the NT1 and NT2 models were developed, six test cases - homogeneous shear flows, normally strained flows, channel flows, zero-pressure-gradient, adverse-pressure-gradient and favourable-pressure-gradient boundary layer - had been assessed, so $\frac{k_P}{k_T}$ and $\frac{\varepsilon_P}{\varepsilon_T}$ were first evaluated in these test cases.

The evolution of these ratios is presented in Figures 6.1 to 6.8.

Starting by looking at the homogeneous shear flow cases, one can observe the evolution of the $\frac{k_P}{k_T}$ and $\frac{\varepsilon_P}{\varepsilon_T}$ in Figures 6.1 and 6.2. Clearly, $\frac{k_P}{k_T}$ in the NG model tends to an asymptotic value; in the CG and KC models, it seems to tend to a asymptotic value, needing perhaps more time to reach it, and, in the TS model, it not only does not tend to an asymptotic value, but increases very fast, especially in the high-shear flow cases, represented by Figure 6.2. In order to understand these behaviours, k_P and k_T are plotted separately in Figure 6.3 for one low, one moderate and one high shear case. One may notice that the reason why $\frac{k_P}{k_T}$ seems to grow exponentially when predicted by the TS model is that this model predicts k_P to grow too fast, much earlier than k_T. This explains the sudden growth followed by a decay and subsequent increase behaviour of the TS model in predicting $\frac{Pk}{\varepsilon_T}$ and $\eta = \frac{k}{\varepsilon_T}\frac{dU}{dy}$ in these two high-shear flow cases as noted earlier in Figures 5.32, 5.33. The evolution of $\frac{\varepsilon_P}{\varepsilon_T}$ behaves nicely, tending to a value close to unity in the low, moderate and high shear flow cases represented in Figures 6.1, 6.2(b) and 6.2(d). Nonetheless, one may notice that although the TS model presents the smallest peak for $\frac{\varepsilon_P}{\varepsilon_T}$ in Figures 6.2(b) and 6.2(d), it presents the highest growth in predicting $\frac{P_k}{\varepsilon_T}$ in Figure 5.32.

Looking now at the evolution of $\frac{k_P}{k_T}$ and $\frac{\varepsilon_P}{\varepsilon_T}$ in the normally strained cases in Figure 6.4

and starting by assessing the $T\&R$ case, one may notice that the CG and TS models which provided the fastest k decay, for this case, as shown in Figure 5.39(c), also return the highest values for the ratios $\frac{k_P}{k_T}$ and $\frac{\varepsilon_P}{\varepsilon_T}$. As the CG model provides a much higher ratio value of $\frac{k_P}{k_T}$ than the TS model, and their prediction of the evolution of $\frac{\varepsilon_P}{\varepsilon_T}$ is similar, it seems that the latter ratio is the more influential one. Profiles of $\frac{k_P}{k_T}$ and $\frac{\varepsilon_P}{\varepsilon_T}$ are not being presented for the $G\&M05$ case because they are expected to be just the same as in the GM0 case, since all MTS models used here are LEV schemes and therefore they have no sensitivity to change in sign of the normal straining, as discussed in Chapter 5.

Moving on to the evolution of the $\frac{k_P}{k_T}$ and $\frac{\varepsilon_P}{\varepsilon_T}$ ratios in the fully developed channel flow cases, one may first look at Figures 6.5(a) and 6.5(b). Only results for the lowest and highest Reynolds number cases will be shown since these are sufficient to provide the features which will be discussed here. The $\frac{\varepsilon_P}{\varepsilon_T}$ ratio was predicted by all MTS models as about unity in the equilibrium part of the flow for all the Reynolds number range. On the other hand, the ratio $\frac{k_P}{k_T}$ increases with the Reynolds number of the flow. For the lowest Reynolds number flow, 6.5(a), most of the models gave the ratio $\frac{k_P}{k_T}$ near to 2 in the equilibrium part. This ratio, however, does increase for the higher Reynolds number flows. One may notice that the TS model clearly returns the highest values of this ratio, specially in the equilibrium part of the flow. In order to understand better the reason why that happens, k_P and k_T were plotted for the highest Reynolds number flow for all LEV MTS models in Figure 6.5(c). One may notice that the TS model predicts k_P to be higher than the other MTS models and k_T to be slightly smaller than the other MTS models. These small differences are amplified when seen in the $\frac{k_P}{k_T}$ ratio form, but do not represent any unexpected behaviour of the TS model.

The evolution of $\frac{k_P}{k_T}$ and $\frac{\varepsilon_P}{\varepsilon_T}$ in the zero pressure gradient boundary layer cases are presented in Figure 6.6. Starting by discussing the behaviour of $\frac{k_P}{k_T}$, one may notice a similarity with the profiles of this ratio in the channel flows presented in Figure 6.5. The evolution of $\frac{k_P}{k_T}$ in the zero pressure gradient boundary layer flow includes the equilibrium part which is characterized by the peaks which are similar in shape to those of the channel flow results, and then an asymptotic part for the outer part of the flow. Again, one may notice the different values of the peaks for the different MTS models. The TS model again returns the highest peak. In Figure 6.6(d), one may notice the individual profiles of k_P and k_T for the Spalart boundary layer case when $Re_\theta = 1410$, showing no significant differences between any models and justifying the different peak values in Figure 6.6 simply by calculating the ratio of these quantities, as already commented on in the channel flow paragraph above. The profiles of $\frac{\varepsilon_P}{\varepsilon_T}$ also show an equilibrium value of around unity (as in the channel flow - Figure 6.5) and in the outer part of the flow this ratio decreases to about 0.5. The profiles of $\frac{k_P}{k_T}$ and $\frac{\varepsilon_P}{\varepsilon_T}$ are presented in Figure 6.6 for $Re_\theta = 1410$, $Re_\theta = 4981$ and $Re_\theta = 13052$ so that one can notice that the ratio $\frac{k_P}{k_T}$ in the equilibrium part of the boundary layer becomes higher, the further the downstream distance.

The evolution of $\frac{k_P}{k_T}$ and $\frac{\varepsilon_P}{\varepsilon_T}$ in the adverse pressure gradient boundary layer flows will not be presented here because they are qualitatively the same as in the zero pressure gradient boundary layer flow just discussed. The TS model always returns the highest peaks for the

equilibrium value of $\frac{k_P}{k_T}$, the level of the peak usually increases with the Re_θ value, except for the NG model where the effect is the opposite due to its LRN treatment. The equilibrium values of $\frac{\varepsilon_P}{\varepsilon_T}$ are slightly above unity showing a small departure from the equilibrium, and in the outer part of the flow they also decrease. The ratio $\frac{k_P}{k_T}$ in the equilibrium part of the boundary layer also becomes higher, the further the downstream distance.

Finally, one can assess the evolution of $\frac{k_P}{k_T}$ and $\frac{\varepsilon_P}{\varepsilon_T}$ in Figure 6.7 for the K150 favourable pressure gradient boundary layer case. One may notice a different behaviour for the outer part of the flow. Within the boundary layer, Figures 6.7(b) and 6.7(d), $\frac{k_P}{k_T}$ and $\frac{\varepsilon_P}{\varepsilon_T}$ present values similar to those in the channel flow, zero and adverse pressure gradient boundary layer cases. However, in the outer part, these ratios grow significantly for the CG, KC and NG models. This same behaviour occurs for the other two higher acceleration parameter cases, K250 and K275, and therefore it was decided not to show the latter's profiles since they would not contribute to the analysis. However, by looking at Figure 6.8, also for the K150 case, one may notice that, again, these high levels of $\frac{k_P}{k_T}$ are caused by expressing k_P and k_T into ratio forms which magnifies their difference. What is more interesting at this moment, is that one may conclude that there is no unexpected behaviour in any MTS model related to the behaviours presented in Figure 6.7.

From the above analyses it was possible to understand the behaviour of the ratios $\frac{k_P}{k_T}$ and $\frac{\varepsilon_P}{\varepsilon_T}$ in the different flows. All tested models provided similar trends to the development of these ratios, however the TS and CG models presented a rather too fast growth of k_P and k_T in homogeneous high shear flows, compared to the other models, which might be not desirable. The next sections will then investigate the possible causes for this and will form the starting point for the development of the new schemes.

6.1.2 Homogeneous Shear Flow Asymptotic Analysis

After examining the evolutions of $\frac{k_P}{k_T}$ and $\frac{\varepsilon_P}{\varepsilon_T}$, it can be noted that the only flow where these ratios performed sometimes oddly was the homogeneous shear flow. As this is a relatively simple flow, one may try to derive, for each turbulence model, what would be the expected value for these ratios when the asymptotic state of the flow is reached.

Asymptotic states for homogeneous shear flows have also been studied in MTS models by Kim and Benson (1992), Nagano et al. (1997), Stawiarski and Hanjalic (2002), Cadiou et al. (2004) and Stawiarski and Hanjalic (2005), among others. These studies were extended here.

Thus in the next subsections, an asymptotic analysis for a homogeneous shear flow will be carried out, primarily for the TS model which is the model under investigation, and the results will be presented for all MTS LEV models considered so far.

In the analysis that follows the transport equations are simplified by neglecting the diffusion terms, because the flow is homogeneous and also by neglecting any model damping functions, since the flows considered are high-Reynolds-number flows.

The asymptotic analysis thus consists of assuming that the substantial derivatives of the ratios of the turbulent quantities become zero when the asymptotic state is reached. For

example, one may say that $\frac{D}{Dt}\left(\frac{k}{\varepsilon_T}\right)$, $\frac{D}{Dt}\left(\frac{k_T}{\varepsilon_T}\right)$, $\frac{D}{Dt}\left(\frac{k_P}{k_T}\right)$, $\frac{D}{Dt}\left(\frac{k_P}{\varepsilon_T}\right)$, $\frac{D}{Dt}\left(\frac{k_P}{\varepsilon_P}\right)$, $\frac{D}{Dt}\left(\frac{k_T}{\varepsilon_P}\right)$ and $\frac{D}{Dt}\left(\frac{\varepsilon_P}{\varepsilon_T}\right)$ are all zero in the asymptotic state.

In order to carry out the asymptotic analysis not all these ratios are necessary. So the ones that will be directly employed here are:

$$\frac{D}{Dt}\left(\frac{k_T}{\varepsilon_T}\right) = \frac{1}{\varepsilon_T}\frac{Dk_T}{Dt} - \frac{k_T}{\varepsilon_T^2}\frac{D\varepsilon_T}{Dt} = 0 \tag{6.1}$$

$$\frac{D}{Dt}\left(\frac{k}{\varepsilon_T}\right) = \frac{1}{\varepsilon_T}\frac{Dk}{Dt} - \frac{k}{\varepsilon_T^2}\frac{D\varepsilon_T}{Dt} = \frac{1}{\varepsilon_T}\left(\frac{Dk_P}{Dt} + \frac{Dk_T}{Dt}\right) - \frac{k}{\varepsilon_T^2}\frac{D\varepsilon_T}{Dt} = 0 \tag{6.2}$$

$$\frac{D}{Dt}\left(\frac{k_P}{\varepsilon_P}\right) = \frac{1}{\varepsilon_P}\frac{Dk_P}{Dt} - \frac{k_P}{\varepsilon_P^2}\frac{D\varepsilon_P}{Dt} = 0 \tag{6.3}$$

6.1.3 TS model

Starting with the TS model, which is the chosen base model and which exhibited some odd behaviour in the evolutions of $\frac{k_P}{k_T}$ and $\frac{\varepsilon_P}{\varepsilon_T}$, one may write the transport equations for k_P, k_T, ε_P and ε_T when applied in a homogeneous shear flow case:

$$\frac{Dk_P}{Dt} = P_k - \varepsilon_P \tag{6.4}$$

$$\frac{Dk_T}{Dt} = \varepsilon_P - \varepsilon_T \tag{6.5}$$

$$\frac{D\varepsilon_P}{Dt} = C_{P1}P_k\frac{\varepsilon_P}{k_P} - C_{P2}\frac{\varepsilon_P^2}{k_P} + C'_{P1}k_P\left(\frac{\partial U}{\partial y}\right)^2 = C_{P1}P_k\frac{\varepsilon_P}{k_P} - C_{P2}\frac{\varepsilon_P^2}{k_P} + \frac{C'_{P1}}{c_\mu}\frac{k_P}{k}P_k\frac{\varepsilon_P}{k_P} \tag{6.6}$$

$$\frac{D\varepsilon_T}{Dt} = C_{T1}\frac{\varepsilon_P\varepsilon_T}{k_T} - C_{T2}\frac{\varepsilon_T^2}{k_T} \tag{6.7}$$

One may notice in equation 6.6 that the term $C'_{P1}k_P\frac{\partial U_l}{\partial x_m}\frac{\partial U_i}{\partial x_j}\epsilon_{lmk}\epsilon_{ijk}$, originally in equation 3.45, reduces here to $C'_{P1}k_P\left(\frac{\partial U}{\partial y}\right)^2$. Since $P_k = \nu_t\left(\frac{\partial U}{\partial y}\right)^2$, one may write $\left(\frac{\partial U}{\partial y}\right)^2 = \frac{P_k}{\nu_t}$. In the TS model, $\nu_t = c_\mu\frac{kk_P}{\varepsilon_P}$ and thus one arrives at the final form presented in equation 6.6. The reason for this algebraic manipulation was an attempt to write the terms associated with C_{P1} and C'_{P1} in as similar manner as possible.

Now replacing the derivatives in the asymptotic state equations 6.1, 6.2 and 6.3 by equations 6.4 to 6.7, one arrives at the equations below where the SF subscript indicates the asymptotic value of the quantity in a homogeneous shear flow case:

$$
\begin{aligned}
0 &= \frac{1}{\varepsilon_T}\frac{Dk_T}{Dt} - \frac{k_T}{\varepsilon_T^2}\frac{D\varepsilon_T}{Dt} \\
&= \frac{1}{\varepsilon_T}(\varepsilon_P - \varepsilon_T) - \frac{k_T}{\varepsilon_T^2}(C_{T1}\frac{\varepsilon_P\varepsilon_T}{k_T} - C_{T2}\frac{\varepsilon_T^2}{k_T}) \\
&= \frac{1}{\varepsilon_T}[\varepsilon_P(1-C_{T1}) - \varepsilon_T(1-C_{T2})] \\
\Rightarrow &\left(\frac{\varepsilon_P}{\varepsilon_T}\right)_{SF} = \left(\frac{1-C_{T2}}{1-C_{T1}}\right)_{SF}
\end{aligned} \tag{6.8}
$$

$$
\begin{aligned}
0 &= \frac{1}{\varepsilon_T}\left(\frac{Dk_P}{Dt} + \frac{Dk_T}{Dt}\right) - \frac{k}{\varepsilon_T^2}\frac{D\varepsilon_T}{Dt} \\
&= \frac{1}{\varepsilon_T}(P_k - \varepsilon_P + \varepsilon_P - \varepsilon_T) - \frac{k}{\varepsilon_T^2}(C_{T1}\frac{\varepsilon_P\varepsilon_T}{k_T} - C_{T2}\frac{\varepsilon_T^2}{k_T}) \\
&= \frac{1}{\varepsilon_T}\left[P_k - \varepsilon_T - C_{T1}(k_P+k_T)\frac{\varepsilon_P}{k_T} + C_{T2}(k_P+k_T)\frac{\varepsilon_T}{k_T}\right] \\
&= \frac{P_k}{\varepsilon_T} - 1 + \left(C_{T2} - C_{T1}\frac{\varepsilon_P}{\varepsilon_T}\right)\left(\frac{k_P}{k_T}+1\right) \\
\Rightarrow &\frac{k_P}{k_T} = \frac{\frac{P_k}{\varepsilon_T}-1}{C_{T1}\frac{\varepsilon_P}{\varepsilon_T} - C_{T2}} - 1 \qquad \text{but from equation 6.8,} \qquad C_{T1}\frac{\varepsilon_P}{\varepsilon_T} - C_{T2} = \frac{\varepsilon_P}{\varepsilon_T} - 1 \\
\Rightarrow &\left(\frac{k_P}{k_T}\right)_{SF} = \left(\frac{\frac{P_k}{\varepsilon_T} - \frac{\varepsilon_P}{\varepsilon_T}}{\frac{\varepsilon_P}{\varepsilon_T} - 1}\right)_{SF}
\end{aligned} \tag{6.9}
$$

$$
\begin{aligned}
0 &= \frac{1}{\varepsilon_P}\frac{Dk_P}{Dt} - \frac{k_P}{\varepsilon_P^2}\frac{D\varepsilon_P}{Dt} \\
&= \frac{1}{\varepsilon_P}(P_k - \varepsilon_P) - \frac{k_P}{\varepsilon_P^2}\left[C_{P1}P_k\frac{\varepsilon_P}{k_P} - C_{P2}\frac{\varepsilon_P^2}{k_P} + \frac{C'_{P1}}{c_\mu}\frac{k_P}{k}P_k\frac{\varepsilon_P}{k_P}\right] \\
&= \frac{P_k}{\varepsilon_P} - 1 - \left[C_{P1} + \frac{C'_{P1}}{c_\mu}\frac{k_P}{k}\right]\frac{P_k}{\varepsilon_P} + C_{P2} \\
&= \left[1 - C_{P1} - \frac{C'_{P1}}{c_\mu}\right]\frac{P_k}{\varepsilon_P} - (1-C_{P2}) \\
\Rightarrow &\left(\frac{P_k}{\varepsilon_P}\right)_{SF} = \left[\frac{1-C_{P2}}{1-\left(C_{P1} + \frac{C'_{P1}}{c_\mu}\frac{k_P}{k}\right)}\right]_{SF}
\end{aligned} \tag{6.10}
$$

Now, one should substitute the coefficients values into equations 6.8, 6.9 and 6.10 in order to arrive at the asymptotic values the TS model predicts for each ratio.

Starting with equation 6.8, one may notice, from Table 3.19, that the coefficient $C_{T2} = 1.15$ is a constant while $C_{T1} = 1.08\frac{\varepsilon_P}{\varepsilon_T}$ is a function of the ratio $\frac{\varepsilon_P}{\varepsilon_T}$. Equation 6.8 thus becomes a second order equation for $\frac{\varepsilon_P}{\varepsilon_T}$ which provides two solutions: $\frac{\varepsilon_P}{\varepsilon_T} = 1.0573$ or $\frac{\varepsilon_P}{\varepsilon_T} = -0.1313$. The latter solution should not be considered since the ratio $\frac{\varepsilon_P}{\varepsilon_T}$ must be positive. One may

check in Figures 6.1 and 6.2 that the value of 1.0573 for $\frac{\varepsilon_P}{\varepsilon_T}$ is reasonably close to that obtained in the computations.

One may now look at equations 6.9 and 6.10. One may substitute the former into the latter, considering that $\frac{k_P}{k} = (1 + \frac{k_T}{k_P})^{-1}$, in order to remain with only one unknown, $\frac{P_k}{\varepsilon_T}$. By substituting the coefficients values from Table 3.19, taking into account that the coefficient C_{P2} depends on the ratio $\frac{k_P}{k_T}$, and using the previous calculated results for $\frac{\varepsilon_P}{\varepsilon_T} = 1.0573$, after some algebraic manipulation, one arrives again at a second order equation for $\frac{P_k}{\varepsilon_T}$ which can be solved to give: $\frac{P_k}{\varepsilon_T} = 1.0698$ or $\frac{P_k}{\varepsilon_T} = -20.7076$. Again, the latter must be discarded since $\frac{P_k}{\varepsilon_T}$ must be positive and the former implies, from equation 6.9, that $\frac{k_P}{k_T} = 0.2186$.

One may notice though, that this asymptotic value for $\frac{k_P}{k_T}$ was not observed in Figures 6.1 and 6.2 and neither was the asymptotic value of $\frac{P_k}{\varepsilon_T}$ observed in Figures 5.8(c), 5.23(c) and 5.32(c). Instead, the ratio of $\frac{k_P}{k_T}$ increases exponentially and $\frac{P_k}{\varepsilon_T}$ provides a sudden growth profile which ends up not tending to an asymptotic value. Besides that, one may also notice that the asymptotic value estimated for $\frac{P_k}{\varepsilon_T}$, 1.0698, is far lower than the asymptotic value provided by DNS calculations as shown in Figures 5.8(c), 5.23(c) and 5.32(c).

The reason for this behaviour was attributed to the C'_{P1} term in equation 3.45 which makes the calculation of the asymptotic values of $\frac{k_P}{k_T}$ and $\frac{P_k}{\varepsilon_T}$ in equations 6.9 and 6.10 less straightforward.

An attempt to verify this hypothesis consisted of incorporating the C'_{P1} term into the C_{P1} term, assuming $\frac{k_P}{k}$ to take the value of $\frac{2}{3}$, thus $C_{P1_{new}} = C_{P1_{original}} + \frac{C'_{P1}}{c_\mu}\frac{k_P}{k} = 2.2 - \frac{0.11}{0.09}\frac{2}{3} = 1.3852$. Therefore, the C'_{P1} term was eliminated and the C_{P1} term became 1.3852. In this new configuration, the asymptotic analysis gives the value for $\frac{k_P}{k_T}$ to be 8.24 and for $\frac{P_k}{\varepsilon_T}$, 1.55. It is of value to mention though, that the elimination of the C'_{P1} term could not avoid a second order equation in $\frac{P_k}{\varepsilon_T}$ to find its asymptotic value, since the C_{P2} term remained as a function of $\frac{k_P}{k_T}$ and again, the negative solution value was discarded.

Figure 6.9 shows computed results of $\frac{k_P}{k_T}$ in the homogeneous shear flows using the above modified C_{P1} and C'_{P1} values for the W2, HM1 and HM2 cases, respectively representing the low, moderate and high shear flow cases. One may notice that the exponential growth of $\frac{k_P}{k_T}$ was eliminated by this modification, $\frac{k_P}{k_T}$ now being consistent with the asymptotic value of 8.24. In Figure 6.9 one may also notice that now the modified TS model started to approach the value predicted by the asymptotic analysis for the $\frac{P_k}{\varepsilon_T}$ ratio which was not happening before. These results thus confirm the hypothesis that the C'_{P1} term was responsible for the sudden growth behaviours of the TS model in the homogeneous shear flows.

Other MTS LEV models

The same procedure described above was carried out for the other three MTS LEV models which are being evaluated in this work, the CG, the KC and the NG models.

It is important to mention that the KC model also resulted in quadratic asymptotic equations for $\frac{\varepsilon_P}{\varepsilon_T}$ and $\frac{P_k}{\varepsilon_T}$ and the negative solutions were discarded.

Asymptotic analysis for the NG model was more straightforward since all coefficients are

constants and the final asymptotic equations are the same as those presented for the TS model, but with no C'_{P1} term.

On the other hand, the CG model presented a few problems to calculate the asymptotic values of the ratios $\frac{\varepsilon_P}{\varepsilon_T}$, $\frac{k_P}{k_T}$ and $\frac{P_k}{\varepsilon_T}$. The vorticity terms in equations 3.53 and 3.54 reduce to a form which has $\frac{dU}{dy}$ which does not allow one to express it as a function of $\frac{P_k}{\varepsilon_T}$. That makes the analysis more complicated since another asymptotic state must be found for an expression such as $\frac{k}{\varepsilon_P}\frac{dU}{dy}$. A system of four equations and four unknowns ($\frac{\varepsilon_P}{\varepsilon_T}$, $\frac{P_k}{\varepsilon_T}$, $\frac{P_k}{\varepsilon_T}$ and $\frac{k}{\varepsilon_P}\frac{dU}{dy}$) was derived, but no real solution (with no complex numbers) could be found. That is indeed in agreement with Figures 5.8(c), 5.23(c) and 5.32(c) where one can see that the ratio $\frac{P_k}{\varepsilon_T}$ does not approach an asymptotic value. Nonetheless, $\frac{\varepsilon_P}{\varepsilon_T}$ and $\frac{k_P}{k_T}$ do seem to tend to an asymptotic value in Figures 6.1 and 6.2. This is consistent with the fact that this model did not exhibit any stability problems, in contrast to the behaviour of the TS model.

It is actually interesting to note the similarities between the extra terms proposed by the CG and the TS models. The vorticity term in the CG model is $W = \sqrt{\left(\frac{dU_i}{dx_j} - \frac{dU_j}{dx_i}\right)^2}$ and the term $\frac{\partial U_l}{\partial x_m}\frac{\partial U_i}{\partial x_j}\epsilon_{lmk}\epsilon_{ijk}$ in the TS model can be shown to be $\frac{1}{2}\left(\frac{dU_i}{dx_j} - \frac{dU_j}{dx_i}\right)^2$. It is interesting then that the term in the TS model is actually a vorticity term and these terms seem to be preventing the CG and TS models from reaching an asymptotic state for $\frac{P_k}{\varepsilon_T}$ in homogeneous shear flows.

The asymptotic states for each model considered so far (except the CG model due to the above reasons) are summarized in Table 6.1. One may also note in Figures 6.1, 6.2, 5.8(c), 5.23(c) and 5.32(c) that the predicted values for the KC and NG models are consistent with the outcomes of the asymptotic analysis.

It is also of interest to draw attention to the predicted asymptotic values of the ratio $\frac{P_k}{\varepsilon_T}$, since DNS data suggests this ratio to be around 2, as presented in Figures 5.8(c), 5.23(c) and 5.32(c). As already commented on before, the original TS model provides a too low value which is not in agreement with DNS. From these figures and Table 6.1 one may indeed notice that the NG model provides the most reasonable result which is actually closer to the one predicted by the STS models, the CG tending to a too high value and the KC to a still rather low value.

Table 6.1: Asymptotic state predicted by each MTS LEV model for the homogeneous shear flow.

Model	$\frac{\varepsilon_P}{\varepsilon_T}$	$\frac{P_k}{\varepsilon_T}$	$\frac{k_P}{k_T}$
TS	1.0573	1.0698	0.2186
KC	1.1012	1.5086	4.0258
CG	-	-	-
NG	1.3000	1.8000	1.6667
TS modified	1.0573	1.5454	8.5206

6.1.4 Decaying Grid Turbulence Flow Asymptotic Analysis

After studying the homogeneous shear flow cases, one may study a decaying grid turbulence flow. This flow has also been studied in MTS models by Hanjalic et al. (1980), Nagano et al. (1997), Stawiarski and Hanjalic (2002), Cadiou et al. (2004) and Stawiarski and Hanjalic (2005).

Decaying grid turbulence is set up by generating turbulence by, for example, making an equilibrium flow pass through a grid and then letting it develop, which means indeed to let it decay since no production mechanism will be present in the flow and only dissipation will act, up to the point the flow reaches a new equilibrium state.

This is perhaps the simplest flow one could consider and it is usually used to define the C_{ε_2} coefficient in the ε equation in STS models and can be used to determine C_{P2} in the ε_P equation as will be shown below. Besides that, the TS model was developed taking into account this flow and thus its features will be discussed here.

The asymptotic analysis of this flow involves the assumption that diffusion terms can be neglected as well as production. This analysis will again be carried out in detail for the TS model, and the asymptotic results for the other LEV MTS models will then be presented for the sake of comparison.

TS model

Applying the TS model for the decaying grid turbulence flow case, one can reduce equations 3.43, 3.44, 3.45 and 3.46 to:

$$\frac{Dk_P}{Dt} = -\varepsilon_P \tag{6.11}$$

$$\frac{Dk_T}{Dt} = \varepsilon_P - \varepsilon_T \tag{6.12}$$

$$\frac{D\varepsilon_P}{Dt} = -C_{P2}\frac{\varepsilon_P^2}{k_P} \tag{6.13}$$

$$\frac{D\varepsilon_T}{Dt} = C_{T1}\frac{\varepsilon_P\varepsilon_T}{k_T} - C_{T2}\frac{\varepsilon_T^2}{k_T} \tag{6.14}$$

From experiments, one knows that the evolution (or decay) of k with time is proportional to t^{-n}. According to Hanjalic et al. (1980), there are many reported values for n in the literature, but $n = 1.25$ would be a reasonable estimate and that is how it will be dealt here too.

Assuming that the ratio $\frac{k_P}{k_T}$ becomes constant during the decay process, as did Hanjalic et al. (1980), one may say that both k_P and k_T decay proportionally to t^{-n}. Substituting this into equations 6.11 and 6.13, one concludes that the C_{P2} coefficient in the decaying grid turbulence flow (indicated in subscripts by DF) should be $C_{P2_{DF}} = \frac{n+1}{n}$. By considering $n = 1.25$, that implies $C_{P2_{DF}} = 1.8$.

From the above assumption, one may also conclude that the substantial derivatives of the ratios $\frac{k_P}{k_T}$ and $\frac{\varepsilon_P}{\varepsilon_T}$ should be zero since these quantities reach constant values. The same procedure as that carried out in the homogeneous shear flow analysis could then be repeated here:

$$\begin{aligned}
0 &= \frac{D}{Dt}\left(\frac{\varepsilon_P}{\varepsilon_T}\right) \\
&= \frac{1}{\varepsilon_T}\frac{D\varepsilon_P}{Dt} - \frac{\varepsilon_P}{\varepsilon_T^2}\frac{D\varepsilon_T}{Dt} \\
&= \frac{1}{\varepsilon_T}\left[-C_{P2}\frac{\varepsilon_P^2}{k_P}\right] - \frac{\varepsilon_P}{\varepsilon_T^2}\left[C_{T1}\frac{\varepsilon_P\varepsilon_T}{k_T} - C_{T2}\frac{\varepsilon_T^2}{k_T}\right] \\
&= \frac{\varepsilon_P}{k_P}\left[-C_{P2}\frac{\varepsilon_P}{\varepsilon_T} - C_{T1}\frac{\varepsilon_P}{\varepsilon_T}\frac{k_P}{k_T} + C_{T2}\frac{k_P}{k_T}\right] \\
&\Rightarrow \frac{\varepsilon_P}{\varepsilon_T}\left(C_{P2} + C_{T1}\frac{k_P}{k_T}\right) = C_{T2}\frac{k_P}{k_T} \\
&\Rightarrow \left(\frac{\varepsilon_P}{\varepsilon_T}\right)_{DF} = \frac{C_{T2}\frac{k_P}{k_T}}{C_{P2} + C_{T1}\frac{k_P}{k_T}}
\end{aligned} \tag{6.15}$$

$$\begin{aligned}
0 &= \frac{D}{Dt}\left(\frac{k_P}{k_T}\right) \\
&= \frac{1}{k_T}\frac{Dk_P}{Dt} - \frac{k_P}{k_T^2}\frac{Dk_T}{Dt} \\
&= -\frac{\varepsilon_T}{k_T} - \frac{k_P}{k_T^2}(\varepsilon_P - \varepsilon_T) \\
&= \frac{\varepsilon_T}{k_T}\left[-\frac{\varepsilon_P}{\varepsilon_T} - \frac{k_P}{k_T}\left(\frac{\varepsilon_P}{\varepsilon_T} - 1\right)\right] \\
&\Rightarrow \left(\frac{k_P}{k_T}\right)_{DF} = \frac{\frac{\varepsilon_P}{\varepsilon_T}}{1 - \frac{\varepsilon_P}{\varepsilon_T}}
\end{aligned} \tag{6.16}$$

By solving the system formed by equations 6.15 and 6.16, one arrives at expressions for $\frac{k_P}{k_T}$ and $\frac{\varepsilon_P}{\varepsilon_T}$ as a function of the model's coefficients:

$$\left(\frac{k_P}{k_T}\right)_{DF} = \left(\frac{C_{P2} - C_{T2}}{C_{T2} - C_{T1}}\right)_{DF} \tag{6.17}$$

$$\left(\frac{\varepsilon_P}{\varepsilon_T}\right)_{DF} = \left(\frac{C_{T2} - C_{P2}}{C_{T1} - C_{P2}}\right)_{DF} \tag{6.18}$$

The latter equations can also be obtained by solving equations 6.12 and 6.14 within the assumptions already discussed.

Now, by looking at the TS model coefficients in Table 3.19, one may solve the system formed by equations 6.17 and 6.18 to find the constant values the ratios $\frac{k_P}{k_T}$ and $\frac{\varepsilon_P}{\varepsilon_T}$ are expected to take when the asymptotic state of the decaying grid turbulence flow is reached.

The solution of the mentioned system provides: $\left(\frac{k_P}{k_T}\right)_{DF_{TS}} = 1.08$ and $\left(\frac{\varepsilon_P}{\varepsilon_T}\right)_{DF_{TS}} = 0.52$.

One may then identify here a slight inconsistency in the TS model. In decaying grid turbulence $C_{P2} = 1.8 + 0.3(\frac{k_P}{k_T} - 1)/(\frac{k_P}{k_T} + 1)$ should take the value of 1.8 which is achieved because $\left(\frac{k_P}{k_T}\right)_{DF_{TS}} = 1.0$. That would then imply $\left(\frac{\varepsilon_P}{\varepsilon_T}\right)_{DF_{TS}} = 0.5$, which is slightly different then the values just calculated. This minor inconsistency will be addressed through further developments introduced later in this chapter.

Other MTS models

The same procedure described above can be applied to the other three LEV MTS models and thereby their expected constant values for $\left(\frac{k_P}{k_T}\right)_{DF}$ and $\left(\frac{\varepsilon_P}{\varepsilon_T}\right)_{DF}$ are presented in Table 6.2, together with the results for the TS model in order to make them comparable.

It may be noted from Table 6.2 that $\left(\frac{\varepsilon_P}{\varepsilon_T}\right)_{DF}$ is a value smaller than one as expected from equation 6.16. One may also notice that the NG model predicts the same value for $\frac{k_P}{k_T}$ in both homogeneous shear and decaying grid turbulence flows. This is inconsistent because one would expect $\left(\frac{k_P}{k_T}\right)_{SF} > \left(\frac{k_P}{k_T}\right)_{DF}$ since in decaying grid turbulence there is no turbulent kinetic energy production. As these two ratios characterize the turbulent kinetic energy spectrum, one may notice how different the tested MTS models predict the spectrum to be.

Table 6.2: Asymptotic state predicted by each MTS model for the decaying grid turbulence flow

Model	$\frac{\varepsilon_P}{\varepsilon_T}$	$\frac{k_P}{k_T}$
TS	0.52	1.08
KC	0.407	0.687
CG	0.83	4.84
NG	0.625	1.667

6.1.5 Transport Equations for the First Versions of the NT1 and NT2 models

In this section the main conclusions about the asymptotic analysis of the homogeneous shear flow cases and the decaying grid turbulence will be presented. They resulted in some modifications to the original TS model which will then be used as a base for the developed NT1 and NT2 models.

From the homogeneous shear flow analysis one could identify that the term associated with C'_{P1} was responsible for some instabilities of the TS model, besides providing unreasonable asymptotic ratios for $\frac{P_k}{\varepsilon_T}$, which is expected to be around 2. Therefore it was decided to remove this term.

From the decaying grid turbulence, one could identify that the coefficients C_{P2}, C_{T1} and/or C_{T2} needed some small adjustments in order to attain correctly the physical constraints of this flow and the assumptions of the model. Therefore one should bear in mind the necessity of further adjustment of these coefficients.

At this point, working towards the development of an improved MTS model, one may summarize the transport equations which will be considered for the first version of the models as:

$$\frac{Dk_P}{Dt} = P_k - \varepsilon_P + \frac{\partial}{\partial x_j}\left[\left(\nu + \frac{\nu_t}{\sigma_{k_P}}\right)\frac{\partial k_P}{\partial x_j}\right] \tag{6.19}$$

$$\frac{Dk_T}{Dt} = \varepsilon_P - \varepsilon_T + \frac{\partial}{\partial x_j}\left[\left(\nu + \frac{\nu_t}{\sigma_{k_T}}\right)\frac{\partial k_T}{\partial x_j}\right] \tag{6.20}$$

$$\frac{D\varepsilon_P}{Dt} = C_{P1}P_k\frac{\varepsilon_P}{k_P} - C_{P2}\frac{\varepsilon_P^2}{k_P} + \frac{\partial}{\partial x_j}\left[\left(\nu + \frac{\nu_t}{\sigma_{\varepsilon_P}}\right)\frac{\partial \varepsilon_P}{\partial x_j}\right] \tag{6.21}$$

$$\frac{D\varepsilon_T}{Dt} = C_{T1}\frac{\varepsilon_P\varepsilon_T}{k_T} - C_{T2}\frac{\varepsilon_T^2}{k_T} + \frac{\partial}{\partial x_j}\left[\left(\nu + \frac{\nu_t}{\sigma_{\varepsilon_T}}\right)\frac{\partial \varepsilon_T}{\partial x_j}\right] \tag{6.22}$$

One may notice in the above equations that the only significant difference between them and the transport equations in the original TS model is the removal of the C'_{P1} term. The turbulent Prandtl numbers σ_{k_P}, σ_{k_T}, σ_{ε_P} and σ_{ε_T} were also introduced in order to use the conventional LEV approaches for the diffusion terms and improve the flexibility of the model in terms of modelling the coefficients. One may notice though, that if $\sigma_{k_P} = \sigma_{k_T} = \sigma_{\varepsilon_P} = \sigma_{\varepsilon_T} = 1$ and the ν_t expression used in the TS model is kept, one remains with the same diffusion terms as these used in the latter.

6.1.6 Fully Turbulent Local Equilibrium Boundary Layer

The next step in the development of an improved MTS model is to test this version for flow in a turbulent boundary layer in local equilibrium. This flow consists of a basic case which turbulence modellers often use as a test to assure the correct behaviour of the velocity (i.e. to follow the log law of the wall) in simple flows such as channel flows and zero pressure gradient boundary layers.

Asymptotic analysis for local equilibrium boundary layers have also been studied in MTS models by Kim and Chen (1989), Nagano et al. (1997), Stawiarski and Hanjalic (2002), Cadiou et al. (2004) and Stawiarski and Hanjalic (2005), among others. These studies were also extended here.

Particular features of this flow are that convection can be neglected and the generation rate of turbulent kinetic energy P_k is equal to the turbulent kinetic energy dissipation rate. In STS models, one would write $P_k = \varepsilon$; in MTS models, one can write $P_k = \varepsilon_P = \varepsilon_T$, since the equilibrium state implies that $\varepsilon_P = \varepsilon_T$. Therefore, one may write $\left(\frac{\varepsilon_P}{\varepsilon_T}\right)_{BL} = 1$, where the subscript BL indicates the asymptotic state in local equilibrium boundary layers.

The asymptotic analysis of a local equilibrium boundary layer thus consists of applying the above mentioned considerations in the transport equations of the turbulent quantities and rewriting them as a function of the wall variables in an attempt to cancel out terms and arrive at a relation between the model's coefficients.

In order to implement the asymptotic analysis of the local equilibrium boundary layer, one should consider the following relations which are valid for this flow:

$$\frac{dU}{dy} = \frac{u_\tau}{\kappa y} \qquad \text{and} \qquad -\overline{uv} = \frac{\tau_w}{\rho} = u_\tau^2 \tag{6.23}$$

The first follows from the logarithmic velocity profile whilst the second comes from the results that the shear stress is constant across such a boundary layer. From the above relations, one may write:

$$P_k = \varepsilon_P = \varepsilon_T = -\overline{uv}\frac{dU}{dy} = \frac{u_\tau^3}{\kappa y} \tag{6.24}$$

$$\nu_t = \frac{-\overline{uv}}{dU/dy} = u_\tau \kappa y \tag{6.25}$$

The asymptotic analysis of the local equilibrium boundary layer will be carried out for the transport equations presented in the previous section, represented by equations 6.19, 6.20, 6.21 and 6.22, since at this stage one is no longer evaluating the tested LEV MTS models, but constructing the basis of an improved MTS model. Hence, applying the above relations (equations 6.23, 6.24 and 6.25) and the simplifications inherent to this flow case, discussed above, into equations 6.21 and 6.22 provides:

$$k_P = \frac{u_\tau^2 \sigma_{\varepsilon_P}}{\kappa^2}(C_{P2} - C_{P1}) \tag{6.26}$$

$$k_T = \frac{u_\tau^2 \sigma_{\varepsilon_T}}{\kappa^2}(C_{T2} - C_{T1}) \tag{6.27}$$

It is easy to see that dividing equation 6.26 by equation 6.27 provides the asymptotic value that $\frac{k_P}{k_T}$ is expected to reach in local equilibrium boundary layers:

$$\left(\frac{k_P}{k_T}\right)_{BL} = \left[\frac{\sigma_{\varepsilon_P}}{\sigma_{\varepsilon_T}}\frac{(C_{P2} - C_{P1})}{(C_{T2} - C_{T1})}\right]_{BL} \tag{6.28}$$

Now, one may observe that in order to arrive at a relation exclusively (without any flow variable) between the coefficients, one needs to find a way to eliminate u_τ, k_P and k_T in equations 6.26 and 6.27. Since substituting the relations of equations 6.24 and 6.25 into equations 6.19 and 6.20 leads nowhere, because the production and sink terms cancel out and one is simply left with diffusion of k_P and k_T equal to zero, the alternative is to look at $\overline{uv}$ again. Considering the original proposition of the TS model for ν_t and applying the relations expressed in equations 6.23 and 6.24, one may find an expression for u_τ^2:

$$-\overline{uv} = c_\mu \frac{k k_P}{\varepsilon_P}\frac{dU}{dy} = u_\tau^2 \Rightarrow u_\tau^4 = c_\mu k k_P \Rightarrow u_\tau^2 = c_\mu^{1/2} k^{1/2} k_P^{1/2} \tag{6.29}$$

By substituting the above equation into equations 6.26 and 6.27, one may find:

$$\left(\frac{k_P}{k}\right)_{BL} = \left[\frac{c_\mu \sigma_{\varepsilon_P}^2}{\kappa^4}(C_{P2} - C_{P1})^2\right]_{BL} \tag{6.30}$$

$$\left(\frac{k_T}{k}\right)_{BL} = \left[\frac{c_\mu \sigma_{\varepsilon_P}\sigma_{\varepsilon_T}}{\kappa^4}(C_{P2} - C_{P1})(C_{T2} - C_{T1})\right]_{BL} \tag{6.31}$$

One can thus finally find a relation between the coefficients, since $\frac{k_P}{k} + \frac{k_T}{k} = 1$. Hence, by summing equations 6.26 and 6.27 one arrives at:

$$\{(C_{P2} - C_{P1})[\sigma_{\varepsilon_P}(C_{P2} - C_{P1}) + \sigma_{\varepsilon_T}(C_{T2} - C_{T1})]\}_{BL} = \left(\frac{\kappa^4}{c_\mu \sigma_{\varepsilon_P}}\right)_{BL} \tag{6.32}$$

One may notice though that the C_{P2} and C_{T1} coefficients may be functions of $\frac{k_P}{k_T}$ and $\frac{\varepsilon_P}{\varepsilon_T}$ and therefore, as indicated in the above equation 6.32, the value of these ratios must be taken at the local equilibrium state. Moreover, the value of the eddy viscosity coefficient c_μ must also be considered in this state. When one is considering STS models, the value of c_μ in the local equilibrium boundary layer is known to be around 0.09. This value comes from the following analysis:

$$P_k = -\overline{uv}\frac{dU}{dy} = \varepsilon \Rightarrow -\overline{uv} = \underbrace{\left(\frac{\overline{uv}}{k}\right)^2}_{c_\mu}\frac{k^2}{\varepsilon}\frac{dU}{dy} \Rightarrow \underbrace{\left(\frac{\overline{uv}}{k}\right)^2}_{c_\mu}\underbrace{\frac{k}{\varepsilon}\frac{dU}{dy}}_{\approx 3.3} = \underbrace{-\frac{\overline{uv}}{k}}_{\approx 0.3}$$

$$\Rightarrow c_\mu \approx 0.09 \tag{6.33}$$

One can notice from the above that the equality $P_k = \varepsilon$ can be rearranged in order to express $\overline{uv}$ in the form $-\overline{uv} = c_\mu \frac{k^2}{\varepsilon}\frac{dU}{dy}$, from where one concludes that $c_\mu = \left(\frac{\overline{uv}}{k}\right)^2$. From experimental results, it is well known that the dimensionless shear $\eta = \frac{k}{\varepsilon}\frac{dU}{dy}$ reaches a value around 3.3 and that the ratio $\frac{-\overline{uv}}{k}$ reaches a value around 0.3 which implies that c_μ should be given a value of around 0.09.

From the above result, one may thus develop the expression for $\overline{uv}$, considering $\nu_t = c_\mu \frac{k k_P}{\varepsilon_P}$, in order to identify what should be the value of c_μ in the local equilibrium boundary layer when predicted by this MTS model:

$$-\overline{uv} = c_\mu \frac{k k_P}{\varepsilon_P}\frac{dU}{dy} \Rightarrow -\frac{\overline{uv}}{k} = c_\mu \underbrace{\frac{k_P}{\varepsilon_P}}_{=\varepsilon_T}\frac{dU}{dy} \Rightarrow \underbrace{-\frac{\overline{uv}}{k}}_{\approx 0.3} = c_\mu \frac{k_P}{k}\underbrace{\frac{k}{\varepsilon_T}\frac{dU}{dy}}_{\approx 3.3}$$

$$\Rightarrow c_\mu \left(\frac{k_P}{k}\right)_{BL} \approx 0.09 \tag{6.34}$$

One may notice that the value of c_μ when $\nu_t = c_\mu \frac{k k_P}{\varepsilon_P}$ must be higher than 0.09, the value it would assume if $\nu_t = c_\mu \frac{k^2}{\varepsilon_T}$, since $\frac{k_P}{k}$ is necessarily smaller than one. One may then substitute equation 6.30 into the above equation and arrive at:

$$\left[\frac{c_\mu \sigma_{\varepsilon_P}}{\kappa^2}(C_{P2} - C_{P1})\right]_{BL} = \sqrt{0.09} \tag{6.35}$$

That concludes this section where one could say the basis for deriving some of the coefficient values for the improved MTS model has been established.

6.1.7 c_μ as a function of η

Before final adjustment of the coefficients of the proposed model, one may look again at the homogeneous shear flow cases and observe that the performance of the models does vary as a function of the dimensionless shear ($\eta = \frac{k}{\varepsilon}\frac{dU}{dy}$). For eddy viscosity formulations, that makes one think of c_μ varying as a function of η. Also considering this flow, Craft et al. (1996b) proposed $c_\mu = \frac{0.3}{1+0.35\eta^{1.5}} f_{rs}$ where $f_{rs} = 1 - \exp\left[\frac{-0.36}{\exp(-0.75\eta)}\right]$ in order to reduce the predicted value of $\frac{\overline{uv}}{k}$ at high shear rates. The f_{rs} function will be effective only for very low shear values which are not encountered in the present homogeneous shear flow cases. Therefore, in this work, it was decided to start testing a general expression for c_μ of the form $c_\mu = \frac{a}{b+\eta^c}$.

It was also questioned, since one is working with MTS models and instead of k and ε one has k_P, k_T, ε_P and ε_T, if the more appropriate expression to take for η would be $\frac{k}{\varepsilon_T}\frac{dU}{dy}$ or $\frac{k_P}{\varepsilon_P}\frac{dU}{dy}$. However, some tests were performed and indicated that if $\eta = \frac{k_P}{\varepsilon_P}\frac{dU}{dy}$, the exponent of η in the c_μ expression, c, would have to be near 2, a relatively high value which could cause some instabilities for other flow cases as found by Craft et al. (1999).

It was also noticed that in order to obtain good predictions over the entire η range which has been tested, $\approx 1 < \eta < 30$, one would need two sets of values for the c_μ coefficients a, b and c, one for the low and moderate shear cases and the other for the high shear ones. It was then identified that a better expression for c_μ would be:

$$c_\mu = c_1 + c_2 \exp(-c_3 \eta) \tag{6.36}$$

6.1.8 Development of the First Version of the NT1 model

The development of the NT1 model thus consisted of determining the set of coefficients of the model. As an LEV model, the Reynolds stresses would be calculated as $\overline{u_i u_j} = -\nu_t\left(\frac{dU_i}{dx_j} + \frac{dU_j}{dx_i}\right) + \frac{2}{3}k\delta_{ij}$, ν_t was here kept as $\nu_t = c_\mu \frac{k k_P}{\varepsilon_P}$ and c_μ would be given by equation 6.36 with $\eta = \frac{k}{\varepsilon_T}\frac{dU}{dy}$. The transport equations for k_P, k_T, ε_P and ε_T are those presented in equations 6.19 to 6.22 and the coefficients' structure was kept as in the original TS model: C_{P1} and C_{T2} would be constants, $C_{T1} \equiv c_{t1}\frac{\varepsilon_P}{\varepsilon_T}$ and $C_{P2} \equiv c_{p21} - c_{p22}\left(\frac{k_P}{k_T} - 1\right)/\left(\frac{k_P}{k_T} + 1\right)$. It can be noted that c_{t1}, c_{p21} and c_{p22} were introduced to make the determination of the

model's coefficients easier and do not appear explicitly in the model's coefficients when their final forms are eventually presented.

In order to define the model's coefficients, a system of equations was built based on the asymptotic analyses carried out in the previous sections, together with some assumptions.

From the decaying grid turbulence flow, one has that C_{P2} should assume a value of 1.8. In order to match this, one could either keep $\left(\frac{k_P}{k_T}\right)_{DF}$ and $\left(\frac{\varepsilon_P}{\varepsilon_T}\right)_{DF}$ as unknowns or simply set $\left(\frac{k_P}{k_T}\right)_{DF} = 1$ which would imply, from equation 6.16, $\left(\frac{\varepsilon_P}{\varepsilon_T}\right)_{DF} = 0.5$ as proposed by Hanjalic et al. (1980) who argued that in decaying grid turbulence flows, an equal amount of energy would be stored by the large and small scales, implying $\left(\frac{k_P}{k_T}\right)_{DF} = 1$, and as this flow has no turbulence production, any other flow would have to predict k_P to be higher then k_T. This argument was accepted here and therefore, from equation 6.15, one may write:

$$\frac{1}{2} = \frac{C_{T2} - 1.8}{\frac{1}{2}c_{t1} - 1.8} \tag{6.37}$$

This equation assumes that $c_{p21} = 1.8$, $\left(\frac{k_P}{k_T}\right)_{DF} = 1$ and $\left(\frac{\varepsilon_P}{\varepsilon_T}\right)_{DF} = 0.5$. Therefore the above equation provides a relation between the coefficients c_{t1} and C_{T2}.

From the homogeneous shear flow analysis, one may notice that equation 6.8 also provides a relation between the C_{T1} and C_{T2} coefficients. By observing the behaviour of the MTS models when applied to homogeneous shear flows, Figures 6.1 and 6.2, one can infer that $\left(\frac{\varepsilon_P}{\varepsilon_T}\right)_{SF}$ tends to be around unity. However, from equation 6.9, one may notice that it could not be exactly 1.0 since that would imply a singularity, giving $\left(\frac{k_P}{k_T}\right)_{SF}$ infinite. Nonetheless, one could say a reasonable value for $\left(\frac{\varepsilon_P}{\varepsilon_T}\right)_{SF}$ would be between 1.01 and 1.4, which would imply $C_{T2} - c_{t1}$ being between 0.01 and 0.33. That would then allow one to arrive at values for the coefficients C_{T1} and C_{T2}.

Another relation which can be inferred from the homogeneous shear flow cases is the asymptotic value of $\left(\frac{P_k}{\varepsilon_T}\right)_{SF}$ which, from the cases studied and presented in Figures 5.8(c), 5.23(c) and5.32(c), is expected to reach a value of around 1.9 as also predicted by the STS models.

One may notice though that, since the C'_{P1} term no longer exists in the new model, equation 6.10 becomes:

$$\left(\frac{P_k}{\varepsilon_P}\right)_{SF} = \left(\frac{1 - C_{P2}}{1 - C_{P1}}\right)_{SF} \tag{6.38}$$

The asymptotic value of $\left(\frac{P_k}{\varepsilon_T}\right)_{SF}$ can thus be easily found by combining equations 6.38 and 6.8 which then provide the following relation between the coefficients:

$$\left(\frac{P_k}{\varepsilon_T}\right)_{SF} = \left(\frac{P_k}{\varepsilon_P}\right)_{SF}\left(\frac{\varepsilon_P}{\varepsilon_T}\right)_{SF} = 1.9 = \frac{\left[1 - c_{p21} + c_{p22}\frac{\left(\frac{k_P}{k_T}\right)_{SF} - 1}{\left(\frac{k_P}{k_T}\right)_{SF} + 1}\right]\left(1 - C_{T2}\right)}{\left(1 - C_{P1}\right)\left[1 - c_{t1}\left(\frac{\varepsilon_P}{\varepsilon_T}\right)_{SF}\right]} \tag{6.39}$$

One may notice that in the above equation, $\left(\frac{\varepsilon_P}{\varepsilon_T}\right)_{SF}$ and $\left(\frac{k_P}{k_T}\right)_{SF}$ are known. The former is first calculated from equation 6.8, since C_{T1} and C_{T2} have already been defined as discussed above, and the latter can then be calculated from equation 6.9. One may notice then that at this point one has two unknowns, c_{p22} and C_{P1}, and only one equation, equation 6.39.

One should look now at the asymptotic analysis developed for the local equilibrium boundary layer. A set of relations between the coefficients can then be obtained from equations 6.28, 6.32 and 6.35 which can be written making all variables explicit:

$$\left(\frac{k_p}{k_t}\right)_{BL} = \frac{\sigma_{\varepsilon p}}{\sigma_{\varepsilon t}} \frac{\left(c_{p21} - c_{p22}\frac{\left(\frac{k_P}{k_T}\right)_{BL}-1}{\left(\frac{k_P}{k_T}\right)_{BL}+1} - C_{P1}\right)}{(C_{T2}-c_{t1})} \tag{6.40}$$

$$\left(c_{p21}-c_{p22}\frac{\left(\frac{k_P}{k_T}\right)_{BL}-1}{\left(\frac{k_P}{k_T}\right)_{BL}+1}-C_{P1}\right)\left[\sigma_{\varepsilon p}\left(c_{p21}-c_{p22}\frac{\left(\frac{k_P}{k_T}\right)_{BL}-1}{\left(\frac{k_P}{k_T}\right)_{BL}+1}-C_{P1}\right)+\sigma_{\varepsilon t}(C_{T2}-c_{t1})\right] = \frac{\kappa^4}{c_{\mu_{BL}}\sigma_{\varepsilon p}} \tag{6.41}$$

$$\frac{c_{\mu_{BL}}\sigma_{\varepsilon p}}{\kappa^2}\left(c_{p21} - c_{p22}\frac{\left(\frac{k_P}{k_T}\right)_{BL}-1}{\left(\frac{k_P}{k_T}\right)_{BL}+1} - C_{P1}\right) = \sqrt{0.09} \tag{6.42}$$

In the above equations, it is implicit that $\left(\frac{\varepsilon_P}{\varepsilon_T}\right)_{BL} = 1$ which implies $C_{T1} = c_{t1}\left(\frac{\varepsilon_P}{\varepsilon_T}\right)_{SF} = c_{t1}$.

Equations 6.39, 6.40, 6.41 and 6.42 thus form a system of four equations and six unknowns (C_{P1}, c_{p22}, $\left(\frac{k_p}{k_t}\right)_{BL}$, $c_{\mu_{BL}}$, σ_{ε_P} and σ_{ε_T}), besides the three coefficients in the c_μ expression presented in equation 6.36.

An optimization procedure was then carried out in order to determine the values of the coefficients which would provide the best fit of the homogeneous shear flows and satisfy all the relations related to the three cases whose asymptotic analysis was studied.

Since there are more variables then equations, there are also many ways of treating and optimizing this system. The way found here to provide the best results is thus described below.

A program was written in Matlab and a loop to vary $D = C_{T2} - c_{t1}$ from 0.01 to 2.0 by a 0.01 increment was initially built in order to define the value of the coefficients C_{T1} and C_{T2}. Inside this loop, a new loop for c_{p22} was built, making it vary from 0.1 to 1.4, by a 0.01 increment. C_{P1} would be then directly calculated from equation 6.39. Inside the c_{p22} loop, another loop was built to specify the value of σ_{ε_P} which was let to vary from 0.1 to 1.5 by a 0.1 increment and then, from solving the system composed of equations 6.40, 6.41 and 6.42, the values of $\left(\frac{k_p}{k_t}\right)_{BL}$, $c_{\mu_{BL}}$ and σ_{ε_T} were determined. Inside the σ_{ε_P} loop, a new loop varying c_2 from 0.2 to 0.4 by a 0.001 increment and within this, a new loop varying c_3 from 0.2 to 0.4 by a 0.001 increment were also built to determine the c_μ coefficients from equation 6.36. The c_1 coefficient was then calculated by $c_1 = c_{\mu_{BL}} - c_2\exp(-c_3 * 3.3)$ in order to guarantee that the $c_{\mu_{BL}}$ would be associated with $\eta \approx 3.3$ according to above discussions.

Inside the last loop the system formed by the transport equations for k_P, k_T, ε_P and ε_T

was then solved for the homogeneous shear flow cases since this is a rather simple differential equation system. The rms "error" would be then computed comparing the results provided by each set of coefficients and the DNS data. The set of coefficients which provided the smallest rms "error" would be then chosen. It is of value to mention that for some sets of coefficients the system of differential equations would not converge and then the intervals mentioned above to vary each of the coefficients had to be manually changed.

When a set of coefficients was then chosen, a channel flow test would be performed with it in the STREAM code. It was noticed that if σ_{ε_P} and σ_{ε_T} were too different from each other, the channel flows would not converge which could be explained by noticing that ε_P and ε_T would be diffusing at rather different rates, thus compromising convergence. Therefore, just after σ_{ε_T} was computed inside the loop, a check was inserted not to allow $|\sigma_{\varepsilon_P} - \sigma_{\varepsilon_T}| > 0.5$.

It is also of value to comment that σ_{k_P} and σ_{k_T} were not used for any asymptotic analysis and therefore both were set to unity as is usually done in LEV models ($\sigma_{k_P} = \sigma_{k_P} = 1.0$).

Another important issue which is worth commenting upon is that one could find a set of coefficients for c_μ in equation 6.36 which would provide very accurate results for the full range of η values in the homogeneous shear flows, including the lowest shears cases. However to match the latter, one would need to let c_μ assume relatively high values. That would cause instabilities and odd behaviours in wall-bounded flows, for example in the outer part of boundary layers, where only diffusion plays a role, and η can reach very low values, making c_μ become too large. In order to avoid this problem, it was decided to clip c_μ with the value it would reach in local equilibrium boundary layers.

The coefficients of the NT1 model are thus summarized in Table 6.3 and the asymptotic values this model is expected to provide in the three studied cases (homogeneous shear flow, decaying grid turbulence flow and local equilibrium boundary layer) are presented in Table 6.4 for later comparison with the NT2 and other MTS models.

Table 6.3: Coefficients of the first version of the NT1 model

c_μ	C_{P1}	C_{P2}	σ_{ε_P}	C_{T1}	C_{T2}	σ_{ε_T}
$min[0.1324, 0.0223 + 0.343e^{-0.341\eta}]$	1.2391	$1.8 - 0.5\frac{\frac{k_P}{k_T}-1}{\frac{k_P}{k_T}+1}$	1.0	$1.04\frac{\varepsilon_P}{\varepsilon_T}$	1.16	1.4945

Table 6.4: Values expected to be provided by the first version of the NT1 model in the asymptotic states studied

$\left(\frac{P_k}{\varepsilon_T}\right)_{SF}$	$\left(\frac{k_P}{k_T}\right)_{SF}$	$\left(\frac{\varepsilon_P}{\varepsilon_T}\right)_{SF}$	$\left(\frac{k_P}{k_T}\right)_{DF}$	$\left(\frac{\varepsilon_P}{\varepsilon_T}\right)_{DF}$	$\left(\frac{k_P}{k_T}\right)_{BL}$	$\left(\frac{\varepsilon_P}{\varepsilon_T}\right)_{BL}$	$c_{\mu_{BL}}$
1.9	7.8897	1.1012	1.0	0.5	2.1243	1.0	0.1324

6.1.9 Development of the First Version of the NT2 model

The NT2 model arose from the idea of testing a different expression for ν_t than the one proposed by Hanjalic et al. (1980) and adopted in the NT1 model. It was decided it would

be worth testing the conventional ν_t expression employed in single scale models to check if that could bring any kind of improvement.

The NT2 model thus consists of the same transport equations used for the NT1 model, equations 6.19, 6.20, 6.21 and 6.22 and the Reynolds stresses will also be calculated by $\overline{u_i u_j} = -\nu_t\left(\frac{dU_i}{dx_j} + \frac{dU_j}{dx_i}\right) + \frac{2}{3}k\delta_{ij}$, given this is also an LEV model, where $\nu_t = c_\mu \frac{k^2}{\varepsilon_T}$ and c_μ is given by the same general expression presented in equation 6.36. The coefficients will again be kept in the form proposed by Hanjalic et al. (1980) and one only needs to determine the new coefficients which satisfy all the asymptotic analysis constraints.

The asymptotic analyses carried out for the homogeneous shear flow and the decaying grid turbulence flow cases are not affected by this change in the ν_t expression. Therefore the way to determine c_{p21}, C_{T1} and C_{T2} remains the same. Equation 6.39 also remains unchanged.

However, setting $\nu_t = c_\mu \frac{k^2}{\varepsilon_T}$ does affect the asymptotic analysis of the local equilibrium boundary layer flows and therefore one must revise it. Equations 6.26 and 6.27 remain the same, which implies that equation 6.28 also remains the same, however the expression for u_τ^2 will change to:

$$-\overline{uv} = c_\mu \frac{k^2}{\varepsilon_T}\frac{dU}{dy} = u_\tau^2 \Rightarrow u_\tau^4 = c_\mu k^2 \Rightarrow u_\tau^2 = c_\mu^{1/2} k \tag{6.43}$$

Substituting then the above results into equations 6.26 and 6.27, one has respectively:

$$\frac{k_P}{k} = \frac{c_\mu^{1/2}\sigma_{\varepsilon_P}}{\kappa^2}(C_{P2} - C_{P1}) \tag{6.44}$$

$$\frac{k_T}{k} = \frac{c_\mu^{1/2}\sigma_{\varepsilon_T}}{\kappa^2}(C_{T2} - C_{T1}) \tag{6.45}$$

By summing the above equations and equating the result to 1, since $\frac{k_P}{k} + \frac{k_T}{k} = 1$, one finally arrives at a relation between the coefficients when $\nu_t = c_\mu \frac{k^2}{\varepsilon_T}$:

$$\sigma_{\varepsilon_P}(C_{P2} - C_{P1}) + \sigma_{\varepsilon_T}(C_{T2} - C_{T1}) = \frac{\kappa^2}{c_\mu^{1/2}} \tag{6.46}$$

One may notice that it is not necessary to calculate a value for $c_{\mu_{BL}}$ since it falls into the same analysis usually done for STS LEV models, described in equation 6.33, which then implies $c_{\mu_{BL}} = 0.09$. However, if on one hand this reduces by one the number of equations, on the other hand, the number of unknowns is also reduced by one since one has no longer to calculate $c_{\mu_{BL}}$.

The system of equations thus necessary to determine the coefficients of the NT2 model is formed by three equations (6.39, 6.28 and 6.46) and five unknowns (C_{P1}, c_{p22}, $\left(\frac{k_p}{k_t}\right)_{BL}$, σ_{ε_P} and σ_{ε_T}), and in addition the coefficients of the c_μ expression in equation 6.36.

The optimization procedure used to determine the coefficients of the NT2 model was similar to that used to determine the coefficients in the NT1 model and was also based on

adjusting the values to provide the best prediction for the homogeneous shear flows and, at the same time, to satisfy the constraints imposed by the asymptotic analysis.

The same clipping in the c_μ expression was necessary and again $\sigma_{k_P} = \sigma_{k_P} = 1.0$ was set.

The values of the coefficients determined in the NT2 model are presented in Table 6.5 and the values this model is expected to provide in the asymptotic states of a homogeneous shear flow, a decaying grid turbulence flow and a local equilibrium boundary layer are presented in Table 6.6.

Table 6.5: Coefficients of the first version of the NT2 model

c_μ	C_{P1}	C_{P2}	σ_{ε_P}	C_{T1}	C_{T2}	σ_{ε_T}
$min[0.09, 0.012 + 0.225e^{-0.318\eta}]$	1.1052	$1.8 - 1.1\frac{\frac{k_P}{k_T}-1}{\frac{k_P}{k_T}+1}$	0.7	$0.9333\frac{\varepsilon_P}{\varepsilon_T}$	1.1333	1.1258

Table 6.6: Values expected to be provided by the first version of the NT2 model in the asymptotic states studied

$\left(\frac{P_k}{\varepsilon_T}\right)_{SF}$	$\left(\frac{k_P}{k_T}\right)_{SF}$	$\left(\frac{\varepsilon_P}{\varepsilon_T}\right)_{SF}$	$\left(\frac{k_P}{k_T}\right)_{DF}$	$\left(\frac{\varepsilon_P}{\varepsilon_T}\right)_{DF}$	$\left(\frac{k_P}{k_T}\right)_{BL}$	$\left(\frac{\varepsilon_P}{\varepsilon_T}\right)_{BL}$	$c_{\mu_{BL}}$
1.9	3.7036	1.1913	1.0	0.5	1.4887	1.0	0.09

One may notice that the NT1 and NT2 models are very similar, however some differences can be pointed out.

First of all, the expression for ν_t is, of course, different. It is possible to say that by comparing the performance of the two proposed MTS models, one may be able to identify the importance of the timescale $\frac{k_P}{\varepsilon_P}$ (in the NT1 model) against $\frac{k}{\varepsilon_T}$ (in the NT2 model).

One may also notice that the ratio $\left(\frac{k_P}{k_T}\right)_{SF}$ is much lower for the NT2 model than for the NT1, implying that the latter concentrates more energy in the large scales. Consistent with this, the ratio $\left(\frac{k_P}{k_T}\right)_{BL}$ is also higher in the NT1 model, the value predicted by it being closer to the $\frac{2}{3}$ generally estimated for local equilibrium boundary layers.

6.1.10 Other MTS Models Tested in Local Equilibrium Boundary Layer

Before proceeding with the analysis of the performance of the newly developed NT1 and NT2 models, it is worth completing the asymptotic analyses of the CG, KC, NG and TS models. Their asymptotic states in decaying grid turbulence and homogeneous shear flows were already discussed so it remains to evaluate their asymptotic states in local equilibrium boundary layers.

As commented upon above, as all models follow the spectrum framework proposed by Hanjalic et al. (1980), they all adopt $\left(\frac{\varepsilon_P}{\varepsilon_T}\right)_{BL} = 1$. In local equilibrium, $P_k = \varepsilon_P = \varepsilon_T$ which then implies $\left(\frac{P_k}{\varepsilon_T}\right)_{BL} = 1$. It remains then to calculate the asymptotic states for $\left(\frac{k_P}{k_T}\right)_{BL}$.

The same procedure outlined above with the NT1 and NT2 models to arrive at the expression for $\left(\frac{k_P}{k_T}\right)_{BL}$ was carried out for the four LEV MTS models in study. Table 6.7 shows the calculated values for this ratio.

Table 6.7: Asymptotic state predicted by each MTS model for equilibrium boundary layers

Model	$\frac{\varepsilon_P}{\varepsilon_T}$	$\frac{k_P}{k_T}$
TS	1.0	6.23
KC	1.0	4.33
CG	1.0	2.52
NG	1.0	1.67

One can evaluate $\frac{k_P}{k_T}$ in the different flows studied for asymptotic analysis. In principle, one would expect $\left(\frac{k_P}{k_T}\right)_{DF} < \left(\frac{k_P}{k_T}\right)_{BL} < \left(\frac{k_P}{k_T}\right)_{SF}$. The reason for that is, as pointed out by Hanjalic et al. (1980), $\left(\frac{k_P}{k_T}\right)_{DF}$ should represent the minimum ratio $\frac{k_P}{k_T}$ would assume since there is no production in decaying grid turbulence. In homogeneous shear flows, the ratio $\frac{P_k}{\varepsilon_T} \approx 1.9$, according to DNS and experimental data, against $\left(\frac{P_k}{\varepsilon_T}\right)_{BL} = 1$ in local equilibrium boundary layers, hence one would expect k_P to store a higher ratio of the total turbulent kinetic energy in homogeneous shear flows than in local equilibrium boundary layers.

Comparing Tables 6.1, 6.2 and 6.7, one can see that only the KC model satisfies the expected relation between the $\frac{k_P}{k_T}$ ratio in the different flow situations, even though it predicts $\left(\frac{k_P}{k_T}\right)_{BL}$ only slightly smaller than $\left(\frac{k_P}{k_T}\right)_{SF}$.

Another important comment is that the coefficients of both CG and TS models do not reproduce the behaviour of the asymptotic state of local equilibrium boundary layers. When an equation similar to equations 6.32 and 6.46 is constructed for these models, one can check that it is not in balance. One could then expect these models not to provide an accurate log law prediction as Figure 5.61(c) suggests.

6.1.11 Performance of the First Versions of the NT1 and NT2 Models

The first versions of the NT1 and NT2 models were then assessed in the following test cases: homogeneous shear flows, normally strained flows, fully developed channel flows, zero, adverse and favourable pressure gradient boundary layers. It was decided to compare their results to those provided by the HR, SG and TS models, since these models represent each class tested before - one STS linear-eddy-viscosity, one STS Reynolds-stress-transport and one two-time-scale LEV model. The latter being the model used as the base for the development of the NT1 and NT2 models. Besides, all these models were used together with wall functions which makes the comparison between them fairer, although it is known that the wall function can affect different models in different levels. As the new NT1 and NT2 models use the linear-eddy-viscosity scheme, predictions of the Reynolds normal stresses will not be discussed here. A sample of results, showing the main features of the performance of the first versions of the NT1 and NT2 models, will be then discussed. In the results, the first versions of the NT1 and NT2 models will be presented as NT1 v1 and NT2 v1 respectively.

In order to assess the performance of the first versions of the NT1 and NT2 models in the homogeneous shear flow cases, one low, one moderate and one high shear case will be used. In Figure 6.10, the prediction of the evolution in time of the turbulent kinetic energy,

the eddy dissipation rate and the Reynolds shear stress are presented for the lowest shear case of Matsumoto et al. (1991) which is also the lowest shear case here tested. One can see that the new NT1 and NT2 models do not perform as well as the SG model, though they do present improvements when compared to the HR and TS models. The reason for this, as also mentioned before, is the clipping in c_μ: it was found during the process of tunning the coefficients for the NT1 and NT2 models that in order to match the DNS data of homogeneous low shear cases, high values of c_μ would be necessary. However, in order to guarantee stability in wall-bounded flows where the dimensionless shear parameter η can assume rather low values, c_μ was clipped with the value it is supposed to assume in equilibrium boundary layers, $c_{\mu_{BL}}$. The profile of c_μ can be seen in Figure 6.11 for the first version of both NT1 and NT2 models as a function of the dimensionless shear η. When looking at Figures 6.12 and 6.13 to assess the performance of the NT1 and NT2 models in moderate and high shear cases, one can see clear improvements provided by the new models, even when compared to the SG model which is an RST model, thus much more complex.

The performance of the first versions of the NT1 and NT2 models in the normally strained cases is presented in Figure 6.14. The new models provide clear improvements compared to the TS model, similar results compared to the HR model and worse results compared to the SG model. These results are expected since the NT1 and NT2 models are linear-eddy-viscosity models and therefore they are limited to predict these normally strained flows, as commented upon on Chapter 5.

The performance of the new models in the fully developed channel flow with $Re = 41441$ can be seen in Figure 6.15. The models perform reasonably well and satisfy the log law of the wall, as designed through the asymptotic analyses carried out. The TS model slightly overpredicts the velocity profile which is consistent with its coefficients not satisfying the asymptotic analyses as comment upon above. Only the results for the highest Reynolds number channel flow are shown, since the results are qualitatively similar for the lower Reynolds number cases.

The performance of the first versions of the NT1 and NT2 models in the zero pressure gradient boundary layer cases was reasonably good as also expected in the fully developed channel flow cases. It can be seen in Figure 6.16 for the profile of the velocity and turbulent quantities at $Re_\theta = 1410$. Again, this case is useful to confirm the models reproduce the behaviour of the asymptotic analysis carried out for local equilibrium boundary layers.

In order to evaluate the performance of the models in the adverse pressure gradient boundary layer cases, only the $M\&P30$ case will be used. It can be considered representative and provides qualitatively similar results to the other cases. The velocity profiles at four positions downstream of the imposed pressure gradient can be seen in Figure 6.17. The NT1 and NT2 models are not able to follow the subtle changes in the velocity profile just as the other STS models. In Chapter 5, it was seen that only the FM and WM models, which were designed to capture these changes, could follow the experimental data. The prediction of the turbulent kinetic energy and Reynolds shear stress profiles downstream are presented in Figures 6.19 and 6.18 respectively. It can be seen that these first versions of the NT1 and NT2

models provide similar results to the other models presented, providing a slight improvement in the prediction of the Reynolds shear stress. It can be also noted that the new models as well as the SG and the TS models predict the diffusion of the turbulent quantities better than the HR model which tends to produce a slower diffusion rate towards the outer layer.

The lowest acceleration parameter case, $K150$, will be used to assess the performance of the first versions of the NT1 and NT2 models in the favourable pressure gradient boundary layer cases. Again, the reason why only this case will be used is that it represents qualitatively the results for the other acceleration parameter cases. Results are presented in Figure 6.20. It can be seen that the new models provide slight improvements compared to the other models tested: while the TS model tends to provide a too fast decay of the turbulent kinetic energy and the Reynolds shear stress, the HR and SG models tend to provide a too slow decay of these turbulent quantities and the NT1 and NT2 models tend to provide results closer to the DNS data. The velocity and eddy dissipation rate profiles were reasonably well predicted by all the five models tested.

On the whole, it may be noted that the first versions of the NT1 and NT2 models provided either improvements or similar results in the first six test cases used to assess the performance of the turbulence models. Clear improvements could be noticed in the homogeneous moderate and high shear cases. The new models were then tested in three more cases: oscillatory boundary layer, fully developed oscillatory and ramp up pipe flows.

Again, only a sample of the results in these cases will be shown in order to discuss the performance of the first versions of the NT1 and NT2 models. In order to assess the performance of these models in the JSF oscillatory boundary layer case, the prediction of the Reynolds shear stress at four stages in the cycle is presented in Figure 6.21. It can be seen that the models perform just as the other STS models and the TS model. That is consistent with the results presented in Chapter 5 where most models performed similarly, showing this was not a very challenging case.

The prediction of the Reynolds shear stress at four stages in the cycle will also be used to assess the performance of the new models in the $TuR05$ oscillatory pipe flow case. Looking at Figure 6.22, one can see that, again, the first versions of the NT1 and NT2 models perform similarly to the other models, not providing improvements, but not performing in a worse manner. Results for the $TuR36$ case will not be shown, since the predictions of the new models were similar to those of the other models which predicted frozen turbulence as the turbulent profiles do not change along the cycle. The $T3RE14A20$ case will be discussed though. This case, where an intermediate frequency of oscillation is applied, shows more interesting features to compare the results with. The velocity and Reynolds shear stress amplitudes and phase shifts are presented in Figure 6.23. One may notice that the TS model performs best overall. The first versions of the NT1 and NT2 models provide reasonable predictions for the amplitude and phase shift of the velocity, however they tend to underpredict the phase shift of the Reynolds shear stress. The Reynolds shear stress amplitude was well predicted by the NT1 v1, but considerably overpredicted by the first version of the NT2 model. Despite these pointed drawbacks, it is worth noticing that the predictions of the new models are not worse

than those of the HR and SG models. The improved performance of the TS model seems to be related to the fact that it fails to reproduce the equilibrium asymptotic states. It was decided not to keep testing the $T3RE10A20$ and $T10RE7A20$ cases, since the wall function seemed to be affecting their results due to the rather low Reynolds number of these cases.

In order to examine the performance of the first versions of the NT1 and NT2 models in the ramp up flow, the prediction of the turbulent kinetic energy at three different positions in the radial direction are now discussed. The prediction of the velocity and of the Reynolds shear stress is not being presented since all models tend to behave similarly and provide reasonably good predictions. Differences in the predictions are more noticeable in the turbulent kinetic energy profile. One may notice in Figure 6.24 that, overall, both NT1 v1 and NT2 v1 perform well. The former, however, tends to perform better at $r/R = 0.47$ and the latter at the centre of the pipe. Both models present an improvement compared to the TS model in terms of the prediction of the moment when the turbulent kinetic energy starts to build up, though the NT1 v1 tends to provide an overpredicted level of k at the last second of the acceleration. As noted in the previous Chapter, when a model predicts well the profile of the turbulent kinetic energy at the centre of the pipe, it tends to underpredict the level of this quantity at $r/R = 0.47$ and vice versa. That is then what is being observed here again with the first versions of the NT1 and NT2 models.

One could then conclude that the new versions of the NT1 and NT2 models provide overall good predictions in all nine test cases evaluated above and provide clear improvements in the homogeneous moderate and high shear flow cases. Nevertheless, one could expect to improve the models' predictions in the intermediate frequency case of the oscillatory pipe flows.

6.1.12 Comparison of the Potential of STS and MTS Models

The comparisons presented so far have established that the first versions of the NT1 and NT2 models have improved the predictions of the homogeneous shear flows. The main reason for that is that the eddy viscosity is now sensitive to the dimensionless shear η. As discussed before, LEV models which use a constant c_μ cannot follow the changes in the turbulent kinetic energy and eddy dissipation rate evolution profiles as the dimensionless shear η of the flow is increased.

The question then arises as to whether the improvements seen in the first versions of the NT1 and NT2 models were only due to the new expression for c_μ or if the two-time-scale approach did contribute to improve the predictions as well.

In order to answer this question, the same procedure of asymptotic analyses carried out for the MTS models was performed with the standard $k - \varepsilon$ model, but using c_μ as in equation 6.36. As there is no partition of variables in STS models, the number of equations and unknowns resulting from the asymptotic analyses is rather smaller. Besides, the model's coefficients cannot vary with the spectrum-related ratios $\frac{k_P}{k_T}$ and $\frac{\varepsilon_P}{\varepsilon_T}$ which then implies that these coefficients must remain constants.

Indeed, as commented in the literature review in Chapter 2, C_{ε_2} is straight away calculated

from the decaying grid turbulence analysis, implying $C_{\varepsilon_2} = (C_{P2})_{DF} = 1.8$.

From homogeneous shear flows analysis, only one equation arises which is $\frac{P_k}{\varepsilon} = 1.9 = (1 - C_{\varepsilon_2})/(1 - C_{\varepsilon_1})$. As C_{ε_2} is already known, C_{ε_1} is easily obtained as 1.4211.

There then remains only one equation from local equilibrium boundary layer, $(C_{\varepsilon_2} - C_{\varepsilon_1}) = \frac{\kappa^2}{c_\mu^{1/2}\sigma_\varepsilon}$, where the only variable to be calculated is σ_ε which then ends up as 1.4787.

Comparing the above values for C_{ε_1}, C_{ε_2} and σ_ε with those used by the standard $k - \varepsilon$ model, presented in Table 3.1, one can notice they are similar. The differences arise from slight different assumptions such as the decay ration of k in grid decaying turbulence ($k \propto t^{-n}$) and the asymptotic value for $\frac{P_k}{\varepsilon}$ in homogeneous shear flows.

The only coefficients then remained to be calculated are c_2 and c_3 from c_μ in equation 6.36. Recall that c_1 is taken by assuming $c_\mu = 0.09$ when $\eta = 3.3$. Thereby two loops were built and both c_2 and c_3 were allowed to vary from 0.1 to 1.0 by a 0.01 increment. The lowest rms "error" was returned when $c_2 = 0.22$ and $c_3 = 0.31$ which implied $c_1 = 0.0117$.

One can now compare the lowest rms "error" provided by the standard $k - \varepsilon$ model using c_μ as in equation 6.36, which is 2.7670, and the first versions of the NT1 and NT2 models, which is 2.0460 and 2.2429 respectively. These results show that even using a non-constant c_μ, the standard STS $k - \varepsilon$ model cannot return as good predictions of homogeneous shear flows as the first versions of the NT1 and NT2 models. Indeed, when examining the results, it turns out that the modified standard STS $k - \varepsilon$ model predicts reasonably well the moderate shear case, but cannot return very good predictions in both low and high shear cases.

This simple test then answers the question above and shows that two-time-scale approaches do contribute to improve prediction of the homogeneous shear flow cases and the main reason for that is apparently the presence of the spectrum-related ratios $\frac{k_P}{k_T}$ and $\frac{\varepsilon_P}{\varepsilon_T}$ which arise as important parameters to sensitize the models.

6.1.13 Tests with σ_{k_P} and σ_{k_T}

In order to test the sensitivity of the new models in terms of predicting the $T3RE14A20$ oscillatory pipe flow case, it was decided to carry out a few tests with σ_{k_P} and σ_{k_T}. These parameters were initially assigned to unity since that is the general practice and since they are not present in any of the resulting equations of the asymptotic analyses. This last fact indeed allows one to change these parameters without compromising the asymptotic analyses carried out, that is, by changing these parameters, all equilibrium states previously studied remain valid. One should bear in mind though that these parameters do play a role in the diffusion terms and the effects of changing them would have to be studied as well.

The first attempt was to both increase and decrease σ_{k_P} and σ_{k_T} to understand which kind of change they would produce. It was noted that by increasing both σ_{k_P} and σ_{k_T} the NT1 and NT2 models would increase the prediction of both phase shift and amplitude of the Reynolds shear stress in the $T3RE14A20$ oscillatory pipe flow case. That would improve the prediction of the phase shift, but jeopardize the prediction of the amplitude which was either being well predicted by the NT1 model or already being overpredicted by the NT2 model.

Decreasing both σ_{k_P} and σ_{k_T} would then jeopardize both amplitude and phase shift of the Reynolds shear stress. Attempts of increasing only either σ_{k_P} or σ_{k_T} were also performed and it was found that increasing only σ_{k_P} would be more effective than increasing only σ_{k_T}.

When performing these same tests in the ramp up flow, it was noticed that a rather opposite effect would occur: by increasing either both σ_{k_P} and σ_{k_T} or only σ_{k_P}, the prediction of the turbulent kinetic energy would become worse. Few tests indicated then that improvements could be achieved by varying σ_{k_P} and/or σ_{k_T} with the turbulent Reynolds number, $Re_t = \frac{k^2}{\nu\varepsilon}$. A function such as that in equation 6.47 was then used in order to provide different asymptotic values at very low and very high Re_t values and a smooth increase from one to the other, as shown in Figure 6.25 with the parameters of equation 6.47 indicated.

$$\sigma_k = \frac{A_1 - A_2}{1 + \exp[(Re_t - R_1)/R_2} + A_2 \tag{6.47}$$

As a general rule, it was observed that the combinations of A_1, A_2, R_1 and R_2 values which worked well for the ramp up flow, would cause a stronger underprediction of phase shift of the Reynolds shear stress in the intermediate frequency oscillatory pipe flow than the original NT1 and NT2, meaning that no test was able to improve prediction in both unsteady cases.

Moreover, preliminary tests changing σ_{k_P} and/or σ_{k_T} disturbed the prediction of adverse pressure gradient boundary layers and low frequency oscillatory pipe flows.

It was then concluded that using both σ_{k_P} and σ_{k_T} as unity was a more appropriate choice.

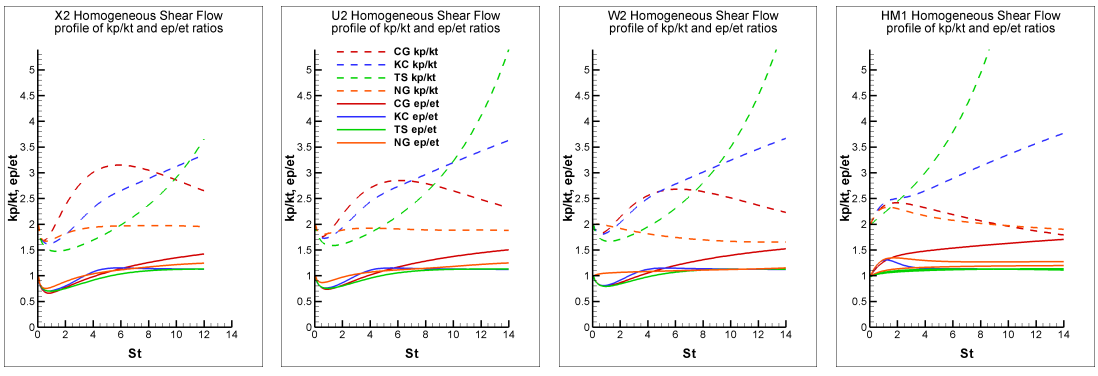

(a) (b) (c) (d)

Figure 6.1: Study of the ratios $\frac{k_P}{k_T}$ and $\frac{\varepsilon_P}{\varepsilon_T}$ in the homogeneous low and moderate shear flow cases: (a) lowest shear case $X2$ (b) low shear case $U2$, (c) low shear case $W2$ (d) moderate shear case $HM1$. Models as in Table 3.25.

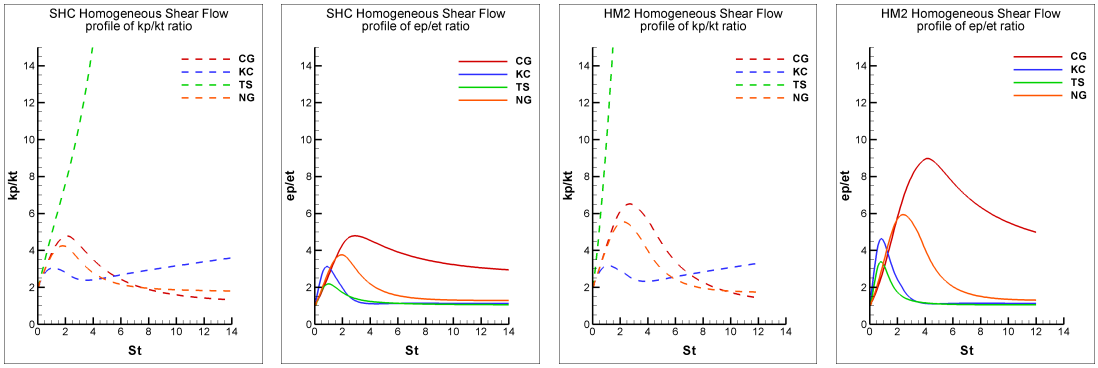

(a) (b) (c) (d)

Figure 6.2: Study of $\frac{k_P}{k_T}$ and $\frac{\varepsilon_P}{\varepsilon_T}$ in the homogeneous high shear flow cases: (a) $\frac{k_P}{k_T}$ in the high shear case SHC (b) $\frac{\varepsilon_P}{\varepsilon_T}$ in the high shear case SHC, (c) $\frac{k_P}{k_T}$ in the highest shear case $HM2$ (d) $\frac{\varepsilon_P}{\varepsilon_T}$ in the highest shear case $HM2$. Models as in Table 3.25.

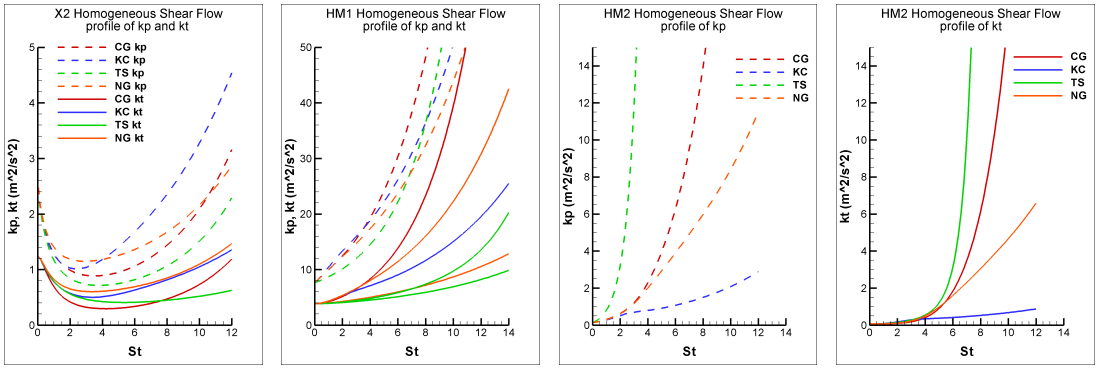

(a) (b) (c) (d)

Figure 6.3: k_P and k_T in the homogeneous shear flow cases: (a) k_P and k_T in the lowest shear case $X2$ (b) k_P and k_T in the moderate shear case $HM1$, (c) k_P in the highest shear case $HM2$ (d) k_T in the highest shear case $HM2$. Models as in Table 3.25.

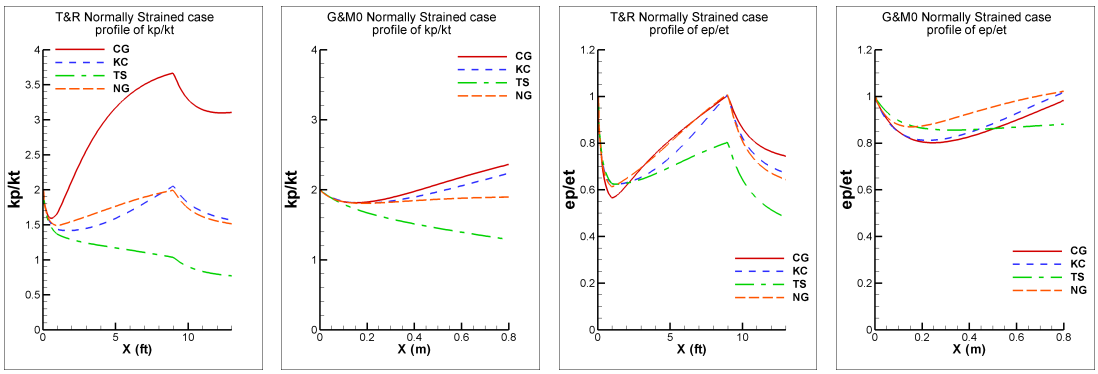

(a) (b) (c) (d)

Figure 6.4: Study of the ratios $\frac{k_P}{k_T}$ and $\frac{\varepsilon_P}{\varepsilon_T}$ in the pure normally strained cases $T\&R$ and $G\&M0$. (a) $\frac{k_P}{k_T}$ in $T\&R$ (b) $\frac{k_P}{k_T}$ in $G\&M0$ (c) $\frac{\varepsilon_P}{\varepsilon_T}$ in $T\&R$ (d) $\frac{\varepsilon_P}{\varepsilon_T}$ in $G\&M0$. Models as in Table 3.25.

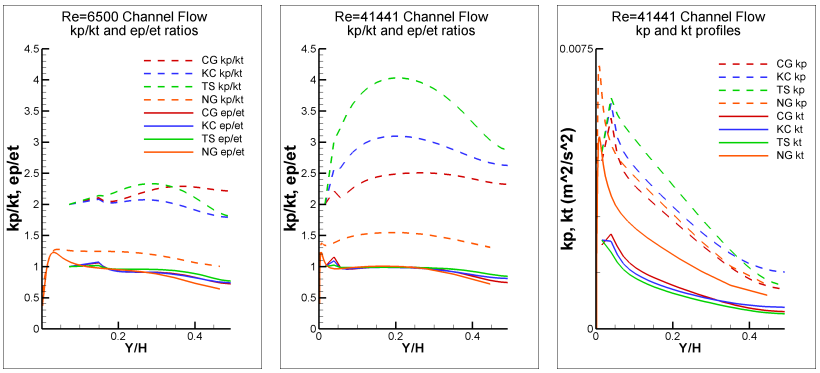

(a) (b) (c)

Figure 6.5: Study of the ratios $\frac{k_P}{k_T}$ and $\frac{\varepsilon_P}{\varepsilon_T}$ in the channel flow cases. (a) $Re = 6500$. (b) $Re = 41441$. (c) Profiles of k_P and k_T in the case with $Re = 41441$. Models as in Table 3.25.

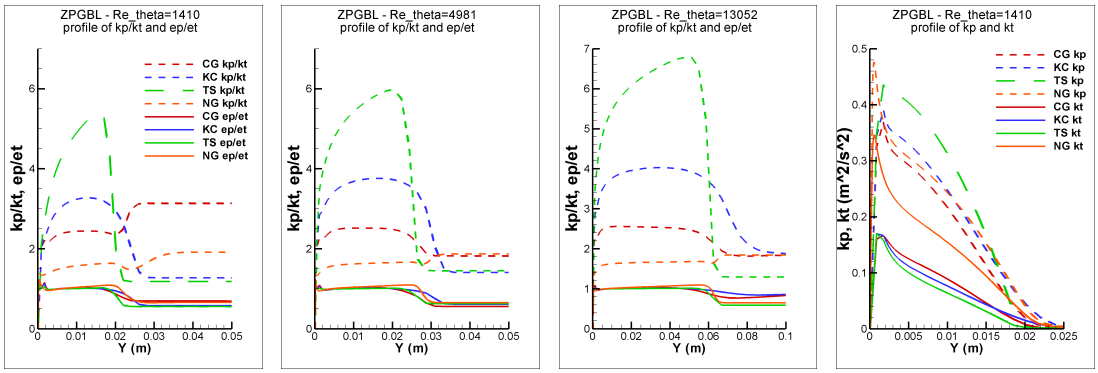

(a) (b) (c) (d)

Figure 6.6: Study of the ratios $\frac{k_P}{k_T}$ and $\frac{\varepsilon_P}{\varepsilon_T}$ in the zero pressure gradient boundary layer cases. Profiles evaluated at: (a) $Re_\theta = 1410$ (b) $Re_\theta = 4981$ and (c) $Re_\theta = 13052$. (d) k_P and k_T at k_T. Models as in Table 3.25.

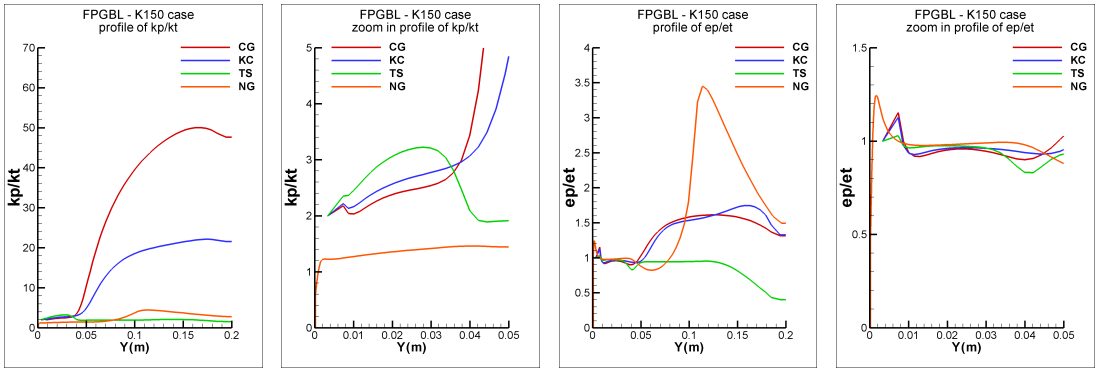

(a) (b) (c) (d)

Figure 6.7: Study of the ratios $\frac{k_P}{k_T}$ and $\frac{\varepsilon_P}{\varepsilon_T}$ in the lowest acceleration parameter ($K = 1.5 \times 10^{-6}$) case of the favourable pressure gradient boundary layer cases. (a) $\frac{k_P}{k_T}$ (b) zoom in $\frac{k_P}{k_T}$, (c) $\frac{\varepsilon_P}{\varepsilon_T}$ (d) zoom in $\frac{\varepsilon_P}{\varepsilon_T}$. Models as in Table 3.25.

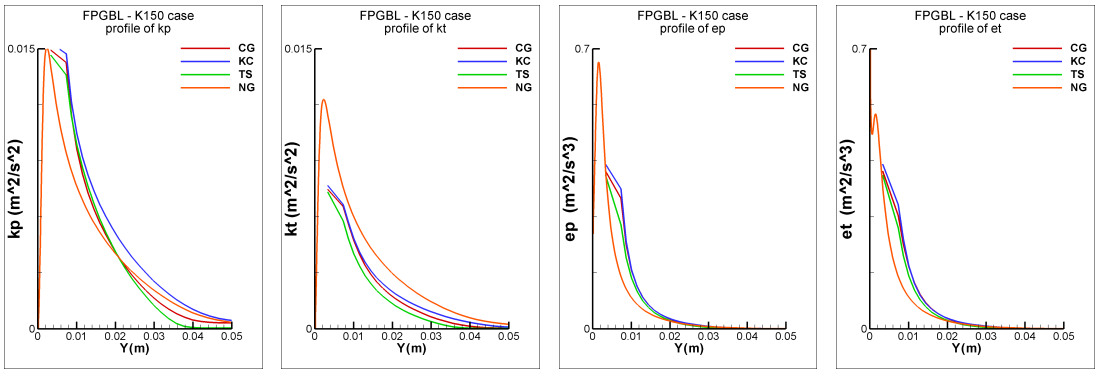

(a) (b) (c) (d)

Figure 6.8: Study of the profiles of k_P, k_T, ε_P and ε_T in the lowest acceleration parameter ($K = 1.5 \times 10^{-6}$) case of the favourable pressure gradient boundary layer cases. (a) k_P (b) k_T (c) ε_P and (d) ε_T. Models as in Table 3.25.

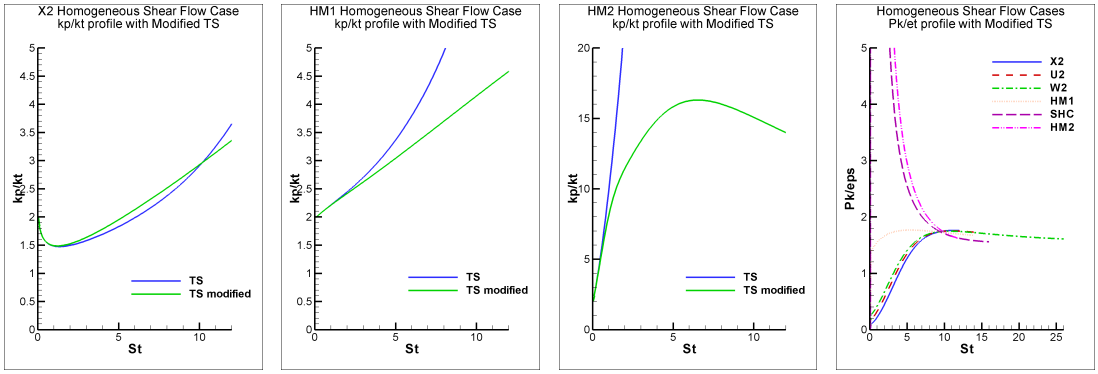

(a) X2 case (b) HM1 case (c) HM2 case (d) all cases

Figure 6.9: Evolution of the ratio $\frac{k_P}{k_T}$ and $\frac{P_k}{\varepsilon_T}$ in the homogeneous shear flow cases, testing the modified TS model where the C'_{P1} term was removed and incorporated into the C_{P1} term.

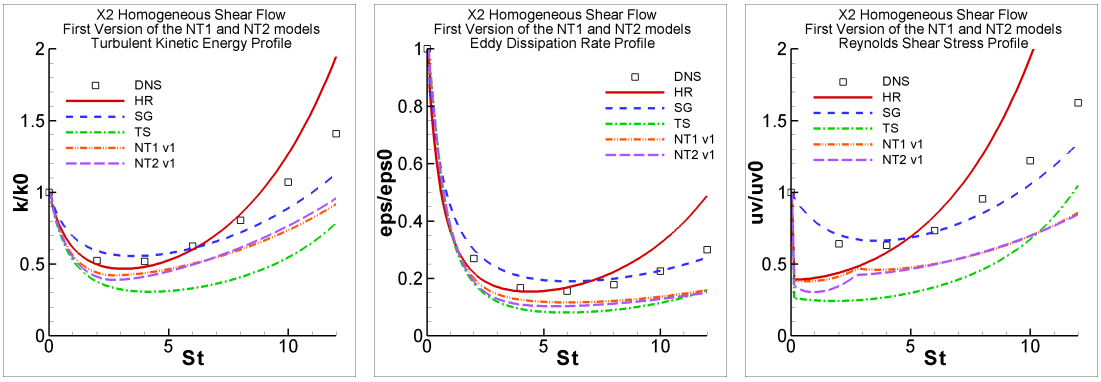

(a) k Profile (b) ε Profile (c) $\overline{uv}$ Profile

Figure 6.10: Performance of the first versions of the NT1 and NT2 models compared with the results provided by the HR, SG and TS models in the homogeneous lowest shear flow case $X2$. Models as in Table 3.25.

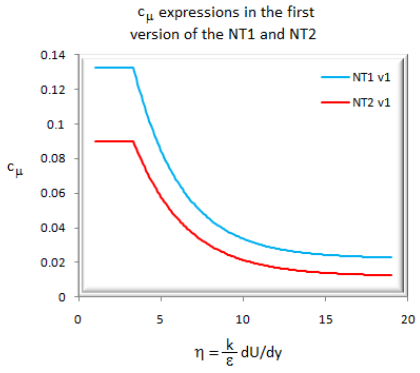

Figure 6.11: c_μ as in Tables 6.3 and Table 6.5 for the first versions of the NT1 and NT2 models

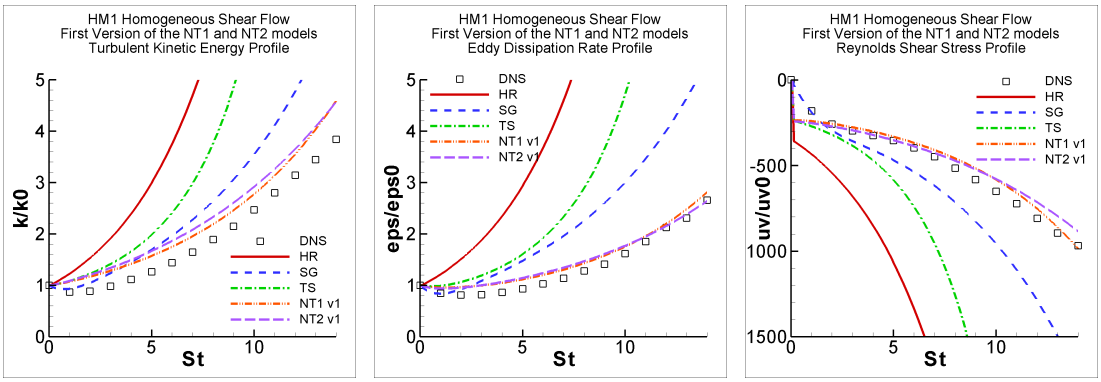

(a) k Profile (b) ε Profile (c) $\overline{uv}$ Profile

Figure 6.12: Performance of the first versions of the NT1 and NT2 models compared with the results provided by the HR, SG and TS models in the homogeneous moderate shear flow case $HM1$. Models as in Table 3.25.

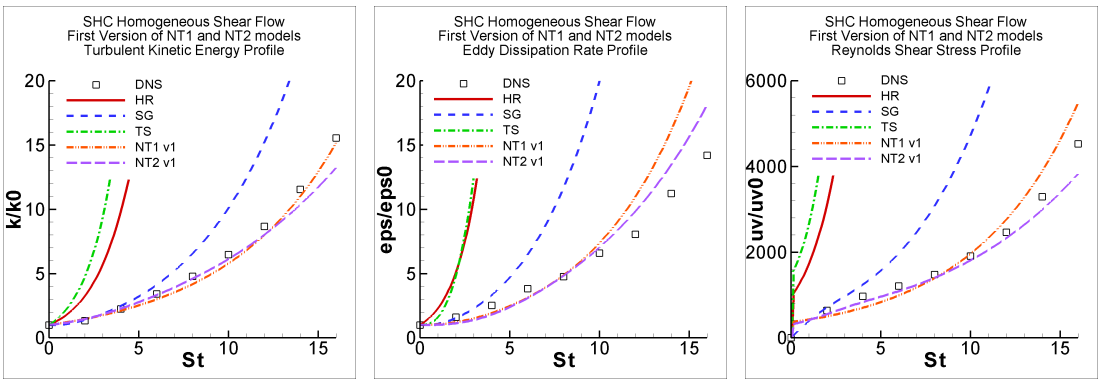

(a) k Profile (b) ε Profile (c) $\overline{uv}$ Profile

Figure 6.13: Performance of the first versions of the NT1 and NT2 models compared with the results provided by the HR, SG and TS models in the homogeneous high shear flow case SHC. Models as in Table 3.25.

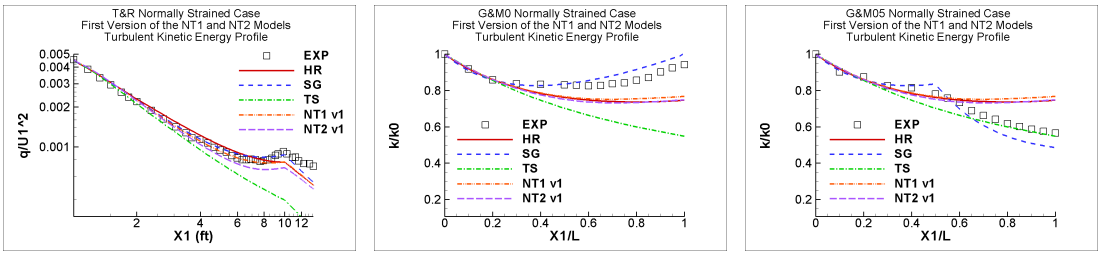

(a) $T\&R$ case (b) $G\&M0$ case (c) $G\&M05$ case

Figure 6.14: Performance of the first versions of the NT1 and NT2 models compared with the results provided by the HR, SG and TS models in the normally strained cases. Models as in Table 3.25.

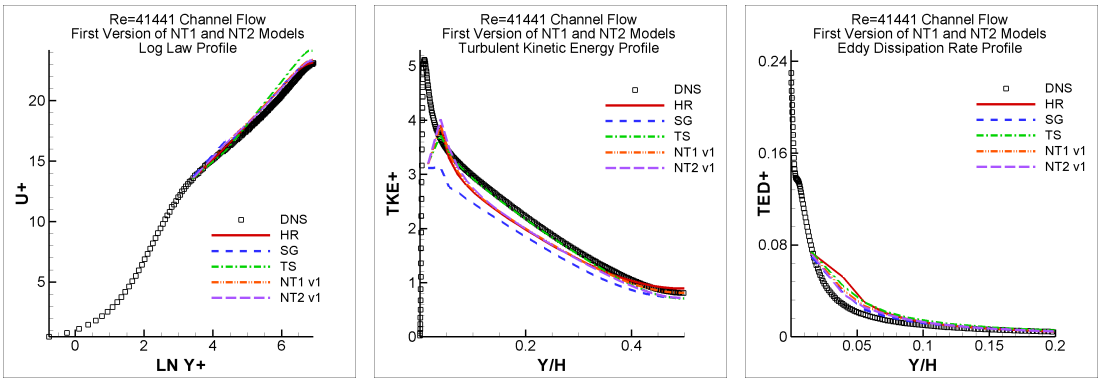

(a) Velocity Profile (b) k Profile (c) ε Profile

Figure 6.15: Performance of the first versions of the NT1 and NT2 models compared with the results provided by the HR, SG and TS models in the fully developed channel flow case with $Re = 41441$. Models as in Table 3.25.

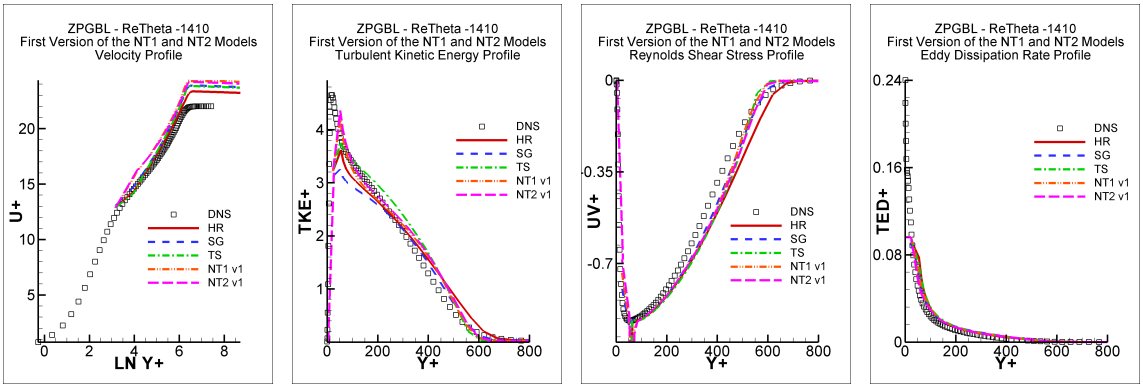

(a) Velocity Profile (b) k Profile (c) $\overline{uv}$ Profile (d) ε Profile

Figure 6.16: Performance of the first versions of the NT1 and NT2 models compared with the results provided by the HR, SG and TS models in the zero pressure gradient boundary layer at $Re_\theta = 1410$. Models as in Table 3.25.

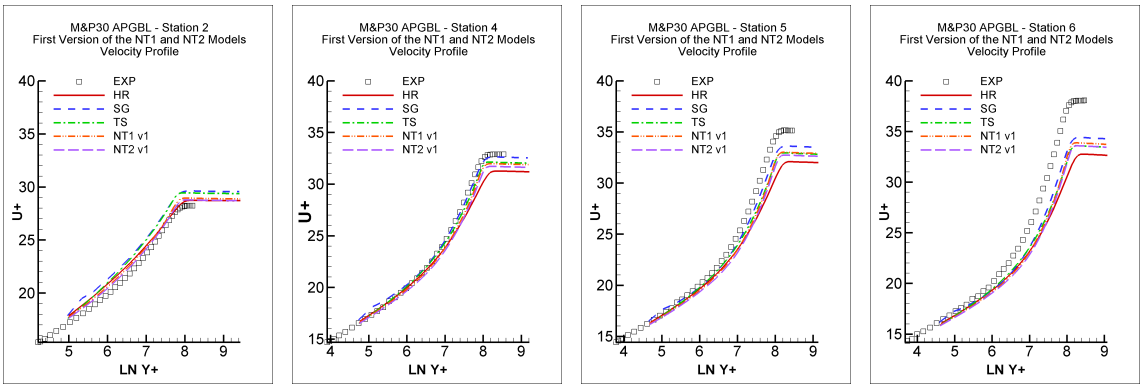

(a) Station 2 (b) Station 4 (c) Station 5 (d) Station 6

Figure 6.17: Prediction of the velocity profile by the first versions of the NT1 and NT2 models compared with the results provided by the HR, SG and TS models in the adverse pressure gradient boundary layer case $M\&P30$. Models as in Table 3.25.

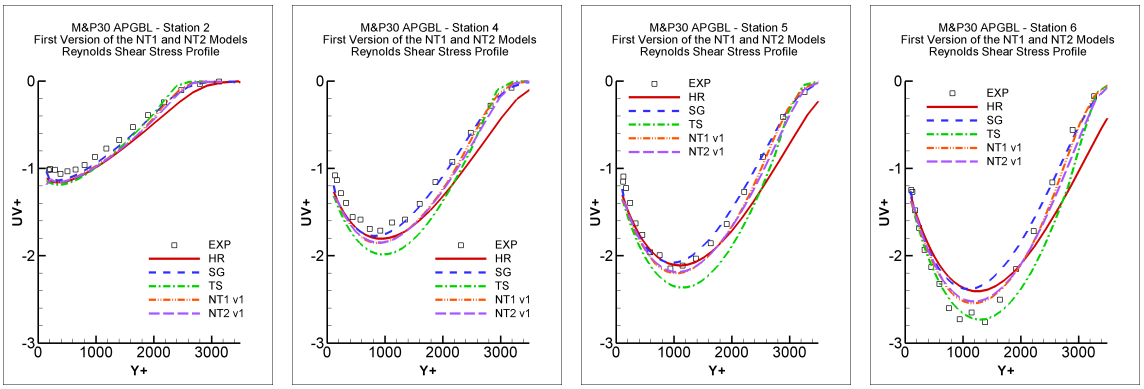

(a) Station 2 (b) Station 4 (c) Station 5 (d) Station 6

Figure 6.18: Prediction of the Reynolds shear stress by the first versions of the NT1 and NT2 models compared with the results provided by the HR, SG and TS models in the adverse pressure gradient boundary layer case $M\&P30$. Models as in Table 3.25.

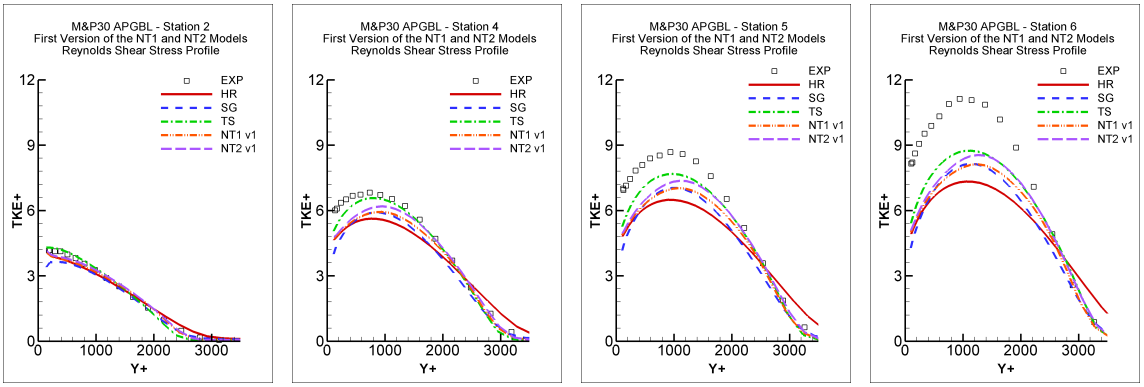

(a) Station 2 (b) Station 4 (c) Station 5 (d) Station 6

Figure 6.19: Prediction of the turbulent kinetic energy by the first versions of the NT1 and NT2 models compared with the results provided by the HR, SG and TS models in the adverse pressure gradient boundary layer case $M\&P30$. Models as in Table 3.25.

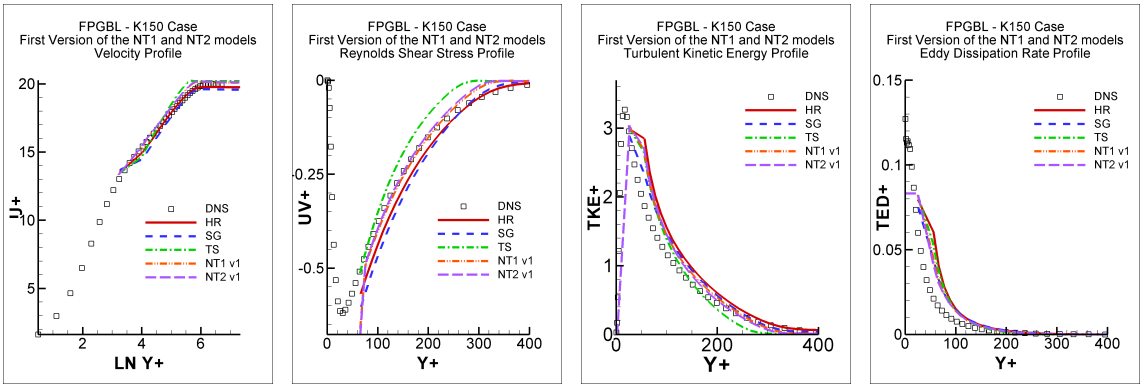

(a) Velocity Profile (b) $\overline{uv}$ Profile (c) k Profile (d) ε Profile

Figure 6.20: Performance of the first versions of the NT1 and NT2 models compared with the results provided by the HR, SG and TS models in the $K150$ favourable pressure gradient case. Models as in Table 3.25.

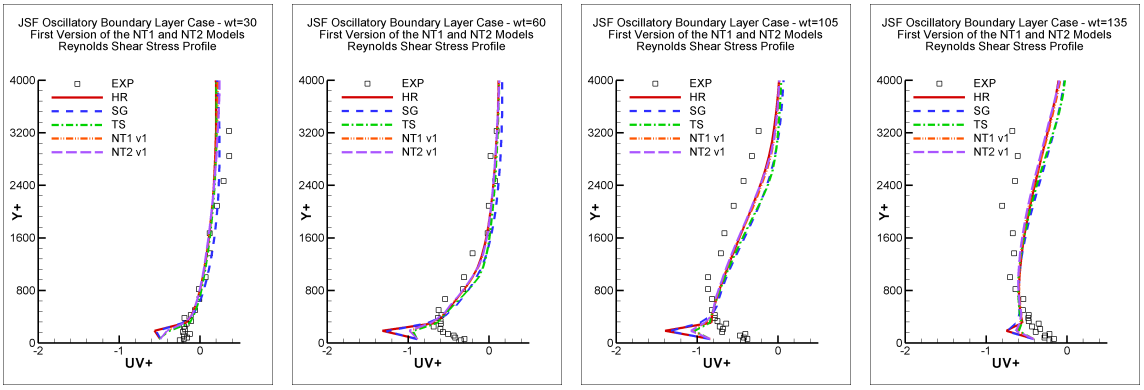

(a) $\omega t = 30^o$ (b) $\omega t = 60^o$ (c) $\omega t = 105^o$ (d) $\omega t = 135^o$

Figure 6.21: Prediction of the Reynolds shear stress by the first versions of the NT1 and NT2 models compared with the results provided by the HR, SG and TS models in the oscillatory boundary layer case JSF. Models as in Table 3.25.

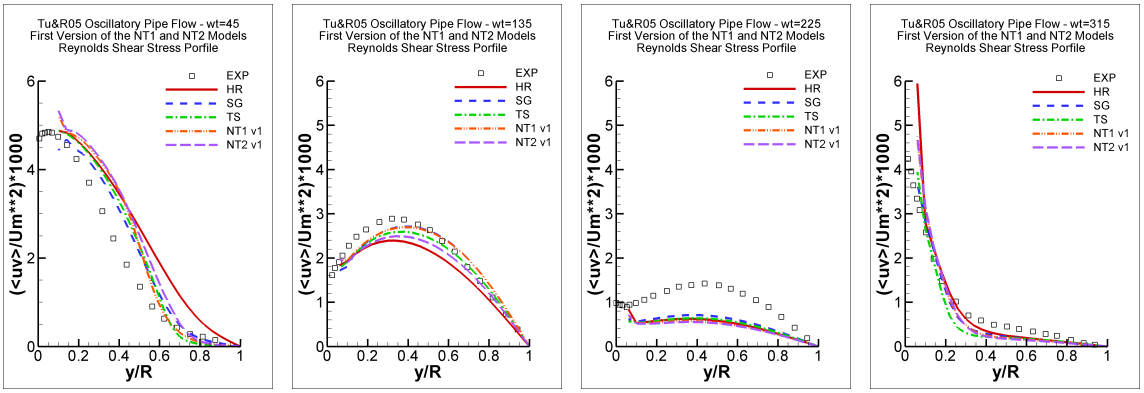

(a) $\omega t = 45^o$ (b) $\omega t = 135^o$ (c) $\omega t = 225^o$ (d) $\omega t = 315^o$

Figure 6.22: Prediction of the Reynolds shear stress by the first versions of the NT1 and NT2 models compared with the results provided by the HR, SG and TS models in the oscillatory pipe flow case $Tu\&R05$. Models as in Table 3.25.

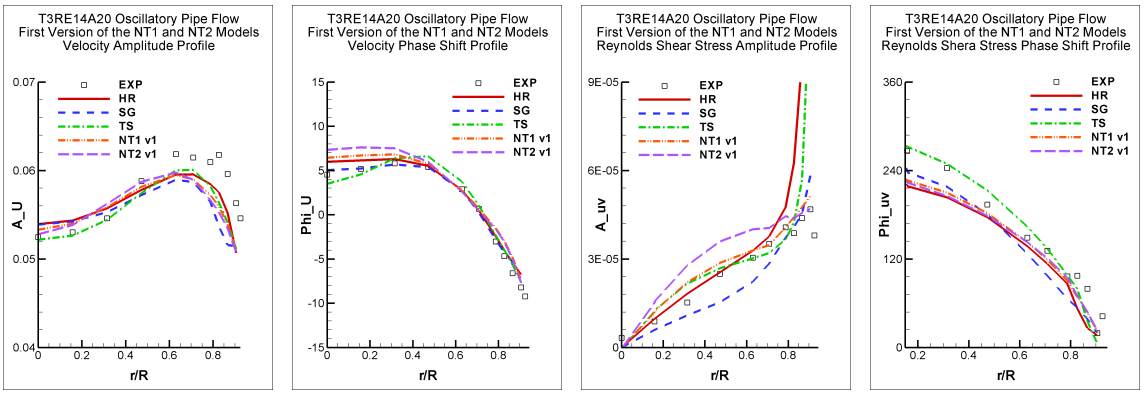

(a) Velocity Amplitude (b) Velocity Phase Shift (c) Shear Stress Amplitude (d) Shear Stress Phase Shift

Figure 6.23: Performance of the first versions of the NT1 and NT2 models compared with the results provided by the HR, SG and TS models in the oscillatory pipe flow case $T3RE14A20$. Models as in Table 3.25.

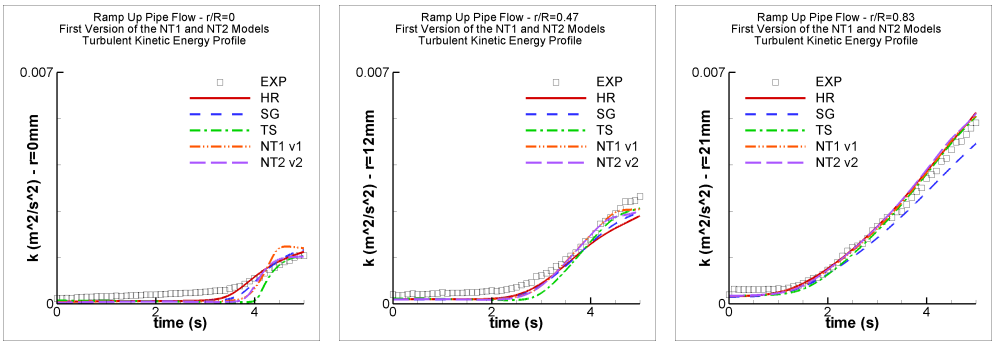

(a) Pipe centre ($r/R = 0$) (b) $r/R = 0.47$ (c) $r/R = 0.83$

Figure 6.24: Prediction of the turbulent kinetic energy by the first versions of the NT1 and NT2 models compared with the results provided by the HR, SG and TS models in the ramp up pipe flow. Models as in Table 3.25.

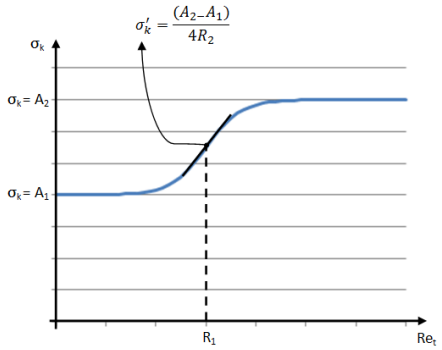

Figure 6.25: Example of σ_{k_P} and/or σ_{k_T} variation as a function of Re_t

6.2 Second versions of the NT1 and NT2 models

The procedures which led to the second versions of the NT1 and NT2 models are described here.

The first versions of the NT1 and NT2 models were identified to be working generally well in the range of nine tested flows. It was recognised though that the performance of the models could be improved in the fully developed oscillatory pipe flows and that their performance was limited in homogeneous low shear and normally strained cases. A few attempts were made in order to change σ_{k_P} and/or σ_{k_T}, however these parameters seemed to result in more reliable predictions when assigned the value of unity.

It can be noted that the first versions of the NT1 and NT2 models are very similar to the original TS model, used as starting point for their development. The extra source term in the ε_P equation was removed and the coefficients constants were changed, however all general expressions such as for C_{P2} and C_{T1} were kept.

6.2.1 Study of Time and Length Scales

In order to introduce a possible extra term which could improve the prediction of the oscillatory pipe flows, it was decided to calculate the ratio between the time and length scales associated with the large and small eddies. The time scale of the small eddies is defined as $\tau_T = \frac{k_T}{\varepsilon_T}$ while the time scale for the large eddies is $\tau_P = \frac{k_P}{\varepsilon_P}$. Similarly, the length scale for the small and large eddies are $\ell_T = \frac{k_T^{3/2}}{\varepsilon_T}$ and $\ell_P = \frac{k_P^{3/2}}{\varepsilon_P}$ respectively.

According to the turbulent kinetic energy spectrum and the cascade process, one would expect the ratio between the small and large time and length scales to be always smaller than unity, that is $\frac{\tau_T}{\tau_P} < 1$ and $\frac{\ell_T}{\ell_P} < 1$.

However, when evaluating these ratios in all nine test cases where the first versions of the NT1 and NT2 models was used, it was found that, except for the homogeneous flows, in all non-homogeneous wall-bounded flows the NT1 and NT2 models were tending to provide growing ratios of the time and length scale ratios, resulting in $\frac{\tau_T}{\tau_P} > 1$ and $\frac{\ell_T}{\ell_P} > 1$ at the edge of the boundary layer. The first version of the NT2 model would usually produce ratios significantly higher than unity, while the first version of the NT1 model would result in ratios very close to unity and eventually slightly higher than that.

An example of the time scale ratio profile in zero pressure gradient boundary layers is presented in Figure 6.26. One can clearly notice what was just commented on above.

It is interesting to notice that only the first versions of the NT1 and NT2 models provide time-scale ratios $\frac{\tau_T}{\tau_P}$ greater than unity. The other LEV MTS models seem to result in physically acceptable time scale ratios. It is worth commenting though that the CG model did provide higher values for $\frac{\tau_T}{\tau_P}$, even higher than unity, in a few other flows such as the homogeneous high shear cases. As far as the first versions of the NT1 and NT2 models are concerned, the high time scale ratios occur basically at the edge of the boundary layer, after which, all models predict a constant lower $\frac{\tau_T}{\tau_P}$.

In order to investigate the reason for that, the ratios of $\frac{k_P}{k_T}$ and $\frac{\varepsilon_P}{\varepsilon_T}$ were also studied for the first versions of the NT1 and NT2 models, presented in Figures 6.27 and 6.28 respectively. The reason why they provide a high time scale ratio seems to be associated with their low $\frac{k_P}{k_T}$ ratio combined with a peak in the $\frac{\varepsilon_P}{\varepsilon_T}$ profile at the edge of the boundary layer. This led to the question whether the low turbulent kinetic energy partitions ratio at the equilibrium boundary layer $\left(\frac{k_P}{k_T}\right)_{BL}$ was responsible for that. The fact that $\left(\frac{k_P}{k_T}\right)_{BL} \approx 2$ for the first version of the NT1 model and $\left(\frac{k_P}{k_T}\right)_{BL} \approx 1.5$ for the first version of the NT2 model together with the NT2 model providing systematically higher time scale ratios than the NT1 model also helped to support this hypothesis.

6.2.2 The Second Version of the NT1 Model

Based on the analysis above, it was decided to re-optimize the model's coefficients and impose $\left(\frac{k_P}{k_T}\right)_{BL}$ to be higher than 3. Stawiarski and Hanjalic (2005) support that 3 would be a reasonable value for the ratio $\frac{k_P}{k_T}$ in equilibrium boundary layers and states that experiments would suggest that this ratio could be even higher than 3.

When determining the coefficients of the first versions of the NT1 and NT2 models, no restrictions were imposed for $\left(\frac{k_P}{k_T}\right)_{BL}$ and the best overall set of coefficients provided low values for this parameter. That would then make one wonder that if $\left(\frac{k_P}{k_T}\right)_{BL}$ is imposed to be higher than 3, the set of coefficients would not perform as well as the original NT1 and NT2 models.

Because of this, it was decided to consider different assumptions than those made in the development of the original TS model, regarding the expected ratio of $\left(\frac{k_P}{k_T}\right)_{DF}$ in decaying grid turbulence and the coefficients' constants and expressions.

The original expression used for the coefficient C_{P2} was that suggested by Hanjalic et al. (1980) where $C_{P2} = c_{p21} - c_{p22}\left(\frac{k_P}{k_T} - 1\right)/\left(\frac{k_P}{k_T} + 1\right)$ and $c_{p21} = 1.8$ and $c_{p22} = 0.3$ and $\left(\frac{k_P}{k_T}\right)_{DF} = 1$ in order to be consistent with the asymptotic analysis behaviour of decaying grid flows. In the first versions of the NT1 and NT2 models, this general expression was retained and c_{p22} was assigned different values, presented in Tables 6.3 and 6.5. The possibility was then studied of having C_{P2} as suggested by Chen and Guo (1991): $C_{P2} = 1.90\left(1 - 0.2\frac{k_T}{k_P} + 0.2\frac{k_P^2}{k_T^2}\right)$. However, here, instead of 1.9, the value of 1.8 was used (the value C_{P2} is supposed here to reach in decaying grid turbulence). An expression such as that used in equation 6.47 (σ_k replaced by C_{P2} and Re_t replaced by $\frac{k_P}{k_T}$) was also tried and is referred to as C_{P2} *test* in Figure 6.29(a) where the three curves considered for C_{P2} are presented.

The expressions for C_{P2} different from that used by the TS model did not show any potential of improving prediction in the homogeneous shear flow cases and therefore were discarded. For the re-optimization procedure, it was then decided to use $C_{P2} = c_{p21} - c_{p22}\left(\frac{k_P}{k_T} - 1\right)/\left(\frac{k_P}{k_T} + 1\right)$, this time allowing c_{p22} to be zero as well, that is allowing C_{P2} to be a constant, in this case $C_{P2} = 1.8$.

The coefficient C_{P1}, originally used as a constant was also allowed to vary with $\frac{k_P}{k_T}$, but in this case, the coefficient C_{P1} was allowed to vary as a function of $\frac{k_P}{k_T}$ only until its value in

local equilibrium boundary layers, $\left(\frac{k_P}{k_T}\right)_{BL}$, was reached. The reason for that was to improve prediction in homogeneous low shear cases, by allowing C_{P1} to reduce at low $\frac{k_P}{k_T}$ values, and at the same time not disturb the asymptotic analyses carried out for local equilibrium boundary layers where C_{P1} would then reduce to a simple constant.

Two different expressions were then tested:

$$C_{P1} = c_{p11} + c_{p12} \min\left[0, \frac{k_P}{k_T} - \left(\frac{k_P}{k_T}\right)_{BL}\right] \Big/ \left[\frac{k_P}{k_T} + \left(\frac{k_P}{k_T}\right)_{BL}\right] \tag{6.48}$$

$$C_{P1} = \begin{cases} c_{p11} - c_{p11}\exp(-c_{p12}\frac{k_P}{k_T}) & \text{if } \frac{k_P}{k_T} < \left(\frac{k_P}{k_T}\right)_{BL} \\ c_{p11} & \text{if } \frac{k_P}{k_T} > \left(\frac{k_P}{k_T}\right)_{BL} \end{cases} \tag{6.49}$$

Equation 6.48 is a similar expression to that of C_{P2} in the TS model, but to reduce the coefficient, and is referred to as C_{P1} TS in Figure 6.29(b) where the curves for C_{P1} are presented; and equation 6.49 is referred to as C_{P1} *test*, where a rather smoother reduction in this coefficient is proposed. Again, the C_{P1} TS proved to be more efficient and was then chosen for the re-optimization procedure.

Two other differences were introduced in the re-optimization procedure when compared to the general model form proposed by Hanjalic et al. (1980). First, the C_{T1} coefficient, originally used as $C_{T1} = c_{t1}\frac{\varepsilon_P}{\varepsilon_T}$, was allowed to be a constant and both forms were tested. Second, the assumption of $\left(\frac{k_P}{k_T}\right)_{DF} = 1$ in decaying grid turbulence was no longer imposed. This parameter was allowed to vary from 0.5 up to $\frac{1}{2}\left(\frac{k_P}{k_T}\right)_{BL}$, the idea being to have $\left(\frac{k_P}{k_T}\right)_{BL}$ up to twice $\left(\frac{k_P}{k_T}\right)_{DF}$ and thereby respect the different levels of magnitude this ratio should assume in the different flows, the decaying grid turbulence representing the minimum ratio one should expect to find in any flow, since this is when no production is present.

The asymptotic analysis carried out before for the first version of the NT1 model remains valid, the system of equations being: equations 6.8, 6.9 and 6.39 for homogeneous shear flows, equations 6.16 and 6.18 for decaying grid turbulence and equations 6.34, 6.28 and 6.32 for local equilibrium boundary layers. This time though, one more equation must be added to the asymptotic analysis of decaying grid turbulence:

$$C_{P2_{DF}} = 1.8 = c_{p21} - c_{p22}\left[\frac{\left(\frac{k_P}{k_T}\right)_{DF} - 1}{\left(\frac{k_P}{k_T}\right)_{DF} + 1}\right] \tag{6.50}$$

This is the same C_{P2} expression used in the TS model, but not considering $\left(\frac{k_P}{k_T}\right)_{DF} = 1$. The reoptimization procedure for the second version of the NT1 model consisted then of 9 equations (just mentioned above) and 14 unknowns ($\left(\frac{k_P}{k_T}\right)_{BL}$, $\left(\frac{k_P}{k_T}\right)_{DF}$, $\left(\frac{k_P}{k_T}\right)_{SF}$, $\left(\frac{\varepsilon_P}{\varepsilon_T}\right)_{DF}$, $\left(\frac{\varepsilon_P}{\varepsilon_T}\right)_{SF}$, c_{p11}, c_{p12}, c_{p21}, c_{p22}, C_{T1}, C_{T2}, $c_{\mu_{BL}}$, σ_{ε_P} and σ_{ε_T}). A program was written in Matlab and in an outer loop, $c_{\mu_{BL}}$ was varied from 0.109 (which provides $\left(\frac{k_P}{k_T}\right)_{BL} \approx 4.7$ through equation 6.34) to 0.12 (which provides $\left(\frac{k_P}{k_T}\right)_{BL} = 3$ through equation 6.34) by a 0.001 increment. Inside this loop, c_{t1} and C_{T2} were varied from 0.6 to 1.7 and 0.65 to 1.75 respectively by a 0.05 increment and $\left(\frac{\varepsilon_P}{\varepsilon_T}\right)_{DF}$, $\left(\frac{k_P}{k_T}\right)_{DF}$ and $\left(\frac{\varepsilon_P}{\varepsilon_T}\right)_{SF}$ were calculated from

equations 6.18, 6.16 and 6.8 respectively, since the condition $0.5 < \left(\frac{k_P}{k_T}\right)_{DF} < \frac{1}{2}\left(\frac{k_P}{k_T}\right)_{BL}$ were satisfied. As $\left(\frac{P_k}{\varepsilon_T}\right)_{SF} = 1.9$, $\left(\frac{k_P}{k_T}\right)_{SF}$ could also be calculated from equation 6.9. Inside the C_{T2} loop, c_{p22} was set to vary from 0 to 1.5 by a 0.1 increment and c_{p21} was calculated through equation 6.50. c_{p11} was then calculated from equation 6.39, since c_{p12} was not included in the asymptotic analysis, since $C_{P1} = c_{p11}$ for $\frac{k_P}{k_T} > \left(\frac{k_P}{k_T}\right)_{BL}$ and $\left(\frac{k_P}{k_T}\right)_{SF} > \left(\frac{k_P}{k_T}\right)_{BL}$, as already discussed. Finally, the system formed by equations 6.28 and 6.32 and by the only two so-far unknowns, σ_{ε_P} and σ_{ε_T}, was solved, and it was imposed that $|\sigma_{\varepsilon_P} - \sigma_{\varepsilon_T}| < 0.5$ to avoid instability in wall-bounded flows as commented on before. Inside the c_{p22} loop, a loop for c_2 and c_3 from the c_μ expression in equation 6.36 was built where these parameters varied from 0.2 to 0.4 by a 0.05 increment and c_1 could then be calculated as $c_1 = c_{\mu_{BL}} - c_2 \exp(-3.3c_3)$ in order to ensure $c_{\mu_{BL}}$ would be associated with $\eta = 3.3$, as also discussed before. The last inner loop then was built to vary c_{p12} from 0 to 2.5 by a 0.1 increment. The same criteria used for the first version of the NT1 model to chose the best set of coefficients was used in this second version: for each set of coefficients, homogeneous low, moderate and high shear cases were calculated and a minimum rms "error" was calculated by comparing these results with DNS data. The set of coefficients which provided the smallest rms "error" was then chosen. A simplified diagram representing this procedure can be seen in Figure 6.30.

The second version of the NT1 model, where $\nu_t = c_\mu k \frac{k_P}{\varepsilon_P}$, involves the following equations with the coefficients presented in Table 6.8.

$$\frac{Dk_P}{Dt} = P_k - \varepsilon_P + \frac{\partial}{\partial x_j}\left[\left(\nu + \frac{\nu_t}{\sigma_{k_P}}\right)\frac{\partial k_P}{\partial x_j}\right] \tag{6.51}$$

$$\frac{Dk_T}{Dt} = \varepsilon_P - \varepsilon_T + \frac{\partial}{\partial x_j}\left[\left(\nu + \frac{\nu_t}{\sigma_{k_T}}\right)\frac{\partial k_T}{\partial x_j}\right] \tag{6.52}$$

$$\frac{D\varepsilon_P}{Dt} = C_{P1}P_k\frac{\varepsilon_P}{k_P} - C_{P2}\frac{\varepsilon_P^2}{k_P} + \frac{\partial}{\partial x_j}\left[\left(\nu + \frac{\nu_t}{\sigma_{\varepsilon_P}}\right)\frac{\partial \varepsilon_P}{\partial x_j}\right] \tag{6.53}$$

$$\frac{D\varepsilon_T}{Dt} = C_{T1}\frac{\varepsilon_P\varepsilon_T}{k_T} - C_{T2}\frac{\varepsilon_T^2}{k_T} + \frac{\partial}{\partial x_j}\left[\left(\nu + \frac{\nu_t}{\sigma_{\varepsilon_T}}\right)\frac{\partial \varepsilon_T}{\partial x_j}\right] \tag{6.54}$$

Table 6.8: Coefficients of the second version of the NT1 model

c_μ	C_{P1}	C_{P2}	σ_{ε_P}	C_{T1}	C_{T2}	σ_{ε_T}
$min[0.115, 0.023 + 0.25e^{-0.30\eta}]$	$1.4921 + 2.5\frac{min(0, \frac{k_P}{k_T} - 3.6)}{\frac{k_P}{k_T} + 3.6}$	1.8	1.4202	1.6	1.7	1.2181

It is instructive to comment on the resulting coefficients and asymptotic states presented in Tables 6.8 and 6.9 above. One may notice that this second version of the NT1 model is rather different from the original TS model. Both C_{P2} and C_{T1} coefficients are now constants and the C_{P1} coefficient varies as a function of $\frac{k_P}{k_T}$. It is also worth commenting that for values

Table 6.9: Values expected to be provided by the second version of the NT1 model in the asymptotic states studied

$\left(\frac{P_k}{\varepsilon_T}\right)_{SF}$	$\left(\frac{k_P}{k_T}\right)_{SF}$	$\left(\frac{\varepsilon_P}{\varepsilon_T}\right)_{SF}$	$\left(\frac{k_P}{k_T}\right)_{DF}$	$\left(\frac{\varepsilon_P}{\varepsilon_T}\right)_{DF}$	$\left(\frac{k_P}{k_T}\right)_{BL}$	$\left(\frac{\varepsilon_P}{\varepsilon_T}\right)_{BL}$	$c_{\mu_{BL}}$
1.9	4.4	1.1667	1.0	0.5	3.6	1.0	0.115

of $\frac{k_P}{k_T} > 1$, this coefficient is positive, as one would expect, and that $\frac{k_P}{k_T}$ is not expected to assume values lower than 1, since that was the value calculated for $\left(\frac{k_P}{k_T}\right)_{DF}$. This ratio was also used in the first version of the NT1 model, but in the latter this ratio was not allowed to be different from unity. The values calculated for $\frac{k_P}{k_T}$ in the three simple cases studied for asymptotic analysis follow the expected relation $\left(\frac{k_P}{k_T}\right)_{DF} < \left(\frac{k_P}{k_T}\right)_{BL} < \left(\frac{k_P}{k_T}\right)_{SF}$ which has already been discussed before.

It is of value to mention that the procedure described above in detail is the procedure which led to the actual second version of the NT1 model. As the optimization procedure is actually a tuning process of the coefficients, since some parameters were discretely varied through the loops, a few different ways of finding the parameters were tested in order to increase the set of coefficients tested. Sometimes, an rms "error" lower than that provided by the actual second version of the NT1 model was found, however, when analysing the predictions of the set of homogeneous shear flows tested, the performance in the low shear cases was not very satisfactory. It will be thus shown later, when the performance of the second versions of the NT1 and NT2 models will be presented and discussed, that the second version of the NT1 model presented improved significantly the prediction of homogeneous low shear cases and kept the good predictions of the moderate and high shear cases.

6.2.3 The Second Version of the NT2 Model

The considerations described above for the second version of the NT1 model also led to the second version of the NT2 model, but taking into account their main difference which is the eddy viscosity expression, $\nu_t = c_\mu \frac{k^2}{\varepsilon_T}$.

When re-optimizing the coefficients of the NT2 model, it was noticed that when imposing $\left(\frac{k_P}{k_T}\right)_{BL}$ to be higher than 3, the NT2 model returned worse predictions of the set of homogeneous shear flow cases than the first version of the model, even after trying different expressions for C_{P1}, C_{P2} and C_{T1} and also after allowing $\left(\frac{k_P}{k_T}\right)_{DF}$ to be different from unity. It was then concluded that when using the total time scale, $\tau = \frac{k}{\varepsilon_T}$, in the eddy viscosity, lower rates for $\left(\frac{k_P}{k_T}\right)_{BL}$ were required in order to have an overall good performance of the model in a wide range of dimensionless shear η in the homogeneous shear flows, which is consistent with the first version of the NT2 model presenting $\left(\frac{k_P}{k_T}\right)_{BL} \approx 1.5$.

It was then decided to try to re-incorporate the extra term in the ε_P equation proposed by Hanjalic et al. (1980), presented in equation 3.45, in order to check if the presence of this term could help to improve the overall prediction of homogeneous shear flows. Since this term was initially identified to cause instabilities, the magnitude of the coefficient C'_{P1} was

set to be at most ten times smaller than the value originally used in the TS model.

Owing to the insertion of the term $C'_{P1}k_P\frac{\partial U_l}{\partial x_m}\frac{\partial U_i}{\partial x_j}\epsilon_{lmk}\epsilon_{ijk}$, which reduces to $C'_{P1}k_P\left(\frac{dU}{dy}\right)^2$ in purely shear flows, some equations of the asymptotic analyses previously used had to be modified.

The equations from the asymptotic analysis of decaying grid turbulence were not altered since the extra term is zero in this flow. Therefore equations 6.16 and 6.18 could be kept. In homogeneous shear flows and equilibrium boundary layer, ε_P equation is no longer the same as that used in the first version of the NT2 model and therefore equations 6.39, 6.28 and 6.46 had to be replaced by equations 6.55, 6.56 and 6.57 respectively:

$$\left(\frac{P_k}{\varepsilon_T}\right)_{SF} = \left(\frac{P_k}{\varepsilon_P}\right)_{SF}\left(\frac{\varepsilon_P}{\varepsilon_T}\right)_{SF} = 1.9 = \frac{\left[1 - c_{p21} + c_{p22}\frac{\left(\frac{k_P}{k_T}\right)_{SF}-1}{\left(\frac{k_P}{k_T}\right)_{SF}+1}\right]}{\left[1 - C_{P1} - \frac{C'_{P1}}{c_\mu}\left(\frac{k_P}{k}\right)^2\left(\frac{\varepsilon_T}{\varepsilon_P}\right)\right]_{SF}}\left(\frac{\varepsilon_P}{\varepsilon_T}\right)_{SF} \tag{6.55}$$

$$\left(\frac{k_P}{k_T}\right)_{BL} = \left\{\frac{\sigma_{\varepsilon_P}}{\sigma_{\varepsilon_T}}\frac{\left[C_{P2} - C_{P1} - \frac{C'_{P1}}{c_{\mu_{BL}}}\left(\frac{k_P}{k}\right)^2\right]}{(C_{T2} - C_{T1})}\right\}_{BL} \tag{6.56}$$

$$\sigma_{\varepsilon_P}\left[C_{P2} - C_{P1} - \frac{C'_{P1}}{c_\mu}\left(\frac{k_P}{k}\right)^2\right]_{BL} + \sigma_{\varepsilon_T}(C_{T2} - C_{T1})_{BL} = \frac{\kappa^2}{c_\mu^{1/2}} \tag{6.57}$$

Thereby, the system of equations from the asymptotic analyses it formed by equations 6.16, 6.18 and 6.50 from the decaying grid turbulence, equations 6.8, 6.9 and 6.55 from the homogeneous shear flows and equations 6.56 and 6.57 from local equilibrium boundary layers. It is of value to recall that $c_{\mu_{BL}} = 0.09$ in the NT2 model due to its eddy viscosity formulation, which is the same used in LEV STS models. However, by including the C'_{P1} term in the analyses, it is now necessary to find the value c_μ is supposed to assume in homogeneous shear flows, $c_{\mu_{SF}} = c_1 + c_2\exp(-c_3\eta_{SF})$, which actually means that one needs to find the value $\eta = \frac{k}{\varepsilon_T}\frac{dU}{dy}$ assumes in the asymptotic state of these flows. After some algebraic manipulation, one can arrive at the following expression:

$$\left(\frac{k}{\varepsilon_T}\frac{dU}{dy}\right)_{SF} = \eta_{SF} = \frac{1}{c_{\mu_{SF}}^{1/2}}\left(\frac{P_k}{\varepsilon_T}\right)_{SF}^{1/2}\left(\frac{k}{k_P}\right)_{SF}\left(\frac{\varepsilon_P}{\varepsilon_T}\right)_{SF}^{1/2} \tag{6.58}$$

The re-optimization procedure then consisted of a program in Matlab similar to that used for the second version of the NT1 model, but considering the particularities of this case. A loop for C_{T1} and C_{T2} made these vary from 0.8 to 1.2 by a 0.02 increment and thereby $\left(\frac{\varepsilon_P}{\varepsilon_T}\right)_{DF}$, $\left(\frac{k_P}{k_T}\right)_{DF}$ and $\left(\frac{\varepsilon_P}{\varepsilon_T}\right)_{SF}$ could be calculated from equations 6.18, 6.16 and 6.8 respectively. Since $\frac{P_k}{\varepsilon_T} = 1.9$ in homogeneous shear flows, $\left(\frac{k_P}{k_T}\right)_{SF}$ could also be calculated using equation 6.9. Inside these loops, a new loop was built for c_{p22} and $\left(\frac{k_P}{k_T}\right)_{BL}$, the former varying from 0 to 1.0 by a 0.1 increment and the latter varying from 3.0 to 4.5 by a 0.1 increment. c_{p21} could now be calculated through equation 6.50, considering that $C_{P2_{DF}} = 1.8$. Inside the $\frac{k_P}{k_T}$ loop, three

new loops were built for c_2, c_3 (from c_μ expression) and C'_{P1}. c_2 was set to vary from 0.2 to 0.3 by a 0.1 increment while c_3 varied from 0.25 to 0.4 by a 0.01 increment which allowed c_1 to be calculated using $c_1 = 0.09 - c2 * exp(-3.3c_3)$ so that $c_\mu = 0.09$ when $\eta = 3.3$. The value of $c_{\mu_{SF}}$ was then iteratively calculated using the Newton Raphson method and C'_{P1} was varied from -0.01 to 0 by a 0.001 increment. Now c_{p11} could be calculated using equation 6.55. Finally, σ_{ε_P} and σ_{ε_T} could be calculated by solving the system formed by equations 6.56 and 6.57. A last inner loop was set to vary c_{p21} from 0 to 3.0 by a 0.1 increment, since this parameter does not affect any asymptotic analysis as discussed before.

The simplest set of coefficients which provided the smallest rms "error" when comparing predictions and DNS data of a homogeneous low, moderate and high shear flows was chosen as the second version of the NT2 model. The transport equations for the NT2 model is then presented below and its coefficients and asymptotic states are presented in Tables 6.10 and 6.11 respectively.

$$\frac{Dk_P}{Dt} = P_k - \varepsilon_P + \frac{\partial}{\partial x_j}\left[\left(\nu + \frac{\nu_t}{\sigma_{k_P}}\right)\frac{\partial k_P}{\partial x_j}\right] \tag{6.59}$$

$$\frac{Dk_T}{Dt} = \varepsilon_P - \varepsilon_T + \frac{\partial}{\partial x_j}\left[\left(\nu + \frac{\nu_t}{\sigma_{k_T}}\right)\frac{\partial k_T}{\partial x_j}\right] \tag{6.60}$$

$$\frac{D\varepsilon_P}{Dt} = C_{P1}P_k\frac{\varepsilon_P}{k_P} - C_{P2}\frac{\varepsilon_P^2}{k_P} + C'_{P1}k_P\frac{\partial U_l}{\partial x_m}\frac{\partial U_i}{\partial x_j}\epsilon_{lmk}\epsilon_{ijk} + \frac{\partial}{\partial x_j}\left[\left(\nu + \frac{\nu_t}{\sigma_{\varepsilon_P}}\right)\frac{\partial \varepsilon_P}{\partial x_j}\right] \tag{6.61}$$

$$\frac{D\varepsilon_T}{Dt} = C_{T1}\frac{\varepsilon_P^2}{k_T} - C_{T2}\frac{\varepsilon_T^2}{k_T} + \frac{\partial}{\partial x_j}\left[\left(\nu + \frac{\nu_t}{\sigma_{\varepsilon_T}}\right)\frac{\partial \varepsilon_T}{\partial x_j}\right] \tag{6.62}$$

Table 6.10: Coefficients of the second version of the NT2 model

c_μ	C_{P1}	C_{P2}	σ_{ε_P}	C_{T1}	C_{T2}	σ_{ε_T}	C'_{P1}
$min[0.09, 0.0117 + 0.22e^{-0.31\eta}]$	$1.5697 + 2.5\frac{min(0,\frac{k_P}{k_T}-3.7)}{\frac{k_P}{k_T}+3.7}$	1.8	1.6664	1.0	1.1	1.1922	-0.005

Table 6.11: Values expected to be provided by the second version of the NT2 model in the asymptotic states studied

$\left(\frac{P_k}{\varepsilon_T}\right)_{SF}$	$\left(\frac{k_P}{k_T}\right)_{SF}$	$\left(\frac{\varepsilon_P}{\varepsilon_T}\right)_{SF}$	$\left(\frac{k_P}{k_T}\right)_{DF}$	$\left(\frac{\varepsilon_P}{\varepsilon_T}\right)_{DF}$	$\left(\frac{k_P}{k_T}\right)_{BL}$	$\left(\frac{\varepsilon_P}{\varepsilon_T}\right)_{BL}$	$c_{\mu_{BL}}$	$c_{\mu_{SF}}$
1.9	8.8245	1.0916	1.3166	0.5683	3.7	1.0	0.09	0.0336

Commenting on the new coefficients and asymptotic states of the second version of the NT2 model, one may notice that this model is also rather different from the original TS model, starting with the different expression for the eddy viscosity. As in the second version

of the NT1 model, now C_{P2} is a constant and C_{P1} varies with $\frac{k_P}{k_T}$. C_{T1} remained as a function of $\frac{\varepsilon_P}{\varepsilon_T}$. However, by incorporating $\frac{\varepsilon_P}{\varepsilon_T}$ into the source term of the ε_T equation, the resulting transport equation for this quantity is equation 6.62 and C_{T1} can be expressed as a constant. Here, the asymptotic states also respect the relation $\left(\frac{k_P}{k_T}\right)_{DF} < \left(\frac{k_P}{k_T}\right)_{BL} < \left(\frac{k_P}{k_T}\right)_{SF}$, but $\left(\frac{k_P}{k_T}\right)_{DF}$ is no longer 1.0, but 1.3166. As a consequence, $\left(\frac{\varepsilon_P}{\varepsilon_T}\right)_{DF}$ is no longer 0.5, but a slightly higher value, 0,5683, which is also smaller than one as expected. $\left(\frac{k_P}{k_T}\right)_{BL}$ is almost the same as in the second version of the NT1 model, however $\left(\frac{k_P}{k_T}\right)_{SF}$ is almost twice the value predicted by the second version of the NT1 model. The extra source term, followed by the C'_{P1} coefficient, was found to be important in improving prediction of the homogeneous low shear cases and due to its new absolute lower magnitude (now -0.005 against -0.11 in the TS model), this term no longer produces instabilities.

As will be seen when the performance of the second versions of the NT1 and NT2 models will be discussed, the second version of the NT2 model provided improvements over the first version of the model, specially regarding the prediction of homogeneous low shear cases.

6.2.4 Attempt of Introducing Extra Source Term in the Second Version of the NT1 Model

As the second version of the NT2 model showed that the addition of the extra source term in the ε_P equation, proposed by Hanjalic et al. (1980), $C'_{P1} k_P \frac{\partial U_l}{\partial x_m} \frac{\partial U_i}{\partial x_j} \epsilon_{lmk} \epsilon_{ijk}$, improved prediction of homogeneous shear flows, it was worth testing if the addition of this term into the NT1 formulation, keeping a low magnitude of the coefficient C'_{P1}, could improve even more the predictions of the second version of the NT1 model.

The same procedure already outlined before about the asymptotic states was then carried out in order to include the new term in the ε_P equation. The flexibilities used before about the C_{P1}, C_{P2} and C_{T1} coefficients as well as about the value $\left(\frac{k_P}{k_T}\right)_{DF}$ should assume were also applied in these tests.

It was then confirmed that for the NT1 formulation, where $\nu_t = c_\mu \frac{k k_P}{\varepsilon_P}$, the extra source term initially used in the TS model would not contribute to improve prediction of homogeneous shear flows. When the best overall set of coefficients, which provided the minimum rms "error", were displayed, C'_{P1} would come out as zero.

The reason why only predictions of the homogeneous shear flows are being mentioned here is that these flows were used in order to tune the coefficients as already commented on before. Only the set of coefficients which performs well in these flows were further tested in the other flows.

6.2.5 Turbulent Viscosity Study

Two different turbulent viscosities were tested so far in the MTS models which are being developed: one considering the time scales associated with the large eddies, $\nu_t = c_\mu \frac{k k_P}{\varepsilon_P}$, used in the NT1 model and another considering the total time scale, $\nu_t = c_\mu \frac{k^2}{\varepsilon_T}$, used in the NT2 model. So far, no significant difference could be noticed in the predictive capabilities of the

two eddy viscosity formulations, though the eddy viscosity based on the total time scale, NT2 model, needed an extra term in the ε_P equation in order to provide as good results as the NT1 formulations, based on the large eddies' time scale.

An analysis of other eddy viscosity formulations was then carried out in order to identify if other expressions should be considered for further development.

The eddy viscosity is usually generally expressed as $\nu_t = c_\mu \vartheta \ell$: the product of a coefficient, c_μ, a velocity scale, ϑ, and a length scale, ℓ. The latter can be expressed as a function of the time scale $\ell = \vartheta\tau$ which then allows one to express the eddy viscosity as:

$$\nu_t = c_\mu \vartheta^2 \tau \tag{6.63}$$

This way of expressing the eddy viscosity is convenient when dealing with multiple-time-scale models, because it allows one to make the time scale explicit in the ν_t expression. In the current two-time-scale framework, one has three possible velocity scales and three possible time scales. The velocity scale can refer to the large eddies, $k_P^{1/2}$, to the small eddies, $k_T^{1/2}$ or to the total spectrum, $k^{1/2}$, the latter being the one used in STS models. The time scale can also be related to these three partitions, respectively, $\frac{k_P}{\varepsilon_P}$, $\frac{k_T}{\varepsilon_T}$ and $\frac{k}{\varepsilon_T}$.

There are therefore eight different possible expressions for the eddy viscosity, as summarized in Table 6.12. One may notice that ν_{t_1} and ν_{t_3} are the eddy viscosities used in the NT1 and NT2 formulations respectively. It remains then to evaluate the other six possibilities.

Table 6.12: Possible expressions for ν_t in two-time-scale models.

	$\tau = \frac{k_P}{\varepsilon_P}$	$\tau = \frac{k_T}{\varepsilon_T}$	$\tau = \frac{k}{\varepsilon_T}$
$\vartheta^2 = k$	$\nu_{t_1} = c_\mu \frac{k k_P}{\varepsilon_P}$	$\nu_{t_2} = c_\mu \frac{k k_T}{\varepsilon_T}$	$\nu_{t_3} = c_\mu \frac{k^2}{\varepsilon_T}$
$\vartheta^2 = k_P$	$\nu_{t_4} = c_\mu \frac{k_P^2}{\varepsilon_P}$	$\nu_{t_5} = c_\mu \frac{k_P k_T}{\varepsilon_T}$	$\nu_{t_6} = c_\mu \frac{k_P k}{\varepsilon_T}$
$\vartheta^2 = k_T$	$\nu_{t_7} = c_\mu \frac{k_T k_P}{\varepsilon_P}$	$\nu_{t_8} = c_\mu \frac{k_T^2}{\varepsilon_T}$	$\nu_{t_9} = \nu_{t_2}$

The first criteria to evaluate the eddy viscosity expressions was to calculate what would be the expected values of c_μ in local equilibrium boundary layer, considering that $\left(\frac{k_P}{k_T}\right)_{BL} \geq 3$. A procedure similar to that carried out in equation 6.34 was implemented for each ν_t expression in Table 6.12. The results are summarized in Table 6.13, including those already known for ν_{t_1} and ν_{t_3} for the sake of comparison.

Examining Table 6.13, it is possible to eliminate straight away ν_{t_2}, ν_{t_5}, ν_{t_7} and ν_{t_8}. The reason for that is that using any of these expressions, $c_{\mu_{BL}}$ would have to assume rather high values which are expected to cause instabilities in wall-bounded flows. Indeed, the maximum possible value for $c_{\mu_{BL}}$ when using ν_{t_4} is quite high as well, however that is the maximum expected value and one could study if such high value would be really necessary. So from the six extra possible eddy viscosity expressions, the analysis of $c_{\mu_{BL}}$ narrowed down the possibilities to two: ν_{t_4} and ν_{t_6}.

The asymptotic analyses carried out before for decaying grid turbulence, homogeneous

Table 6.13: Expected values of $c_{\mu_{BL}}$ according to ν_t expressions in Table 6.12.

ν_{t_1}	$c_{\mu_{BL}}\left(\frac{k_P}{k}\right)_{BL} = 0.09 \rightarrow c_{\mu_{BL}} \leq 0.12$
ν_{t_2}	$c_{\mu_{BL}}\left(\frac{k_T}{k}\right)_{BL} = 0.09 \rightarrow c_{\mu_{BL}} \geq 0.36$
ν_{t_3}	$c_{\mu_{BL}} = 0.09$
ν_{t_4}	$c_{\mu_{BL}}\left(\frac{k_P}{k}\right)^2_{BL} = 0.09 \rightarrow c_{\mu_{BL}} \leq 0.16$
ν_{t_5}	$c_{\mu_{BL}}\left(\frac{k_P}{k}\right)_{BL}\left(\frac{k_T}{k}\right)_{BL} = 0.09 \rightarrow c_{\mu_{BL}} \geq 0.48$
ν_{t_6}	$c_{\mu_{BL}}\left(\frac{k_P}{k}\right)_{BL} = 0.09 \rightarrow c_{\mu_{BL}} \leq 0.12$
ν_{t_7}	$c_{\mu_{BL}}\left(\frac{k_P}{k}\right)_{BL}\left(\frac{k_T}{k}\right)_{BL} = 0.09 \rightarrow c_{\mu_{BL}} \geq 0.48$
ν_{t_8}	$c_{\mu_{BL}}\left(\frac{k_T}{k}\right)^2_{BL} = 0.09 \rightarrow c_{\mu_{BL}} \geq 1.44$

shear flows and local equilibrium boundary layers were also carried out using both ν_{t_4} and ν_{t_6} expressions. Tests were carried out considering all the flexibilities allowed before in the C_{P1}, C'_{P1}, C_{P2} and C_{T1} coefficients and $\left(\frac{k_P}{k_T}\right)_{DF}$ was not imposed to be 1. It is worth noting that if C'_{P1} is zero, the asymptotic state equations used in the NT1 model remain exactly the same for ν_{t_6}, since this expression would only be necessary in local equilibrium boundary layer analysis (equation 6.29) and in this situation, $\varepsilon_P = \varepsilon_T$, thus making $\nu_{t_1} = \nu_{t_6}$. If C'_{P1} is not zero, the asymptotic state equation of $\frac{P_k}{\varepsilon_T}$ in homogeneous shear flows would be different from those used in the NT1 and NT2 models when ν_{t_1} and ν_{t_3} were used. When using ν_{t_4}, the asymptotic state equations for local equilibrium boundary layers are different from those presented for the NT1 and NT2 models independently of C'_{P1} being zero or not. However, if C'_{P1} is zero, the asymptotic state equations for decaying grid turbulence and homogeneous shear flows remain the same presented here before and $\frac{P_k}{\varepsilon_T}$ in homogeneous shear flows assumes a different form if C'_{P1} is not zero.

The tests carried out with ν_{t_4} provided good overall prediction of homogeneous shear flows, however, to achieve these good results, $c_{\mu_{BL}}$ had to assume its highest possible imposed value, $c_{\mu_{BL}} = 0.16$, according to Table 6.13. Although these results were good, the overall rms "error" returned when determining the model's coefficients by predicting homogeneous shear flows was still higher than the overall rms "error" returned by the second versions of the NT1 and NT2 models. For this reason, combined with a relatively higher value of $c_{\mu_{BL}}$, whose stability would have to be investigated in wall-bounded flows, the ν_{t_4} expression was abandoned.

The tests carried out with ν_{t_6} did not provide overall good prediction of homogeneous shear flows, specially in the low shear cases, even when C'_{P1} was allowed to be different from zero. For this reason, this expression of the eddy viscosity was also abandoned.

After all these analyses, the eddy viscosity expressions used by the NT1 and NT2 models, ν_{t_1} and ν_{t_3} respectively, proved to be the most appropriate for two-time-scale models. It is interesting to notice that the NG and TS models also used the ν_{t_1} formulation, the KC model used the ν_{t_3} expression, however the CG model used $\nu_t = \frac{k^2}{\varepsilon_P}$. This expression was

not considered here, since it would imply the time scale to be $\tau = \frac{k}{\varepsilon_P}$ which apparently does not have a clear physical meaning once k is the total turbulent kinetic energy and ε_P is the energy transfer rate between the large and small eddies.

6.2.6 Turbulent Kinetic Energy Spectrum Study

As multiple-time-scale models have been the main focus of attention here, more precisely, two-time-scale models, it was decided to briefly investigate the turbulent kinetic energy spectrum in order to understand it better and try to find any eventual parameter or correlation which could be useful in the turbulence modelling process.

The turbulent kinetic energy spectrum will be evaluated through the Kolmogorov hypotheses which are considered a good approximation and match several experimental works (Tennekes and Lumley, 1972).

Kolmogorov examined both the small and the large scales of motions and his three hypotheses led to a formal mathematical expression for the turbulent kinetic energy spectrum.

The first two hypotheses are related to the small scales and state that they are statistically isotropic and have a universal form which depends only on the kinematic viscosity ν and the eddy dissipation rate ε. Based on this, he defined the small scales' length, time and velocity through dimensional analysis. These became known as the Kolmogorov length, time and velocity scales which can be expressed as $\eta = (\nu^3/\varepsilon)^{1/4}$, $\tau_\eta = (\nu/\varepsilon)^{1/2}$ and $u_\eta = (\varepsilon\nu)^{1/4}$ respectively.

The simplified spectrum proposed by Kolmogorov is divided into two main regions: the energy-containing range and the universal equilibrium range. The latter is further divided into two subregions: the inertial range and the dissipation range. The sketch is represented in Figure 6.31 from Pope (2000), where $\kappa = 2\pi/\ell$ is the wavenumber of an eddy of averaged size ℓ.

Kolmogorov then proposed that, at very high Reynolds numbers, there would be a range of length, velocity and time scales which are smaller than the main flow's ones, but still significantly higher than those from the very smallest eddies. The third hypothesis regards these intermediate scales of motions and states that they also have a universal form which depends only on the eddy dissipation rate ε.

Comparing the Kolmogorov spectrum with the spectrum proposed by Hanjalic et al. (1980), one can say that the latter is rather aligned with the former. The Universal-equilibrium range would be represented by both the Transfer and Dissipation zones defined by Hanjalic et al. (1980) which then match the Inertial and Dissipation subranges proposed by Kolmogorov. The Production zone of Hanjalic et al. (1980) is then obviously the Energy-containing range of the Kolmogorov spectrum. That means, the Kolmogorov spectrum also assumes equilibrium between the transfer and dissipation zones ($\varepsilon_T = \varepsilon$) which is exactly what Hanjalic et al. (1980) proposed.

Pope (2000) also drew attention to the fact that, as a consequence of the third Kolmogorov hypothesis, which states that the scale motions in the inertial subrange depend only on inertial

effects, therefore only on the eddy dissipation rate, both velocity and time scales decrease as the eddy length scale ℓ increases in the spectrum, or equivalently, as the wave number κ of this eddy increases in the turbulent kinetic energy spectrum. That is again in agreement with expecting the ratio between small and large eddies time scales in the two-time-scale models to be smaller than unity, $\frac{\tau_T}{\tau_P} < 1$.

It remains then to understand where in the spectrum $\frac{k_P}{k_T}$ is expected to be. The turbulent kinetic energy associated with eddies confined between two wavenumbers κ_1 and κ_2 is formally expressed as a function of the energy density per unit wave number $E(\kappa)$, also referred to as the energy-spectrum function:

$$k(\kappa_1 \text{ until } \kappa_2) = \int_{\kappa_1}^{\kappa_2} E(\kappa) d\kappa \tag{6.64}$$

The most important result of the Kolmogorov hypotheses is that they led to an expression for the energy-spectrum function in the Inertial subrange also known as the Kolmogorov $-\frac{5}{3}$ spectrum:

$$E(\kappa) = C\varepsilon^{2/3}\kappa^{-5/3} \tag{6.65}$$

In the above equation, C is considered a universal constant determined through experiments to be 1.5 (Tennekes and Lumley (1972), Pope (2000)).

In order to calculate k, the $E(\kappa)$ function is often non-dimensionalized either with the large or the small length scales. In the former case, kL (k, the total turbulent kinetic energy and L that length scale associated with the large eddies) is usually used and in the latter, ηu_η^2. In order to proceed with the turbulent kinetic energy spectrum analysis, the latter will be used:

$$E(\kappa)\eta^{-5/3} = C\varepsilon^{2/3}(\kappa\eta)^{-5/3} = E(\kappa)\frac{\nu^{-5/4}}{\varepsilon^{-5/12}} \Rightarrow \frac{E(\kappa)}{\nu^{5/4}\varepsilon_{1/4}} = \frac{E(\kappa)}{\eta u_\eta^2} = C(\kappa\eta)^{-5/3} \tag{6.66}$$

This equation is usually known as the Kolmogorov $-\frac{5}{3}$ power law.

In order to calculate the total turbulent kinetic energy, by integrating equation 6.64, it is necessary to know $E(\kappa)$ in the Energy-containing and Dissipation ranges as well. Both Tennekes and Lumley (1972) and Pope (2000) present non-dimensional functions which match experiments satisfactorily. Using the ones presented by Pope (2000), the energy-spectrum function can be expressed for the whole domain as:

$$\frac{E(\kappa)}{\eta u_\eta^2} = C(\kappa\eta)^{-5/3} f_L(\kappa L) f_\eta(\kappa\eta) \tag{6.67}$$

Where f_L and f_η are the functions to model the Energy-containing and Dissipation ranges

presented in equations 6.68 and 6.69 respectively. Both these functions reduce to unity in the Inertial subrange where the $-\frac{5}{3}$ power law rules the spectrum.

$$f_L(\kappa L) = \left(\frac{\kappa L}{[(\kappa L)^2 + 6.78]^{1/2}} \right)^{5/3+2} \tag{6.68}$$

$$f_\eta(\kappa\eta) = \exp\{-5.2([(\kappa\eta)^4 + 0.4^4]^{1/4} - 0.4)\} \tag{6.69}$$

Although f_L is presented in equation 6.68 as a function of κL, which is the natural large eddies scaling, L can be easily converted into η, using the turbulent Reynolds number, $Re_t = \frac{k^2}{\nu\varepsilon} = \frac{u_0 L}{\nu}$, and the relation $\varepsilon = \frac{u_0^3}{L}$ which comes from assuming equilibrium between the three ranges in the spectrum (Pope, 2000). In these relations, u_0 is the velocity scale of the large eddies.

$$\eta = (\nu^3/\varepsilon)^{1/4} = \frac{\nu^{3/4} L^{1/4}}{u_0^{3/4}} \Rightarrow \frac{\eta}{L} = \frac{\nu^{3/4}}{u_0^{3/4} L^{3/4}} \Rightarrow \frac{\eta}{L} = Re_t^{-3/4} \tag{6.70}$$

Using equations 6.67, 6.68, 6.69 and 6.70, the spectrum was reproduced here for two Reynolds Taylor numbers: $Re_\lambda = 50$ and $Re_\lambda = 2000$, presented in Figures 6.32 and 6.33. The Reynolds Taylor number can be directly obtained by the turbulent Reynolds number through the relation $Re_\lambda = \left(\frac{20}{3} Re_t\right)^{1/2}$. Equation 6.64 was integrated in the ranges shown in these Figures and the total turbulent kinetic energy as well as the energy of each range were calculated. The ranges are defined through the black vertical lines in Figures 6.32 and 6.33. Additionally, it is also presented the value of $\kappa\eta$ which provides the different values of $\frac{k_P}{k_T}$ in equations 6.71 and 6.72 and these are marked in orange vertical lines. In the spectrum of Hanjalic et al. (1980), the turbulent kinetic energy is stored only in the production and transfer zones, since no turbulent kinetic energy is considered in the dissipation zone. Thereby, the way k_P and k_T were calculated is:

$$k_P = \int_{10^{-5}}^{\kappa\eta} E(\kappa\eta) d(\kappa\eta) \tag{6.71}$$

$$k_T = \int_{\kappa\eta}^{10} E(\kappa\eta) d(\kappa\eta) \tag{6.72}$$

Tests were carried out in order to test the limits of integration. No significant difference in the values of the total and partial turbulent kinetic energy were found if integrated from $\kappa\eta < 10^{-5}$ and $\kappa\eta > 10^1$.

In Figures 6.32 and 6.33, the green line is the $-\frac{5}{3}$ power law and the blue line is the total turbulent kinetic energy as in equation 6.67. That confirms that both f_L and f_η functions are different from unity only out of the Inertial subrange.

The first important observation to make is that $1 < \frac{k_P}{k_T} < 10$ is within the Inertial

subrange. This result is desirable, since the NT1 and NT2 models predict $\frac{k_P}{k_T}$ to be in this range and it means the spectrum is being split yet in a region where viscous effects are negligible, but where the length, velocity and time scales are expected to be smaller than those of the main flow.

Through the calculation of the turbulent kinetic energy stored in each range of the Kolmogorov spectrum, also presented in Figures 6.32 and 6.33, one may notice that the assumption of Hanjalic et al. (1980) that no turbulent kinetic energy is stored in the dissipation zone is in agreement with the calculations shown in these Figures. The amount of turbulent kinetic energy stored in this zone is definitely much smaller than that stored in the other two zones and the higher the Reynolds number, the more negligible it is.

It is of value then to evaluate the range of the Reynolds Taylor number, Re_λ, in the different test cases studied, using the second version of the NT1 and NT2 models. The Reynolds Taylor number, which is equivalent to the turbulent Reynolds number, might arise as a useful parameter to improve the performance of the models in the oscillatory pipe flows, for example. The ranges of Re_λ in the different test cases are presented in Table 6.14 for the region far from the wall, where this parameter goes to zero due to the no-slip conditions. Values of Re_λ in homogeneous shear flows and normally strained flows are not being shown since these flows are unbounded flows and therefore are expected to have very high Reynolds numbers.

Table 6.14 thus shows that the Reynolds Taylor numbers of these flows are not very high, however an Inertial range is still expected to exist. Besides, by analysing Table 6.14, one can see that most test cases share similar ranges of Re_λ which then does not make it an interesting parameter to improve prediction of only oscillatory pipe flows.

Table 6.14: Ranges of the Reynolds Taylor number in the different test cases studied.

Test Case	Re_λ
Channel Flows	30 - 80
ZPGBL	50 - 180
APGBL	90 - 250
FPGBL	30 - 40
Oscillatory Boundary Layers	30 - 120
Oscillatory Pipe Flows	80 - 200
Ramp Up Flow	30 - 80

6.2.7 Performance of the Second versions of the NT1 and NT2 models

The second versions of the NT1 and NT2 models were then tested in all test cases used for the first versions and then they were also tested in steady and pulsated flows in backward facing steps. A brief discussion of the results will be then carried out by comparing the performance of the first and second versions of the NT1 and NT2 models.

Firstly though, it is important to check whether the increase in the predicted value for $\left(\frac{k_P}{k_T}\right)_{BL}$, the turbulent kinetic energy partitions ratio in the local equilibrium regions of boundary layers, did solve the problem of the ratio between the small and large time scales being

higher or too close to 1. The prediction of the time scale ratio as well as of $\frac{k_P}{k_T}$ and $\frac{\varepsilon_P}{\varepsilon_T}$ are presented in Figures 6.34, 6.35 and 6.36 respectively and one can see that now the time scale ratio is well below unity and $\frac{k_P}{k_T}$ is consistent with the predicted values, presented in Tables 6.8 and 6.10 for $\left(\frac{k_P}{k_T}\right)_{BL}$. Besides, the increase in the latter did avoid that peak in $\frac{\varepsilon_P}{\varepsilon_T}$ at the edge of the boundary layer previously presented by the first versions of the NT1 and NT2 models in Figure 6.28.

The results for homogeneous shear flows are shown for the lowest shear case $X2$, the moderate case $HM1$ and the high shear case SHC (Table 5.1). The prediction of the turbulent kinetic energy, the eddy dissipation rate and the Reynolds shear stress for each of these cases are presented in Figures 6.37, 6.38 and 6.39. One can see that the second version of the models clearly improved prediction of the low shear case and maintained the good prediction of the moderate and high shear cases.

Another clear improvement provided by the second version of the models can be seen in the prediction of the turbulent kinetic energy in the normally strained cases, presented in Figure 6.40. For both $T\&R$ and $G\&M0$ cases, the prediction of the second versions of the NT1 and NT2 models is closer to the experimental data when compared to the predictions provided by the first version of the models. The prediction for the $G\&M05$ case was not improved, however that is expected since the second versions of the NT1 and NT2 models are still linear-eddy-viscosity schemes and therefore insensitive to changes in the sign of the normal straining.

The prediction of the velocity, turbulent kinetic energy and eddy dissipation rate in the channel flow with $Re = 41441$ is presented in Figure 6.41. As one would expect, no significant difference can be seen in the prediction of these quantities in channel flows. However, that ensures the second versions of the NT1 and NT2 models do reproduce the expected behaviour for the asymptotic state of local equilibrium boundary layer.

The prediction of the velocity and Reynolds shear stress profiles in the zero pressure gradient boundary layer cases are presented at $Re_\theta = 1410$ and $Re_\theta = 13052$ in Figure 6.42. One can notice that both versions of the models result in the prediction of identical velocity profiles, however the second version of the models did improve the decay rate of the Reynolds shear stress at the outer layer.

The velocity, Reynolds shear stress and turbulent kinetic energy profiles at four measurement stations are respectively presented in Figures 6.43, 6.44 and 6.45 for the $M\&P30$ adverse pressure gradient boundary layer case. One may notice that the second version of the models perform similarly to the first versions, still not being able to follow the subtle changes the experiments do. These results are similar to the other two adverse pressure gradient boundary layer cases and therefore are not being presented here.

Very similar predictions between the two versions of the NT1 and NT2 models can also be seen in the favourable pressure gradient boundary layer case with the lowest acceleration parameter case, presented in Figure 6.46. These results are similar for the other acceleration parameter cases and therefore are not being shown now.

With regard to the prediction of the oscillatory boundary layer and pipe flows, the only

case where there was a noticeable difference in the prediction of the two versions of the models was the $T3RE14A20$ case, where an intermediate frequency of oscillation is used. That is actually expected, since the oscillatory boundary layer is often well predicted by all models and the oscillatory pipe flow cases $Tu\&R05$ and $Tu\&R36$ present either too low or too high frequencies which reduces the cases to either a series of steady state profiles or frozen turbulence, as seen before, also not presenting much difference in the prediction of the different models. The prediction of the velocity and Reynolds shear stress amplitude and phase shift are presented in Figure 6.47. One may notice that the second versions of the NT1 and NT2 models did not improve the prediction of the Reynolds shear stress phase shift, which was the main focus of attention for improvements in the first version of the models, however they provide slightly worse predictions which do not compromise the performance of the models. The prediction of the Reynolds shear stress amplitude is slightly worse for the second version of the NT1 model and slightly better for the second version of the NT2 models when compared to their first version counterparts. The prediction of the velocity phase shift is slightly improved at the centre of the pipe by the second version of the models and the prediction of the velocity amplitude is equivalent for both versions of the models.

Finally, the performance of the second versions of the NT1 and NT2 models in the ramp up flow is being assessed by the prediction of the turbulent kinetic energy at different positions in the radial direction, presented in Figure 6.48. The prediction of the velocity profile and Reynolds shear stress are usually reasonable for all models and so it is for the second versions of the NT1 and NT2 models. The second version of the NT1 model clearly improved the prediction of k at the centre of the pipe, however it tended to provide a low level of this quantity at $r/R = 0.47$. The opposite effect occurred with the second version of the NT2 model which improved the prediction of the turbulent kinetic energy at $r/R = 0.47$ and overpredicted it at the centre of the pipe. Both models provided good predictions at $r/R = 0.83$.

The second versions of the NT1 and NT2 models were then used to simulate the three backward facing step cases considered in this work, presented in Chapter 5. The prediction of the time-averaged location of the reattachment point and the velocity profiles at $x/H = -0.02, 1, 3, 5, 7, 9$ are discussed. The time-averaged locations of the reattachment points predicted by the second versions of the NT1 and NT2 models are presented in Table 6.15, where they are also compared to those predicted by the HR, SG KC and TS models for each backward facing step case. The KC model are used here because the TS model did not converge for the unsteady backward facing step cases and it is interesting to compare the results with other LEV MST model.

In Table 6.15 one can see that the second version of the NT1 model performs similarly to the KC model, overpredicting the time-averaged reattachment point in the steady and high frequency cases and is not able to reduce the time-averaged reattachment length enough in the low frequency case, thus completely overpredicting this parameter. The second version of the NT2 model provided even more highly over-predicted values, thus not performing well in any of the three cases.

Table 6.15: Performance of the second version of the NT1 and NT2 in predicting the time-averaged reattachment point in the three backward facing step cases.

Model/Experiment	St=0	St=0.275	St=1
Experiment	7.8	5.0	8.1
HR	6.42	5.01	6.67
SG	6.95	5.51	7.66
KC	8.44	7.21	9.15
TS	4.14	-	-
NT1_V2	8.63	8.16	9.3
NT2_V2	9.5	9.25	10.2

The velocity profiles at different positions downstream of the step clearly reflect the overpredicted location of the reattachment points. In Figure 6.49, one may notice that the second versions of the NT1 and NT2 models performed reasonably well in the $BFS - St0$ case until $x/H = 7$ and not very well at $x/H = 9$, which is already after the reattachment point. The NT1 model provides similar velocity profiles to those of the SG model, which actually underpredicts the location of the reattachment point at the steady state. That is due to the low post-channel profile recovery characteristic of RST models discussed before. The HR model performs apparently best, however, as also discussed before, that is due to its underprediction of the location of the reattachment point. The TS model which completely underpredicts the location of the reattachment point in the steady state, does not provide such reasonably good velocity profiles, as also commented on before.

The time-averaged velocity profile at the five positions downstream of the step in the $BFS-St0275$ case is presented in Figure 6.50. One may notice that in this case, only the HR model performed reasonably well, since it predicted correctly the time-averaged reattachment point, as can be seen in Table 6.15. The second version of both NT1 and NT2 models perfomed poorly due to its big overprediction of the location of the reattachment point. Although the SG model provided reasonable prediction for the reattachment point at this low frequency case, it still overpredicts the velocity profile. The KC model provided a slightly better profile of the velocity than the NT1 model and that is probably related to its better prediction of the time-averaged reattachment point, which is still far above the experimental data.

In the $BFS - St1$ case the time-averaged velocity profile, presented in Figure 6.51, is reasonably well predicted up to $x/H = 9$ by all models. As discussed before, that is probably due to the long reattachment length ($x/H = 8.1$) together with the last position where experimental data is available for comparison being at $x/H = 9$. In this case, although the NT1 and NT2 models provide overpredicted values for this parameter, the prediction of velocity is still reasonably good.

On the whole, one can say that the second versions of the NT1 and NT2 models solved the problem of high time scale ratios, now fully respecting the turbulent kinetic energy spectrum, and clearly improved prediction of the homogeneous shear flows and normally strained flows and performed reasonable well in all tested flows, but the backward facing step cases which clearly indicated that some more improvements were needed in the NT1 and NT2 models.

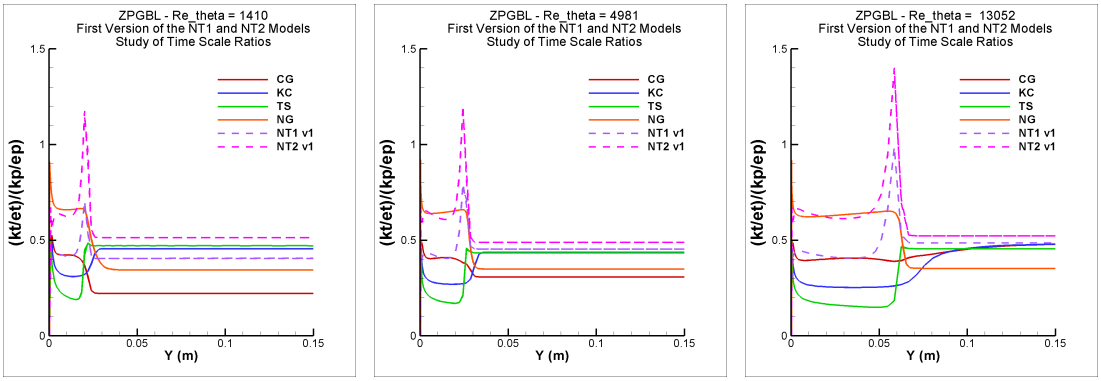

(a) $Re_\theta = 1410$ (b) $Re_\theta = 4981$ (c) $Re_\theta = 13052$

Figure 6.26: Time scale ratio, $\frac{\tau_T}{\tau_P} = \frac{k_T/\varepsilon_T}{k_P/\varepsilon_P}$, in the zero pressure gradient boundary layer: assessing the first versions of the NT1 and NT2 models. Models as in Table 3.25.

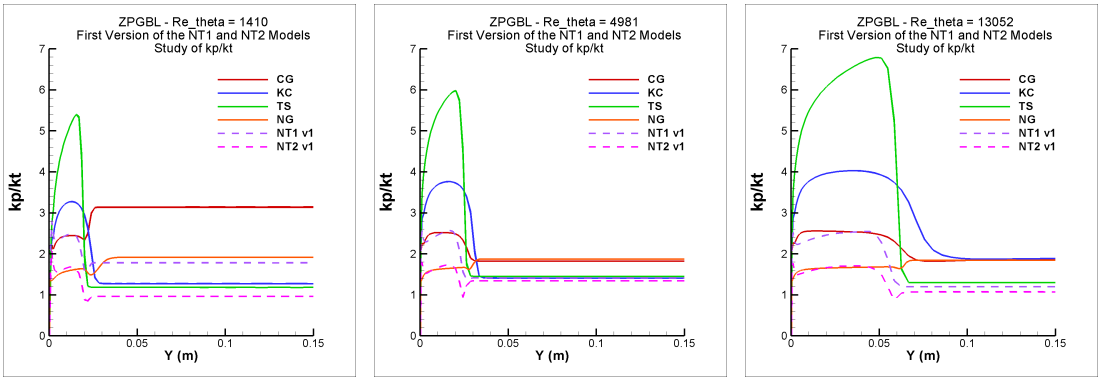

(a) $Re_\theta = 1410$ (b) $Re_\theta = 4981$ (c) $Re_\theta = 13052$

Figure 6.27: Turbulent kinetic energy partitions ratio, $\frac{k_P}{k_T}$, in the zero pressure gradient boundary layer: assessing the first versions of the NT1 and NT2 models. Models as in Table 3.25.

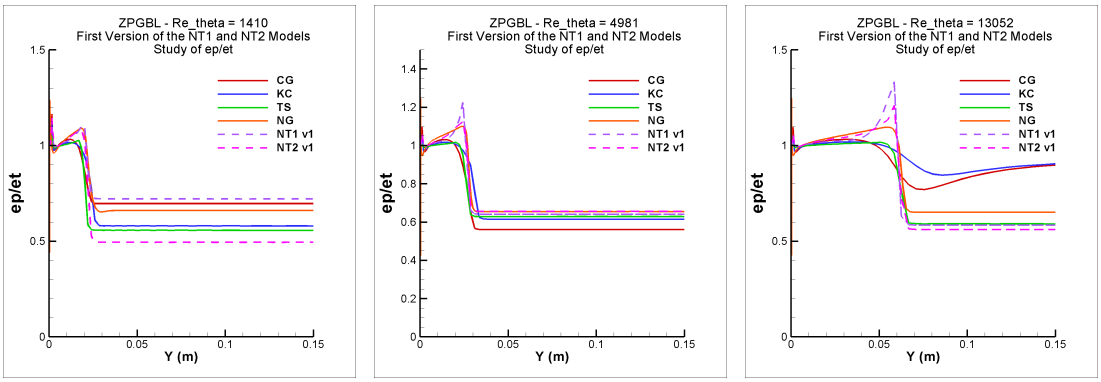

(a) $Re_\theta = 1410$ (b) $Re_\theta = 4981$ (c) $Re_\theta = 13052$

Figure 6.28: Turbulent kinetic energy transfer rates ratio, $\frac{\varepsilon_P}{\varepsilon_T}$, in the zero pressure gradient boundary layer: assessing the first versions of the NT1 and NT2 models. Models as in Table 3.25.

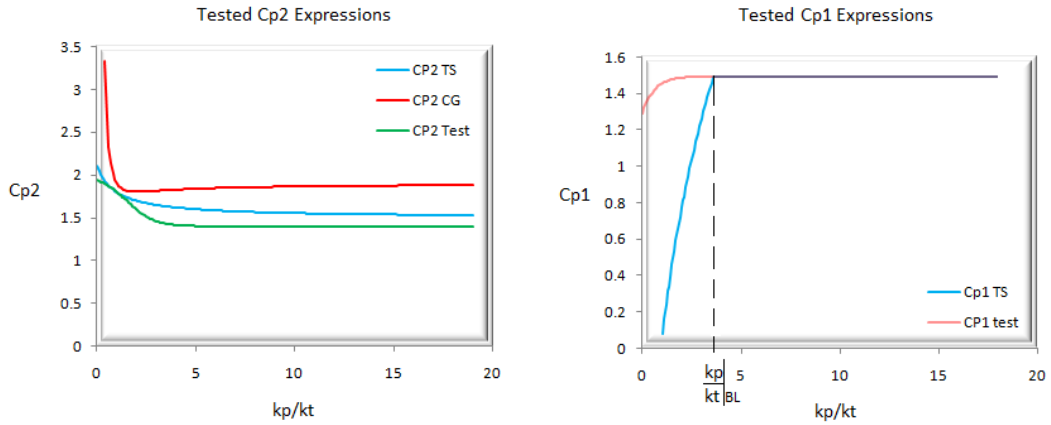

(a) C_{P2} profiles (b) C_{P1} profiles

Figure 6.29: Curves for C_{P1} and C_{P2} as a function of $\frac{k_P}{k_T}$.

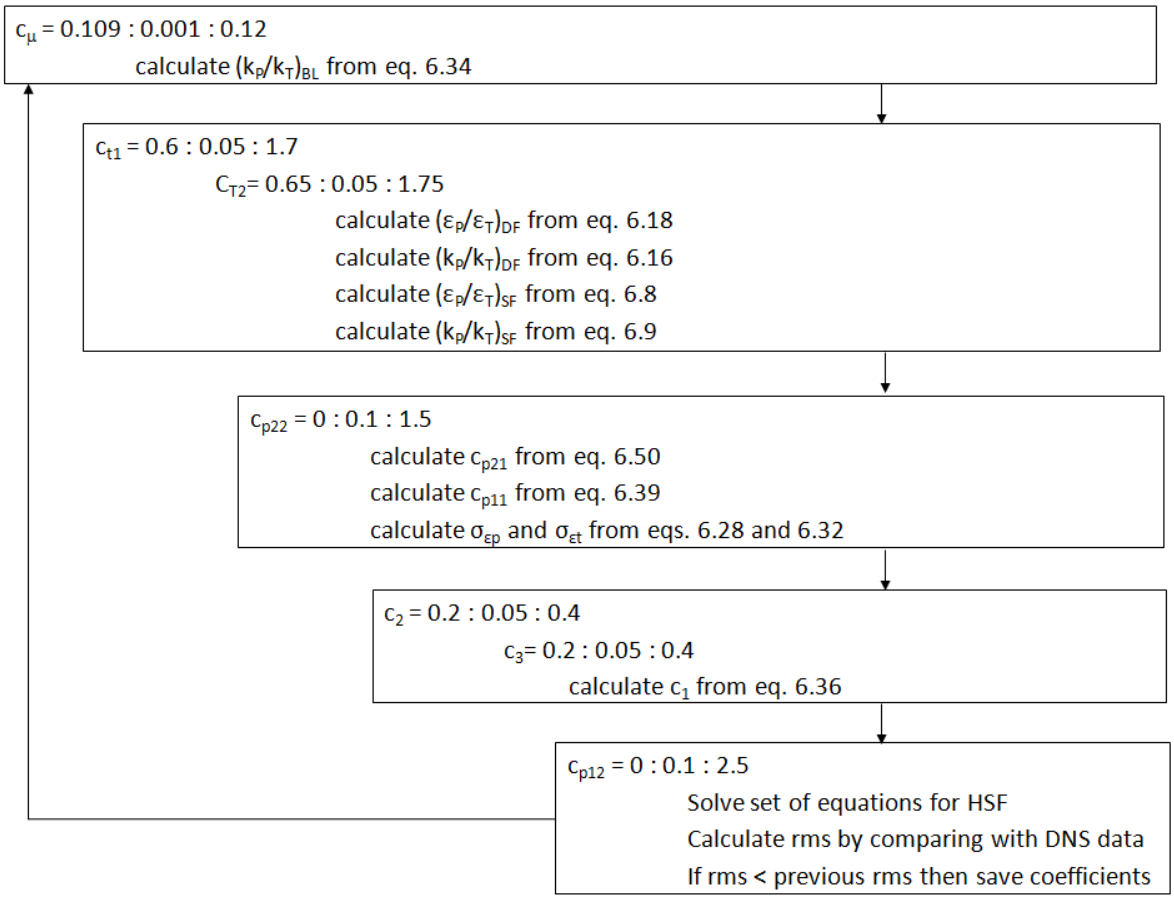

Figure 6.30: Simplified scheme of the optimization procedure to determine the coefficients of the second version of the NT1 model.

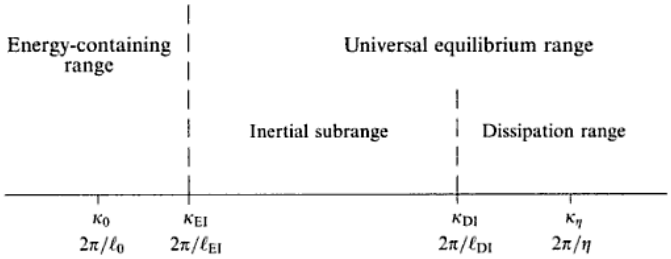

Figure 6.31: Sketch of the spectrum proposed by Kolmogorov presented in Pope (2000)

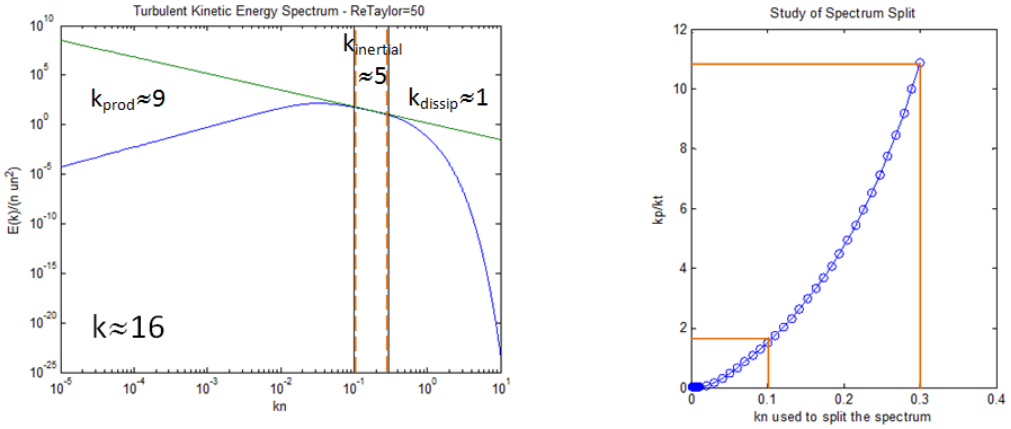

Figure 6.32: Study of the turbulent kinetic energy spectrum at $Re_\lambda = 50$

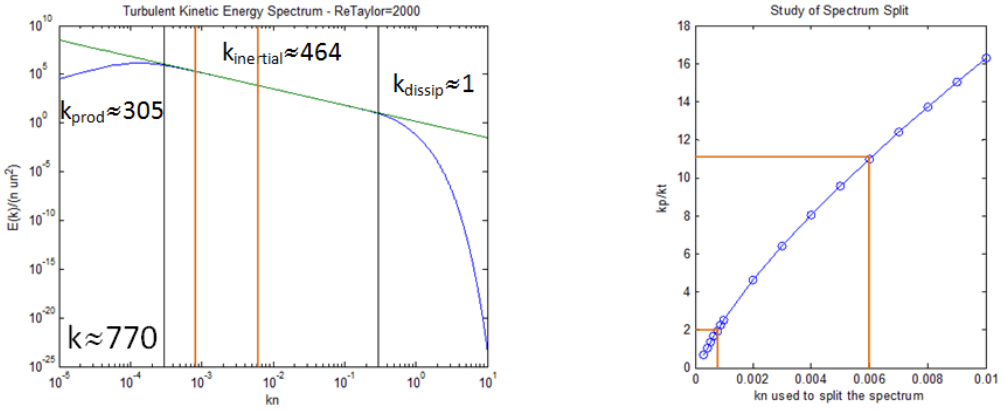

Figure 6.33: Study of the turbulent kinetic energy spectrum at $Re_\lambda = 2000$

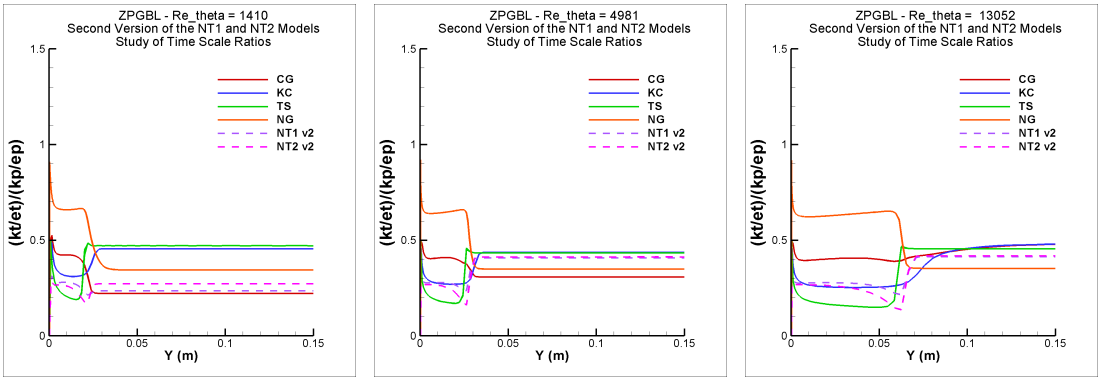

(a) $Re_\theta = 1410$ (b) $Re_\theta = 4981$ (c) $Re_\theta = 13052$

Figure 6.34: Time scale ratio, $\frac{\tau_T}{\tau_P} = \frac{k_T/\varepsilon_T}{k_P/\varepsilon_P}$, in the zero pressure gradient boundary layer: assessing the second versions of the NT1 and NT2 models. Models as in Table 3.25.

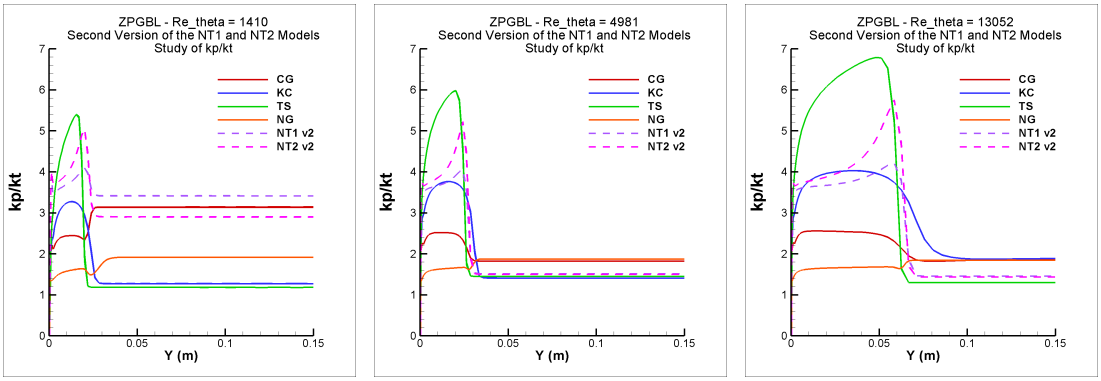

(a) $Re_\theta = 1410$ (b) $Re_\theta = 4981$ (c) $Re_\theta = 13052$

Figure 6.35: Turbulent kinetic energy partitions ratio, $\frac{k_P}{k_T}$, in the zero pressure gradient boundary layer: assessing the second versions of the NT1 and NT2 models. Models as in Table 3.25.

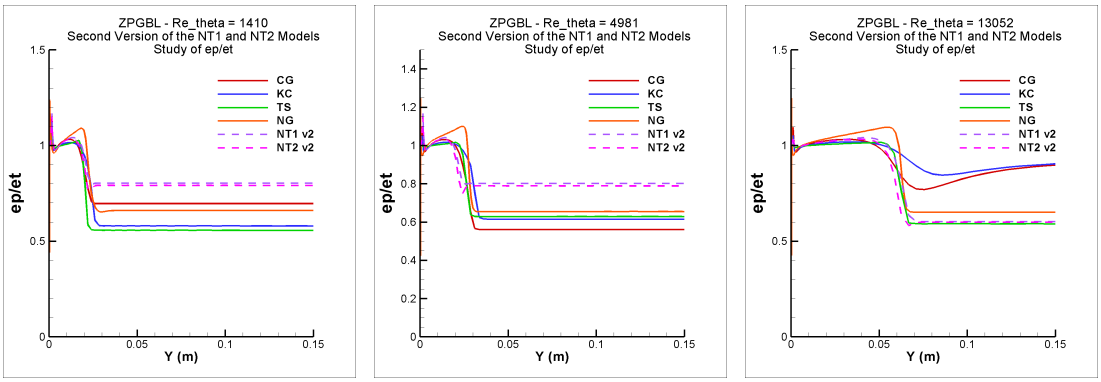

(a) $Re_\theta = 1410$ (b) $Re_\theta = 4981$ (c) $Re_\theta = 13052$

Figure 6.36: Turbulent kinetic energy transfer rates ratio, $\frac{\varepsilon_P}{\varepsilon_T}$, in the zero pressure gradient boundary layer: assessing the second versions of the NT1 and NT2 models. Models as in Table 3.25.

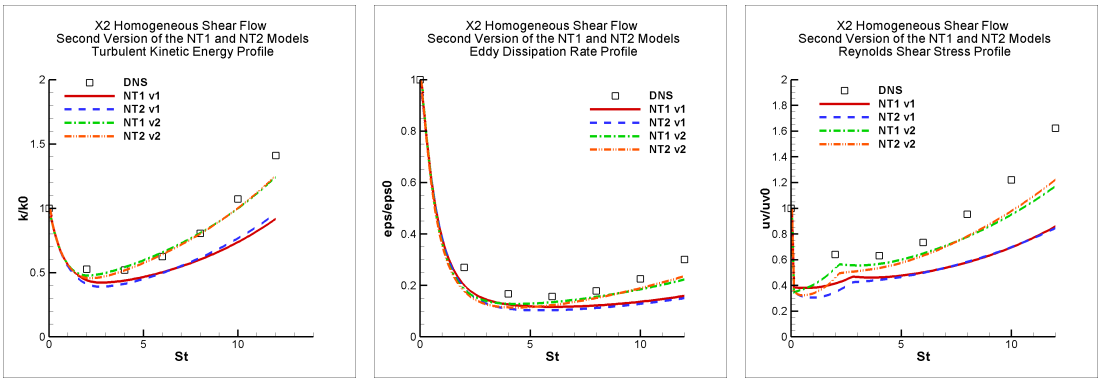

(a) k Profile (b) ε Profile (c) $\overline{uv}$ Profile

Figure 6.37: Performance of the second versions of the NT1 and NT2 models compared with the first version of the models in the homogeneous lowest shear flow case $X2$.

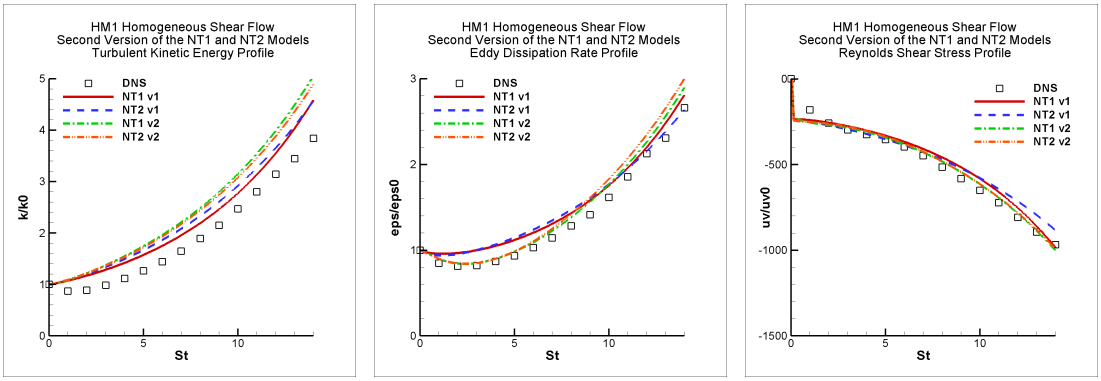

(a) k Profile (b) ε Profile (c) $\overline{uv}$ Profile

Figure 6.38: Performance of the second versions of the NT1 and NT2 models compared with the first version of the models in the homogeneous moderate shear flow case $HM1$.

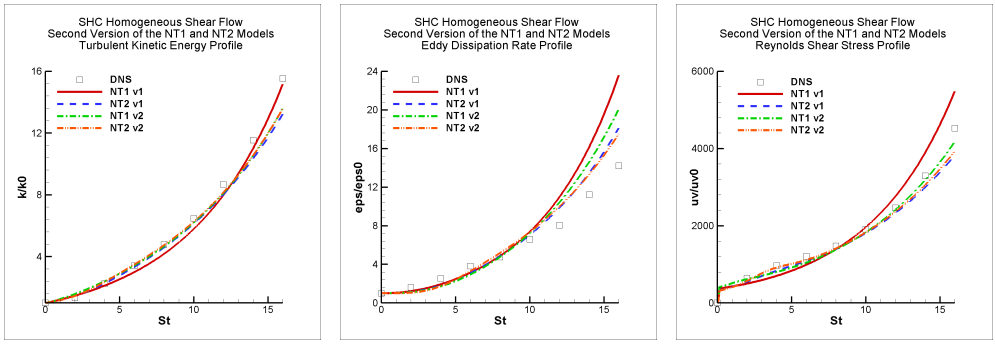

(a) k Profile (b) ε Profile (c) $\overline{uv}$ Profile

Figure 6.39: Performance of the second versions of the NT1 and NT2 models compared with the first version of the models in the homogeneous high shear flow case SHC.

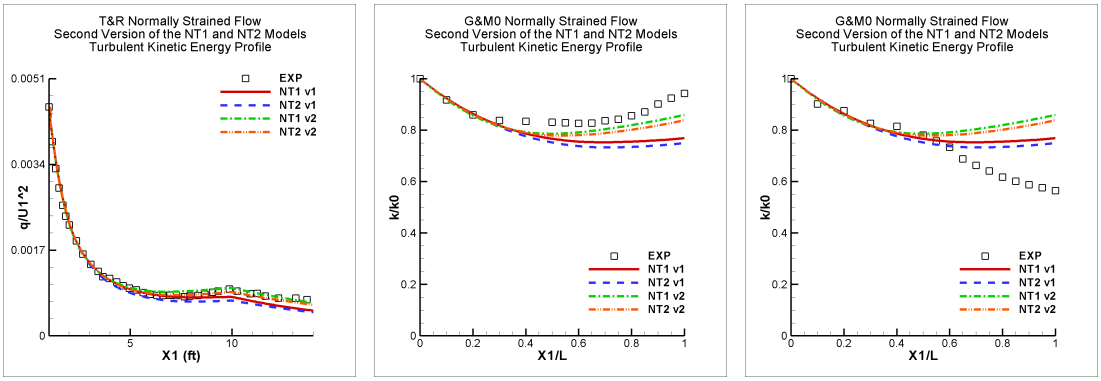

(a) $T\&R$ case (b) $G\&M0$ case (c) $G\&M05$ case

Figure 6.40: Performance of the second versions of the NT1 and NT2 models compared with the first version of the models in the normally strained cases.

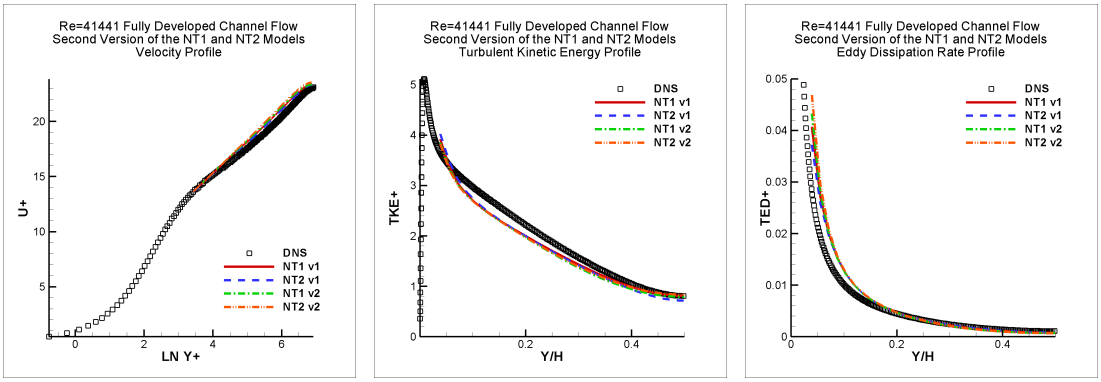

(a) Velocity Profile (b) k Profile (c) ε Profile

Figure 6.41: Performance of the second versions of the NT1 and NT2 models compared with the first version of the models in the fully developed channel flow case with $Re = 41441$.

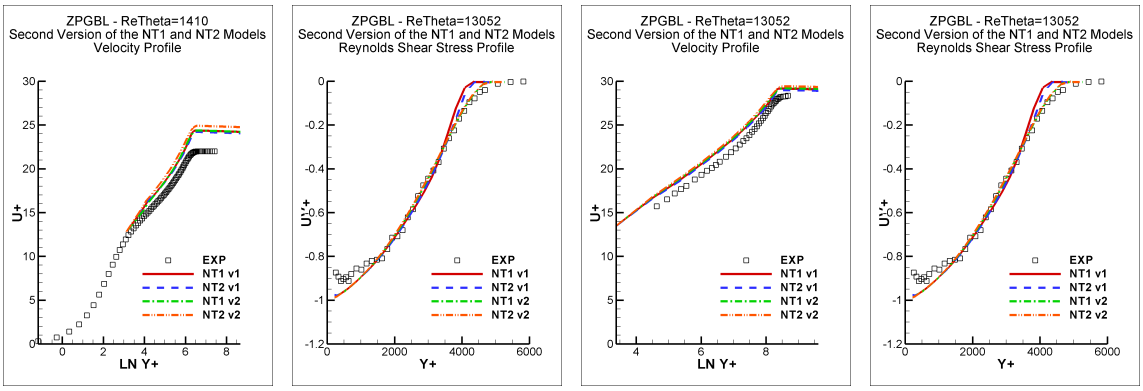

(a) Velocity Profile at $Re_\theta = 1410$ (b) Shear Stress Profile at $Re_\theta = 1410$ (c) Velocity Profile at $Re_\theta = 13052$ (d) Shear Stress Profile at $Re_\theta = 13052$

Figure 6.42: Performance of the second versions of the NT1 and NT2 models compared with the first version of the models in zero pressure gradient boundary layer.

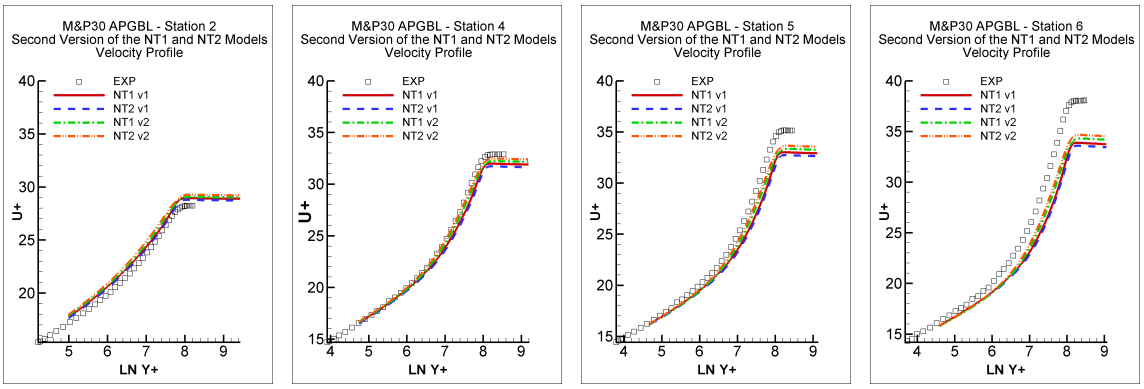

(a) Station 2 (b) Station 4 (c) Station 5 (d) Station 6

Figure 6.43: Prediction of the velocity profile by the second versions of the NT1 and NT2 models compared with the first version of the models in the adverse pressure gradient boundary layer case $M\&P30$.

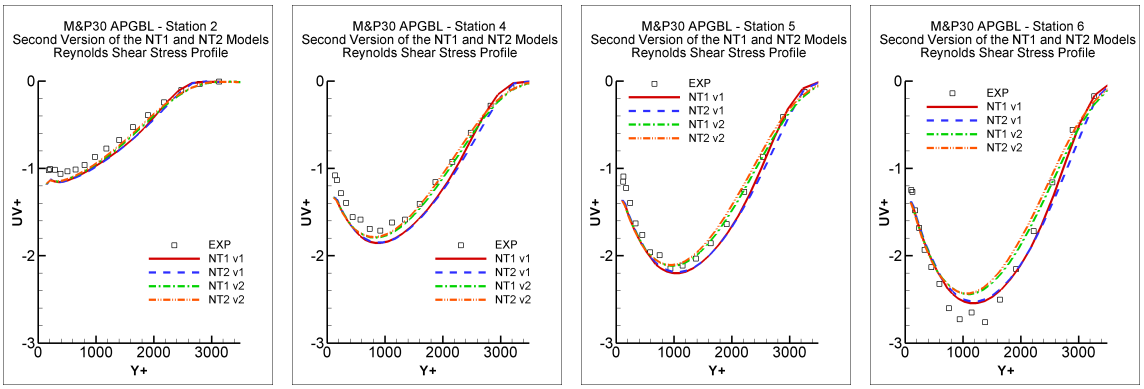

(a) Station 2 (b) Station 4 (c) Station 5 (d) Station 6

Figure 6.44: Prediction of the Reynolds shear stress by the second versions of the NT1 and NT2 models compared with the first version of the models in the adverse pressure gradient boundary layer case $M\&P30$.

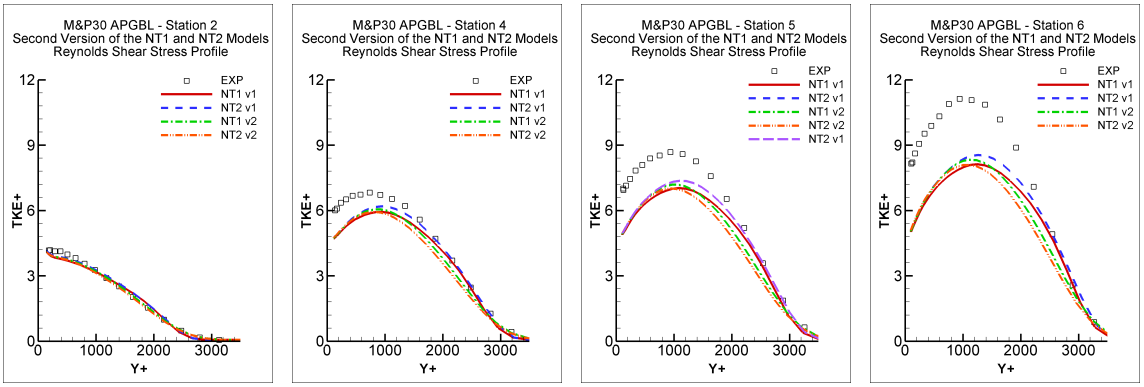

(a) Station 2 (b) Station 4 (c) Station 5 (d) Station 6

Figure 6.45: Prediction of the turbulent kinetic energy by the second versions of the NT1 and NT2 models compared with the first version of the models in the adverse pressure gradient boundary layer case $M\&P30$.

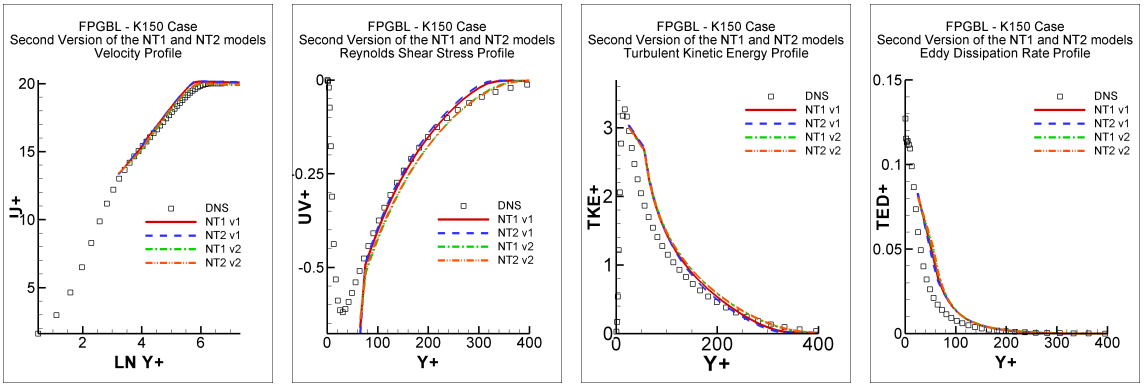

(a) Velocity Profile (b) $\overline{uv}$ Profile (c) k Profile (d) ε Profile

Figure 6.46: Performance of the first versions of the NT1 and NT2 models compared with the first version of the models in the $K150$ favourable pressure gradient case.

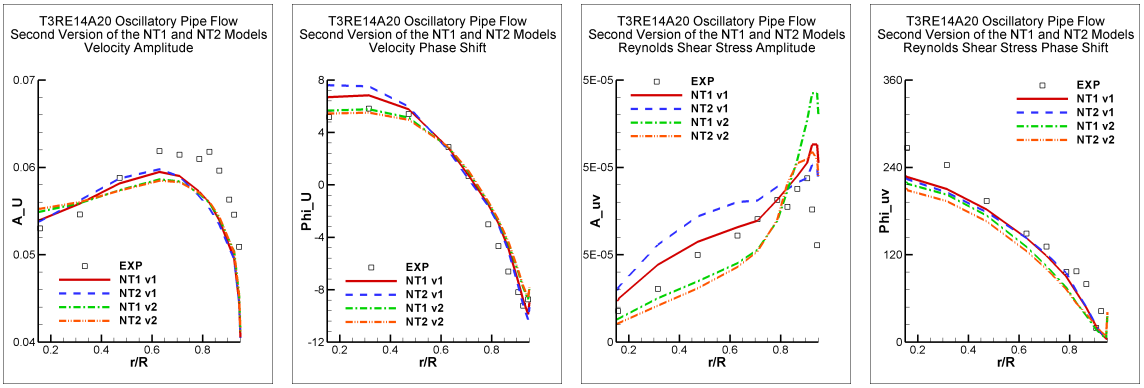

(a) Velocity Amplitude (b) Velocity Phase Shift (c) Shear Stress Amplitude (d) Shear Stress Phase Shift

Figure 6.47: Performance of the second versions of the NT1 and NT2 models compared with the first version of the models in the oscillatory pipe flow case $T3RE14A20$.

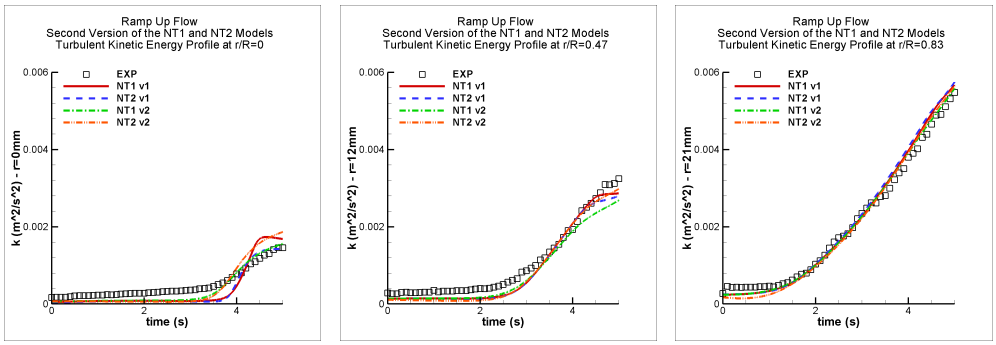

(a) Pipe centre ($r/R = 0$) (b) $r/R = 0.47$ (c) $r/R = 0.83$

Figure 6.48: Prediction of the turbulent kinetic energy by the second versions of the NT1 and NT2 models compared with the first version of the models in the ramp up pipe flow.

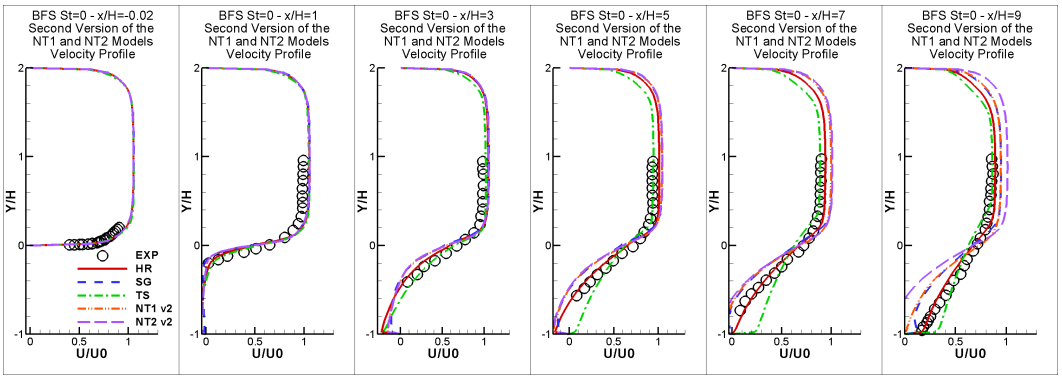

Figure 6.49: Prediction of the velocity profile before the step $x/H = -0.02$ and at five positions downstream of the step $x/H = 1, 3, 5, 7, 9$ by the second versions of the NT1 and NT2 models in the steady state backward facing step case of Chun and Sung (1996). Models as in Table 3.25.

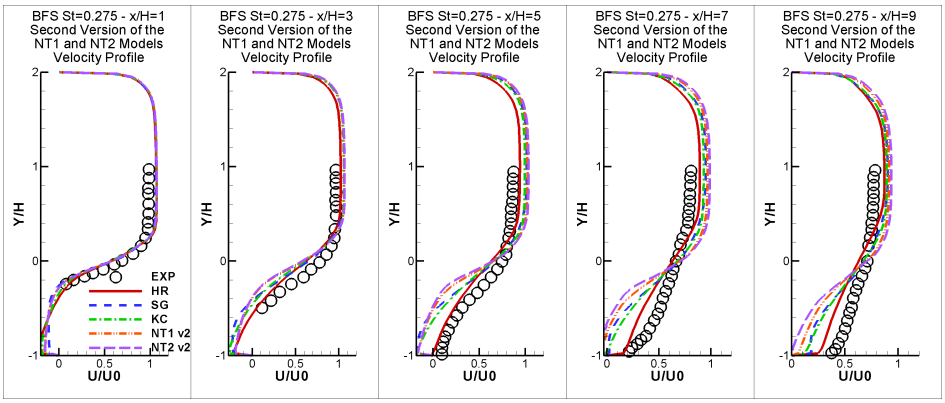

Figure 6.50: Prediction of the time-averaged velocity profile at five positions downstream of the step $x/H = 1, 3, 5, 7, 9$ by the second versions of the NT1 and NT2 models in the unsteady backward facing step case with of $St = 0.275$ Chun and Sung (1996). Models as in Table 3.25.

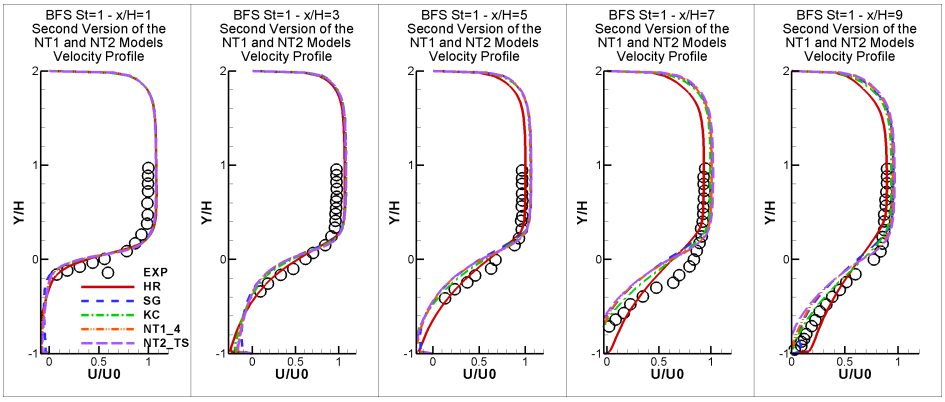

Figure 6.51: Prediction of the time-averaged velocity profile at five positions downstream of the step $x/H = 1, 3, 5, 7, 9$ by the second versions of the NT1 and NT2 models in the unsteady backward facing step case with $St = 1$ of Chun and Sung (1996). Models as in Table 3.25.

6.3 Final Versions of the NT1 and NT2 Models

The performance of the second versions of the NT1 and NT2 models indicated that improvements were needed in the backward facing step cases. The final versions of the NT1 and NT2 models thus focused on these improvements without disturbing the prediction of the other test cases where the second versions of the NT1 and NT2 models are performing well.

By analysing the performance of the LEV MTS models in backward facing step flows, it was concluded that when the coefficients of the model satisfy reasonably well the asymptotic states of local equilibrium boundary layers and homogeneous shear flows, the models tend to overpredict the reattachment point of the steady state and high frequency cases and it is not able to reduce the reattachment length enough in the low frequency cases. That is what happened to the KC model and the second versions of the NT1 and NT2 models. Clearly, when the coefficients are tuned to satisfy the equilibrium states of boundary layers and homogeneous shear flows, they are not able to perform well in strongly non-equilibrium flows such as the backward facing step flows. That would then imply the necessity of extra terms which do not disturb the asymptotic analyses carried out to arrive at the second versions of the NT1 and NT2 models but which make the models more sensitive to strong non-equilibrium flows.

As both CG and TS models, whose coefficients do not satisfy the above mentioned asymptotic states, provided underprediction of the location of the reattachment point in all steady and unsteady backward facing step cases, it was worth comparing the profiles of $\frac{k_P}{k_T}$ and $\frac{\varepsilon_P}{\varepsilon_T}$ provided by the second versions of the NT1 and NT2 models and the TS model, for example, in order to understand which mechanisms would lead to a decrease of the predicted reattachment length.

The profiles of $\frac{\varepsilon_P}{\varepsilon_T}$ provided by the TS and the second versions of the NT1 and NT2 models did not show any particular difference which would allow one to conclude why these models predicted such different reattachment lengths. However, in Figure 6.52, one can see the prediction of $\frac{k_P}{k_T}$ in the steady state backward facing step case provided by the TS and the second versions of the NT1 and NT2 models. The profiles of $\frac{k_P}{k_T}$ provided by the second versions of the NT1 and NT2 models only are presented in Figure 6.53. Clearly, the TS model provided far higher levels of $\frac{k_P}{k_T}$ in the shear region than the second version of the NT1 and NT2 models. As these models overpredict the reattachment length and the TS model underpredicts this parameter, one knows that in order to reduce the predicted reattachment length, one needs extra terms which increase the ratio of $\frac{k_P}{k_T}$ in the shear region.

6.3.1 Tests Towards the Final version of the NT1 Model

Firstly, the tests which led to the final version of the NT1 model will be presented and discussed.

In order to increase the ratio $\frac{k_P}{k_T}$, one needs either to increase the generation of k_P or decrease the generation of k_T. Looking at equations 6.51 to 6.54, ε_P is directly the sink term of $\frac{Dk_P}{Dt}$ and the source term of $\frac{Dk_T}{Dt}$. One can then either decrease C_{P1} or increase C_{P2} in the

ε_P equation (equation 6.53) in order to have the desired effect.

The first attempt was then to rewrite C_{P1} as:

$$C_{P1} = 1.4912 + 2.5\frac{\min\left[\frac{k_P}{k_T} - f_{BL}, 0\right]}{\frac{k_P}{k_T} + f_{BL}} \tag{6.73}$$

where in the second version of the NT1 model $f_{BL} = \left(\frac{k_P}{k_T}\right)_{BL} = 3.6$. Tests in changing f_{BL} are only reported in Table 6.16. Firstly it was noticed that by increasing f_{BL}, the prediction of the reattachment point in both steady and high frequency backward facing step cases would be improved, as can be seen in Test 1 in Table 6.16. The change in this parameter as a constant would affect the asymptotic states previously carried out since C_{P1} would no longer be 1.4912 in local equilibrium boundary layers.

Table 6.16: Tests performed in the backward facing step cases with the NT1 model, exploring f_1 in f_{BL} which is used in C_{P1} in equation 6.73.

Test NT1	f_1	f_{BL}	Reattachment Point		
			St=0	St=0.275	St=1
1	4.5	f_1	7.5	7.5	8.2
2	$2\max\left(\frac{\varepsilon_P}{\varepsilon_T} - 1, 0\right)$	$\left(\frac{k_P}{k_T}\right)_{BL}(1 + f_1)$	7.8	7.4	8.5
3	$1.7\left(\frac{k_P}{k_T} - 1\right)\min\left(\frac{P_k}{\varepsilon_T} - 1.9, 0\right)\max\left(\frac{\varepsilon_P}{\varepsilon_T} - 1, 0\right)$	$\left(\frac{k_P}{k_T}\right)_{BL}(1 - f_1)$	7.8	7.9	8.6
EXP	-	-	7.8	5.0	8.1

Looking at the profiles of $\frac{\varepsilon_P}{\varepsilon_T}$ in Figure 6.54, one can see that this ratio, which in equilibrium boundary layers is equal to 1, exceeds the value of 1 within the shear region. Test 2 in Table 6.16 then showed that it was possible to substitute f_{BL} by an expression involving $\max(\frac{\varepsilon_P}{\varepsilon_T} - 1, 0)$ and reduce the reattachment length in both steady and high frequency backward facing step cases and keep $f_{BL} = 3.6$ in local equilibrium boundary layers. The problem of the form adopted by f_{BL} in Test 2 in Table 6.16 was that when tested in the homogeneous shear flow cases, it disturbed the prediction of the high shear cases since in these cases, $\frac{\varepsilon_P}{\varepsilon_T}$ reaches levels significantly higher than unity in spite of $\left(\frac{\varepsilon_P}{\varepsilon_T}\right)_{SF}$ being so close to unity.

So in order to use $\max(\frac{\varepsilon_P}{\varepsilon_T} - 1, 0)$ in the desired extra term, it is necessary to propose a term which would not affect the homogeneous shear flows, but which would still be active in the shear region in the backward facing step cases. Looking at the profile of $\frac{P_k}{\varepsilon_T}$ in Figure 6.55, one may notice that this ratio peaks at about 2 which is very close to $\left(\frac{P_k}{\varepsilon_T}\right)_{SF} = 1.9$. So a term such as $\min(\frac{P_k}{\varepsilon_T} - 1.9, 0)$ would probably cancel any significant effect in homogeneous shear flows. Test 3 in Table 6.16 shows a term involving both $\max(\frac{\varepsilon_P}{\varepsilon_T} - 1, 0)$ and $\min(\frac{P_k}{\varepsilon_T} - 1.9, 0)$ in f_{BL} which also produces the desired reduction in the reattachment length in both steady and high frequency backward facing step cases and does not affect the asymptotic states studied. This term was then adopted in C_{P1} which now is expressed as in equation 6.73 with:

$$f_{BL} = \left(\frac{k_P}{k_T}\right)_{BL}(1 - f_1) = 3.6(1 - f_1) \tag{6.74}$$

$$f_1 = 1.7\left(\frac{k_P}{k_T} - 1\right)\min\left(\frac{P_k}{\varepsilon_T} - 1.9, 0\right)\max\left(\frac{\varepsilon_P}{\varepsilon_T} - 1, 0\right) \tag{6.75}$$

In equation 6.75, the term $\left(\frac{k_P}{k_T} - 1\right)$ was also included for two reasons: to increase the overall level of the whole term implying a small coefficient such as 1.7 and to reduce any eventual effect of the f_1 term in local low turbulence level regions, such as the core region of channel flows and the outer part of boundary layers, where $\frac{k_P}{k_T}$ is expected to reach minimum levels such as $\left(\frac{k_P}{k_T}\right)_{DF}$ which are unity in the NT1 model. The general shape of the f_1 term predicted by the second version of the NT1 model can be seen in Figure 6.56. This term is either zero or negative, since $\left(\frac{k_P}{k_T} - 1\right) \geq 0$, $\max(\frac{\varepsilon_P}{\varepsilon_T} - 1, 0) \geq 0$ and $\min(\frac{P_k}{\varepsilon_T} - 1.9, 0) \leq 0$, and that is why the f_1 has a minus sign in f_{BL} which is intended to be increased.

The adopted form for C_{P1} given by equations 6.73, 6.74 and 6.75 reduced the reattachment length in all backward facing step cases, as can be seen in Test 3 in Table 6.16, though not enough sufficiently for the low frequency case where the experiments indicate $X_R = 5.0$. Another extra term is then needed, but now one looks for a term which has no effect in the steady state backward facing step case, little effect in the high frequency case and a strong effect in the low frequency case.

A large number of tests were then performed in order to arrive at a second extra term, which would provide the expected sensitivity to the prediction of the reattachment point in different forcing frequencies, and a selection of them will be presented and discussed below.

Still looking at the profiles provided by the second version of the NT1 model, but now considering the three backward facing step cases, it was found that the term SW, presented in equation 6.76, is nearly zero in the shear region of the steady state and high frequency cases and non-zero in the low frequency backward facing step case.

$$SW = \frac{S_{ij}S_{ij} - W_{ij}W_{ij}}{S_{ij}S_{ij} + W_{ij}W_{ij}} \tag{6.76}$$

where $S_{ij} = \frac{\partial U_i}{\partial x_j} + \frac{\partial U_j}{\partial x_i}$ and $W_{ij} = \frac{\partial U_i}{\partial x_j} - \frac{\partial U_j}{\partial x_i}$. In 2-D flows, these terms reduce to:

$$S_{ij}S_{ij} = S_{11}^2 + S_{22}^2 + 2S_{12}^2 = \left(2\frac{\partial U}{\partial x}\right)^2 + \left(2\frac{\partial V}{\partial y}\right)^2 + 2\left(\frac{\partial U}{\partial y} + \frac{\partial V}{\partial x}\right)^2 \tag{6.77}$$

$$W_{ij}W_{ij} = 2W_{12}^2 = 2\left(\frac{\partial U}{\partial y} - \frac{\partial V}{\partial x}\right)^2 \tag{6.78}$$

The SW term is quite convenient to be used since it is zero in simple shear flows which means both local equilibrium boundary layers and homogeneous shear flows asymptotic analyses would not be affected.

As the shear region in the backward facing step cases is the crucial one for modelling in the backward facing step cases, it is sensible to think of a term such as $\max(\frac{\varepsilon_P}{\varepsilon_T} - 1, 0)SW$ to be included in one of the model's coefficients. In order to reduce the coefficient needed, the

term $\frac{P_k}{\varepsilon_P}$ was initially used. The profile of $\frac{P_k}{\varepsilon_P}\max(\frac{\varepsilon_P}{\varepsilon_T}-1,0)SW$ for the second version of the NT1 model is presented in Figure 6.58 for the three backward facing step cases where one can see it is clearly non-zero in the low frequency case and negligible in the steady state and high frequency cases. This same profile is also shown in Figure 6.61 for the NT1 model with C_{P1} given by equations 6.73, 6.74 and 6.75 where one can see that no significant difference in this parameter's profile was noticed when running the updated model.

It was observed that by decreasing C_{T1}, the desired effect of reducing significantly the reattachment length in the low frequency backward facing step case could be achieved. Test 4 in Table 6.17 shows that, while the term $\frac{P_k}{\varepsilon_P}\max(\frac{\varepsilon_P}{\varepsilon_T}-1,0)SW$ had negligible effect in the steady state, as expected from the profiles shown in Figure 6.58 for the second version of the NT1 model, in the high frequency case, this term had a huge effect reducing the reattachment length to the same level as in the low frequency case which was not expected nor desired.

It was then decided to shed some light on the results of Test 4 in Table 6.17 in order to understand the reason for the unexpected behaviours in the high frequency backward facing step case described above. It was then noticed that C_{T1} became negative in the shear region and that the reason for that was the very high peaks in the $\frac{\varepsilon_P}{\varepsilon_T}$ profiles throughout the cycle. In order to capture the effects of these strongly shear flows, without compromising the performance of the model, the first hypothesis was that by either clipping this coefficient and not allowing it to become negative - $\max(C_{T1},0)$ - or by clipping $\frac{\varepsilon_P}{\varepsilon_T}$ such as $\min[4,\max(\frac{\varepsilon_P}{\varepsilon_T}-1,0)]$ or by taking the square root of $\max(\frac{\varepsilon_P}{\varepsilon_T}-1,0)$ one could have the desired effect in the high frequency backward facing step case. Tests 5, 6 and 7 in Table 6.17 thus show that by using one of these clips the undesired effect in the high frequency case was reduced, but was still too strong.

The profiles of $\max(\frac{\varepsilon_P}{\varepsilon_T},0)$ and $\frac{P_k}{\varepsilon_P}\max(\frac{\varepsilon_P}{\varepsilon_T}-1,0)SW$ for the NT1 model with Test 5 are presented in Figures 6.63 and 6.64 respectively where one can notice that the introduction of $\frac{P_k}{\varepsilon_P}\max(\frac{\varepsilon_P}{\varepsilon_T}-1,0)SW$ in C_{T1} produced much higher levels of this term as well as of $\frac{\varepsilon_P}{\varepsilon_T}$ throughout the cycle than the second version of the NT1 model (Figures 6.54 and 6.58) and even when the NT1 is run with C_{P1} given by equations 6.73, 6.74 and 6.75 (Figures 6.60 and 6.61).

The dynamic of the differential equations clearly changed when the term $\frac{P_k}{\varepsilon_P}\max(\frac{\varepsilon_P}{\varepsilon_T}-1,0)SW$ was introduced in C_{T1}. It was decided to study which effects it would have if $\frac{P_k}{\varepsilon_P}$ were exchanged by $\frac{k_P}{k_T}$. The former can reach very high values in strongly non-equilibrium flows while the latter is expected not to vary that much. Test 8 in Table 6.17 shows that the term $\frac{k_P}{k_T}\max(\frac{\varepsilon_P}{\varepsilon_T}-1,0)SW$ can produce the same effect in the low frequency case, but still reduces too much the reattachment length in the high frequency case. The profile of $\frac{k_P}{k_T}\max(\frac{\varepsilon_P}{\varepsilon_T}-1,0)SW$ for the second version of the NT1 model and for the NT1 with C_{P1} given by equations 6.73, 6.74 and 6.75 is presented in Figures 6.59 and 6.62. One can see that its profile is similar to the profile of $\frac{P_k}{\varepsilon_P}\max(\frac{\varepsilon_P}{\varepsilon_T}-1,0)SW$ which is expected since $\frac{P_k}{\varepsilon_P}$ and $\frac{k_P}{k_T}$ are being introduced mainly to increase the magnitude of the term $\max(\frac{\varepsilon_P}{\varepsilon_T}-1,0)SW$ and therefore decrease the value of the coefficient needed.

As C_{T1} becoming negative is an issue, it was worth evaluating the effect of the term

Table 6.17: Tests performed in the backward facing step cases with the NT1 model, using C_{P1} given by equations 6.73, 6.74 and 6.75, and exploring f_2 in C_{T1}.

Test NT1	f_2	C_{T1}	Reattachment Point		
			St=0	St=0.275	St=1
4	$0.7\frac{P_k}{\varepsilon_P}\max\left(\frac{\varepsilon_P}{\varepsilon_T}-1,0\right)SW$	$C_{T1}-f_2$	7.8	5.0	5.2
5	$2.5\frac{P_k}{\varepsilon_P}\max\left(\frac{\varepsilon_P}{\varepsilon_T}-1,0\right)SW$	$\max(C_{T1}-f_2,0)$	7.9	5.1	5.8
6	$0.8\frac{P_k}{\varepsilon_P}\min\left[4,\max\left(\frac{\varepsilon_P}{\varepsilon_T}-1,0\right)\right]SW$	$C_{T1}-f_2$	7.8	5.1	5.6
7	$\frac{P_k}{\varepsilon_P}\sqrt{\max\left(\frac{\varepsilon_P}{\varepsilon_T}-1,0\right)}SW$	$C_{T1}-f_2$	7.9	4.9	5.5
8	$2\frac{k_P}{k_T}\max\left(\frac{\varepsilon_P}{\varepsilon_T}-1,0\right)SW$	$\max(C_{T1}-f_2,0)$	7.9	5.2	6.2
EXP	-	-	7.8	5.0	8.1

$\frac{k_P}{k_T}\max(\frac{\varepsilon_P}{\varepsilon_T}-1,0)SW$ when added to C_{T2}. That was done in Test 9, presented in Table 6.18. As one can see the same result as in Test 8 can be achieved, making C_{T2} a more interesting coefficient to be changed. However, even in C_{T2} the effect of $\frac{k_P}{k_T}\max(\frac{\varepsilon_P}{\varepsilon_T}-1,0)SW$ is far stronger than the expected according to the profiles of this term with the second version of the NT1 model (Figure 6.59) and the NT1 with C_{P1} given by equations 6.73, 6.74 and 6.75 (Figure 6.62). The profiles of $\frac{\varepsilon_P}{\varepsilon_T}$ in Test 9 are similar to those of Test 5 which are presented in Figure 6.63 where this ratio reaches relatively higher values in the low frequency case than in the high frequency case. It was then decided to try clipping $\frac{\varepsilon_P}{\varepsilon_T}$ at values higher than one in order to try to cancel the effects of the extra term in the high frequency case. Tests 10, 11 and 12 in Table 6.18 shows these results. Again, the extra term in C_{T2} seems to affect the high frequency case.

Table 6.18: Tests performed in the backward facing step cases with the NT1 model, using C_{P1} given by equations 6.73, 6.74 and 6.75, and exploring f_2 in C_{T2}.

Test NT1	f_2	C_{T2}	Reattachment Point		
			St=0	St=0.275	St=1
9	$2\frac{k_P}{k_T}\max\left(\frac{\varepsilon_P}{\varepsilon_T}-1,0\right)SW$	$C_{T2}+f_2$	7.9	5.1	5.7
10	$2.5\frac{k_P}{k_T}\max\left(\frac{\varepsilon_P}{\varepsilon_T}-1.2,0\right)SW$	$C_{T2}+f_2$	7.8	5.1	5.6
11	$2.5\frac{k_P}{k_T}\max\left(\frac{\varepsilon_P}{\varepsilon_T}-1.4,0\right)SW$	$C_{T2}+f_2$	7.8	5.3	5.9
12	$4\frac{k_P}{k_T}\max\left(\frac{\varepsilon_P}{\varepsilon_T}-1.6,0\right)SW$	$C_{T2}+f_2$	7.8	5.0	5.6
EXP	-	-	7.8	5.0	8.1

As changes in both C_{T1} and C_{T2} seemed to change drastically the dynamics of the partitions variables (k_P, k_T, ε_P and ε_T), it was decided to investigate what effect a second extra term such as $\frac{k_P}{k_T}\max(\frac{\varepsilon_P}{\varepsilon_T}-1,0)SW$ in C_{P1} would cause. Test 13 in Table 6.19 shows that C_{P1} seems much more appropriate since the effect of the second extra term has very little effect in the high frequency case when inserted in C_{T1} and C_{T2}. The term $\frac{k_P}{k_T}\max(\frac{\varepsilon_P}{\varepsilon_T}-1,0)SW$ is mostly positive, particularly when it reaches the high values responsible for reducing sufficiently the reattachment length in the low frequency case, but can be negative since SW is expected to vary from -1 to 1. Test 14 in Table 6.19 shows that by using only the positive part of $\frac{k_P}{k_T}\max(\frac{\varepsilon_P}{\varepsilon_T}-1,0)SW$, there are no effects in the unsteady cases and even smaller effects in the steady state case. That indicated that $\max\left[\frac{k_P}{k_T}\max\left(\frac{\varepsilon_P}{\varepsilon_T}-1,0\right)SW,0\right]$ seemed a more appropriate form for the second extra term.

Test 15 (essentially Test 14, but with a slightly higher coefficient) in Table 6.19 is the best test so far, though one would expect the reattachment length in the high frequency case to be slightly higher, since experiments indicate $X_R = 8.1$. When looking at the profile of $\max\left[\frac{k_P}{k_T}\max\left(\frac{\varepsilon_P}{\varepsilon_T}-1,0\right)SW,0\right]$ provided by the second version of the NT1 model (Figure 6.59) and the NT1 with C_{P1} given by equations 6.73, 6.74 and 6.75 (Figure 6.62), it is difficult to believe that such smaller magnitude of this term in the high frequency case could cause such a big reduction of the reattachment length in the $BFS - St1$ case.

It was then decided to investigate if there would be any other location in the flow, apart from $x/H = -0.02, 1, 3, 5, 7, 9$, where the term $\max\left[\frac{k_P}{k_T}\max\left(\frac{\varepsilon_P}{\varepsilon_T}-1,0\right)SW,0\right]$ reached higher values in the high frequency case. In Figure 6.57 one can see a contour plot of this term at $\omega t = 180^o$, which is representative of other positions in the cycle. One may see that $\max\left[\frac{k_P}{k_T}\max\left(\frac{\varepsilon_P}{\varepsilon_T}-1,0\right)SW,0\right]$ is mostly near zero, as indicated in Figure 6.62, but very high values can be observed very close to the step edge. That should explain why the term $\max\left[\frac{k_P}{k_T}\max\left(\frac{\varepsilon_P}{\varepsilon_T}-1,0\right)SW,0\right]$ was having such high influence in the high frequency case. Looking at Figure 6.62, where this term does not exceed unity in the low frequency case, suggests that if a term such as $\min\left\{1.0,\max\left[\frac{k_P}{k_T}\max\left(\frac{\varepsilon_P}{\varepsilon_T}-1,0\right)SW,0\right]\right\}$ were used, the desired effects in all three backward facing step cases should be achieved. However, Tests 16, 17 and 18 (where the maximum limit of the term was varied from 1 to 10) show that no improvements were achieved by clipping the maximum value of the term $\max\left[\frac{k_P}{k_T}\max\left(\frac{\varepsilon_P}{\varepsilon_T}-1,0\right)SW,0\right]$.

Table 6.19: Tests performed in the backward facing step cases with the NT1 model, using C_{P1} given by equations 6.73, f_1 given by equation 6.75, and exploring f_2 in C_{P1} too through f_{BL}.

Test NT1	f_2	f_{BL}	Reattachment Point		
			St=0	St=0.275	St=1
13	$5\frac{k_P}{k_T}\max\left(\frac{\varepsilon_P}{\varepsilon_T}-1,0\right)SW$	$\left(\frac{k_P}{k_T}\right)_{BL}(1-f_1+f_2)$	7.9	5.4	7.2
14	$5\max\left[\frac{k_P}{k_T}\max\left(\frac{\varepsilon_P}{\varepsilon_T}-1,0\right)SW,0\right]$	$\left(\frac{k_P}{k_T}\right)_{BL}(1-f_1+f_2)$	7.8	5.4	7.2
15	$5.5\max\left[\frac{k_P}{k_T}\max\left(\frac{\varepsilon_P}{\varepsilon_T}-1,0\right)SW,0\right]$	$\left(\frac{k_P}{k_T}\right)_{BL}(1-f_1+f_2)$	7.8	5.2	7.0
16	$5.5\min\left\{1.0,\max\left[\frac{k_P}{k_T}\max\left(\frac{\varepsilon_P}{\varepsilon_T}-1,0\right)SW,0\right]\right\}$	$\left(\frac{k_P}{k_T}\right)_{BL}(1-f_1+f_2)$	7.8	5.1	6.9
17	$5.5\min\left\{3.0,\max\left[\frac{k_P}{k_T}\max\left(\frac{\varepsilon_P}{\varepsilon_T}-1,0\right)SW,0\right]\right\}$	$\left(\frac{k_P}{k_T}\right)_{BL}(1-f_1+f_2)$	7.8	5.1	7.2
18	$5.5\min\left\{10.0,\max\left[\frac{k_P}{k_T}\max\left(\frac{\varepsilon_P}{\varepsilon_T}-1,0\right)SW,0\right]\right\}$	$\left(\frac{k_P}{k_T}\right)_{BL}(1-f_1+f_2)$	-	-	7.1
EXP	-	-	7.8	5.0	8.1

A term such as $\min\left\{1.0,\max\left[\frac{k_P}{k_T}\max\left(\frac{\varepsilon_P}{\varepsilon_T}-1,0\right)SW,0\right]\right\}$ was then tried in C_{P2} in order to test the effects of an extra term in this coefficient. Tests 19 and 20 were then performed, allowing the maximum value of the term $\max\left[\frac{k_P}{k_T}\max\left(\frac{\varepsilon_P}{\varepsilon_T}-1,0\right)SW,0\right]$ to be 2 and 3 respectively. These tests confirmed again that the C_{P1} was the most appropriate term to be changed through equation 6.73.

When looking at the profiles of $\frac{\varepsilon_P}{\varepsilon_T}$ in Figure 6.60, where the NT1 model is used with C_{P1} given by equations 6.73, 6.74 and 6.75 (Test 3 in Table 6.16), one may notice that there is not such difference in the levels of this ratio in the high and low frequency cases, however, the levels are higher in the low frequency case. It was then decided to try a term such as $\max\left[\frac{k_P}{k_T}\max\left(\frac{\varepsilon_P}{\varepsilon_T}-1.1,0\right)SW,0\right]$ which would not present high values in the step edge when

Table 6.20: Tests performed in the backward facing step cases with the NT1 model, using C_{P1} given by equations 6.73, 6.74 and 6.75, and exploring f_2 in C_{P2}.

Test NT1	f_2	C_{P2}	Reattachment Point		
			St=0	St=0.275	St=1
19	$2.5\min\left\{2.0, \max\left[\frac{k_P}{k_T}\max\left(\frac{\varepsilon_P}{\varepsilon_T}-1,0\right)SW,0\right]\right\}$	$C_{P2}+f_2$	-	5.1	6.4
20	$2.5\min\left\{3.0, \max\left[\frac{k_P}{k_T}\max\left(\frac{\varepsilon_P}{\varepsilon_T}-1,0\right)SW,0\right]\right\}$	$C_{P2}+f_2$	-	5.1	6.4
EXP	-	-	7.8	5.0	8.1

evaluating the profile provided by Test 3 in Table 6.16 due to the clip $\max\left(\frac{\varepsilon_P}{\varepsilon_T}-1.1,0\right)$ which can be interpreted as a flag to indicate when $\frac{\varepsilon_P}{\varepsilon_T}$ is at least 10% higher than its expected value in local equilibrium boundary layers, $\left(\frac{\varepsilon_P}{\varepsilon_T}\right)_{BL}=1$. Test 21 in Table 6.21 was the first attempt in this sense and although the reattachment length in the low frequency case was not reduced enough, the location of the reattachment point in the high frequency case was finally at the desired magnitude, close to $X_R=8.1$. Tests 22 and 23 in Table 6.21 tuned the coefficient associated with the term $\max\left[\frac{k_P}{k_T}\max\left(\frac{\varepsilon_P}{\varepsilon_T}-1.1,0\right)SW,0\right]$ in order to match the steady state, low and high frequency cases which is eventually achieved with Test 23.

As two extra terms are now being incorporated in C_{P1} to reduce its value in the shear region, one could wonder whether C_{P1} becomes negative. That would not be a problem in principle, since the source term in ε_P equation (equation 6.53) is associated with P_k which can be negative, however one could argue that only P_k should attribute a minus sign to the source term. As LEV models always predict P_k as positive, it makes perhaps more sense to have C_{P1} always positive.

By checking the profiles of C_{P1}, it was noticed that this coefficient was mainly positive, reaching very low negative values very close to the step edge. Test 24 was then perfomed to study the influence of the "negative" C_{P1} by clipping this coefficient and not allowing it to be negative. The results were slightly better in the high frequency case than when not clipping C_{P1} which then made this the best model so far.

Table 6.21: Further tests performed in the backward facing step cases with the NT1 model, using C_{P1} given by equations 6.73, f_1 given by equation 6.75, and exploring f_2 in C_{P1} too through f_{BL}.

Test NT1	f_2	f_{BL}	Reattachment Point		
			St=0	St=0.275	St=1
21	$10\max\left[\frac{k_P}{k_T}\max\left(\frac{\varepsilon_P}{\varepsilon_T}-1.1,0\right)SW,0\right]$	$\left(\frac{k_P}{k_T}\right)_{BL}(1-f_1+f_2)$	7.8	6.1	8.0
22	$15\max\left[\frac{k_P}{k_T}\max\left(\frac{\varepsilon_P}{\varepsilon_T}-1.1,0\right)SW,0\right]$	$\left(\frac{k_P}{k_T}\right)_{BL}(1-f_1+f_2)$	7.8	5.5	8.0
23	$20\max\left[\frac{k_P}{k_T}\max\left(\frac{\varepsilon_P}{\varepsilon_T}-1.1,0\right)SW,0\right]$	$\left(\frac{k_P}{k_T}\right)_{BL}(1-f_1+f_2)$	7.8	5.1	7.9
24	$20\max\left[\frac{k_P}{k_T}\max\left(\frac{\varepsilon_P}{\varepsilon_T}-1.1,0\right)SW,0\right]$	$\left(\frac{k_P}{k_T}\right)_{BL}(1-f_1+f_2)$ $\max(C_{P1},0)$	7.8	5.1	8.0
EXP	-	-	7.8	5.0	8.1

So now, f_{BL} is given by equation 6.79 below and with f_1 as in equation 6.75.

$$f_{BL}=\left(\frac{k_P}{k_T}\right)_{BL}(1-f_1+f_2)=3.6(1-f_1+f_2) \tag{6.79}$$

$$f_2 = 20 \max\left[\frac{k_P}{k_T}\max\left(\frac{\varepsilon_P}{\varepsilon_T} - 1.1, 0\right)SW, 0\right] \tag{6.80}$$

To finish the set of tests with the NT1 model, since a satisfactory final form was already achieved, it was decided to study the effect of the term $\max\left[\frac{k_P}{k_T}\max\left(\frac{\varepsilon_P}{\varepsilon_T} - 1.1, 0\right)SW, 0\right]$ if incorporated in the C_{P2} or C_{T2} coefficients. One may then look at Tests 25 and 26 in Table 6.22. It can be noted that, again, when incorporating the extra term in C_{T2} the dynamic of the differential equations is changed and the high frequency case presents a too low reattachment length. When the term $\max\left[\frac{k_P}{k_T}\max\left(\frac{\varepsilon_P}{\varepsilon_T} - 1.1, 0\right)SW, 0\right]$ was added to C_{P2} reasonable results were also achieved. However, they are not better than the ones provided by Test 24 in Table 6.21. It is worth knowing though about this behaviour for future tests.

Table 6.22: Tests performed in the backward facing step cases with the NT1 model, using C_{P1} given by equations 6.73, 6.74 and 6.75, and exploring f_2 similar to equation 6.80 in C_{P2} or C_{T2}.

Test NT1	f_2	Coefficient Changed	Reattachment Point		
			St=0	St=0.275	St=1
25	$2\max\left[\frac{k_P}{k_T}\max\left(\frac{\varepsilon_P}{\varepsilon_T} - 1.1, 0\right)SW, 0\right]$	$C_{T2} + f_2$	-	5.0	5.3
26	$10\max\left[\frac{k_P}{k_T}\max\left(\frac{\varepsilon_P}{\varepsilon_T} - 1.1, 0\right)SW, 0\right]$	$C_{P2} + f_2$	-	4.9	7.6
EXP	-	-	7.8	5.0	8.1

In Tables 6.16 to 6.22 whenever the reattachment point was indicated by a dashed sign it meant these test cases were not run, because the models have already been shown to fail in one of the other cases tested.

It might be worth commenting that the changes in C_{P1} might have seemed more attractive due to the way they were being incorporated, through f_{BL} in C_{P1} instead of being directly added or subtracted into the other coefficients. However, as could be noted in Test 26, the direct addition of $\max\left[\frac{k_P}{k_T}\max\left(\frac{\varepsilon_P}{\varepsilon_T} - 1.1, 0\right)SW, 0\right]$ in C_{P2} had the expected effect.

6.3.2 The Final Version of the NT1 Model

In this section the full final version of the NT1 model is presented. According to the tests presented above, the final version of the NT1 model is the second version of the NT1 model with C_{P1} given by equations 6.73, 6.79, 6.75 and 6.80 which correspond to Test 24, in Table 6.21.

The transport equations for the final form of the NT1 model are presented in equations 6.51 to 6.54 and are repeated here for the sake of presenting the whole model.

$$\frac{Dk_P}{Dt} = P_k - \varepsilon_P + \frac{\partial}{\partial x_j}\left[\left(\nu + \frac{\nu_t}{\sigma_{k_P}}\right)\frac{\partial k_P}{\partial x_j}\right] \tag{6.81}$$

$$\frac{Dk_T}{Dt} = \varepsilon_P - \varepsilon_T + \frac{\partial}{\partial x_j}\left[\left(\nu + \frac{\nu_t}{\sigma_{k_T}}\right)\frac{\partial k_T}{\partial x_j}\right] \tag{6.82}$$

$$\frac{D\varepsilon_P}{Dt} = C_{P1}P_k\frac{\varepsilon_P}{k_P} - C_{P2}\frac{\varepsilon_P^2}{k_P} + \frac{\partial}{\partial x_j}\left[\left(\nu + \frac{\nu_t}{\sigma_{\varepsilon P}}\right)\frac{\partial \varepsilon_P}{\partial x_j}\right] \tag{6.83}$$

$$\frac{D\varepsilon_T}{Dt} = C_{T1}\frac{\varepsilon_P\varepsilon_T}{k_T} - C_{T2}\frac{\varepsilon_T^2}{k_T} + \frac{\partial}{\partial x_j}\left[\left(\nu + \frac{\nu_t}{\sigma_{\varepsilon T}}\right)\frac{\partial \varepsilon_T}{\partial x_j}\right] \tag{6.84}$$

The Reynolds stresses are calculated through the linear-eddy-viscosity scheme given by:

$$\overline{u_i u_j} = -\nu_t\left(\frac{dU_i}{dx_j} + \frac{dU_j}{dx_i}\right) + \frac{2}{3}k\delta_{ij} \tag{6.85}$$

where the eddy viscosity ν_t is defined as:

$$\nu_t = c_\mu\frac{kk_P}{\varepsilon_P} \tag{6.86}$$

The coefficients of the final version of the NT1 model are presented in Table 6.23 where:

$$\eta = \max\left[\frac{k}{\varepsilon_T}\sqrt{\frac{1}{2}S_{ij}S_{ij}}, \frac{k}{\varepsilon_T}\sqrt{\frac{1}{2}W_{ij}W_{ij}}\right] \tag{6.87}$$

$$S_{ij} = \frac{\partial U_i}{\partial x_j} + \frac{\partial U_j}{\partial x_i} \tag{6.88}$$

$$W_{ij} = \frac{\partial U_i}{\partial x_j} - \frac{\partial U_j}{\partial x_i} \tag{6.89}$$

$$f_{BL} = \left(\frac{k_P}{k_T}\right)_{BL}(1 - f_1 + f_2) = 3.6(1 - f_1 + f_2) \tag{6.90}$$

$$f_1 = 1.7\left(\frac{k_P}{k_T} - 1\right)\min\left(\frac{P_k}{\varepsilon_T} - 1.9, 0\right)\max\left(\frac{\varepsilon_P}{\varepsilon_T} - 1, 0\right) \tag{6.91}$$

$$f_2 = 20\max\left[\frac{k_P}{k_T}\max\left(\frac{\varepsilon_P}{\varepsilon_T} - 1.1, 0\right)SW, 0\right] \tag{6.92}$$

$$SW = \frac{S_{ij}S_{ij} - W_{ij}W_{ij}}{S_{ij}S_{ij} + W_{ij}W_{ij}} \tag{6.93}$$

The expression for the dimensionless shear η presented in equation 6.87 is the general expression proposed by Craft et al. (1996b) which reduces to $\frac{k}{\varepsilon_T}\frac{dU}{dy}$ in simple shear flows.

And finally, the asymptotic states predicted by the final version of the NT1 model are presented in Table 6.24 below for latter comparison with the NT2 model.

Now that the final version of the NT1 model has been presented, a few comments on the model's coefficients and asymptotic states are worthwhile. The final version of the NT1

Table 6.23: Coefficients of the final version of the NT1 model

c_μ	C_{P1}	C_{P2}	σ_{ε_P}	C_{T1}	C_{T2}	σ_{ε_T}
$min[0.115, 0.023 + 0.25e^{-0.30\eta}]$	$max\left[1.4921 + 2.5\frac{min(0, \frac{k_P}{k_T} - f_{BL})}{\frac{k_P}{k_T} + f_{BL}}, 0\right]$	1.8	1.4202	1.6	1.7	1.2181

Table 6.24: Values expected to be provided by the second version of the NT1 model in the asymptotic states studied

$\left(\frac{P_k}{\varepsilon_T}\right)_{SF}$	$\left(\frac{k_P}{k_T}\right)_{SF}$	$\left(\frac{\varepsilon_P}{\varepsilon_T}\right)_{SF}$	$\left(\frac{k_P}{k_T}\right)_{DF}$	$\left(\frac{\varepsilon_P}{\varepsilon_T}\right)_{DF}$	$\left(\frac{k_P}{k_T}\right)_{BL}$	$\left(\frac{\varepsilon_P}{\varepsilon_T}\right)_{BL}$	$c_{\mu_{BL}}$
1.9	4.4	1.1667	1.0	0.5	3.6	1.0	0.115

model differs from its second version due to the new C_{P1} expression only. The f_1 and f_2 terms, presented in equations 6.91 and 6.92 respectively, incorporated in C_{P1} (now equation 6.73) through the new parameter f_{BL}, defined in equation 6.90, are not expected to disturb the asymptotic analyses carried out for the second version of the NT1 model nor to affect significantly the prediction of the test cases other than the backward facing step ones.

As commented on before where each term in f_1 and f_2 were discussed, the f_{BL} is designed to reduce to $f_{BL} = \left(\frac{k_P}{k_T}\right)_{BL} = 3.6$ in the asymptotic states as well as in flows where f_1 and f_2 are expected to be negligible. The asymptotic state of decaying grid turbulence was not mentioned during the development of the f_1 and f_2 terms since these are straightaway negligible in this equilibrium state where $\frac{\varepsilon_P}{\varepsilon_T}$ is necessarily smaller than unity and after all, as $P_{k_{DF}} = 0$, any change in C_{P1} would not affect this flow which is one more advantage of incorporating the f_1 and f_2 terms into this coefficient.

The f_2 term has a rather high constant, 20, which is not expected to create instabilities due to the expected low magnitude of $\max\left[\frac{k_P}{k_T}\max\left(\frac{\varepsilon_P}{\varepsilon_T} - 1, 0\right)SW, 0\right]$. This hypothesis was confirmed when running the other test cases.

6.3.3 Tests Towards the Final version of the NT2 Model

The same procedures followed to arrive at the final version of the NT1 model were carried out to arrive at the final version of the NT2 model. They will be then presented in a briefer way here, since the main reasons for choosing the extra terms are the same as those discussed in the NT1 section.

Firstly, C_{P1} can be expressed as:

$$C_{P1} = 1.5697 + 2.5\frac{\min\left[\frac{k_P}{k_T} - f_{BL}, 0\right]}{\frac{k_P}{k_T} + f_{BL}} \tag{6.94}$$

where in the second version of the NT2 model $f_{BL} = \left(\frac{k_P}{k_T}\right)_{BL} = 3.7$. In Table 6.25 are presented the tests which led to the final form of the f_1 term, similar to that in equation 6.75. From Test 3 in Table 6.25 one can write:

$$f_{BL} = \left(\frac{k_P}{k_T}\right)_{BL}(1 - f_1) = 3.7(1 - f_1) \tag{6.95}$$

$$f_1 = 5.4\left(\frac{k_P}{k_T} - 1.3166\right)\min\left(\frac{P_k}{\varepsilon_T} - 1.9, 0\right)\max\left(\frac{\varepsilon_P}{\varepsilon_T} - 1, 0\right) \tag{6.96}$$

There are two main differences between the f_1 term in the final versions of the NT1 and NT2 models: in the former, the coefficient is rather lower than in the latter (1.7 in equation 6.75 against 5.4 in equation 6.96) and, as in the second version of the NT2 model, $\left(\frac{k_P}{k_T}\right)_{DF} = 1.3166$, that is the value used in f_1 instead of unity which is $\left(\frac{k_P}{k_T}\right)_{DF}$ in the NT1 model. The reason for needing such higher constant in f_1 is mainly due to the fact that the second version of the NT2 model strongly over-estimates the reattachment length in the backward facing step cases and therefore a stronger extra term was needed.

Table 6.25: Tests performed in the backward facing step cases with the NT2 model, exploring f_1 in C_{P1} in equation 6.94.

Test NT2	f_1	f_{BL}	Reattachment Point		
			St=0	St=0.275	St=1
1	6.0	f_1	7.7	8.4	8.7
2	$9\max\left(\frac{\varepsilon_P}{\varepsilon_T} - 1, 0\right)$	$\left(\frac{k_P}{k_T}\right)_{BL}(1 + f_1)$	7.8	8.0	8.7
3	$5.4\left(\frac{k_P}{k_T} - 1\right)\min\left(\frac{P_k}{\varepsilon_T} - 1.9, 0\right)\max\left(\frac{\varepsilon_P}{\varepsilon_T} - 1, 0\right)$	$\left(\frac{k_P}{k_T}\right)_{BL}(1 - f_1)$	7.9	8.7	8.9
EXP	-	-	7.8	5.0	8.1

The same tests performed in the NT1 model with the terms $\frac{P_k}{\varepsilon_P}\max\left(\frac{\varepsilon_P}{\varepsilon_T} - 1, 0\right)SW$ and $\frac{k_P}{k_T}\max\left(\frac{\varepsilon_P}{\varepsilon_T} - 1, 0\right)SW$ in C_{T1} were also performed with the NT2 model and are presented in Table 6.26. It is worth noticing though that if Test 4 Table 6.26 is used without clipping C_{T1} or $\frac{\varepsilon_P}{\varepsilon_T}$ convergence is not reached which shows a less stable feature of this model compared to the NT1 formulation. On the other hand, by comparing Tables 6.17 and 6.26, one may notice that by applying the clippings shown in Tests 4, 6 and 7 the reattachment length in the high frequency case is not reduced by as much as when the same clippings were applied in the NT1 model.

Table 6.26: Tests performed in the backward facing step cases with the NT2 model, using C_{P1} given by equations 6.94, 6.95 and 6.96, and exploring f_2 in C_{T1}.

Test NT2	f_2	C_{T1}	Reattachment Point		
			St=0	St=0.275	St=1
4	$1.7\frac{P_k}{\varepsilon_P}\max\left(\frac{\varepsilon_P}{\varepsilon_T} - 1, 0\right)SW$	$\max(C_{T1} - f_2, 0)$	7.9	5.0	6.4
5	$1.25\frac{P_k}{\varepsilon_P}\min\left[4, \max\left(\frac{\varepsilon_P}{\varepsilon_T} - 1, 0\right)\right]SW$	$C_{T1} - f_2$	7.9	5.0	5.9
6	$1.3\frac{P_k}{\varepsilon_P}\sqrt{\max\left(\frac{\varepsilon_P}{\varepsilon_T} - 1, 0\right)SW}$	$C_{T1} - f_2$	7.9	5.4	6.7
7	$\frac{k_P}{k_T}\max\left(\frac{\varepsilon_P}{\varepsilon_T} - 1, 0\right)SW$	$\max(C_{T1} - f_2, 0)$	7.9	5.5	6.5
EXP	-	-	7.8	5.0	8.1

As tests in the C_{T1} did not succeed, just as in the NT1 model, the same tests performed in C_{T2} were carried out and are presented in Table 6.27, where it can be seen that, as in the

NT1 model, incorporating an extra term in C_{T1} or C_{T2} is equivalent and in both the dynamic of the differential equations changes and the reattachment length is excessively reduced.

Table 6.27: Tests performed in the backward facing step cases with the NT2 model, using C_{P1} given by equations 6.94, 6.95 and 6.96, and exploring f_2 in C_{T2}.

Test NT2	f_2	C_{T2}	Reattachment Point		
			St=0	St=0.275	St=1
8	$2.5\frac{k_P}{k_T}\max\left(\frac{\varepsilon_P}{\varepsilon_T}-1,0\right)SW$	$C_{T2}+f_2$	8.0	5.2	6.6
9	$3.5\frac{k_P}{k_T}\max\left(\frac{\varepsilon_P}{\varepsilon_T}-1.2,0\right)SW$	$C_{T2}+f_2$	7.9	5.0	6.2
10	$5\frac{k_P}{k_T}\max\left(\frac{\varepsilon_P}{\varepsilon_T}-1.4,0\right)SW$	$C_{T2}+f_2$	7.9	4.8	5.8
11	$6.6\frac{k_P}{k_T}\max\left(\frac{\varepsilon_P}{\varepsilon_T}-1.6,0\right)SW$	$C_{T2}+f_2$	7.9	5.1	5.7
EXP	-	-	7.8	5.0	8.1

The main difference between the behaviour of the NT1 and NT2 models occurred when tests in incorporating a second extra term in C_{P1} were carried out. These tests are presented in Table 6.28. As in the NT1 model, when a term such as $\max\left[\frac{k_P}{k_T}\max\left(\frac{\varepsilon_P}{\varepsilon_T}-1,0\right)SW\right]$ was included in C_{P1} without an upper limit, Test 12 in Table 6.28, the reattachment length in the high frequency case was increased to 7.2, but that was still rather low, since experiments indicated $X_R = 8.1$. However, when $\max\left[\frac{k_P}{k_T}\max\left(\frac{\varepsilon_P}{\varepsilon_T}-1,0\right)SW\right]$ was imposed an upper limit, such as in Tests 13 to 16 in Table 6.28, the reattachment length in the high frequency case was significantly increased and in the low frequency case it remained about 5 which matched the experimental value. Different upper limits were studied in Tests 13, 14 and 15 in Table 6.28. The NT2 model behaved as expected, differently than the NT1 model where an upper limit did not increase the reattachment length in the high frequency case. The clipping with 1.5 or 1.8 (Tests 13 and 14) seemed equivalent while when clipping with 2.0 (Test 15) the reattachment length at the $BFS-St1$ case started to decrease, indicating that the f_2 term should not increase as high as 2.0. In Test 16, it was studied the influence of clipping C_{P1} and not allowing it to become negative. This test performed best and was adopted as the final version of the NT2 model.

So now f_{BL} can be defined as:

$$f_{BL} = \left(\frac{k_P}{k_T}\right)_{BL}(1-f_1+f_2) = 3.7(1-f_1+f_2) \tag{6.97}$$

$$f_2 = 11\min\left\{1.8, \max\left[\frac{k_P}{k_T}\max\left(\frac{\varepsilon_P}{\varepsilon_T}-1,0\right)SW, 0\right]\right\} \tag{6.98}$$

Just as a matter of testing, it would be interesting to check whether the same f_2 expression used in the NT1 model, equation 6.80, would also work in the NT2 model. Test 17 still in Table 6.28 shows that even using a high constant such as 25, the reattachment length in the low frequency case could not be reduced enough to match the experiments which provide $X_R = 5.0$.

Also for the sake of closing the set of tests with the NT2 model, the f_2 terms used for both NT1 and NT2 models were tested in the C_{P2} and C_{T2} coefficients as shown in Table 6.29. When f_2 was used as $\min\left\{1.8, \max\left[\frac{k_P}{k_T}\max\left(\frac{\varepsilon_P}{\varepsilon_T}-1,0\right)SW, 0\right]\right\}$ in C_{P2} (Test

Table 6.28: Tests performed in the backward facing step cases with the NT2 model, using C_{P1} given by equations 6.94, f_1 given by equation 6.96, and exploring f_2 in C_{P1} too through f_{BL}.

Test NT2	f_2	f_{BL}	Reattachment Point		
			St=0	St=0.275	St=1
12	$11\max\left[\frac{k_P}{k_T}\max\left(\frac{\varepsilon_P}{\varepsilon_T}-1,0\right)SW,0\right]$	$\left(\frac{k_P}{k_T}\right)_{BL}(1-f_1+f_2)$	-	5.1	7.2
13	$11\min\left\{1.5,\max\left[\frac{k_P}{k_T}\max\left(\frac{\varepsilon_P}{\varepsilon_T}-1,0\right)SW,0\right]\right\}$	$\left(\frac{k_P}{k_T}\right)_{BL}(1-f_1+f_2)$	7.8	5.1	7.7
14	$11\min\left\{1.8,\max\left[\frac{k_P}{k_T}\max\left(\frac{\varepsilon_P}{\varepsilon_T}-1,0\right)SW,0\right]\right\}$	$\left(\frac{k_P}{k_T}\right)_{BL}(1-f_1+f_2)$	7.84	5.12	7.7
15	$11\min\left\{2.0,\max\left[\frac{k_P}{k_T}\max\left(\frac{\varepsilon_P}{\varepsilon_T}-1,0\right)SW,0\right]\right\}$	$\left(\frac{k_P}{k_T}\right)_{BL}(1-f_1+f_2)$	7.84	5.12	7.6
16	$11\min\left\{1.8,\max\left[\frac{k_P}{k_T}\max\left(\frac{\varepsilon_P}{\varepsilon_T}-1,0\right)SW,0\right]\right\}$	$\left(\frac{k_P}{k_T}\right)_{BL}(1-f_1+f_2)$ $\max(C_{P1},0)$	7.84	5.05	7.8
17	$25\max\left[\frac{k_P}{k_T}\max\left(\frac{\varepsilon_P}{\varepsilon_T}-1.1,0\right)SW,0\right]$	$\left(\frac{k_P}{k_T}\right)_{BL}(1-f_1+f_2)$	-	7.95	-
EXP	-	-	7.8	5.0	8.1

18 in Table 6.29) and in C_{T2} (Test 20 in Table 6.29), the reattachment length in the low frequency case was reduced enough, however, in the high frequency case it became too low, as happened in the previous tests with C_{T1} and C_{T2}. When f_2 was adopted as in the NT1 model, $\max\left[\frac{k_P}{k_T}\max\left(\frac{\varepsilon_P}{\varepsilon_T}-1.1,0\right)SW,0\right]$, and applied in C_{P2}, it was noticed that rather high constants would be necessary, since with 15, the reattachment length in the low frequency case reduced only to 7.8 against the expected value of 5.0 suggested by the experiments. When applied in C_{T2}, again the reattachment length in the high frequency case was excessively reduced.

Table 6.29: Tests performed in the backward facing step cases with the NT2 model, using C_{P1} given by equations 6.94, 6.95 and 6.96, and exploring f_2 similar to equations 6.80 or 6.98 in C_{P2} or C_{T2}.

Test NT2	f_2	Coefficient Changed	Reattachment Point		
			St=0	St=0.275	St=1
18	$4.5\min\left\{1.8,\max\left[\frac{k_P}{k_T}\max\left(\frac{\varepsilon_P}{\varepsilon_T}-1,0\right)SW,0\right]\right\}$	$C_{P2}+f_2$	7.8	5.0	6.5
19	$15\max\left[\frac{k_P}{k_T}\max\left(\frac{\varepsilon_P}{\varepsilon_T}-1.1,0\right)SW,0\right]$	$C_{P2}+f_2$	-	7.8	-
20	$2.6\min\left\{1.8,\max\left[\frac{k_P}{k_T}\max\left(\frac{\varepsilon_P}{\varepsilon_T}-1,0\right)SW,0\right]\right\}$	$C_{T2}+f_2$	7.8	5.4	6.8
21	$2.6\max\left[\frac{k_P}{k_T}\max\left(\frac{\varepsilon_P}{\varepsilon_T}-1.1,0\right)SW,0\right]$	$C_{T2}+f_2$	7.8	5.4	6.8
EXP	-	-	7.8	5.0	8.1

In Tables 6.25 to 6.29 whenever the reattachment point was indicated by a dashed sign it meant those test cases were not run, because the models have already been shown to fail in one of the other cases tested.

6.3.4 The Final Version of the NT2 Model

The full final version of the NT2 model can now be presented.

According to the tests presented above, the final version of the NT2 model is the second version of the NT2 model with C_{P1} given by equations 6.94, 6.97, 6.96 and 6.98 which correspond to Test 16 in Table 6.28.

The transport equations for the final form of the NT2 model is presented in equations

6.59 to 6.62 and will be repeated here for the sake of presenting the whole model.

$$\frac{Dk_P}{Dt} = P_k - \varepsilon_P + \frac{\partial}{\partial x_j}\left[\left(\nu + \frac{\nu_t}{\sigma_{k_P}}\right)\frac{\partial k_P}{\partial x_j}\right] \tag{6.99}$$

$$\frac{Dk_T}{Dt} = \varepsilon_P - \varepsilon_T + \frac{\partial}{\partial x_j}\left[\left(\nu + \frac{\nu_t}{\sigma_{k_T}}\right)\frac{\partial k_T}{\partial x_j}\right] \tag{6.100}$$

$$\frac{D\varepsilon_P}{Dt} = C_{P1}P_k\frac{\varepsilon_P}{k_P} - C_{P2}\frac{\varepsilon_P^2}{k_P} + C'_{P1}k_P\frac{\partial U_l}{\partial x_m}\frac{\partial U_i}{\partial x_j}\epsilon_{lmk}\epsilon_{ijk} + \frac{\partial}{\partial x_j}\left[\left(\nu + \frac{\nu_t}{\sigma_{\varepsilon_P}}\right)\frac{\partial \varepsilon_P}{\partial x_j}\right] \tag{6.101}$$

$$\frac{D\varepsilon_T}{Dt} = C_{T1}\frac{\varepsilon_P^2}{k_T} - C_{T2}\frac{\varepsilon_T^2}{k_T} + \frac{\partial}{\partial x_j}\left[\left(\nu + \frac{\nu_t}{\sigma_{\varepsilon_T}}\right)\frac{\partial \varepsilon_T}{\partial x_j}\right] \tag{6.102}$$

The Reynolds stresses are calculated through the linear-eddy-viscosity scheme given by:

$$\overline{u_i u_j} = -\nu_t\left(\frac{dU_i}{dx_j} + \frac{dU_j}{dx_i}\right) + \frac{2}{3}k\delta_{ij} \tag{6.103}$$

where the eddy viscosity ν_t is defined as:

$$\nu_t = c_\mu\frac{k^2}{\varepsilon_T} \tag{6.104}$$

The coefficients of the final version of the NT2 model are presented in Table 6.30 where:

$$\eta = \max\left[\frac{k}{\varepsilon_T}\sqrt{\frac{1}{2}S_{ij}S_{ij}}, \frac{k}{\varepsilon_T}\sqrt{\frac{1}{2}W_{ij}W_{ij}}\right] \tag{6.105}$$

$$S_{ij} = \frac{\partial U_i}{\partial x_j} + \frac{\partial U_j}{\partial x_i} \tag{6.106}$$

$$W_{ij} = \frac{\partial U_i}{\partial x_j} - \frac{\partial U_j}{\partial x_i} \tag{6.107}$$

$$f_{BL} = \left(\frac{k_P}{k_T}\right)_{BL}(1 - f_1 + f_2) = 3.7(1 - f_1 + f_2) \tag{6.108}$$

$$f_1 = 5.4\left(\frac{k_P}{k_T} - 1.3166\right)\min\left(\frac{P_k}{\varepsilon_T} - 1.9, 0\right)\max\left(\frac{\varepsilon_P}{\varepsilon_T} - 1, 0\right) \tag{6.109}$$

$$f_2 = 11\min\left\{1.8, \max\left[\frac{k_P}{k_T}\max\left(\frac{\varepsilon_P}{\varepsilon_T} - 1, 0\right)SW, 0\right]\right\} \tag{6.110}$$

$$SW = \frac{S_{ij}S_{ij} - W_{ij}W_{ij}}{S_{ij}S_{ij} + W_{ij}W_{ij}} \tag{6.111}$$

The expressions for η, S_{ij}, W_{ij} and SW are the same for the NT1 model, however they are being repeated here in order to present the full final version of the NT2 model.

Table 6.30: Coefficients of the final version of the NT2 model

c_μ	C_{P1}	C_{P2}	σ_{ε_P}
$min[0.09, 0.0117 + 0.22e^{-0.31\eta}]$	$max\left[1.5697 + 2.5\frac{min(0, \frac{k_P}{k_T} - f_{BL})}{\frac{k_P}{k_T} + f_{BL}}, 0\right]$	1.8	1.6664
C_{T1}	C_{T2}	σ_{ε_T}	C'_{P1}
1.0	1.1	1.1922	-0.005

And finally, the asymptotic states predicted by the final version of the NT2 model are presented in Table 6.31 below. Comparing Tables 6.24 and 6.31, it should be noted that both NT1 and NT2 models satisfy the asymptotic constraints such as $\left(\frac{P_k}{\varepsilon_T}\right)_{SF} \approx 2$, $\left(\frac{k_P}{k_T}\right)_{DF} < \left(\frac{k_P}{k_T}\right)_{BL} < \left(\frac{k_P}{k_T}\right)_{SF}$ and $\left(\frac{\varepsilon_P}{\varepsilon_T}\right)_{DF} < 1$, thus arising as more consistent than the other LEV MTS models studied.

Table 6.31: Values expected to be provided by the second version of the NT2 model in the asymptotic states studied

$\left(\frac{P_k}{\varepsilon_T}\right)_{SF}$	$\left(\frac{k_P}{k_T}\right)_{SF}$	$\left(\frac{\varepsilon_P}{\varepsilon_T}\right)_{SF}$	$\left(\frac{k_P}{k_T}\right)_{DF}$	$\left(\frac{\varepsilon_P}{\varepsilon_T}\right)_{DF}$	$\left(\frac{k_P}{k_T}\right)_{BL}$	$\left(\frac{\varepsilon_P}{\varepsilon_T}\right)_{BL}$	$c_{\mu_{BL}}$	$c_{\mu_{SF}}$
1.9	8.8245	1.0916	1.3166	0.5683	3.7	1.0	0.09	0.0336

One may notice that the final version of the NT2 model reduces to its second version when f_1 and f_2, presented in equations 6.109 and 6.110, diminish. As a result, as these terms become zero, the final version of the model also satisfies all asymptotic states used to derive the coefficients of the second version of the NT2 model.

6.3.5 Performance of The Final Versions of the NT1 and NT2 Models

Although the final versions of the NT1 and NT2 models are not expected to provide significantly different results from those of their second versions in all test cases, but the backward facing step cases, the performance of the final versions of the NT1 and NT2 models is discussed for all test cases presented in Chapter 5, since this is the final result of this work.

As the NT1 and NT2 models are linear-eddy-viscosity schemes, prediction of the Reynolds normal stresses will not be considered here. The results provided by the final versions of the NT1 and NT2 models, from now on simply referred to as the NT1 and NT2 models, will be compared to those of the HR, SG and TS models and the respective experimental or DNS data of each case. In the cases where the TS model did not converge - only the unsteady backward facing step cases - the KC model will be used for comparison, representing an existing linear-eddy-viscosity two-time-scale model.

The prediction of the turbulent kinetic energy, eddy dissipation rate and Reynolds shear stress in the homogeneous shear flows are presented for the six cases described in Chapter

5 in Figures 6.65 to 6.70. One may notice that the NT1 and NT2 models performed best in the set of cases, validating them in a wide range of dimensionless shear values such as $1 < \eta = \frac{k}{\varepsilon}\frac{dU}{dy} < 30$. The NT1 and NT2 models performed overall even better than the SG model, which is a much more complex model and designed for homogeneous shear flows, thus being one of the significant improvements they provided.

The predictions of the turbulent kinetic energy in the three normally strained cases are presented in Figure 6.71 where one can see the improvements the NT1 and NT2 models provided compared to the HR and TS models. The NT1, NT2 and SG models perform equally well in the $T\&R$ and $G\&M0$ cases which is again an improvement of the new models that must be highlighted, and as expected, only the SG model, which does not use the linear-eddy-viscosity approach, is able to respond to the change in sign of the normal straining in the $G\&M05$ case.

Evaluating the performance of the NT1 and NT2 models in the channel flow cases, the prediction of the velocity, turbulent kinetic energy and eddy dissipation rate for the cases with Reynolds number equal to 6500 and 41441 are presented in Figures 6.72 and 6.73 respectively. As commented on before, the prediction of channel flows are useful to guarantee the models behave well in such simple flows and that the velocity profile does satisfy the log law of the wall. As expected, the NT1 and NT2 models as well as the HR, SG and TS models provide reasonable results in the channel flow cases. In the relatively low Reynolds number cases such as with $Re = 6500$, the profiles are compromised by the use of the wall function, since a far first near-wall node is required to provide $y^+ \approx 30$. The important conclusion here about the channel flow cases though is that the terms introduced in C_{P1}, which differentiate the final version from the second versions of the NT1 and NT2 models, did not cause any undesired effect on the prediction of these flows.

The performance of the NT1 and NT2 models in zero pressure gradient boundary layers can be assessed in Figures 6.74 to 6.76. The profiles of velocity, turbulent kinetic energy, eddy dissipation rate and Reynolds shear stress across the boundary layer at $Re_\theta = 1410$ is presented in Figure 6.74 and the velocity and Reynolds shear stress profiles at $Re_\theta = 4981$ and at $Re_\theta = 13052$ are presented in Figure 6.76. One may notice that the NT1 and NT2 models perform reasonably well and so do the other models, as expected. As was the case with the channel flows, the zero pressure gradient boundary layer is a test case used to ensure the correct behaviour of the models in such basic, but important, flows. The predictions of the skin-friction coefficient, shape factor and boundary layers thickness are presented in Figure 6.75 for the Spalart boundary layer case which is representative of the other two ZPGBL cases described in Chapter 5. One may notice that the NT1 and NT2 models provide reasonable results as well as the other models.

The velocity and Reynolds shear stress profiles at two measurement positions in the $S\&J$ adverse pressure gradient boundary layer case are presented in Figure 6.77. As commented on before, all models perform well until station 5 and no model is actually able to follow the change in the velocity profile from this station to station 6 where the pressure gradient presents the strongest increase, as discussed in Chapter 5. The SG model performs best in

the prediction of the Reynolds shear stress profile, with the NT1 and NT2 models performing reasonably well and resulting in slight improvements.

The profiles of the velocity, Reynolds shear stress and turbulent kinetic energy at four measurement positions in the $M\&P30$ adverse pressure gradient boundary layer case are presented in Figures 6.78 to 6.80. One may notice that none of the models are able to capture the subtle changes in the velocity profile presented in in Figure 6.78. The SG model performs slightly better in predicting the Reynolds shear stress, presented in Figure 6.79, than the NT1 and NT2 models which perform slightly better than the HR model and better than the TS model which overpredicts this quantity. None of the models though are able to capture the level of the turbulent kinetic energy, specially in the last station where again the pressure gradient is the steepest. Similar analyses can be extended to the $M\&P10$ case which is then not being presented here. The prediction of the boundary layer parameters is presented in Figure 6.81 for the $M\&P30$ case representing the other APGBL cases. Again, these parameters are similarly and well predicted by all models. If one compares the prediction of the Reynolds shear stress and turbulent kinetic energy provided by the second versions of the model in this case, presented in Figures 6.44 and 6.45 respectively, one may notice that the final versions of the NT1 and NT2 models tend to provide a rather lower decay of these quantities towards the outer layer. That can be then associated with the two extra terms introduced in C_{P1}, however this does not disturb the overall performance of the NT1 and NT2 models.

The performance of the NT1 and NT2 models in the favourable pressure gradient boundary layer cases is presented in Figures 6.82 to 6.84. The velocity, Reynolds shear stress, turbulent kinetic energy and eddy dissipation rate profiles in the three cases described in Chapter 5 are presented in Figures 6.82, 6.83 and 6.84 for acceleration parameters equal to 1.5×10^{-6}, 2.5×10^{-6} and 2.75×10^{-6} respectively. One may notice that the NT1 and NT2 models as well as the HR and SG model perform similarly and better than the TS model at the lowest acceleration parameter case, where the TS provides a too fast decay of the turbulent quantities, especially the Reynolds shear stress. On the other hand, for the higher acceleration parameter cases, the TS model seems to capture better the turbulent quantity profiles and the NT1 and NT2 models as well as the HR and SG models tend to provide a rather slow decay of k, $\overline{uv}$ and ε, thus overpredicting them. That actually shows that none of the models is able to capture the changes in the profiles as the flow is accelerated, though the NT1 and NT2 models perform reasonably well in all cases.

The predictions of the NT1 and NT2 models of the velocity and Reynolds shear stress profiles at selected positions in the cycle and throughout the cycle in the JSF oscillatory boundary layer cases are presented in Figures 6.85 to 6.88. As commented on before, in this test case all turbulence models tend to perform similarly and reasonably well and the NT1 and NT2 models are no exception.

More challenging cases though are the fully developed oscillatory pipe flows with different forcing frequencies. Starting by looking at the results for the low frequency case, one may confirm the expected bulk velocity profile and assess the prediction of the wall shear stress

and Reynolds shear stress at $y/R = 0.07$ and $y/R = 0.63$ in Figure 6.89. The wall shear stress is well predicted by all models, the Reynolds shear stress at $y/R = 0.07$, closer to the wall, is best predicted by the SG model, the other models tending to overpredict this quantity at this position when the bulk velocity assumes the highest levels and none of the models were actually capable of capturing the intensity and position of the Reynolds shear stress peak at $y/R = 0.63$. The Reynolds shear stress profiles at four positions in the cycle are presented in Figure 6.90 where the models perform similarly and predict reasonably well this quantity at some positions in the cycle and not very well in others. The performance of the NT1 and NT2 models is overall reasonably good and, as noticed in the adverse pressure gradient boundary layer case, the final versions of the models tended to provide a slower decay of $\overline{uv}$ at $\omega t = 45^o$. That is again associated with the extra terms introduced in C_{P1} and again that does not compromise the performance of the models.

The final versions of the NT1 and NT2 models also predicted frozen turbulence for the high frequency case $Tu\&R36$ and therefore profiles at selected positions in the cycle are not shown here.

Among the oscillatory pipe flow cases, the more challenging one is the $T3RE14A20$ case which uses an intermediate forcing frequency. The amplitude and phase shift of the velocity and Reynolds shear stress in the radial direction is presented in Figure 6.91. One may notice that the velocity amplitude and phase shift are reasonably well predicted by all models, the TS model perhaps performing best. The Reynolds shear stress amplitude is well predicted by all models as well. This represents an improvement from the second to the final versions of the NT1 and NT2 models, since the former were underpredicting the amplitude of $\overline{uv}$ and now this quantity is well predicted. On the other hand, the Reynolds shear stress phase shift is underpredicted by the NT1 and NT2 models. That also happened with the second version of the models, so in this case it can be said that the extra terms introduced in C_{P1} contributed positively to the performance of the NT1 and NT2 models, however could not improve the prediction of the Reynolds shear stress phase shift. The positive effects must have come from the f_1 terms (equations 6.91 and 6.109) since the SW term in f_2 (equations 6.92 and 6.110) is expected to be zero in fully developed pipe flows where the only non-zero velocity gradient is $\frac{dU}{dy}$.

The performance of the NT1 and NT2 models in the fully developed ramp up pipe flow case can be assessed in Figures 6.92 and 6.93 for the turbulent kinetic energy and Reynolds shear stress profiles varying in time at three positions in the radial direction respectively. The velocity profiles are not being shown because they are all well predicted by all models. The same can be said of the Reynolds shear stress which is presented in Figure 6.92. The prediction of the turbulent kinetic energy though is more challenging, since it was already noted that the models tended to perform well either at the centre of the pipe ($r/R = 0$) or in the mid distance from the centre to the wall, $r/R = 0.47$. The NT1 and NT2 models are thus best predicting this quantity at $r/R = 0.47$ and overpredicting its profile at $r/R = 0$. The second versions of the NT1 and NT2 models tended to predict better the profile of k at the centre of the pipe. Considering the predictions of the versions of the developed models at

both $r/R = 0$ and $r/R = 0.47$, by comparing Figures 6.48 and 6.93, one might say that the final versions of the NT1 and NT2 models are performing better than their previous versions.

Finally, the performance of the models in the backward facing step cases is assessed.

As before, the predicted time-averaged location of the reattachment point for each case is evaluated before looking at the time-averaged velocity profiles, since the former provides a quicker initial comparison to assess the model predictive effectiveness than the latter.

It can be noted in Table 6.32 that the NT1 and NT2 models are the only models which predict correctly the time-averaged reattachment point at the three forcing frequencies. That is again a clear improvement provided by the NT1 and NT2 models when compared to other existing models, even much more complex ones such as the SG model which is a RST model.

Table 6.32: Performance of the second version of the NT1 and NT2 in predicting the time-averaged reattachment point in the three backward facing step cases.

Model/Experiment	St=0	St=0.275	St=1
Experiment	7.8	5.0	8.1
HR	6.42	5.01	6.67
SG	6.95	5.51	7.66
KC	8.44	7.21	9.15
TS	4.14	-	-
NT1	7.82	5.05	7.96
NT2	7.84	5.05	7.81

Looking now at the time-averaged velocity profiles for each case, presented in Figures 6.94, 6.97 and 6.98 for the $BFS - St0$, $BFS - St0275$ and $BFS - St1$ cases respectively, one can see that the NT1 and NT2 models perform reasonably well in all cases. In the steady state case, the NT1 and NT2 models still overpredict the velocity in the shear region at $x/H = 9$ which means the models are also presenting a rather slow recovery process. The time-averaged velocity profiles provided by the NT1 and NT2 models in the case where $St = 0.275$ are clearly improved compared to the second version of the models which were strongly overpredicting the reattachment length in this case. By comparing the time-averaged velocity profiles predicted by the NT1 and NT2 models with those of the HR model for the low frequency case, where the three models predicted correctly the reattachment point, one may say that these three models return practically identical predictions at this frequency. This suggests that the post-reattachment recovery process is similar and rather slow for the three models. This supports the hypothesis expressed earlier about the HR model providing the best velocity profile at the steady state case where it underpredicts the reattachment point. At the high frequency case, where all models tended to provide a reasonable time-averaged velocity profile, it can be said that the NT1 and NT2 models provide the best prediction. As commented on before, it is thought that the low recovery characteristic of the models is not seen in this case because the last position downstream of the step where there are experimental data available is too close to the reattachment point.

As the stream function contour plots for all models were presented for the steady state in Chapter 5, these contour plots are also being presented here for the final versions of the NT1 and NT2 models in Figures 6.95 and 6.96 respectively. One may notice that the new models

could not capture the small recirculation bubble at the corner of the step which circulates fluid in a direction opposite to that of the main recirculation loop indicated in the experiments and that might be related to the use of wall functions, as discussed in Chapter 5.

The profiles of the time-averaged wall shear stress and wall-pressure coefficient are presented in Figures 6.99 and 6.100 for the $BFS - St0$, $BFS - St0275$ and $BFS - St1$ cases respectively. These results just confirm overall reasonably good performance of the NT1 and NT2 models.

Finally, in order to further assess the final versions of the NT1 and NT2 models and test the consistency of the effect of the introduced terms in C_{P1}, only these two models were used to run a series of different frequency cases. These cases are detailed in Table 6.33 where the specifications needed to set up all unsteady cases are also shown for both NT1 and NT2 models. Recalling the set up of the unsteady backward facing step cases, the velocity at $y/H = 0.01$ in the steady case used as $Q_{unforced}$ to calculate the forcing amplitude as $A_0 = 0.07$ was $8.4m/s$ in the NT1 model and $8.5m/s$ in the NT2 model.

Table 6.33: Specifications for the unsteady backward facing step cases run with the final versions of the NT1 and NT2 models.

St	frequency (Hz)	time step	Jet amplitude B at $(x/H, y/H) = (0, 0)$	
			$NT1$	$NT2$
0.025	7	3.571429E-04	$1.1\sqrt{2}$	$1.15\sqrt{2}$
0.05	14	1.785714E-04	$1.18\sqrt{2}$	$1.2\sqrt{2}$
0.1	28	8.928571E-05	$1.24\sqrt{2}$	$1.25\sqrt{2}$
0.14	39.2	6.377551E-05	$1.25\sqrt{2}$	$1.27\sqrt{2}$
0.2	56	4.464286E-05	$1.31\sqrt{2}$	$1.31\sqrt{2}$
0.275	77	3.246753E-05	$1.38\sqrt{2}$	$1.4\sqrt{2}$
0.4	112	2.232143E-05	$1.58\sqrt{2}$	$1.54\sqrt{2}$
0.6	168	1.488095E-05	$1.81\sqrt{2}$	$1.7\sqrt{2}$
0.8	224	1.116071E-05	$1.97\sqrt{2}$	$1.85\sqrt{2}$
1	280	8.928571E-06	$2.02\sqrt{2}$	$1.91\sqrt{2}$
1.5	420	5.952381E-06	$2.0\sqrt{2}$	$1.89\sqrt{2}$
2	560	4.464286E-06	$1.85\sqrt{2}$	$1.78\sqrt{2}$

Although the final versions of the NT1 and NT2 models were defined using C_{P1} clipped so that it could not become negative, the unsteady cases in Table 6.33 were also run with a version of the models where C_{P1} was not clipped. The idea of this test was to verify whether any stability issue would arise or if any significant difference in the predictions would be noted.

The prediction of the time-averaged reattachment point for each of the backward facing step cases run with the NT1 and NT2 models are presented in Figure 6.101 for the version where C_{P1} was not clipped and in Figure 6.102 for the final version of the models where C_{P1} is not allowed to become negative.

One may notice that NT1 and NT2 models performed just the same whether C_{P1} was clipped or not and no stability issues were identified. The biggest difference being on the prediction of the time-averaged reattachment point by the NT1 model in the case where

$St = 1.5$ where the version with C_{P1} clipped provided $X_R = 8.4$ and the version where there was no clip in C_{P1} provided $X_R = 7.9$.

Looking now at the results themselves, it is possible to say that they are quite promising, showing that the terms introduced in C_{P1} do capture the effects of the different forcing frequencies. Both models followed reasonably well the experimental pattern, confirming the lowest time-averaged reattachment point at $St = 0.275$ and providing approximately constant time-averaged reattachment length for $St > 1$. However, the NT1 model provided a too fast recovery of the time-averaged reattachment point while the NT2 model provided a rather slow one. These differences are nevertheless rather modest. Overall agreement with experimental data remains close.

In Figure 6.103 prediction of the time-averaged reattachment point by NT1 and NT2 models is compared with the prediction provided by the HR, SG and KC models in the three cases the single-time-scale models were run with. The graphs clearly show that the tested single-time-scale models are not able to follow the experimental pattern, as already discussed. In Figure 6.103(a) the time-averaged reattachment point is not normalized allowing one to identify the models which underpredict and overpredict this parameter. In Figure 6.103(b) the time-averaged reattachment point at each case is normalized by the reattachment point predicted by each model in the steady state so that one can see how flexible the models are in terms or decreasing or increasing the time-averaged reattachment length according to each forcing frequency case.

So that concludes the analysis about the performance of the final versions of the NT1 and NT2 models. The new models can be considered to perform well in all test cases and to particularly improve the prediction of homogeneous shear flows, normally strained flows and steady and unsteady backward facing step cases. The new models show a wider range of applicability than other MTS and STS models and, in cases like the pulsated backward facing step flows and shear flows, they are the only models which predict the correct behaviour.

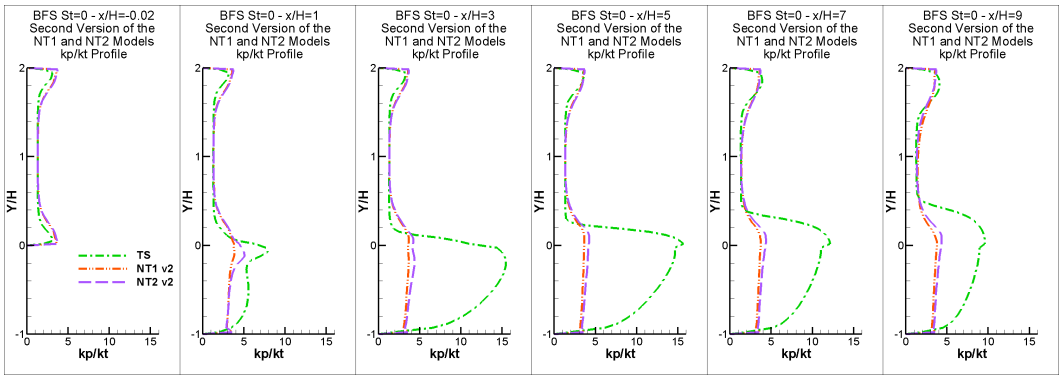

Figure 6.52: Profile of $\frac{k_P}{k_T}$ predicted by the TS and second versions of the NT1 and NT2 models before the step $x/H = -0.02$ and at five positions downstream of the step $x/H = 1, 3, 5, 7, 9$ in the steady state backward facing step case of Chun and Sung (1996).

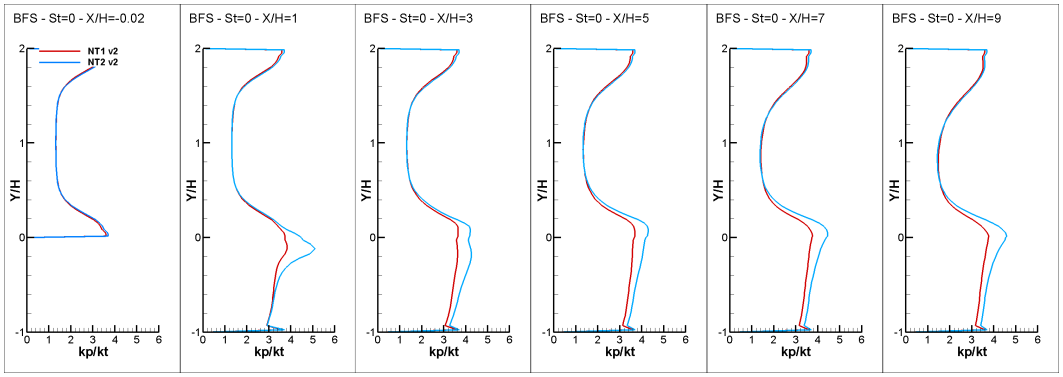

Figure 6.53: Profile of $\frac{k_P}{k_T}$ predicted by the second versions of the NT1 and NT2 models before the step $x/H = -0.02$ and at five positions downstream of the step $x/H = 1, 3, 5, 7, 9$ in the steady state backward facing step case of Chun and Sung (1996).

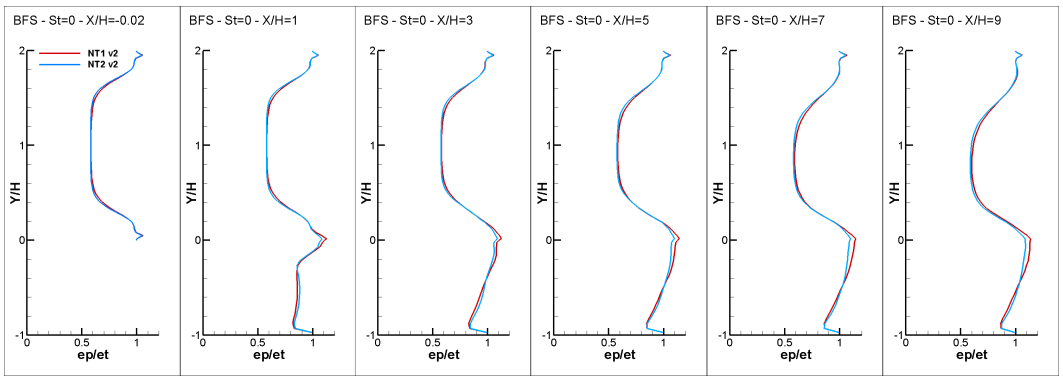

Figure 6.54: Profile of $\frac{\varepsilon_P}{\varepsilon_T}$ predicted by the second versions of the NT1 and NT2 models before the step $x/H = -0.02$ and at five positions downstream of the step $x/H = 1, 3, 5, 7, 9$ in the steady state backward facing step case of Chun and Sung (1996).

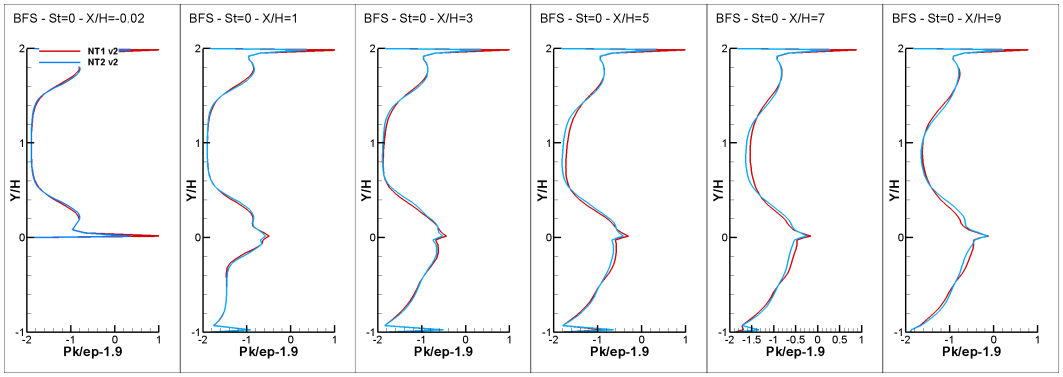

Figure 6.55: Profile of $\frac{P_k}{\varepsilon_T} - 1.9$ predicted by the second versions of the NT1 and NT2 models before the step $x/H = -0.02$ and at five positions downstream of the step $x/H = 1, 3, 5, 7, 9$ in the steady state backward facing step case of Chun and Sung (1996).

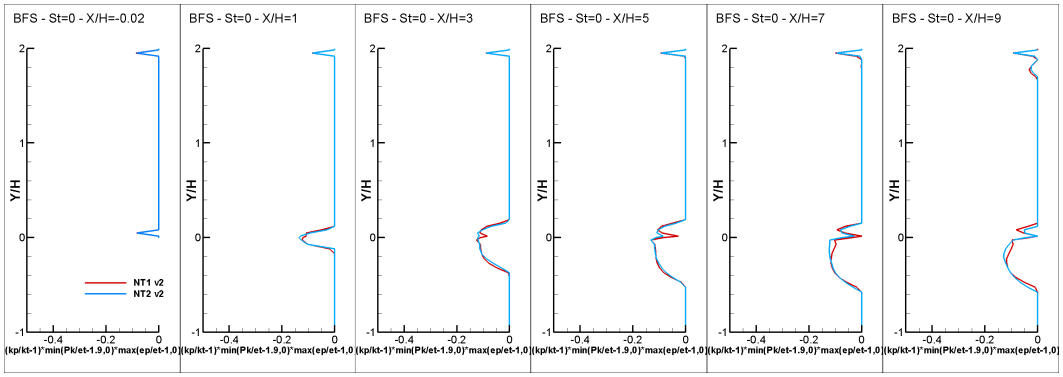

Figure 6.56: Profile of $\left(\frac{k_P}{k_T} - 1\right) \min\left(\frac{P_k}{\varepsilon_T} - 1.9, 0\right) \max\left(\frac{\varepsilon_P}{\varepsilon_T} - 1, 0\right)$ predicted by the second versions of the NT1 and NT2 models before the step $x/H = -0.02$ and at five positions downstream of the step $x/H = 1, 3, 5, 7, 9$ in the steady state backward facing step case of Chun and Sung (1996).

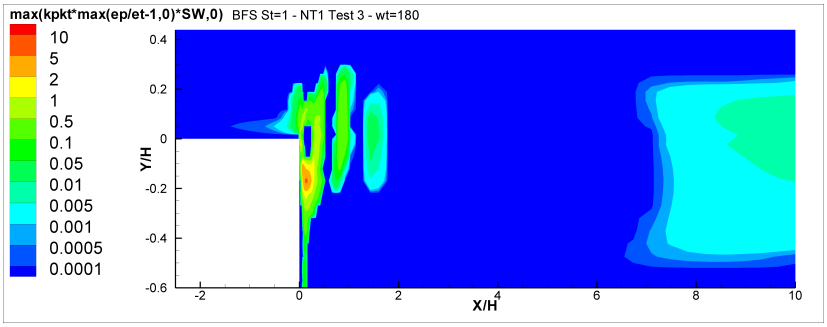

Figure 6.57: Contour plot of $\frac{k_P}{k_T} \max\left(\frac{\varepsilon_P}{\varepsilon_T} - 1, 0\right) SW$ predicted by the NT1 model with Test 3 in Table 6.16 at $\omega t = 180^o$ in the unsteady backward facing step case with $St = 1$ of Chun and Sung (1996).

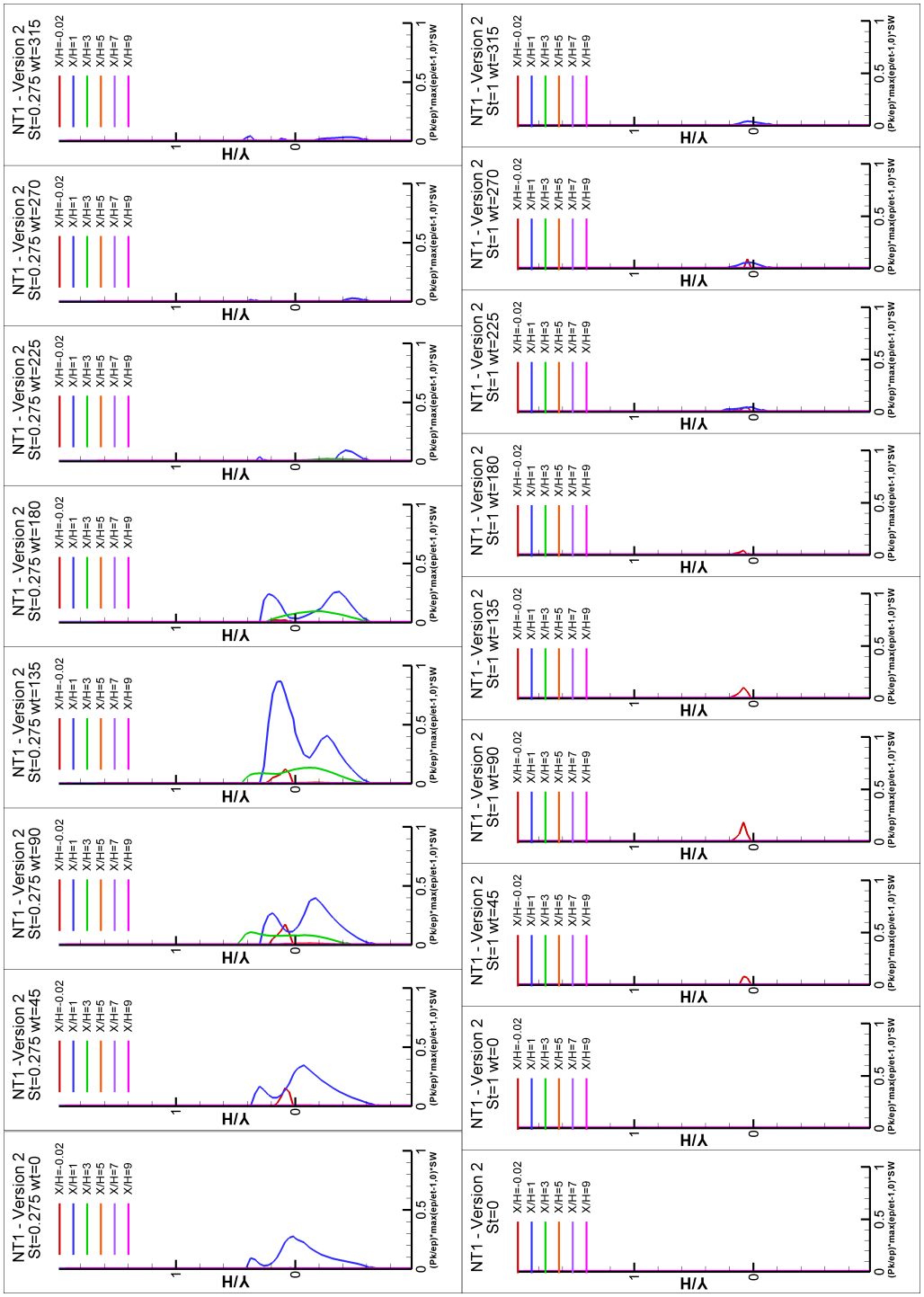

Figure 6.58: Profile of $\frac{P_k}{\varepsilon}\max\left(\frac{\varepsilon}{\varepsilon}\frac{P}{T}-1,0\right)SW$ predicted by the second version of the NT1 model before the step $x/H=-0.02$ and at five positions downstream of the step $x/H=1,3,5,7,9$ in the steady state backward facing step case of Chun and Sung (1996).

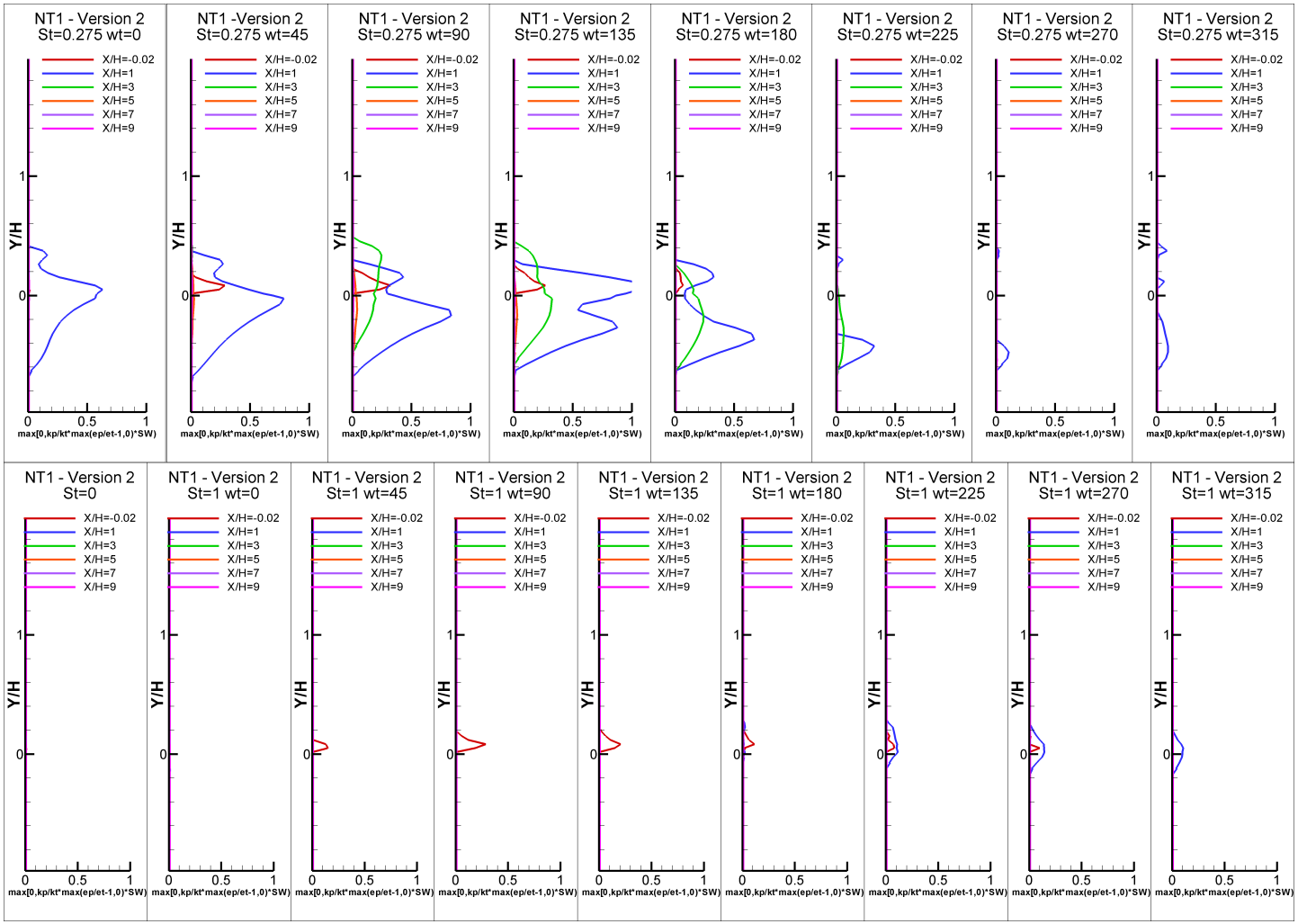

Figure 6.59: Profile of $\frac{k_P}{k_T}\max\left(\frac{\varepsilon_P}{\varepsilon_T}-1,0\right)SW$ predicted by the second version of the NT1 model before the step $x/H=-0.02$ and at five positions downstream of the step $x/H=1,3,5,7,9$ in the steady state backward facing step case of Chun and Sung (1996).

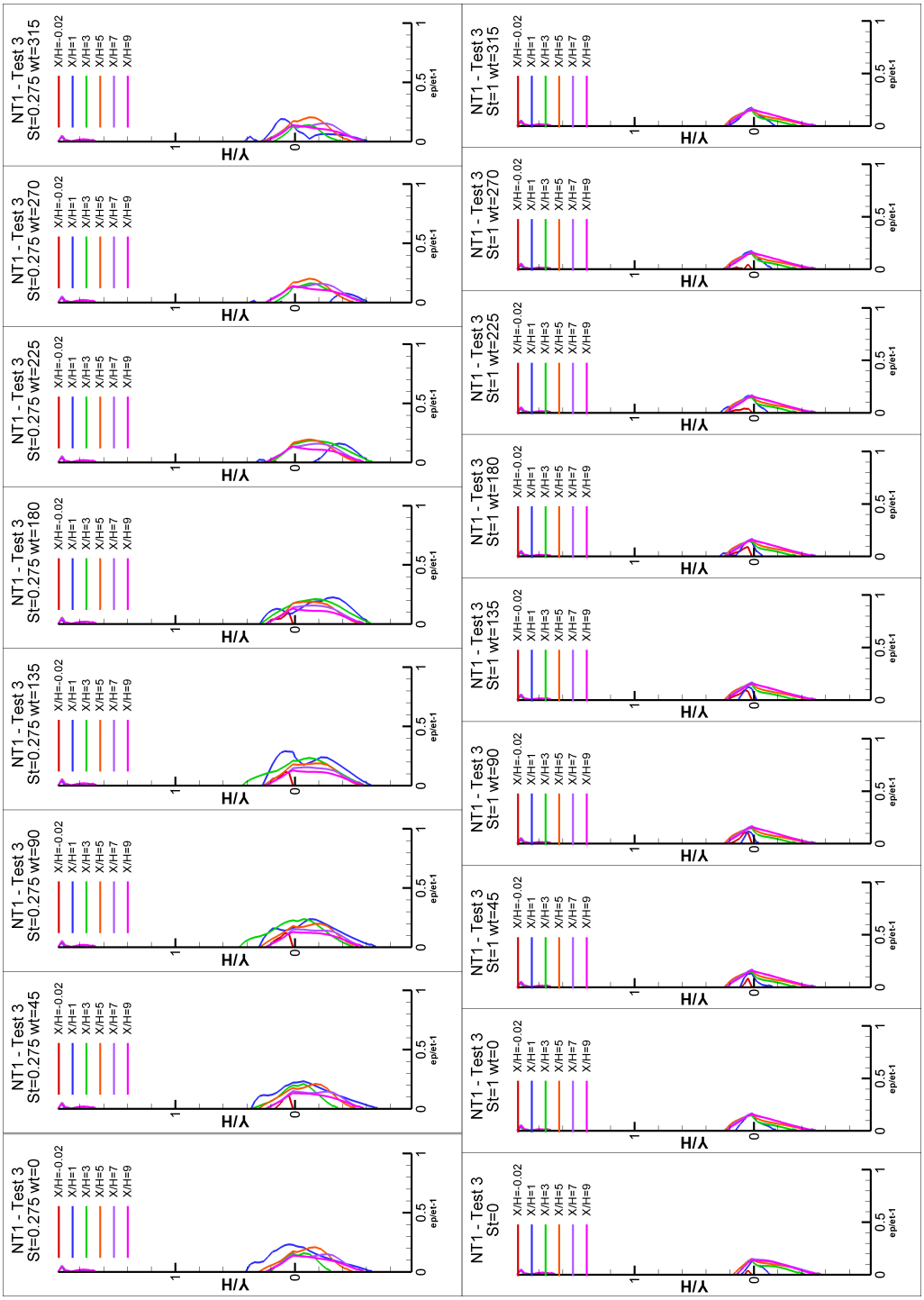

Figure 6.60: Profile of $\max\left(\frac{\varepsilon_P}{\varepsilon_T} - 1, 0\right)S$ predicted by the NT1 model with Test 3 in Table 6.16 before the step $x/H = -0.02$ and at five positions downstream of the step $x/H = 1, 3, 5, 7, 9$ in the three backward facing step cases of Chun and Sung (1996): 8 cycles positions with $St = 0.275$ at the top, $St = 0$ at the bottom left and 8 cycle positions with $St = 1$ at the bottom.

Figure 6.61: Profile of $\frac{P_k}{\varepsilon_T}\max\left(\frac{\varepsilon_P}{\varepsilon_T}-1,0\right)SW$ predicted by the NT1 model with Test 3 in Table 6.16 before the step $x/H=-0.02$ and at five positions downstream of the step $x/H=1,3,5,7,9$ in the three backward facing step cases of Chun and Sung (1996): 8 cycles positions with $St=0.275$ at the top, $St=0$ at the bottom left and 8 cycle positions with $St=1$ at the bottom.

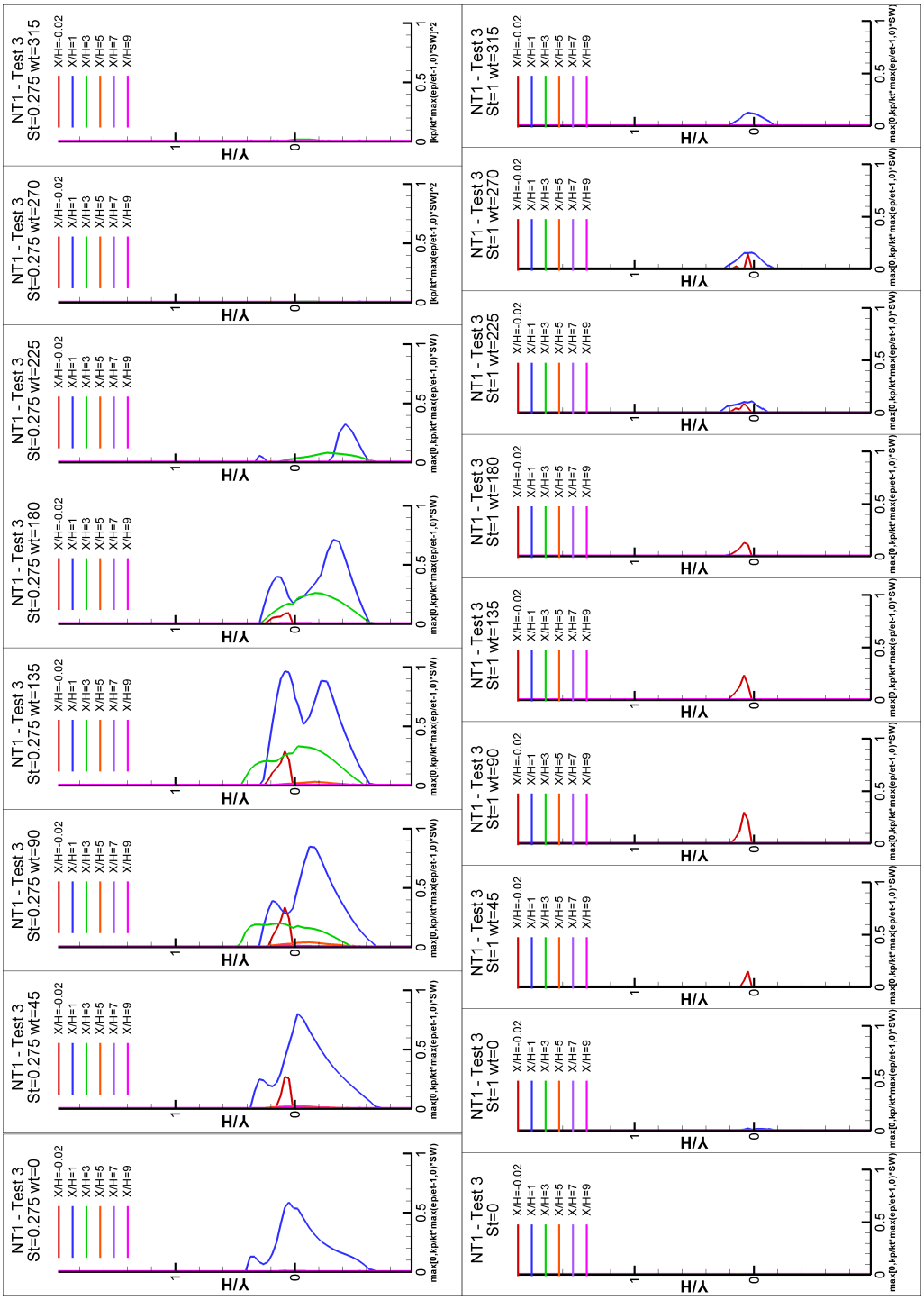

Figure 6.62: Profile of $\frac{k_P}{k_T}\max\left(\frac{\varepsilon_P}{\varepsilon_T}-1,0\right)SW$ predicted by the NT1 model with Test 3 in Table 6.16 before the step $x/H=-0.02$ and at five positions downstream of the step $x/H=1,3,5,7,9$ in the three backward facing step cases of Chun and Sung (1996): 8 cycles positions with $St=0.275$ at the top, $St=0$ at the bottom left and 8 cycle positions with $St=1$ at the bottom.

Figure 6.63: Profile of $\max\left(\frac{\varepsilon_P}{\varepsilon_T} - 1, 0\right)$ predicted by the NT1 model with Test 5 in Table 6.16 before the step $x/H = -0.02$ and at five positions downstream of the step $x/H = 1, 3, 5, 7, 9$ in the three backward facing step cases of Chun and Sung (1996): 8 cycles positions with $St = 0.275$ at the top, $St = 0$ at the bottom left and 8 cycle positions with $St = 1$ at the bottom.

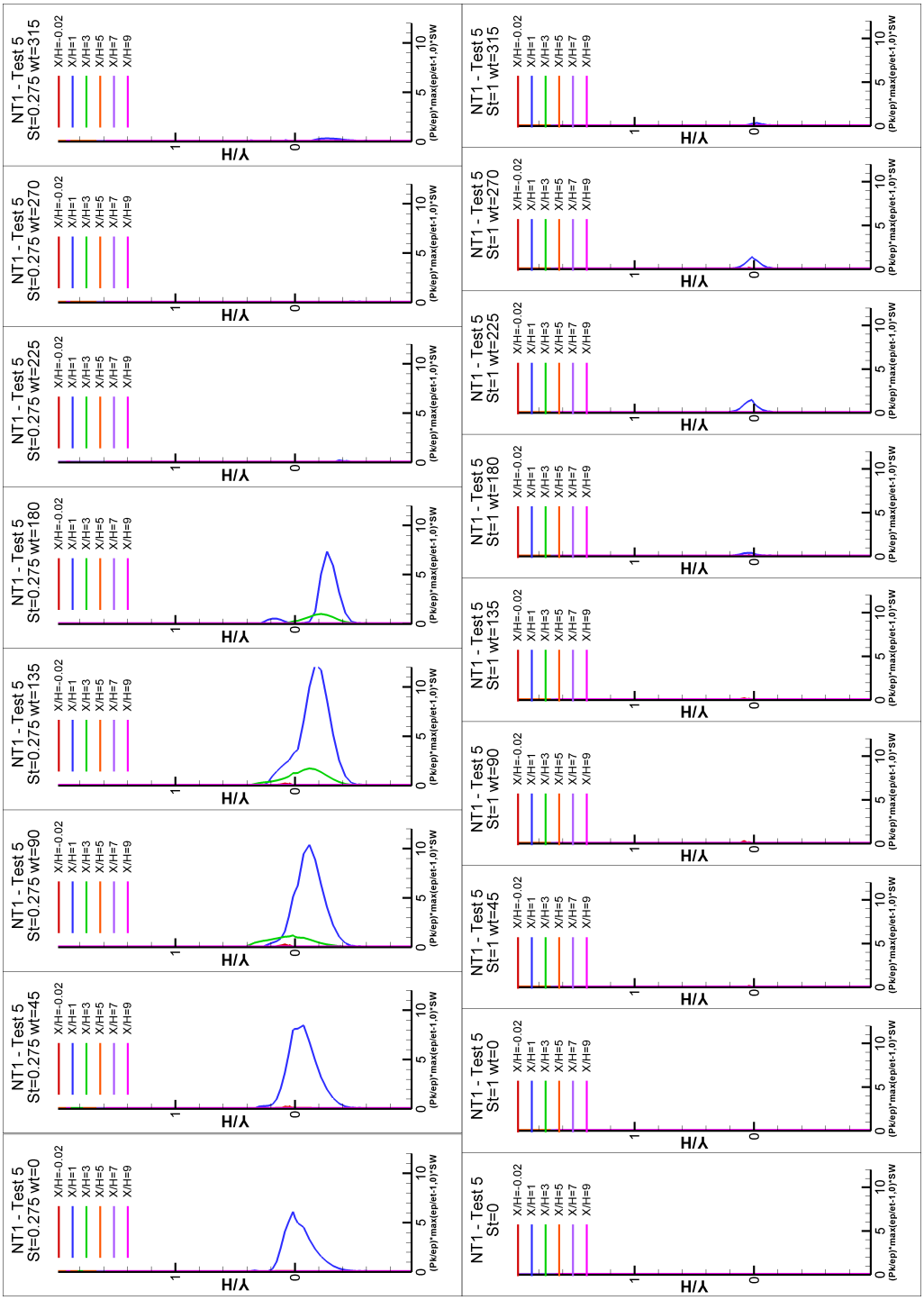

Figure 6.64: Profile of $\frac{k_P}{k_T}\max\left(\frac{\varepsilon_P}{\varepsilon_T}-1,0\right)SW$ predicted by the NT1 model with Test 5 in Table 6.16 before the step $x/H=-0.02$ and at five positions downstream of the step $x/H=1,3,5,7,9$ in the three backward facing step cases of Chun and Sung (1996): 8 cycles positions with $St=0.275$ at the top, $St=0$ at the bottom left and 8 cycle positions with $St=1$ at the bottom.

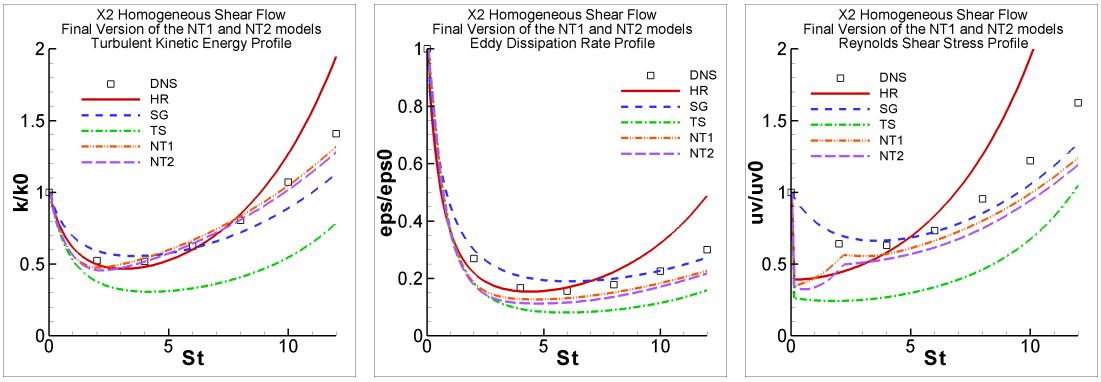

(a) k Profile (b) ε Profile (c) $\overline{uv}$ Profile

Figure 6.65: Performance of the final versions of the NT1 and NT2 models compared with the results provided by the HR, SG and TS models in the homogeneous lowest shear flow case $X2$. Models as in Table 3.25.

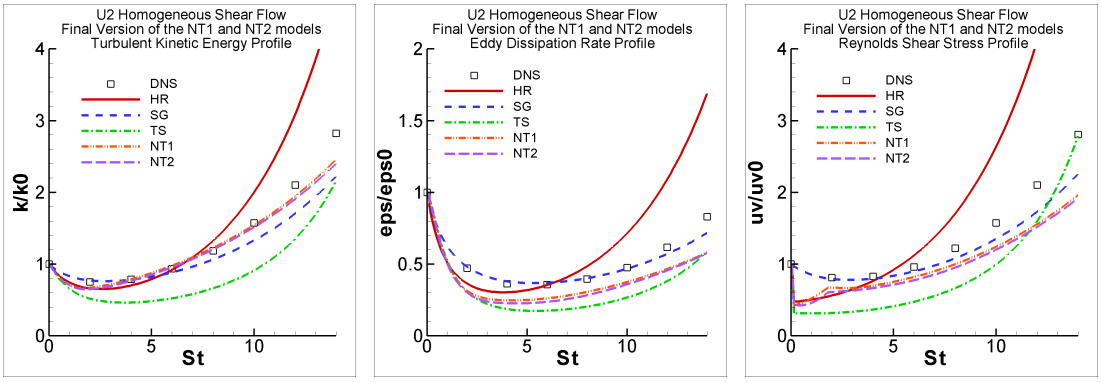

(a) k Profile (b) ε Profile (c) $\overline{uv}$ Profile

Figure 6.66: Performance of the final versions of the NT1 and NT2 models compared with the results provided by the HR, SG and TS models in the homogeneous low shear flow case $U2$. Models as in Table 3.25.

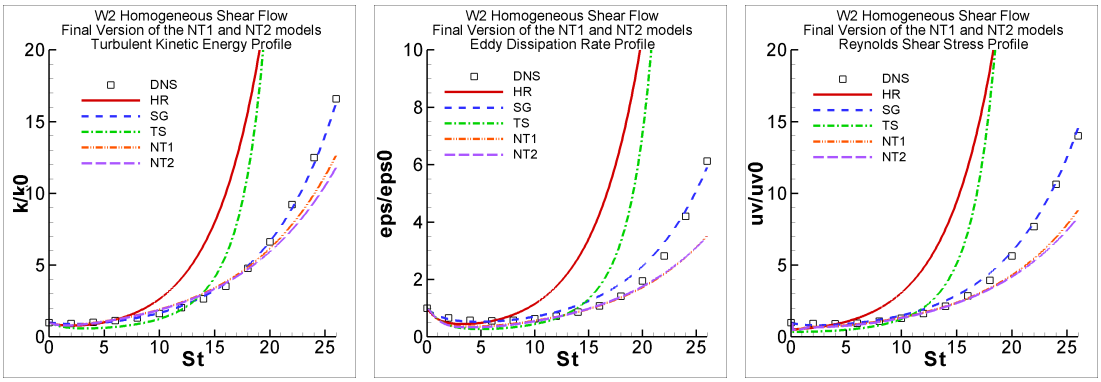

(a) k Profile (b) ε Profile (c) $\overline{uv}$ Profile

Figure 6.67: Performance of the final versions of the NT1 and NT2 models compared with the results provided by the HR, SG and TS models in the homogeneous low shear flow case $W2$. Models as in Table 3.25.

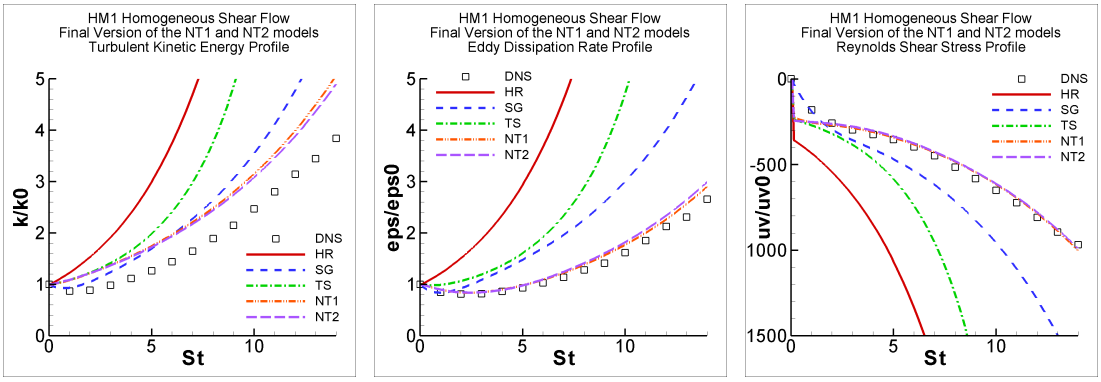

(a) k Profile (b) ε Profile (c) $\overline{uv}$ Profile

Figure 6.68: Performance of the final versions of the NT1 and NT2 models compared with the results provided by the HR, SG and TS models in the homogeneous moderate shear flow case $HM1$. Models as in Table 3.25.

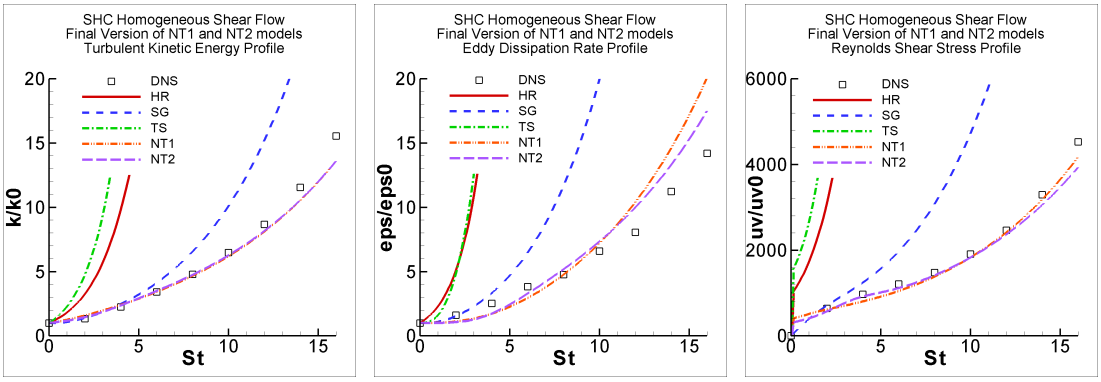

(a) k Profile (b) ε Profile (c) $\overline{uv}$ Profile

Figure 6.69: Performance of the final versions of the NT1 and NT2 models compared with the results provided by the HR, SG and TS models in the homogeneous high shear flow case SHC. Models as in Table 3.25.

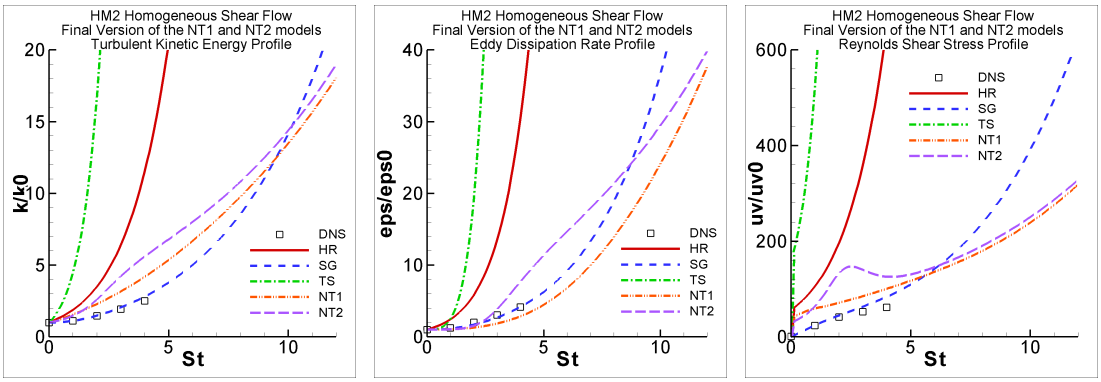

(a) k Profile (b) ε Profile (c) $\overline{uv}$ Profile

Figure 6.70: Performance of the final versions of the NT1 and NT2 models compared with the results provided by the HR, SG and TS models in the homogeneous highest shear flow case $HM2$. Models as in Table 3.25.

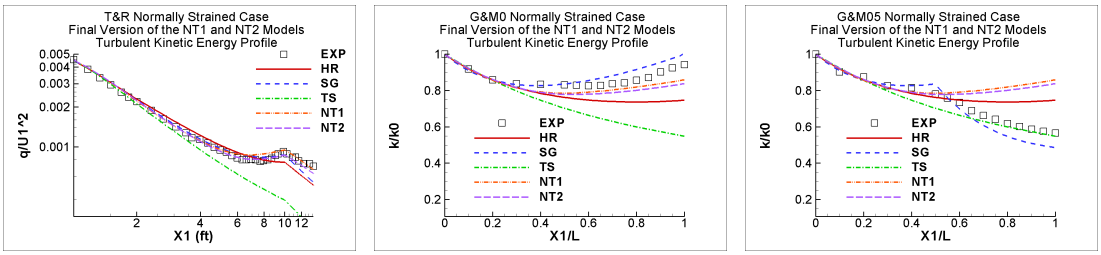

(a) $T\&R$ case (b) $G\&M0$ case (c) $G\&M05$ case

Figure 6.71: Performance of the final versions of the NT1 and NT2 models compared with the results provided by the HR, SG and TS models in the normally strained cases. Models as in Table 3.25.

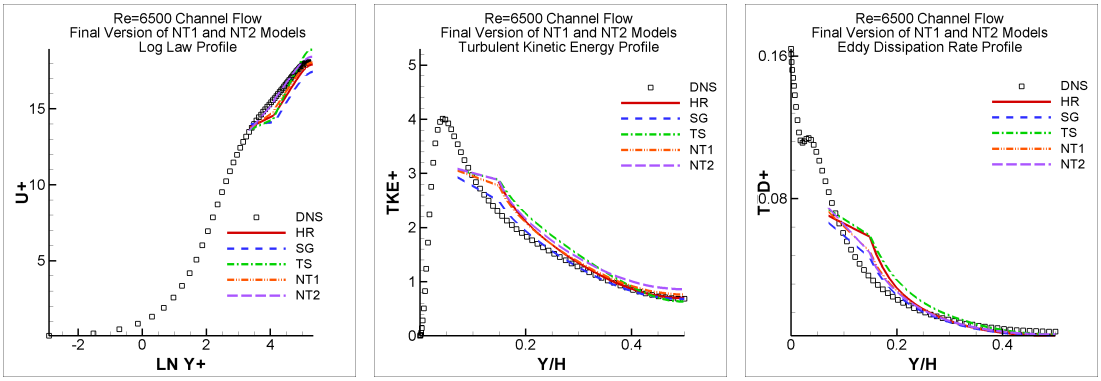

(a) Velocity Profile (b) k Profile (c) ε Profile

Figure 6.72: Performance of the final versions of the NT1 and NT2 models compared with the results provided by the HR, SG and TS models in the fully developed channel flow case with $Re = 6500$. Models as in Table 3.25.

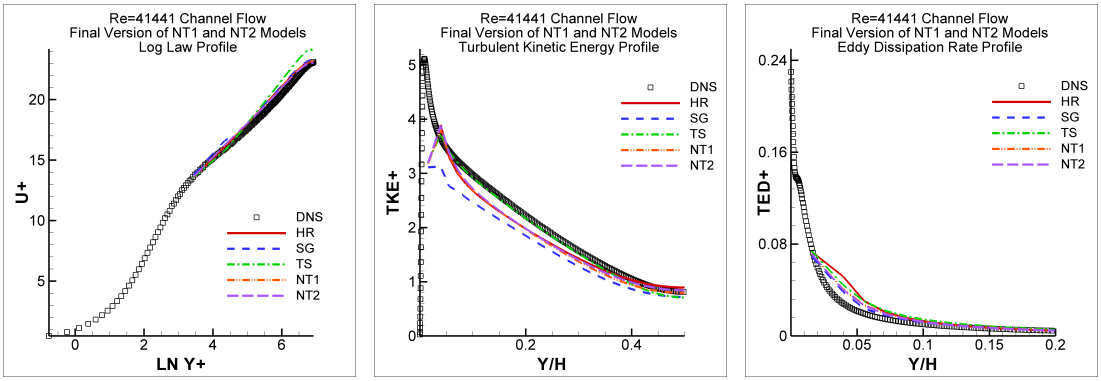

(a) Velocity Profile (b) k Profile (c) ε Profile

Figure 6.73: Performance of the final versions of the NT1 and NT2 models compared with the results provided by the HR, SG and TS models in the fully developed channel flow case with $Re = 41441$. Models as in Table 3.25.

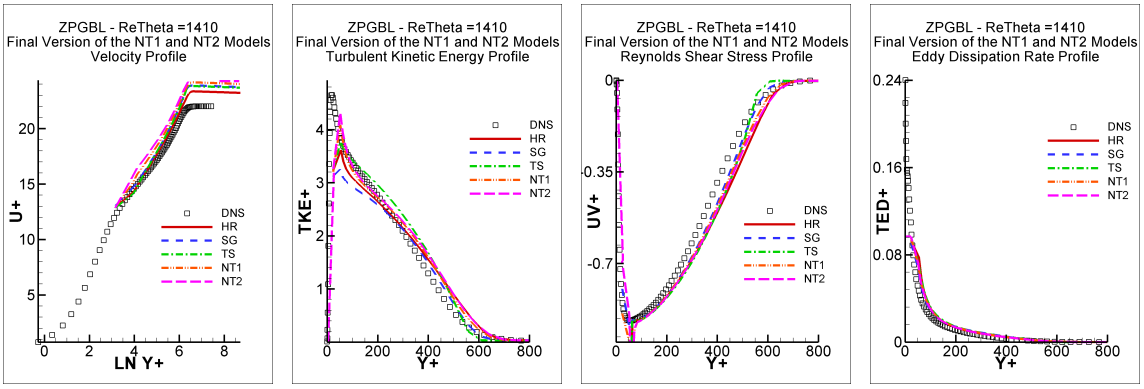

(a) Velocity Profile (b) k Profile (c) $\overline{uv}$ Profile (d) ε Profile

Figure 6.74: Performance of the final versions of the NT1 and NT2 models compared with the results provided by the HR, SG and TS models in the zero pressure gradient boundary layer at $Re_\theta = 1410$. Models as in Table 3.25.

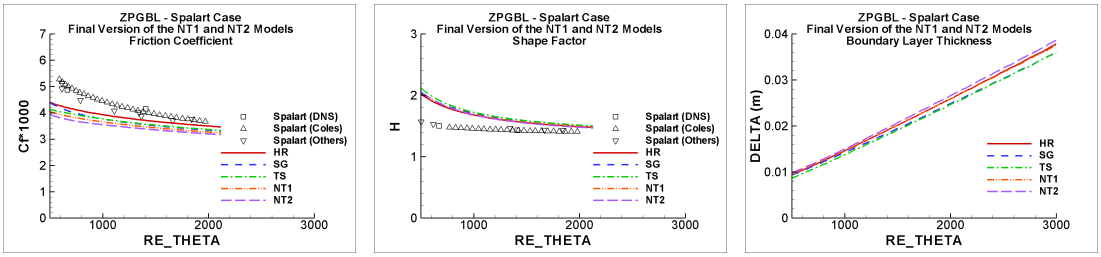

(a) skin-friction coefficient (b) Shape Factor (c) BL Thickness

Figure 6.75: Boundary layer parameters predicted by the final versions of the NT1 and NT2 models and compared with the results provided by the HR, SG and TS models in a zero pressure gradient boundary layer compared to the DNS of Spalart (1988). Models as in Table 3.25.

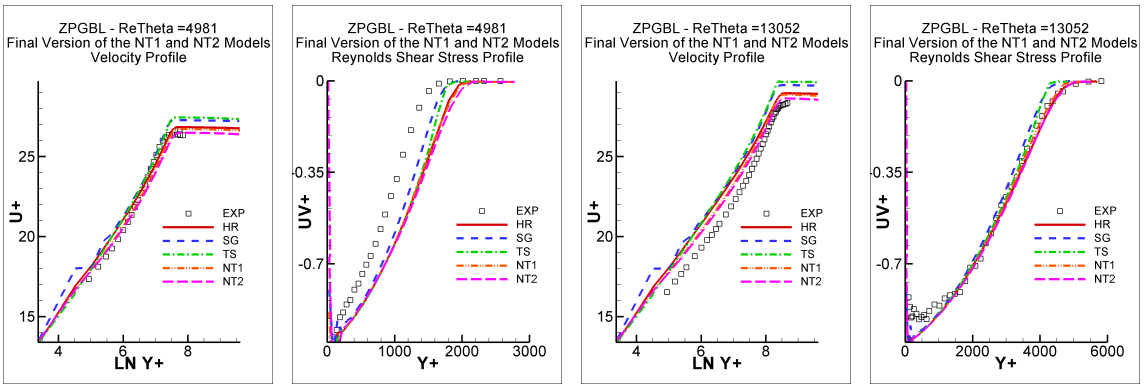

(a) $Re_\theta = 4981$ (b) $Re_\theta = 4981$ (c) $Re_\theta = 13052$ (d) $Re_\theta = 13052$

Figure 6.76: Performance of the final versions of the NT1 and NT2 models compared with the results provided by the HR, SG and TS models in zero pressure gradient boundary layer. Models as in Table 3.25.

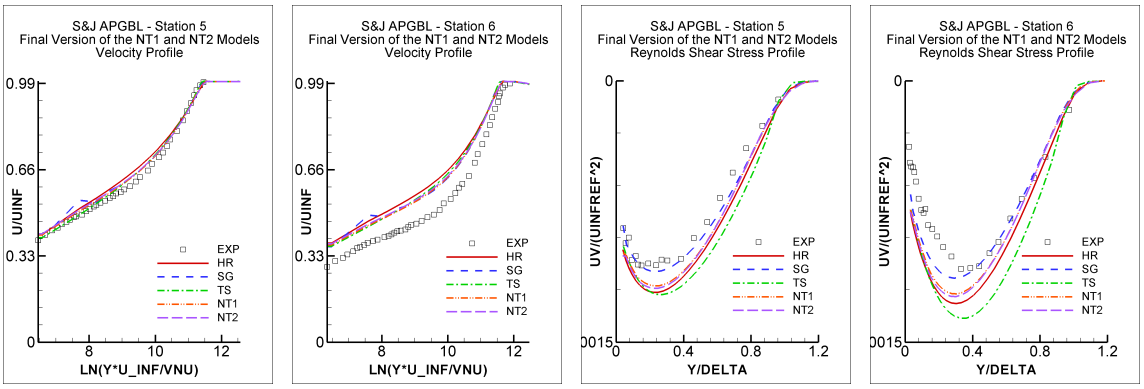

(a) U at Station 5 (b) U at Station 6 (c) $\overline{uv}$ at Station 5 (d) $\overline{uv}$ at Station 6

Figure 6.77: Prediction of the velocity and Reynolds shear stress profiles by the final versions of the NT1 and NT2 models compared with the results provided by the HR, SG and TS models in the adverse pressure gradient boundary layer case $S\&J$. Models as in Table 3.25.

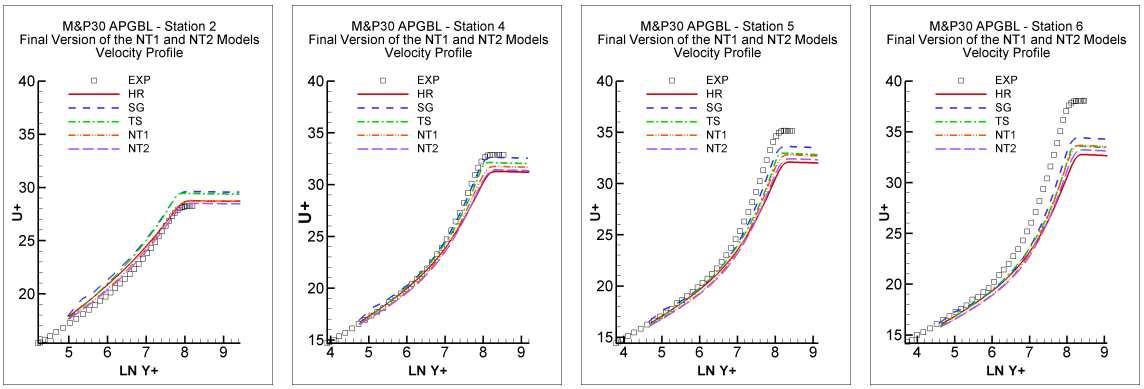

(a) Station 2 (b) Station 4 (c) Station 5 (d) Station 6

Figure 6.78: Prediction of the velocity profile by the final versions of the NT1 and NT2 models compared with the results provided by the HR, SG and TS models in the adverse pressure gradient boundary layer case $M\&30$. Models as in Table 3.25.

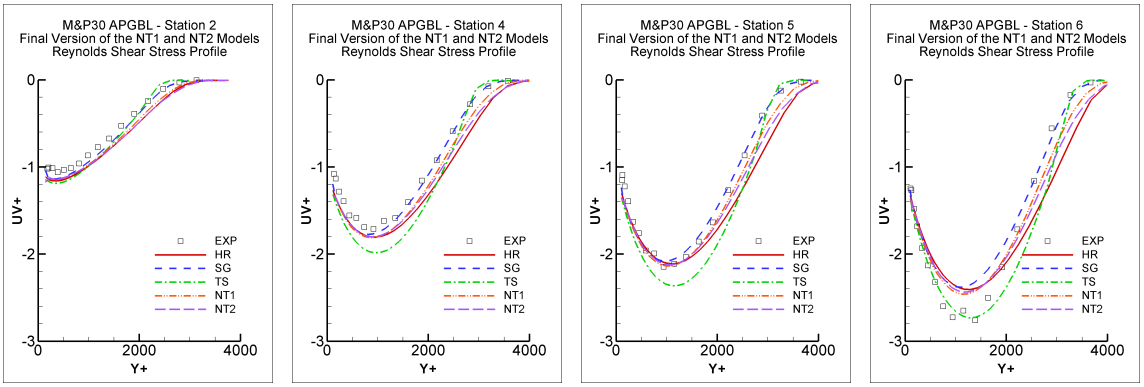

(a) Station 2 (b) Station 4 (c) Station 5 (d) Station 6

Figure 6.79: Prediction of the Reynolds shear stress by the final versions of the NT1 and NT2 models compared with the results provided by the HR, SG and TS models in the adverse pressure gradient boundary layer case $M\&30$. Models as in Table 3.25.

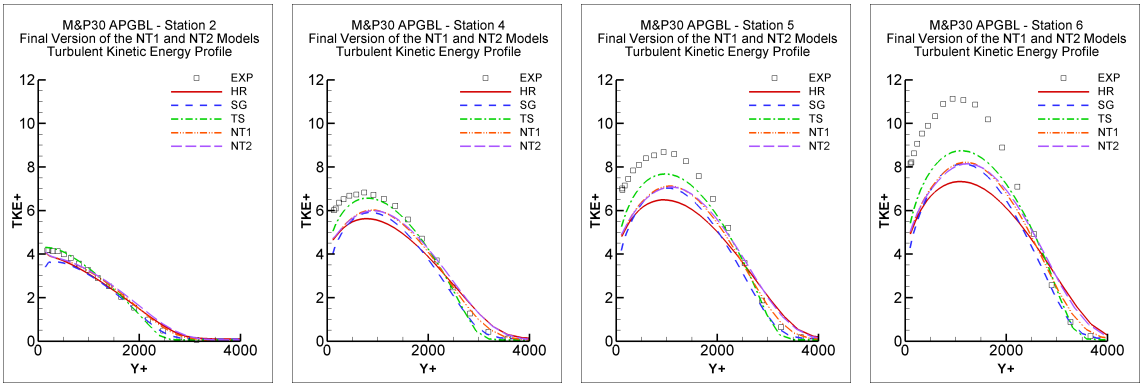

(a) Station 2 (b) Station 4 (c) Station 5 (d) Station 6

Figure 6.80: Prediction of the turbulent kinetic energy by the final versions of the NT1 and NT2 models compared with the results provided by the HR, SG and TS models in the adverse pressure gradient boundary layer case $M\&30$. Models as in Table 3.25.

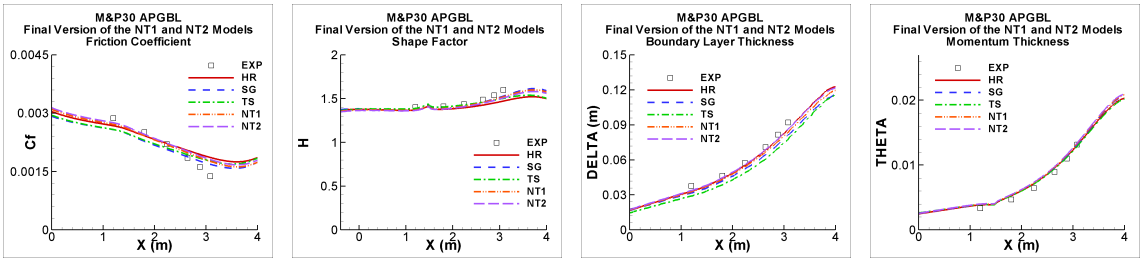

(a) skin-friction coefficient (b) Shape factor (c) BL thickness (d) Momentum Thickness

Figure 6.81: Prediction of the boundary layer parameters by the final versions of the NT1 and NT2 models compared with the results provided by the HR, SG and TS models in the adverse pressure gradient boundary layer case $M\&P10$. Models as in Table 3.25.

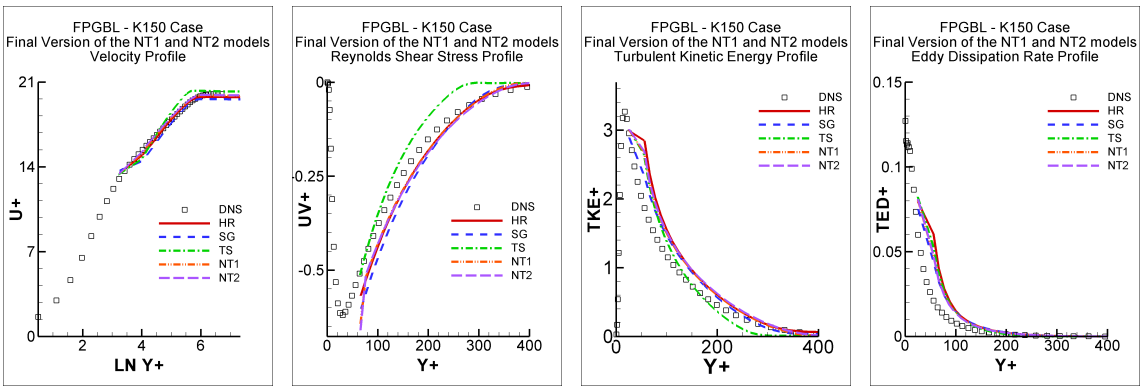

(a) Velocity Profile (b) $\overline{uv}$ Profile (c) k Profile (d) ε Profile

Figure 6.82: Performance of the final versions of the NT1 and NT2 models compared with the results provided by the HR, SG and TS models in the $K150$ favourable pressure gradient boundary layer case. Models as in Table 3.25.

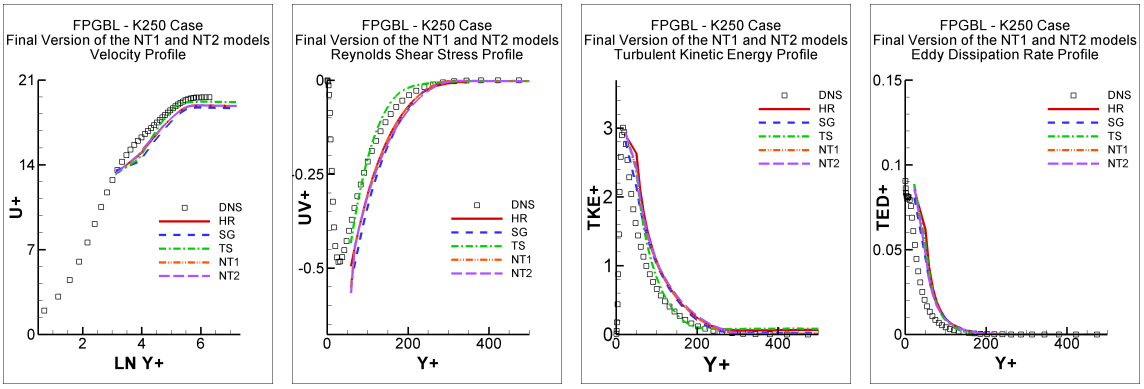

(a) Velocity Profile (b) $\overline{uv}$ Profile (c) k Profile (d) ε Profile

Figure 6.83: Performance of the final versions of the NT1 and NT2 models compared with the results provided by the HR, SG and TS models in the $K250$ favourable pressure gradient boundary layer case. Models as in Table 3.25.

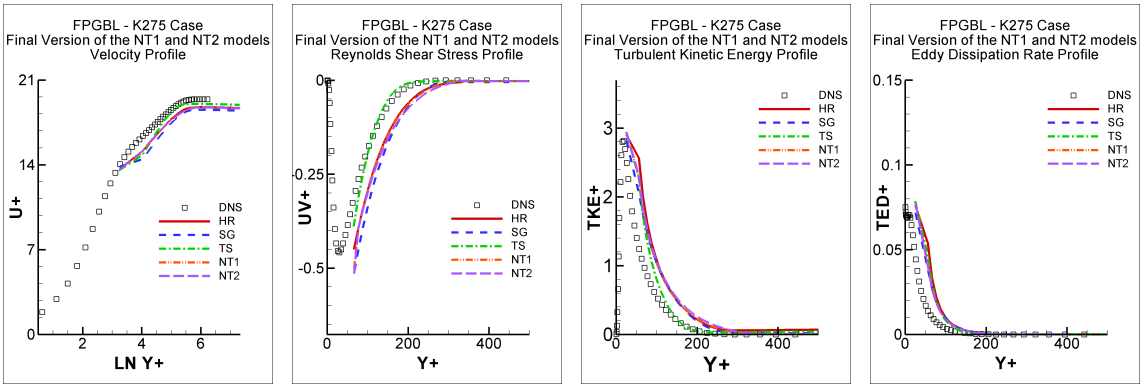

(a) Velocity Profile (b) $\overline{uv}$ Profile (c) k Profile (d) ε Profile

Figure 6.84: Performance of the final versions of the NT1 and NT2 models compared with the results provided by the HR, SG and TS models in the $K275$ favourable pressure gradient boundary layer case. Models as in Table 3.25.

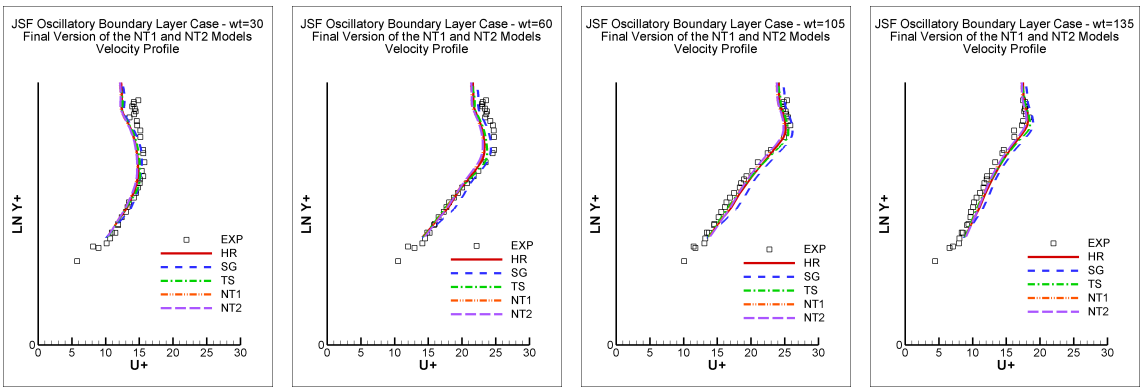

(a) $\omega t = 30^o$ (b) $\omega t = 60^o$ (c) $\omega t = 105^o$ (d) $\omega t = 135^o$

Figure 6.85: Prediction of the velocity profile by the final versions of the NT1 and NT2 models compared with the results provided by the HR, SG and TS models in the oscillatory boundary layer case JSF. Models as in Table 3.25.

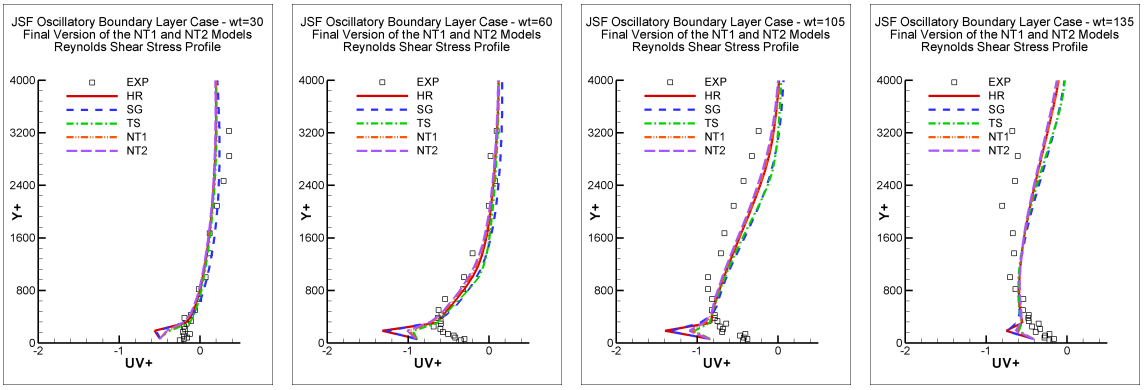

(a) $\omega t = 30^o$ (b) $\omega t = 60^o$ (c) $\omega t = 105^o$ (d) $\omega t = 135^o$

Figure 6.86: Prediction of the Reynolds shear stress by the final versions of the NT1 and NT2 models compared with the results provided by the HR, SG and TS models in the oscillatory boundary layer case JSF. Models as in Table 3.25.

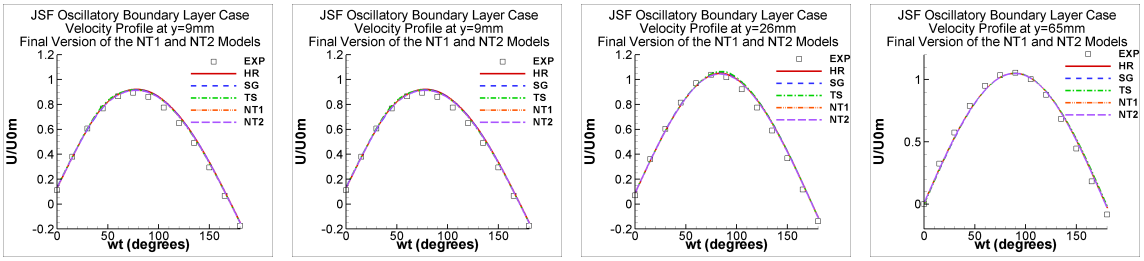

(a) $y = 4mm$ (b) $y = 9mm$ (c) $y = 26mm$ (d) $y = 25mm$

Figure 6.87: Prediction of the velocity profile at four positions in the y direction by the final versions of the NT1 and NT2 models compared with the results provided by the HR, SG and TS models in the JSF oscillatory boundary layer case. Models as in Table 3.25.

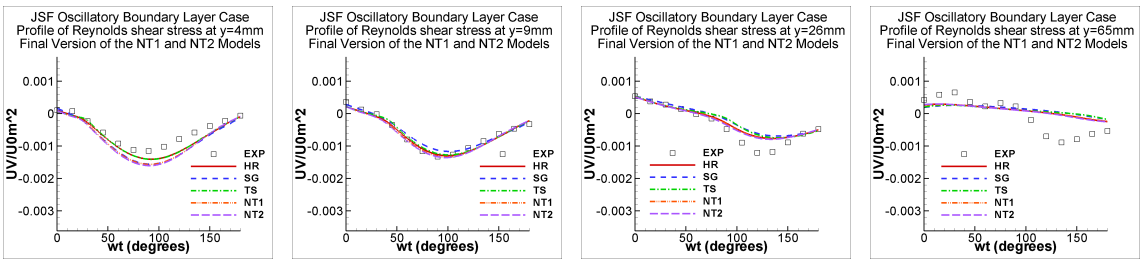

(a) $y = 4mm$ (b) $y = 9mm$ (c) $y = 26mm$ (d) $y = 25mm$

Figure 6.88: Prediction of the Reynolds shear stress at four positions in the y direction by the final versions of the NT1 and NT2 models compared with the results provided by the HR, SG and TS models in the JSF oscillatory boundary layer case. Models as in Table 3.25.

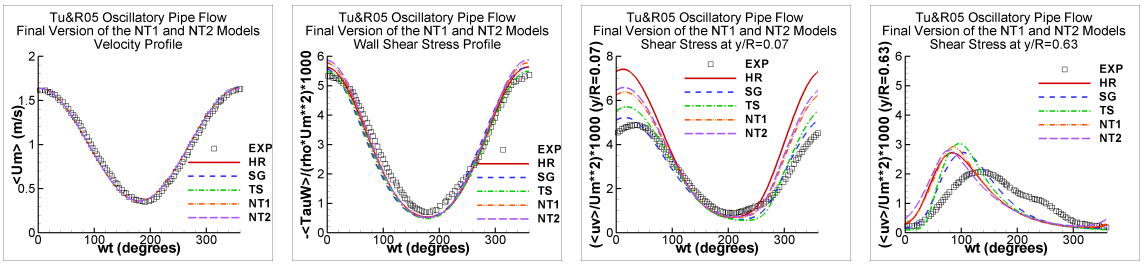

(a) velocity (b) wall shear stress (c) $\overline{uv}$ at y/R=0.07 (d) $\overline{uv}$ at y/R=0.63

Figure 6.89: Prediction of the velocity, wall shear stress and Reynolds shear stress at two radial positions throughout the cycle by the final versions of the NT1 and NT2 models compared with the results provided by the HR, SG and TS models in the $Tu\&R05$ oscillatory pipe flow case of Tu and Ramaprian (1983a). Models as in Table 3.25.

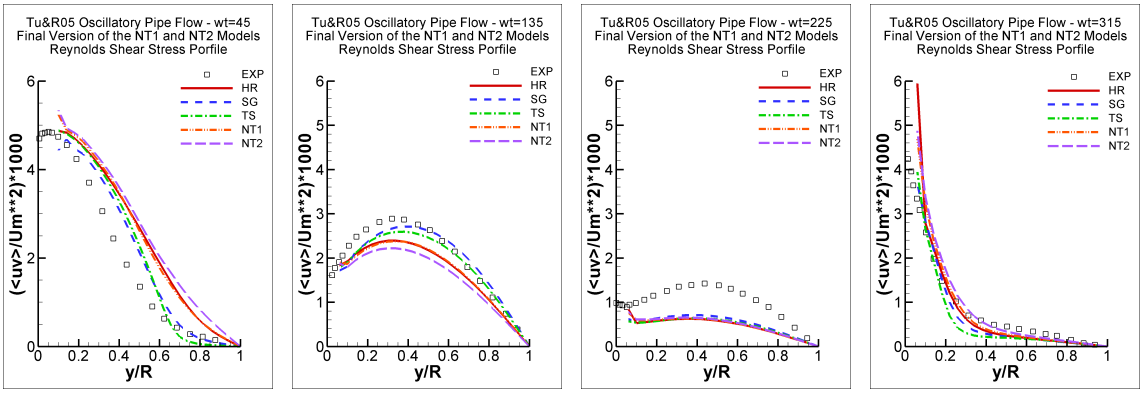

(a) $\omega t = 45^o$ (b) $\omega t = 135^o$ (c) $\omega t = 225^o$ (d) $\omega t = 315^o$

Figure 6.90: Prediction of the Reynolds shear stress by the final versions of the NT1 and NT2 models compared with the results provided by the HR, SG and TS models in the oscillatory pipe flow case $Tu\&R05$. Models as in Table 3.25.

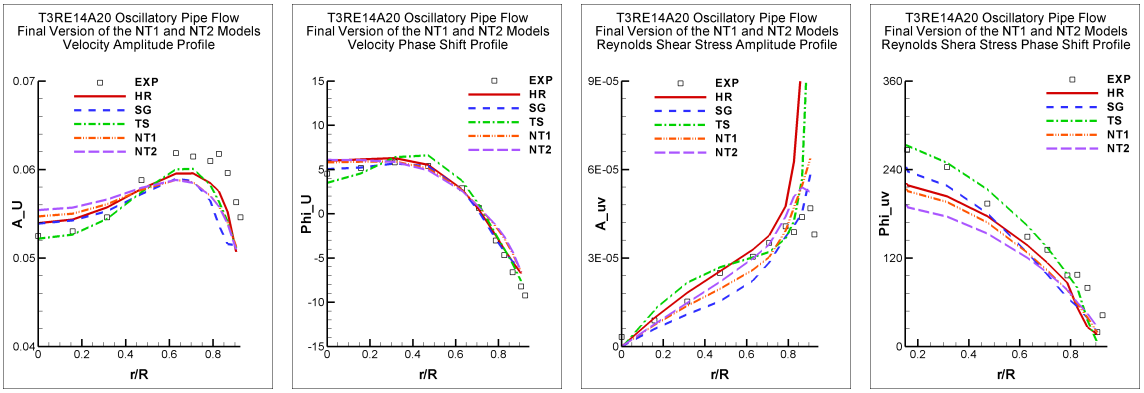

(a) Velocity Amplitude (b) Velocity Phase Shift (c) Shear Stress Amplitude (d) Shear Stress Phase Shift

Figure 6.91: Performance of the final versions of the NT1 and NT2 models compared with the results provided by the HR, SG and TS models in the oscillatory pipe flow case $T3RE14A20$. Models as in Table 3.25.

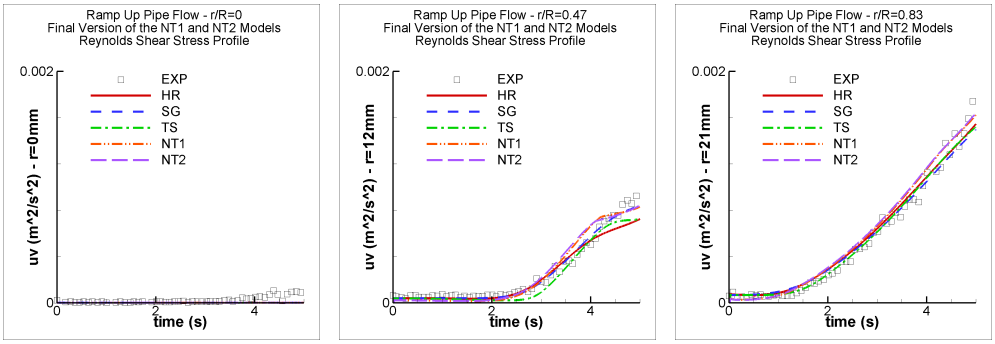

(a) Pipe centre ($r/R = 0$) (b) $r/R = 0.47$ (c) $r/R = 0.83$

Figure 6.92: Prediction of the Reynolds shear stress by the final versions of the NT1 and NT2 models compared with the results provided by the HR, SG and TS models in the ramp up pipe flow. Models as in Table 3.25.

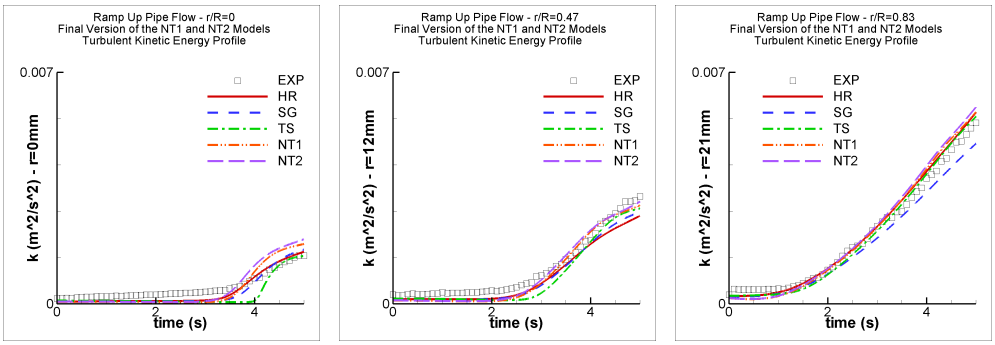

(a) Pipe centre ($r/R = 0$) (b) $r/R = 0.47$ (c) $r/R = 0.83$

Figure 6.93: Prediction of the turbulent kinetic energy by the final versions of the NT1 and NT2 models compared with the results provided by the HR, SG and TS models in the ramp up pipe flow. Models as in Table 3.25.

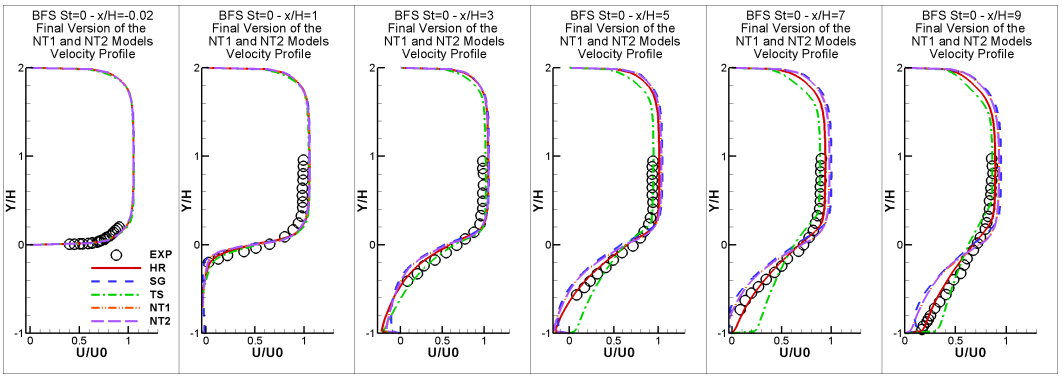

Figure 6.94: Prediction of the velocity profile before the step $x/H = -0.02$ and at five positions downstream of the step $x/H = 1, 3, 5, 7, 9$ by the final versions of the NT1 and NT2 models compared with the results provided by the HR, SG and TS models in the steady state backward facing step case of Chun and Sung (1996). Models as in Table 3.25.

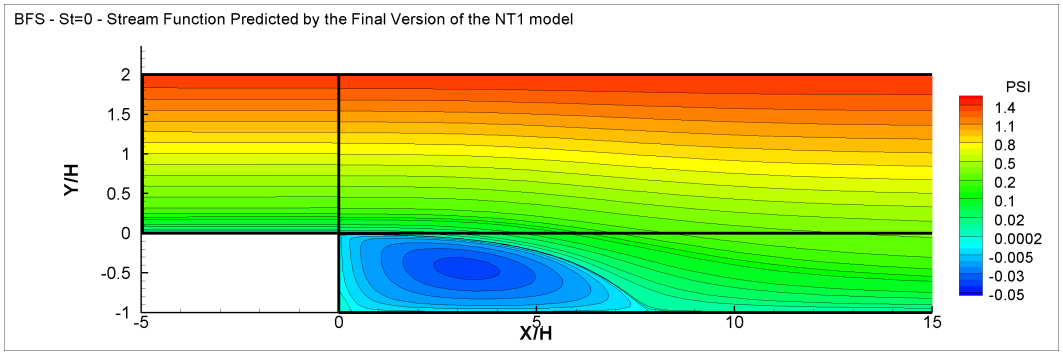

Figure 6.95: Prediction of the stream function by the final version of the NT1 model in the steady state backward facing step case of Chun and Sung (1996).

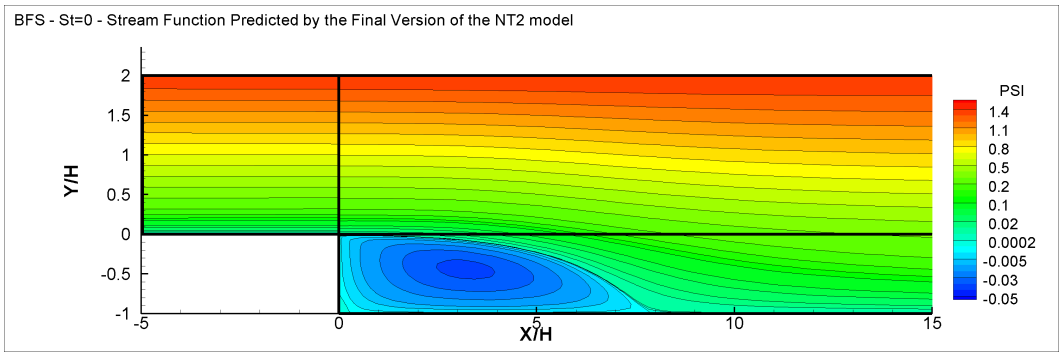

Figure 6.96: Prediction of the stream function by the final version of the NT2 model in the steady state backward facing step case of Chun and Sung (1996).

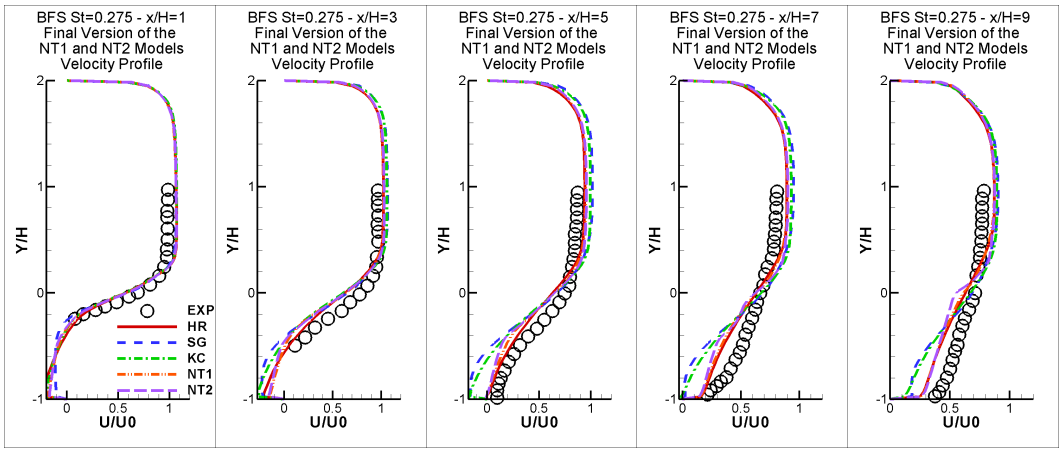

Figure 6.97: Prediction of the time-averaged velocity profile at five positions downstream of the step $x/H = 1, 3, 5, 7, 9$ by the final versions of the NT1 and NT2 models compared with the results provided by the HR, SG and KC models in the unsteady backward facing step case with St=0.275 of Chun and Sung (1996). Models as in Table 3.25.

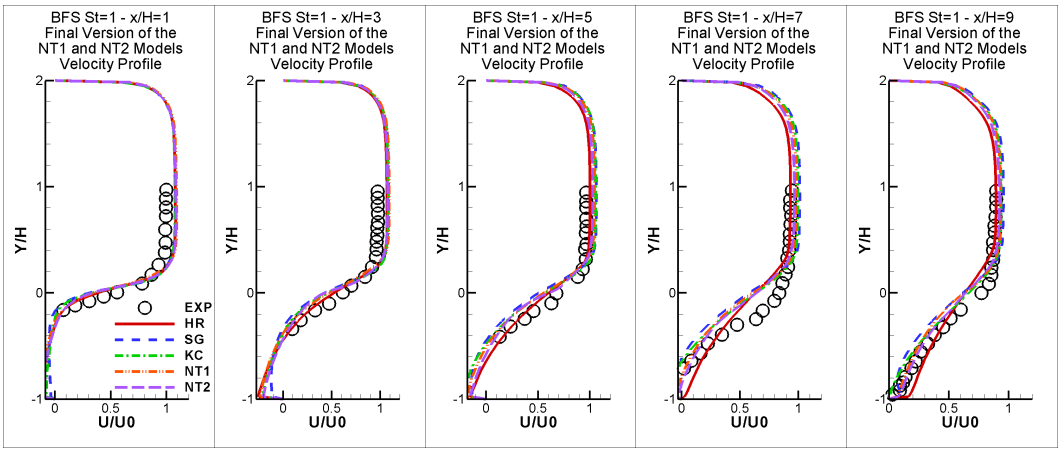

Figure 6.98: Prediction of the time-averaged velocity profile at five positions downstream of the step $x/H = 1, 3, 5, 7, 9$ by the final versions of the NT1 and NT2 models compared with the results provided by the HR, SG and KC models in the unsteady backward facing step case with St=1 of Chun and Sung (1996). Models as in Table 3.25.

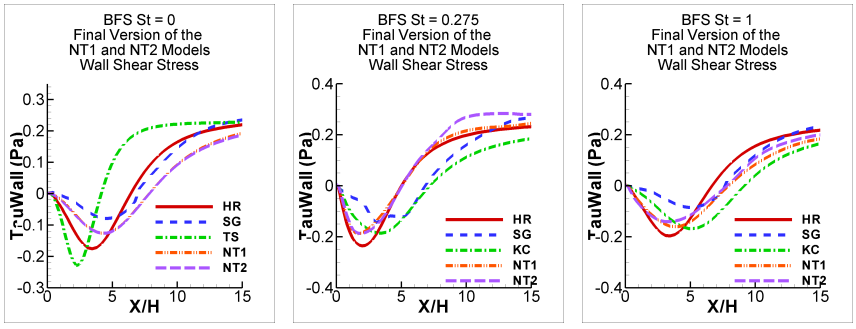

(a) St=0 (b) St=0.275 (c) St=1

Figure 6.99: Prediction of the time-averaged wall-shear-stress by the final versions of the NT1 and NT2 models compared with the results provided by the HR, SG and TS models in the backward facing step cases of Chun and Sung (1996). Models as in Table 3.25.

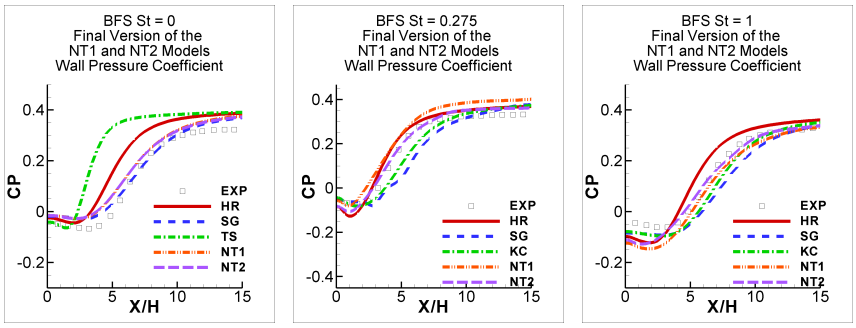

(a) St=0 (b) St=0.275 (c) St=1

Figure 6.100: Prediction of the time-averaged wall-pressure coefficient by the final versions of the NT1 and NT2 models compared with the results provided by the HR, SG and TS models in the backward facing step cases of Chun and Sung (1996). Models as in Table 3.25.

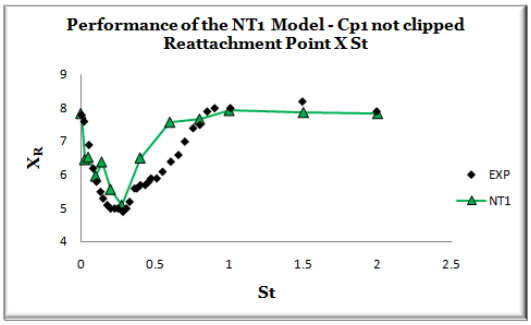

(a) NT1 Model - C_{P1} not clipped

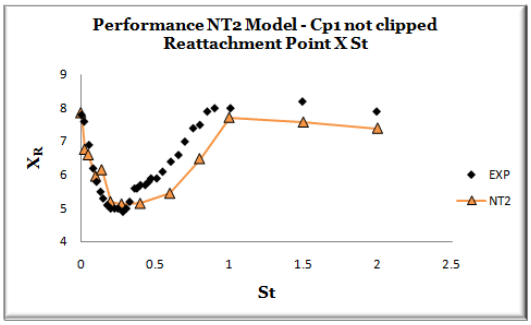

(b) NT2 Model - C_{P1} not clipped

Figure 6.101: Individual performance of the final versions of the NT1 and NT2 models, but with C_{P1} not clipped and allowed to become negative, in predicting the time-averaged reattachment point of unsteady backward facing step cases with different oscillation frequencies.

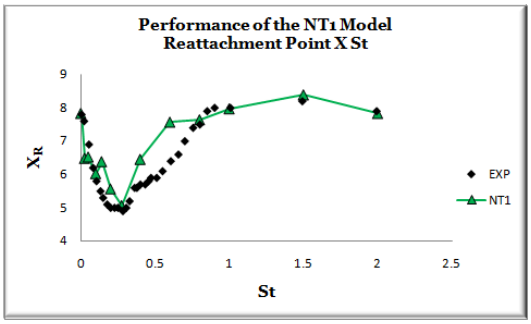

(a) NT1 Model

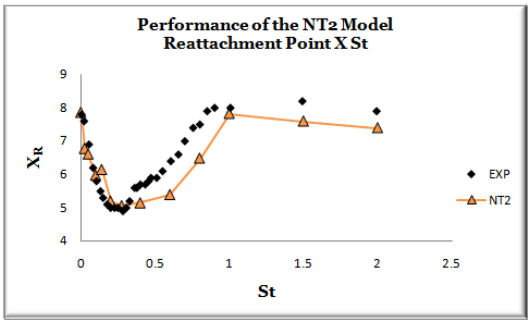

(b) NT2 Model

Figure 6.102: Individual performance of the final versions of the NT1 and NT2 models in predicting the time-averaged reattachment point of unsteady backward facing step cases with different oscillation frequencies.

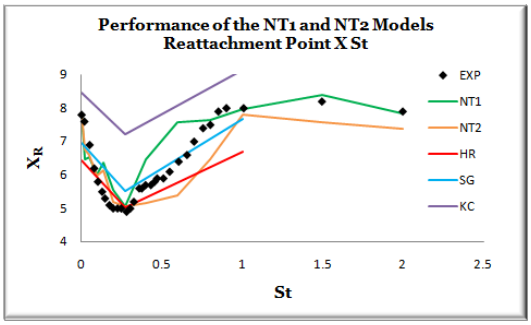

(a) Time-averaged reattachment point X_R

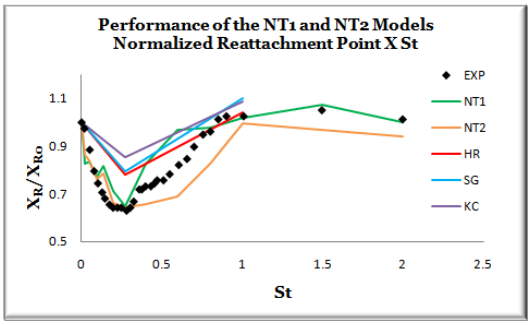

(b) X_R normalized with $X_{R_{St=0}}$

Figure 6.103: Prediction of the time-averaged reattachment point by the final versions of the NT1 and NT2 models compared with the results provided by the HR, SG and KC models in unsteady backward facing step cases with different oscillation frequencies. Models as in Table 3.25.

6.4 Concluding Remarks

In this chapter the development of the final versions of the NT1 and NT2 models has been presented.

The new developed models are significantly different to the original TS model, initially used as the base model for the modelling process.

The models' coefficients were determined so that they satisfied the asymptotic states for homogeneous shear flows, decaying grid turbulence and local equilibrium boundary layers thus ensuring the correct behaviour of the models in these flows and avoiding odd predictions in other flows.

Different time-scales were studied as possibilities for the expression of the turbulent viscosity and it was concluded that the ones used in the NT1 and NT2 models appeared to be the most appropriate.

The models also satisfy the physical constraints related to the turbulent kinetic energy spectrum such as keeping the ratio between the time scale associated with the small and large eddies smaller than one and splitting the spectrum in the inertial subrange.

The models proved to be stable and to perform well in a wide range of non-equilibrium flows providing predictions either as good as or even better than benchmarked traditional models, including simpler models such as the standard $k-\varepsilon$ model and more complex Reynolds stress transport models.

It has not been possible so far to choose either the NT1 or the NT2 model as the best model since both perform similarly well in all flows and are similarly stable.

It can be thus stated that the main objective of this work has been achieved since two two-time-scale linear-eddy-viscosity models have been successfully developed.

Chapter 7

Development of Two-Time-Scale Non-Linear-Eddy-Viscosity Models

Two-time-scale linear-eddy-viscosity models were developed in the previous chapter and were shown to perform well over a range of fairly challenging flows. However, there are a number of inherent weaknesses in the LEV formulation that are likely to limit the performance of such schemes in flows with complex strain fields. As STS NLEV models have been shown to often perform better than linear ones in complex strain fields, the present chapter hence describes an initial attempt to apply the modelling practices developed in the previous chapter to a NLEV scheme.

In this work high Reynolds number NLEV schemes have been built based on importing the two-time-scale equations developed in Chapter 6 into the NLEV scheme of Craft et al. (1996b). Following the linear schemes developed, the two-time-scale non-linear-eddy-viscosity models differ in the eddy viscosity expression. The model which uses the same eddy viscosity formulation as that used in the NT1 model will be referred to as NL1 model. Similarly, the model using the eddy viscosity expression used by the NT2 model will be referred to as NL2 model.

Most test cases presented in Chapter 5, where good agreement was achieved with the linear two-time-scale models developed, are shear dominated flows and therefore one only expects to see improvements with the NLEV models in the normal stresses, although these will not directly affect the mean field greatly. However, there is potential to see greater improvements in the normally-strained flows, where the normal stresses are responsible for turbulent kinetic energy generation.

In this chapter the initial investigation carried out to develop two-time-scale non-linear-eddy-viscosity models will be described.

7.1 Non-Linear-Eddy-Viscosity Scheme

As mentioned before, the two two-time-scale non-linear-eddy-viscosity models were developed in order to identify what advantages they could add on top of the performance of their linear-eddy-viscosity counterparts. Hence, the NL1 will inherit features from the NT1 model, whilst the NL2 will be build from elements of the NT2 scheme. Both will incorporate a non-linear stress-strain formulation to model the Reynolds stresses.

Non-linear-eddy-viscosity models can be thought of as simplified versions of Algebraic Reynolds Stress (ARS) models. While the latter solve coupled non-linear algebraic equations for the Reynolds stresses, the former provide explicit algebraic equations. Pope (1975) derived a general expression for the Reynolds stresses as a function of the dimensionless strain rate and vorticity tensors up to the fifth order, as shown in equations 2.27, 2.28 and 2.29. Most non-linear-eddy-viscosity models, such as those proposed by Speziale (1987), Rubinstein and Barton (1990) and Craft et al. (1996b), among others, thus use linearly independent combinations of these tensors. Most non-linear eddy-viscosity formulations found in the literature are of quadratic type, such as those of Speziale (1987) and Rubinstein and Barton (1990). Craft et al. (1996b) proposed a cubic stress-strain relation arguing, amongst other things, that the cubic terms are important for capturing streamline curvature effects.

The general non-linear-eddy-viscosity expression for the Reynolds stresses thus adopted here was the cubic one proposed by Craft et al. (1996b), presented in equation 2.19, but re-written as in equation 7.1 below in order to take into account the spectrum partition variables, by exploring different time scales. It can be noted that ν_t used in equation 2.19 can be expressed as $\nu_t = c_\mu k \tau_1$ and $\frac{k}{\varepsilon}$ can be used as a second time scale τ_2.

$$\begin{aligned}\overline{u_i u_j} =& \frac{2}{3}\delta_{ij}k - \nu_t S_{ij} \\ &+ c_\mu k\tau_1 \Bigg[c_1\tau_2 \Bigg(S_{ik}S_{jk} - \frac{1}{3}S_{kl}S_{kl}\delta_{ij} \Bigg) + c_2\tau_2 \Bigg(W_{ik}S_{jk} + W_{jk}S_{ik} \Bigg) + c_3\tau_2 \Bigg(W_{ik}W_{jk} - \frac{1}{3}W_{kl}W_{kl}\delta_{ij} \Bigg) \\ &+ c_4\tau_2^2 \Bigg(S_{ki}W_{lj} + S_{kj}W_{li} \Bigg) S_{kl} + c_5\tau_2^2 \Bigg(W_{il}W_{lm}S_{mj} + S_{il}W_{lm}W_{mj} - \frac{2}{3}S_{lm}W_{mn}W_{nl}\delta_{ij} \Bigg) \\ &+ c_6\tau_2^2 S_{ij}S_{kl}S_{kl} + c_7\tau_2^2 S_{ij}W_{kl}W_{kl} \Bigg] \end{aligned} \tag{7.1}$$

In the above equation, τ_1 and τ_2 are time scales and the dimensionless strain rate and vorticity tensors are $S_{ij} = \left(\frac{\partial U_i}{\partial x_j} + \frac{\partial U_j}{\partial x_i}\right)$ and $W_{ij} = \left(\frac{\partial U_i}{\partial x_j} - \frac{\partial U_j}{\partial x_i}\right)$ respectively. As can be noted in equation 7.1, the time scales are explicit and that will allow one to explore the use of the two time scales considered so far in the NT1 and NT2 models: the large eddies time scale, $\tau_P = \frac{k_P}{\varepsilon_P}$, and the total time scale, $\tau_{tot} = \frac{k}{\varepsilon_T}$.

The study and full optimization of the coefficients' form is not the main purpose here, and therefore the general form adopted by Craft et al. (1996b) will be used. As can be seen in Table 3.7, Craft et al. (1996b) proposed the coefficient c_5 in equation 7.1 to be zero and so it will be taken as such here. With this simplification, the above form can be expanded

out for each of the Reynolds stress components, giving:

$$\begin{aligned}\overline{u^2} =& \frac{2}{3}k - \nu_t S_{11} \\ &+ c_\mu k\tau_1 \Bigg\{ \frac{c_1\tau_2}{3}\Big(2S_{11}^2 + S_{12}^2 + S_{13}^2 - S_{22}^2 - 2S_{23}^2 - S_{33}^2\Big) \\ &+ 2c_2\tau_2\Big(S_{12}W_{12} + S_{13}W_{13}\Big) + \frac{c_3\tau_2}{3}\Big(W_{12}^2 + W_{13}^2 - 2W_{23}^2\Big) \\ &- 2c_4\tau_2^2\Big[S_{11}\Big(S_{12}W_{12} + S_{13}W_{13}\Big) + S_{23}\Big(S_{12}W_{13} + S_{13}W_{12}\Big) + S_{22}S_{12}W_{12} + S_{33}S_{13}W_{13}\Big] \\ &+ c_6\tau_2^2 S_{11}\Big(S_{11}^2 + S_{22}^2 + S_{33}^2 + 2S_{12}^2 + 2S_{13}^2 + 2S_{23}^2\Big) + 2c_7\tau_2^2 S_{11}\Big(W_{12}^2 + W_{13}^2 + W_{23}^2\Big)\Bigg\} \end{aligned} \tag{7.2}$$

$$\begin{aligned}\overline{v^2} =& \frac{2}{3}k - \nu_t S_{22} \\ &+ c_\mu k\tau_1 \Bigg\{ \frac{c_1\tau_2}{3}\Big(2S_{22}^2 + S_{12}^2 + S_{23}^2 - S_{11}^2 - 2S_{13}^2 - S_{33}^2\Big) \\ &+ 2c_2\tau_2\Big(S_{23}W_{23} - S_{12}W_{12}\Big) + \frac{c_3\tau_2}{3}\Big(W_{12}^2 + W_{23}^2 - 2W_{13}^2\Big) \\ &- 2c_4\tau_2^2\Big[S_{22}\Big(S_{23}W_{23} - S_{12}W_{12}\Big) + S_{13}\Big(S_{12}W_{23} - S_{23}W_{12}\Big) + S_{33}S_{23}W_{23} - S_{11}S_{12}W_{12}\Big] \\ &+ c_6\tau_2^2 S_{22}\Big(S_{11}^2 + S_{22}^2 + S_{33}^2 + 2S_{12}^2 + 2S_{13}^2 + 2S_{23}^2\Big) + 2c_7\tau_2^2 S_{22}\Big(W_{12}^2 + W_{13}^2 + W_{23}^2\Big)\Bigg\} \end{aligned} \tag{7.3}$$

$$\begin{aligned}\overline{w^2} =& \frac{2}{3}k - \nu_t S_{33} \\ &+ c_\mu k\tau_1 \Bigg\{ \frac{c_1\tau_2}{3}\Big(2S_{33}^2 + S_{23}^2 + S_{13}^2 - S_{11}^2 - 2S_{12}^2 - S_{22}^2\Big) \\ &- 2c_2\tau_2\Big(S_{13}W_{13} + S_{23}W_{23}\Big) + \frac{c_3\tau_2}{3}\Big(W_{13}^2 + W_{23}^2 - 2W_{12}^2\Big) \\ &+ 2c_4\tau_2^2\Big[S_{33}\Big(S_{13}W_{13} + S_{23}W_{23}\Big) + S_{12}\Big(S_{13}W_{23} + S_{23}W_{13}\Big) + S_{11}S_{13}W_{13} + S_{22}S_{23}W_{23}\Big] \\ &+ c_6\tau_2^2 S_{33}\Big(S_{11}^2 + S_{22}^2 + S_{33}^2 + 2S_{12}^2 + 2S_{13}^2 + 2S_{23}^2\Big) + 2c_7\tau_2^2 S_{33}\Big(W_{12}^2 + W_{13}^2 + W_{23}^2\Big)\Bigg\} \end{aligned} \tag{7.4}$$

$$\begin{aligned}\overline{uv} =& -\nu_t S_{12} \\ &+ c_\mu k\tau_1 \Bigg\{ c_1\tau_2\Big[S_{12}\Big(S_{11} + S_{22}\Big) + S_{13}S_{23}\Big] + c_2\tau_2\Big[W_{12}\Big(S_{22} - S_{11}\Big) + S_{23}W_{13} + S_{13}W_{23}\Big] + c_3\tau_2\Big(W_{13}W_{23}\Big) \\ &+ c_4\tau_2^2\Big[W_{12}\Big(S_{11}^2 - S_{22}^2 + S_{13}^2 - S_{23}^2\Big) - W_{13}\Big(S_{12}S_{13} + S_{22}S_{23} + S_{23}S_{33}\Big) - W_{23}\Big(S_{11}S_{13} + S_{12}S_{23} + S_{13}S_{33}\Big)\Big] \\ &+ c_6\tau_2^2 S_{12}\Big(S_{11}^2 + S_{22}^2 + S_{33}^2 + 2S_{12}^2 + 2S_{13}^2 + 2S_{23}^2\Big) + 2c_7\tau_2^2 S_{12}\Big(W_{12}^2 + W_{13}^2 + W_{23}^2\Big)\Bigg\} \end{aligned} \tag{7.5}$$

$$\begin{aligned}\overline{uw} = &-\nu_t S_{13} \\ &+ c_\mu k\tau_1 \Big\{ c_1\tau_2 \Big[S_{13}\Big(S_{11}+S_{33}\Big) + S_{12}S_{23} \Big] + c_2\tau_2 \Big[W_{13}\Big(S_{33}-S_{11}\Big) - S_{12}W_{23} + S_{23}W_{12} \Big] - c_3\tau_2 \Big(W_{12}W_{23} \Big) \\ &+ c_4\tau_2^2 \Big[W_{13}\Big(S_{11}^2 - S_{33}^2 + S_{12}^2 - S_{23}^2\Big) + W_{23}\Big(S_{11}S_{12} + S_{12}S_{22} + S_{13}S_{23}\Big) - W_{12}\Big(S_{12}S_{13} + S_{22}S_{23} + S_{23}S_{33}\Big) \Big] \\ &+ c_6\tau_2^2 S_{13}\Big(S_{11}^2 + S_{22}^2 + S_{33}^2 + 2S_{12}^2 + 2S_{13}^2 + 2S_{23}^2\Big) + 2c_7\tau_2^2 S_{13}\Big(W_{12}^2 + W_{13}^2 + W_{23}^2\Big) \Big\} \end{aligned} \tag{7.6}$$

$$\begin{aligned}\overline{vw} = &-\nu_t S_{23} \\ &+ c_\mu k\tau_1 \Big\{ c_1\tau_2 \Big[S_{23}\Big(S_{22}+S_{33}\Big) + S_{12}S_{13} \Big] + c_2\tau_2 \Big[W_{23}\Big(S_{33}-S_{22}\Big) - S_{12}W_{13} - S_{13}W_{12} \Big] + c_3\tau_3 \Big(W_{12}W_{13} \Big) \\ &+ c_4\tau_2^2 \Big[W_{23}\Big(S_{22}^2 - S_{33}^2 + S_{12}^2 - S_{13}^2\Big) + W_{12}\Big(S_{11}S_{13} + S_{12}S_{23} + S_{13}S_{33}\Big) + W_{13}\Big(S_{11}S_{12} + S_{12}S_{22} + S_{13}S_{23}\Big) \Big] \\ &+ c_6\tau_2^2 S_{23}\Big(S_{11}^2 + S_{22}^2 + S_{33}^2 + 2S_{12}^2 + 2S_{13}^2 + 2S_{23}^2\Big) + 2c_7\tau_2^2 S_{23}\Big(W_{12}^2 + W_{13}^2 + W_{23}^2\Big) \Big\} \end{aligned} \tag{7.7}$$

7.2 Asymptotic Analyses

The transport equations for the non-linear schemes are the same as those in the linear versions. In the present work, as in Craft et al. (1996b), the coefficient c_6 is taken as $-c_7$, so the non-linear terms do not contribute to the shear stress in a simple shear flow, and consequently the various asymptotic analyses for such flows reported in chapter 6 are still valid for these non-linear schemes. The NL1 and NL2 models were initially developed based on the second version of the NT1 and NT2 models, so the NL1 and NL2 models share the same coefficients and asymptotic states of the second version of the NT1 and NT2 models respectively, presented in Tables 6.8 and 6.10.

Although the non-linear stress-strain relation used here is based on that of Craft et al. (1996b), some re-tuning of the coefficients in equation 7.1 is appropriate, since the timescales used in the present models will be different from those of the single-scale version. This re-tuning was primarily done through considering the homogeneous shear and normally strained flows, as described below.

7.2.1 Homogeneous Shear Flows

In homogeneous shear flows the mean velocity gradient $\frac{dU}{dy}$ is constant and the only non-zero elements of the strain rate and vorticity tensors are S_{12} and W_{12} (and, by symmetry, S_{21} and W_{21}). One can check that all terms in equations 7.6 and 7.7 are multiplied by either S_{13}, S_{23} or S_{33}, thus ensuring the model will return $\overline{uw} = \overline{vw} = 0$. From equations 7.2 to 7.5 one can then derive the expressions for the Reynolds normal and shear stresses in this case:

$$\overline{u^2}_{SF} = \frac{2}{3}k + \frac{c_\mu k \tau_1 \tau_2 S_{12}^2}{3}(c_1 + 6c_2 + c_3) \tag{7.8}$$

$$\overline{v^2}_{SF} = \frac{2}{3}k + \frac{c_\mu k \tau_1 \tau_2 S_{12}^2}{3}(c_1 - 6c_2 + c_3) \tag{7.9}$$

$$\overline{w^2}_{SF} = \frac{2}{3}k - \frac{2c_\mu k \tau_1 \tau_2 S_{12}^2}{3}(c_1 + c_3) \tag{7.10}$$

$$\overline{uv}_{SF} = -\nu_t S_{12} + 2c_\mu k \tau_1 \tau_2^2 S_{12}^3 (c_6 + c_7) \tag{7.11}$$

As noted above, the choice $c_6 = -c_7$ has the benefit that it leaves $\overline{uv} = -\nu_t S_{12}$, and hence the previously carried out asymptotic analysis for local equilibrium boundary layer and homogeneous shear flows is still valid for these models.

From the homogeneous shear flows it thus becomes clear that one can look for the best values of $c_1 + c_3$ and c_2 to return accurate representations of the normal stresses compared to the DNS in these flows.

7.2.2 Normally Strained Flows

A second convenient set of test cases for tuning the non-linear coefficients is provided by the normally strained homogeneous flows. These again are simple geometrical flows, but as noted earlier linear schemes show some significant weaknesses in them due to misrepresentation of the normal stresses. Since one improvement expected from the non-linear schemes is better normal stress prediction, these flows are thus good test cases for tuning of the models.

In these normally strained flows, the only non-zero strains are the S_{22} and S_{33} components (with $S_{22} = -S_{33}$) and all vorticity components are zero and the only non-zero Reynolds stresses are the normal ones. One can check that in equations 7.5, 7.6 and 7.7 all terms are multiplied by either S_{12}, S_{13} or S_{23} confirming $\overline{uv} = \overline{uw} = \overline{vw}$. The modelled expressions for the Reynolds stresses then become:

$$\overline{u^2}_{NS} = \frac{2}{3}(k - c_1 c_\mu k \tau_1 \tau_2 S_{22}^2) \tag{7.12}$$

$$\overline{v^2}_{NS} = \frac{2}{3}k - \nu_t S_{22} + \frac{c_1 c_\mu k \tau_1 \tau_2 S_{22}^2}{3} + 2c_6 c_\mu k \tau_1 \tau_2^2 S_{22}^3 \tag{7.13}$$

$$\overline{w^2}_{NS} = \frac{2}{3}k + \nu_t S_{22} + \frac{c_1 c_\mu k \tau_1 \tau_2 S_{22}^2}{3} - 2c_6 c_\mu k \tau_1 \tau_2^2 S_{22}^3 \tag{7.14}$$

One can therefore tune the coefficients c_1 and c_6 for this case and, together with equations 7.11 to 7.10 for the homogeneous shear flows, the coefficients c_1, c_2, c_3, c_6 and c_7 can thus be determined.

A closer look at the terms followed by the coefficient c_4 in equations 7.2 to 7.7 shows that these terms are only non-zero in 3-D flows (since $S_{11}+S_{22}=0$ from continuity in 2-D). As all test cases studied in this work are 2-D flows, the c_4 coefficients will not be determined here, remaining to be adjusted when the models are tried in 3-D flows. However, as a starting point, one could use $c_4 = 2c_6$, as taken by Craft et al. (1996b).

7.3 The NL1 and NL2 Models

As mentioned before, the NL1 and NL2 models have initially been developed from the second version of the NT1 and NT2 schemes, whose coefficients are presented in Tables 6.8 and 6.10. As discussed in the previous chapter, the difference between the final and second versions of the NT1 and NT2 models are those extra terms inserted into the C_{P1} coefficient which are meant to improve the prediction of shear regions in strongly non-equilibrium flows, and the effect of adding such corrections into the non-linear versions will be looked at separately, after the initial model development. By starting the development of the NL1 and NL2 models using the second version of the NT1 and NT2 models, one can have a better idea of the effects of the non-linear-eddy-viscosity approach.

As also commented on before, the use of different time scale combinations in the two-time-scale non-linear-eddy-viscosity models were explored. The expression for the Reynolds stresses is used as presented in equation 7.1. Note that ν_t must be always used as in the NT1 and NT2 models in the linear term $(-\nu_t S_{ij})$ in equation 7.1 so that the asymptotic analyses carried out for the linear two-time-scale models remain valid. In Table 7.1 are presented the three different combinations of time scales tested in the NL1 and NL2 models, together with the identifiers that will be used to distinguish them below.

Table 7.1: Study of time scale in the two-time-scale non-linear-eddy-viscosity models

Model	τ_1	τ_2
$NL1-P-P$	$\frac{k_P}{\varepsilon_P}$	$\frac{k_P}{\varepsilon_P}$
$NL1-T-T$	$\frac{k}{\varepsilon_T}$	$\frac{k}{\varepsilon_T}$
$NL1-P-T$	$\frac{k_P}{\varepsilon_P}$	$\frac{k}{\varepsilon_T}$
$NL2-P-P$	$\frac{k_P}{\varepsilon_P}$	$\frac{k_P}{\varepsilon_P}$
$NL2-T-T$	$\frac{k}{\varepsilon_T}$	$\frac{k}{\varepsilon_T}$
$NL2-T-P$	$\frac{k}{\varepsilon_T}$	$\frac{k_P}{\varepsilon_P}$

So for both non-linear versions of the NT1 and NT2 models, three different non-linear approaches for the Reynolds stresses were tried. The idea would be to choose as the NL1 and NL2 models the ones in Table 7.1 which perform best.

7.3.1 The NL1 Model

Initially, a tuned set of coefficients was obtained for each of the three time scale options for the NL1 model, presented in Table 7.1. In order to do so, a program in Matlab was written so that the coefficients' values could be varied through incrementing loops and the set of

coefficients which best matched the DNS of homogeneous shear flows and the experiments of normally strained flows could be chosen.

Firstly a loop to vary $c_1 + c_3$ from -1 to 1 in increments of 0.01 was build and inside this loop, another loop was built to vary c_2 also from -1 to 1 by 0.01 increments. Three homogeneous shear flow cases (a low, a moderate and a high shear case) were solved for each combination of $c_1 + c_3$ and c_2 values and the rms "error" was computed by comparing the resultant normal stresses predicted with the DNS data. Thereby, the best sum of c_1 and c_3 and the coefficient c_2 itself were determined using the homogeneous shear flow cases.

After this, another loop was started to vary c_1 from -1 to 1 in increments of 0.01 and an inside loop was built to vary c_6 from -5 to 5 in increments of 0.01. For each set of c_1 and c_6 values, the $G\&M0$ case was solved and an rms "error" was computed by comparing the Reynolds normal stresses predicted with those provided by the experiments. Only this case was used because it is the only completely pure strain case studied. The best c_1 and c_6 could then be chosen. c_3 could then be easily computed since from the homogeneous shear flows one knows $c_1 + c_3$ and c_7 was taken as $-c_6$ for the reasons outlined earlier.

It should be noted that when optimizing the coefficients of the non-linear terms in the Reynolds stress expression only the prediction of the Reynolds normal stresses were considered. In the normally strained flows these are the only non-zero stresses, whilst in the homogeneous shear flows the prediction of the other turbulent quantities such as the Reynolds shear stress, the turbulent kinetic energy and the eddy dissipation rate depend only on the coefficients of the transport equations such as C_{P1}, C_{P2}, C_{T1}, C_{T2} and C'_{P1} and the turbulent viscosity formulation and as these are the same as those used in the linear NT1 model, their predictions should not be altered.

The best set of coefficients for each of the NL1 formulations in Table 7.1 is presented in Table 7.2 together with their rms "error" for both homogeneous shear flows (HSF) and normally strained flows (NSF). As commented on before, the general form of the coefficients is the one adopted by Craft et al. (1996b) and that is why c_1, c_2 and c_3 were taken as constants and c_6 and c_7 as functions of c_μ, which also varies with the dimensionless shear η.

Table 7.2: Best set of coefficients for the NL1 formulations in Table 7.1

Model	c_1	c_2	c_3	c_6	c_7	rms "error" in HSF	rms "error" in NSF
$NL1-P-P$	0.22	0.16	-0.12	$-0.48c_\mu^2$	$0.48c_\mu^2$	5.1402	0.9891
$NL1-T-T$	0.13	0.04	-0.11	$-0.27c_\mu^2$	$0.27c_\mu^2$	6.9146	1.0048
$NL1-P-T$	0.17	0.09	-0.09	$-0.34c_\mu^2$	$0.34c_\mu^2$	5.7298	0.9934

As one can see from Table 7.2, the different time scales do have an impact on the achievable accuracy of both the homogeneous shear and normally strained cases, although the greater differences are seen in the shear flow cases. The $NL1-P-P$ model performed slightly better than the $NL1-P-T$ model which performed better than the $NL1-T-T$ model. However, before choosing which timescale combination to use for the NL1 model simulations of the channel flow cases were carried out to test for accuracy and stability in such wall-bounded flows as well.

When running the channel flows, both $NL1-P-P$ and $NL1-T-T$ models exhibited a few instability problems. Since the $NL1-T-T$ provided the less good results in the homogeneous shear and normally strained flows it was thus discarded. The two remaining forms of the NL1 model were then used to simulate all test cases presented in Chapter 5. The instability problems found with the $NL1-P-P$ model in the channel flow were also found in most of the other flows, and so this version was also discarded and the $NL1-P-T$ formulation was thus adopted as the NL1 model.

For the sake of completeness, the form of the NL1 model and its coefficients is summarised below:

$$\frac{Dk_P}{Dt} = P_k - \varepsilon_P + \frac{\partial}{\partial x_j}\left[\left(\nu + \frac{\nu_t}{\sigma_{k_P}}\right)\frac{\partial k_P}{\partial x_j}\right] \tag{7.15}$$

$$\frac{Dk_T}{Dt} = \varepsilon_P - \varepsilon_T + \frac{\partial}{\partial x_j}\left[\left(\nu + \frac{\nu_t}{\sigma_{k_T}}\right)\frac{\partial k_T}{\partial x_j}\right] \tag{7.16}$$

$$\frac{D\varepsilon_P}{Dt} = C_{P1}P_k\frac{\varepsilon_P}{k_P} - C_{P2}\frac{\varepsilon_P^2}{k_P} + \frac{\partial}{\partial x_j}\left[\left(\nu + \frac{\nu_t}{\sigma_{\varepsilon_P}}\right)\frac{\partial \varepsilon_P}{\partial x_j}\right] \tag{7.17}$$

$$\frac{D\varepsilon_T}{Dt} = C_{T1}\frac{\varepsilon_P\varepsilon_T}{k_T} - C_{T2}\frac{\varepsilon_T^2}{k_T} + \frac{\partial}{\partial x_j}\left[\left(\nu + \frac{\nu_t}{\sigma_{\varepsilon_T}}\right)\frac{\partial \varepsilon_T}{\partial x_j}\right] \tag{7.18}$$

The Reynolds stresses are given by:

$$\begin{aligned}\overline{u_iu_j} =& \frac{2}{3}\delta_{ij}k - \nu_t S_{ij} \\ &+ c_\mu k\tau_1\left[c_1\tau_2\left(S_{ik}S_{jk} - \frac{1}{3}S_{kl}S_{kl}\delta_{ij}\right) + c_2\tau_2\left(W_{ik}S_{jk} + W_{jk}S_{ik}\right) + c_3\tau_2\left(W_{ik}W_{jk} - \frac{1}{3}W_{kl}W_{kl}\delta_{ij}\right)\right. \\ &+ c_4\tau_2^2\left(S_{ki}W_{lj} + S_{kj}W_{li}\right)S_{kl} + c_5\tau_2^2\left(W_{il}W_{lm}S_{mj} + S_{il}W_{lm}W_{mj} - \frac{2}{3}S_{lm}W_{mn}W_{nl}\delta_{ij}\right) \\ &\left.+ c_6\tau_2^2 S_{ij}S_{kl}S_{kl} + c_7\tau_2^2 S_{ij}W_{kl}W_{kl}\right]\end{aligned} \tag{7.19}$$

with the eddy viscosity defined as in the NT1 model:

$$\nu_t = c_\mu\frac{kk_P}{\varepsilon_P} \tag{7.20}$$

The coefficients and asymptotic states determined for the NL1 model are presented in Tables 7.3 and 7.4 respectively where:

$$\eta = \max\left[\frac{k}{\varepsilon_T}\sqrt{\frac{1}{2}S_{ij}S_{ij}}, \frac{k}{\varepsilon_T}\sqrt{\frac{1}{2}W_{ij}W_{ij}}\right] \tag{7.21}$$

$$S_{ij} = \frac{\partial U_i}{\partial x_j} + \frac{\partial U_j}{\partial x_i} \tag{7.22}$$

$$W_{ij} = \frac{\partial U_i}{\partial x_j} - \frac{\partial U_j}{\partial x_i} \tag{7.23}$$

Table 7.3: Coefficients of the NL1 model

C_{P1}	C_{P2}	σ_{ε_P}	C_{T1}	C_{T2}	σ_{ε_T}	
$1.4921 + 2.5\frac{min(0,\frac{k_P}{k_T}-3.6)}{\frac{k_P}{k_T}+3.6}$	1.8	1.4202	1.6	1.7	1.2181	
c_μ	c_1	c_2	c_3	c_4	c_6	c_7
$min[0.115, 0.023 + 0.25e^{-0.30\eta}]$	0.17	0.09	-0.09	$-0.68c_\mu^2$	$-0.34c_\mu^2$	$0.34c_\mu^2$

Table 7.4: Values expected to be provided by the NL1 model in the asymptotic states studied.

$\left(\frac{P_k}{\varepsilon_T}\right)_{SF}$	$\left(\frac{k_P}{k_T}\right)_{SF}$	$\left(\frac{\varepsilon_P}{\varepsilon_T}\right)_{SF}$	$\left(\frac{k_P}{k_T}\right)_{DF}$	$\left(\frac{\varepsilon_P}{\varepsilon_T}\right)_{DF}$	$\left(\frac{k_P}{k_T}\right)_{BL}$	$\left(\frac{\varepsilon_P}{\varepsilon_T}\right)_{BL}$	$c_{\mu_{BL}}$
1.9	4.4	1.1667	1.0	0.5	3.6	1.0	0.115

One may notice that the asymptotic states presented in Table 7.4 are the same as those presented in Table 6.24 for the NT1 model, thus ensuring the desired consistency with the asymptotic analyses.

7.3.2 The NL2 Model

The same procedure described above to determine the coefficients of the three NL1 schemes was used to determine the coefficients of the three NL2 formulations presented in Table 7.1, and the resulting optimized coefficients can be found in Table 7.5, together with the rms "error" of each model for both homogeneous shear and normally strained flows, referred to as HSF and NSF respectively.

Table 7.5: Best set of coefficients for the NL2 formulations in Table 7.1

Model	c_1	c_2	c_3	c_6	c_7	rms "error" in HSF	rms "error" in NSF
$NL2-P-P$	0.30	0.21	-0.10	$-1.54c_\mu^2$	$1.54c_\mu^2$	3.5873	0.9698
$NL2-T-T$	0.18	0.09	-0.10	$-0.83c_\mu^2$	$0.83c_\mu^2$	5.6571	0.9785
$NL2-T-P$	0.23	0.14	-0.10	$-1.23c_\mu^2$	$1.23c_\mu^2$	4.3217	0.9775

As one can see in Table 7.5, the different time scales have little effect on the accuracy achievable in the normally strained flows, although do have a slightly larger impact in the shear flows. Comparing Tables 7.2 and 7.5 one may see that better results are apparently achieved with the NL2 formulations. Among these, the $NL2-P-P$ model performs better than the $NL2-T-P$ model which performs better than the $NL2-T-T$.

Again, before picking one of the three to be the first version of the NL2 model, the three schemes were used to run the channel flows. None of the models presented instability problems and therefore the $NL2-T-T$, which performed less well in the homogeneous shear and normally strained flows, was discarded. The other two versions, $NL2-P-P$ and

$NL2-T-P$ were then used to simulate all other test cases presented in Chapter 5. Both models performed similarly and proved to be stable. As the $NL2-P-P$ performed best in the homogeneous shear and normally strained flows, it was therefore taken as the NL2 model.

Again, for the sake of completeness, the NL2 model formulation and coefficients are summarized below:

$$\frac{Dk_P}{Dt} = P_k - \varepsilon_P + \frac{\partial}{\partial x_j}\left[\left(\nu + \frac{\nu_t}{\sigma_{k_P}}\right)\frac{\partial k_P}{\partial x_j}\right] \tag{7.24}$$

$$\frac{Dk_T}{Dt} = \varepsilon_P - \varepsilon_T + \frac{\partial}{\partial x_j}\left[\left(\nu + \frac{\nu_t}{\sigma_{k_T}}\right)\frac{\partial k_T}{\partial x_j}\right] \tag{7.25}$$

$$\frac{D\varepsilon_P}{Dt} = C_{P1}P_k\frac{\varepsilon_P}{k_P} - C_{P2}\frac{\varepsilon_P^2}{k_P} + C'_{P1}k_P\frac{\partial U_l}{\partial x_m}\frac{\partial U_i}{\partial x_j}\epsilon_{lmk}\epsilon_{ijk} + \frac{\partial}{\partial x_j}\left[\left(\nu + \frac{\nu_t}{\sigma_{\varepsilon_P}}\right)\frac{\partial \varepsilon_P}{\partial x_j}\right] \tag{7.26}$$

$$\frac{D\varepsilon_T}{Dt} = C_{T1}\frac{\varepsilon_P^2}{k_T} - C_{T2}\frac{\varepsilon_T^2}{k_T} + \frac{\partial}{\partial x_j}\left[\left(\nu + \frac{\nu_t}{\sigma_{\varepsilon_T}}\right)\frac{\partial \varepsilon_T}{\partial x_j}\right] \tag{7.27}$$

The Reynolds stresses are given by:

$$\begin{aligned}\overline{u_iu_j} =& \frac{2}{3}\delta_{ij}k - \nu_t S_{ij} \\ &+ c_\mu k\tau_1\left[c_1\tau_2\left(S_{ik}S_{jk} - \frac{1}{3}S_{kl}S_{kl}\delta_{ij}\right) + c_2\tau_2\left(W_{ik}S_{jk} + W_{jk}S_{ik}\right) + c_3\tau_2\left(W_{ik}W_{jk} - \frac{1}{3}W_{kl}W_{kl}\delta_{ij}\right)\right. \\ &+ c_4\tau_2^2\left(S_{ki}W_{lj} + S_{kj}W_{li}\right)S_{kl} + c_5\tau_2^2\left(W_{il}W_{lm}S_{mj} + S_{il}W_{lm}W_{mj} - \frac{2}{3}S_{lm}W_{mn}W_{nl}\delta_{ij}\right) \\ &\left.+ c_6\tau_2^2 S_{ij}S_{kl}S_{kl} + c_7\tau_2^2 S_{ij}W_{kl}W_{kl}\right]\end{aligned} \tag{7.28}$$

with the eddy viscosity defined as in the NT2 model:

$$\nu_t = c_\mu\frac{k^2}{\varepsilon_T} \tag{7.29}$$

The coefficients and asymptotic states determined for the NL2 model are presented in Tables 7.6 and 7.7 respectively where η, S_{ij} and W_{ij} are given by equations 7.21, 7.22 and 7.23 respectively.

7.4 Performance of the NL1 and NL2 Models

The performance of the NL1 and NL2 models as defined above will be assessed in all test cases presented in Chapter 5. As commented on before, most of these cases are shear dominated flows and therefore differences in the prediction of the velocity, Reynolds shear stress,

Table 7.6: Coefficients of the NL2 model

C_{P1}	C_{P2}	σ_{ε_P}	C_{T1}	C_{T2}	σ_{ε_T}	C'_{P1}
$1.5697 + 2.5\frac{min(0,\frac{k_P}{k_T}-3.7)}{\frac{k_P}{k_T}+3.7}$	1.8	1.6664	1.0	1.1	1.1922	-0.005
c_μ	c_1	c_2	c_3	c_4	c_6	c_7
$min[0.09, 0.0117 + 0.22e^{-0.31\eta}]$	0.23	0.14	-0.10	$-2.46c_\mu^2$	$-1.23c_\mu^2$	$1.23c_\mu^2$

Table 7.7: Values expected to be provided by the second version of the NL2 model in the asymptotic states studied

$\left(\frac{P_k}{\varepsilon_T}\right)_{SF}$	$\left(\frac{k_P}{k_T}\right)_{SF}$	$\left(\frac{\varepsilon_P}{\varepsilon_T}\right)_{SF}$	$\left(\frac{k_P}{k_T}\right)_{DF}$	$\left(\frac{\varepsilon_P}{\varepsilon_T}\right)_{DF}$	$\left(\frac{k_P}{k_T}\right)_{BL}$	$\left(\frac{\varepsilon_P}{\varepsilon_T}\right)_{BL}$	$c_{\mu_B L}$	$c_{\mu_S F}$
1.9	8.8245	1.0916	1.3166	0.5683	3.7	1.0	0.09	0.0336

turbulent kinetic energy and eddy dissipation rate are not expected between the NL1 and NT1 and NL2 and NT2 models. This expectation was confirmed when running all test cases and therefore the discussion of the performance of the NL1 and NL2 models will be mainly based on the predictions of the Reynolds normal stresses.

The predictions provided by the NL1 and NL2 models will be compared to those provided by the KS and SG models, besides the final version of the NT1 and NT2 models. The idea is to compare these two-time-scale non-linear-eddy-viscosity models with the single-time-scale model they were based on (the KS model), with the two-time-scale linear schemes they were also based on (the NT1 and NT2 models), and with a stress transport model (the SSG model).

Starting by evaluating the performance of the NL1 and NL2 models in the homogeneous shear flows, the predictions of the Reynolds normal stresses are presented in Figure 7.1 to 7.11. In Figures 7.1 and 7.2 the prediction of the Reynolds normal stresses and of the normal components of the Reynolds stress anisotropy tensor $a_{ij} = \frac{u_i u_j}{k} - \frac{2}{3}\delta_{ij}$ are respectively presented for the lowest shear case. One may notice that the NL1 and NL2 models perform overall better than the KS and SG models. One can also clearly see the improvements of the NLEV and RST models over the LEV schemes, which predict an isotropic state for the normal stresses. The predictions in the $U2$ low shear case are presented in Figure 7.3 where again, the NL1 and NL2 models can be considered to perform best. In the $W2$ low shear case, presented in Figures 7.4 and 7.5, the NL1 and NL2 models again perform well (although the KS and SG models return slightly better results than them in this case). However, none of the models entirely capture the development of the a_{ij} profiles, particularly a_{11}. Although the NL1 and NL2 models perform similarly to the KS and SG models in predicting $\overline{u^2}$ in the $HM1$ moderate shear case, presented in Figures 7.6 and 7.7, the SG model performs best in predicting the normal components of the Reynolds stress anisotropy tensor, specially the a_{11}. In the SHC high shear case, presented in Figures 7.8 and 7.9, the SG model predicts well $\overline{u^2}$, but overpredicts the other normal stresses, while the NL1 and NL2 models appear to predict $\overline{v^2}$ and $\overline{w^2}$ better. A closer examination of the NL1 results for $\overline{v^2}$ shows that it actually returned negative values for this stress component up to $St \approx 6$. For the sake of plotting,

these negative values have been clipped to zero. This is clearer from the a_{22} profile in Figure 7.8(b). Nevertheless, the a_{ij} profile is not very well predicted by any of the models. In the $HM2$ highest shear case the SG model performed clearly better than the other models and one can notice that both NL1 and NL2 models results have been clipped where they produced negative $\overline{v^2}$ predictions. These negative values of $\overline{v^2}$ returned by the models indicate that the non-linear terms are capable of returning non-realizable stress values at quite high strain rates, and this could be an avenue to explore further in future work.

Among the normally strained flow cases studied, two cases will be assessed: the $T\&R$ and the $G\&M0$ cases. Both cases present pure normal straining, however the former has the straining started after some initial development of the flow (decay of turbulence), and stopped before the end of the duct, so there is some relaxation of the flow. The turbulent kinetic energy development is presented in Figure 7.12. All models predict well the development of k, the SG model predicting a rather fast decay after the removal of the straining. The NL1 and NL2 models provided a rather fast decay of $\overline{u^2}$ and a rather steep growth in the $\overline{w^2}$ profile before the interruption of the straining. The KS model performed best in predicting the Reynolds normal stresses, however, as a NLEV model, it fails after the deactivation of the straining, when only the SG model performs reasonably. The profile of the Reynolds stress anisotropy tensor, presented in Figure 7.14, was also best predicted by the KS model before the straining was interrupted.

Moving now to the $G\&M0$ case, the prediction of the turbulent kinetic energy is presented in Figure 7.15. One may see that the NL1 and NL2 models clearly improve the prediction of the turbulent kinetic energy. The Reynolds normal stresses, presented in Figure 7.16, were overall best predicted by the SG model, but the NL1 and NL2 models best predicted $\overline{v^2}$. This analysis can be extended to the prediction of the Reynolds stress anisotropy tensor components in Figure 7.17. The NL1 and NL2 models predict fairly well $\overline{u^2}$ and $\overline{w^2}$ in the second half of the channel, however fail in the first half due to the wrong starting levels of these quantities which is an inherent limitation of eddy-viscosity models.

The prediction of the turbulent kinetic energy and the Reynolds normal stresses in the channel flow with $Re = 41441$ are presented in Figure 7.18. One may confirm that there is no difference in the prediction of the turbulent kinetic energy between the linear and non-linear two-time-scale models, but the latter did improve the prediction of the Reynolds normal stresses which are as good as those provided by the KS and SG models. These results are representative of the cases at other Reynolds numbers and therefore the other cases will not be presented here.

The prediction of the turbulent kinetic energy and the Reynolds normal stresses in the zero pressure gradient boundary layer at $Re_\theta = 1410$ are presented in Figure 7.19. As in the channel flow, the prediction of the turbulent kinetic energy is nearly the same for the linear and non-linear two-time-scale models. None of the models were actually able to correctly predict the near wall peak of $\overline{u^2}$, however, of the models shown, only the KS is a LRN scheme, and those employing wall-functions might not be expected to fully capture the near-wall peak of $\overline{u^2}$. One can say that the NL1 and NL2 models predicted the normal stresses

better than the KS model and similarly to the SG model. At $Re_\theta = 4981$ and $Re_\theta = 13052$ there are only experimental data for $\overline{u^2}$ and $\overline{v^2}$. These are presented in Figure 7.20 where one can see that the conclusions drawn from the $Re_\theta = 1410$ location remain valid.

In order to assess the performance of the NL1 and NL2 models in the adverse pressure gradient boundary layer cases, profiles of the turbulent kinetic energy and Reynolds normal stresses will be discussed for the $M\&P30$ case which is representative of the other two cases. Looking at the profiles of k in Figure 7.21 it can be noted that the NL1 and NL2 models tend to return slightly higher peak levels of k than the other models as the flow develops in the x direction, but these are still lower than the measurements. The profile of $\overline{u^2}$ is presented in Figure 7.22 where, again, none of the models are able to follow the experiments. Nonetheless, it can be noted that the NL1 and NL2 models perform similarly to the KS and SG models. The profiles of $\overline{v^2}$ and $\overline{w^2}$, respectively presented in Figures 7.23 and 7.24, were perhaps best predicted by the NL1 and NL2 models.

The performance of the NL1 and NL2 models in the favourable pressure gradient boundary layer cases will be discussed only for the lowest acceleration parameter case, since it is representative of the other cases as well. The profiles of the turbulent kinetic energy and the Reynolds normal stresses for the $K150$ case are presented in Figure 7.25. Again, the turbulent kinetic energy profile shows no difference in the predictions of the LEV and NLEV two-time-scale models. Although the NL1 and NL2 models are high Reynolds number models which were used together with wall functions, they provided the best predictions of the near-wall peak of $\overline{u^2}$. On the other hand, they overpredicted the near-wall peak of the other two normal stresses. Overall, they performed as well as the KS and SG models.

Turning now to the JSF oscillatory boundary layer case, the profiles of the Reynolds shear stress and of the streamwise and wall-normal Reynolds normal stresses through the cycle at four y locations are presented in Figures 7.26 to 7.28. The profiles of the Reynolds shear stress show little difference between the LEV and NLEV two-time-scale model predictions. The predictions of the streamwise and wall-normal Reynolds normal stresses show that the NL1 and NL2 models perform similarly to the SG and KS models and, as expected, better than their linear counterparts. A closer look at the Reynolds normal stresses profiles is presented in Figures 7.29 to 7.31 for four positions in the cycle. Again, it can be seen that all models perform similarly, overpredicting $< u^2 >^{1/2}$ and predicting well $< v^2 >^{1/2}$ and $< w^2 >^{1/2}$.

For the low frequency oscillatory pipe flow, predictions of the wall shear stress and streamwise fluctuating velocity through the cycle at three radial locations are shown in Figure 7.32. The prediction of the wall shear stress is slightly improved by the NLEV MTS models, compared to their LEV counterparts. The profiles of u'/U_m at three y/R positions are similarly predicted by the NLEV and RST models. The same analysis can be extended to the prediction of u'/U_m across the radial direction at four cycle positions, presented in Figure 7.33, where again it can be seen the NL1 and NL2 perform well and similarly to the KS and SG models. In the $Tu\&R36$ high frequency case, the prediction of the wall shear stress is presented in Figure 7.34 where the NL1 and NL2 models perform similarly to the other models,

but the KS model returns a slightly higher level for this quantity. None of the models are able to predict the kink in the $< \tau_w >$ profile. Figure 7.34 also presents profiles of u'/U_m at three y/R positions. Although in this case the models mainly exhibit a frozen turbulence behaviour, it can be seen that all models predict some oscillation in the rms streamwise fluctuating velocity profile. The KS model seems to be more in phase with the experiments, while the NL1 and NL2 models perform similarly to the SG model. Particularly at $y/R = 0.07$ this behaviour might be related to the use of wall functions for the latter models. Closer to the centre of the pipe, at $y/R = 0.98$ one can observe frozen turbulence. Looking at the profiles of u'/U_m across the radial direction at four cycle positions in Figure 7.35, one can see that only very close to the wall is there any difference in the predictions, confirming frozen turbulence from $y/R \approx 0.25$ on. Again, the NL1 and NL2 models performed reasonably well and similarly to the KS and SG models. For the intermediate frequency case, the prediction of the amplitude and phase shift of the rms streamwise and wall-normal fluctuating velocities are presented in Figure 7.36 where perhaps the KS model performs best, although none of the models perform very accurately. The NL1 and NL2 models performed similarly to the SG model and as this case has a relatively low Reynolds number, $Re = 14000$, it makes one wonder whether the use of a wall function might be adversely affecting these predictions.

For the fully developed ramp up pipe flow case, only Reynolds stress and turbulent kinetic energy profiles will be presented, since the mean velocity is well predicted by all models, as shown already in Chapters 5 and 6. The time histories of the Reynolds shear stress at three radial positions are presented in Figure 7.37 where one can see the NL1 and NL2 models performing very similarly to the NT1 and NT2 models and also to the SG model, providing better results than the KS model which shows the increase in shear stress occurring rather too late. The prediction of the turbulent kinetic energy is presented in Figure 7.38. Whereas the NL1 and NL2 models perform well, the interesting aspect to be noted is how similar these models perform compared to their linear counterpart. As commented on before, the version of the NT1 and NT2 models which is being presented is the final one where the extra terms in C_{P1} are present. The NL1 and NL2 models perform similarly to them in spite of not having any of these terms included. That might point to an underlying benefit of the NLEV schemes, although it should be noted that the terms were added to the linear models specifically to address problems in the forced backstep flows, and it still remains to be seen how the corresponding non-linear schemes behave in those flows. The time histories of the rms streamwise fluctuating velocity are presented in Figures 7.39 and 7.40. One can notice that none of the models are able to predict the initial slow increase in u' levels, especially at the centre of the pipe, however the NL1 and NL2 models seems to best capture the levels of this quantity after the building up process. When looking at the profiles of u' normalized by the local bulk velocity, it can be seen that all models follow correctly the experimental trend, the KS model slightly out of phase due to its delay in predicting the building up process. Similar analysis can be extended to the profiles of v' and w'. These two normal stresses present similar profiles so only results for v' are being shown and can be found in Figures 7.41 and 7.42. In all the fluctuating velocities profiles the SG model tends to predict correctly

the level of these quantities at the centre of the pipe and underpredict them at $r/R = 0.47$. On the other hand, the NL1 and NL2 models tend to correctly predict the profiles at this position and overpredict them in the centre of the pipe.

Finally, the performance of the NL1 and NL2 models in the backward facing step cases will be discussed. The prediction of the reattachment point in the steady and unsteady cases is presented in Table 7.8 where the predictions provided by the second version of the NT1 and NT2 models are also included. It can be noted that the NL1 and NL2 models perfomed similarly to the second version of the NT1 and NT2 models which shows that the non-linear approach is not improving prediction, as expected, since the backward facing step flows are shear dominated flows. The reason why the final version of the NT1 and NT2 models actually perform best is due to the extra terms inserted into C_{P1} as already discussed.

The velocity profiles provided by the NL1 and NL2 models are very similar to those of the second version of the NT1 and NT2 models (Figure 6.49) and therefore are not being presented here, since no additional comments are worthwhile for the discussion.

Summarizing, the NL1 and NL2 models perform generally well over the range of flows studied, bringing some of the benefits noted earlier from the introduction of the two-time scales, and also the benefits of better normal stress predictions from the non-linear stress-strain relation.

Whilst the backstep flow predictions of reattachment location are close to those of the underlying NT1 and NT2 models, further modifications were introduced into these linear models, as described in Section 6.3, to specifically address their weaknesses in this case. The following section therefore explores the possibility of including such modifications within the non-linear model versions.

Table 7.8: Performance of the NL1 and NL2 models in predicting the reattachment point in the three backward facing step cases.

Model/Experiment	St=0	St=0.275	St=1
Experiment	7.8	5.0	8.1
SG	6.95	5.51	7.66
KS	8.03	-	-
NT1_V2	8.63	8.16	9.30
NT2_V2	9.50	9.25	10.2
NT1	7.82	5.05	7.96
NT2	7.84	5.05	7.81
NL1	8.63	8.02	9.45
NL2	9.49	9.00	10.4

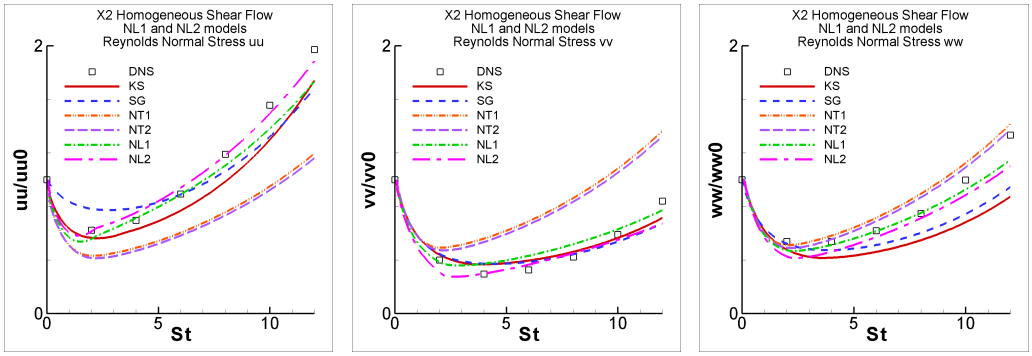

(a) $\overline{u^2}$ Profile (b) $\overline{v^2}$ Profile (c) $\overline{w^2}$ Profile

Figure 7.1: Performance of the NL1 and NL2 models compared with the results provided by the KS, SG, NT1 and NT2 models in predicting the Reynolds normal stresses in the homogeneous lowest shear flow case $X2$. Models as in Table 3.25.

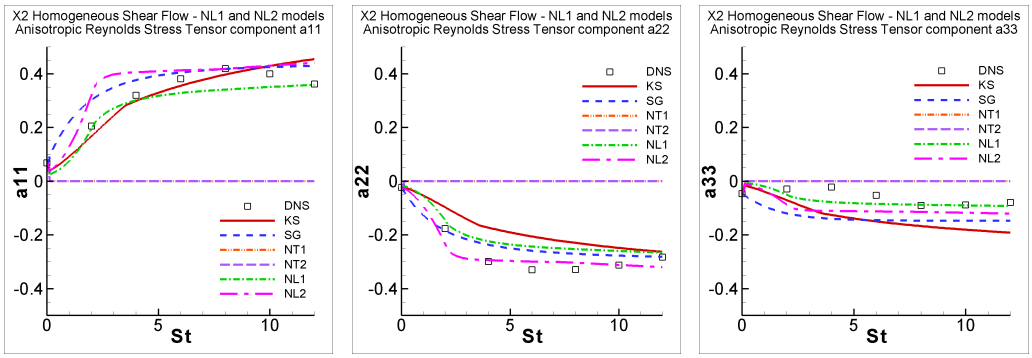

(a) a_{11} Profile (b) a_{22} Profile (c) a_{33} Profile

Figure 7.2: Performance of the NL1 and NL2 models compared with the results provided by the KS, SG, NT1 and NT2 models in predicting the normal components of the Reynolds stress anisotropy tensor in the homogeneous lowest shear flow case $X2$. Models as in Table 3.25.

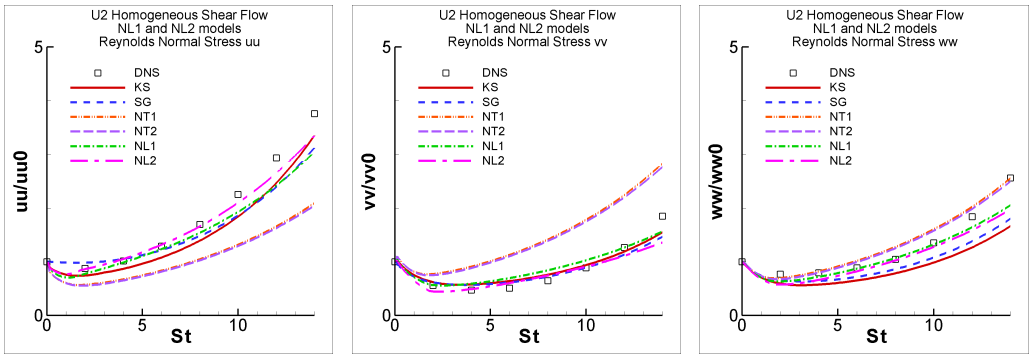

(a) $\overline{u^2}$ Profile (b) $\overline{v^2}$ Profile (c) $\overline{w^2}$ Profile

Figure 7.3: Performance of the NL1 and NL2 models compared with the results provided by the KS, SG, NT1 and NT2 models in predicting the Reynolds normal stresses in the homogeneous low shear flow case $U2$. Models as in Table 3.25.

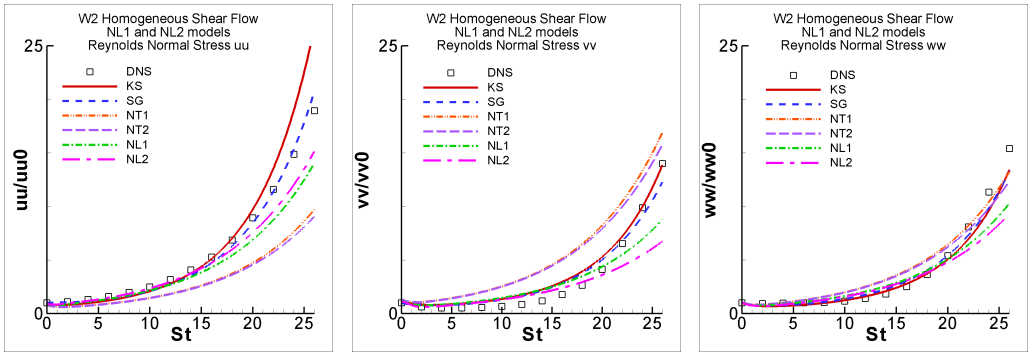

(a) $\overline{u^2}$ Profile (b) $\overline{v^2}$ Profile (c) $\overline{w^2}$ Profile

Figure 7.4: Performance of the NL1 and NL2 models compared with the results provided by the KS, SG, NT1 and NT2 models in predicting the Reynolds normal stresses in the homogeneous low shear flow case $W2$. Models as in Table 3.25.

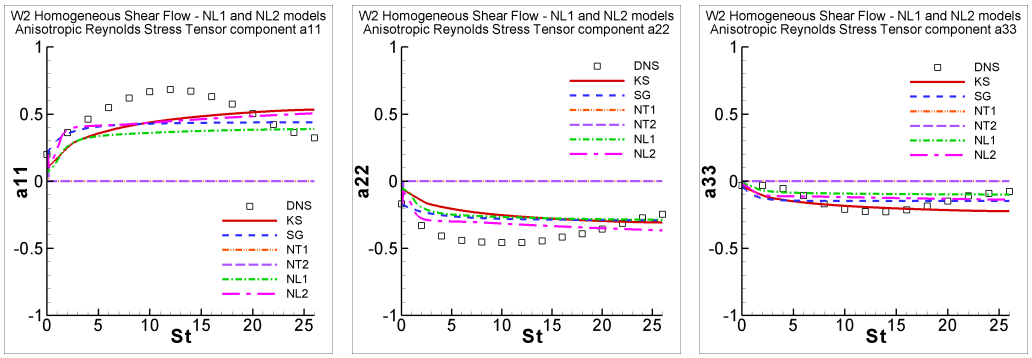

(a) a_{11} Profile (b) a_{22} Profile (c) a_{33} Profile

Figure 7.5: Performance of the NL1 and NL2 models compared with the results provided by the KS, SG, NT1 and NT2 models in predicting the normal components of the Reynolds stress anisotropy tensor in the homogeneous low shear flow case $W2$. Models as in Table 3.25.

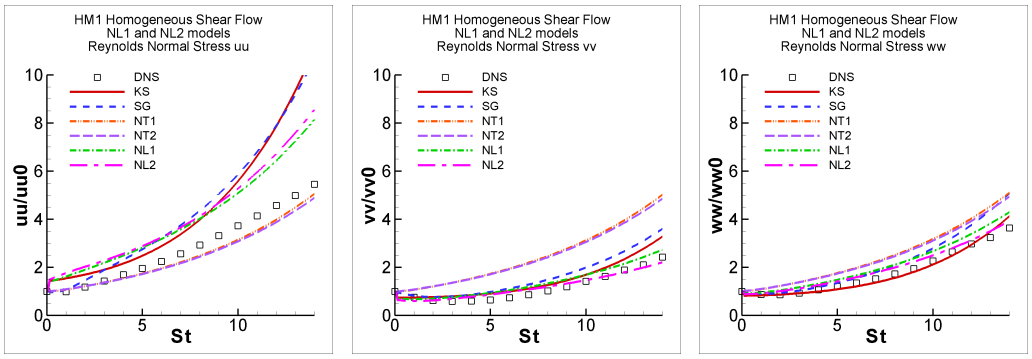

(a) $\overline{u^2}$ Profile (b) $\overline{v^2}$ Profile (c) $\overline{w^2}$ Profile

Figure 7.6: Performance of the NL1 and NL2 models compared with the results provided by the KS, SG, NT1 and NT2 models in predicting the Reynolds normal stresses in the homogeneous moderate shear flow case $HM1$. Models as in Table 3.25.

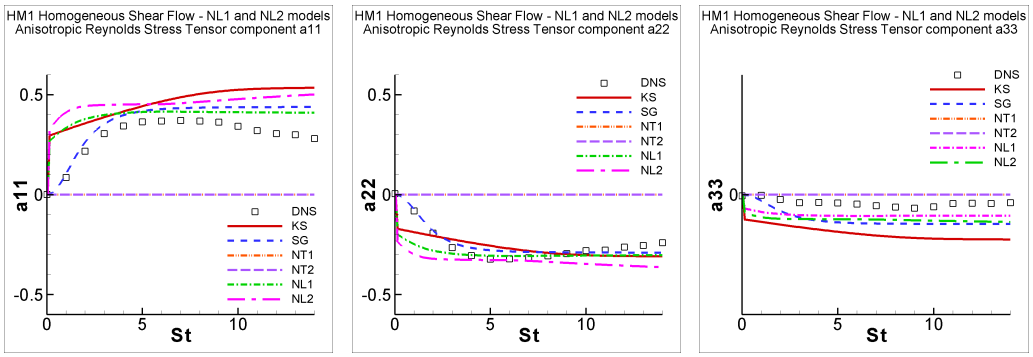

(a) a_{11} Profile (b) a_{22} Profile (c) a_{33} Profile

Figure 7.7: Performance of the NL1 and NL2 models compared with the results provided by the KS, SG, NT1 and NT2 models in predicting the normal components of the Reynolds stress anisotropy tensor in the homogeneous moderate shear flow case $HM1$. Models as in Table 3.25.

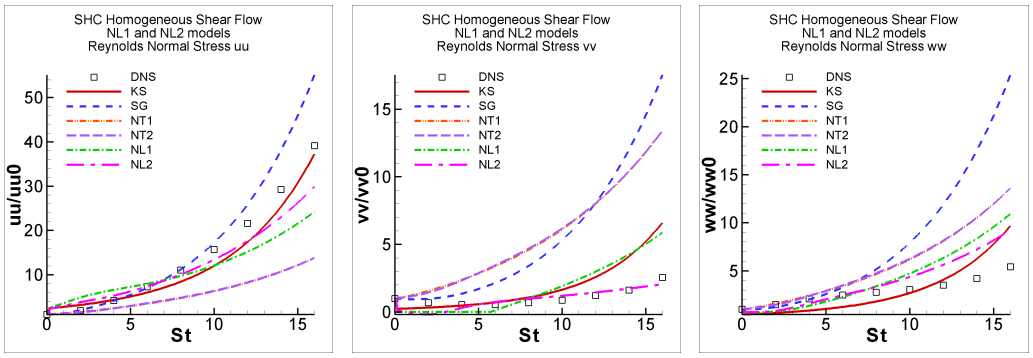

(a) $\overline{u^2}$ Profile (b) $\overline{v^2}$ Profile (c) $\overline{w^2}$ Profile

Figure 7.8: Performance of the NL1 and NL2 models compared with the results provided by the KS, SG, NT1 and NT2 models in predicting the Reynolds normal stresses in the homogeneous high shear flow case SHC. Models as in Table 3.25.

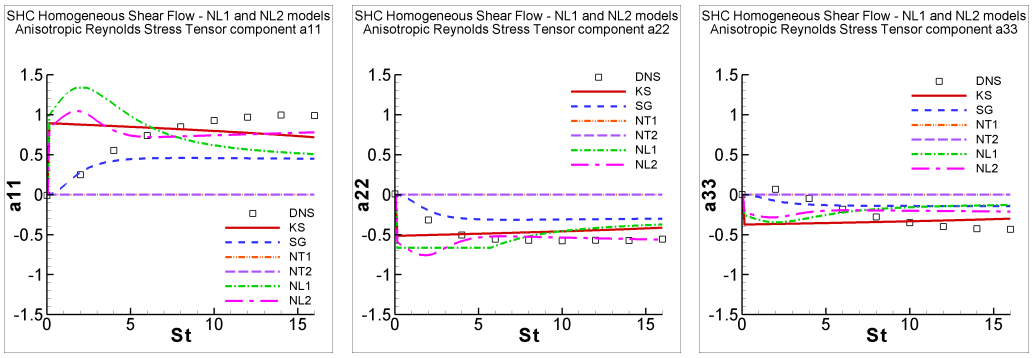

(a) a_{11} Profile (b) a_{22} Profile (c) a_{33} Profile

Figure 7.9: Performance of the NL1 and NL2 models compared with the results provided by the KS, SG, NT1 and NT2 models in predicting the normal components of the Reynolds stress anisotropy tensor in the homogeneous high shear flow case SHC. Models as in Table 3.25.

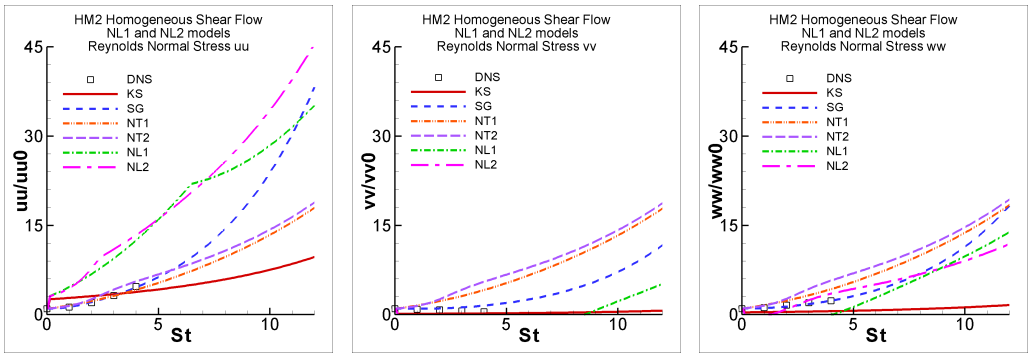

(a) $\overline{u^2}$ Profile (b) $\overline{v^2}$ Profile (c) $\overline{w^2}$ Profile

Figure 7.10: Performance of the NL1 and NL2 models compared with the results provided by the KS, SG, NT1 and NT2 models in predicting the Reynolds normal stresses in the homogeneous highest shear flow case $HM2$. Models as in Table 3.25.

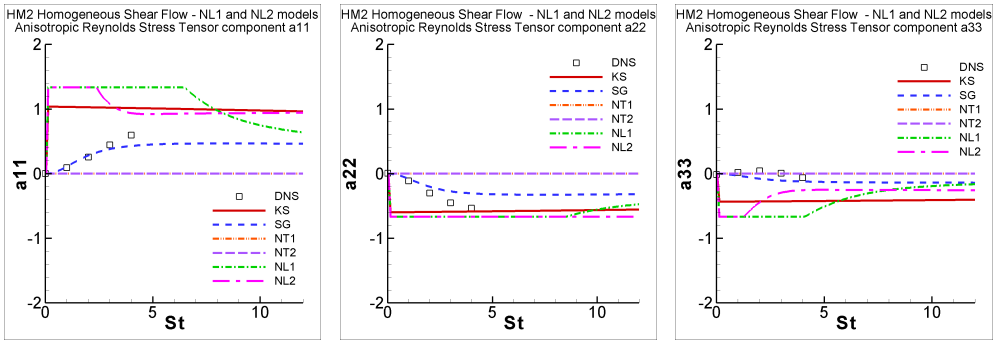

(a) a_{11} Profile (b) a_{22} Profile (c) a_{33} Profile

Figure 7.11: Performance of the NL1 and NL2 models compared with the results provided by the KS, SG, NT1 and NT2 models in predicting the normal components of the Reynolds stress anisotropy tensor in the homogeneous highest shear flow case $HM2$. Models as in Table 3.25.

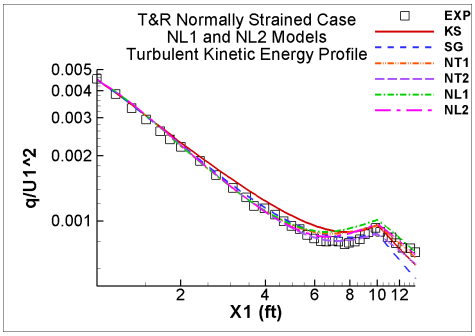

Figure 7.12: Performance of the NL1 and NL2 models compared with the results provided by the KS, SG, NT1 and NT2 models in predicting the turbulent kinetic energy ($q = 2k$) in the $T\&R$ normally strained flow case. Models as in Table 3.25.

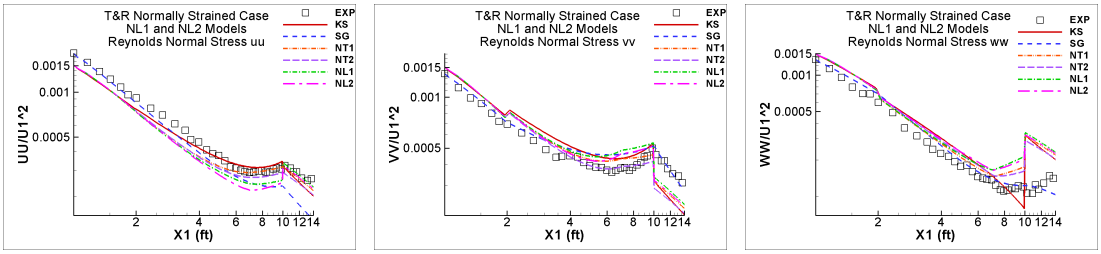

(a) $\overline{u^2}$ profile (b) $\overline{v^2}$ profile (c) $\overline{w^2}$ profile

Figure 7.13: Performance of the NL1 and NL2 models compared with the results provided by the KS, SG, NT1 and NT2 models in predicting the Reynolds normal stresses in the $T\&R$ normally strained flow case. Models as in Table 3.25.

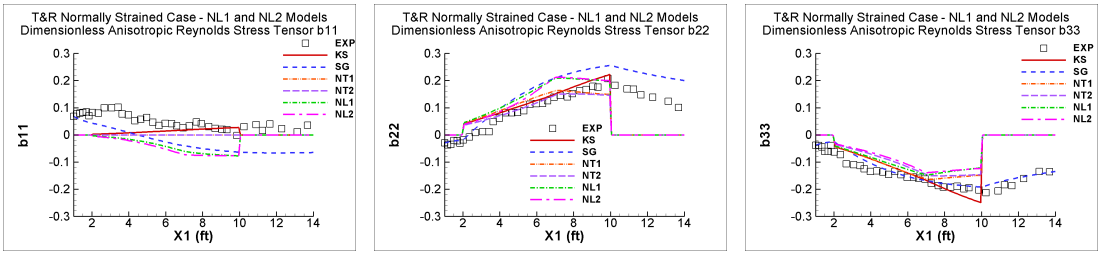

(a) b_{11} profile (b) b_{22} profile (c) b_{33} profile

Figure 7.14: Performance of the NL1 and NL2 models compared with the results provided by the KS, SG, NT1 and NT2 models in predicting the normal components of the Reynolds stress anisotropy tensor in the $T\&R$ normally strained flow case. Models as in Table 3.25.

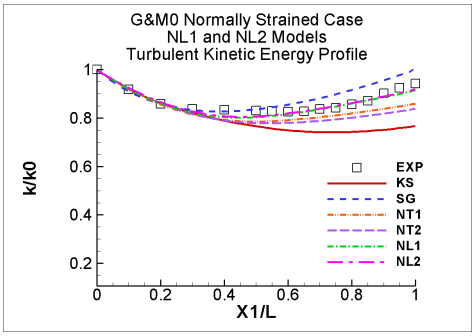

Figure 7.15: Performance of the NL1 and NL2 models compared with the results provided by the KS, SG, NT1 and NT2 models in predicting the turbulent kinetic energy in the $G\&M0$ normally strained flow case. Models as in Table 3.25.

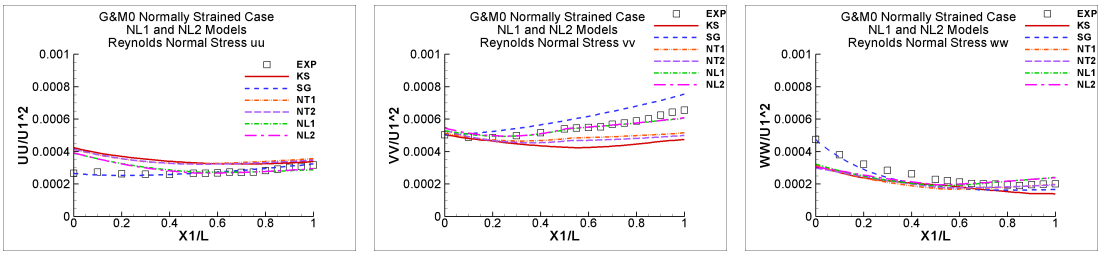

(a) $\overline{u^2}$ profile (b) $\overline{v^2}$ profile (c) $\overline{w^2}$ profile

Figure 7.16: Performance of the NL1 and NL2 models compared with the results provided by the KS, SG, NT1 and NT2 models in predicting the Reynolds normal stresses in the $G\&M0$ normally strained flow case. Models as in Table 3.25.

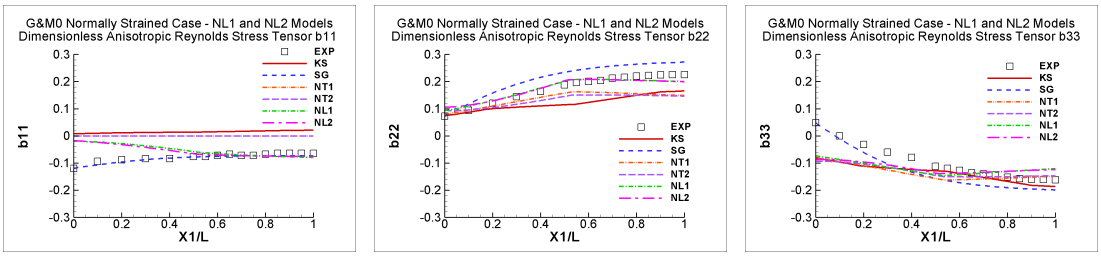

(a) b_{11} profile (b) b_{22} profile (c) b_{33} profile

Figure 7.17: Performance of the NL1 and NL2 models compared with the results provided by the KS, SG, NT1 and NT2 models in predicting the normal components of the Reynolds stress anisotropy tensor in the $G\&M0$ normally strained flow case. Models as in Table 3.25.

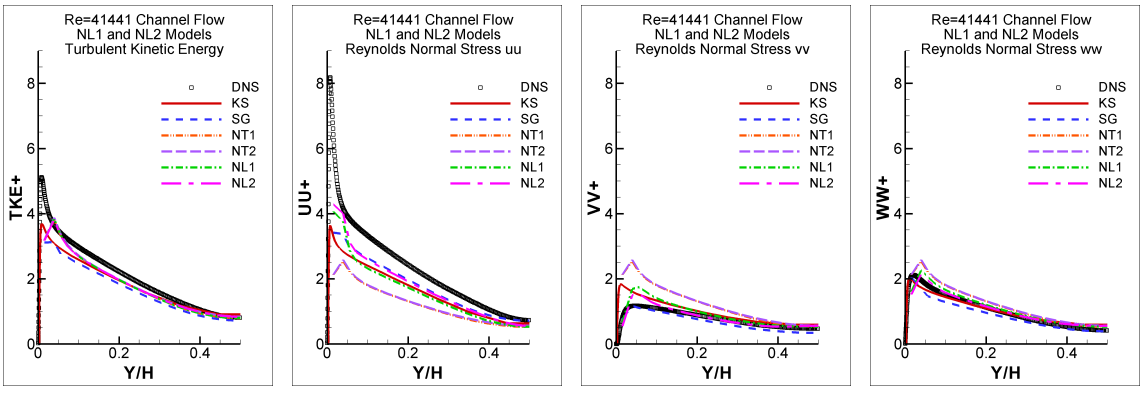

(a) k Profile (b) $\overline{u^2}$ Profile (c) $\overline{v^2}$ Profile (d) $\overline{w^2}$ Profile

Figure 7.18: Performance of the NL1 and NL2 models compared with the results provided by the KS, SG, NT1 and NT2 models in the fully developed channel flow case with $Re = 41441$. Models as in Table 3.25.

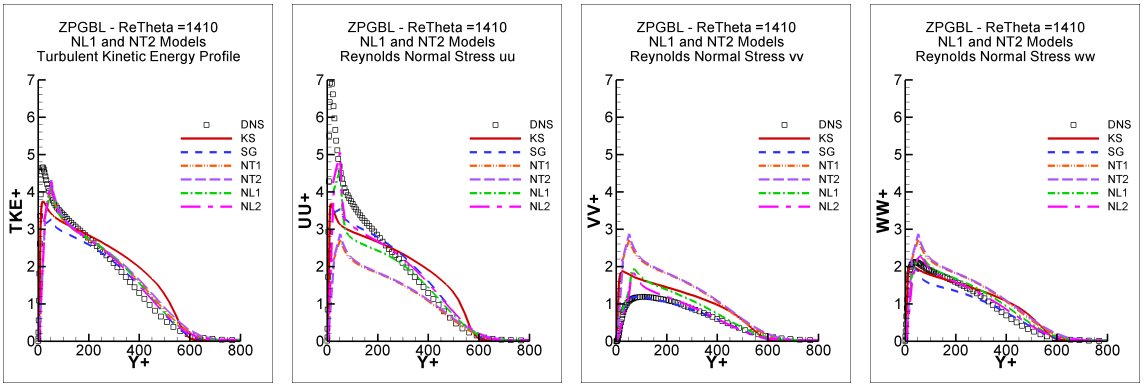

(a) k Profile (b) $\overline{u^2}$ Profile (c) $\overline{v^2}$ Profile (d) $\overline{w^2}$ Profile

Figure 7.19: Performance of the NL1 and NL2 models compared with the results provided by the KS, SG, NT1 and NT2 models in the zero pressure gradient boundary layer at $Re_\theta = 1410$. Models as in Table 3.25.

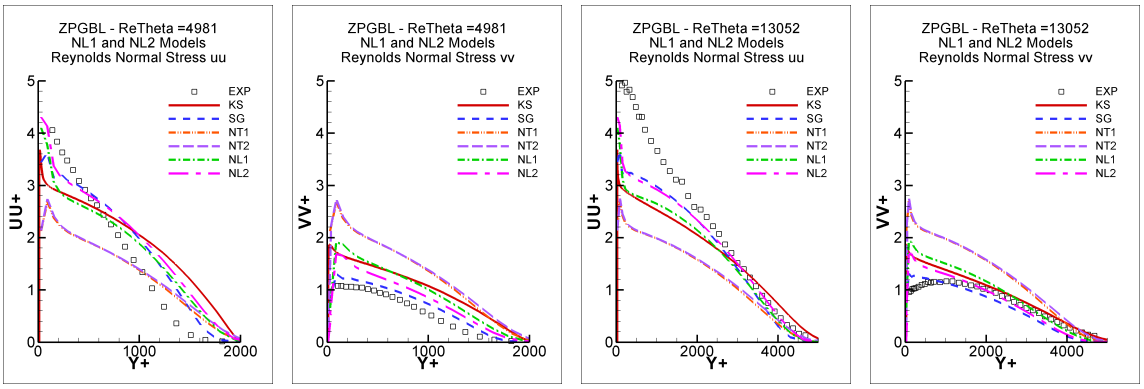

(a) $\overline{u^2}$ at $Re_\theta = 4981$ (b) $\overline{v^2}$ at $Re_\theta = 4981$ (c) $\overline{u^2}$ at $Re_\theta = 13052$ (d) $\overline{v^2}$ at $Re_\theta = 13052$

Figure 7.20: Performance of the NL1 and NL2 models compared with the results provided by the KS, SG, NT1 and NT2 models in the zero pressure gradient boundary layer at $Re_\theta = 4981$ and $Re_\theta = 13052$. Models as in Table 3.25.

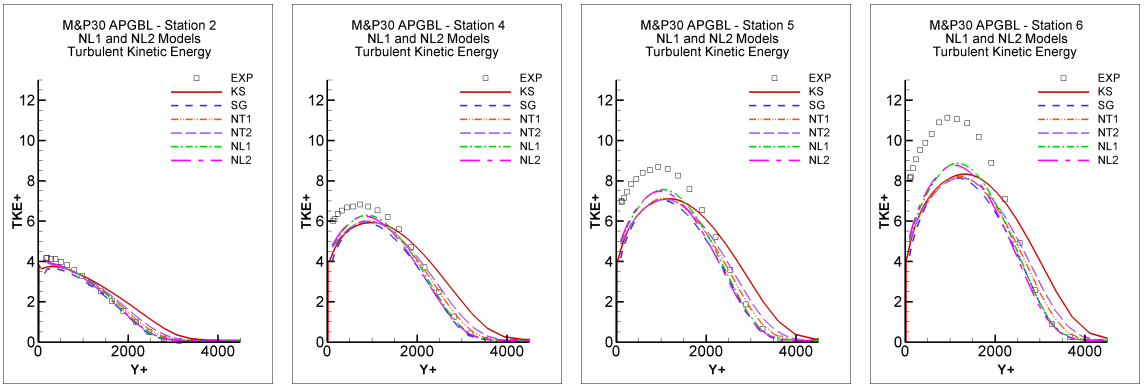

(a) Station 2 (b) Station 4 (c) Station 5 (d) Station 6

Figure 7.21: Prediction of the turbulent kinetic energy by the NL1 and NL2 models compared with the results provided by the KS, SG, NT1 and NT2 models in the adverse pressure gradient boundary layer case $M\&30$. Models as in Table 3.25.

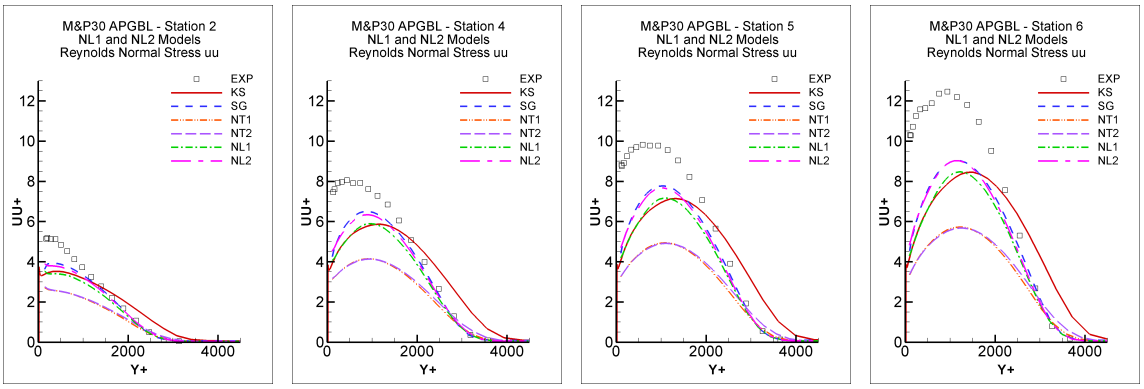

(a) Station 2 (b) Station 4 (c) Station 5 (d) Station 6

Figure 7.22: Prediction of the Reynolds normal stress $\overline{u^2}$ by the NL1 and NL2 models compared with the results provided by the KS, SG, NT1 and NT2 models in the adverse pressure gradient boundary layer case M&30. Models as in Table 3.25.

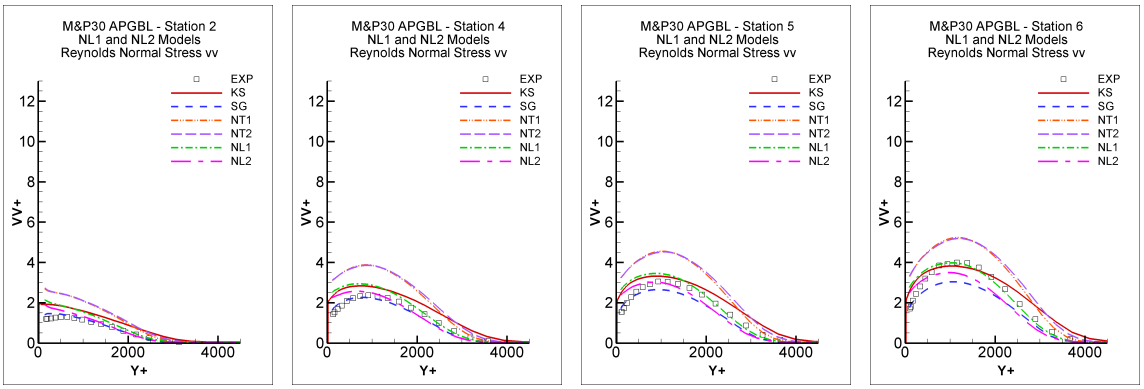

(a) Station 2 (b) Station 4 (c) Station 5 (d) Station 6

Figure 7.23: Prediction of the Reynolds normal stress $\overline{v^2}$ by the NL1 and NL2 models compared with the results provided by the KS, SG, NT1 and NT2 models in the adverse pressure gradient boundary layer case M&30. Models as in Table 3.25.

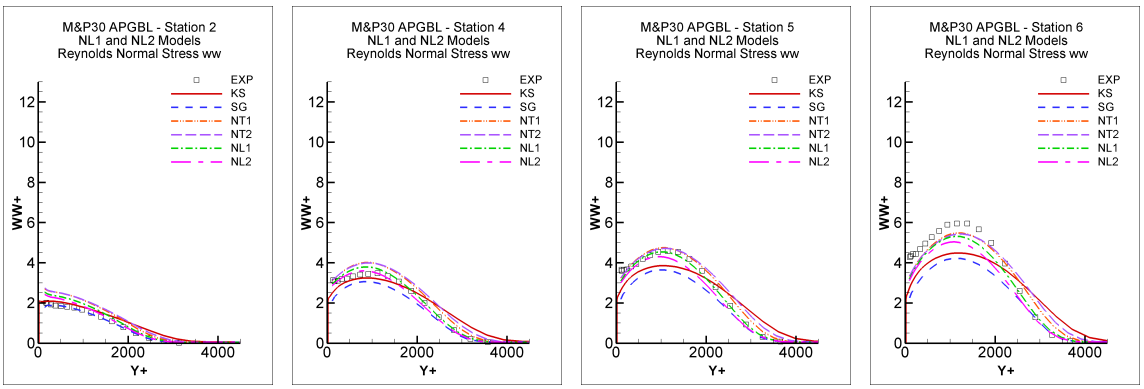

(a) Station 2 (b) Station 4 (c) Station 5 (d) Station 6

Figure 7.24: Prediction of the Reynolds normal stress $\overline{w^2}$ by the NL1 and NL2 models compared with the results provided by the KS, SG, NT1 and NT2 models in the adverse pressure gradient boundary layer case M&30. Models as in Table 3.25.

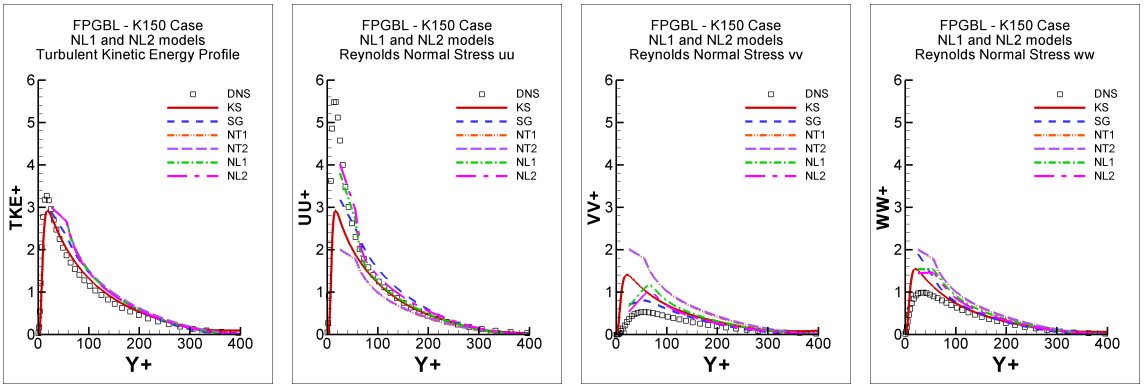

(a) k Profile (b) $\overline{u^2}$ Profile (c) $\overline{v^2}$ Profile (d) $\overline{w^2}$ Profile

Figure 7.25: Performance of the NL1 and NL2 models compared with the results provided by the KS, SG, NT1 and NT2 models in the $K150$ favourable pressure gradient boundary layer case. Models as in Table 3.25.

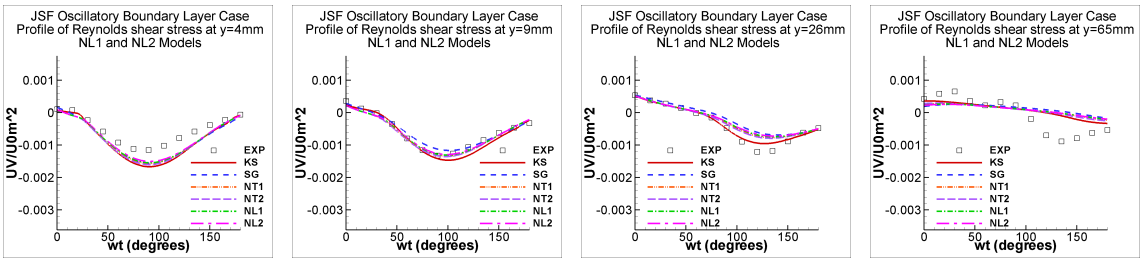

(a) $y = 4mm$ (b) $y = 9mm$ (c) $y = 26mm$ (d) $y = 25mm$

Figure 7.26: Prediction of the Reynolds shear stress at four positions in the y direction by the NL1 and NL2 models compared with the results provided by the KS, SG, NT1 and NT2 models in the JSF oscillatory boundary layer case. Models as in Table 3.25.

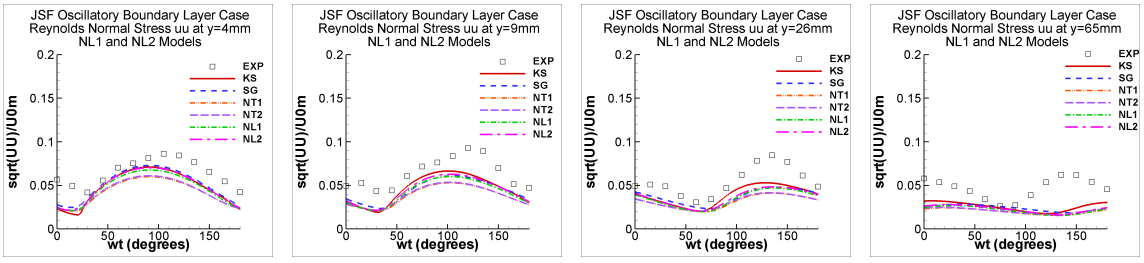

(a) $y = 4mm$ (b) $y = 9mm$ (c) $y = 26mm$ (d) $y = 25mm$

Figure 7.27: Prediction of the normalized rms of the streamwise fluctuating velocity $< u^2 >^{1/2}$ at four positions in the y direction by the NL1 and NL2 models compared with the results provided by the KS, SG, NT1 and NT2 models in the JSF oscillatory boundary layer case. Models as in Table 3.25.

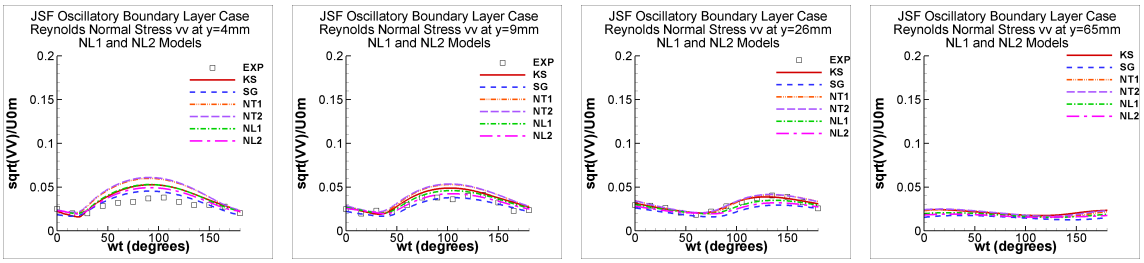

(a) $y = 4mm$ (b) $y = 9mm$ (c) $y = 26mm$ (d) $y = 25mm$

Figure 7.28: Prediction of the normalized rms of the wall-normal fluctuating velocity $< v^2 >^{1/2}$ at four positions in the y direction by the NL1 and NL2 models compared with the results provided by the KS, SG, NT1 and NT2 models in the JSF oscillatory boundary layer case. Models as in Table 3.25.

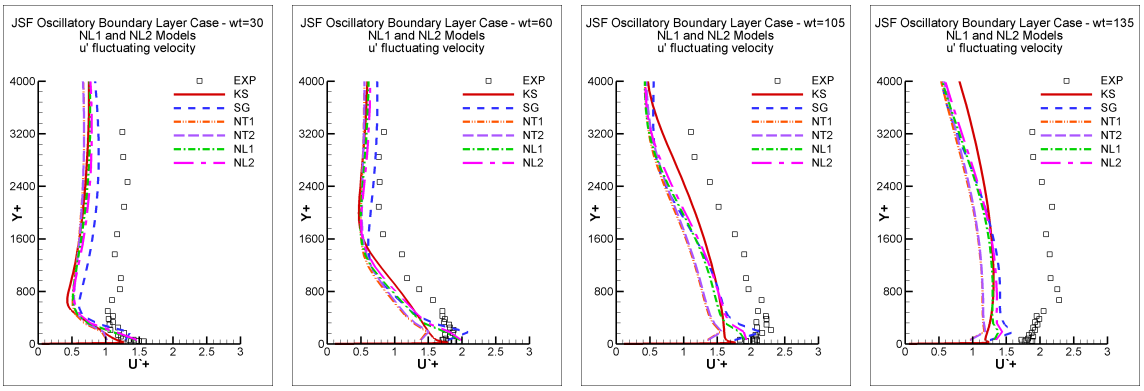

(a) $\omega t = 30^o$ (b) $\omega t = 60^o$ (c) $\omega t = 105^o$ (d) $\omega t = 135^o$

Figure 7.29: Prediction of the rms fluctuating velocity u' by the NL1 and NL2 models compared with the results provided by the KS, SG, NT1 and NT2 models in the oscillatory boundary layer case JSF. Models as in Table 3.25.

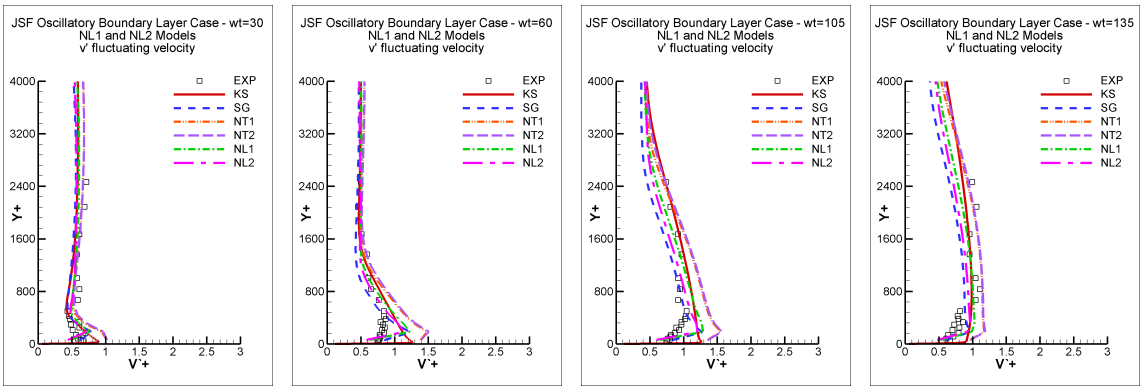

(a) $\omega t = 30^o$ (b) $\omega t = 60^o$ (c) $\omega t = 105^o$ (d) $\omega t = 135^o$

Figure 7.30: Prediction of the rms fluctuating velocity v' by the NL1 and NL2 models compared with the results provided by the KS, SG, NT1 and NT2 models in the oscillatory boundary layer case JSF. Models as in Table 3.25.

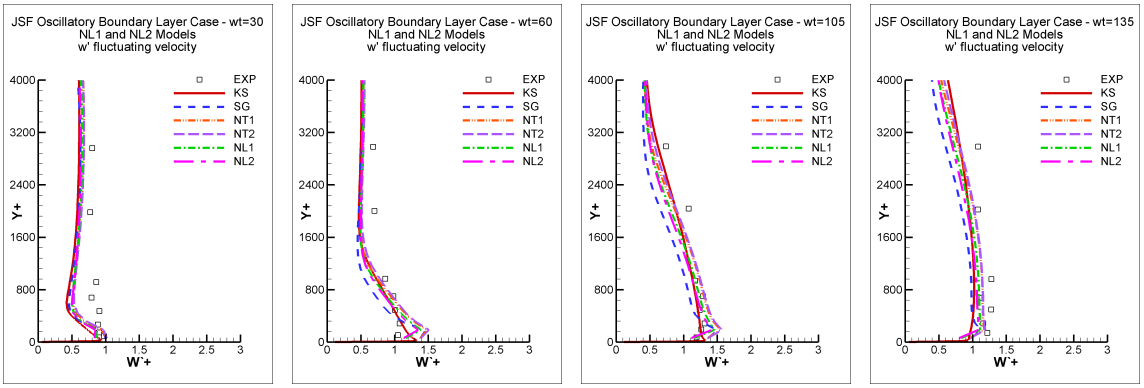

(a) $\omega t = 30^o$ (b) $\omega t = 60^o$ (c) $\omega t = 105^o$ (d) $\omega t = 135^o$

Figure 7.31: Prediction of the rms fluctuating velocity w' by the NL1 and NL2 models compared with the results provided by the KS, SG, NT1 and NT2 models in the oscillatory boundary layer case JSF. Models as in Table 3.25.

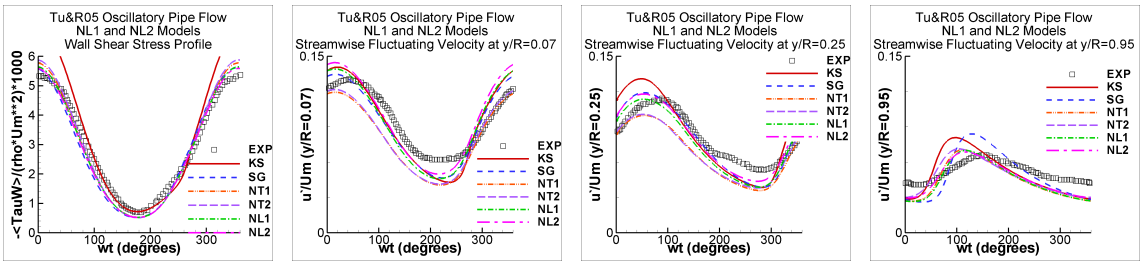

(a) wall shear stress (b) u'/U_m at y/R=0.07 (c) u'/U_m at y/R=0.25 (d) u'/U_m at y/R=0.95

Figure 7.32: Prediction of the wall shear stress and rms fluctuating velocity u' normalized with time-averaged bulk velocity at three radial positions throughout the cycle by the NL1 and NL2 models compared with the results provided by the KS, SG, NT1 and NT2 models in the $Tu\&R05$ oscillatory pipe flow case of Tu and Ramaprian (1983a). Models as in Table 3.25.

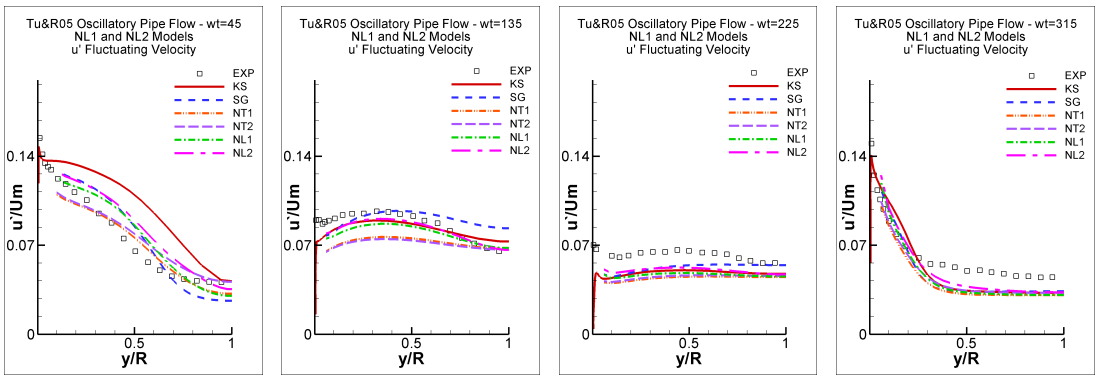

(a) $\omega t = 45^o$ (b) $\omega t = 135^o$ (c) $\omega t = 225^o$ (d) $\omega t = 315^o$

Figure 7.33: Prediction of the rms fluctuating velocity u' normalized with the time-averaged bulk velocity by the NL1 and NL2 models compared with the results provided by the KS, SG, NT1 and NT2 models in the oscillatory pipe flow case $Tu\&R05$. Models as in Table 3.25.

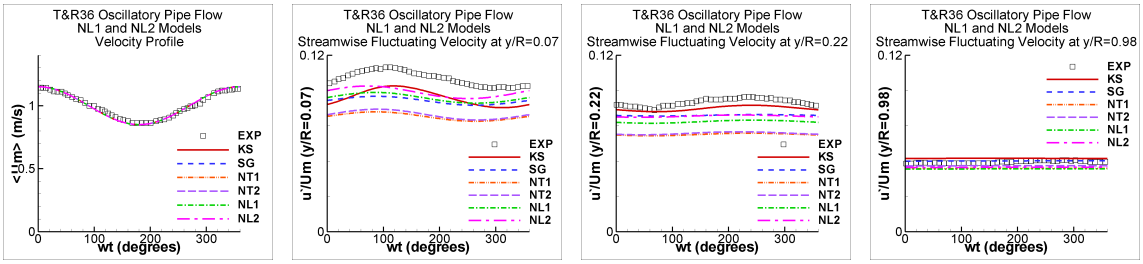

(a) wall shear stress (b) u'/U_m at y/R=0.07 (c) u'/U_m at y/R=0.22 (d) u'/U_m at y/R=0.98

Figure 7.34: Prediction of the wall shear stress and rms fluctuating velocity u' normalized with the time-averaged bulk velocity at three radial positions throughout the cycle by the NL1 and NL2 models compared with the results provided by the KS, SG, NT1 and NT2 models in the $Tu\&R36$ oscillatory pipe flow case of Tu and Ramaprian (1983a). Models as in Table 3.25.

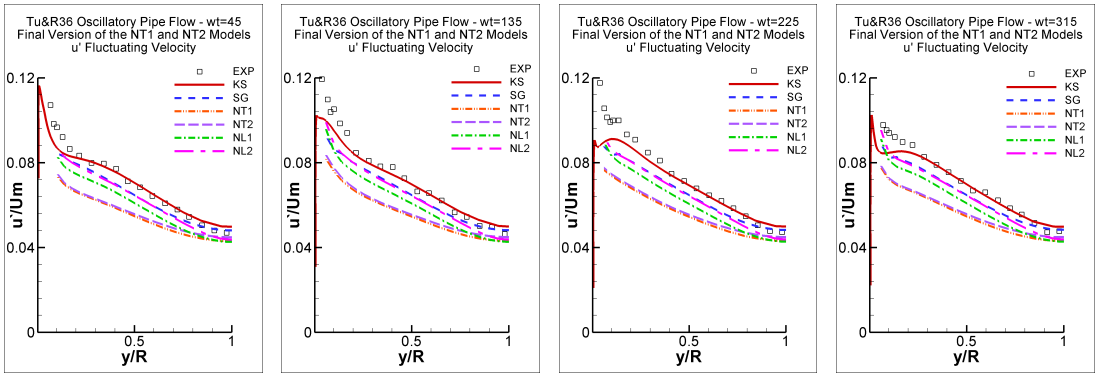

(a) $\omega t = 45^o$ (b) $\omega t = 135^o$ (c) $\omega t = 225^o$ (d) $\omega t = 315^o$

Figure 7.35: Prediction of the rms fluctuating velocity u' normalized with the time-averaged bulk velocity by the NL1 and NL2 models compared with the results provided by the KS, SG, NT1 and NT2 models in the oscillatory pipe flow case $Tu\&R36$. Models as in Table 3.25.

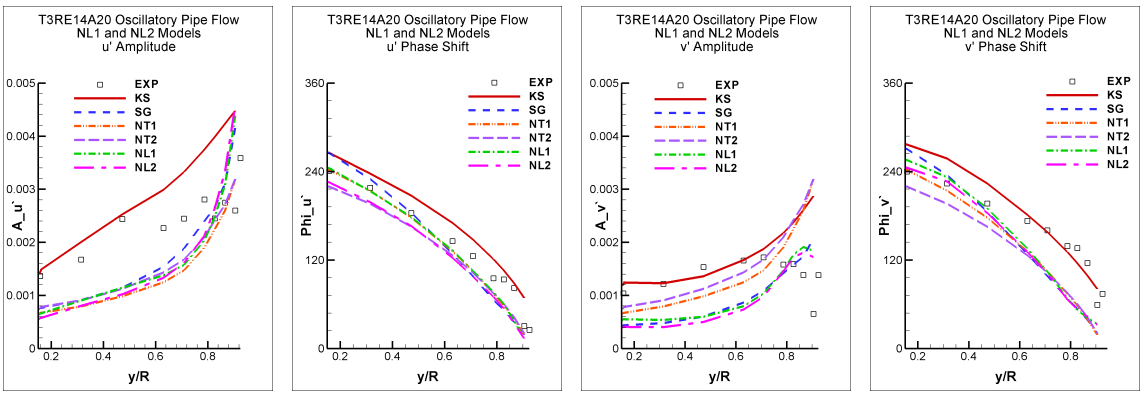

(a) u' Amplitude (b) u' Phase Shift (c) v' Amplitude (d) v' Phase Shift

Figure 7.36: Performance of the NL1 and NL2 models compared with the results provided by the KS, SG, NT1 and NT2 models in the oscillatory pipe flow case $T3RE14A20$. Models as in Table 3.25.

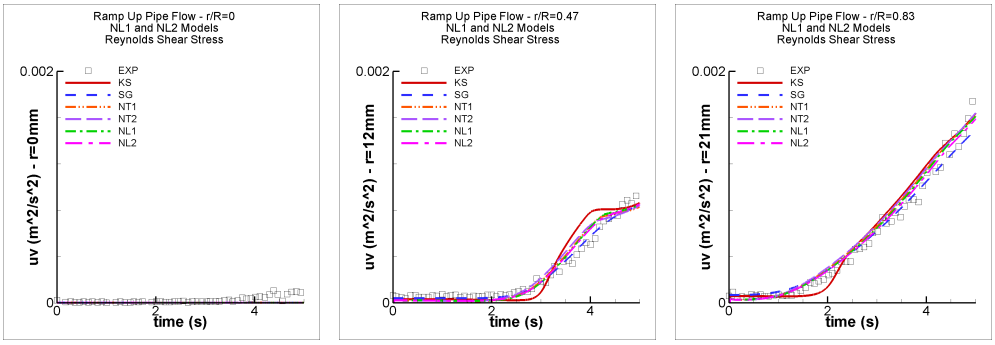

(a) Pipe centre ($r/R = 0$) (b) $r/R = 0.47$ (c) $r/R = 0.83$

Figure 7.37: Prediction of the Reynolds shear stress at selected radial positions by the NL1 and NL2 models compared with the results provided by the KS, SG, NT1 and NT2 models in the ramp up pipe flow. Models as in Table 3.25.

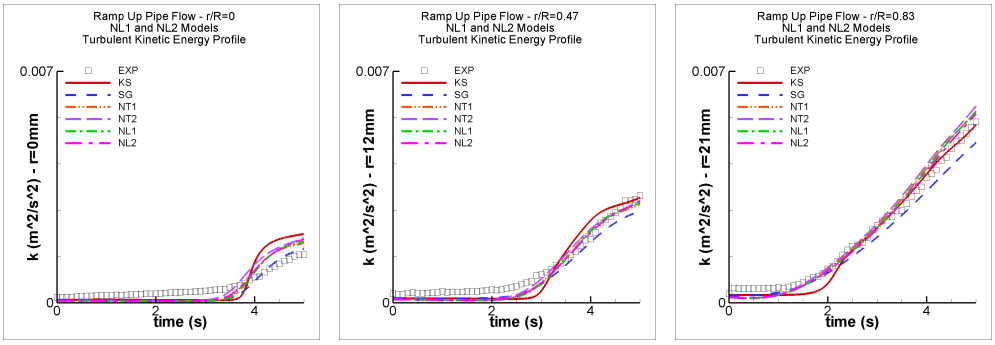

(a) Pipe centre ($r/R = 0$) (b) $r/R = 0.47$ (c) $r/R = 0.83$

Figure 7.38: Prediction of the turbulent kinetic energy at selected radial positions by the NL1 and NL2 models compared with the results provided by the KS, SG, NT1 and NT2 models in the ramp up pipe flow. Models as in Table 3.25.

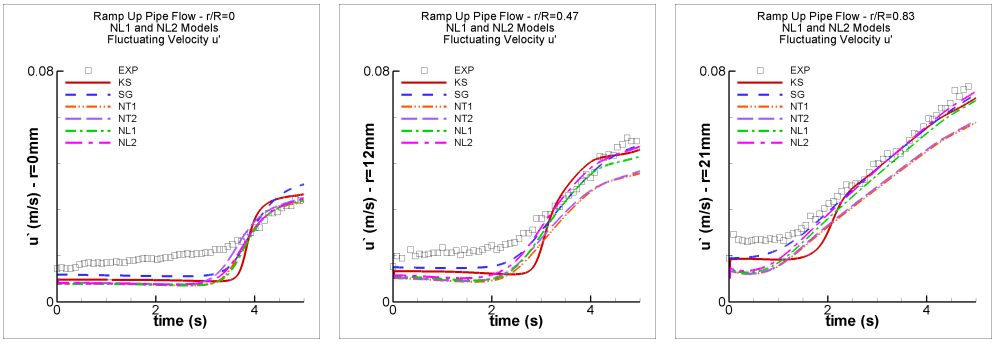

(a) Pipe centre ($r/R = 0$) (b) $r/R = 0.47$ (c) $r/R = 0.83$

Figure 7.39: Prediction of the rms fluctuating velocity u' at selected radial positions by the NL1 and NL2 models compared with the results provided by the KS, SG, NT1 and NT2 models in the ramp up pipe flow. Models as in Table 3.25.

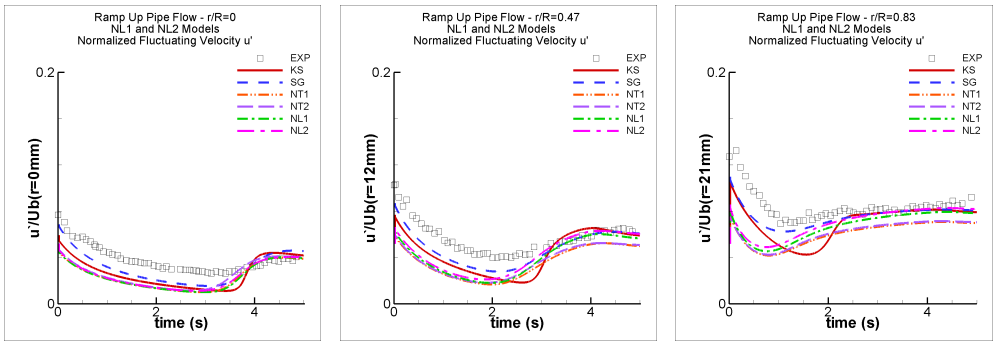

(a) Pipe centre ($r/R = 0$) (b) $r/R = 0.47$ (c) $r/R = 0.83$

Figure 7.40: Prediction of the u' normalized by the bulk velocity at selected radial positions by the NL1 and NL2 models compared with the results provided by the KS, SG, NT1 and NT2 models in the ramp up pipe flow. Models as in Table 3.25.

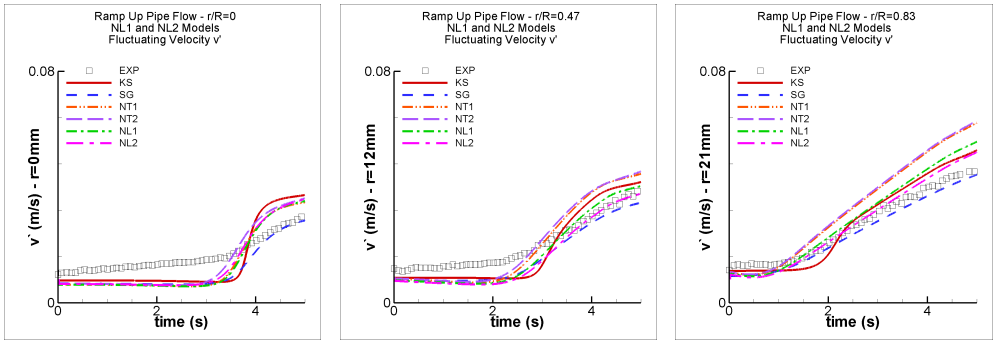

(a) Pipe centre ($r/R = 0$) (b) $r/R = 0.47$ (c) $r/R = 0.83$

Figure 7.41: Prediction of the rms fluctuating velocity v' at selected radial positions by the NL1 and NL2 models compared with the results provided by the KS, SG, NT1 and NT2 models in the ramp up pipe flow. Models as in Table 3.25.

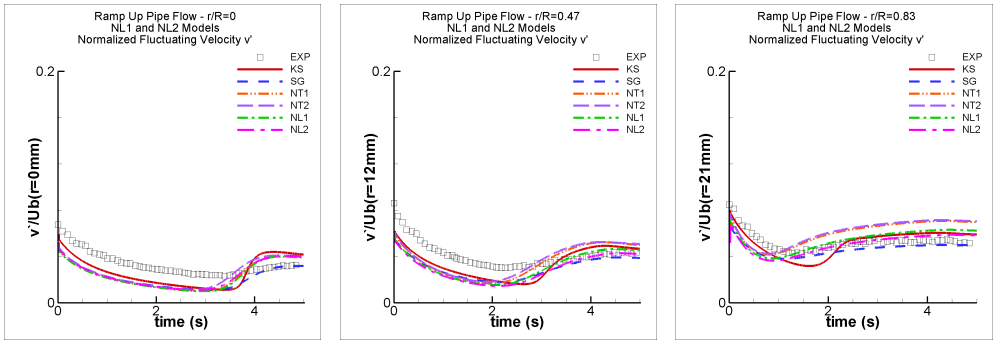

(a) Pipe centre ($r/R = 0$) (b) $r/R = 0.47$ (c) $r/R = 0.83$

Figure 7.42: Prediction of the v' normalized by the bulk velocity at selected radial positions by the NL1 and NL2 models compared with the results provided by the KS, SG, NT1 and NT2 models in the ramp up pipe flow. Models as in Table 3.25.

7.5 Further Investigations in the NL1 and NL2 Models

The predictions provided by the NL1 and NL2 models of the reattachment point in the steady and unsteady backward facing step cases have indicated that similar adjustments in the MTS NLEV models as those done in the NT1 and NT2 models might be necessary. As the NL1 and NL2 models performed very similarly to the second version of the NT1 and NT2 models, the first attempt was to try the same extra terms in C_{P1} for the NL1 and NL2 models. So the three backward facing step cases were run with the NL1 model using C_{P1} as in Table 6.23 (f_{BL}, f_1 and f_2 given by equations 6.90, 6.91 and 6.92) and with the NL2 model using C_{P1} as in Table 6.30 (f_{BL}, f_1 and f_2 given by equations 6.108, 6.109 and 6.110).

In the steady state backward facing step cases, these tests succeeded and both the NL1 and NL2 models predicted the reattachment point as 7.9, a significant improvement compared to the results presented in Table 7.8. However, in the unsteady cases, some instability problems were encountered in both NL1 and NL2 models. By reducing the under-relaxation factors (using 0.25 for the velocity and turbulent quantities and using 0.15 for the pressure correction) it was possible to get a fully converged and periodic solution for the NL1 model, which then predicted a reattachment length of 6.2 in the low frequency $BFS-St0275$ case. Whilst this is less than in the unforced case, it does not show as large a reduction as in the measurements (nor as large as was achieved with the final NT1 version). With the modified NL2 model a fully periodic state was not achieved, and so further results with this are not shown.

In order to try reducing further the predicted reattachment length in the forced case with the NL1 model, the coefficient f_2 (equation 6.92) was increased from 20 to 30. However, this only resulted in a small further decrease of reattachment length to 6.0, and so simply increasing this coefficient does not sufficiently reduce the reattachment length in the low frequency case. Moreover, in the high frequency $BFS-St1$ case, the predicted reattachment length using the larger f_2 coefficient was around $x/H = 7.2$, which is rather low compared to the experimental data.

As Test 26 in Table 6.22 indicated some positive results in the NT1 model, it was decided to try the NL1 model with an expression for f_2 such as $f_2 = 15 \max\left[\frac{k_P}{k_T} \max\left(\frac{\varepsilon_P}{\varepsilon_T} - 1.1, 0\right) SW, 0\right]$ within C_{P2} instead. In this case, f_{BL} included only f_1 as in equation 6.74. However, not much difference in behaviour was encountered: the predicted reattachment point for the $BFS-St0275$ case was 5.8 and for the $BFS-St1$ was 7.1. Increases in the f_2 coefficient from 15 to 20 and 25 were also tried, however no fully periodic result was achieved.

A number of further tests were also tried for the NL2 model, by varying the coefficient in f_2 and by trying f_2 as in the NL1 model, however none of these tests managed to provide a periodic state result. It was then decided to go back to the $NL2-T-P$ formulation of the NL2 model, presented in Table 7.1, in order to check if stability could be achieved with this scheme and with C_{P1} as in Table 6.30 (f_{BL}, f_1 and f_2 given by equations 6.108, 6.109 and 6.110), however this test also failed and could not provide a fully periodic result.

Finally, in order to identify which of the f_1 or f_2 terms were causing the instabilities, it was decided to run the three backward facing step cases with only the f_1 term included,

since this is the term responsible for adjusting the reattachment point in the steady state case. So the NL1 model was run with C_{P1} as in Table 6.23, but with f_{BL} and f_1 given by equations 6.74 and 6.75 respectively, and the NL2 model was run using C_{P1} as in Table 6.30, but with f_{BL} and f_1 given by equations 6.95 and 6.96 respectively. Using under-relaxation factors of 0.25 for velocity and turbulent quantities and 0.15 for the pressure correction, the NL1 model converged and provided a fully periodic result. However, the NL2 model, again failed to provide a fully periodic result. It was decided to try again the $NL2-T-P$ formulation of the NL2 model, presented in Table 7.1, but again using only f_1, that is, with C_{P1} as in Table 6.30 with f_{BL} and f_1 given by equations 6.95 and 6.96 respectively. This case converged and provided a fully periodic result. After some further small adjustments to the f_1 term coefficients the predicted reattachment points returned by these tests with the NL1 and NL2-T-P models are given in Table 7.9, together with the exact forms used for f_1.

Table 7.9: Reattachment point predicted by the NL1 and NL2 models in the BFS cases.

Model/Experiment	f_1	St=0	St=0.275	St=1
Experiment	-	7.8	5.0	8.1
NL1	$2\left(\frac{k_P}{k_T}-1\right)\min\left(\frac{P_k}{\varepsilon_T}-1.9,0\right)\max\left(\frac{\varepsilon_P}{\varepsilon_T}-1,0\right)$	7.74	7.64	8.66
NL2-T-P	$6\left(\frac{k_P}{k_T}-1\right)\min\left(\frac{P_k}{\varepsilon_T}-1.9,0\right)\max\left(\frac{\varepsilon_P}{\varepsilon_T}-1,0\right)$	7.78	8.33	8.96

A positive feature of the results in Table 7.9 is that they provide good predictions for the steady state and high frequency $BFS-St1$ cases, actually very similar to those provided by Test 3 in Table 6.16 for the NT1 model and Test 3 in Table 6.25 for the NT2 model. This further suggests that the f_2 term is at least a contributor to the stability problems noted above, and it seems that further work could be done on finding a form that could improve predictions of the non-linear schemes in the $BFS-St0275$ case.

As commented on before, all test cases were also simulated with the $NL2-T-P$ formulation of the NL2 model, presented in Table 7.1 and the difference in prediction from the adopted NL2 model, that is, the $NL2-P-P$ formulation in Table 7.1, were minimal.

7.6 Concluding Remarks

The two two-time-scale non-linear-eddy-viscosity models so far developed performed well in all test cases discussed in Chapter 5, with the exception of the unsteady backward facing step flow, where some further improvements are needed in the low frequency case.

The predictions of the normal stresses provided by the NL1 and NL2 models are comparable to those of the KS and SG models in most cases, although these improvements did not significantly affect other predictions in most cases which were shear dominated. The cases where improvements were clearly noticed were the normally strained flows where the NL1 and NL2 predictions of k returned the closest results to the experiments.

The NL1 and NL2 models can thus be considered to have provided very satisfactory results and one could expect that in flows where the Reynolds normal stresses play a role these models would improve predictions when compared to their linear counterpart.

Chapter 8

Conclusions and Future Work

In this chapter, the main conclusions about the work carried out and described in the other chapters of this thesis will be presented. The chapter is divided into three main sections: the performance of the existing turbulence models, the performance of the developed two-time-scale linear-eddy-viscosity models and the performance of the developed two-time-scale non-linear-eddy-viscosity models. The last section will finally discuss proposals for further advancement of the present work.

The next sections thus show that the present work carried out an extensive investigation of different classes of turbulence models by testing them in a wide variety of non-equilibrium flows and developed successful multiple-time-scale models which over a wide range of test cases demonstrate their superiority and consistency, by either matching or improving the best predictions of the existing models.

8.1 Conclusions About the Existing Turbulence Models

Thirteen existing turbulence models have been used to simulate all test cases presented in Chapter 5. By comparing their performance in each of these test cases a number of conclusions have been reached, which are now presented.

All turbulence models perform well in fully developed channel flows and zero pressure gradient boundary layers and that is expected since the coefficients of all these models were determined with reference to fully developed flows.

In homogeneous shear flows, which are shear dominated, the RST models performed clearly better. The KS non-linear-eddy-viscosity model also performed well, because of the sensitivity of c_μ in the turbulent viscosity expression to the dimensionless shear η, rather than its capacity to return anisotropic Reynolds stresses.

The adverse pressure gradient boundary layer cases were best predicted by the FM and WM models, both ω based models which were developed to provide accurate prediction in such flows, specially with regard to the velocity profile which changes significantly as the freestream pressure is increased. None of the other models were able to follow these subtle changes in the velocity profiles. Apart from the velocity profile, the turbulence kinetic energy

levels are also not well captured by any of the turbulence models, specially where the pressure gradient increases sharply. The Reynolds shear stress is reasonably well captured, specially by the RST models and some KC MTS LEV models. Despite the mentioned drawbacks, overall all turbulence models can be considered to perform reasonably well.

The favourable pressure gradient boundary layer cases, which reach a self-similar state, were best predicted by the KS model. This turbulence model, together with the LS model are the only ones expected to correctly predict the laminarization process since they are the only ones which possess an E term (which accounts for the second derivative of the mean velocities. Besides that, the usage of an equation for $\tilde{\varepsilon}$, which goes to zero at the wall and provides an exact expression for ε at the wall, shows how underpredicted is the turbulent kinetic energy growth rate at the wall, implying the underprediction of ε itself. Despite that, the NG MTS LEV model also performed very well which might indicate the importance of LRN approaches in these accelerating flows.

The normally strained flow cases were also clearly better predicted by the NLEV and RST models. In these cases, the anisotropy of the Reynolds normal stresses clearly plays a role. The LEV models could only be expected to perform well in predicting the turbulent kinetic energy in the pure strain cases, however even in these cases, they fail to provide as good predictions as the other models.

The oscillatory boundary layer case was similarly predicted by all models as far as the velocity and Reynolds shear stress variations are concerned. The streamwise Reynolds normal stress tended to be underpredicted by all models, including the RST ones and the other normal stresses were well predicted by all models. This case did not represent a challenging case and anisotropy did not seem to play an important role.

In the oscillatory pipe flow cases studied, the influence of the forcing frequency was confirmed in affecting the turbulence. The low frequency case, where the turbulence behaved as in a series of steady states, all models performed similarly, not matching the velocity and turbulent profiles in every single cycle position. In the high frequency case, frozen turbulence was predicted by all models, apart from very close to the wall, whereas experiments have not shown such high level of frozen turbulence. In the intermediate frequency cases the amplitude and phase shift of the velocity and turbulent quantities were reasonably well predicted by all models, the MTS models showing perhaps some improvements. It has been observed that apparently the use of wall functions could be distorting the predictions, since the Reynolds number of these flows was not very high.

In the fully developed ramp up pipe flows, it has been observed that the models were either able to predict the profile of the turbulent quantities at the centre of the pipe or at the mid distance between the centre and the wall. None of the models managed to provide profiles which would match the experiments at both positions. Most importantly though, most models predicted correctly the time delay for the turbulent quantities to build up after the acceleration of the bulk velocity.

Finally, in the backward facing step cases, the turbulence models have shown an inability to be sensitive enough to the forcing frequency as far as the prediction of the reattachment

point is concerned. Besides that, it was confirmed that all models, to some extent, recover rather slowly the post-reattachment channel flow profile. The LS and FM models best predicted these flows and that again makes one wonder the influence of LRN approaches in these flows. Again, the anisotropy of the Reynolds normal stresses did not prove to play an important role in these backward facing step cases which are also shear dominated flows.

Generally speaking about the numerical stability of the models, the HJ, KS, TC, TS and WM models proved to be the less stable ones. The HJ, TC and WM models also tended to provide not well behaved profiles of the Reynolds normal stresses in some flows. The KS model showed instability problems in only the unsteady backward facing step flows. That was associated with its LRN approach which became too sensitive to the rapid changes in the eddy dissipation profile at the step height where the grid was still quite refined, but there was no longer a wall. The TS model was identified as unstable in some cases such as homogeneous high shear flows and unsteady backward facing step flows and that was associated with its extra source term in the ε_P equation.

Among the single-time-scale linear-eddy-viscosity models, the standard $k-\varepsilon$ model proved to behave generally well, either in its HRN form (HR model) or LRN form (LS model). The FM model also performed reasonable well in most flows. These turbulence models are the simplest models tested and still provided reasonable results for most flows. They particularly failed in the homogeneous shear and normally strained flows.

The single-time-scale non-linear-eddy-viscosity models performed well in most flows, however proved to be unstable in the unsteady backward facing step cases. It was noticed that the strain-rate-dependent c_μ was an important feature in homogeneous shear flows.

Among the Reynolds-stress-transport models, the SG and GL models proved to be the best models, although they were used together with wall functions. The HJ and WM did not converge in the backward facing step cases and the TC model proved to be a much more complex RST scheme which did not bring clear advantages in prediction in the cases here tested.

Among the multiple-time-scale linear eddy viscosity models, the KC and NG models were shown to approach asymptotic states of homogeneous shear flows and equilibrium boundary layers, however their predicted ratios for the partition variables in these asymptotic states were rather questionable. The CG and TS models were shown not to completely approach these asymptotic states and that would make them perform badly in some flows, but to improve prediction in some other flows.

That concludes the analysis of the performance of the existing turbulence models which were assessed in this work. None of these models, from the simplest to the most complex ones, performed consistently well in all test cases studied thus indicating the need of a model which provides consistent good results in a wide range of non-equilibrium flows.

8.2 Conclusions About the MTS LEV Models Developed

Two two-time-scale linear-eddy-viscosity models have been developed in this work and referred to as NT1 and NT2 models. Their essential difference is the different time scales used in their eddy viscosity expression: $\nu_t = c_\mu \frac{k k_P}{\varepsilon_P}$ for the NT1 model and $\nu_t = c_\mu \frac{k^2}{\varepsilon_T}$ for the NT2 model.

Indeed, a study about the possible time-scales to be used in the turbulent viscosity has been carried out and the ones used in the NT1 and NT2 models have been shown to be the most appropriate ones.

The coefficients of the models have been determined by requiring the resulting predictions to approach the asymptotic analyses of decaying grid turbulence, homogeneous shear flows and local equilibrium boundary layers. The different expressions for the turbulent viscosity thus implied different transport equations for the energy transfer rate ε_P and for the eddy dissipation rate ε_T. As a consequence, the final forms of these models are quite different from the TS model (Hanjalic et al., 1980) which is the model used as a base for their development.

The extra source term in the ε_P equation in the TS model, followed by the C'_{P1} coefficient and which has been identified to cause instabilities in some flows, has been found to be unnecessary in the NT1 scheme, but essential in the NT2 scheme for the improvement of predictions of homogeneous shear flows. In order to avoid stability problems in the NT2 model, the C'_{P1} coefficient was assigned a much lower value than that used in the TS model.

A study of the turbulent kinetic energy spectrum has also been carried out and it was identified that one would expect the two-time-scale models to split the spectrum within the inertial subrange which was then confirmed to be the case in the NT1 and NT2 models.

The eddy viscosity coefficient, c_μ, was sensitized to the dimensionless mean strain rates which is unusual in linear-eddy-viscosity models, but which proved to be essential for the correct prediction of homogeneous shear flows.

An important conclusion on turbulence modelling practice was reached regarding the coefficients ensemble. It was noticed that if the resulting solutions approached the asymptotic states in homogeneous shear flows and equilibrium boundary layer, the models would need extra source terms to adjust to strongly non-equilibrium flows. That implied extra terms which do not affect the asymptotic states studied should be included in order to improve prediction, for instance, of the backward facing step flows.

Extra terms to be included into the C_{P1} coefficient in both NT1 and NT2 models were determined to make them sensitive to the different forcing frequencies in the backward facing step cases. These terms were designed not to affect shear dominated flows and therefore they did not disturb the prediction in the other test cases. The C_{P1} coefficient was identified as the most appropriate coefficient to insert these extra terms.

Another important turbulence modelling conclusion, also reached from this work is the potential of multiple-time-scale models in improving prediction of non-equilibrium flows. The main reason for this, besides solving transport equations for each of the partition variables, is the availability of terms related to the spectral behaviour, such as $\frac{k_P}{k_T}$ and $\frac{\varepsilon_P}{\varepsilon_T}$, which cannot

be employed by single-time-scale models.

The main achievements of the NT1 and NT2 two-time-scale linear-eddy-viscosity models developed here are that they perform well in all test cases, being the models which best perfomed in the wide range of dimensionless shear values of homogeneous shear flows, the only linear-eddy-viscosity models which predicted well the turbulent kinetic energy in the normally strained cases and the only models which showed enough sensitivity in predicting correctly the reattachment point in the pulsated backward facing step cases with different forcing frequencies.

So it can be said that the developed NT1 and NT2 models are two rather simple models which performed either as well as or even better than the existing single and multiple-time-scale models, many of them being of much more complex formulations, thus emerging as promising models for future use in non-equilibrium flows.

8.3 Conclusions About the MTS NLEV Models Developed

The NL1 and NL2 two-time-scale non-linear-eddy-viscosity models have been developed in an attempt to investigate the influence of better predicting the Reynolds normal stresses. They were based on the NT1 and NT2 two-time-scale linear-eddy-viscosity models respectively and on the KS single-time-scale non-linear-eddy-viscosity model.

As noted above, since most of the test cases performed in this work are shear dominated flows, it was found that in such flows, the non-linear-eddy-viscosity schemes improve prediction of the Reynolds normal stresses, but do not improve significantly the prediction of mean velocity, Reynolds shear stress and turbulent kinetic energy. That is expected though, since in shear dominated flows only the Reynolds shear stress plays a role in the turbulent kinetic energy production term.

In the normally strained flows, where Reynolds normal stresses are influential in the generation rate of turbulence, P_k, the developed NL1 and NL2 models predicted best the turbulent kinetic energy in the pure strained cases.

The prediction of the Reynolds normal stresses provided by the NL1 and NL2 models are comparable to those provided by the KS single-time-scale non-linear-eddy-viscosity model and the single-time-scale Reynolds-stress-transport models tested, which suggests that these models are suitable for future use in flows with complex strain fields where the normal stresses play a role.

In the homogeneous high shear cases the NL1 and NL2 models provided non realizable solutions as one of the normal stresses became negative and therefore further refinement of the non-linear stress-strain relationship is needed.

Further adjustments in the NL1 and NL2 models are also required in order to improve prediction of unsteady backward facing step cases. The terms introduced in C_{P1} in the NT1 and NT2 models have been identified to cause instability problems in the NL1 and NL2 models and therefore that should become the focus of future work.

8.4 Future Work

In order to continue this work, the two-time-scale linear-eddy-viscosity NT1 and NT2 models developed should be assessed in other non-equilibrium flows so that one can further assess and validate their performance. Flows such as those through diffusers under steady and unsteady conditions, 3-D backward facing step flows, flows through square ducts and curved ducts and impinging flows, are examples of flows which can be simulated to evaluate the performance of the new models.

It would also be interesting to continue to compare the performance of the final versions of the NT1 and NT2 models and their second versions in order to assess the effects of the extra terms inserted into the C_{P1} coefficient. These terms have been designed to have little or no effect in equilibrium flows, but their effect in flows where $\frac{k_P}{k_T}$, $\frac{\varepsilon_P}{\varepsilon_T}$ and $\frac{P_k}{\varepsilon_T}$ reach values far from equilibrium were only assessed in the pulsated backward facing step cases.

With regard to the two-time-scale non-linear-eddy-viscosity models, NL1 and NL2, two most urgent investigations are needed: one to ensure realizable predictions in homogeneous high shear cases and the other in order to improve prediction of the unsteady backward facing step cases. Evaluation of the profiles of the $\frac{k_P}{k_T}$, $\frac{\varepsilon_P}{\varepsilon_T}$, $\frac{P_k}{\varepsilon_T}$ and of the Reynolds stresses is needed in order to better understand the reason for the instability problems and to identify the most appropriate terms to be included into one of the models' transport equations coefficients. Further testing of these MTS NLEV models is also needed in other flows such as those mentioned above to assess both performance and numerical stability.

As noted in many of the test cases, low-Reynolds-number approaches might improve the prediction of turbulent flows which do not present a high enough Reynolds number. The study of LRN schemes to be included in two-time-scale models is also another possible and worthy objective. As noted in the backward facing step cases, LRN approaches might lead to numerical instabilities. This feature must also be studied and an approach using the isotropic part of ε_T, similarly to the LS and KS models, is also a possible tool to be explored.

Although non-linear-eddy-viscosity models improve prediction of the Reynolds normal stresses, they still present inherent limitations such as those observed in the normally strained flows when the straining was either deactivated or had its sign changed. Within the RANS framework, Reynolds stress transport models could be expected to improve the predictions of these flows because, as they solve transport equations for the stresses, sudden changes in the strain field are felt by the stress generation terms (as opposed to EV models where only the turbulent kinetic energy production rate, P_k, is considered) and so some lag is naturally built into how the stresses themselves behave. Further improvements in the RST models might also be achievable by introducing multi-scale modelling ideas into them, to account for changes in the spectral shape of not only the turbulent kinetic energy, but of the individual stresses. However, a similar approach as taken in this work (splitting each stress into large and intermediate scale regions and solving transport equations for both and all transfer rates) would result in a rather large set of equations. In order to apply multiple-time-scale approaches into RST models for practical cases, it thus seems more sensible to propose

transport equations for the Reynolds stresses contributions associated with the large scales of motion and employ a simpler algebraic form - such as an eddy-viscosity representation - for the intermediate/small scale contributions. This approach could be justified by arguing that the smaller scales are likely to be more isotropic than the large scales. The eddy viscosity used for the small scale contributions could thus be based on k_T and ε_T, and ε_T could be solved for similarly as presented in this work. With regard to the energy transfer rate between the large and the intermediate/small scales, individually solved ε_P transfer rates for each of the stresses would not be recommended due again to the large number of equations needed. So a single ε_P equation could be solved, and a model developed for the contribution of this to each stress component. In this case, the often adopted isotropic dissipation representation in stress transport models ($\varepsilon_{ij} = \frac{2}{3}\varepsilon\delta_{ij}$) should not, of course, be carried over and used for this process, as the energy transfer from large to intermediate scales is very unlikely to be isotropic. According to the Kolmogorov spectrum discussed in Chapter 6, the intermediate/small scales where local isotropy can be considered are contained in the equilibrium range which comprises the inertial subrange and the dissipation range. Therefore, in order to support the above assumptions in MTS RST models, one should bear in mind that the ratio $\frac{k_P}{k_T}$ should be placed within the inertial subrange as already discussed. Another modelling advantage offered by MTS models is the availability of terms related to the spectral behaviour, such as $\frac{k_P}{k_T}$ and $\frac{\varepsilon_P}{\varepsilon_T}$, which could be used, for example, to sensitize redistribution and other processes to the spectral shape. This is the next logical step through which the experience gained in this study could be directed towards the refinement of second-moment closures. It will be interesting to explore how this could be exploited within the second-moment modelling framework.

Multiple-time-scale approaches can also be extended to turbulent convective heat transfer applications. The most straightforward way of doing that is by exploring different time scales in the eddy diffusivity, similarly to what was done with the eddy viscosity in this work. Spectral relations could also be studied in order to enhance prediction of turbulent heat fluxes.

The future work proposals outlined above thus indicate that the present work has developed successful modelling strategies and has opened several other research branches which might help the development of widely applicable turbulence models.

Bibliography

H. Abe, H. Kawamura, and Y. Matsuo. Surface heat-flux fluctuations in a turbulent channel flow up to Re-tau=1020 with Pr=0.025 and 0.71. *Int. J. Heat and Fluid Flow*, 25:404–419, 2004.

S. F. Al-Sharif. Personal communication, 2007.

B. S. Baldwin and T. J. Barth. A one-equation turbulence transport model for high Reynolds number wall-bounded flows. *NASA TM-102847*, 1990.

B. S. Baldwin and H. Lomax. Thin-layer approximation and algebraic model for separated turbulent flows. *AIAA Paper*, 78:257.

G. Binder, S. Tardu, and P. Vezin. Cyclic modulation od Reynolds stresses and length scales in pulsed turbulent channel flow. *Proc. R. Soc. Lond. A*, 451:121–139, 1995.

P. Bradshaw and H. Ferriss, D. Applications of a general method of calculating turbulent shear layers. *J. Basic Eng., Trans. ASME, Series D*, 94:345, 1973.

P. Bradshaw and H. andd Atwell N. P. Ferriss, D. Calculation of boundary layer development using the turbulent energy equation. *J. Fluid Mech.*, 28:593–616, 1967.

G. J. Brereton, W. C. Reynolds, and R. Jayaraman. Response of a turbulent boundary layer to sinusoidal free-stream unsteadiness. *J . Fluid Mech.*, 221:131–159, 1990.

A. Cadiou, K. Hanjalic, and K. Stawiarski. A two-scale second-moment turbulence closure based on weighted spectrum integration. *Theoret. Comput. Fluid Dynamics*, 18:1–26, 2004.

T. Cebeci and A. M. O. Smith. Analysis of turbulent boundary layers. Academic Press, New York, 1974.

C. P. Chen and K. L. Guo. A non-isotropic multiple-scale turbulence model. *Applied Mathematics and Mechanics*, 12:981–991, 1991.

W. L. Chen. *Turbulence Modelling for Highly-Loaded Cascade Blades*. PhD thesis, University of Manchester Institute of Science and Technology, 1996.

T. S. Cheng and W. J. Yang. Numerical simulation of three-dimensional turbulent separated and reattaching flows using a modified turbulence model. *Computers & Fluids*, 37:194–206, 2008.

C. C. Chieng and B. E. Launder. On the calculation of turbulent heat transport downstream from an abrupt pipe expansion. *Numerical Heat Transfer, Part A: Applications*, 3:189–207, 1980.

K. B. Chun and H. J. Sung. Control of turbulent separated flow over a backward-facing step by local forcing. *Experiments in Fluids*, 21:417–426, 1996.

D. E. Coles. The turbulent boundary layer in a compressible fluid. Rand. Rep. R403-PR, ARC 24473 : Appendix A : A manual of experimental practice for low-speed flow., 1962.

T. J. Craft. Developments in a low-Reynolds-number second-moment closure and its application to separating and reattachment flows. *International Journal of Heat and Fluid Flow*, 19:541–548, 1998.

T. J. Craft and B. E. Launder. A Reynolds stress closure designed for complex geometries. *Dynamics of Atmospheres and Oceans*, 23:99–114, 1996.

T. J. Craft, N. Z. Ince, and B. E. Launder. Recent developments in second-moment closure for buoyancy-affected flows. *Dynamics of Atmospheres and Oceans*, 23:99–114, 1996a.

T. J. Craft, B. E. Launder, and K. Suga. Development and application of a cubic eddy-viscosity model of turbulence. *International Journal of Heat and Fluid Flow*, 17(2):108–115, 1996b.

T. J. Craft, B. E. Launder, and K. Suga. Prediction of turbulent transitional phenomena with a nonlinear eddy-viscosity model. *International Journal of Heat and Fluid Flow*, 18 (1):15–28, 1997.

T. J. Craft, H. Iacovides, and J. H. Yoon. Progress in the use of non-linear two-equation models in the computation of convective heat-transfer in impinging and separated flows. *Flow, Turbulence and Combustion*, 63:59–80, 1999.

T.J. Craft, L.J.W. Graham, and B.E. Launder. Impinging jet studies for turbulence model assessmentii. an examination of the performance of four turbulence models. *International Journal of Heat and Mass Transfer*, 36:2685 – 2697, 1993.

B. J. Daly and F. H. Harlow. Transport equations in turbulence. *Phys. Fluids*, 13:2634–2649, 1970.

M. T. Deevy. *Development and validation of low-Reynolds-number turbulence models for flows with complex strains.* PhD thesis, University of Manchester. School of Mechanical, Aerospace and Manufacturing Engineering, 2004.

E.R. van Driest. On turbulent ow near a wall. *J. Aero. Sci.*, 23:1007–1011, 1956.

B. S. Duncan, W. W. Liou, and T. H. Shih. A multiple-scale turbulence model for incompressible flow. NASA Technical Memorandum 106113, 1993.

P.A. Durbin. Near-wall turbulence closure modelling without "damping functions". *Theoret. Comput. Fluid Dynamics*, 3:1–13, 1991.

J. H. Ferziger and M. Peric. *Computational methods for fluid dynamics*. Springer, Berlin ; London, 2002.

R. Friedrich, T. J. Httl, M. Manhart, and C. Wagner. Direct numerical simulation of incompressible turbulent flows. *Computers & Fluids*, 30(5):555–579, 2001.

S. Gant. *Development and Application of a New Wall Function for Complex Turbulent Flows*. PhD thesis, University of Manchester Institute of Science and Technology, 2002.

T. B. Gatski and C. G. Speziale. On explicit algebraic stress models for complex turbulent flows. *Journal of Fluid Mechanics*, 254:59–78, 1993.

T. B. Gatski, M. Y. Hussaini, and J. L. Lumley, editors. *Simulation and Modeling of Turbulent Flows*. Oxford University Press, New York;Oxford, 1996.

J. N. Gence and J. Mathieu. On the application of successive plane strains to grid-generated turbulence. *J. Fluid Mech.*, 93:501–513, 1979.

M. M. Gibson and B. E. Launder. Ground effects on pressure fluctuations in the atmospheric boundary layer. *J. Fluid Mech.*, 86:491–511, 1978.

M.M. Gibson and B. E. Launder. On the calculation of horizontal, turbulent, free shear flows under gravitational influence. *Trans. A.S.M.E., J. Heat Transfer C*, 98:81–87, 1976.

U. Goldberg and D. Apsley. A wall-distance-free low Re k -ε turbulence model. *Computer Methods in Applied Mechanics and Engineering*, 145(3-4):227–238, 1997.

K. Hanjalic and S. Jakirlic. A model of stress dissipation in second-moment closures. *Applied Scientific Research*, 51:513–518, 1993.

K. Hanjalic and B. E. Launder. A Reynolds stress model of turbulence and its application to thin shear flows. *Journal of Fluid Mechanics*, 52:609–638, 1972.

K. Hanjalic, B. E. Launder, and R. Schiestel. Multiple-time-scale concepts in turbulent transport modelling. July 2-4 1980.

K. Hanjalic, S. Jakirlic, and I. Hadzic. Expanding the limits of "equilibrium" second-moment turbulence closures. *Fluid Dynamics Research*, 20:25–41, 1997.

S. He and J. D. Jackson. A study of turbulence under conditions of transient flow in a pipe. *J . Fluid Mech.*, 408:1–38, 2000.

S. He and J. D. Jackson. An experimental study of pulsating turbulent flow in a pipe. *European Journal of Mechanics B/Fluids*, 28:309320, 2009.

J. O. Hinze. *Turbulence*. McGraw-Hill, New York; London (etc.), 2nd edition, 1976.

H. Iacovides and M. Raisee. Computation of flow and heat transfer in 2d rib roughened passages. In K. Hanjalic and T. Peeters, editors, *Proceedings of the Second International Symposium on Turbulence, Heat and Mass Transfer*, pages Addendum 21–30, Delft, 1997. Delft University Press.

F. G. Jacobitz, S. Sarkar, and C. W. van Atta. Direct numerical simulations of the turbulence evolution in a uniformly sheared and stably stratifed flow. *J. Fluid Mech.*, 342:231–261, 1997.

B. L. Jensen, B. M. Sumer, and J. Fredsoe. Turbulent oscillatory boundary layers at high Reynolds numbers. *J. Fluid Mech.*, 206:265–297, 1989.

D. A. Johnson and L. S. King. Mathematically simple turbulence closure model for attached and separated turbulent boundary layers. *AIAA Journal*, 23:1684–1692, 1985.

W . P. Jones and B. E. Launder. Some properties of sink-flow turbulent boundary layers. *J. Fluid Mech*, 56:347–351, 1972a.

W . P. Jones and B. E. Launder. The prediction of laminarization with a two-equation model of turbulence. *Int. J. Heat Mass Transfer.*, 15:301–314, 1972b.

W. P. Jones and B. E. Launder. The calculation of low-Reynolds-number phenomena with a two-equation model of turbulence. *International Journal of Heat and Mass Transfer*, 16 (6):1119–1130, 1973.

N. Kasagi and A. Matsunaga. Turbulence measurement in a separated and reattaching flow over a backward-facing step with the aid of three-dimensional particle tracking velocimetry. *Journal of Wind Engineering and Industrial Aerodynamics*, 46 & 47:821–829, 1993.

J. Kim, P. Moin, and R. Moser. Turbulence statistics in fully developed channel flow at low Reynolds number. *J. Fluid Mech*, 177, 1987.

S. W. Kim. Calculation of divergent channel flows with a multiple-time-scale turbulence model. *AIAA Journal*, 29:547–554, 1991.

S. W. Kim and T. J. Benson. Calculation of a circular jet in crossflow with a multiple-time-scale turbulence model. *International Journal of Heat and Mass Transfer*, 35(10): 2357–2365, 1992.

S. W. Kim and C. P. Chen. A multiple-time-scale turbulence model based on variable partitioning of the turbulent kinetic energy spectrum. *Numerical Heat Transfer*, 16:193–211, 1989.

B. Launder and N. Sandham. *Closure Strategies for Turbulent and Transitional Flows*. Cambridge University Press, United Kingdom, 2002.

B. E. Launder and K. Hanjalic. Contribution towards a Reynolds-stress closure for low-Reynolds-number turbulence. *J . Fluid Mech.*, 74:593–610, 1976.

B. E. Launder and B. I. Sharma. Application of the energy-dissipation model of turbulence to the calculation of flow near a spinning disc. *Letters in Heat and Mass Transfer*, 1:131–138, 1974.

B. E. Launder and D. B. Spalding. The numerical computation of turbulent flows. *Computer Methods in Applied Mechanics and Engineering*, 3(2):269–289, 1974.

B. E. Launder, G. J. Reece, and W. Rodi. Progress in the development of a Reynolds-stress turbulence closure. *Journal of Fluid Mechanics*, 68:537–566, 1975.

B. E. Launder, W. C. Reynolds, and W. Rodi. *Turbulence models and their applications; Modeles de turbulence et leurs applications*, volume 2 of *Collection de la Direction des Etudes et Recherches d'Electricite de France*. Editions Eyrolles, Paris, 1984.

M. J. Lee, J. Kim, and P. Moin. Structure of turbulence at high shear rate. *J. Fluid Mech*, 216:561–583, 1990.

F. S. Lien and M. A. Leschziner. A pressure-velocity solution strategy for compressible flow and its application to shock/boundary-layer interaction using second-moment turbulence closure,. *ASME J. Fluids Engrg*, 115:717, 1993.

F. S. Lien and M. A. Leschziner. A general non-orthogonal collocated finite volume algorithm for turbulent flow at all speeds incorporating second-moment turbulence-transport closure, part 1: Computational implementation. *Computer Methods in Applied Mechanics and Engineering*, 114:123–148, 1994a.

F. S. Lien and M. A. Leschziner. Upstream monotonic interpolation for scalar transport with application to complex turbulent flows. *Int. J . for Numerical Method in Fluids*, 19:527548, 1994b.

F. S. Lien and M. A. Leschziner. Assessment of turbulence-transport models including non-linear rng eddy-viscosity formulation and second-moment closure for flow over a backward-facing step. *Computers Fluids*, 23:983–1004, 1994c.

M. Manna and A. Vacca. Spectral dynamic of pulsating turbulent pipe flow. *Computers & Fluids*, 37:825–835, 2008.

Z. H. Mao and T. J. Hanratty. Studies of the wall shear stress in a turbulent pulsating pipe flow. *J. Fluid Mech.*, 170:545–564, 1986.

I. Marusic and A. E. Perry. A wall-wake model for the turbulence structure of boundary layers. part 2. further experimental support. *J. Fluid Mech*, 298:389–407, 1995.

J. Mathieu and J. Scott. *An Introduction to Turbulent Flow*. Topics in applied physics. Cambridge University Press, 2000.

A. Matsumoto, Y. Nagano, and T. Tsuji. Direct numerical simulation of homogeneous turbulent shear flow. 5th Symposium on Computational Fluid Dynamics, Tokyo, 1991.

G. L. Mellor and H. J. Herring. A survey of the mean turbulent field closure models. *AIAA Journal*, 11, 1973.

A. N. Menendez and B. R. Ramaprian. Prediction of periodic boundary layers. *INTERNATIONAL JOURNAL FOR NUMERICAL METHODS IN FLUIDS*, 4:781–800, 1984.

F. R. Menter. Two-equation eddy-viscosity turbulence models for engineering applications. *AIAA Journal*, 32:1598–1605, 1994.

P. Moin and K. Mahesh. Direct numerical simulation: A tool in turbulence research. *Annual Review of Fluid Mechanics*, 30:539–578, 1998.

P. Momeni. *Modelling the effect of pulsation on flow and heat transfer in turbulent separated and reattaching flows*. PhD thesis, University of Manchester. School of Mechanical, Aerospace and Civil Engineering, 2008.

N. A. Mostafa. *Computational Fluid Dynamics Modelling of Three-Dimensional Jet Impingement Cooling On Concave Surfaces*. PhD thesis, University of Manchester, 2007.

Y. Nagano, M. Kondoh, and M. Shimada. Multiple time-scale turbulence model for wall and homogeneous shear flows based on direct numerical simulations. *International Journal of Heat and Fluid Flow*, 18(4):346–359, 1997.

T. Nomura, Y. Takahashi, T. Ishima, and T. Obokata. Analysis on flow around a rectangular cube by means of LDA, PIV and the numerical simulation by PCC method-in the case of inclined cube. In *11th international symposium on application of laser techniques to fluid mechanics*, Lisbon, Portugal, 2002.

L. H. Norris and W. C. Reynolds. Turbulent channel flow with a moving wavy boundary. Report No. FM- 10, Stanford University, Mechanical Engineering Department, USA, 1975.

T. S. Park and H.J. Sung. A nonlinear low-Reynolds-number $k - \varepsilon$ model for turbulent separated and reattaching flows - i. flow field computations. *Int. J. Heat Mass Transfer*, 38:2657–2666, 1995.

S. V. Patankar and D. B. Spalding. A calculation procedure for heat, mass and momentum transfer in three-dimensional parabolic flows. *Int. J. Heat Mass Transfer*, 15:1787–1806, 1972.

S. B. Pope. A more general effective-viscosity hypothesis. *Journal of Fluid Mechanics*, 72: 331–340, 1975.

S. B. Pope. *Turbulent Flows*. Cambridge University Press, 2000.

L. Prandtl. Uber die ausgebildete turbulenz. *ZAMM*, 5:136–139, 1925.

S.H. Ra, P.K. Chang, and S.O. Park. Measurement of the forward-flow fraction using a split film sensor. *Experiments in Fluids*, 10:57–59, 1990.

M .M. Rahman and T. Siikonen. Near-wall turbulence modelling with enhanced dissipation. *International Journal for Numerical Methods in Fluids*, 42:979997, 2003.

M. M. Rahman and T. Siikonen. Low Reynolds number k-e model for near-wall flow. *International Journal for Numerical Methods in Fluids*, 47(4):325–338, 2005. 10.1002/fld.809.

O. Reynolds. An experimental investigation of the circumstances which determine whether the motion of water in parallel channels shall be direct or sinuous and of the law of resistance in parallel channels. *Philos. Trans. R. Soc.*, 174:935982, 1883.

W. Rodi. *Turbulence models and their application in hydraulics : a state-of-the-art.* A.A.Balkema, Rotterdam, 3rd edition, 1993.

W. Rodi and N. N. Mansour. Low Reynolds number k-e modelling with the aid of direct simulation data. *Journal of Fluid Mechanics*, 250:509–529, 1993.

M. M. Rogers and P. Moin. The structure of the vorticity field in homogeneous turbulent flows. *J. Fluid Mech*, 176:33–66, 1987.

J. Rotta. Statistische theorie nichthomogener turbulenz. *Z. Phys.*, 129:547–572, 1951.

R. Rubinstein. Formulation of a two-scale model of turbulence. ICASE Report No. 2000-5, 2000.

R. Rubinstein and J. M. Barton. Nonlinear Reynolds stress models and the renormalization group. *Physics of Fluids A*, 2(8):1472–1476, 1990.

H. Sakamoto and H. Haniu. A study on wortex shedding from spheres in a uniform flow. *Journal of Fluids Engineering*, 112:386–392, 1990.

A. E. Samuel and P. N. Joubert. A boundary layer developing in an increasingly adverse pressure gradient. *J. Fluid Mech*, 66:481–505, 1974.

A. Scotti and U. Piomelli. Numerical simulation of pulsating turbulent channel flow. *PHYSICS OF FLUIDS*, 13:1367–1384, 2001.

L. Shemer, I. Wygnanski, and E. Kit. Pulsating flow in a pipe. *J . Fluid Mech.*, 153:313–337, 1985.

C. C. Shir. A preliminary numerical study of atmospheric turbulent flows in the idealized planetary boundary layer. *J. Atmos. Sci.*, 30:1327–1339, 1973.

R. L. Simpson. Aspects of turbulent boundary-layer separation. *Prog. Aerospace Sci.*, 32: 457–521, 1996.

J. Smagorinsky. General circulation experiments with the primitive equations. *Mon. Wheather Review*, 91:99–165, 1963.

R. W. Smith. *Effect of Reynolds Number on the Structure of Turbulent Boundary Layers*. PhD thesis, Department of Mechanical and Aerospace Engineering, Princeton University, 1994.

I. J. Sobey. Oscillatory flows at intermediate strouhal number in asymmetric channels. *J . Fluid Mech.*, 125:359–373, 1982.

P. R. Spalart. Numerical study of sink-flow boundary layers. *J. Fluid Mech*, 172:307–328, 1986.

P. R. Spalart and S. R. Allmaras. A one-equation turbulence model for aerodynamic flows. *AIAA Paper*, 92:439, 1992.

P.R. Spalart. Direct simulation of a turbulent boundary layer up to r=1410. *J. Fluid Mech*, 187, 1988.

C. G. Speziale. On nonlinear k-l and k-ε models of turbulence. *J. Fluid Mech.*, 178:459–475, 1987.

C. G. Speziale. Analytical methods for the development of Reynolds-stress closures in turbulence. *Annual Review of Fluid Mechanics*, 23(1):107–157, 1991.

C. G. Speziale. A review of Reynolds stress models for turbulent shear flows, research supported by the national aeronautics and space administration under nasa contract. NASA Langley Research Center, Hampton, 1995.

C. G. Speziale, S. Sarkar, and T. B. Gatski. Modelling the pressure-strain correlation of turbulence: an invariant dynamical systems approach. *J. Fluid Mech.*, 227:245–272, 1991.

K. Stawiarski and K. Hanjalic. A two-scale second-moment one-point turbulence closure. In *Engineering Turbulence Modelling and Experiments - 5*, Mallorca, Spain, 2002.

K. Stawiarski and K. Hanjalic. On physical constraints for multi-scale turbulence closure models. *Progress in Computational Fluid Dynamics*, 5:120–135, 2005.

S. F. Tardu, G. Binder, and R. F. Blackwelder. Turbulent channel flow with large-amplitude velocity oscillations. *J. Fluid Mech.*, 267:109–151, 1994.

D. B. Taulbee. An improved algebraic Reynolds stress model and corresponding nonlinear stress model. *Physics of Fluids A*, 4:2555–2561, 1992.

H. Tennekes and J.L. Lumley. *A First Course in Turbulence*. The MIT Press, 1972.

A. A. Townsend. The uniform distortion of homogeneous turbulence. *Quart. J. Mech. Appl. Math.*, 7:104–127, 1954.

S. W. Tu and B. R. Ramaprian. Fully developed periodic turbulent pipe flow. part 1. main experimental results and comparison with predictions. *J. Fluid Mech.*, 137:31–58, 1983a.

S. W. Tu and B. R. Ramaprian. Fully developed periodic turbulent pipe flow. part 2. the detailed structure of the flow. *J. Fluid Mech.*, 137:59–81, 1983b.

H. J. Tucker and A. J. Reynolds. The distortion of turbulence by irrotational plane strain. *J . Fluid Mech.*, 32:657–673, 1968.

H. K. Versteeg and W. Malalasekera. *An introduction to computational fluid dynamics : the finite volume method*. Longman, Harlow, 1995.

D. C. Wilcox. Reassessment of the scale-determining equation for advanced turbulence models. *AIAA Journal*, 26:1299–1310, 1988a.

D. C. Wilcox. Multiscale model for turbulent flows. *AIAA Journal*, 26:1311–1320, 1988b.

D. C. Wilcox. Progress in hypersonic turbulence modeling. *AIAA Paper*, 1785, 1991.

V. Yakhot and S. A. Orszag. Renormalization group analysis of turbulence. i. basic theory. *Journal of Scientific Computing*, 1:3–51, 1986.

C. J. Yap. *Turbulent Heat and Momentum Transfer in Recirculating and Impinging Flows*. PhD thesis, Faculty of Technology, University of Manchester, United Kingdom, 1987.

S. Yoshioka, S. Obi, and S. Masuda. Turbulence statistics of periodically perturbed separated flow over backward-facing step. *International Journal of Heat and Fluid Flow*, 22:393–401, 2001.